Dissertation zur Erlangung des Doktorgrades
der Fakultät Chemie und Pharmazie
der Ludwig-Maximilians-Universität München

Spin Caloric Transport and Related Phenomena from First Principles

Sebastian Wimmer

aus

München, Deutschland

2018

Erklärung

Diese Dissertation wurde im Sinne von § 7 der Promotionsordnung vom 28. November 2011 von Herrn Prof. Dr. H. Ebert betreut.

Eidesstattliche Versicherung

Diese Dissertation wurde eigenständig und ohne unerlaubte Hilfe erarbeitet.

München, den 17.07.2018

Sebastian Wimmer

Dissertation eingereicht am	17.07.2018
1. Gutachter:	Prof. Dr. H. Ebert
2. Gutachter:	Prof. Dr. C. Heiliger
Mündliche Prüfung am	23.11.2018

"Being a PhD student is like being a prisoner of war: Your first duty is to escape."[1]

Balázs László Győrffy (1938 – 2012)

[1] I heard, but I did not (want to) understand...

Abstract

The present dissertation gives an account of a first-principles description of linear response phenomena in the field of spin caloric transport or spincaloritronics and closely related areas of condensed matter physics and materials science. Embedded into the priority program SPP 1538 "Spin Caloric Transport (SpinCaT)" of the DFG, the major aim was the development and application of computational methods suitable for a parameter-free determination of material specific response coefficients in metals and alloys. The underlying band structure method, the Korringa-Kohn-Rostoker multiple scattering framework, provides an ideal basis for an accurate and versatile representation of the systems under study in terms of the single-electron Green function. Most importantly, this quantity serves as the fundamental variable in Kubo's linear response formalism that is employed for the calculation of charge and spin conductivities as well as related electric-field-induced response coefficients. Using and extending an approach to temperature-induced phenomena based on the energy dependence of the electrical conductivity put forward by Mott, the diffusion contribution to thermoelectric and spincaloritronic response properties can be assessed. Making furthermore use of an efficient description of substitutional as well as thermally-induced disorder by means of the coherent potential approximation and the closely-related alloy analogy model for finite-temperature effects, a reliable description of charge-, heat-, and spin-related transport properties of dilute as well as concentrated alloys under realistic conditions can be achieved. The methodology just outlined has been applied to various thermoelectric and spincaloritronic phenomena such as the Seebeck effect and its magnetic anisotropy, the anomalous and spin Nernst effects as well as to the corresponding electric-field-induced material properties: anisotropic magnetoresistance, anomalous and spin Hall conductivity. In addition so-called spinorbitronic responses have been studied, namely the spin-orbit torque and the Edelstein or inverse spin-galvanic effect. Accompanying space-time symmetry considerations on the transformation properties of the respective operator-operator correlation functions in terms of the Kubo formula allowed the model-independent determination of symmetry-restricted response tensor shapes for direct and inverse effects, based on the crystallographic and magnetic structure. The predictions of the occurrence and relation of tensor elements were verified numerically by first-principles calculations in collinear, non-collinear as well as non-coplanar magnetic configurations, providing in addition reliable estimates of their magnitude.

Kurzzusammenfassung

Die vorliegende Arbeit erstattet Bericht über eine *ab initio*-Beschreibung linearer Antwortphänomene im Feld des spinkalorischen Transports oder der Spinkaloritronik und eng verwandter Bereiche der Festkörperphysik und Materialwissenschaften. Eingebettet in das Schwerpunktprogramm SPP 1538 „Spin Caloric Transport (SpinCaT)“ der DFG, war das Hauptanliegen die Entwicklung und Anwendung rechnergestützter Verfahren zur parameterfreien Bestimmung materialspezifischer Antwortgrößen von Metallen und Legierungen. Das zugrundeliegende Bandstrukturverfahren, die Korringa-Kohn-Rostoker-Vielfachstreumethode, stellt eine ideale Basis für die akkurate und vielseitige Darstellung der zu beschreibenden Systeme durch ihre Ein-Elektronen-Greensche Funktion dar. Insbesondere dient diese Größe als fundamentale Variable in Kubos linearem Antwortformalismus, der zur Berechnung elektrischer und spinpolarisierter Leitfähigkeiten sowie verwandter, ebenfalls durch ein elektrisches Feld hervorgerufene Prozesse beschreibende, Koeffizienten verwendet wird. Durch Anwendung und Erweiterung eines auf Mott zurückgehenden Ansatzes zur Beschreibung thermisch induzierter Phänomene mittels der Energieabängigkeit der elektrischen Leitfähigkeit, kann der diffusive Anteil thermoelektrischer und spinkaloritronischer Antwortgrößen ermittelt werden. Des Weiteren kann unter Verwendung einer effizienten Beschreibung substitutioneller sowie thermisch induzierter Unordnung mittels der sogenannten *Coherent Potential Approximation* und des nahe verwandten *Alloy Analogy Model* für endliche Temperaturen eine verlässliche Beschreibung von Ladungs-, Wärme- und Spintransporteigenschaften in sowohl verdünnten als auch konzentrierten Legierungen unter realistischen Bedingungen erreicht werden. Die soeben vorgestellte Methodik wurde auf eine Reihe thermoelektrischer und spinkaloritronischer Phänomene wie den Seebeck-Effekt und seine magnetische Anisotropie, den Anomalen und den Spin-Nernst-Effekt angewendet, sowie auf die entsprechenden elektrisch induzierten Materialeigenschaften, den anisotropen Magnetwiderstand, die anomale und die Spin-Hall-Leitfähigkeit. Zusätzlich wurden sogenannte spinorbitronische Antwortprozesse untersucht, namentlich der *Spin Orbit Torque* und der Edelstein- oder inverse spingalvanische Effekt. Begleitende Überlegungen zur Raum-Zeit-Symmetrie der zugrundeliegenden Operator-Operator-Korrelationsfunktionen, ausgedrückt durch die Kubo-Formel, erlaubten eine modellunabängige Bestimmung der symmetriekonformen Tensorstruktur für die direkten und inversen Effekte auf Basis der kristallographischen und magnetischen Struktur. Die Vorhersagen zum Auftreten von Tensorelementen und ihrer Beziehung wurden nummerisch durch *ab initio*-Berechnungen in kollinearen, nichtkollinearen, sowie nichtkoplanaren Anordnungen magnetischer Momente verifiziert. Gleichzeitig konnten hierdurch belastbare Aussagen über ihre Größe gemacht werden.

Contents

Chapter 1

Introduction

The relatively new area of condensed matter physics termed *Spin Caloritronics* [1] is, as the portmanteau of *spintronics*[1] and the Latin *calor* (heat) suggests, dealing with the coupling of spin, charge, and energy or heat transport on the micro- to nanometre scale. This sub-field emerged from the connection of thermoelectrics, which is concerned with the coupling of charge and heat currents, to the field of spintronics, where the intrinsic spin angular momentum of the electron acts as a degree of freedom (partially) separated from its charge. Spin Caloritronics, spin caloric transport or, preferentially, spincaloritronics was probably initiated by theoretical work on non-equilibrium thermodynamics of spin, charge, and heat in layered metallic structures by Johnson and Silsbee [2], but gained considerable momentum only about two decades later with the discovery[2] of the spin Seebeck effect by Uchida *et al.* [4]. Since then a vast number of investigations have been performed, both theoretically and experimentally, to some extent [3, 5–12] but by far not exclusively [13–21] on the spin Seebeck effect. The rapidly developing field, see Ref. 22 for an early (2010) and Ref. 23 for a current (as of 2018) collection of articles, has been reviewed, e.g., by Bauer *et al.* [24] and Boona *et al.* [25]. For an overview focusing on theoretical aspects, see Ref. 26.

Bauer *et al.* [24] give a classification scheme for the various directions of research, dividing them into (i) independent electron, (ii) collective, and (iii) relativistic effects. Class (i) is closest to what was initiated by Johnson and Silsbee [2], namely the thermoelectrics of layered systems employing the concept of explicitly spin-dependent transport properties and their behaviour at interfaces [14, 16–18, 27]. This has been recently extended to superconductor-ferromagnet tunnel junctions [28–30]. In fact, the origin of the spin Seebeck effect was initially believed to be explicable on these grounds [4]. As it turned out soon after, collective excitations such as phonons and, in particular, magnons play an important, if not the most prominent, role in this [31–36] and related effects [37–40], which therefore have to be assigned to a class of their own, (ii). One might add a fourth class (iv) to this scheme, namely the thermal analogues of spin torque effects such as the spin transfer torque [41–44] and its inverse (more frequently called spin pumping [45–49] or spin-motive force [50–52]) as well as the just recently discovered spin-orbit torque [53–56] and its inverse [57, 58] (also called charge pumping). These include the thermal spin

[1] Which by itself is a contraction of *spin electronics*.

[2] Not really that of the transverse spin Seebeck effect as was originally stated [3], but it nevertheless ignited the whole field.

transfer torque [38, 59–61], thermal spin pumping [34], which can be regarded as its reciprocal, as well as the direct and inverse thermal spin-orbit torques [62, 63] which remain a theoretical conjecture to date. The same applies to the thermally-induced Edelstein effect [64] and its reciprocal, which are the thermal analogues of the Edelstein or inverse spin-galvanic effect [65, 66] and the inverse Edelstein or spin-galvanic effect [67]. The former is however believed to contribute to the so-called spin Nernst magneto-thermopower [21] employed for the detection of the spin Nernst effect [68].

The present work is almost exclusively concerned with class (iii), the thermoelectric generalisation of spin-orbit-induced response phenomena such as anisotropic magnetoresistance (AMR) [69, 70], the anomalous Hall effect (AHE) [71–75], and the spin Hall effect (SHE) [76–80]. Contact will to some extent be made nevertheless to the other classes, since there is of course a certain overlap between the three of them. Treated only *in passing*, but also part of class (iii) are the thermal Hall effect or Righi-Leduc effect [81] and the Maggi-Righi-Leduc effect [82] or thermal AMR. Corresponding quasi-particle phenomena like the phonon Hall effect [83] and the magnon Hall effect [84] belonging to class (ii) will not be considered herein.

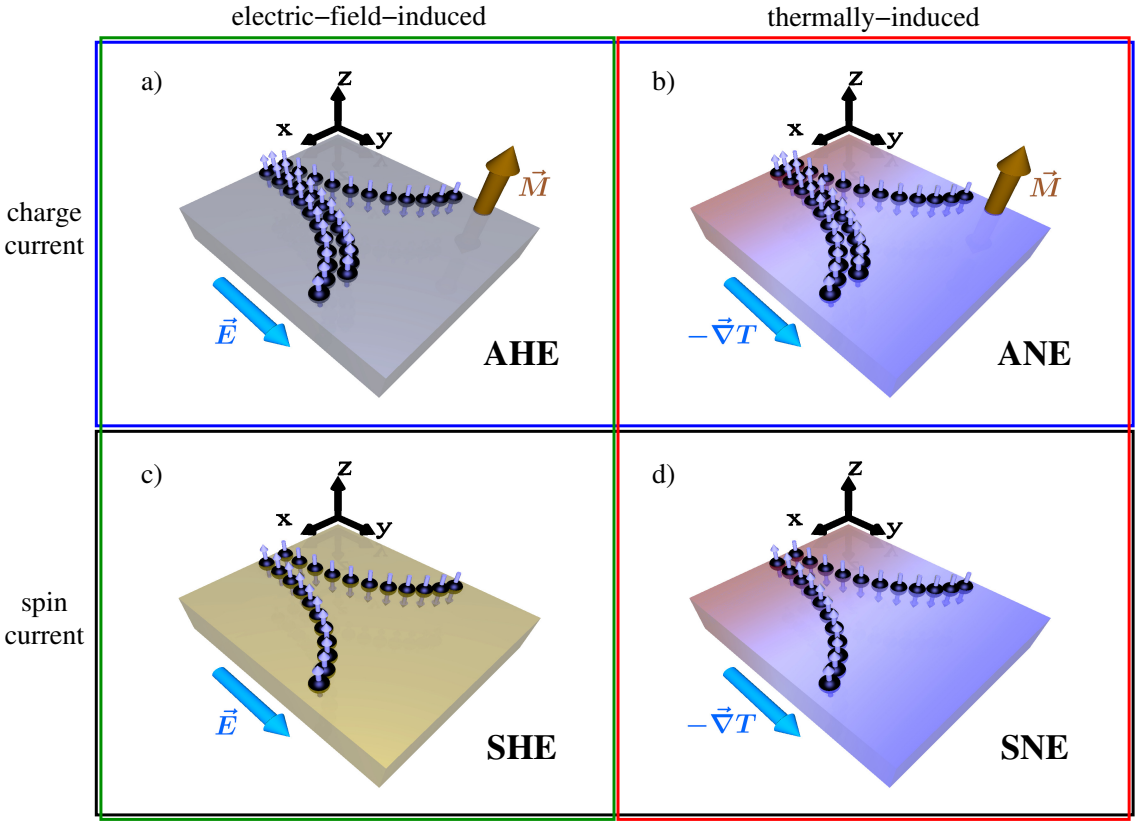

Figure 1.1: Transverse transport effects in response to electric fields (left column) and temperature gradients (right column) in the form of spin-polarised charge (top row) and pure spin currents (bottom row). From top left to bottom right, a)–d), the effects are called anomalous Hall effect (AHE), anomalous Nernst effect (ANE), spin Hall effect (SHE), and spin Nernst effect (SNE). While the former two occur only in magnetic systems, symbolised by the magnetisation $\vec{M}$, the latter two are present in non-magnetic systems as well.

To a considerable extent the present work will be concerned with transverse transport effects, where transverse means that the response (a current or a generalised flux, see Section 2.3.2.1) to an external perturbation (a field or a generalised force,

Figure 1.2: Overview of linear response phenomena within the scope of this work. Each coloured rectangle represents the response tensor associated with a correlation of two fluxes/forces depicted on the left and on top: charge- (c), heat- (q), spin (s) currents, and magnetic torque (t). The symbols L^{AB}, $\mathcal{L}^{AB}$, and $\tilde{\mathcal{L}}^{AB}$ will be used for the corresponding linear response coefficients. For each tensor the rank is given at the bottom right and the most prominent effects are named.

ibid.) is observed perpendicular to the latter. Those effects are associated with the anti-symmetric part of the corresponding response tensor and are visualised in Fig. 1.1. The anomalous Hall effect in the top left panel a) describes the occurrence of a transverse spin-polarised charge current in response to an electric field $\vec{E}$. Its thermoelectric analogue is the anomalous Nernst effect shown at the top right in panel b), here the perturbation is a temperature gradient $\vec{\nabla}T$. The pure spin currents generated by the spin Hall (bottom left, c)) and the spin Nernst effect (bottom right, d)) can occur in any magnetic as well as non-magnetic system, while AHE and ANE require, at least locally, a finite magnetisation $\vec{M}$. The ordinary Hall [71] and Nernst [85] effects observable in non-magnetic samples in an externally applied field, that can be explained in terms of the Lorentz force, will not be discussed. The focus clearly will be on phenomena induced by spin-orbit coupling which manifests itself in spin-dependent electron deflection or scattering leading to currents perpendicular to the driving force.

Figure 1.2 depicts the *zoo* of linear response phenomena that will be, to varying extents, covered in this work. The pictograms at the left and above represent the generalised fluxes and forces that will be considered herein, each rectangle corresponds to the tensor of associated response coefficients. The second rank tensor $\underline{\boldsymbol{L}}^{cc}$ at the top left is related to the electrical conductivity tensor, the galvanomagnetic phenomena of interest are the above-mentioned AMR and AHE. The tensors to

the right and below describe thermo(magneto)electric effects, the Seebeck effect [86] and its magnetic anisotropy [87] are determined by the diagonal elements of the former, their reciprocals (anisotropic) Peltier effect [82, 88, 89] are given in terms of the latter. The anomalous Nernst conductivity [85, 90] corresponds to the anti-symmetric off-diagonal elements of $\underline{\boldsymbol{L}}^{cq}$, the inverse anomalous Nernst or anomalous Ettingshausen effect [82, 85, 91] accordingly to those of $\underline{\boldsymbol{L}}^{qc}$. The thermal conductivity is associated with the tensor $\underline{\boldsymbol{L}}^{qq}$, the Maggi-Righi-Leduc effect [82] due to an anisotropy of the diagonal, in analogy to the AMR, will not be discussed, while the thermal analogue of the AHE, the Righi-Leduc effect [81] will play a minor role. Non-electronic related effects such as the phonon and magnon Hall effects are beyond the scope of this work.

The correlation between charge currents and static or dynamic spin polarisation is described by the third rank tensor $\underline{\boldsymbol{\mathcal{L}}}^{sc}$, encompassing spintronic effects such as the already mentioned spin Hall and Edelstein effects, as well as the longitudinal spin conductivity occurring in magnetic but also certain non-magnetic systems [92]. Corresponding inverse effects such as the inverse spin Hall effect [93–95], the inverse Edelstein or spin-galvanic effect already mentioned, as well as a hypothetical inverse longitudinal spin conductivity are described by the elements of the tensor $\underline{\boldsymbol{\mathcal{L}}}^{cs}$ in the first row. The thermally-induced analogues of these spintronic phenomena, i.e., spincaloritronic effects in the proper sense of the word are encoded by the tensor $\underline{\boldsymbol{\mathcal{L}}}^{sq}$. These encompass of course the spin Seebeck effect that shall however not be discussed in this work, the spin-dependent Seebeck effect (SDSE) [14, 15], which will be briefly treated,[3] the spin Nernst effect and the thermal Edelstein effect (TEE). The corresponding inverse or reciprocal effects, the spin Peltier effect [40], the spin-dependent Peltier effect [16], as well as the inverse spin Nernst or spin Ettingshausen and the inverse thermal Edelstein effects, both of which are theoretical conjectures based on space-time symmetry arguments discussed herein, are represented by $\underline{\boldsymbol{\mathcal{L}}}^{qs}$. Thermomagnetoelectric and spincaloritronic effects in layered heterostructures, i.e., the *independent electron* effects of class (i) in the scheme of Bauer *et al.* [24] will be referred to only occasionally. These include the (anisotropic) magneto-thermoelectric power (MTEP [96, 97] or AMTEP [98]), the (tunnelling) magneto-Seebeck effect in magnetic tunnel junctions (TMS) [17, 18], the tunnelling anisotropic magneto-Seebeck effect [99], and the tunnelling anisotropic spin Seebeck effect (TASS) [100], as well as their reciprocals such as the magneto-Peltier effect [101] (inverse magneto-Seebeck effect).

The fourth rank tensor $\underline{\tilde{\boldsymbol{\mathcal{L}}}}^{ss}$ describing spin-spin response phenomena will play only a minor role in this work. The magnetic torque-related effects in the rightmost column and the bottom row of Fig. 1.2 will be, except for elements of $\underline{\boldsymbol{\mathcal{L}}}^{st}$ and $\underline{\boldsymbol{\mathcal{L}}}^{ts}$, covered. Most importantly the so-called spin-orbit torque (SOT) will feature quite prominently, its inverse (ISOT) and both of their thermal analogues, TSOT and ITSOT, will only be discussed w.r.t. their symmetry properties. Finally, the torque-torque correlation described by the Gilbert damping tensor at the bottom right will be again mentioned only in passing.

An introduction to work concerned with materials properties relevant for spin transport cannot do without advertising the great potential of this field in future micro-

[3] As a bulk effect belonging to class (iii).

and nanoelectronics. To considerable extent this is already exploited, usually the giant magnetoresistance (GMR) effect is cited in this respect, but the promises a completely spin-based logic holds are by far not explored yet [102]. To the very active and, for quite some time already, application-oriented research in spintronics the field of spincaloritronics adds in particular another source for the generation of pure spin currents: heat. It is inevitably generated in all electronic devices and usually considered a parasitic effect, detrimental to their performance. Although this certainly is a very promising field of research, it has to be noted that it is still very much in its infancy. The field of spinorbitronics [103], that will also be entered herein to some extent, on the other hand has seen a remarkably fast rise from first theoretical predictions [104–106], their almost immediate experimental realisation [55, 56, 107], to application-oriented research [108].

The aim of the present dissertation is to give an account of recent activities in the first-principles description and symmetry analysis of linear response coefficients relevant to the field of spincaloritronics (and beyond), and to introduce the methods and formalisms that were employed to this end. The structure is as follows:

Chapter 2 gives a brief overview of the theoretical methods and formalisms that have been used to calculate linear response coefficients for spin, charge, and heat transport from first principles. Starting with the fundamental electronic structure method of choice, density functional theory (Section 2.1), followed by a brief introduction (Section 2.2) into the Korringa-Kohn-Rostoker multiple-scattering framework employed to obtain a representation of the ordered or disordered system under study in terms of its single-electron Green function, finally the Kubo linear response formalism will be outlined (Section 2.3), with an emphasis on its application to the description of thermoelectric and spin caloric transport. This last part of the chapter includes a brief overview on the history of the field, a comparison of alternative formulations of the relevant linear response coefficients, an extended discussion of the Mott formula for the thermopower and various generalisations of it, as well as a short introduction into a general group-theoretical approach to the space-time symmetry of linear response coefficients.

In Chapter 3 applications and extensions of the methodology just outlined will be presented, in the form of published articles and manuscripts to be submitted. In Section 3.1 the thermomagnetoelectric or thermogalvanomagnetic transport properties of ferromagnetic $Co_{1-x}Pd_x$ alloys, in particular the magnetic anisotropy of the Seebeck effect and the anomalous Nernst effect, are investigated in comparison to the corresponding galvanomagnetic phenomena anisotropic magnetoresistance and anomalous Hall effect. In addition a combined experimental and theoretical study of the electrical and thermal conductivity and the Seebeck coefficient in $Co_{1-x}Fe_x$ is presented, with an emphasis on possible non-electronic contributions. Section 3.2 then focuses on a truly spincaloritronic phenomenon, the spin Nernst effect. First, its relation to the spin Hall effect is investigated in $Cu_{1-x}Au_x$ alloys, furthermore, in another cooperation with experimentalists, its first observation via the so-called spin Nernst magneto-thermopower was supported by first principles calculations. Section 3.3 deals with the space-time symmetry of linear response phenomena within the Kubo formalism. The occurrence and interrelation of tensor elements of electrical and spin conductivity is derived in a model-independent group-theoretical framework. One of the predictions made is numerically confirmed in low-symmetric

non-magnetic systems: the occurrence of longitudinal spin-polarised currents in non-magnetic materials. In Section 3.4 a study on transverse transport and related magneto-optical properties of non-collinear antiferromagnets is presented. Additionally the occurrence of chirality-induced contributions in non-coplanar spin configurations is investigated. Section 3.5 gives an account of the work done on the spin-orbit torque and the Edelstein effect. Again this is a combination of group-theoretical considerations and supporting first-principles calculations in a non-centrosymmetric tri-layer alloy system. Results on finite-temperature transport properties will be presented in Section 3.6. A mean field description of the effect of uncorrelated lattice displacements and spin fluctuations, the so-called alloy analogy model, is applied to the temperature-dependent spin Hall effect in $Au_{1-x}Pt_x$ alloys. Once more this is a joint experimental-theoretical work. Furthermore, the behaviour of resistivity and anomalous Hall conductivity in a, at $T = 0\,\mathrm{K}$, compensated ferrimagnetic Heusler alloy is studied as a function of temperature.

In the Appendices A.1-A.4 remarks on the phenomenological transport equations of Kubo *et al.* [109] (Appendix A.1), supporting information and materials on the first-principles description of thermoelectric and spincaloritronic response phenomena (Appendix A.2), a concise comparison of spin-projected and -polarised formulations (Appendix A.3), and additional notes on space-time symmetry considerations (Appendix A.4) can be found. Appendix A.5 presents an implementation of a two-dimensional formulation of the Kubo formalism and Appendix A.6 that of the non-equilibrium Green function formalism for layered systems, both of which have no immediate relevance for the remainder of this work, but are presently used within other research projects.

In summary, the present thesis aims at investigating the symmetry and magnitude of spincaloritronic and related response properties in transition metals and their alloys from first principles based on the linear response Kubo formalism and a generalisation of Mott's formula for thermally-induced phenomena. Predictions for and comparison with experiment will be shown to be on a qualitative and often even quantitative level of agreement.

Chapter 2

Theoretical Framework

The following gives a brief introduction into the formal basis for determining the electronic structure of the systems investigated in the present thesis and for calculating, based on this, their physical – in particular response – properties. Section 2.1 outlines the essential aspects of density functional theory (DFT), the method of choice for treating solid state compounds, as it allows mapping the many-electron problem of extended systems composed of several, possibly heavy atoms onto a single-particle problem of just one electron moving in an effective potential. In the subsequent section (2.2) the Korringa-Kohn-Rostoker Green function method (KKR-GF) will be introduced, an ansatz based on multiple scattering theory for solving the electronic problem via the (single-particle) Green function. Particular emphasis will be put on the advantages of this method when dealing with disorder due to random occupation of lattice sites or due to thermally-induced vibrations and/or spin fluctuations, and, when including these effects, calculating expectation values of single-particle operators. Of central relevance to this work is the description of electronic transport in solid state systems, which will be treated on the level of linear response theory in Section 2.3. Starting with general remarks on Kubo's linear response formalism, tractable equations for the electrical conductivity on several levels of complexity will be presented briefly. This is followed by a discussion of the Mott formula for the thermoelectric power and its generalisations to temperature-dependent thermoelectric and spin caloritronic transport coefficients. Finally, a group-theoretical approach to the space-time symmetry of the relevant response tensors will be outlined. If not noted otherwise, atomic Rydberg units will be assumed throughout, that is, the settings $\hbar = 2m_e = e^2/2 = k_\mathrm{B} = 4\pi\epsilon_0 = 1$ are used. The elementary charge e is furthermore distinguished from the electronic charge $q = -|e|$.

2.1 Density functional theory

Density functional theory has a quite long and successful history. The real breakthrough came with the pioneering works of Hohenberg and Kohn [110] and Kohn and Sham [111]. Originally DFT was formulated on a non-relativistic level aiming at the ground state properties of non-spin-polarised systems, but since then it has seen many extensions. The spin-polarised case was considered first by von Barth and Hedin [112] and Rajagopal and Callaway [113] leading to spin density functional theory (SDFT). Relativistic effects (RDFT) were included by the works of Ramana and Rajagopal [114] and MacDonald and Vosko [115]. An improved framework to

deal with orbital magnetism was set up by Vignale and Rasolt [116–118] who introduced current density functional theory or CDFT. Another important aspect of magnetism is the occurrence of non-collinear spin configurations. The technical issues of such situations have been considered in particular by Kübler *et al.* [119], Sandratskii [120] as well as Nordström and Singh [121]. Finally, the latest fundamental steps forward were superconducting density functional theory (SCDFT) [122] and time-dependent density functional theory (TD-DFT). The latter was introduced by Runge and Gross [123], providing a firm basis for linear response calculations and investigations of the dynamics of electronic systems as for example encountered in an ultra-fast demagnetisation process induced by a laser pulse [124].

The major achievements of the work of Kohn and Sham [111] were the introduction of the auxiliary non-interacting particle system and the local density approximation (LDA) that turned DFT from a mere concept into a practicable scheme. Since then several refinements have been worked out to go beyond that simplification. These developments are well documented in numerous review articles (e.g., [125–127]) and text books (e.g., [128–130]). In particular the book of Engel and Dreizler [130] gives a detailed overview over the various aspects mentioned above. In the following only the key features of DFT relevant to this thesis will be summarised.

2.1.1 Non-relativistic formulation

In density functional theory the absolute square of the N-particle wave function $\Psi(\boldsymbol{r}_1, \boldsymbol{r}_2, ..., \boldsymbol{r}_N)$, the single-particle probability or, in case of electronic systems, electron density $n(\boldsymbol{r}) = \langle\Psi|\hat{n}(\boldsymbol{r})|\Psi\rangle = \langle\Psi(\boldsymbol{r}_1, ..., \boldsymbol{r}_N)|\Psi(\boldsymbol{r}_1, ..., \boldsymbol{r}_N)\rangle$[1] is taken as the fundamental property of a system. As such, it is formally sufficient for a complete description of its ground state properties involving arbitrary interactions. The energy of the system is given as a functional of the density and the electronic structure problem expressed in the time-independent Schrödinger- or, in case of a relativistic description, Dirac-like equation $\hat{H}\Psi = E\Psi$ is solved by functional variation in three rather than $3N$ dimensions.

The Hamiltonian $\hat{H}$ of the system under consideration is – within the Born-Oppenheimer approximation [131], assuming a complete decoupling of electronic and nuclear degrees of freedom due to their different time and energy scales[2] – composed of a kinetic part $\hat{T}$, describing the motion of the electrons, a potential (energy) term accounting for all electron-electron interactions $\hat{U}$, and a static external potential (energy) $\hat{V}_{\text{ext}}$,

$$\hat{H} = \hat{T} + \hat{U} + \hat{V}_{\text{ext}} \ . \tag{2.1}$$

The last term is the sum over local one-particle potentials

$$\hat{V}_{\text{ext}} = \sum_{i}^{N} v_{\text{ext}}(\boldsymbol{r}_i) \ , \tag{2.2}$$

which represent the potential energy associated with an external field. In the most simple case this is just the Coulomb interaction of electrons and nuclei, which are

[1] The concise Dirac bra-ket notation hides the fact that this is actually an integral in $(N-1) \times 3$ dimensions, leading to a three dimensional (ignoring spin and time dependence for now) object.

[2] In solids, this corresponds in particular to neglecting (non-adiabatic) electron-phonon coupling.

– as stated above – assumed to remain fixed on the timescale of the electronic motion, and the repulsion of the nuclei $\hat{V}_{nn}$, which then just amounts to an additive constant. Accordingly, it is omitted in the following. Furthermore, the nuclei usually are treated as point particles with a resulting singular Coulomb potential. The kinetic and the electron-electron parts, $\hat{T}$ and $\hat{U}$, are on the other hand system-independent or *universal*. Obviously, the many-body problem is connected to the latter of the two. In contrast to wave function-based methods of Quantum Chemistry or the diagrammatic approach to many-body perturbation theory that rely on systematic expansion of Ψ or $\hat{H}$, respectively, DFT provides an exact mapping of the many-particle problem onto an effective single-particle problem without the complex electron-electron interaction operator $\hat{U}$.
The use of the density as the central quantity for the description of an electronic system had been proposed already quite early, namely just one year after Schrödinger published his seminal work [132], independently by Thomas [133] and Fermi [134]. However, it took about 40 years until a theory emerged that could be used for actual calculation of bound states, namely density functional theory introduced by Hohenberg and Kohn [110].

The (first)[3] theorem of Hohenberg and Kohn [110] states that the external potential in Eq. (2.1) is uniquely defined up to an arbitrary constant by the electron density. This implies a bijective mapping between $\hat{V}_{\text{ext}}$ (or $\hat{H}$) and the electronic wave function Ψ as well as between Ψ and the electron density $n(\boldsymbol{r})$. Since according to this the wave function of any given system can be formulated as a functional of $n(\boldsymbol{r})$, the same is true for any ground-state observable:

$$O[n(\boldsymbol{r})] = \langle \Psi[n(\boldsymbol{r})] | \hat{O} | \Psi[n(\boldsymbol{r})] \rangle \ . \tag{2.3}$$

In the original work [110] this was proven, by *reductio ad absurdum*, only for a non-degenerate ground state Ψ_0, but even if several degenerate ground-state wave functions Ψ_0^i would reproduce the same density n_0, they all would also have the same energy eigenvalue E_0, which hence is a unique functional of $n(\boldsymbol{r})$. An alternative proof of the Hohenberg-Kohn theorem including the possibility of degenerate ground states was given independently by Levy [135, 136] and Lieb [137, 138] based on a constraint minimisation procedure.

What is sometimes called the second theorem of Hohenberg and Kohn [110] now states that the energy eigenvalue of an electronic system without an external potential exists, being a particular case of Eq. (2.3), as a universal functional of its density, $F[n(\boldsymbol{r})] = \langle \Psi | (\hat{T} + \hat{U}) | \Psi \rangle$[4], that does not depend explicitly on the external potential. Furthermore the sum $E[n] = F[n] + V_{\text{ext}}[n]$ becomes minimal for the density of the actual ground state in the presence of V_{ext}. This is the central idea of the aforementioned constrained-search proof of the (first) Hohenberg-Kohn theorem. This minimum principle, derived from the Rayleigh-Ritz variational principle, implies that by starting from an arbitrary test density, which only has to obey

[3] There is some dissens in the literature concerning the number of theorems, ranging from one to three.

[4] The real space position vector $\boldsymbol{r} \equiv \vec{r}$ will be dropped in the following for functionals of the density, i.e., $X[n] \equiv X[n(\boldsymbol{r})]$.

$N[n] \equiv \int d^3r\, n(\boldsymbol{r}) = N$,[5] with N being the particle number, and with knowledge of the exact energy functional, the global minimum of the energy $E_0 = E[n_0]$ could be found by functional variation,

$$\frac{\delta}{\delta n(\boldsymbol{r})} \left\{ E[n] - \mu \left(\int d^3r\; n(\boldsymbol{r}) - N \right) \right\} \Bigg|_{n(\boldsymbol{r})=n_0(\boldsymbol{r})} = 0\ . \tag{2.4}$$

With μ as a Lagrange multiplier[6], the above is equivalent to the Euler-Lagrange equation

$$\frac{\delta F[n]}{\delta n(\boldsymbol{r})} + V_{\text{ext}}[n] = \mu\ , \tag{2.5}$$

and the subsidiary condition in Eq. (2.4) ensures correct normalisation of the density. This equation shows that the external potential is uniquely defined by the density of the ground state. The minimum principle just outlined, that can be expressed as $E[n_0] \leq E[n']$, is of such central importance that it is sometimes given the status of an additional Hohenberg-Kohn theorem [126]. Although density functional theory is formally rigorous, extremely versatile and has proven its usefulness beyond doubt, the obvious caveat of the above lies in the expression "knowledge of the exact energy functional". This problem will be addressed below.

Hence, the greatest challenge of this method lies in the search for an appropriate density functional accurately describing the system under investigation. The basic principle for this is the ansatz of Kohn and Sham [111], where the energy functional

$$E_s[n] = T_s[n] + J[n] + E_{\text{xc}}[n] + \int d^3r\, v_{\text{ext}}(\boldsymbol{r}) n(\boldsymbol{r})\ , \tag{2.6}$$

is composed of the kinetic energy of the fictitious non-interacting Kohn-Sham system[7], $T_s[n]$, the Coulomb energy $J[n]$, the exchange-correlation energy $E_{\text{xc}}[n]$ and finally the potential energy term arising from the external potential, $V_{\text{ext}}[n]$. In the most simple case this comprises only the Coulomb interaction between electrons and nuclei. With this, the exchange-correlation functional containing all many-particle interactions is defined as

$$E_{\text{xc}}[n] \equiv T[n] - T_s[n] + U[n] - J[n]\ , \tag{2.7}$$

the difference between exact kinetic energy as well as electron-electron interaction ($T[n] + U[n]$) and the sum of $T_s[n]$ and the bare Coulomb interaction $J[n]$ (or Hartree potential). This energy functional is obviously system-independent or *universal*, since it only depends on quantities which are independent on V_{ext} and since it is the same for any particle number.

The Kohn-Sham equations, which correspond to the Schrödinger equation for the Kohn-Sham system, represented by the Kohn-Sham wave function $\Psi_s(\boldsymbol{r}_1, \boldsymbol{r}_2, ..., \boldsymbol{r}_N)$

[5] In addition it has to be connected to an anti-symmetric N-particle wave function as its probability density, a non-trivial issue termed N-representability problem [139, 140].

[6] It can be interpreted as the chemical potential according to $\dfrac{\partial E}{\partial N} = \mu$.

[7] This requires the density to be *non-interacting ν-representable*, i.e., a non-interacting ground state $\Psi_s[n]$ with $n_s(\boldsymbol{r}) = n(\boldsymbol{r})$ has to exist.

describing the inhomogeneous electron system, are usually expressed (in atomic Rydberg units) as

$$[-\boldsymbol{\nabla}^2 + V_{eff}(\boldsymbol{r})]\phi_i = \varepsilon_i \phi_i \; . \tag{2.8}$$

The effective Kohn-Sham potential $V_{eff}(\boldsymbol{r})$ occurring in Eq. (2.8) is given by

$$\begin{aligned} V_{eff}(\boldsymbol{r}) &= V_{\rm ext}(\boldsymbol{r}) + V_{\rm H}(\boldsymbol{r}) + V_{\rm xc}(\boldsymbol{r}) \\ &= V_{\rm ext}(\boldsymbol{r}) + 2\int d^3r' \frac{n(\boldsymbol{r'})}{|\boldsymbol{r}-\boldsymbol{r'}|} + \frac{\delta E_{\rm xc}[n]}{\delta n(\boldsymbol{r})} \; , \end{aligned} \tag{2.9}$$

with

$$\frac{\delta E_{\rm xc}(n)}{\delta n(\boldsymbol{r})} = \epsilon_{\rm xc}[n(\boldsymbol{r})] + n(\boldsymbol{r})\frac{\partial \epsilon[n(\boldsymbol{r})]}{\partial n(\boldsymbol{r})} \tag{2.10}$$

and the particle density

$$n(\boldsymbol{r}) = \sum_i^N \sum_s |\psi_i(\boldsymbol{r}, s)|^2 \; , \tag{2.11}$$

expressed as a sum over N one-particle orbitals ψ_i with spin s. The Lagrange multipliers ε_i again are introduced to satisfy the above-mentioned condition of particle number conservation and in this case can be interpreted as single-particle energy eigenvalues. The Kohn-Sham wave function $\Psi_s(\boldsymbol{r}_1, \boldsymbol{r}_2, ...\boldsymbol{r}_N)$ is constructed from the Kohn-Sham orbitals $\phi_i(\boldsymbol{r}, s)$ as a single Slater determinant [141][8], obeying the Pauli principle [144]. These effective one-particle equations, Eqs. (2.8)-(2.11), obtained via an *exact* mapping of the many-body problem, are to be solved self-consistently by iteration, as they are implicit differential equations with the solutions themselves being contained in the Hartree and exchange-correlation potentials, V and $V_{\rm xc}$, respectively.

As mentioned above, the greatest challenge of density functional theory remains the problem to construct the universally "correct" exchange-correlation functional for realistic systems. A simple, yet extremely – not to say astonishingly – successful approximation to it is the so-called *local density approximation* (LDA)[9], in which the exchange-correlation energy is determined exclusively by $n(\boldsymbol{r})$ at $\boldsymbol{r}$, by setting

$$E_{\rm xc}^{LDA}[n(\boldsymbol{r})] = E_{\rm xc}^{heg}[n(\boldsymbol{r})] = \int d^3\, r\, \varepsilon_{\rm xc}^{heg}(n(\boldsymbol{r}))\, n(\boldsymbol{r}) \; , \tag{2.12}$$

which is the exchange-correlation functional of the interacting homogeneous electron gas[10] (heg), which has a locally constant density n by construction. The expression $\varepsilon_{\rm xc}^{heg}(n(\boldsymbol{r}))$ represents the mean exchange-correlation energy density per electron of the homogeneous electron gas, where the exchange part can be determined analytically to be [145]

$$\varepsilon_x^{heg}(n) = -\frac{3}{4}\left(\frac{3}{\pi}\right)^{\frac{1}{3}} n^{\frac{4}{3}} \; , \tag{2.13}$$

leading to the simple expression

$$E_x^{LDA}[n] = -\frac{3}{4}\left(\frac{3}{\pi}\right)^{\frac{1}{3}} \int d^3\, r\, n(\boldsymbol{r})^{\frac{4}{3}} \; . \tag{2.14}$$

[8] Actually, Heisenberg [142] as well as Dirac [143] proposed this ansatz already some years earlier.
[9] This idea in fact dates back already to the Thomas-Fermi model [133, 134].
[10] To stress the importance of the electron-electron interaction some authors speak of a liquid here.

The correlation energy $\varepsilon_{\mathrm{c}}^{heg}$ however is a complicated many-body problem on its own and not known exactly. Approximations for it used to be based on perturbation theory, such as, e.g., the random-phase approximation [112], but nowadays usually are obtained by parametrisation of results from Quantum Monte Carlo calculations for the electron liquid (such as Ref. 146). The sum $\varepsilon_{\mathrm{x}}^{heg} + \varepsilon_{\mathrm{c}}^{heg} = \varepsilon_{\mathrm{xc}}^{heg}$, representing the interacting homogeneous electron liquid, enters the Kohn-Sham equations for the inhomogeneous electron gas Eq. (2.8) via Eq. (2.12) and the last term of Eq. (2.9).

As stated already above, the LDA proved to be remarkably successful. This is to a large extent caused by a cancellation of errors in the exchange and correlation terms. Nevertheless, the accuracy necessary for investigations on the stability and energetics of molecules (*chemical accuracy*) is normally not achieved [126]. For this reason ongoing research is aimed at developing more accurate schemes that however (ideally) keep the simplicity of the local density approximation. For example an improvement over the local ansatz in Eq. (2.12) is the so-called *generalised gradient approximation* (GGA) [147–149] which considers in addition to the local density also its gradient via the expression

$$E_{\mathrm{xc}}^{GGA}[n(\boldsymbol{r}), \nabla n(\boldsymbol{r})] = \int d^3r\, f(n(\boldsymbol{r}), \nabla n(\boldsymbol{r}))\ . \tag{2.15}$$

For both approximation schemes (LDA and GGA) a vast number of parametrised functionals has been developed over the last decades, usually separated into an exchange and a correlation part, E_{x} and E_{c}, respectively. Still today there is an ever increasing demand for more accurate and preferentially at the same time more general and still computationally feasible approximations. To a good extent motivated by the increasing interest of chemists in density functional theory for calculating molecular properties, in recent years the inclusion of a wave-function based description of "exact" (Hartree-Fock) exchange, derived from the Kohn-Sham orbitals rather than the density, has led to the so-called hybrid density functionals [150, 151]. Another noteworthy extension of Kohn-Sham-DFT are dispersion corrections, which allow for example the description of van-der-Waals interactions [152]. For further extensions fully within the framework of DFT see for example Refs. 153–155.

A completely different approach to remedy the shortcomings of the local density approximation concerning the description of electronic correlation is to combine it with many-body approaches. A simple version of such a scheme is the LDA+U method [156, 157]. A more sophisticated treatment of electron-electron interaction is the combination of dynamical mean field theory (DMFT) [158, 159] with the LDA, leading to LDA+DMFT [160].

In this work, if not stated otherwise, the combined exchange-correlation parametrisation of Vosko, Wilk, and Nusair [161] within the local spin density approximation (LSDA) that extends Eqs. (2.8-2.11) to the spin-polarised case has been used (see below).

2.1.2 Relativistic formulation

For most of the spincaloritronic phenomena studied in this work a proper treatment of relativistic effects, in particular of the spin-orbit interaction, is essential. Hence the so-called scalar-relativistic corrections to the Schrödinger or Kohn-Sham equations, i.e., the mass-velocity correction and the Darwin term connected to the *Zitterbewegung* of the electrons, are not sufficient. A corresponding relativistic version of density functional theory (RDFT) has been worked out by various authors [113–115]. With the electric four-current density as the fundamental electronic variable this scheme in particular accounts for all magnetic aspects of a system. Accordingly, replacing the Kohn-Sham Hamiltonian by the Dirac-(Kohn-Sham) Hamiltonian one arrives at the Dirac-Kohn-Sham-equations (in SI units)

$$[-i\hbar c\boldsymbol{\alpha}\cdot\boldsymbol{\nabla}+\beta mc^2+V_{eff}(\boldsymbol{r})+e\boldsymbol{\alpha}\boldsymbol{A}_{eff}(\boldsymbol{r})]\Psi_i(\boldsymbol{r})=\epsilon_i\Psi_i(\boldsymbol{r})\;, \tag{2.16}$$

where m is the electron's rest mass, c the speed of light in vacuum, and α_i and β are the 4×4 Dirac matrices [162]

$$\alpha_{i=x,y,z}=\begin{pmatrix}0 & \sigma_i\\ \sigma_i & 0\end{pmatrix}\;, \tag{2.17}$$

with the usual 2×2 Pauli spin matrices

$$\sigma_{\mathrm{x}}=\begin{pmatrix}0 & 1\\ 1 & 0\end{pmatrix}\;,\;\sigma_{\mathrm{y}}=\begin{pmatrix}0 & -i\\ i & 0\end{pmatrix}\;\text{and}\;\sigma_{\mathrm{z}}=\begin{pmatrix}1 & 0\\ 0 & -1\end{pmatrix}\;, \tag{2.18}$$

and the Dirac beta matrix

$$\beta=\begin{pmatrix}\mathrm{I}_2 & 0_2\\ 0_2 & -\mathrm{I}_2\end{pmatrix}\;, \tag{2.19}$$

where I_2 is the two-dimensional unity. Accordingly, the wave function $\Psi_i(\boldsymbol{r})$ is a four-dimensional object as well, the so-called Dirac or bi-spinor.
The first term in Eq. (2.16) is the relativistic kinetic energy operator[11], while the second is the rest energy (or mass) term. Analogous to the non-relativistic case there is an effective scalar potential,

$$V_{eff}(\boldsymbol{r})=V_{\mathrm{ext}}(\boldsymbol{r})+e^2\int d^3r'\frac{n(\boldsymbol{r'})}{|\boldsymbol{r}-\boldsymbol{r'}|}+\frac{\delta E_{\mathrm{xc}}[n(\boldsymbol{r}),\boldsymbol{j}(\boldsymbol{r})]}{\delta n(\boldsymbol{r})}\;, \tag{2.20}$$

that is again composed of an external, a classical or Hartree, and an exchange-correlation part. In addition Eq. (2.16) however contains now a second potential term, the effective vector potential $\boldsymbol{A}_{eff}(\boldsymbol{r})$ given by

$$\boldsymbol{A}_{eff}(\boldsymbol{r})=\boldsymbol{A}_{\mathrm{ext}}(\boldsymbol{r})-\frac{e}{c}\int d^3r'\frac{\boldsymbol{j}(\boldsymbol{r'})}{|\boldsymbol{r}-\boldsymbol{r'}|}+\frac{e}{c}\frac{\delta E_{\mathrm{xc}}[n(\boldsymbol{r}),\boldsymbol{j}(\boldsymbol{r})]}{\delta\boldsymbol{j}(\boldsymbol{r})}\;, \tag{2.21}$$

which is like the relativistic effective potential once more composed of an external, a classical[12], and an exchange-correlation part.

[11] Note that the Laplacian of the Schrödinger or Pauli equation has been replaced by a first-order differential operator.
[12] That arises from the so-called Breit interaction, see Ref. 163 and references therein.

These two may be seen as the components of a four-component effective potential $V^{\mu}_{eff} = (V_{eff}, -e\boldsymbol{A}_{eff})$. The complete single-particle density has accordingly to be seen as a four-component object, the relativistic four-current density $J^{\mu} = (J^0, \boldsymbol{j})$ with $\frac{1}{c}J^0 = n$ being the electron density and the three remaining parts the spatial components of the electric current density. In comparison to Eq. (2.9), the last term of Eq. (2.20) obviously implies a coupling between charge and current density also for the effective potential. There is however no simple approximation to this modified exchange-correlation potential, making relativistic CDFT impracticable.

Applying a Gordon decomposition of $\boldsymbol{j}$ into an orbital and a spin part and retaining only the coupling of the spin current density to the magnetic field, neglecting the orbital current density altogether, one arrives at relativistic spin density functional theory (RSDFT) [113–115]. In this approach, the coupling of the spin current density to the vector potential $\boldsymbol{A}_{eff}$ is represented by

$$-\boldsymbol{m}\boldsymbol{B}_{eff} \,, \tag{2.22}$$

with the spin magnetisation density

$$\boldsymbol{m} = \langle\Psi|\beta\boldsymbol{\sigma}|\Psi\rangle \tag{2.23}$$

and the effective magnetic field

$$\boldsymbol{B}_{eff}(\boldsymbol{r}) = \boldsymbol{B}_{\mathrm{ext}}(\boldsymbol{r}) + \frac{\delta E_{\mathrm{xc}}[n(\boldsymbol{r}), \boldsymbol{m}(\boldsymbol{r})]}{\delta \boldsymbol{m}(\boldsymbol{r})} \,, \tag{2.24}$$

leading to the simplified Dirac-Kohn-Sham-equations

$$[-i\hbar c\boldsymbol{\alpha}\cdot\boldsymbol{\nabla} + \beta mc^2 + V_{eff}(\boldsymbol{r}) + \beta\boldsymbol{\sigma}\boldsymbol{B}_{eff}(\boldsymbol{r})]\Psi_i(\boldsymbol{r}) = \epsilon_i\Psi_i(\boldsymbol{r}) \,, \tag{2.25}$$

with a modified exchange-correlation potential

$$V_{\mathrm{xc}} = \frac{\delta E_{\mathrm{xc}}[n(\boldsymbol{r}), \boldsymbol{m}(\boldsymbol{r})]}{\delta n(\boldsymbol{r})} \,. \tag{2.26}$$

Assuming moreover collinear magnetisation (at least locally), one can further simplify Eq. (2.25) to the form

$$[-i\hbar c\boldsymbol{\alpha}\cdot\boldsymbol{\nabla} + \beta mc^2 + V_{eff}(\boldsymbol{r}) + \beta\sigma_{\mathrm{z}}B_{eff}(\boldsymbol{r})]\Psi_i(\boldsymbol{r}) = \epsilon_i\Psi_i(\boldsymbol{r}) \,, \tag{2.27}$$

where the spin magnetisation as well as the effective magnetic field are oriented along the local z axis according to $\boldsymbol{B}_{eff}(\boldsymbol{r}) = B_{eff}(\boldsymbol{r})\hat{e}_{\mathrm{z}}$. With this, the magnetisation can be represented by a scalar field as well, leading to the following basic variables of the system

$$n(\boldsymbol{r}) = n^{\uparrow}(\boldsymbol{r}) + n^{\downarrow}(\boldsymbol{r}) \tag{2.28}$$

$$\boldsymbol{m}(\boldsymbol{r}) = m(\boldsymbol{r})\hat{e}_{\mathrm{z}} = n^{\uparrow}(\boldsymbol{r}) - n^{\downarrow}(\boldsymbol{r}) \,, \tag{2.29}$$

where the total density $n(\boldsymbol{r})$ and the magnetisation $\boldsymbol{m}(\boldsymbol{r})$ have been expressed in terms of the spin-dependent densities $n^{\uparrow(\downarrow)}(\boldsymbol{r})$ projected on the local z axis. All

calculations presented in the following are based on Eq. (2.27) using, if not noted otherwise, the local spin density approximation to

$$V_{\mathrm{xc}} = \frac{\delta E_{\mathrm{xc}}[n(\boldsymbol{r}), m(\boldsymbol{r})]}{\delta n(\boldsymbol{r})} \tag{2.30}$$

with the parametrisation as given by Vosko *et al.* [161].

In summary, density functional theory is a formally exact, extremely versatile, and ever increasingly successful[13] method for electronic structure calculations (and beyond). Given a suitable description of the exchange-correlation part of the energy, highly accurate and reproducible [169] results can be obtained with comparably modest computational effort.

[13] Among the most cited articles of *Physical Review* (as of July 2018), a majority is work related to density functional theory, including that of Hohenberg and Kohn [110] and Kohn and Sham [111], as well as on functional parametrisation [164–168].

2.2 Multiple scattering theory

In multiple scattering theory, which is the basis of the Korringa-Kohn-Rostoker (KKR) method for electronic structure calculations used throughout in this thesis, the Green function $G(\boldsymbol{r}, \boldsymbol{r}', E)$ is the central object representing the time-independent electronic structure of the system under investigation.[14] It is equivalent to the propagator of the system and hence describes the motion of a particle, usually an electron, from $\boldsymbol{r}'$ to $\boldsymbol{r}$, reflecting the scattering properties of the system. In contrast to most other band structure methods the concept of the Green function is not restricted to translation invariant systems as the use of Bloch wave functions. This allows the treatment of disordered systems of arbitrary dimensions (0-3D) and scattering-based phenomena in spectroscopy and transport in a rather straightforward manner [173–176]. System properties like the aforementioned but also much simpler ones, as the particle density, can be directly obtained from the Green function determined within the framework of density functional theory.

2.2.1 Green operators and functions

The central quantity of multiple scattering theory is the single-particle Green function, that can be formally defined as the solution of an inhomogeneous Schrödinger-like linear differential equation, as [173, 174, 177]

$$(E - \hat{H})\hat{G}(E) = \hat{1} \ . \tag{2.31}$$

The Green operator is accordingly defined as

$$\hat{G} = (E - \hat{H})^{-1} \ . \tag{2.32}$$

It is the so-called resolvent of the Hamiltonian with the associated boundary conditions, that contains all information on the spectrum of its solutions. Being the Kernel of the integral operator inverse to the Hermitian differential operator $\hat{H}$ it gives access to the solutions of any related inhomogeneous problem without having to actually perform the differential operation.[15] Moreover these solutions are automatically satisfying the required homogeneous boundary conditions (i.e., continuity of the wave function and its gradient, and finite or zero value at infinity) by construction since the Green function fulfils them [173, 177].

An important property of the Green function is that it is analytic in the complex energy plane. For a Hermitian Hamilton operator $\hat{H}$ one has in particular the property

$$G^{\dagger}(z) = G(z^*) \ , \tag{2.33}$$

where the complex energy argument has been emphasised by writing z. The spectrum of the Hamiltonian is reflected by poles and a continuous branch cut on the real energy axis corresponding to localised and extended band states, respectively. For that reason one is in general interested in the side limits

$$G^{\pm}(E) = \lim_{\varepsilon \to 0} G(E \pm i\varepsilon) \ , \tag{2.34}$$

[14] While the original works of Korringa [170] and Kohn and Rostoker [171] were aiming at Bloch wave functions, it was Beeby [172] who introduced the use of Green functions.

[15] This can in particular be a numerical advantage, which was actually the original motivation of the work of Korringa [170].

leading to the so-called retarded (G^+) and advanced (G^-) Green functions with the connection $[G^+(E)]^\dagger = G^-(E)$ via Eq. (2.33). Because of this relation the following will be restricted to $G^+(E)$ and the "+" sign will be in general omitted.
According to Eq. (2.31) the real space representation of the Green function $G(\boldsymbol{r}, \boldsymbol{r}', E)$ is defined as the solution to the inhomogeneous equation

$$(E - \hat{H})G(\boldsymbol{r}, \boldsymbol{r}', E) = \delta(\boldsymbol{r} - \boldsymbol{r}') \; . \tag{2.35}$$

For the case of a free electron, i.e., in case of $\hat{V} = 0$ it is straightforward to derive the following expression:

$$G^0(\boldsymbol{r}, \boldsymbol{r}', E) = -\frac{1}{4\pi} \frac{e^{ik|\boldsymbol{r}-\boldsymbol{r}'|}}{|\boldsymbol{r} - \boldsymbol{r}'|} \; , \tag{2.36}$$

with $k = \sqrt{E}$. For a system of scatterers, the retarded Green function can be expressed by means of the so-called Lehmann spectral representation of the Green operator $\hat{G}$

$$G(\boldsymbol{r}, \boldsymbol{r}', E) = \lim_{\varepsilon \to 0} \sum_j \frac{\Psi_j(\boldsymbol{r}) \Psi_j^*(\boldsymbol{r}')}{E - E_j + i\varepsilon} \; . \tag{2.37}$$

Here the sum runs over the eigenstates j and corresponding eigenenergies E_j of the Hamiltonian.

This becomes more complicated in case of a relativistic treatment, i.e., when $\hat{H}$ is the Dirac Hamiltonian and the eigenstates are bi-spinors, as the complex conjugation has to be replaced by taking the Hermitian adjoint (†). Moreover left-hand-side and right-hand-side solutions can no longer be assumed to be identical. In case of general non-local and complex potentials (self energies) further complications arise [178–180], leading to the most general expression

$$G(\boldsymbol{r}, \boldsymbol{r}', z) = \sum_j \frac{\Phi_j(\boldsymbol{r}, z) \Psi_j^\dagger(\boldsymbol{r}', z)}{z - E_j(z)} \; . \tag{2.38}$$

For the work presented herein this distinction however is not relevant and left- and right-hand solutions will from now on be assumed to be identical.

As mentioned above, the Green function gives access to all physical properties of the system under investigation. For example the particle density can be obtained from it using the Dirac identity

$$-\frac{1}{\pi} \mathrm{Im} \lim_{\varepsilon \to 0} \frac{1}{x + i\varepsilon} = \delta(x) \; , \tag{2.39}$$

leading via

$$-\frac{1}{\pi} \mathrm{Im}\, G(\boldsymbol{r}, \boldsymbol{r}', E) = \sum_j \phi_j(\boldsymbol{r})\, \phi_j(\boldsymbol{r}')^*\, \delta(E - E_j) \tag{2.40}$$

to

$$\begin{aligned} n(\boldsymbol{r}) &= \sum_{j\mathrm{occ}} \phi_j(\boldsymbol{r}) \phi_j(\boldsymbol{r}')^* \\ &= \int^{E_\mathrm{F}} dE\, \phi_j(\boldsymbol{r})\, \phi_j(\boldsymbol{r}')^*\, \delta(E - E_j) \\ &= -\frac{1}{\pi} \int^{E_\mathrm{F}} dE\, G(\boldsymbol{r}, \boldsymbol{r}', E) \; , \end{aligned} \tag{2.41}$$

where the energy integration runs up to the Fermi level corresponding to a sum over all occupied states.

Similarly the density of states (DOS) is given by

$$\begin{aligned} n(E) &= \sum_j \delta(E - E_j) \\ &= \sum_i \int_\Omega d^3r\ \phi_j(\boldsymbol{r})\ \phi_j(\boldsymbol{r}')^*\ \delta(E - E_j) \\ &= -\frac{1}{\pi}\mathrm{Im}\int_\Omega d^3r\ G(\boldsymbol{r}, \boldsymbol{r}', E)\ . \end{aligned} \tag{2.42}$$

A natural choice of basis in solids are of course lattice periodic Bloch eigenstates, leading for the Lehmann representation to

$$G(\boldsymbol{r}, \boldsymbol{r}', E) = \lim_{\varepsilon\to 0}\sum_{j\boldsymbol{k}} \frac{\Psi_{j\boldsymbol{k}}(\boldsymbol{r})\Psi^\dagger_{j\boldsymbol{k}}(\boldsymbol{r}')}{E - E_{j\boldsymbol{k}} + i\varepsilon}\ , \tag{2.43}$$

with the sum over the band index j and the $\boldsymbol{k}$-vectors [181]. Although of course formally fully correct its application is in practice very tedious, as one would need the whole spectrum of solutions. A much more efficient and versatile alternative to this presents multiple scattering theory, which will be detailed in the following.

2.2.2 Single-site scattering

The basic electronic structure problem is to find a solution to the stationary Schrödinger equation

$$\hat{H}\Psi(\boldsymbol{r}) = \left[\hat{T} + \hat{V}\right]\Psi(\boldsymbol{r}) = E\Psi(\boldsymbol{r})\ , \tag{2.44}$$

or, within a relativistic treatment, to the Dirac equation. Within a spin-polarised relativistic formulation the corresponding Dirac Hamiltonian [182] is

$$-i\hbar c\boldsymbol{\alpha}\cdot\boldsymbol{\nabla} + \beta mc^2 + V(\boldsymbol{r})\ , \tag{2.45}$$

where in the most general case the potential is [179]

$$V(\boldsymbol{r}) = \bar{V}(\boldsymbol{r}) + \beta\boldsymbol{\sigma}\cdot\boldsymbol{B}(\boldsymbol{r}) + e\boldsymbol{\alpha}\cdot\boldsymbol{A}(\boldsymbol{r})\ . \tag{2.46}$$

In addition one may add a non-local potential or an energy-dependent self-energy to the Hamiltonian of Eq. (2.45) [180]. It is however conventionally employed in a simplified version,

$$-i\hbar c\boldsymbol{\alpha}\cdot\boldsymbol{\nabla} + \beta mc^2 + \overline{V}(\boldsymbol{r}) + \beta\boldsymbol{\sigma}\cdot\boldsymbol{B}_{eff}(\boldsymbol{r})\ , \tag{2.47}$$

where $\overline{V}(\boldsymbol{r})$ is the spin-independent part of the potential and the full dependence on the electromagnetic vector potential is approximated by $\beta\boldsymbol{\sigma}\cdot\boldsymbol{B}_{eff}$. Assuming collinear magnetism within an atomic cell this is normally further simplified using the expression $\beta\sigma_z B_{eff}$.

In Eqs. (2.45)-(2.47) m is the electron's rest mass, c the speed of light in vacuum, and $\boldsymbol{\alpha}$ and β are the 4×4 Dirac matrices [162]

$$\alpha_{i=x,y,z} = \gamma_{j=1,2,3} = \begin{pmatrix} 0 & \sigma_i \\ \sigma_i & 0 \end{pmatrix} , \tag{2.48}$$

with the usual 2×2 Pauli spin matrices

$$\sigma_{\mathrm{x}} = \begin{pmatrix} 0 & 1 \\ 1 & 0 \end{pmatrix} , \sigma_{\mathrm{y}} = \begin{pmatrix} 0 & -i \\ i & 0 \end{pmatrix} \text{ and } \sigma_{\mathrm{z}} = \begin{pmatrix} 1 & 0 \\ 0 & -1 \end{pmatrix} \tag{2.49}$$

and

$$\beta = \gamma_0 = \begin{pmatrix} \mathrm{I}_2 & 0_2 \\ 0_2 & -\mathrm{I}_2 \end{pmatrix} , \tag{2.50}$$

where I_2 is the two-dimensional unit matrix. The wave function in Eq. (2.44) accordingly has to be a four-dimensional object.

Dealing with atomic-like potentials it is most convenient to work with the Dirac equation in spherical coordinates [180] and using atomic Rydberg units:[16]

$$\begin{aligned} \hat{H}(\boldsymbol{r}) &= -ic\boldsymbol{\alpha} \cdot \boldsymbol{\nabla} + \frac{1}{2}c^2(\beta - 1) + V(\boldsymbol{r}) \\ &= i\gamma_5\sigma_r c \left(\frac{\partial}{\partial r} + \frac{1}{r} - \frac{\beta}{r}K \right) + \frac{1}{2}c^2(\beta - 1) + V(\boldsymbol{r}) , \end{aligned} \tag{2.51}$$

where $\sigma_r = \boldsymbol{\sigma} \cdot \boldsymbol{r}/r$ stands for the radial projection of the Pauli matrices, K is the spin-orbit operator $\boldsymbol{\sigma} \cdot \boldsymbol{l} + 1$ [183],

$$\gamma_5 = i\gamma_0\gamma_1\gamma_2\gamma_3 = \begin{pmatrix} 0 & \mathrm{I}_2 \\ \mathrm{I}_2 & 0 \end{pmatrix} , \tag{2.52}$$

and the rest mass energy $\frac{1}{2}c^2$ has been subtracted.

Instead of applying Eq. (2.44) to a solid directly, the problem is solved by dealing first with the individual atoms seen as independent objects. Employing the so-called muffin-tin approximation (MTA), the corresponding scattering potentials are obtained by decomposing the space into two distinct areas, the so-called *muffin-tin* spheres with radius r_{MT} where the actual scattering takes place, and the remaining interstitial region where the potential is taken to be constant,

$$V(\boldsymbol{r}) = \begin{cases} V(r) & \text{for } r < r_{\mathrm{MT}} \\ \text{const.} & \text{for } r \geq r_{\mathrm{MT}} \end{cases} . \tag{2.53}$$

Note that the muffin-tin construction implies non-overlapping and isotropic potentials. Approaches beyond this like the *atomic sphere approximation* (ASA) and the *full potential* (FP) scheme will be discussed below.

In the following introduction to the KKR-GF method we will first deal with the non-relativistic Schrödinger equation

$$\left[-\boldsymbol{\nabla}^2 + V(\boldsymbol{r}) \right] \Psi(\boldsymbol{r}) = E\Psi(\boldsymbol{r}) . \tag{2.54}$$

[16] Atomic Rydberg units (ARU): $\hbar = 1$, $m = 1/2$, $e^2 = 2$.

As an ansatz for the solution to the spherically symmetric single-site problem problem represented by Eq. (2.54) one inserts

$$\varphi_L(\boldsymbol{r}) = R_\ell(r, E)\; Y_L(\hat{r}) \text{ with } L \mathrel{\hat{=}} (l, m)\;, \tag{2.55}$$

i.e., the product of a complex spherical harmonics $Y_L(\hat{r})$ (with the short-hand combined angular momentum index $L = (\ell, m)$) and the regular (constant for $r \to 0$) solutions to the radial differential equation

$$\left[(-\frac{1}{r}\frac{d^2}{dr^2}\,r + \frac{l(l+1)}{r^2}) + V(r) - E\right] R_\ell(r, E) = 0\;. \tag{2.56}$$

In the interstitial region outside of the scattering potential the radial wave function is constructed as a linear combination of spherical Bessel and von Neumann functions, j_ℓ and n_ℓ, which are the free-space ($V(r) = 0$) solutions to Eq. (2.56),

$$R_\ell(r, E) = e^{i\eta_\ell(E)}\left[\cos\eta_\ell(E)\, j_\ell(kr) - \sin\eta_\ell(E)\, n_\ell(kr)\right]\;. \tag{2.57}$$

where $E = k^2$ is the free electron energy (in ARU) and k the corresponding wave vector. The phase shift $\eta_\ell(E)$ that is acquired upon interaction with the scattering potential can be obtained from the boundary conditions for the wave function, namely by demanding that at $r = r_{\mathrm{MT}}$ the function itself as well as its first derivative have to be continuous. Using the logarithmic derivative w.r.t. the radius r,

$$L_\ell(E) = \left.\frac{d\ln R_\ell(r, E)}{dr}\right|_{r=r_{\mathrm{MT}}}\;, \tag{2.58}$$

the phase shift can be expressed by

$$\tan\eta_\ell(E) = \left.\frac{L_\ell(E)\, j_\ell(kr) - dj_\ell(kr)/dr}{L_\ell(E)\, n_\ell(kr) - dn_\ell(kr)/dr}\right|_{r=r_{\mathrm{MT}}}\;. \tag{2.59}$$

For $r > r_{\mathrm{MT}}$ the incoming and outgoing (scattered) waves hence obviously are expected to show the same oscillatory behaviour in the radial part, only shifted by $\eta_\ell(E)$ corresponding to elastic or *on the energy shell* scattering. Within the *muffin-tin* sphere the radial part of the wave function exhibits a structure determined by $V(r)$, accordingly the solutions to Eq. (2.56) have to be obtained numerically. By subsequently evaluating Eqs. (2.58) and (2.59) the scattered wave within the interstitial region is given.

If the scattering at a potential $V(\boldsymbol{r})$ is described as the perturbation of an incoming plane wave $\varphi^0(\boldsymbol{r})$ via the Hamilton operator

$$H = H^0 + \Delta V(\boldsymbol{r}) \text{ with } H^0 = -\nabla^2 + V^0(\boldsymbol{r})\;, \tag{2.60}$$

where in case of the muffin-tin construction $\Delta V(\boldsymbol{r})$ corresponds to $V(r)$ and $V^0 =$ const., the perturbed wave $\varphi(\boldsymbol{r})$ can be expressed, with the help of the free-electron Green function $G^0(\boldsymbol{r}, \boldsymbol{r}', E)$ obeying

$$(E - H^0)\, G^0(\boldsymbol{r}, \boldsymbol{r}', E) = \delta(\boldsymbol{r} - \boldsymbol{r}')\;, \tag{2.61}$$

via an implicit integral equation of Fredholm type as

$$\varphi(\boldsymbol{r}) = \varphi^0(\boldsymbol{r}) + \int d^3r'\, G^0(\boldsymbol{r}, \boldsymbol{r}', E)\, V(\boldsymbol{r}')\, \varphi(\boldsymbol{r}')\;. \tag{2.62}$$

This is the Lippmann-Schwinger equation [184], an equivalent to the time-independent Schrödinger (or Dirac) equation, but already including boundary conditions. In Dirac bra-ket notation and using a short-hand operator formulation omitting all arguments, it reads

$$|\varphi\rangle = |\varphi^0\rangle + \hat{G}^0\,\hat{V}\,|\varphi\rangle\ , \tag{2.63}$$

with the formal solution

$$|\varphi\rangle = (1 - \hat{G}^0\hat{V})^{-1}|\varphi^0\rangle\ . \tag{2.64}$$

Expanding this by a geometric series one arrives at the so-called Born series [185], corresponding to a repeated insertion of the r.h.s. of Eq. (2.63) into itself.
By constructing the transition operator $\hat{T}$

$$\hat{T} = \hat{V}(1 - \hat{G}^0\hat{V})^{-1}\ , \tag{2.65}$$

one gets the relation

$$\hat{T}|\varphi^0\rangle = \hat{V}|\varphi\rangle\ , \tag{2.66}$$

that allows to recast Eq. (2.63) into

$$|\varphi\rangle = (1 + \hat{G}^0\,\hat{T})|\varphi^0\rangle\ . \tag{2.67}$$

Hence, formally the task of computing the scattered states from the incoming ones is reduced to an inversion of the operator $(1 - \hat{G}^0\hat{V})$, assuming $\hat{G}^0$ is available.

In analogy to the Lippmann-Schwinger equation, Eq. (2.63), the Green function $G(\boldsymbol{r}, \boldsymbol{r}', E)$ of the perturbed system can be connected to the free-electron reference system represented by $G^0(\boldsymbol{r}, \boldsymbol{r}'; E)$ via a Dyson equation. In operator notation with position and energy arguments again omitted this important relation reads

$$\hat{G} = \hat{G}^0 + \hat{G}^0\hat{V}\hat{G} \tag{2.68}$$

$$= \hat{G}^0 + \hat{G}^0\hat{T}\hat{G}^0\ . \tag{2.69}$$

Comparison of Eqs. (2.68) and (2.69) leads to the relation

$$\hat{T}\hat{G}^0 = \hat{V}\hat{G}\ , \tag{2.70}$$

that is a counterpart to Eq. (2.66). Multiplying Eq. (2.68) from the left by T one obtains via Eq. (2.70) an implicit equation for the transition operator,

$$\hat{T} = \hat{V} + \hat{T}\,\hat{G}^0\,\hat{V} = \hat{V} + \hat{V}\,\hat{G}^0\,\hat{T}\ . \tag{2.71}$$

For the single-site scattering problem Eq. (2.62) is now used to obtain the wave function $\varphi_L(\boldsymbol{r}, E) = R_\ell(r, E)\,Y_L(\hat{r})$ from the incoming spherical wave $\varphi^0(\boldsymbol{r}, E) = j_\ell(kr)\,Y_L(\hat{r})$ and the Green function for the free particle $G^0(\boldsymbol{r}, \boldsymbol{r}', E)$ using

$$R_\ell(r, E) = j_\ell(kr) + \int_0^{r_{\mathrm{MT}}} r'^2\,dr'\,G^0_\ell(r, r', E)\,V(r')\,R_\ell(r', E)\ . \tag{2.72}$$

For $r \geq r_{\mathrm{MT}}$ the integral in Eq. (2.72) can be transformed, via

$$G^0_\ell(r, r', E) = -i\,j_\ell(kr_<)\,h^+_\ell(kr_>)\ , \tag{2.73}$$

where $r_>(r_<)$ assumes the value of either r or r' depending on which is the larger (smaller), and the outgoing wave represented by a Hankel function of 1st kind

$$h_\ell^+(kr) = n_\ell(kr) + ij_\ell(kr) \;, \tag{2.74}$$

into

$$[n_\ell(kr) - ij_\ell(kr)]\, k\langle j_\ell|V|R_\ell\rangle \;, \tag{2.75}$$

where the matrix elements

$$\langle j_\ell|V|R_\ell\rangle = \int_0^{r_{\rm MT}} r^2 dr j_\ell(kr)V(r)R_\ell(r,E) \tag{2.76}$$

can now be identified with the angular momentum representation of the transition operator for a single scatterer. This means the $t_\ell(E)$ are the diagonal elements of the single-site t matrix in the combined azimuthal and orbital quantum number index L,

$$t_\ell(E) = \delta_{LL'}t_{LL'}(E) = \delta_{LL'}\langle\varphi_L^0|\hat{T}|\varphi_{L'}^0\rangle = \delta_{LL'}\langle\varphi_L^0|V|\varphi_{L'}\rangle = \langle j_\ell|V|R_\ell\rangle \;. \tag{2.77}$$

Inserting this first into Eq. (2.75), subsequently into Eq. (2.72), and comparing the result to Eq. (2.57), one obtains

$$e^{i\eta_\ell(E)}\cos\eta_\ell(E) = 1 - ikt_\ell(E) \tag{2.78}$$

$$\text{or } -e^{i\eta_\ell(E)}\sin\eta_\ell(E) = kt_\ell(E) \;, \tag{2.79}$$

and thus an expression for the t matrix in terms of the phase shift η_ℓ:

$$t_\ell(E) = -\frac{1}{k}\sin\eta_\ell(E)\, e^{i\eta_\ell(E)} \;. \tag{2.80}$$

With the t-matrix determined, the regular wave function $R_L(\boldsymbol{r},E)$ is completely fixed by its asymptotic behaviour outside the muffin-tin regime:

$$R_L(\boldsymbol{r},E) = j_L(\boldsymbol{r},E) - ikt_\ell(E)h_L^+(\boldsymbol{r},E) \;, \tag{2.81}$$

with $j_L(\boldsymbol{r},E) = j_\ell(kr)\,Y_L(\hat{r})$ and analogously for $h_L^+(\boldsymbol{r},E)$.
In addition one can introduce an irregular solution $H_L(\boldsymbol{r},E)$ to the Schrödinger equation by the boundary conditions for $r \geq r_{\rm MT}$,

$$H_L(\boldsymbol{r},E) = h_L^+(\boldsymbol{r},E) \;, \tag{2.82}$$

while for $r \leq r_{\rm MT}$ it is a numerical solution for the finite single-site potential $V(\boldsymbol{r})$. The properly normalised set of functions, $R_L(\boldsymbol{r},E)$ and $H_L(\boldsymbol{r},E)$, allows now expressing the single-site Green function

$$G(\boldsymbol{r},\boldsymbol{r}',E) = -ik\sum_L Y_L(\hat{r})R_\ell(r_<,E)H_\ell^+(r_>,E)Y_L(\hat{r}') \tag{2.83}$$

as a solution of the differential equation Eq. (2.35) for an isolated potential well [186].

Dealing with the Dirac equation instead of the Schrödinger equation, the corresponding derivation of the expression for the single-site t-matrix is conceptually

analogous. Working with the Dirac Hamiltonian in spherical coordinates, as given by Eq. (2.51), the corresponding spherical functions for the free-electron situation $V(\boldsymbol{r}) = 0$ are given by the bi-spinors

$$j_\Lambda(\boldsymbol{r}, E) = \begin{pmatrix} j_\ell(pr)\chi_\Lambda(\hat{r}) \\ \frac{ipcS_\kappa}{E+c^2}\, j_{\bar{\ell}}(pr)\chi_{-\Lambda}(\hat{r}) \end{pmatrix} \tag{2.84}$$

and analogously for $h^+_\Lambda(\boldsymbol{r}, E)$, where Λ stands for the combined spin-orbit and magnetic quantum numbers (κ, μ), $-\Lambda = (-\kappa, \mu)$, $p = \sqrt{E(1 + E/c^2)}$ is the relativistic momentum, $S_\kappa = \mathrm{sign}(\kappa)$, $\bar{\ell} = \ell - S_\kappa$, and $\chi_\Lambda(\hat{r})$ are the spin-angular functions

$$\chi_\Lambda(\hat{r}) = \sum_{m_s} C^{m_s}_\Lambda \mathcal{Y}^{\mu-m_s}_\ell \, \chi_{m_s} \tag{2.85}$$

with the Clebsch-Gordon coefficients[17] $C^{m_s}_\Lambda$, real spherical harmonics $\mathcal{Y}^{\mu-m_s}_\ell$, and the Pauli spinors χ_{m_s} [162]. These functions are eigenfunctions to the spin-orbit operator K

$$K\chi_\Lambda(\hat{r}) = -\kappa\chi_\Lambda(\hat{r}) \tag{2.86}$$

and obey the symmetry relation

$$\sigma_r\chi_\Lambda(\hat{r}) = -\chi_{-\Lambda}(\hat{r}) \; . \tag{2.87}$$

This allows to construct the free-electron Green function as a 4×4 matrix function [180]:

$$\begin{aligned} G^0(\boldsymbol{r}, \boldsymbol{r}', E) = -i(1 + E/c^2)p \sum_\Lambda \quad & j_\Lambda(\boldsymbol{r}, E)\, h^{+\times}_\Lambda(\boldsymbol{r}', E)\, \theta(r' - r) \\ & + h^+_\Lambda(\boldsymbol{r}, E)\, j^\times_\Lambda(\boldsymbol{r}', E)\, \theta(r - r') \; , \end{aligned} \tag{2.88}$$

where

$$j^\times_\Lambda(\boldsymbol{r}', E) = \left(j_\ell(pr)\chi^\dagger_\Lambda\hat{r}), \frac{-ipcS_\kappa}{E + c^2} j_{\bar{\ell}}(pr)\chi^\dagger_{-\Lambda}(\hat{r}) \right) \tag{2.89}$$

and the corresponding $h^{+\times}_\Lambda$ are the left-hand side solutions to the Dirac equation. When applying the Dirac Hamiltonian of Eq. (2.47) involving a spin-dependent potential the corresponding solutions have in general no pure spin-angular character any more, i.e., one has for example

$$\Psi_\Lambda(\boldsymbol{r}, E) = \sum_{\Lambda'} \Psi_{\Lambda'\Lambda}(\boldsymbol{r}, E) \; , \tag{2.90}$$

with the bi-spinors

$$\Psi_{\Lambda'\Lambda}(\boldsymbol{r}, E) = \begin{pmatrix} g_{\Lambda'\Lambda}(r, E)\chi_{\Lambda'}(\hat{r}) \\ if_{\Lambda'\Lambda}(r, E)\chi_{-\Lambda'}(\hat{r}) \end{pmatrix} \; . \tag{2.91}$$

This implies that the corresponding t-matrix is not diagonal w.r.t. Λ. Nevertheless, properly normalised regular and irregular scattering solutions, $R_\Lambda(\boldsymbol{r}, E)$ and $H_\Lambda(\boldsymbol{r}, E)$, respectively, to the Dirac equation can be given in analogy to Eqs. (2.81)

[17] Transforming from the non-relativistic (ℓ, m, m_s) to the relativistic (κ, μ) representation.

and (2.82). This normalisation is often called Jülich convention, as it was introduced by Dederichs and co-workers [187]. An alternative normalisation, introduced by Faulkner and Stocks [188, 189] and commonly called Bristol-Oak-Ridge convention, has some advantages in particular when dealing with alloys (see below). In this case one has the regular and irregular solutions

$$Z_\Lambda(\boldsymbol{r}, E) = \sum_{\Lambda'} j_{\Lambda'}(\boldsymbol{r}, E)\, m_{\Lambda'\Lambda}(E) - ip h^+_\Lambda(\boldsymbol{r}, E) \tag{2.92}$$

$$J_\Lambda(\boldsymbol{r}, E) = j_\Lambda(\boldsymbol{r}, E)\ , \tag{2.93}$$

with $\underline{m}(E) = \underline{t}^{-1}(E)$ being the inverse of the single-site t matrix in relativistic spin-angular representation. Comparing with the normalisation in Eq. (2.81) and Eq. (2.82) one finds the relations between the regular (R and Z) and irregular (H and J) solutions to be

$$R_\Lambda(\boldsymbol{r}, E) = \sum_{\Lambda'} Z_{\Lambda'}(\boldsymbol{r}, E)\, t_{\Lambda'\Lambda}(E) \tag{2.94}$$

$$-ipH_\Lambda(\boldsymbol{r}, E) = Z_\Lambda(\boldsymbol{r}, E) - \sum_{\Lambda'} J_{\Lambda'}(\boldsymbol{r}, E)\, m_{\Lambda'\Lambda}(E)\ . \tag{2.95}$$

Again, with the free-electron Green function $G^0(\boldsymbol{r}, \boldsymbol{r}', E)$ and the properly normalised regular and irregular solutions for an isolated potential well available, one can construct the corresponding relativistic single-site Green function

$$G(\boldsymbol{r}, \boldsymbol{r}', E) = -i\bar{p} \sum_\Lambda R_\Lambda(\boldsymbol{r}, E)\, H^{+\times}_\Lambda(\boldsymbol{r}', E)\, \theta(r' - r) + H^+_\Lambda(\boldsymbol{r}, E)\, R^\times_\Lambda(\boldsymbol{r}', E)\, \theta(r - r')\ , \tag{2.96}$$

where $\bar{p} = (1 + E/c^2)p$ and $\times$ labels again the left-hand side solutions to the Dirac equation (see above and Refs. 179 and 180).

2.2.3 Multiple scatterers

As stated above, the electronic structure problem of many-atom systems can be recast into solving the multiple scattering equations for an electron moving in an array of potentials and being subjected to repeated scattering events at these individual potentials. The most simple ansatz for the geometry of the potential is the so-called *muffin-tin approximation* (MTA) that goes back to work of Slater [190]. In this case the potentials are non-overlapping and spherically symmetric, separated by a region of constant potential which is taken as the energy reference (*muffin-tin zero*). The radii of the atomic spheres are usually chosen to minimise this interstitial region, since the description of the electronic structure therein by free-electron solutions is certainly not accurate.

The *atomic sphere approximation* (ASA) [191] goes one step further by allowing for overlapping spheres and demanding that the sum of their volumina corresponds to the volume of the unit cell. This way the interstitial region is eliminated, leading in general to a better description of the electronic structure. For rather open crystal structures the introduction of so-called *empty spheres*, i.e., atomic cells without a nuclear potential, often is beneficial. This way the interstitial regime is in principle enlarged, but treated as a spherically symmetric problem like regular atomic cells,

and the intersection of the atomic spheres is at the same time reduced. This last point touches a somewhat delicate issue of the ASA, namely that multiple scattering theory is formally based on the assumption that the scattering events are clearly separated in time and space, i.e., the interaction with one potential has to be finished before the electron enters the region of another. Hence, the overlap volume should be kept as small as possible. In spite of this caveat, the ASA has proven extremely successful in particular for the treatment of metallic systems due to its relative simplicity and simultaneous remarkable accuracy. Since the present work deals almost exclusively with transition metals, their compounds and alloys, the ASA has been employed throughout.

An alternative to the ASA, to be mentioned here for the sake of completeness, is the so-called *full potential* ansatz using a Wigner-Seitz construction or Voronoi tessellation resulting in space-filling polyhedra centred at the atomic sites. Formally, such a Voronoi polyhedron or Wigner-Seitz cell V_{WS}^n centred at n can be expressed via a three-dimensional Heaviside step function

$$\Theta^n(\boldsymbol{r}) = \begin{cases} 1 \text{ for } \boldsymbol{r} \in V_{\mathrm{WS}}^n \\ 0 \text{ for } \boldsymbol{r} \notin V_{\mathrm{WS}}^n \end{cases} \tag{2.97}$$

$$= \sum_{\ell}^{\infty} \sum_{m=-\ell}^{+\ell} f_{\ell m}(r)\, \mathcal{Y}_{\ell m}(\hat{r}) \;, \tag{2.98}$$

using real spherical harmonics $\mathcal{Y}_{\ell m}(\hat{r})$ and the so-called *shape functions* $f_{\ell m}(r)$. The latter have to obey the point group symmetry of the unit cell with the additional constraint

$$\sum_n \int d^3r\, \Theta^n(\boldsymbol{r}) = \sum_n V_{\mathrm{WS}}^n = V_{\mathrm{UC}} \;, \tag{2.99}$$

i.e., the sum of all Wigner-Seitz cells V_{WS}^n has to reproduce the volume of the unit cell V_{UC}. The *full potential* (FP) approach to the division of space certainly is most accurate and formally rigorous, yet also technically and computationally demanding. Since most of the systems treated in the present thesis are closed packed and metallic bulk materials, the ASA has been employed assuming the deviations to be of minor importance for the general trends observed.
The decomposition of space via the muffin-tin, ASA, or FP scheme implies a corresponding decomposition of the potential according to

$$V(\boldsymbol{r}) = \sum_i v_i(\boldsymbol{r} - \boldsymbol{R}_i) \equiv \sum_i v_i(\boldsymbol{r}_i) \tag{2.100}$$

$$\text{or } \hat{V} = \sum_i v_i \;. \tag{2.101}$$

In the last equation an operator notation has been used that simplifies the subsequent manipulations for the transition operator $\hat{T}$ of the total system. Omitting energy arguments from now on, one has from Eq. (2.71) and Eq. (2.101)

$$\begin{aligned} \hat{T} &= \hat{V} + \hat{V}\hat{G}^0\hat{V} + \hat{V}\hat{G}^0\hat{V}\hat{G}^0\hat{V} + \ldots \\ &= \sum_i v_i + \sum_{i,j} v_i\hat{G}^0 v_j + \sum_{i,j,k} v_i\hat{G}^0 v_j\hat{G}^0 v_k + \ldots \\ &= \sum_i \hat{T}_i \;. \end{aligned} \tag{2.102}$$

with the auxiliary operators

$$\hat{T}_i = v_i \hat{G}^0 \sum_j \hat{T}_j \ . \tag{2.103}$$

Introducing the single-site transition operator

$$\hat{t}_i = \hat{v}_i + \hat{v}_i \hat{G}^0 \hat{t}_i \ , \tag{2.104}$$

that is related to $\hat{T}_i$ via

$$\hat{T}_i = \hat{t}_i + \hat{t}_i \hat{G}^0 \sum_{j \neq i} \hat{T}_j \ , \tag{2.105}$$

Eq. (2.102) can be transformed into a Born series in terms of $t_i G^0$

$$\begin{aligned} \hat{T} = & \sum_i \hat{t}_i + \sum_{j \neq i} \hat{t}^i \hat{G}^0 \hat{t}_j \\ & + \sum_{j \neq i} \sum_{k \neq j} \hat{t}_i \hat{G}^0 \hat{t}_j \hat{G}^0 \hat{t}_k + \ldots \\ = & \sum_{i,j} \hat{\tau}_{ij} \ . \end{aligned} \tag{2.106}$$

In the last line the so-called scattering path operator τ_{ij} [192] has been introduced that accounts for all scattering events on an arbitrary path connecting sites i and j. For this operator one has the defining equation of motion

$$\begin{aligned} \hat{\tau}_{ij} &= \hat{t}_i \delta_{ij} + \hat{t}_i \hat{G}^0 \sum_{k \neq i} \hat{\tau}_{kj} \\ &= \hat{t}_i \delta_{ij} + \sum_{k \neq j} \hat{\tau}_{ik} \hat{G}^0 \hat{t}_j \ . \end{aligned} \tag{2.107}$$

For practical applications a suitable set of basis functions has to be chosen for the real space representation of the operators $\hat{t}_i$, $\hat{G}^0$, and $\hat{\tau}_{ij}$. Moreover, this expansion will always have to be truncated at some point, otherwise one would have to deal with matrices of infinite dimensions when dealing with real solids. From Eq. (2.107) one obtains this way

$$\begin{aligned} \underline{\underline{\tau}} &= \underline{\underline{t}} + \underline{\underline{t}}\, \underline{\underline{G}}^0\, \underline{\underline{\tau}} \\ &= \left(\underline{\underline{t}}^{-1} - \underline{\underline{G}}^0 \right)^{-1} \ , \end{aligned} \tag{2.108}$$

where the double underline stands for matrices in the site index i and the combined angular momentum index of the chosen representation. This is the fundamental equation of multiple scattering theory since it gives the scattering path operators $\underline{\tau}_{ij}$ connecting sites i and j in terms of the t-matrix $\underline{t}_i$ representing the scattering properties of the individual atoms or potential wells, and the so-called structure constants $\underline{G}^0_{ij}$ containing information on the geometric arrangements of the scatterers, via

$$\underline{\tau}_{ij} = \left[\left(\underline{\underline{t}}^{-1} - \underline{\underline{G}}^0 \right)^{-1} \right]_{ij} \ . \tag{2.109}$$

Having solved the multiple scattering problem the real space representation of the Green function $G(\boldsymbol{r}, \boldsymbol{r}', E)$ can now be given in terms of the scattering path operator. For the non-relativistic case these steps have been described in detail by

Faulkner and Stocks [189]. For the relativistic case the derivation runs completely analogously [180], and one is led to

$$\begin{aligned} G(\boldsymbol{r}_i, \boldsymbol{r}'_j, E) \;=\; & \sum_{\Lambda\Lambda'} Z_\Lambda(\boldsymbol{r}_i, E)\, \tau^{ij}_{\Lambda\Lambda'}(E)\, Z^\times_{\Lambda'}(\boldsymbol{r}'_j, E) \\ & -\delta_{ij} \sum_{\Lambda} \big[Z_\Lambda(\boldsymbol{r}, E)\, J^\times_\Lambda(\boldsymbol{r}', E)\, \theta(\boldsymbol{r}' - \boldsymbol{r}) \\ & + J_\Lambda(\boldsymbol{r}, E)\, Z^\times_\Lambda(\boldsymbol{r}', E)\, \theta(\boldsymbol{r} - \boldsymbol{r}') \big] \;. \end{aligned} \tag{2.110}$$

Here $Z_\Lambda(\boldsymbol{r}, z)$ and $J_\Lambda(\boldsymbol{r}, z)$ are the regular and irregular single-site scattering solutions to the radial Dirac equation as defined in Eqs. (2.92) and (2.93), where $\times$ denotes left-hand-side solutions.
The elements of the scattering path operator matrix, $\tau^{ij}_{\Lambda\Lambda'}(E)$, can formally (for finite systems also in practice) be obtained by inversion of the equation of motion Eq. (2.107)

$$\tau^{ij}_{\Lambda\Lambda'}(E) = \left\{ \left[\underline{\underline{t}}^{-1}(E) - \underline{\underline{G}}^0(E) \right]^{-1}_{ij} \right\}_{\Lambda\Lambda'} \;. \tag{2.111}$$

For three-dimensional periodic, i.e., infinite systems a proper solution to the problem can be obtained via lattice Fourier transformation leading to

$$\tau^{ij}_{\Lambda\Lambda'}(E) = \frac{1}{\Omega_{BZ}} \int_{\Omega_{BZ}} d^3k \, [\underline{t}^{-1}(E) - \underline{G}^0(\boldsymbol{k}, E)]^{-1}_{\Lambda\Lambda'} \, e^{i\boldsymbol{k}(\boldsymbol{R}_i - \boldsymbol{R}_j)} \;, \tag{2.112}$$

as an integral over the first Brillouin zone (BZ). Here $G^0(\boldsymbol{k}, z)$ is the Fourier transform of the real space free-electron Green function. The computational effort for the integration can be considerably reduced by use of the point group symmetry of the lattice allowing restriction to the irreducible part of the BZ.

Equations (2.111) and (2.112) are central to the Korringa-Kohn-Rostoker Green function method, connecting the scattering properties of the system under investigation, expressed in terms of the single-site t-matrix, with the geometric arrangement of the scatterers, defined via the structure constants $G^{0ij}_{LL'}(z)$ or structural Green function matrix $\underline{g}^{ij}(z)$. The corresponding infinite sum over lattice vectors

$$\underline{G}^0(\boldsymbol{k}, E) = \frac{1}{N} \sum_{i,j} \underline{G}^{0ij}(E) e^{i\boldsymbol{k}(\boldsymbol{R}_i - \boldsymbol{R}_j)} \tag{2.113}$$

to get the Fourier transformed structure constants is in practice evaluated by splitting into separate sums of real and reciprocal lattice vectors. This method, named Ewald summation [193] after its discoverer who developed it for calculating the electrostatic or Madelung potential in ionic crystals, considerably speeds up convergence.

2.2.4 Calculating ground-state properties

The electron density can now be obtained from the single-particle Green function as given by Eq. (2.110) via integration over energy up to the Fermi energy E_F,

$$n(\boldsymbol{r}) = -\frac{1}{\pi} \,\mathrm{Im}\mathrm{Tr} \int_{-\infty}^{E_\mathrm{F}} dz \; G(\boldsymbol{r}, \boldsymbol{r}, z) \;, \tag{2.114}$$

where the trace refers to the 4×4 matrix structure of the relativistic Green function. Here only the Green function for coinciding position arguments is required and accordingly only the diagonal elements of the scattering path operator of Eq. (2.111) have to be computed. Since $G(\boldsymbol{r},\boldsymbol{r}',z)$ is analytic on the whole complex plane – emphasised by writing z for the energy argument in Eq. (2.114) – except for the real axis, this integration can in practice be performed on a complex path. Due to the broadening of the structure of the integrand with increasing imaginary part of the complex energy $z = E + i\eta$, the computational effort is reduced considerably. The exact form of the path can be chosen according to specific needs, for the results presented herein a semi-circular contour has been used. Details on computational parameters can be found in Appendix A.7.

In practice, the energy integration is not starting from $-\infty$, but from an energy below the bottom of the valence band. Hence, the treatment of core states (atomic-like) and valence states is separated. Depending on the situation, that is, the structure and in particular chemical composition of a system, it might be necessary to include high-lying so-called *semi-core* states into the valence band in order to correctly describe these. An example for this are rare earth metals with their incompletely localised f electrons.

Eq. (2.114) constitutes the basis for a self-consistent determination of the electronic ground state within the framework of density functional theory described in Section 2.1. It is obviously a special case of the more general expression for the expectation value

$$\langle A\rangle = -\frac{1}{\pi}\mathrm{Im}\mathrm{Tr}\int_{-\infty}^{E_\mathrm{F}} dz\hat{A}G(\boldsymbol{r},\boldsymbol{r},z) \tag{2.115}$$

of a single-particle operator $\hat{A}$. The (spin) magnetisation for the local frame of reference quantisation axis along z is correspondingly obtained by setting $\hat{A}$ to the z component of the spin operator $\beta\boldsymbol{\sigma}$:[18]

$$m(\boldsymbol{r}) = \frac{1}{\pi}\,\mathrm{Im}\mathrm{Tr}\int_{-\infty}^{E_\mathrm{F}} dz\ \beta\sigma_\mathrm{z}G(\boldsymbol{r},\boldsymbol{r},z)\ . \tag{2.116}$$

The electronic density of states (DOS) is obtained in an analogous fashion by integrating over the volume Ω of interest (atomic or unit cell),

$$n(E) = -\frac{1}{\pi}\,\mathrm{Im}\mathrm{Tr}\int_\Omega d^3r\ G(\boldsymbol{r},\boldsymbol{r},E)\ . \tag{2.117}$$

Spin- and orbital-magnetic moments can accordingly be computed via

$$\mu_\mathrm{spin} = \frac{1}{\pi}\,\mathrm{Im}\mathrm{Tr}\int_{-\infty}^{E_\mathrm{F}} dz\int_\Omega d^3r\ \beta\sigma_\mathrm{z}G(\boldsymbol{r},\boldsymbol{r},z) \tag{2.118}$$

$$\mu_\mathrm{orb} = \frac{1}{\pi}\,\mathrm{Im}\mathrm{Tr}\int_{-\infty}^{E_\mathrm{F}} dz\int_\Omega d^3r\ l_\mathrm{z}G(\boldsymbol{r},\boldsymbol{r},z)\ . \tag{2.119}$$

[18] Note that magnetisation and spin expectation value are anti-parallel.

The band structure $E(\boldsymbol{k})$ of an ideal periodic solid can be derived from the KKR matrix $\underline{M}(\boldsymbol{k}, E) = \underline{t}^{-1}(E) - \underline{G}^0(\boldsymbol{k}, E)$ of Eq. (2.112) as well. Those values of $\boldsymbol{k}$ for which $\tau^{ij}(\boldsymbol{k}, E) = [\underline{M}(\boldsymbol{k}, E)^{-1}]_{ij}$ is diverging indicate the poles of the Green function and therefore the real eigenvalues of the Hamiltonian that correspond to the determinant condition

$$\det |\underline{t}(E)^{-1} - \underline{G}^0(\boldsymbol{k}, E)| = 0 \; . \tag{2.120}$$

This is to be met for a given vector $\boldsymbol{k}$ by varying the energy E to yield the band structure $E(\boldsymbol{k})$, as $\underline{t}(E)$ as well as $\underline{G}^0(\boldsymbol{k}, E)$ explicitly depend on the energy.

The Bloch spectral function (BSF) $A^B(E, \boldsymbol{k})$ also gives a relation between the energy E and the reciprocal lattice vector $\boldsymbol{k}$, but in addition, taking the former two as arguments, it gives a proper measure for the density of states in a $\boldsymbol{k}$-resolved way:

$$n(E) = \frac{1}{\Omega_{\mathrm{BZ}}} \int_{\Omega_{\mathrm{BZ}}} d^3k A^B(E, \boldsymbol{k}) \; . \tag{2.121}$$

This makes it applicable also for the description of the band structure (or remnants thereof) in disordered systems such as alloys. For an ordered system $A^B(E, \boldsymbol{k})$ is just a sum of δ-functions for $E = E(\boldsymbol{k})$, i.e., it follows the dispersion relation, while for a disordered system it shows a broadening in energy due to the disorder in the system (see below). In the formulation given by Faulkner and Stocks [189] the definition for the BSF reads

$$A^B(E, \boldsymbol{k}) = -\frac{1}{\pi} \mathrm{Im} \tilde{G}(\boldsymbol{k} = \boldsymbol{k'}, E) \; , \tag{2.122}$$

where

$$\tilde{G}(\boldsymbol{k}, \boldsymbol{k'}, E) = \sum_n G(\boldsymbol{k} + \boldsymbol{K}_n, \boldsymbol{k'} + \boldsymbol{K}_n, E) \; , \tag{2.123}$$

is the Fourier transformed Green function of, e.g., Eq. (2.110) for $\boldsymbol{k}$ and $\boldsymbol{k'}$ within the first Brillouin zone and the reciprocal lattice vectors $\boldsymbol{K}_i$ reflect the periodicity of the underlying lattice. Alternatively one may write in a compact way

$$A^B(E, \boldsymbol{k}) = \lim_{z \to E^+} -\frac{1}{\pi} \mathrm{Im} \mathrm{Tr} \frac{1}{N} \sum_{i,j}^{N} e^{ik(\boldsymbol{R}_i - \boldsymbol{R}_j)} \int_{\Omega} d^3r \, G(\boldsymbol{r} + \boldsymbol{R}_i, \boldsymbol{r'} + \boldsymbol{R}_j, z) \; . \tag{2.124}$$

The corresponding approximation to the scattering path operator and thereby the Green function made in this work for the treatment of disordered alloys that provides the basis to apply Eqs. (2.122) or (2.124) to such systems will be introduced in the following section.

2.2.5 Treatment of disorder

In order to describe the electronic structure of disordered systems within the framework of multiple scattering theory access to the configurational average of the Green function $\langle G \rangle_c$ is required. For a lattice of N sites occupied by, in the simplest case, two different types of scatterers, A and B, with probabilities $c_A = 1 - x$ and $c_B = x$ in principle all possible arrangements of $c_A \cdot N$ atoms of type A and $c_B \cdot N$ atoms of type B have to be taken into consideration. Since this becomes increasingly infeasible with growing number of sites and occupants, an effective medium approach is called for.

The straightforward concentration-weighted superposition of two or more different atomic potentials on a site is often termed *virtual crystal approximation* (VCA) [194, 195] and has a very limited realm of applicability. An improved description of the effective scattering property of a randomly occupied site can be obtained using the *average t-matrix approximation* or ATA [196, 197]. This ad-hoc construction however still can lead to unphysical artefacts such as spurious band gaps. These shortcomings can be cured by demanding for the effective scatterers that on average there should be no further scattering when adding atoms of type A or B to the medium,

$$c_A \bar{t}_A + c_B \bar{t}_B = 0 \;, \tag{2.125}$$

with the effective t matrices

$$\bar{t}_X = (v_X - \overline{v}) + (v_X - \overline{v})\overline{G}^0 \;. \tag{2.126}$$

This requirement is the foundation of the *coherent potential approximation* (CPA) introduced by Soven [198]. Its formulation in terms of the site-diagonal scattering path operators reads as

$$c_A \tau_A^{ii} + c_B \tau_B^{ii} = \tau_{CPA}^{ii} \;. \tag{2.127}$$

The type-projected scattering path operators τ_X^{ii} occurring in this equation can be obtained from the configurationally-averaged one,

$$\tau_{CPA}^{ii} = t_{CPA}^{i}\delta_{ij} + \sum_{i \neq k} t_{CPA}^{i} G^0 \tau_{CPA}^{jk} \;, \tag{2.128}$$

by means of the so-called CPA projectors D_X

$$\tau_X^{ii} = D_X \tau_{CPA}^{ii} = \tau_{CPA}^{ii}[1 + (t_X^{-1} + t_{CPA}^{-1})\tau_{CPA}^{ii}]^{-1} \;, \tag{2.129}$$

which themselves depend on τ_{CPA}^{ii}. Hence, the so-called CPA-equations Eqs. (2.127)-(2.129) have to be solved for the effective single-site t-matrix t_{CPA} and then τ_{CPA} self-consistently by iteration.

The CPA provides a formally rigorous, very efficient and sufficiently accurate access to the scattering properties of statistically randomly disordered systems such as alloys. In particular it compares tremendously favourable to the use of super cells concerning computational effort. However, as a mean-field theory it can neither directly account for changes to the local coordination geometry upon chemical substitution, nor does it allow for local ordering effects. For the former one has to recourse to either self-consistent structural relaxation based on the average potential or use (super cell) structures obtained for specific configurations otherwise. The effect of short-range order, on the other hand, is incorporated in the *non-local coherent potential approximation* (NL-CPA) [199], that shall not be discussed here. The concept of an effective medium approach to disorder based on a suitable averaging of the scattering properties of the individual components can be extended to thermally-induced disorder as well. In Refs. 200–202 a scheme called *alloy analogy model* (AAM) has been introduced, that treats uncorrelated atomic displacements and/or rotated spin moments using the configuration-averaging techniques of the CPA to describe the influence of lattice vibrations and spin fluctuations on the electronic structure. From the corresponding Green functions one can subsequently obtain corresponding finite-temperature values for, in principle, any observable. In

Chapter 3 a few selected results using the AAM will be discussed, in particular concerning its application to thermoelectric (Section 3.1) and spincaloritronic (Section 3.2) response coefficients and the limits of its range of applicability. Spintronic and galvanomagnetic properties at finite temperatures are the subject of Section 3.6.

As all kinds of electronic response properties, regardless of stimulus and transported quantity, are dependent on the type and concentration of scatterers present, a reliable description of disorder-induced scattering as provided by the CPA or the AAM is a mandatory prerequisite for the description of transport in realistic materials. Accordingly the above considerations will also play a role in parts of the following section.

2.3 Linear response theory

This work is mainly concerned with the response of solid state systems to perturbations in the form of gradients of the electrochemical potential, defined as the sum of the chemical potential μ_c and $q = -|e|$ times the electric potential ϕ, $\boldsymbol{\nabla}\mu = \boldsymbol{\nabla}(\mu_\mathrm{c} + q\phi) = \boldsymbol{\nabla}\mu_\mathrm{c} + e\boldsymbol{E}$, of the temperature, $\boldsymbol{\nabla}T$, and of possible spin accumulations, represented by the fictitious field $\underline{\boldsymbol{F}}^s$ [203, 204]. In the linear response regime, the resulting current densities of electronic charge, heat, and spin, $\boldsymbol{j}^c$, $\boldsymbol{j}^q$, and $\underline{\boldsymbol{J}}^s$, respectively, the *fluxes* or *flows* in the language of irreversible thermodynamics [205–210], are assumed to be linearly dependent on the aforementioned perturbations, also termed *generalised forces* or *affinities*. This assumption is usually well justified for a low magnitude of the perturbation. The relationships between these causes and effects can be conveniently expressed by a matrix of response tensors,[19]

$$\begin{pmatrix} \boldsymbol{j}^c \\ \boldsymbol{j}^q \\ \underline{\boldsymbol{J}}^s \end{pmatrix} = \begin{pmatrix} \underline{\boldsymbol{L}}^{cc} & \underline{\boldsymbol{L}}^{cq} & \underline{\boldsymbol{\mathcal{L}}}^{cs} \\ \underline{\boldsymbol{L}}^{qc} & \underline{\boldsymbol{L}}^{qq} & \underline{\boldsymbol{\mathcal{L}}}^{qs} \\ \underline{\boldsymbol{\mathcal{L}}}^{sc} & \underline{\boldsymbol{\mathcal{L}}}^{sq} & \underline{\tilde{\boldsymbol{\mathcal{L}}}}^{ss} \end{pmatrix} \begin{pmatrix} -\boldsymbol{\nabla}\mu \\ -\boldsymbol{\nabla}T/T \\ \underline{\boldsymbol{F}}^s \end{pmatrix} , \tag{2.130}$$

where the quantities $\underline{\boldsymbol{L}}^{AB}$, as well as $\underline{\boldsymbol{J}}^s$ and $\underline{\boldsymbol{F}}^s$ are second rank tensors, usually expressed w.r.t. the Cartesian coordinates x, y, z indexed by $\{\mu, \nu\}$. The sub-tensors $\underline{\boldsymbol{\mathcal{L}}}^{AB}$ are of rank three and $\underline{\tilde{\boldsymbol{\mathcal{L}}}}^{ss}$ is a fourth rank tensor. Here the spin quantisation axis will be indexed by ξ and only second-rank sub-tensors diagonal w.r.t. this will be considered herein. The superscripts $A, B \in \{c, q, s\}$ encode the nature of the respective fluxes and forces whose correlation is expressed by these *kinetic coefficients*, namely electrical, thermal or spin-related phenomena.

Writing Eq. (2.130) without spatial and temporal arguments implies a restriction to a stationary situation with the various quantities representing averages over space and time. In other words, the linear response coefficients $L^{AB}_{\mu\nu}$ are assumed to be local in both space and time, i.e., the generalised flux $\boldsymbol{J}(\boldsymbol{r}, t)$ depends only on the value of the generalised force $\boldsymbol{X}(\boldsymbol{r}, t)$ at the space-time position $(\boldsymbol{r}, t)$ [52, 205]. For a translationally invariant solid that is assumed here, the perturbations and induced current densities are to be seen as the average over the unit cell. The same holds true for the response tensors connecting them. The symmetry and magnitude of these quantities are the central topic of the present thesis.

Assuming the chemical potential to be constant, $\boldsymbol{\nabla}\mu_\mathrm{c} = 0$, certainly justified for bulk systems in the linear response regime, the gradient of the electrochemical potential $\boldsymbol{\nabla}\mu$ is reduced to that of the electric potential, the electric field $\boldsymbol{E}$. If no other driving forces are present and the only response of interest is the electric current density $\boldsymbol{j}^c$, Eq. (2.130) is equivalent to Ohm's law,

$$\boldsymbol{j}^c = \underline{\boldsymbol{\sigma}}\boldsymbol{E} \quad \text{or} \quad \boldsymbol{E} = \underline{\boldsymbol{\rho}}\boldsymbol{j}^c \, , \tag{2.131}$$

with the conductivity or resistivity tensors, $\underline{\boldsymbol{\sigma}}$ and $\underline{\boldsymbol{\rho}}$, respectively. Their explicit shape is determined by the symmetry of the system (see Sections 2.3.4 and 3.3).

[19] That is sometimes called Onsager matrix, see, e.g., Ref. 26.

Going beyond this textbook example, the main focus of this work is to describe linear response phenomena connected with the driving forces electric field $\boldsymbol{E}$, temperature gradient $\boldsymbol{\nabla} T$, and the spin field $\underline{\boldsymbol{F}}^s$, and the resulting electric, heat, and spin current densities $\boldsymbol{j}^c$, $\boldsymbol{j}^q$, and $\underline{\boldsymbol{J}}^s$, respectively. The corresponding effects are usually classified as galvanic/electric when connected to $\boldsymbol{E}$ and thermal or using the prefix *thermo* when related to $\boldsymbol{\nabla} T$. If additional magnetic fields $\boldsymbol{B}$, external or internal (as for spontaneously magnetised materials) are present,[20] effects due this anisotropy are addressed with either a prefix *magneto* or the suffix *magnetic*. The names used for two of the main classes of phenomena that will be discussed in the following illustrate this terminology: galvanomagnetic phenomena are for example the anisotropic magnetoresistance [69, 70] (AMR) or the anomalous Hall effect [71, 73–75], thermomagnetoelectric or thermogalvanomagnetic effects such as the anisotropic magneto-Seebeck effect [87, 211, 212] or the anomalous Nernst effect [85, 90, 213–215] are their direct thermal analogues. Spin-related phenomena are usually termed spintronic when electric fields are the driving force and spingalvanic if they are the response, spincaloritronic effects finally encompass a wide range of $\boldsymbol{\nabla} T$-related phenomena (see Chapter 1). Unfortunately, the terminology is far from uniform throughout the literature though.

The investigation of transport phenomena will be limited to electrons or holes as carriers of charge, heat, and spin(-polarisation) in the present work. Phonons and magnons will merely be considered as additional sources of elastic scattering. Furthermore, as stated above, we restrict ourselves to stationary situations, i.e., only time-independent perturbations will be considered. Finally, it should be stressed that the application of linear response theory is of course not limited to the cases introduced above, besides the already mentioned external magnetic fields, also optical or pressure fields would be other common perturbations of interest, while induced magnetisation, magnetic torque, and light absorption are further responses.

2.3.1 Kubo's formalism

Kubo is the name usually associated with the correlation functions used to describe linear response phenomena. While Green [216, 217] was the first to derive a corresponding expression for transport in liquids[21] it was Kubo [219, 220] who first treated electrical conductivity in solids using the very general linear response formalism outlined below.

The expectation value of an arbitrary operator $\hat{A}$ in terms of the density matrix of a system in thermodynamic equilibrium,

$$\rho_0 = \frac{e^{-\beta \hat{H}_0}}{\mathrm{Tr}(e^{-\beta \hat{H}_0})} \,, \tag{2.132}$$

with $\beta = 1/(k_\mathrm{B} T)$ and $\hat{H}_0$ the Hamiltonian, is given by

$$\langle \hat{A} \rangle = \mathrm{Tr}(\rho_0 \hat{A}) \,. \tag{2.133}$$

[20] They are however not considered as driving force or response here, i.e., no electromagnetic or magnetoelectric effects will be discussed. Also the Shubnikov-de Haas effect, which denotes oscillations of the resistivity as a function of the strength of an external magnetic field, and related phenomena will not be considered here.

[21] Also Mori [218] should be at least mentioned here.

If a time-dependent perturbation $\hat{H}_1(t)$ is applied, the expectation value for the density matrix $\rho(t)$ is itself time-dependent:

$$\langle \hat{A} \rangle_t = \mathrm{Tr}(\rho(t)\hat{A}) \; . \tag{2.134}$$

The von Neumann equation describes the time-evolution of the density matrix,

$$i\hbar \frac{\partial \rho_I(t)}{\partial t} = [\hat{H}_{1,I}(t), \rho_I(t)] \; , \tag{2.135}$$

where both the perturbation and the density matrix have been transformed from the Schrödinger to the interaction picture indicated by the index I, via

$$X_I(t) = e^{i\hat{H}_0 t/\hbar} X(t) e^{-i\hat{H}_0 t/\hbar} \; , \tag{2.136}$$

which allows eliminating $\hat{H}_0$ in the commutator. Transforming back to the Schrödinger picture and integrating over time leads to

$$\rho(t) = \rho_0 - \frac{i}{\hbar} \int_{-\infty}^{t} dt' e^{-i\hat{H}_0(t-t')/\hbar} [\hat{H}_1(t'), \rho(t')] e^{i\hat{H}_0(t-t')/\hbar} \; , \tag{2.137}$$

where $\rho(t' = -\infty) = \rho_0$ represents the unperturbed system and $\rho(t)$ obviously depends on $\rho(t')$ at an earlier time $t' < t$. For small $\hat{H}_1$ it is justified to keep only the first term linear in $\hat{H}_1$ when inserting the r.h.s. repeatedly into itself,

$$\begin{aligned} \rho(t) \approx \tilde{\rho}(t) &= \rho_0 - \frac{i}{\hbar} \int_{-\infty}^{t} dt' e^{-i\hat{H}_0(t-t')/\hbar} [\hat{H}_1(t'), \rho_0] e^{i\hat{H}_0(t-t')/\hbar} \\ &= \rho_0 - \frac{i}{\hbar} \int_{-\infty}^{t} dt' e^{-i\hat{H}_0 t/\hbar} [\hat{H}_{1,I}(t'), \rho_0] e^{i\hat{H}_0 t/\hbar} \; . \end{aligned} \tag{2.138}$$

This leads for the expectation value in Eq. (2.134) to an expression that gives the response in an arbitrary operator only in terms of the commutator of the perturbation and the equilibrium density matrix:

$$\langle \hat{A} \rangle_t - \mathrm{Tr}(\rho_0 \hat{A}) = -\frac{i}{\hbar} \mathrm{Tr} \left(\int_{-\infty}^{t} dt' e^{-i\hat{H}_0 t/\hbar} [\hat{H}_{1,I}(t'), \rho_0] e^{i\hat{H}_0 t/\hbar} \hat{A} \right) \; . \tag{2.139}$$

Or equivalently that of the operators representing perturbation and response,

$$\begin{aligned} \langle \hat{A} \rangle_t - \langle \hat{A} \rangle &= -\frac{i}{\hbar} \int_{-\infty}^{t} dt' \left\langle [\hat{H}_{1,I}(t'), \hat{A}(t)] \right\rangle \\ &= \frac{i}{\hbar} \int_{-\infty}^{\infty} dt' \theta(t-t') \left\langle [\hat{H}_{1,I}(t'), \hat{A}_I(t)] \right\rangle \; , \end{aligned} \tag{2.140}$$

The expectation value in equilibrium, $\langle \hat{A} \rangle = \mathrm{Tr}(\rho_0 \hat{A})$, furthermore vanishes if there is no response in absence of $\hat{H}_1$.

In the following we are primarily interested in the response to an electric field

$$\boldsymbol{E}(t) = \boldsymbol{E}_0 e^{-i(\omega+i\delta)t} \,, \tag{2.141}$$

where the term $i\delta$ with $\delta \to 0^+$ ensures that the perturbation vanishes for $t \to -\infty$. The coupling to the system is described by the interaction

$$\hat{H}_1(t) = -\hat{\boldsymbol{P}}\boldsymbol{E}(t) \,, \tag{2.142}$$

where

$$\hat{\boldsymbol{P}} = \sum_{i=1}^{n} q_i \boldsymbol{r}_i \tag{2.143}$$

is the electric dipole operator. As will be demonstrated below, restricting for the moment the form of $\hat{H}_1(t)$ to Eq. (2.142) does not exclude the discussion of the response of a system to a temperature gradient.

The operator $\hat{A}$ in Eq. (2.139) may represent any observable of interest. In the case of charge transport as expressed in Eq. (2.131) one has for example $\hat{A} = \hat{\boldsymbol{j}}$, where $\hat{j}$ is the electric current density operator with the conductivity tensor as the corresponding response tensor. Another important example is spin transport with the corresponding spin current density operator $\hat{\underline{\boldsymbol{J}}}$ that is obviously a second rank tensor operator. The explicit form of $\hat{\underline{\boldsymbol{J}}}$ has been controversially discussed in the literature [221–224]. It has been stressed in particular that a simple combination of the Pauli spin operator $\hat{\boldsymbol{\sigma}}$ with the electric current density operator does not fulfil an associated continuity equation. Here we use the approach suggested by Vernes *et al.* [222] that focuses on the spin polarisation with the corresponding relativistic spin-polarisation current density operator [221–224]

$$\hat{\boldsymbol{J}}^{\xi} = \left(\beta\Sigma_{\xi} - \frac{\gamma_5\Pi_{\xi}}{mc}\right) ec\boldsymbol{\alpha} \,, \tag{2.144}$$

with the usual definition of the Dirac matrices (see Section 2.2.2), the kinetic momentum $\boldsymbol{\Pi} = (\hat{\boldsymbol{p}} + e/c\boldsymbol{A})I_4$, the canonical momentum $\hat{\boldsymbol{p}}$, and the vector potential $\boldsymbol{A}$. Σ_{ξ} is the 4×4 matrix resulting from the outer product of the 2×2 Pauli matrices σ_{ξ} and I_2, where ξ signifies the direction of polarisation of the spin current.

Apart from the two possibilities for the operator $\hat{A}$ just mentioned in particular two other responses to an electric field have been studied within this thesis. With $\hat{A} = \hat{\boldsymbol{T}}$ the magnetic torque operator one gets access to the so-called spin-orbit torque, while $\hat{A} = \hat{\boldsymbol{m}}$ for the spin magnetisation allows discussion of the Edelstein or inverse spin-galvanic effect. Both phenomena will be the subject of Section 3.5. The shape of the tensors arising from, in principle, arbitrary combinations of operators for perturbation and response will be the subject of Section 2.3.4. In the following we will replace $\hat{A}$ by $\hat{\mathbf{J}}$ without loss of generality.

The next steps to proceed from Eq. (2.139), see, e.g., Ref. 225, lead to the so-called Kubo equation

$$\sigma_{\mu\nu} = V \int_0^{(k_\mathrm{B}T)^{-1}} d\lambda \int_0^{\infty} dt \mathrm{Tr}\left(\rho_0 \hat{j}_\nu \hat{J}_{\mu,I}(t + i\hbar\lambda)\right) e^{i(\omega+i\delta)t} \,, \tag{2.145}$$

that gives the response function, here a conductivity tensor element, in terms of an operator-operator correlation function with $\hat{A} = \hat{\mathbf{J}}$ and $\hat{B} = \hat{\mathbf{j}}$ representing the

perturbation. V is the volume of the system and λ corresponds to a complex time variable [226].

Restricting to the static case ($\omega = 0$) and adopting the independent particle picture one arrives at

$$\sigma_{\mu\nu} = \frac{1}{V} \int_0^{(k_B T)^{-1}} d\lambda \int_0^{\infty} dt \sum_{n,m} \Big\langle e^{-\lambda(E_n - E_m)} f(E_m)\,[1 - f(E_n)]\, e^{it/[\hbar(E_n - E_m + i\hbar\delta)]} \langle m \,|\, \hat{j}_\nu \,|\, n \rangle \langle n \,|\, \hat{J}_\mu \,|\, m \rangle \Big\rangle_c , \tag{2.146}$$

where $f(E) = \left(e^{(E-\mu_c)/(k_B T)} + 1\right)^{-1}$ is the Fermi-Dirac distribution function and μ_c the chemical potential. The angular brackets imply a configurational average over all possible combinations of occupation of alloy sites where perturbation and response are acting. Evaluation of the integrals w.r.t. λ and t leads to the expression

$$\sigma_{\mu\nu} = \frac{i\hbar}{V} \sum_{n,m} \left\langle \frac{f(E_m) - f(E_n)}{(E_n - E_m)(E_n - E_m + i\hbar\delta)} \langle m \,|\, \hat{j}_\nu \,|\, n \rangle \langle n \,|\, \hat{J}_\mu \,|\, m \rangle \right\rangle_c . \tag{2.147}$$

Making use of the definition of the Green function operator $\hat{G}^{\pm}(E) = (E - \hat{H} \pm i\varepsilon)^{-1}$ one finally arrives at the Kubo-Bastin formula [227]

$$\sigma_{\mu\nu} = \frac{i\hbar}{V} \int_{-\infty}^{\infty} dE\, f(E)\, \mathrm{Tr} \left\langle \hat{J}_\mu \frac{dG^+(E)}{dE} \hat{j}_\nu\, \delta(E - \hat{H}) - \hat{J}_\mu\, \delta(E - \hat{H})\, \hat{j}_\nu \frac{dG^-(E)}{dE} \right\rangle_c . \tag{2.148}$$

For practical applications the form (omitting the energy argument of $G^{\pm}(E)$ for simplicity)

$$\sigma_{\mu\nu} = \sigma^I_{\mu\nu} + \sigma^{II}_{\mu\nu} \tag{2.149}$$

$$\sigma^I_{\mu\nu} = -\frac{\hbar}{4\pi V} \int_{-\infty}^{\infty} dE\, \frac{df(E)}{dE}\, \mathrm{Tr} \left\langle \hat{J}_\mu\, (G^+ - G^-)\, \hat{j}_\nu\, G^- - \hat{J}_\mu\, G^+\, \hat{j}_\nu\, (G^+ - G^-) \right\rangle_c \tag{2.150}$$

$$\sigma^{II}_{\mu\nu} = \frac{\hbar}{4\pi V} \int_{-\infty}^{\infty} dE\, f(E)\, \mathrm{Tr} \left\langle \hat{J}_\mu\, G^+\, \hat{j}_\nu \frac{dG^+}{dE} - \hat{J}_\mu \frac{dG^+}{dE} \hat{j}_\nu\, G^+ - \hat{J}_\mu\, G^-\, \hat{j}_\nu \frac{dG^-}{dE} + \hat{J}_\mu \frac{dG^-}{dE} \hat{j}_\nu\, G^- \right\rangle_c \tag{2.151}$$

of the Kubo-Bastin formula is most convenient. It is obtained, following Crépieux and Bruno [228], by splitting the integrand of Eq. (2.148) in two parts and doing a partial integration on one half. The δ functions, that have been replaced by differences of retarded and advanced Green functions, of course cause numerical problems when integrating, but this can be facilitated by going into the complex energy plane.[22] Nevertheless, Eq. (2.149) implies that in the most general case one has contributions to transport not only from electrons in the vicinity of the Fermi level (Fermi surface contribution) but also from all other occupied states (Fermi sea

[22] Details on the implementation can be found in Ref. 229.

contribution). For the case that the perturbation and the observable are represented by the same operator, as for the electrical conductivity, one can simplify Eq. (2.149) for the athermal limit to the so-called Kubo-Středa equation [230]

$$\begin{aligned}\sigma_{\mu\nu} &= \frac{\hbar}{4\pi V}\mathrm{Tr}\langle\hat{j}_\mu(G^+ - G^-)\hat{j}_\nu G^- - \hat{j}_\mu G^+\hat{j}_\nu(G^+ - G^-)\rangle_c \\ &\quad + \frac{e}{4\pi i V}\mathrm{Tr}\langle(G^+ - G^-)(\hat{r}_\mu\hat{j}_\nu - \hat{r}_\nu\hat{j}_\mu)\rangle_c \,, \end{aligned} \tag{2.152}$$

where $\hat{\boldsymbol{J}}$ has been replaced by $\hat{\boldsymbol{j}}$. Here only electrons at the Fermi surface are contributing to the transport, making evaluation of $\sigma_{\mu\nu}$ much simpler. Restricting finally to the symmetric part of the electrical conductivity tensor one arrives at the Kubo-Greenwood equation [231]:

$$\sigma_{\mu\nu} = \frac{i\hbar}{2\pi V}\mathrm{Tr}\langle\hat{j}_\mu \mathrm{Im}G^+\hat{j}_\nu \mathrm{Im}G^+\rangle_c \,. \tag{2.153}$$

Applications of Eqs. (2.148), (2.152), and (2.153) using multiple scattering theory started with the work of Butler [232]. This author worked out in particular an implementation for disordered alloys within the framework of the CPA. His approach led to a clear prescription to deal with the so-called *vertex corrections* that arise from an incomplete configurational average over the product of two Green functions. These play a central role for many response functions of magnetic as well as non-magnetic solids, in particular in the case of anti-symmetric tensor elements. After the non-relativistic implementation of the Kubo-Greenwood equation by Butler and co-workers, Banhart worked out its fully relativistic counterpart for non-magnetic solids [233, 234]. This was followed by a corresponding implementation for magnetic systems by Banhart and Ebert [235]. The full conductivity tensor on the basis of the Kubo-Středa equation was calculated by Lowitzer *et al.* [236], while the Kubo-Bastin equation was finally implemented by Ködderitzsch *et al.* [237]. Similar work was done on the basis of the LMTO method by Turek and co-workers [238, 239].

As this thesis is focusing to a great extent on linear responses to a thermal gradient, the question of how such phenomena can be described within the framework just outlined arises naturally. Luttinger [240] for example points out, that this is not as straightforward as in the electrical case since there is no Hamiltonian that describes a gradient of the temperature – it is a statistical property of the system. To get access to the thermal conductivity this author introduces a gravitational field as the source for energy and heat currents, and then uses an analogue of the Einstein relation [241] to connect the obtained diffusion coefficient to the thermal conductivity. Deo and Behera [242] shortly afterwards gave a corresponding expression in the language of Green functions. In the present work, however, phenomena induced by a temperature gradient will be exclusively dealt with on the basis of the Mott formula [243] and its generalisations [244, 245]. As will be outlined in Sections 2.3.2 and 2.3.3, this way all[23] thermoelectric (spincaloritronic) and thermal transport coefficients can be, under certain assumptions, obtained from the electrical (spin) conductivity.

The symmetry and interrelation of response tensors whose elements can be expressed by a Kubo formula as in Eq. (2.145) with, in principle, arbitrary pairs (or even triples) of operators will be the subject of Section 2.3.4.

[23] This is slightly exaggerated, as will be discussed in Section 2.3.4.

2.3.2 Thermo(magneto)electric transport

The history of thermoelectrics can be said to have begun almost two centuries ago with the experiments of Seebeck [86, 246]. As the title *Magnetische Polarisation der Metalle und Erze durch Temperatur-Differenz* (Magnetic Polarisation of Metals and Ores by a Temperature Difference) clearly indicates, he interpreted his results as a thermomagnetic effect, as the observable was the magnetic field induced by the electric current that arose from the temperature difference applied to his metallic samples.[24] The inverse phenomenon, a temperature difference induced by an applied electric field, was shortly afterwards reported by Peltier [88]. William Thomson (Lord Kelvin) predicted and observed an effect closely related to the two just mentioned, the Thomson effect describing the reversible (i.e., not Joule) heating of a conductor by a temperature gradient [247]. In 1953, Wiedemann and Franz [248] reported that *die Metalle für Elektricität und Wärme eine nahezu gleiche Leitungsfähigkeit besitzen* (metals have almost the same electrical and thermal conductivity), which is nowadays known as the Wiedemann-Franz law.

The first observation of a truly thermomagnetoelectric effect, in the sense of being inherently dependent on either an external magnetic field or the internal magnetisation, was by von Ettingshausen and Nernst [85]. They observed a transversal, i.e., perpendicular to the applied temperature difference, *thermomagnetic* current in a Bi sample when a magnetic field was applied perpendicular to both. This effect is commonly termed Nernst effect or first (von-)Ettingshausen-Nernst effect[25] and can be explained in terms of a Lorentz force that laterally deflects the carriers moving in parallel to the electromotive force generated by the Seebeck effect. If the role of the externally applied magnetic field is taken over by the internal magnetisation of a, say, ferromagnet, the term *anomalous Nernst effect* (ANE) will be employed herein. The first clear observation of the ANE can be attributed to Ky [249]. The inverse phenomenon, the occurrence of a transversal heat current in response to an electric field is called either Ettingshausen or second (von-)Ettingshausen-Nernst effect, in reference to (the first of) the two discoverers of the direct effect, who however did not make a corresponding observation themselves. Most likely Hall and Campbell [82] can be credited with its discovery.

Von Ettingshausen and Nernst did however also observe a longitudinal thermoelectric effect that depended on the strength but apparently not the direction of the magnetic field. This effect, sometimes called longitudinal Nernst-Ettingshausen effect[26], that will be referred to in this thesis as anisotropy of the Seebeck effect (ASE), unfortunately has been given various names throughout the literature. The one most often used by experimentalists is probably *planar Nernst effect* (PNE) [87, 251], in reference to the planar Hall effect that is itself an unnecessary renaming of the anisotropic magnetoresistance, of which the ASE/PNE is the thermoelectric analogue. It might have been first observed by Hall and Campbell [82], who express it as *longitudinal thermomagnetic potential-difference* and unsuccessfully tried to also

[24] One should not forget that at this time electromagnetism was *in statu nascendi*.

[25] Author names appear often reversed.

[26] See for example the Ph.D. thesis of Demars [250], which contains an instructive overview over thermoelectric, thermomagnetic (thermoelectric and thermal effects in magnetic materials or in presence of an applied magnetic field), and galvanomagnetic effects. Another concise overview can be found in the book by Callen [210].

measure its reciprocal *longitudinal electromagnetic temperature-difference*. In analogy to the A(M)SE this just recently confirmed effect has been called anisotropic magneto-Peltier effect (AMPE) [89]. To avoid confusion with the reciprocal of the magneto-Seebeck effect (see below), the prefix *magneto* will be omitted herein.

In analogy to the AMR-like ASE there are of course thermoelectric versions of the GMR effect and related phenomena in 2D systems composed of alternating magnetic and non-magnetic layers, possibly including insulating tunnel barriers (magnetic tunnel junctions, MTJ). These effects, commonly termed (anisotropic) magneto-thermo(electric)power or -Seebeck effect ((A)MTEP) [98, 252], that is related to the MTGV observed by Gravier *et al.* [253], or tunnelling (anisotropic) magneto-Seebeck effect (TMS [18], TAMS [99]), will however, as well as their reciprocals like the (tunnelling) magneto-Peltier effect [101, 254] or a yet to be discovered anisotropic magneto-Peltier effect, not be discussed further here.

To complete this phenomenological overview one has to also mention the class of thermomagnetic effects that encompass in particular the (Righi-)Leduc effect (RLE) [81] that is rightfully often referred to as *thermal Hall effect*, and the Maggi-Righi-Leduc effect (MRLE), correspondingly the *thermal AMR*, which is also sometimes called planar Righi-Leduc effect [255]. Again it might have been observed for the first time already by Hall and Campbell [82], as a *longitudinal thermomagnetic temperature-difference*, although their experimental results were not fully conclusive. Literature on this subject is in general rather scarce. For an overview over these and the aforementioned thermomagnetoelectric effects see, e.g., Ref. 250 or the recent review by Boona *et al.* [25] which includes also spincaloritronic phenomena that will be the subject of Section 2.3.3.

The theoretical treatment of thermoelectrics, although for example also Sommerfeld [256] made an important contribution[27], is inseparable from the name Mott. His derivation of the eponymous Mott formula for the thermoelectric power [243] will be reviewed in some detail in Section 2.3.2.2. It gives a connection between the energy derivative of the electrical conductivity at the Fermi level and the electron diffusion contribution to the TEP or Seebeck effect. Still nowadays, this is the most popular approach to thermoelectrics due to its simplicity and considerably wide range of applicability. More on the shortcomings and possible extensions or generalisations of Mott's expression will be presented below and towards the end of this chapter (see Sections 2.3.2.3, 2.3.3, and 2.3.4). Similar expressions for transverse thermomagnetoelectric (ANE and AEE) and thermal effects (RLE) were given by Sondheimer [258].

A first derivation of the Wiedemann-Franz law was given in terms of the Boltzmann transport theory by Kohler [259], who also made important contributions towards an understanding of the role of defects and their interactions [260]. The so-called Nordheim-Gorter rule [261] can be loosely termed a *Matthiessen's rule for the thermoelectric power*, because of being based on it and because it allows expressing the total TEP due to several scattering mechanisms as a combination of individual contributions. Of course this is a rule based on several assumptions, the most important of which is clearly the same as for Matthiessen's rule: the impurity concentrations have to be close to the dilute limit, for which these have accordingly been devised. Another central work in the theory of thermally induced transport is that by Chester

[27] See also Ref. 257.

and Thellung [244], who proved, on the basis of Kubo's linear response theory and using a wave-function formulation, the Wiedemann-Franz law to be valid for independent electrons interacting with impurities and lattice vibrations, regardless of the interaction strength. Jonson and Mahan [245] later confirmed their findings using a Green function formulation and made corresponding statements also for the Mott formula. As Ref. 245 served as an important basis for this work it will be reviewed in greater detail below (Sections 2.3.2.1 and 2.3.2.3). Only one aspect shall be briefly highlighted here, namely the importance of the formulation chosen for the heat current operator entering the Kubo formulae describing thermal processes. This to some extent still open issue has already been tackled by Luttinger [240] in his work on the thermal conductivity, invoking an analogy of the temperature gradient with that of a gravitational field. This issue, briefly mentioned before, will be picked up at a later time. In this context the interested reader is also referred to a later work by Jonson and Mahan [262] and to references therein.

First actual calculations of thermoelectric coefficients in alloys using the coherent potential approximation have been performed presumably by Levin *et al.* [263], the first KKR-CPA work is that of Butler and Stocks [264], who used the Boltzmann transport equation based on the *band structure* of disordered AgPd alloys represented by the Bloch spectral function. Among the first to employ Kubo's linear response formalism in this context, to be precise the Kubo-Greenwood equation [Eq. (2.153)], were Banhart and Ebert [265].

The first-principles description of thermomagnetoelectric (and later on spincaloritronic) transport phenomena within the framework of the KKR-CPA, that is presented in this thesis starts from the phenomenological transport equations as summarised in Eq. (2.130). This set of equations allows dealing simultaneously with the response to gradients of the electrochemical potential $\mu = \mu_{\mathrm{c}} + q\phi$ with the chemical potential μ_{c} , the charge q ($-|e|$ for electrons), and the electric potential ϕ, of the temperature, $\boldsymbol{\nabla} T$, and of the spin-polarised chemical potential μ^s, represented by $\underline{\boldsymbol{F}}^s$. Neglecting spin transport for the moment, one may write for the induced current densities of charge and heat:

$$\boldsymbol{j}^c = -\underline{\boldsymbol{L}}^{cc}\boldsymbol{\nabla}\mu - \underline{\boldsymbol{L}}^{cq}\boldsymbol{\nabla}T/T \tag{2.154}$$

$$\boldsymbol{j}^q = -\underline{\boldsymbol{L}}^{qc}\boldsymbol{\nabla}\mu - \underline{\boldsymbol{L}}^{qq}\boldsymbol{\nabla}T/T \; . \tag{2.155}$$

The various response functions occurring here may be expressed by the corresponding conductivities according to the *generalised* Mott relations [243, 245, 266, 267]:

$$L^{cc}_{\mu\nu}(T) = -\frac{1}{|e|}\int dE\, \sigma^{(cc)}_{\mu\nu}(E)\left(-\tfrac{\partial f(E,T)}{\partial E}\right) \tag{2.156}$$

$$L^{cq}_{\mu\nu}(T) = -\frac{1}{|e|}\int dE\, \sigma^{(cc)}_{\mu\nu}(E)\left(-\tfrac{\partial f(E,T)}{\partial E}\right)(E - E_F) \tag{2.157}$$

$$L^{qq}_{\mu\nu}(T) = -\frac{1}{|e|}\int dE\, \sigma^{(cc)}_{\mu\nu}(E)\left(-\tfrac{\partial f(E,T)}{\partial E}\right)(E - E_F)^2 \; . \tag{2.158}$$

Here the superscripts c and q again denote the nature of response and perturbation, charge- or heat-related. Note that for each heat current density involved in the process an energy factor $(E - E_{\mathrm{F}})$ appears in the integrand. For the materials and temperature ranges considered in this thesis, E_{F} and μ_{c} can be assumed to be

identical [268]. In the following the temperature argument of the response functions will usually be omitted for brevity. The tensor $\underline{\boldsymbol{L}}^{qc}$ describing the heat current or temperature gradient in response to an electric current or field, related to the reciprocals or time-reversed counterparts of the Seebeck and (anomalous) Nernst effects, the Peltier and the (anomalous) Ettingshausen[28] effect, respectively, is, in part, accessible via its (Onsager) relation to $\underline{\boldsymbol{L}}^{cq}$ (see Section 2.3.4).

Unfortunately there are numerous different formulations of phenomenological equations like Eqs. (2.154) and (2.155) and the corresponding response functions or kinetic coefficients describing charge and heat transport used in the literature. The next section gives an overview over the different approaches, providing relations interconnecting the various notations.

2.3.2.1 Alternative formulations of kinetic coefficients

The transport of charge and heat in response to an electric field and/or a gradient of the temperature as expressed by the spin-independent part of Eq. (2.130) (i.e., the first two rows without the third column of the Onsager matrix) has been discussed by many authors. In the following the most commonly used definitions for response functions are reviewed. Their differences and, if present, shortcomings are highlighted and conversion prescriptions to connect them are given. In order to introduce the general concepts and terminology a short introduction into irreversible thermodynamics is necessary.

Irreversible thermodynamics

The extension to irreversible processes by Onsager [205, 206] has been such a fundamental advancement of thermodynamics that his *reciprocal relations* are sometimes referred to as its fourth law. They relate the *flows* which occur in a system to the *forces* that are responsible in a very general manner under the assumption of microscopic reversibility. Another seminal contribution to the field is the work of Callen and Welton [269], whose *fluctuation-dissipation theorem* relates, on a statistical-mechanical basis, the fluctuations of an equilibrium property of a system with a parameter that characterises an irreversible process. Based on this, first and foremost Kubo [109, 219, 220] developed what is nowadays known as linear response theory.

Following Callen [210] (see also Refs. 243, 270 and 208), we consider a closed system consisting of two parts and an extensive parameter taking the values X_k and X'_k in those subsystems, their sum $X_k + X'_k = c$ being constant. The equilibrium values of the two are then determined by the condition

$$\mathcal{F}_k \equiv \left(\frac{\partial S^\circ}{\partial X_k}\right)_{X_k^\circ} = \left(\frac{\partial (S + S')}{\partial X_k}\right)_{X_k^\circ} = \frac{\partial S}{\partial X_k} - \frac{\partial S'}{\partial X'_k} = F_k - F'_k \stackrel{!}{=} 0 \,, \tag{2.159}$$

for the partial derivatives of the equilibrium entropy S°. Accordingly if the difference of the two intensive parameters F_k and F'_k is non-zero, an irreversible process will

[28] Or second Nernst-Ettingshausen effect, see Chapter 1.

bring the system into equilibrium. This process is said to be driven by the *generalised force* or *affinity* $\mathcal{F}_k$. For example if X_k is the internal energy U then the affinity is

$$\mathcal{F}_k = \frac{\partial S}{\partial U} - \frac{\partial S'}{\partial U'} = \frac{1}{T} - \frac{1}{T'} \tag{2.160}$$

and heat will flow from one subsystem to the other until the difference in inverse temperature vanishes. In general such a *flux* is defined by the rate of change of the extensive parameter,

$$J_k \equiv \frac{dX_k}{dt} \ . \tag{2.161}$$

Fluxes and affinities are complementary or *conjugated* entities, one is defined by the other, and their relationship determines the rates of irreversible processes.
A useful strategy to find the relevant affinities in a system is to consider the rate of entropy production

$$\dot{S} = \frac{dS}{dt} = \sum_k \frac{\partial S}{\partial X_k}\frac{dX_k}{dt} = \sum_k \mathcal{F}_k J_k \ , \tag{2.162}$$

which is a sum over all fluxes multiplied by the associated affinities.
This approach is in particular also applicable to continuous systems out of equilibrium, where the local entropy $S(X_0, X_1, ...)$ is assumed to have the same dependence on the extensive parameters as in equilibrium. Then

$$dS = \sum_k F_k \, dX_k \tag{2.163}$$

with the local intensive parameters F_k also taken to have the same functional dependence on the extensive parameters as in equilibrium. This is in fact what allows defining a continuously varying temperature in a sample, despite temperature strictly being an equilibrium property.
Assuming now a Markovian system in the sense of local fluxes depending only on local affinities present at the same time, one can expand the fluxes J_k in powers of affinities,

$$J_k = \sum_j L_{kj}\mathcal{F}_j + \frac{1}{2!}\sum_i\sum_j L_{kji}\mathcal{F}_j\mathcal{F}_i + ... \ , \tag{2.164}$$

where

$$L_{kj} = \left(\frac{\partial J_k}{\partial \mathcal{F}_j}\right)_0 \tag{2.165}$$

and

$$L_{kji} = \left(\frac{\partial^2 J_k}{\partial \mathcal{F}_j \partial \mathcal{F}_i}\right)_0 \tag{2.166}$$

are called first and second order kinetic coefficients. Both as well as of course all higher orders are functions of the local intensive parameters, for example of an external magnetic field $\boldsymbol{H}$. Neglecting all other intensive parameters this functional dependence obeys for example in non-magnetic systems the symmetry relation

$$L_{jk}(\boldsymbol{H}) = L_{kj}(-\boldsymbol{H}) \tag{2.167}$$

for the linear effects, which is nothing but the famous Onsager reciprocal relation. All phenomena of interest to this thesis can be assumed to depend linearly on the perturbation, that is quadratic and higher order terms in Eq. (2.164) are negligible, since the deviations from equilibrium are small when considering commonly applied voltages and temperature gradients in transport experiments.

Kubo *et al.* & Kleiner

The phenomenological electronic charge and heat transport equations in the notation used by Kleiner [271] based on earlier work of Kubo *et al.* [109] read

$$\boldsymbol{j} = \underline{\boldsymbol{S}}^{(1)}(\boldsymbol{H})\ (\boldsymbol{E} + T/e\boldsymbol{\nabla}\zeta) + \underline{\boldsymbol{S}}^{(2)}(\boldsymbol{H})\ \frac{1}{T}\boldsymbol{\nabla}T \tag{2.168}$$

$$\boldsymbol{q} = -\underline{\boldsymbol{S}}^{(3)}(\boldsymbol{H})\ (\boldsymbol{E} + T/e\boldsymbol{\nabla}\zeta) - \underline{\boldsymbol{S}}^{(4)}(\boldsymbol{H})\ \frac{1}{T}\boldsymbol{\nabla}T, \tag{2.169}$$

with the elementary charge $e = |e|$, the external magnetic field $\boldsymbol{H}$, and the temperature T. The response currents or *fluxes/flows* in the language of irreversible thermodynamics are the electric current density $\boldsymbol{j}$ and the heat current density $\boldsymbol{q}$. The first *generalised force* or *affinity* in Eqs. (2.168) and (2.169) is the combination of an electric field $\boldsymbol{E}$ and the gradient of a reduced chemical potential $\zeta = \varsigma/T$, i.e., altogether the gradient of the electrochemical potential $\mu = \varsigma - e\phi$ (with ϕ the electric potential) divided by e, $\frac{1}{e}\boldsymbol{\nabla}\mu$. The second generalised force is the temperature gradient $\boldsymbol{\nabla}T$ divided by T, $\frac{1}{T}\boldsymbol{\nabla}T$. The kinetic coefficients $\underline{\boldsymbol{S}}^{(n)}$ with $n = 1...4$ that linearly relate fluxes and forces are tensors of rank two. Eqs. (2.168) and (2.169) can be brought into a more convenient matrix form

$$\begin{pmatrix} \boldsymbol{j} \\ \boldsymbol{q} \end{pmatrix} = \begin{pmatrix} \underline{\boldsymbol{S}}^{(1)}(\boldsymbol{H}) & \underline{\boldsymbol{S}}^{(2)}(\boldsymbol{H}) \\ -\underline{\boldsymbol{S}}^{(3)}(\boldsymbol{H}) & -\underline{\boldsymbol{S}}^{(4)}(\boldsymbol{H}) \end{pmatrix} \begin{pmatrix} \frac{1}{e}\boldsymbol{\nabla}\mu \\ \frac{1}{T}\boldsymbol{\nabla}T \end{pmatrix}. \tag{2.170}$$

Kinetic coefficients or response functions such as the $\underline{\boldsymbol{S}}^{(n)}$ can be most generally expressed by means of the Kubo formula

$$\tau_{B_\mu A_\nu}(\omega, \boldsymbol{H}) = \int_0^\infty dt\, e^{-i\omega t} \int_0^\beta d\lambda\, \mathrm{Tr}\rho(\boldsymbol{H})\, A_\nu B_\mu(t + i\hbar\lambda; \boldsymbol{H}), \tag{2.171}$$

where B_μ is a Cartesian component of the operator for the response observable in the Heisenberg picture, $B_\mu(t; \boldsymbol{H}) = e^{iH(\boldsymbol{H})t/\hbar} B_\mu e^{-iH(\boldsymbol{H})t/\hbar}$, and A_ν one of the perturbation operator ($t = 0$), ω is the frequency of the external electric field, $\boldsymbol{H}$ an (optional) external magnetic field, t is the time, $\beta = 1/(k_\mathrm{B}T)$, λ is essentially the complex time, and $\rho(\boldsymbol{H}) = e^{-\beta H(\boldsymbol{H})}/\mathrm{Tr}e^{-\beta H(\boldsymbol{H})}$ is the equilibrium density operator of the canonical ensemble in the presence of $\boldsymbol{H}$. The trace in Eq. (2.171) represents the thermal average of the operator product w.r.t. the canonical distribution.
In the dc limit ($\omega = 0$) and for $\{A, B\} = \{\boldsymbol{j}, \boldsymbol{q}\}$, one obtains

$$S^{(n)}_{\mu\nu}(\boldsymbol{H}) = \int_0^\infty dt \int_0^\beta d\lambda \langle A_\nu B_\mu(t + i\hbar\lambda; \boldsymbol{H})\rangle\ , \tag{2.172}$$

where the angular brackets indicate the thermal average. $\underline{\boldsymbol{S}}^{(1)}$ is the response function tensor for the case $\boldsymbol{A} = \boldsymbol{B} = \boldsymbol{j}$, which is nothing but the electrical conductivity tensor $\boldsymbol{\sigma}$, for $\boldsymbol{A} = \boldsymbol{q}$ and $\boldsymbol{B} = \boldsymbol{j}$, $\underline{\boldsymbol{S}}^{(2)}$ is obviously related to the Seebeck effect, while for $\boldsymbol{A} = \boldsymbol{j}$ and $\boldsymbol{B} = \boldsymbol{q}$ the coefficient $\underline{\boldsymbol{S}}^{(3)}$ describes the reciprocal Peltier effect, finally for the case $\boldsymbol{A} = \boldsymbol{B} = \boldsymbol{q}$, $\underline{\boldsymbol{S}}^{(4)}$ is in essence the electronic thermal conductivity tensor. Kubo *et al.* [109] try to make an explicit connection between the $\underline{\boldsymbol{S}}^{(n)}$ and more familiar transport coefficients electrical resistivity ρ, the heat conductivity κ,

the absolute thermoelectric power per unit temperature difference $-\mathcal{S}/e$, and the Peltier coefficient π. This is done by rewriting Eqs. (2.168) and (2.169) as

$$\boldsymbol{E} = \underline{\boldsymbol{\rho}}\boldsymbol{j} - \frac{1}{e}\mathcal{S}\boldsymbol{\nabla}T - \frac{1}{e}\boldsymbol{\nabla}\zeta \tag{2.173}$$

$$\boldsymbol{q} = \underline{\boldsymbol{\pi}}\boldsymbol{j} - \underline{\boldsymbol{\kappa}}\boldsymbol{\nabla}T + \frac{1}{T}\zeta\boldsymbol{j}, \tag{2.174}$$

with

$$\underline{\boldsymbol{\rho}} = [\underline{\boldsymbol{S}}^{(1)}]^{-1} \tag{2.175}$$

$$\underline{\boldsymbol{\mathcal{S}}} = (e\underline{\boldsymbol{\rho}}\underline{\boldsymbol{S}}^{(2)} - \zeta)/T \tag{2.176}$$

$$\underline{\boldsymbol{\pi}} = -\underline{\boldsymbol{S}}^{(3)}\underline{\boldsymbol{\rho}} - \zeta/T \tag{2.177}$$

$$\underline{\boldsymbol{\kappa}} = (\underline{\boldsymbol{S}}^{(4)} - \underline{\boldsymbol{S}}^{(3)}\underline{\boldsymbol{\rho}}\underline{\boldsymbol{S}}^{(2)})/T\,. \tag{2.178}$$

Unfortunately, there appear to be two misprints in Ref. 109 (see appendix A.1), that have been corrected here. Moreover, the chemical potential is usually assumed to be constant and therefore in general does not appear explicitly in the coefficients. In case of the Peltier coefficient this is an unnecessary complication, most likely meant to obtain a similar structure as the reciprocal $\mathcal{S}$. Presumably for these reasons Kleiner [271] did not give similar explicit expressions.

The Onsager relations [205, 206], valid for the non-magnetic case (or only for the symmetric part of the tensor in the magnetic case), can be expressed as $S^{(1)}_{\mu\nu}(\boldsymbol{H}) = S^{(1)}_{\nu\mu}(-\boldsymbol{H})$, $S^{(4)}_{\mu\nu}(\boldsymbol{H}) = S^{(4)}_{\nu\mu}(-\boldsymbol{H})$, and $\underline{\boldsymbol{S}}^{(2)}(\boldsymbol{H}) = (\underline{\boldsymbol{S}}^{(3)}(-\boldsymbol{H}))^T$. The first two are termed Onsager relations of the first kind, while the last one, connecting time-reversed phenomena, is of the second kind.[29] Here it is a generalisation of the Kelvin relation $TS = \pi$, where S is the thermoelectric or Seebeck coefficient (denoted α in Ref. 271) and π the Peltier coefficient. At least at this stage the additional terms ζ/T have to be dropped however. It should be noted that these relations are certainly also valid in the ac case, i.e., for $\omega \neq 0$. For the anti-symmetric part of $\underline{\boldsymbol{S}}^{(1)}$ in a magnetic material a slightly modified relation holds, $S^{(1),a}_{\mu\nu}(\boldsymbol{H}) = -S^{(1),a}_{\nu\mu}(-\boldsymbol{H})$ (see, e.g., Ref. 219). Furthermore relations for the full, that is symmetric and anti-symmetric, optical conductivity tensor at finite frequency,

$$\mathrm{Re}\,\sigma_{\mu\nu}(\omega, \boldsymbol{H}) = \mathrm{Re}\,\sigma_{\mu\nu}(-\omega, \boldsymbol{H}) \tag{2.179}$$

$$\mathrm{Im}\,\sigma_{\mu\nu}(\omega, \boldsymbol{H}) = -\mathrm{Im}\,\sigma_{\mu\nu}(-\omega, \boldsymbol{H}) = \mathrm{Im}\,\sigma_{\nu\mu}(\omega, -\boldsymbol{H}). \tag{2.180}$$

have been given by Kubo [219, 220].

Jonson and Mahan

In the notation used by Jonson and Mahan [245, 262], which derives from Barnard's work [272] and that was adapted and extended to spincaloritronics by the present author [266, 267], the thermoelectric equations read [245]

$$j_\alpha = L^{11}_{\alpha\beta}\,[-(1/T)\nabla_\beta(\mu + eV)] + L^{12}_{\alpha\beta}\,\nabla_\beta(1/T)] \tag{2.181}$$

$$j_{Q,\alpha} = L^{21}_{\alpha\beta}\,[-(1/T)\nabla_\beta(\mu + eV)] + L^{22}_{\alpha\beta}\,\nabla_\beta(1/T)] \tag{2.182}$$

[29] This will be discussed extensively in Section 2.3.4.

with $e = -|e|$ the electronic charge[30], T the temperature, and no external magnetic field considered. The above-mentioned authors assume electrons interacting only with static impurities and phonons treated in the adiabatic approximation. Concerning the symmetry relations of the coefficients, this is however irrelevant.

The fluxes or response quantities in Eqs. (2.181) and (2.182) are the *electrical*[31] current $\boldsymbol{j}$ and the thermal current $\boldsymbol{j}_Q$, the subscript α stands for the Cartesian component. The misleading notation of vector symbol combined with a subscript, that has not been taken over here, has no further consequences since all response tensors are later on assumed to be isotropic. The conjugated generalised forces or perturbations are the gradients of the sum of the chemical potential μ plus eV, where V is the electrostatic potential, and of the inverse temperature $(1/T)$, respectively. Again β signifies a Cartesian component of the gradients. The frequency-dependent coefficients or response functions are most generally written as

$$L^{ij}(i\omega) = -\frac{iT}{(i\omega)\, d\, \Omega} \int_0^\beta d\tau e^{i\omega\tau} \langle T_\tau j_i(\tau) j_j(0) \rangle \ , \tag{2.183}$$

with now $i, j = 1, 2$ indexing the type of response and perturbation, respectively, according to Eqs. (2.181) and (2.182), the frequency ω, dimensionality d, volume Ω, $\beta = 1/k_\mathrm{B}T$, and T_τ being the time-ordering operator for the complex time τ. Furthermore, the Cartesian indices have been dropped as an isotropic material is assumed from now on.

For independent electrons with scattering on static impurities and phonons treated in the adiabatic approximation one obtains by analytical continuation for the $\omega \to 0$ limit

$$L^{ij} = \frac{T}{e^2} \int_{-\infty}^{\infty} dE (-\frac{\partial n_\mathrm{F}}{\partial E}) E^{i+j-2} \sigma(E) \ , \tag{2.184}$$

where n_F is the Fermi distribution function.
For constant chemical potential one obtains this way from Eqs. (2.181) and (2.182)

$$L^{11} = T/e^2\sigma \tag{2.185}$$

$$L^{12} = -|e|T\, L^{11}\, S = \frac{T^2}{-|e|}\sigma S = L^{21} \tag{2.186}$$

$$L^{22} = T^2 K + \frac{L^{12}L^{21}}{L^{11}} \ , \tag{2.187}$$

where σ is the electrical conductivity, S the thermoelectric or Seebeck coefficient, and K is the electronic contribution to the thermal conductivity. Furthermore the Lorenz number (or rather function) is given by

$$L = \frac{K}{\sigma T} = \frac{1}{e^2T^2} \frac{(L^{11}L^{22} - L^{12}L^{21})}{(L^{11})^2} \ . \tag{2.188}$$

[30] Assumption based on comparing Eq. (1) for the Mott formula in Ref. 245 to, e.g., Eq. (1) of Domenicali [273], who refers to Mott and Jones [243] (see Section 2.3.2.2) for a corresponding expression in terms of the resistivity with a positive prefactor, writing explicitly $|e|$.

[31] Actually the particle current, see below.

Onsager relations as such are not discussed by Jonson and Mahan, who merely state concerning the symmetry properties of the response functions that the tensors $\{L^{ij}\}_{\alpha\beta}$ are diagonal in $\alpha\beta$ for isotropic systems and $L^{12} = L^{21}$.

To make the connection to the conventions used by Kubo *et al.* and Kleiner (see previous section) we first note that Eq. (2.181)) describes in fact the particle current and not the electric current $\boldsymbol{j}_{el} = -|e|\boldsymbol{j}$. With this, $\boldsymbol{E} = -\boldsymbol{\nabla}V$ ($V \leftrightarrow \phi$), and $\boldsymbol{\nabla}(1/T) = -\frac{1}{T^2}\boldsymbol{\nabla}T$, Eqs. (2.181) and (2.182) become (dropping the Cartesian indices)

$$\boldsymbol{j} = \frac{-|e|}{T}L^{11}\ \boldsymbol{E} - \frac{1}{T^2}L^{12}\ \boldsymbol{\nabla}T \tag{2.189}$$

$$\boldsymbol{j}_{el} = \frac{e^2}{T}L^{11}\ \boldsymbol{E} - \frac{-|e|}{T^2}L^{12}\ \boldsymbol{\nabla}T \tag{2.190}$$

$$\boldsymbol{j}_Q = \frac{-|e|}{T}L^{21}\ \boldsymbol{E} - \frac{1}{T^2}L^{22}\ \boldsymbol{\nabla}T\ . \tag{2.191}$$

Comparing these equations with Eqs. (2.168) and (2.169) leads to the following connections between the two formulations for the kinetic coefficients:

$$\frac{e^2}{T}L^{11} = S^1 = \sigma \tag{2.192}$$

$$\frac{-|e|}{T}L^{12} = S^2 \tag{2.193}$$

$$\frac{|e|}{T}L^{21} = S^3 \tag{2.194}$$

$$\frac{1}{T}L^{22} = S^4. \tag{2.195}$$

This correspondence implies a modified second kind of Onsager relation, $\underline{\boldsymbol{L}}^{12} = -(\underline{\boldsymbol{L}}^{21})^T$, in absence of an external magnetic field.

Girvin and Jonson

Based on the works of Luttinger [240] and Mahan [226], Girvin and Jonson [274] give a *fundamental phenomenological expression describing the non-equilibrium particle current density in a system under the influence of temperature (T) and* [electric] *potential (ϕ)* as

$$J_i = L^{11}_{ij}(e/T)\partial_j\phi + L^{12}_{ij}\partial_j(1/T)\ , \tag{2.196}$$

with $-e$ the electronic charge. Accordingly, they define the thermopower via

$$\partial_i\phi = -S_{ij}\partial_j T \tag{2.197}$$

as[32]

$$S_{ij} = (-1/eT)(L^{11})^{-1}_{ik}L^{12}_{kj}\ . \tag{2.198}$$

Obviously, the coefficient L^{12} occurring in Eq. (2.196) differs from the one used by Jonson and Mahan [245] [see Eq. (2.186)] only in sign, reflecting the assumed difference in the definition of e. The relation of L^{11}_{ij} to the electrical conductivity is given as $L^{11}_{ij} = (T/e^2)\sigma_{ij}$, consistent with Eq. (2.185).

[32] There appears to be a misprint in Ref. 274, that gives Eq. (2.198) with $(L^{11})^{-1}_{ij}$ instead of $(L^{11})^{-1}_{ik}$.

For the special case of an ideal 2DEG in a high magnetic field along the z direction, they give the following symmetry relations

$$L_{xx}^{11} = L_{yy}^{11} = 0 \tag{2.199}$$
$$L_{xy}^{11} = -L_{yx}^{11} \neq 0 \tag{2.200}$$
$$L_{xx}^{12} = L_{yy}^{12} = 0 \tag{2.201}$$
$$L_{xy}^{12} = -L_{yx}^{12} \neq 0\,, \tag{2.202}$$

where the detailed expressions for the quantised Hall and Nernst conductivities are omitted here. These relations are consistent with later works of the same authors [275, 276].

Callen

In the works by Callen [207, 210] the particle and heat currents are expressed by the equations

$$-J = L_{11}\frac{1}{T}\boldsymbol{\nabla}\mu + L_{12}\boldsymbol{\nabla}\frac{1}{T} \tag{2.203}$$
$$Q = L_{21}\frac{1}{T}\boldsymbol{\nabla}\mu + L_{22}\boldsymbol{\nabla}\frac{1}{T}\,, \tag{2.204}$$

with the electrochemical potential $\mu = \mu_c + \mu_e = \mu_c + e\phi$. Here $e = -|e|$ is the electronic charge and ϕ the electrostatic potential. Callen furthermore states the conventional Onsager relation of second kind:

$$L_{12}(\boldsymbol{H}) = L_{21}(-\boldsymbol{H})\,. \tag{2.205}$$

The relations of the kinetic coefficients in Eqs. (2.203) and (2.204) to the corresponding experimentally accessible quantities are found by considering special situations. For $\boldsymbol{\nabla}\mu_c = 0$, i.e., $\boldsymbol{\nabla}\mu = \boldsymbol{\nabla}\mu_e$, where $\frac{1}{e}\boldsymbol{\nabla}\mu_e$ is the electric field, and $\boldsymbol{\nabla}T = 0$ one has

$$\sigma = -eJ/\frac{1}{e}\boldsymbol{\nabla}\mu = e^2 L_{11}/T\,. \tag{2.206}$$

For $J = 0$ one obtains in turn the electronic part of the thermal conductivity

$$\kappa \equiv -Q/\boldsymbol{\nabla}T\,. \tag{2.207}$$

Finally, the expression

$$\boldsymbol{\nabla}\mu = \frac{L_{12}}{TL_{11}}\boldsymbol{\nabla}T \tag{2.208}$$

leads to the Seebeck coefficient

$$S = -\frac{1}{eT}\frac{L_{12}}{L_{11}} = \frac{e}{T^2}\sigma^{-1}L_{12}\,. \tag{2.209}$$

In relation to the previously introduced definitions of the kinetic coefficients by Jonson and Mahan, we accordingly have the interrelations:

$$L_{11}^{\mathrm{Cal}} = L_{\mathrm{JM}}^{11} \tag{2.210}$$
$$L_{12}^{\mathrm{Cal}} = L_{\mathrm{JM}}^{12} \tag{2.211}$$
$$L_{21}^{\mathrm{Cal}} = -L_{\mathrm{JM}}^{21} \tag{2.212}$$
$$L_{22}^{\mathrm{Cal}} = L_{\mathrm{JM}}^{22}\,. \tag{2.213}$$

Barnard

Barnard [272], citing de Groot [208], Mott and Jones [243] and Onsager [205, 206] writes

$$J = -L_{11}\frac{1}{T}\boldsymbol{\nabla}\bar{\mu} - L_{12}\frac{1}{T^2}\boldsymbol{\nabla}T \tag{2.214}$$

$$J_Q = -L_{21}\frac{1}{T}\boldsymbol{\nabla}\bar{\mu} - L_{22}\frac{1}{T^2}\boldsymbol{\nabla}T, \tag{2.215}$$

with $\bar{\mu} = \mu - |e|V$ the electrochemical potential and the electric current $I = -|e|J$. The relations of the kinetic coefficients to the experimental parameters σ, S, Π, and κ are

$$\sigma = \frac{e^2 L_{11}}{T} \tag{2.216}$$

$$S = -\frac{1}{|e|T}\frac{L_{12}}{L_{11}} \tag{2.217}$$

$$\Pi = -\frac{1}{|e|}\frac{L_{21}}{L_{11}} \tag{2.218}$$

$$\kappa = \frac{1}{T^2}\left(L_{22} - \frac{L_{21}L_{12}}{L_{11}}\right) \tag{2.219}$$

With the usual Onsager reciprocal relation $L_{12} = L_{21}$, Eqs. (2.217) and (2.218) give of course the (second) Kelvin relation $\Pi = ST$. The connection to the previously introduced formulations is

$$L_{11}^{\mathrm{Bar}} = L_{11}^{\mathrm{Cal}} = L_{\mathrm{JM}}^{11} = \frac{T}{e^2}S^{(1)} \tag{2.220}$$

$$L_{12}^{\mathrm{Bar}} = -L_{12}^{\mathrm{Cal}} = -L_{\mathrm{JM}}^{12} = \frac{T}{|e|}S^{(2)} \tag{2.221}$$

$$L_{21}^{\mathrm{Bar}} = -L_{21}^{\mathrm{Cal}} = L_{\mathrm{JM}}^{21} = \frac{T}{|e|}S^{(3)} \tag{2.222}$$

$$L_{22}^{\mathrm{Bar}} = L_{22}^{\mathrm{Cal}} = L_{\mathrm{JM}}^{22} = TS^{(4)}\,. \tag{2.223}$$

Other contributions in the field

There is of course an abundance of articles, books (or chapters therein), and reviews on the basics of thermoelectric effects in the literature, as for example by Domenicali [273, 277–279], de Groot and Mazur [208, 209, 270], Ziman [280], Chester and Thellung [244], Luttinger [240], Smrčka and Středa [281] , Vilenkin and Taylor [282], Mahan [226], Tauber *et al.* [20], Wimmer *et al.* [266, 267, 283][33]. Most of these authors either build on or are derived from one of the works reviewed above. Unfortunately, often additional conventions are introduced, mistakes or misprints are carried over or added, increasing the already chaotic situation in the literature. For this reason we have reviewed only a few selected contributions to the field, that are the most relevant for the basic formalism used in this work. Aspects connected with spin transport will be considered in Section 2.3.3.

[33] In the beginning repeating the mistake of Jonson and Mahan [245], which was later corrected [283].

2.3.2.2 The Mott formula

The following compilation summarises the relevant expressions and relations in Chapters VII.15 (thermoelectric transport), VII.5 (electric transport), and VI.1 (heat capacity) of the book *The Theory of the Properties of Metals and Alloys* by Mott and Jones [243] . Using Boltzmann transport theory, these authors write the electric and heat current due to a temperature gradient dT/dx and an electric field F as

$$j = \frac{2e}{\hbar}\frac{1}{8\pi^3}\int \frac{\partial E}{\partial k_\mathrm{x}} f(\boldsymbol{k})d\boldsymbol{k} \tag{2.224}$$

$$Q = \frac{2}{\hbar}\frac{1}{8\pi^3}\int E\frac{\partial E}{\partial k_\mathrm{x}} f(\boldsymbol{k})d\boldsymbol{k}\,, \tag{2.225}$$

with $e = -|e|$, E the energy of the electronic state $\boldsymbol{k}$, and $f(\boldsymbol{k})$ the steady state Fermi distribution function. The rate of change of f due to F and dT/dx is given by

$$-\frac{df}{dt} = \frac{\partial f_0}{\partial k_\mathrm{x}}\frac{eF}{\hbar} + \frac{\partial f_0}{\partial x}\frac{dx}{dt}\,, \tag{2.226}$$

with the equilibrium distribution function $f_0 = (e^{(E-\zeta)/k_\mathrm{B}T}+1)^{-1}$, where ζ is here the chemical potential, and $dx/dt = \hbar^{-1}\partial E/\partial k_\mathrm{x}$ the velocity along the x axis. Since

$$\frac{\partial f_0}{\partial x} = -\frac{\partial f_0}{\partial E}\left(\frac{\partial \zeta}{\partial T} + \frac{(E-\zeta)}{T}\right)\frac{\partial T}{\partial x} \tag{2.227}$$

the rate of change of f becomes

$$\frac{df}{dt} = -\frac{1}{\hbar}\frac{\partial f_0}{\partial E}\frac{\partial E}{\partial k_\mathrm{x}}\left[eF - \left(\frac{\partial \zeta}{\partial T} + \frac{(E-\zeta)}{T}\right)\frac{\partial T}{\partial x}\right]. \tag{2.228}$$

As in standard Boltzmann transport theory, i.e., without the temperature gradient, the rate of change of f due to the external stimulus is equated with that due to scattering and accordingly a relaxation time $\tau(\boldsymbol{k})$ is introduced. Since the second term in Eq. (2.228) connected to the temperature gradient is independent of $\boldsymbol{k}$ one can write the displaced Fermi distribution function in complete analogy to the "electric-only" case as[34]

$$f = f_0 - \frac{\tau(\boldsymbol{k})}{\hbar}\frac{\partial E}{\partial k_\mathrm{x}}\frac{\partial f_0}{\partial E}\left[eF - \left(\frac{\partial \zeta}{\partial T} + \frac{(E-\zeta)}{T}\right)\frac{\partial T}{\partial x}\right]. \tag{2.229}$$

The currents from Eqs. (2.224) and (2.225) now become

$$\frac{j}{e} = \left[eF + \left(\frac{\zeta}{T} - \frac{\partial \zeta}{\partial T}\right)\frac{\partial T}{\partial x}\right]K_0 - \frac{1}{T}\frac{\partial T}{\partial x}K_1 \tag{2.230}$$

$$Q = \left[eF + \left(\frac{\zeta}{T} - \frac{\partial \zeta}{\partial T}\right)\frac{\partial T}{\partial x}\right]K_1 - \frac{1}{T}\frac{\partial T}{\partial x}K_2 \tag{2.231}$$

where the (kinetic) coefficients K_n are given by

$$K_n = -\frac{2}{\hbar^2}\frac{1}{8\pi^3}\int E^n\left(\frac{\partial E}{\partial k_\mathrm{x}}\right)^2\frac{\partial f_0}{\partial E}\tau(\boldsymbol{k})d\boldsymbol{k}. \tag{2.232}$$

[34] See Chapter VII, § 6.3 of Ref. 243.

By abbreviating the $\boldsymbol{k}$-space integral over the constant-energy surface $E(\boldsymbol{k}) = E'$

$$\phi(E') = \frac{2}{\hbar^2}\frac{1}{8\pi^3}\int\int\left(\frac{\partial E}{\partial k_\mathrm{x}}\right)^2\tau(\boldsymbol{k})\frac{dS}{|\boldsymbol{\nabla}E|}\,, \tag{2.233}$$

these may be written more compactly as

$$-K_n = \int_0^\infty \phi(E)E^n\frac{\partial f_0}{\partial E}dE\,. \tag{2.234}$$

For low temperatures $\frac{\partial f_0}{\partial E}$ is non-vanishing only close to the Fermi level $E = \zeta$. Accordingly, one can expand Eq. (2.234) in this case in powers of T,

$$K_n = \zeta^n\phi(\zeta) + \frac{\pi^2}{6}(k_\mathrm{B}T)^2\frac{d^2}{d\zeta^2}[\zeta^n\phi(\zeta)]...\,, \tag{2.235}$$

corresponding to the well-known Sommerfeld expansion [256, 284–287] originally employed in the theory of the electronic specific heat. From this one obtains to the first order w.r.t. T for the thermal conductivity under the condition $j = 0$ (i.e., no electric current)

$$Q = \left(\frac{K_1^2}{K_0} - K_2\right)\frac{1}{T}\frac{\partial T}{\partial x} = -\kappa\frac{\partial T}{\partial x} = \frac{\pi^2}{3}k_\mathrm{B}^2T\phi(\zeta) \tag{2.236}$$

and for the electrical conductivity in the case $\partial T/\partial x = 0$

$$\sigma = e^2K_0 = e^2\phi(\zeta). \tag{2.237}$$

Dividing Eq. (2.236) by Eq. (2.237) leads to the Wiedemann-Franz law

$$\frac{\kappa}{\sigma} = \frac{\pi^2}{3}\frac{k^2}{e^2}T \tag{2.238}$$

and further on to the Lorenz number

$$L = \frac{\kappa}{\sigma T} = \frac{\pi^2}{3}\left(\frac{k}{e}\right)^2 \approx 2.45\times10^{-2}\,\mathrm{V}^2\,\mathrm{K}^{-2}\,. \tag{2.239}$$

The thermoelectric power S and the Thomson coefficient μ, connected via

$$S = \int_0^T \frac{\mu}{T}dT\,, \tag{2.240}$$

are finally obtained by considering the energy production per unit time per unit volume in the presence of an electric and a heat current as well as a temperature gradient

$$U = Fj - \partial Q/\partial x\,. \tag{2.241}$$

Solving Eq. (2.230) for F and inserting into Eq. (2.231), one obtains

$$Q = \frac{K_1}{K_0}\frac{j}{e} - \frac{K_0K_2 - K_1^2}{K_0}\frac{1}{T}\frac{\partial T}{\partial x}\,, \tag{2.242}$$

which leads, neglecting contributions from the second term as they go with $\partial^2/\partial x^2$ and $(\partial T/\partial x)^2$ to

$$\frac{\partial Q}{\partial x} = \frac{j}{e}\frac{\partial}{\partial x}\left(\frac{K_1}{K_0}\right). \tag{2.243}$$

With this, Eq. (2.241) becomes

$$U = \frac{j^2}{K_0 e^2} - \frac{j}{e}T\frac{\partial T}{\partial x}\frac{\partial}{\partial T}\left[\frac{1}{T}\left(\frac{K_1}{K_0} - \zeta\right)\right] . \tag{2.244}$$

The term in j^2 is the irreversible Joule heating, hence one has for the remaining reversible part by definition the Thomson coefficient

$$\mu = \frac{T}{e}\frac{\partial}{\partial T}\left[\frac{1}{T}\left(\frac{K_1}{K_0} - \zeta\right)\right] \tag{2.245}$$

and for the Seebeck coefficient via Eq. (2.240)

$$S = \frac{1}{e}\left[\frac{1}{T}\left(\frac{K_1}{K_0} - \zeta\right)\right]. \tag{2.246}$$

Using the coefficients K_n one has to the first order in $k_\mathrm{B}T/\zeta$

$$S = \frac{\pi^2}{3}\frac{k^2 T}{e}\left[\frac{\partial(\log\sigma(E))}{\partial E}\right]_{E=\zeta} , \tag{2.247}$$

i.e., one arrives at the well-known Mott formula for the thermopower, where the energy-dependent electrical conductivity is defined as

$$\sigma(E) = \frac{2e^2}{\hbar^2}\int\left(\frac{\partial E}{\partial k_\mathrm{x}}\right)^2 \tau(\boldsymbol{k})\frac{dS}{|\boldsymbol{\nabla} E|} . \tag{2.248}$$

Comparison with the corresponding expressions of Kubo *et al.* and Kleiner ($S^{(n)}$ for the isotropic case), and Jonson and Mahan (likewise L^{ij}) given above leads to

$$e^2 K_0 = S^1 = \frac{e^2}{T}L^{11} = \sigma \tag{2.249}$$

$$e(K_1 - \zeta K_0) = S^2 = \frac{-|e|}{T}L^{12} = T\sigma S \tag{2.250}$$

$$K_2 = S^4 = \frac{1}{T}L^{22} . \tag{2.251}$$

Obviously Eq. (2.247) is only valid for low temperatures and, assuming the variation of $\sigma(E)$ to be linear in the vicinity of the Fermi level, linear in temperature. From a simplistic phenomenological point of view this *diffusion thermopower* can be interpreted as the charge imbalance built up due to the difference in conductivity for *hot* and *cold* electrons flowing from opposite ends of the sample in response to the applied temperature difference. The sign of the Seebeck coefficient S is then defined by the sign of the derivative in Eq. (2.248), reflecting whether *hotter* electrons are less scattered than *colder* ones or vice versa. An empirical expression devised by Guénault [288] to account for the experimentally observed non-linearity of S in Ag with non-magnetic and (traces of) magnetic impurities,

$$S = AT + BT^3 + C\frac{T}{T + T_0} , \tag{2.252}$$

still assumes the diffusion contribution in the first term to be linear in T, while the non-linearity comes about due to the so-called phonon-drag mechanism represented by the second term (that will have to be discussed later on), and the Kondo effect [289] due to the magnetic impurities with the Kondo temperature T_0 in the third term. However, as will be shown for example in Section 3.1, even without taking such effects as the latter two into account, the electronic contribution to the Seebeck effect can be non-linear even in pure metals and even at relatively low temperatures. Accordingly, one has to go beyond the Sommerfeld approximation employed to arrive at the classical Mott formula in Eq. (2.247).

2.3.2.3 Generalisations and application of the Mott formula

The starting point for the first-principles description of thermo(magneto)electric and, later on, spincaloritronic phenomena presented in this thesis has been the work of Jonson and Mahan [245], whose definitions of the kinetic coefficients was briefly reviewed above in Section 2.3.2.1. In fact, this was a re-derivation of earlier work by Chester and Thellung [244] using the expressions of Kubo *et al.* [109] in a wave function formulation, but instead employing the language of Green functions to prove that the Mott formula for the thermoelectric power and the Wiedemann-Franz law are *exact for independent electrons interacting with static impurities and phonons treated in the adiabatic approximation* [245]. As such it was considered to be the ideal basis for a Kubo linear response description within the DFT-based KKR-CPA framework, in particular having the treatment of chemically- and thermally-induced disorder in mind.

As it had already been recognised by Luttinger [240], a serious problem in the quantum mechanical treatment of thermally-induced processes is to find a proper formulation for the heat current operator. While his *trick* of invoking a gravitational field is certainly elegant and insightful, it does not render tractable expressions that give numerical access to the response coefficients. Jonson and Mahan [245] restricted to the adiabatic approximation for the electron-phonon interaction, which neglects the phonon momentum and effectively turns the interaction into a static potential that is added to other impurity potentials, if present. These authors write the heat current as

$$\boldsymbol{j}_q = \boldsymbol{j}_E - \mu_c \boldsymbol{j} \ , \tag{2.253}$$

with the energy current

$$\boldsymbol{j}_E = \dot{\boldsymbol{R}} = -i[\hat{\boldsymbol{R}}, \hat{H}] \ , \tag{2.254}$$

given by the commutator of the energy position operator $\hat{\boldsymbol{R}} = \sum_i \hat{\boldsymbol{R}}_i \hat{h}_i$ and the Hamilton operator $\hat{H} = \sum_i \hat{h}_i$. The independent-electron many-body Hamiltonian for the interaction with static impurities and phonons is most generally written (in second quantisation) as

$$\hat{H} = \sum_k \varepsilon_k \hat{c}_k^\dagger \hat{c}_k + \frac{1}{\Omega} \sum_q \hat{V}^{imp}(q) \hat{\rho}^{imp}(q) + \sum_{q\lambda} \hat{W}_\lambda(q) \hat{Q}_\lambda(q) \hat{\rho}(q) \ , \tag{2.255}$$

with the single-particle energies ε_k, creation and annihilation operators $c_k^\dagger$ and $\hat{c}_k$, the volume of the system Ω, impurity potential and density operator, $\hat{V}^{imp}(q)$ and $\hat{\rho}^{imp}(q)$, respectively, and the electron-phonon interaction $\hat{W}_\lambda(q)$ as well as the

phonon displacement operator $\hat{Q}_\lambda(q)$ in the last term. With this, Eq. (2.254) becomes

$$\begin{aligned} \boldsymbol{j}_E &= \sum_k \varepsilon_k \boldsymbol{v}_k \hat{c}_k^\dagger \hat{c}_k + \frac{1}{\Omega}\sum_q \hat{V}^{imp}(q)\hat{\rho}^{imp}(q)\boldsymbol{j}(q) \\ &\quad + \sum_{q\lambda} \hat{W}_\lambda(q)\hat{Q}_\lambda(q)\boldsymbol{j}(q) - \frac{i}{M}\sum_{q\lambda}\left(\boldsymbol{\nabla}_q \hat{W}_\lambda(q)\right)\hat{P}_\lambda(q)\rho(q)\,, \end{aligned} \tag{2.256}$$

where $\boldsymbol{v}_k = \boldsymbol{\nabla}_k \varepsilon_k$, $\boldsymbol{j}(q) = \sum_k (\boldsymbol{v}_k + \boldsymbol{v}_q/2)\, c_{k+q}^\dagger c_k$ and $\hat{P}_\lambda(q)$ is the phonon momentum operator. As stated above, Jonson and Mahan [245] set $\hat{P}_\lambda(q)$ to zero and treat $\hat{W}_\lambda(q)\hat{Q}_\lambda(q)$ as a random static potential. Based on this assumption, the authors obtain expressions for the response functions at constant field ($\omega \to 0$) in the form of Eqs. (2.156)-(2.158), compactly given by

$$L^{ij} = \frac{T}{e^2}\int_{-\infty}^{\infty} dE(-\frac{\partial f}{\partial E})\, E^{i+j-2}\,\sigma(E)\,, \tag{2.257}$$

which for low temperatures allows recovering the Mott formula and the Wiedemann-Franz law. The derivation has been coarsely sketched in Section 2.3.2.1 and shall not be extended here, for this and also for a more extensive discussion on the validity of the assumptions made, see Ref. 245. A later work by the same authors, Ref. 262, that goes beyond the adiabatic approximation might also be of interest, moreover the reader is referred to Kontani [290] for a fairly recent perspective on the subject. In conclusion of the above one should stress that, while obviously a more sophisticated treatment of the heat current operator is possible and desirable, in particular concerning inelastic scattering of electrons with phonons and magnons, this would however most certainly lead to a breakdown of the Mott formula and the Wiedemann-Franz law as already stated for example by Jonson and Mahan [245]. In Section 2.3.4 we will return to this issue in terms of a discussion from a group-theoretical perspective.

Expressions like Eq. (2.257), in particular when both $\sigma(E)$ and L^{ij} are written as tensors, have often been termed *generalised* Mott relations, for example by the present author [266]. One should remark here, that *generalised* initially meant first of all an extension to the non-isotropic case due to magnetism. See for example Jonson and Girvin [276], who generalised it to finite magnetic fields for calculating S_{xy} in a non-relativistic 2DEG model, as briefly reviewed on pp. 46 (see also Refs. 274 and 275). Actually already Sondheimer [258] spoke of generalisations to finite temperatures and magnetic fields, when deriving a Mott-like relation for the Ettingshausen-Nernst coefficient often referred to as Sondheimer's formula. He considers the limiting cases of low and high temperature and derives approximate expressions for intermediate situations. In addition he gives corresponding relations also for the Ettingshausen effect and for the Righi-Leduc effect. Concerning the *generalisation* to finite (electronic) temperature one should note that of course already Eq. (2.234) by Mott and Jones [243] is equivalent to Eq. (2.257). An expression for the thermoelectric power in terms of an energy integral over the conductivity is for example also given in Ref. 291.

In the following, *generalised* will be used in the sense of both, an extension to tensorial quantities and finite electronic temperatures, and furthermore the expressions for the elements of $\underline{\boldsymbol{L}}^{ij}$ or, from now on, $\underline{\boldsymbol{L}}^{AB}$ [Eqs. (2.156)-(2.158)]

$$L^{cc}_{\mu\nu}(T) = -\frac{1}{|e|}\int dE\, \sigma^{(cc)}_{\mu\nu}(E)\left(-\tfrac{\partial f(E,T)}{\partial E}\right) \tag{2.258}$$

$$L^{cq}_{\mu\nu}(T) = -\frac{1}{|e|}\int dE\, \sigma^{(cc)}_{\mu\nu}(E)\left(-\tfrac{\partial f(E,T)}{\partial E}\right)(E-E_F) \tag{2.259}$$

$$L^{qq}_{\mu\nu}(T) = -\frac{1}{|e|}\int dE\, \sigma^{(cc)}_{\mu\nu}(E)\left(-\tfrac{\partial f(E,T)}{\partial E}\right)(E-E_F)^2\,, \tag{2.260}$$

will be called *generalised Mott relations*. The term *generalised Mott formula* has probably first been used in this context by Proskurin and Ogata [292], who deal with longitudinal and transverse thermoelectric responses in graphene. As a further generalisation the application to spin transport in terms of $\underline{\boldsymbol{\mathcal{L}}}^{AB}$ might be considered, that will be detailed in the next section (2.3.3).
For convenience, the Onsager matrix, Eq. (2.130), summarising the relevant responses, perturbations and kinetic coefficient tensors connecting them is repeated here:

$$\begin{pmatrix} \boldsymbol{j}^c \\ \boldsymbol{j}^q \\ \underline{\boldsymbol{J}}^s \end{pmatrix} = \begin{pmatrix} \underline{\boldsymbol{L}}^{cc} & \underline{\boldsymbol{L}}^{cq} & \underline{\boldsymbol{\mathcal{L}}}^{cs} \\ \underline{\boldsymbol{L}}^{qc} & \underline{\boldsymbol{L}}^{qq} & \underline{\boldsymbol{\mathcal{L}}}^{qs} \\ \underline{\boldsymbol{\mathcal{L}}}^{sc} & \underline{\boldsymbol{\mathcal{L}}}^{sq} & \underline{\tilde{\boldsymbol{\mathcal{L}}}}^{ss} \end{pmatrix} \begin{pmatrix} -\boldsymbol{\nabla}\mu \\ -\boldsymbol{\nabla}T/T \\ \underline{\boldsymbol{F}}^s \end{pmatrix}\,. \tag{2.261}$$

Neglecting the effect of the "spin force" $\underline{\boldsymbol{F}}^s$ and the associated sub-tensors for now (see Section 2.3.3.1 and Appendix A.3 for considerations including it), i.e., assuming absence of boundary conditions that could lead to a spin accumulation, one obtains from the first row for open circuit conditions,

$$\boldsymbol{j}^c = \boldsymbol{0} = -\underline{\boldsymbol{L}}^{cc}\boldsymbol{\nabla}\mu - \underline{\boldsymbol{L}}^{cq}\boldsymbol{\nabla}T/T\,, \tag{2.262}$$

and assuming a constant chemical potential μ_c, the definition of the Seebeck tensor,

$$\boldsymbol{E} = -\frac{1}{eT}(\underline{\boldsymbol{L}}^{cc})^{-1}\underline{\boldsymbol{L}}^{cq}\boldsymbol{\nabla}T = \underline{\boldsymbol{S}}\boldsymbol{\nabla}T\,, \tag{2.263}$$

relating the electric field to an applied temperature gradient. This corresponds to the usual macroscopic definition of $S = -\Delta V/\Delta T$, since $\Delta \to -\boldsymbol{\nabla}$ and $-\boldsymbol{\nabla}V = \boldsymbol{E}$. With the Nernst or thermoelectric conductivity tensor $\underline{\boldsymbol{\alpha}} = -\frac{1}{T}\underline{\boldsymbol{L}}^{cq}$, which gives the direct relation between charge current density and temperature gradient, and with the electric conductivity tensor $\underline{\boldsymbol{\sigma}} = -|e|\underline{\boldsymbol{L}}^{cc}$, the Seebeck tensor can be more conveniently expressed as

$$\underline{\boldsymbol{S}} = -\underline{\boldsymbol{\sigma}}^{-1}\underline{\boldsymbol{\alpha}}\,. \tag{2.264}$$

Accounting for finite temperatures via the Fermi-Dirac distribution

$$f(E,\mu_\mathrm{c},T) = \frac{1}{e^{(E-\mu_\mathrm{c})/kT}+1} \tag{2.265}$$

with the single-particle energies E, the chemical potential $\mu_\mathrm{c} \approx E_\mathrm{F}$, and what will from now on be called *electronic* temperature T, contained in the definition of the temperature-dependent response functions $L^{cc}(T)$ and $L^{cq}(T)$ [Eqs. (2.258) and (2.259)], the generalised Mott formula for the thermopower is

$$\underline{\boldsymbol{S}} = -\frac{1}{eT}\frac{\int dE\,(E-\mu_\mathrm{c})\,\underline{\boldsymbol{\sigma}}(E)\left(-\frac{\partial f}{\partial E}\right)}{\int dE\,\underline{\boldsymbol{\sigma}}(E)\left(-\frac{\partial f}{\partial E}\right)}\,. \tag{2.266}$$

Note that numerator and denominator just differ by the term $(E-\mu_c)$ in the kernel. As shown in Section 2.3.2.2, for low temperatures employing the Sommerfeld expansion [256, 284–287]

$$\int_{-\infty}^{\infty} dE(E)^n\sigma(E)(-\frac{\partial f}{\partial E}) \approx \sigma(0)\delta_{n,0}+\frac{\pi^2}{6}(k_BT)^2[n(n-1)E^{n-2}\sigma(E) +2nE^{n-1}\sigma'(E)+E^n\sigma''(E)]_{E=0} \quad (2.267)$$

and keeping only first order derivatives, one recovers the *classical* Mott formula [243]

$$\begin{aligned} S &= -\frac{\pi k_B^2 T}{3e}\frac{d\ln\sigma(E)}{dE}\Big|_{E_F} \\ &= \frac{\pi k_B^2 T}{3e}\frac{d\ln\rho(E)}{dE}\Big|_{E_F} . \end{aligned} \quad (2.268)$$

Note the difference in sign when comparing the first line with Eq. (2.247), that comes about due to the, as usual not explicitly stated, different conventions used for e (elementary vs *electronic* [243] charge).

Eq. (2.266) is in use for a first-principles description of thermoelectric properties quite some time already, see for example Refs. 293–295 for applications within the framework of Boltzmann transport theory and Ref. 296 that employs the Kubo formalism. The work of Oshita *et al.* [296] is of particular interest as it makes a direct comparison between Boltzmann transport theory in the commonly employed relaxation time approximation (RTA)[35] and the Kubo-Greenwood equation. Sivan and Imry [297] derived a corresponding expression in terms of conductances or transmission coefficients within the Landauer-Büttiker approach [298–300], which often serves as the basis for calculations of thermoelectric and spincaloritronic properties of 2D systems (cf. Refs. 18, 301–303).

The diagonal elements of the Seebeck tensor in Eq. (2.264) will be called (charge) Seebeck coefficients, transverse effects (Nernst) will be represented by the anti-symmetric part of the thermoelectric conductivity tensor

$$[\underline{\boldsymbol{\alpha}}]_{\mu\nu} = -\frac{1}{T}\int dE(E-\mu_c)\,[\underline{\boldsymbol{\sigma}}(E)]_{\mu\nu}\,(-\frac{\partial f}{\partial E}) , \quad (2.269)$$

which in the low-temperature limit becomes

$$[\underline{\boldsymbol{\alpha}}]_{\mu\nu} = -\frac{\pi k_B^2}{3e}\frac{d\,[\underline{\boldsymbol{\sigma}}(E)]_{\mu\nu}}{dE}|_{E_F} , \quad (2.270)$$

the (anomalous) Nernst conductivity (ANC). This second, Mott-like formula for the ANC is the so-called Sondheimer formula [258], that has been discussed for instance in Refs. 214, 290, 304–307. Other authors, see for example Refs. 20, 215, and 292, formulate off-diagonal anti-symmetric elements of Seebeck tensors and to some extent connection will be made to these definitions later on.[36]

[35] Which assumes the relaxation time appearing in $\sigma(E)$ in both numerator and denominator of Eq. (2.266) to be constant (in energy) and therefore negligible.

[36] These are either related to the ANC (S_{xy} in Refs. 215 and 292) or to a combination of spintronic and spincaloritronic phenomena that will be discussed in Section 2.3.3 (S^s_{yx} in Ref. 20).

Depending on the magnetic space group (see Section 2.3.4), the elements of the Seebeck tensor, both diagonal and off-diagonal, might contain contributions from diagonal as well as off-diagonal elements of the tensors $\underline{\boldsymbol{L}}^{cc} \propto \underline{\boldsymbol{\sigma}}$ and $\underline{\boldsymbol{L}}^{cq} \propto \underline{\boldsymbol{\alpha}}$. As will be demonstrated later on, the latter ones can, in particular in case of them being anti-symmetric tensor elements connected to anomalous transport effects (Hall and Nernst) often be neglected in highly symmetric transition metals and their alloys due to their considerably smaller magnitude in comparison to the diagonal elements. In case of non-magnetic cubic systems the Seebeck effect even becomes isotropic. However, the so-called spin Nernst magneto-thermopower (SMT) that will be discussed in the following section (2.3.3) and is the subject of Ref. 21 (reprinted here in Section 3.2.2 on page 133) is precisely such a small modulation of the Seebeck effect that has been used to indirectly observe the spin Nernst effect.

The electronic contribution to the thermal conductivity κ is in particular connected to the response coefficient L^{qq}, that contains an additional factor of energy in the kernel [Eq. (2.260)] as compared to L^{qc} and L^{cq}, which are giving usually only a small correction for metals. The full expression reads

$$\underline{\boldsymbol{\kappa}} = \frac{1}{T^2}\left(\underline{\boldsymbol{L}}^{qq} - \frac{\underline{\boldsymbol{L}}^{qc}\underline{\boldsymbol{L}}^{cq}}{\underline{\boldsymbol{L}}^{cc}}\right) . \tag{2.271}$$

The relevant elements of $\underline{\boldsymbol{L}}^{qc}$ have been obtained in this thesis exclusively based on their Onsager relation to $\underline{\boldsymbol{L}}^{cq}$ (see Section 2.3.4). Of particular interest in this context is of course the Wiedemann-Franz law (WFL)

$$\frac{\kappa}{\sigma} = LT \tag{2.272}$$

given here for the isotropic case. The Lorenz number L or rather Lorenz function tensor, as it depends on temperature as well and can be anisotropic depending on the magnetic space group, finally is

$$\underline{\boldsymbol{L}} = \underline{\boldsymbol{\kappa}}\,\underline{\boldsymbol{\sigma}}^{-1}T^{-1} = \frac{1}{e^2T^2}\frac{\underline{\boldsymbol{L}}^{cc}\underline{\boldsymbol{L}}^{qq} - \underline{\boldsymbol{L}}^{cq}\underline{\boldsymbol{L}}^{qc}}{(\underline{\boldsymbol{L}}^{cc})^2} . \tag{2.273}$$

Violation of the WFL is a popular catch phrase nowadays [308], occurring if charge and heat transport are not mediated essentially by the electronic subsystem alone, i.e., when the thermal conductivity due to phonons and magnons becomes significant and/or inelastic scattering processes interconnect the subsystems. This issue will be discussed in Ref. 309, reprinted in this thesis in Section 3.1.2. One should note already here, that a temperature-dependent Lorenz number is however not a sufficient precondition for a WFL-violation. Obviously, based on Eqs. (2.258) and (2.260) the temperature dependence of the electrical and the electronic thermal conductivity cannot be assumed to be identical even when only electronic temperatures and elastic scattering are considered.

For the description of finite temperatures beyond the Fermi-Dirac statistics the so-called alloy analogy model [202] (see Section 2.2.5 above and Sections 3.1.2, 3.1.3 and 3.6 for applications) is used to capture the effect of uncorrelated lattice vibrations and transverse spin fluctuations in a mean-field way based on the CPA.[37]

[37] Similar approaches based on the super-cell technique have been used for the former by Liu *et al.* [310] and for the latter by Kováčik *et al.* [303]

Accordingly those additional scattering mechanisms are entering the thermoelectric coefficients only via the conductivity, the generalised Mott relations are left unchanged. This is well justified, since the regime of the adiabatic approximation of Jonson and Mahan [245] is never left. How well this assumption describes the experimental reality is of course a completely different question. In particular phenomena such as phonon drag [311, 312], magnon drag [313–315], and other inelastic scattering mechanisms naturally are missing. But as Jonson and Mahan [262] have shown for the electron-phonon interaction, they can in principle be included by a correction that is small at low as well as high temperatures for metals.

A brief demonstration of the generalised Mott implementation used throughout this thesis can be found in Appendix A.2. Computational details, including such for the underlying electronic structure and Kubo linear response calculations are given in Appendix A.7.

2.3.3 Spin caloric transport

As a brief introduction into the field of spin caloric transport or spincaloritronics has already been given in Chapter 1, we will focus here on the aspects of linear response theory and first-principles description, with a particular emphasis on classes (i) and (iii) in the scheme of Bauer *et al.* [24].

Johnson and Silsbee [2] (see also Refs. 316–318) made the first steps towards a coherent description of spincaloritronic phenomena by extending the formulation of Callen [319] to the case of an electric, thermal, and magnetic perturbation, the *thermomagnetoelectric system*,

$$-\boldsymbol{J}_q = \frac{L_{11}}{T}\boldsymbol{\nabla}V + L_{12}\boldsymbol{\nabla}\frac{1}{T} + \frac{L_{13}}{T}\boldsymbol{\nabla}-H^* \tag{2.274}$$

$$\boldsymbol{J}_Q = \frac{L_{21}}{T}\boldsymbol{\nabla}V + L_{22}\boldsymbol{\nabla}\frac{1}{T} + \frac{L_{23}}{T}\boldsymbol{\nabla}-H^* \tag{2.275}$$

$$-\boldsymbol{J}_M = \frac{L_{31}}{T}\boldsymbol{\nabla}V + L_{32}\boldsymbol{\nabla}\frac{1}{T} + \frac{L_{33}}{T}\boldsymbol{\nabla}-H^* \tag{2.276}$$

with $L_{11} = T\sigma$, $L_{12} = L_{21} = -T^2\sigma\varepsilon$, $L_{22} = T^3\sigma\varepsilon^2 + T^2\kappa$ and the *magnetisation potential* H^*, that combines internal magnetisation and external field. As usual, σ stands for the electrical conductivity, κ for the electronic thermal conductivity, while the thermopower is denoted here by ε. The coefficients describing the magnetisation current are estimated from a free-electron model and following *Aronov's postulate* [320], $J_M = \frac{\beta}{e}J_q$ (where β is the Bohr magneton), to be $L_{31} = p\beta\sigma T/e$, $L_{32} = L_{23} = -p'\beta\sigma T^2\varepsilon/e$, and $L_{33} = \varsigma\beta^2\sigma T/e^2$, with $p \neq p'$ the spin polarisation of the conduction electrons and ς a phenomenological parameter assumed to be close to unity. Johnson and Silsbee [2] also give a short introduction to the general irreversible thermodynamics in terms of entropy change/production, generalised fluxes and forces, later on focusing on FM/NM interfaces. However the explicit expressions given for the response coefficients are strongly simplified on the basis of model considerations. Similar sets of phenomenological equations or Onsager matrices have been for example proposed by Gravier *et al.* [321], Hatami *et al.* [59], Hatami *et al.* [27], Bauer *et al.* [24], Wimmer *et al.* [322], Misiorny and Barnaś [323], Yu *et al.* [26], and Meyer *et al.* [21]. In the following we will, if not stated otherwise,

always refer to the formulation given in Eq. (2.130) or Eq. (2.261).

On this basis, the first-principles approach to spin caloric transport in the diffusion limit has, naively or rather pragmatically, started by replacing σ by σ^{ξ} or L^{cB} by $\mathcal{L}^{sB}$ in the generalised Mott relations for thermoelectric transport [20]. The spin-related response functions occurring in Eq. (2.261) are accordingly, in analogy to Eqs. (2.258) and (2.259), expressed by the corresponding spin conductivities:

$$\mathcal{L}^{sc,\xi}_{\mu\nu}(T) = -\frac{1}{|e|}\int dE\, \sigma^{sc,\xi}_{\mu\nu}(E)\left(-\tfrac{\partial f(E,T)}{\partial E}\right) \tag{2.277}$$

$$\mathcal{L}^{sq,\xi}_{\mu\nu}(T) = -\frac{1}{|e|}\int dE\, \sigma^{sc,\xi}_{\mu\nu}(E)\left(-\tfrac{\partial f(E,T)}{\partial E}\right)(E-E_F)\,. \tag{2.278}$$

The spin(-polarised) conductivity $\underline{\boldsymbol{\sigma}}^{(sc,)\xi}$ is obviously given by $-|e|\underline{\boldsymbol{\mathcal{L}}}^{sc,\xi}$ for $T \to 0$. The *bare* spin Nernst conductivity, i.e., describing the response to $\boldsymbol{\nabla} T$ alone, giving rise to a spin polarised current transverse to the temperature gradient is defined as

$$\alpha^{\xi}_{\mu\nu} = \frac{J^{\xi}_{\mu}}{\nabla_{\nu} T} = -\frac{1}{T}\mathcal{L}^{sq,\xi}_{\mu\nu}\,, \tag{2.279}$$

with $\mathcal{L}^{sq,\xi}_{\mu\nu}$ obtained from the spin Hall conductivity via Eq. (2.278). For a discussion on an *electrical* contribution [20, 324] to the spin Nernst effect due to Seebeck effect and spin Hall effect, see Ref. 266 that is reprinted in this thesis in Section 3.2 on page 122.

In analogy to the spin Hall angle $\theta_{\mathrm{SH}} = \sigma_{\mathrm{SH}}/\sigma$ quantifying the efficiency of conversion of a longitudinal electric current into a transverse spin-polarised current, one can introduce a spin Nernst angle (SNA). There are at least two (reasonable) possibilities for its definition, either relating the spin(-polarised) current $\underline{\boldsymbol{J}}$ in response to a temperature gradient $\boldsymbol{\nabla} T$ to the longitudinal heat current $\boldsymbol{q}$ created by the same driving force [325, 326],

$$\gamma = \frac{J^{i}_{j}}{q_k} = \frac{\alpha^{i}_{jk}}{-\kappa_{kk}}\,. \tag{2.280}$$

Here J^{i}_{j} is the transverse spin current ($i \neq j \neq k$, $i \neq k$), q_k the longitudinal heat current parallel to $\nabla_k T$, α^{i}_{jk} is the spin Nernst conductivity as introduced above in Eq. (2.279), and κ_{kk} is the diagonal heat conductivity of the electrons as defined in Eq. (2.271). Alternatively, one can define the spin Nernst angle as the ratio of the transverse spin Nernst conductivity and a diagonal element of the thermoelectric conductivity tensor defined above [21],

$$\theta_{\mathrm{SN}} = \frac{\alpha^{i}_{jk}}{\alpha_{kk}} = \frac{J^{i}_{j}}{j_k}\,, \tag{2.281}$$

which relates, as the SHA, spin(-polarised) and charge current densities to each other, but now in response to a temperature gradient as opposed to an electric field as in the case of the spin Hall angle. This is equivalent to the definition of the SNA in terms of a transverse spin-dependent Seebeck coefficient (see below) and its longitudinal charge counterpart as proposed in Ref. 20.

Each of the definitions clearly has its advantages. The first one is, by relating the spin current to the primary response connected to the force, closer to the definition

of the spin Hall angle and thus more in the spirit of a conversion efficiency. The second definition on the other hand describes the same observables as the SHA, thus relating two conversions to each other (heat-spin to heat-charge). A direct connection between SHA and SNA can be made for both of them, once by using the Wiedemann-Franz law relating heat and charge conductivity and once by the Seebeck effect relating the thermoelectric or Nernst conductivity α_{kk} to σ_{kk}.

A detailed treatment of spin-dependent contributions to the charge Seebeck effect based on modifying the boundary conditions for the charge and spin current densities can be found in the following Section 2.3.3.1 as well as in Appendix A.3, and in Ref. 21 which is reprinted in Section 3.2 on page 133. A spin-polarised Seebeck coefficient giving in particular access to the spin-dependent Seebeck effect can be obtained from the symmetric part of $\underline{\boldsymbol{\mathcal{L}}}^{sq,\xi}$. It should be noted, that a spin-dependent heat [327] introduced as an affinity in a spin-projected formulation of spincaloritronics is neglected here. Apart from the fact that an analogous spin-polarised temperature gradient is questionable, within the relativistic framework used herein a spin-polarised heat conductivity could of course be calculated using Eq. (2.260) based on the energy-dependent spin conductivity $\sigma_{\mu\nu}^{(sc)\xi}(E)$.

2.3.3.1 Remarks on spin-projected vs. spin-polarised thermoelectrics

Similar to the situation concerning the description of thermoelectric phenomena (see Section 2.3.2.2) also the treatment of spin transport in response to electric fields and/or temperature gradients is handled in various different ways in the literature. Often a spin-projected formalism in the spirit of Mott's two-current model [328, 329] is adopted that assumes a parallel circuit of spin-up and spin-down currents [20]. This is opposed to working with spin-polarised currents as done for the first time in Ref. 266 (reprinted in Section 3.2.1). This approach is based on a continuity equation for the corresponding spin-polarisation current density and accounts coherently for the impact of spin-orbit coupling.

Spincaloritronics in terms of spin-projected response functions

The spin-projected formulation of spin transport starts in a somewhat *ad-hoc* way assuming for the response tensors of non-magnetic cubic materials, fcc Cu with 1 % Ti, Au, and Bi, in a 2D geometry the form [20]:

$$\underline{\boldsymbol{a}}^{b} = \begin{pmatrix} a^{b}_{\mathrm{xx}} & a^{b}_{\mathrm{xy}} & 0 \\ -a^{b}_{\mathrm{xy}} & a^{b}_{\mathrm{xx}} & 0 \\ 0 & 0 & a^{b}_{\mathrm{zz}} \end{pmatrix} \quad \forall\, a \in \{\sigma, L_0, L_1\} \text{ and } \forall\, b \in \{\uparrow, \downarrow\}\,. \tag{2.282}$$

Furthermore, $L_{1'}$ and L_2 should also have the same symmetry, with an Onsager relationconnecting L_1 and $L_{1'}$ (see below). This is however not explicitly stated by Tauber *et al.* [20]. More details on the relation and shapes of response tensors due to symmetry restrictions of the magnetic Laue group can be found in the following section (2.3.4) and in Ref. 283 (reprinted in Section 3.3).

Imposing time and space inversion symmetry leads to the interrelations

$$a^{\uparrow}_{\mathrm{xx}} = a^{\downarrow}_{\mathrm{xx}}, \quad a^{\uparrow}_{\mathrm{xy}} = -a^{\downarrow}_{\mathrm{xy}} \quad \text{and} \quad a^{\uparrow}_{\mathrm{zz}} = a^{\downarrow}_{\mathrm{zz}} \tag{2.283}$$

or in matrix notation

$$\underline{\boldsymbol{a}}^{\downarrow} = \begin{pmatrix} a^{\downarrow}_{\mathrm{xx}} & a^{\downarrow}_{\mathrm{xy}} & 0 \\ -a^{\downarrow}_{\mathrm{xy}} & a^{\downarrow}_{\mathrm{xx}} & 0 \\ 0 & 0 & a^{\downarrow}_{\mathrm{zz}} \end{pmatrix} = \begin{pmatrix} a^{\uparrow}_{\mathrm{xx}} & -a^{\uparrow}_{\mathrm{xy}} & 0 \\ a^{\uparrow}_{\mathrm{xy}} & a^{\uparrow}_{\mathrm{xx}} & 0 \\ 0 & 0 & a^{\uparrow}_{\mathrm{zz}} \end{pmatrix} = (\underline{\boldsymbol{a}}^{\uparrow})^{T} \, , \tag{2.284}$$

where the z axis has been chosen as the the quantisation axis. It should be mentioned that a film or bar geometry is considered, as already reflected in Eq. (2.282), i.e, the considered sample is assumed to be infinitely long in x, narrow in y and flat in z direction.

As spin-flip scattering is not explicitly accounted for one has for the spin-averaged and the spin(-polarised) conductivities

$$\underline{\boldsymbol{\sigma}} = \underline{\boldsymbol{\sigma}}^{\uparrow} + \underline{\boldsymbol{\sigma}}^{\downarrow} \tag{2.285}$$

$$\underline{\boldsymbol{\sigma}}^{s} = \underline{\boldsymbol{\sigma}}^{\uparrow} - \underline{\boldsymbol{\sigma}}^{\downarrow} \, , \tag{2.286}$$

respectively. The corresponding set of relevant transport equations reads [14]

$$\begin{pmatrix} \mathbf{j}^{\uparrow} \\ \mathbf{j}^{\downarrow} \\ \mathbf{j}^{q} \end{pmatrix} = \begin{pmatrix} \underline{\boldsymbol{L}}^{\uparrow}_{0} & 0 & \underline{\boldsymbol{L}}^{\uparrow}_{1} \\ 0 & \underline{\boldsymbol{L}}^{\downarrow}_{0} & \underline{\boldsymbol{L}}^{\downarrow}_{1} \\ \underline{\boldsymbol{L}}^{\uparrow}_{1'} & \underline{\boldsymbol{L}}^{\downarrow}_{1'} & \underline{\boldsymbol{L}}^{\uparrow}_{2} + \underline{\boldsymbol{L}}^{\downarrow}_{2} \end{pmatrix} \begin{pmatrix} \boldsymbol{\nabla}\mu^{\uparrow} \\ \boldsymbol{\nabla}\mu^{\downarrow} \\ -\frac{1}{T}\boldsymbol{\nabla}T \end{pmatrix} \, , \tag{2.287}$$

with

$$\underline{\boldsymbol{L}}^{\uparrow(\downarrow)}_{n}(T) = -\frac{1}{e}\int d\,E\; \underline{\boldsymbol{\sigma}}^{\uparrow(\downarrow)}(E) \left(-\frac{d\,f_0(E,T)}{d\,E}\right) (E-\mu_{\mathrm{c}})^{n} \, . \tag{2.288}$$

Here the quantities $\underline{\boldsymbol{L}}^{\uparrow(\downarrow)}_{1'}$ are the reciprocal coefficients of $\underline{\boldsymbol{L}}^{\uparrow(\downarrow)}_{1}$, connected via the Onsager relation [283]

$$\underline{\boldsymbol{L}}^{\uparrow(\downarrow)}_{1'} = -(\underline{\boldsymbol{L}}^{\uparrow(\downarrow)}_{1})^{T} \, . \tag{2.289}$$

Of course the symmetry of $\underline{\boldsymbol{\sigma}}^{\uparrow(\downarrow)}(E)$ is carried over to the response functions $\underline{\boldsymbol{L}}^{\uparrow(\downarrow)}_{n}(T)$.

Eq. (2.287) excludes a spin-dependent temperature gradient [327] with the response sub-tensor related to the thermal conductivity, the bottom right element in the tensor of Eq. (2.287), being simply the sum of both electronic contributions with different spin, $\kappa = \kappa^{\uparrow} + \kappa^{\downarrow}$, following, e.g., Ref. 24. This is not explicitly considered by Tauber *et al.* [20].

Starting now from the spin-projected currents as responses to a spin-dependent chemical potential $\boldsymbol{\nabla}\mu^{\uparrow(\downarrow)}$ and to a temperature gradient $\boldsymbol{\nabla}T$,

$$\mathbf{j}^{\uparrow(\downarrow)} = -\underline{\boldsymbol{L}}^{\uparrow(\downarrow)}_{0}\boldsymbol{\nabla}\mu^{\uparrow(\downarrow)} - \frac{1}{T}\underline{\boldsymbol{L}}^{\uparrow(\downarrow)}_{1}\boldsymbol{\nabla}T \tag{2.290}$$

$$\mathbf{j} = \mathbf{j}^{\uparrow} + \mathbf{j}^{\downarrow} = -(\underline{\boldsymbol{L}}^{\uparrow}_{0}\boldsymbol{\nabla}\mu^{\uparrow} + \underline{\boldsymbol{L}}^{\downarrow}_{0}\boldsymbol{\nabla}\mu^{\downarrow}) - \frac{1}{T}(\underline{\boldsymbol{L}}^{\uparrow}_{1} + \underline{\boldsymbol{L}}^{\downarrow}_{1})\boldsymbol{\nabla}T \tag{2.291}$$

$$\mathbf{j}^{s} = \mathbf{j}^{\uparrow} - \mathbf{j}^{\downarrow} = -(\underline{\boldsymbol{L}}^{\uparrow}_{0}\boldsymbol{\nabla}\mu^{\uparrow} - \underline{\boldsymbol{L}}^{\downarrow}_{0}\boldsymbol{\nabla}\mu^{\downarrow}) - \frac{1}{T}(\underline{\boldsymbol{L}}^{\uparrow}_{1} - \underline{\boldsymbol{L}}^{\downarrow}_{1})\boldsymbol{\nabla}T \, , \tag{2.292}$$

one can, by setting the respective current $\mathbf{j}^{b}$ with $b \in \{\uparrow, \downarrow, , s\}$ to 0, derive spin-dependent Seebeck coefficients $\underline{\boldsymbol{S}}^{\uparrow(\downarrow)}$ from Eq. (2.290):

$$\frac{1}{e}\boldsymbol{\nabla}\mu^{\uparrow(\downarrow)} = -\frac{1}{eT}(\underline{\boldsymbol{L}}^{\uparrow(\downarrow)}_{0})^{-1}\underline{\boldsymbol{L}}^{\uparrow(\downarrow)}_{1}\boldsymbol{\nabla}T = \underline{\boldsymbol{S}}^{\uparrow(\downarrow)}\boldsymbol{\nabla}T \, . \tag{2.293}$$

For $b =\uparrow$ one obtains for example the explicit expression for $\underline{\boldsymbol{S}}^{\uparrow}$,

$$\begin{aligned}
\underline{\boldsymbol{S}}^{\uparrow} &= -\frac{1}{eT}\begin{pmatrix} L^{\uparrow}_{0,\mathrm{xx}} & L^{\uparrow}_{0,\mathrm{xy}} & 0 \\ -L^{\uparrow}_{0,\mathrm{xy}} & L^{\uparrow}_{0,\mathrm{xx}} & 0 \\ 0 & 0 & L^{\uparrow}_{0,\mathrm{zz}} \end{pmatrix}^{-1}\begin{pmatrix} L^{\uparrow}_{1,\mathrm{xx}} & L^{\uparrow}_{1,\mathrm{xy}} & 0 \\ -L^{\uparrow}_{1,\mathrm{xy}} & L^{\uparrow}_{1,\mathrm{xx}} & 0 \\ 0 & 0 & L^{\uparrow}_{1,\mathrm{zz}} \end{pmatrix} \\
&= -\frac{1}{eT}\begin{pmatrix} \frac{L^{\uparrow}_{0,\mathrm{xx}}L^{\uparrow}_{1,\mathrm{xx}}+L^{\uparrow}_{0,\mathrm{xy}}L^{\uparrow}_{1,\mathrm{xy}}}{{L^{\uparrow}_{0,\mathrm{xx}}}^2+{L^{\uparrow}_{0,\mathrm{xy}}}^2} & \frac{L^{\uparrow}_{0,\mathrm{xx}}L^{\uparrow}_{1,\mathrm{xy}}-L^{\uparrow}_{0,\mathrm{xy}}L^{\uparrow}_{1,\mathrm{xx}}}{{L^{\uparrow}_{0,\mathrm{xx}}}^2+{L^{\uparrow}_{0,\mathrm{xy}}}^2} & 0 \\ \frac{L^{\uparrow}_{0,\mathrm{xy}}L^{\uparrow}_{1,\mathrm{xx}}-L^{\uparrow}_{0,\mathrm{xx}}L^{\uparrow}_{1,\mathrm{xy}}}{{L^{\uparrow}_{0,\mathrm{xx}}}^2+{L^{\uparrow}_{0,\mathrm{xy}}}^2} & \frac{L^{\uparrow}_{0,\mathrm{xx}}L^{\uparrow}_{1,\mathrm{xx}}+L^{\uparrow}_{0,\mathrm{xy}}L^{\uparrow}_{1,\mathrm{xy}}}{{L^{\uparrow}_{0,\mathrm{xx}}}^2+{L^{\uparrow}_{0,\mathrm{xy}}}^2} & 0 \\ 0 & 0 & (L^{\uparrow}_{0,\mathrm{zz}})^{-1}L^{\uparrow}_{1,\mathrm{zz}} \end{pmatrix} \\
&= \begin{pmatrix} S^{\uparrow}_{\mathrm{xx}} & S^{\uparrow}_{\mathrm{xy}} & 0 \\ -S^{\uparrow}_{\mathrm{xy}} & S^{\uparrow}_{\mathrm{xx}} & 0 \\ 0 & 0 & S^{\uparrow}_{\mathrm{zz}} \end{pmatrix} , \qquad (2.294)
\end{aligned}$$

that obviously has the same tensor shape as the responses quantities represented by Eq. (2.282).

Analogously a charge Seebeck tensor $\underline{\boldsymbol{S}}$ can be obtained from Eq. (2.291) by making use of the relations given by Eq. (2.284),

$$\begin{aligned}
\mathbf{0} = \mathbf{j} &= -(\underline{\boldsymbol{L}}^{\uparrow}_0\boldsymbol{\nabla}\mu^{\uparrow} + \underline{\boldsymbol{L}}^{\downarrow}_0\boldsymbol{\nabla}\mu^{\downarrow}) - \frac{1}{T}(\underline{\boldsymbol{L}}^{\uparrow}_1 + \underline{\boldsymbol{L}}^{\downarrow}_1)\boldsymbol{\nabla}T \\
&= -(\underline{\boldsymbol{L}}^{\uparrow}_0\boldsymbol{\nabla}\mu^{\uparrow} + (\underline{\boldsymbol{L}}^{\uparrow}_0)^T\boldsymbol{\nabla}\mu^{\downarrow}) - \frac{1}{T}(\underline{\boldsymbol{L}}^{\uparrow}_1 + (\underline{\boldsymbol{L}}^{\uparrow}_1)^T)\boldsymbol{\nabla}T \, . \qquad (2.295)
\end{aligned}$$

Using again matrix notation, this is

$$\begin{aligned}
\begin{pmatrix} 0 \\ 0 \\ 0 \end{pmatrix} = &-\left[\begin{pmatrix} L^{\uparrow}_{0,xx} & L^{\uparrow}_{0,xy} & 0 \\ -L^{\uparrow}_{0,xy} & L^{\uparrow}_{0,xx} & 0 \\ 0 & 0 & L^{\uparrow}_{0,zz} \end{pmatrix}\begin{pmatrix} \nabla_{\mathrm{x}}\mu^{\uparrow} \\ \nabla_{\mathrm{y}}\mu^{\uparrow} \\ \nabla_{\mathrm{z}}\mu^{\uparrow} \end{pmatrix} + \begin{pmatrix} L^{\downarrow}_{0,xx} & L^{\downarrow}_{0,xy} & 0 \\ -L^{\downarrow}_{0,xy} & L^{\downarrow}_{0,xx} & 0 \\ 0 & 0 & L^{\downarrow}_{0,zz} \end{pmatrix}\begin{pmatrix} \nabla_{\mathrm{x}}\mu^{\downarrow} \\ \nabla_{\mathrm{y}}\mu^{\downarrow} \\ \nabla_{\mathrm{z}}\mu^{\downarrow} \end{pmatrix}\right] \\
&-\frac{1}{T}\left[\begin{pmatrix} L^{\uparrow}_{1,xx} & L^{\uparrow}_{1,xy} & 0 \\ -L^{\uparrow}_{1,xy} & L^{\uparrow}_{1,xx} & 0 \\ 0 & 0 & L^{\uparrow}_{1,zz} \end{pmatrix} + \begin{pmatrix} L^{\downarrow}_{1,xx} & L^{\downarrow}_{1,xy} & 0 \\ -L^{\downarrow}_{1,xy} & L^{\downarrow}_{1,xx} & 0 \\ 0 & 0 & L^{\downarrow}_{1,zz} \end{pmatrix}\right]\begin{pmatrix} \nabla_{\mathrm{x}}T \\ \nabla_{\mathrm{y}}T \\ \nabla_{\mathrm{z}}T \end{pmatrix} \\
= &-\begin{pmatrix} L^{\uparrow}_{0,\mathrm{xx}}(\nabla_{\mathrm{x}}\mu^{\uparrow} + \nabla_{\mathrm{x}}\mu^{\downarrow}) + L^{\uparrow}_{0,\mathrm{xy}}(\nabla_{\mathrm{y}}\mu^{\uparrow} - \nabla_{\mathrm{y}}\mu^{\downarrow}) \\ -L^{\uparrow}_{0,\mathrm{xy}}(\nabla_{\mathrm{x}}\mu^{\uparrow} - \nabla_{\mathrm{x}}\mu^{\downarrow}) + L^{\uparrow}_{0,\mathrm{xx}}(\nabla_{\mathrm{y}}\mu^{\uparrow} + \nabla_{\mathrm{y}}\mu^{\downarrow}) \\ L^{\uparrow}_{0,\mathrm{zz}}(\nabla_{\mathrm{z}}\mu^{\uparrow} + \nabla_{\mathrm{z}}\mu^{\downarrow}) \end{pmatrix} \\
&-\frac{1}{T}\begin{pmatrix} 2L^{\uparrow}_{1,\mathrm{xx}} & 0 & 0 \\ 0 & 2L^{\uparrow}_{1,\mathrm{xx}} & 0 \\ 0 & 0 & 2L^{\uparrow}_{1,\mathrm{zz}} \end{pmatrix}\begin{pmatrix} \nabla_{\mathrm{x}}T \\ \nabla_{\mathrm{y}}T \\ \nabla_{\mathrm{z}}T \end{pmatrix} . \qquad (2.296)
\end{aligned}$$

The first term on the r.h.s. of the second line containing sums and differences of spin-dependent chemical potentials can be decomposed again into a response to an electric

field $\mathbf{E} = \frac{1}{2e}(\boldsymbol{\nabla}\mu^{\uparrow} + \boldsymbol{\nabla}\mu^{\downarrow})$ and one to a spin accumulation $\boldsymbol{\nabla}\mu^{s} = \frac{1}{2e}(\boldsymbol{\nabla}\mu^{\uparrow} - \boldsymbol{\nabla}\mu^{\downarrow}) \stackrel{!}{=} \frac{1}{2e}\boldsymbol{\nabla}(\mu^{\uparrow} - \mu^{\downarrow})$:

$$\begin{aligned}\begin{pmatrix}0\\0\\0\end{pmatrix} =& -2e\begin{pmatrix}L^{\uparrow}_{0,\mathrm{xx}} & 0 & 0\\ 0 & L^{\uparrow}_{0,\mathrm{xx}} & 0\\ 0 & 0 & L^{\uparrow}_{0,\mathrm{xx}}\end{pmatrix}\begin{pmatrix}E_{\mathrm{x}}\\E_{\mathrm{y}}\\E_{\mathrm{z}}\end{pmatrix} - 2e\begin{pmatrix}0 & L^{\uparrow}_{0,\mathrm{xy}} & 0\\ -L^{\uparrow}_{0,\mathrm{xy}} & 0 & 0\\ 0 & 0 & 0\end{pmatrix}\begin{pmatrix}\nabla_{\mathrm{x}}\mu^{s}\\\nabla_{\mathrm{y}}\mu^{s}\\\nabla_{\mathrm{z}}\mu^{s}\end{pmatrix}\\ &-\frac{2}{T}\begin{pmatrix}L^{\uparrow}_{1,\mathrm{xx}} & 0 & 0\\ 0 & L^{\uparrow}_{1,\mathrm{xx}} & 0\\ 0 & 0 & L^{\uparrow}_{1,\mathrm{xx}}\end{pmatrix}\begin{pmatrix}\nabla_{\mathrm{x}}T\\\nabla_{\mathrm{y}}T\\\nabla_{\mathrm{z}}T\end{pmatrix}. \end{aligned} \tag{2.297}$$

From this expression one can derive Seebeck coefficients for two different scenarios. Assuming closed spin current boundary condition, i.e., if a spin accumulation at the edges (x or y direction) perpendicular to the applied temperature gradient (y or x direction) cannot build up, the second term vanishes and one obtains by solving for the electric field

$$\begin{aligned}\mathbf{E} =& -\frac{1}{eT}\begin{pmatrix}L^{\uparrow}_{0,\mathrm{xx}} & 0 & 0\\ 0 & L^{\uparrow}_{0,\mathrm{xx}} & 0\\ 0 & 0 & L^{\uparrow}_{0,\mathrm{zz}}\end{pmatrix}^{-1}\begin{pmatrix}L^{\uparrow}_{1,\mathrm{xx}} & 0 & 0\\ 0 & L^{\uparrow}_{1,\mathrm{xx}} & 0\\ 0 & 0 & L^{\uparrow}_{1,\mathrm{zz}}\end{pmatrix}\boldsymbol{\nabla}T\\ =& -\frac{1}{eT}\begin{pmatrix}\frac{L^{\uparrow}_{1,\mathrm{xx}}}{L^{\uparrow}_{0,\mathrm{xx}}} & 0 & 0\\ 0 & \frac{L^{\uparrow}_{1,\mathrm{xx}}}{L^{\uparrow}_{0,\mathrm{xx}}} & 0\\ 0 & 0 & \frac{L^{\uparrow}_{1,\mathrm{zz}}}{L^{\uparrow}_{0,\mathrm{zz}}}\end{pmatrix}\boldsymbol{\nabla}T = \underline{\tilde{\boldsymbol{S}}}\boldsymbol{\nabla}T. \end{aligned} \tag{2.298}$$

This corresponds to the expression for the charge Seebeck coefficient given by us in Eq. (6) of Ref. 266, that was derived without considering a response to a spin accumulation or the field F^{s} in Eq. (2.130). This will be detailed in the following part.

For open spin current boundary conditions on the other hand, i.e., if a spin accumulation in x or y direction is present, this can be expressed by setting the spin current in Eq. (2.292) to 0. Noting that the z component is irrelevant since it does not mix in, one is led to

$$\begin{aligned}\begin{pmatrix}0\\0\\0\end{pmatrix} =& -\left[\begin{pmatrix}L^{\uparrow}_{0,xx} & L^{\uparrow}_{0,xy} & 0\\ -L^{\uparrow}_{0,xy} & L^{\uparrow}_{0,xx} & 0\\ 0 & 0 & L^{\uparrow}_{0,zz}\end{pmatrix}\begin{pmatrix}\nabla_{\mathrm{x}}\mu^{\uparrow}\\\nabla_{\mathrm{y}}\mu^{\uparrow}\\\nabla_{\mathrm{z}}\mu^{\uparrow}\end{pmatrix} - \begin{pmatrix}L^{\downarrow}_{0,xx} & L^{\downarrow}_{0,xy} & 0\\ -L^{\downarrow}_{0,xy} & L^{\downarrow}_{0,xx} & 0\\ 0 & 0 & L^{\downarrow}_{0,zz}\end{pmatrix}\begin{pmatrix}\nabla_{\mathrm{x}}\mu^{\downarrow}\\\nabla_{\mathrm{y}}\mu^{\downarrow}\\\nabla_{\mathrm{z}}\mu^{\downarrow}\end{pmatrix}\right]\\ &-\frac{1}{T}\left[\begin{pmatrix}L^{\uparrow}_{1,xx} & L^{\uparrow}_{1,xy} & 0\\ -L^{\uparrow}_{1,xy} & L^{\uparrow}_{1,xx} & 0\\ 0 & 0 & L^{\uparrow}_{1,zz}\end{pmatrix} - \begin{pmatrix}L^{\downarrow}_{1,xx} & L^{\downarrow}_{1,xy} & 0\\ -L^{\downarrow}_{1,xy} & L^{\downarrow}_{1,xx} & 0\\ 0 & 0 & L^{\downarrow}_{1,zz}\end{pmatrix}\right]\begin{pmatrix}\nabla_{\mathrm{x}}T\\\nabla_{\mathrm{y}}T\\\nabla_{\mathrm{z}}T\end{pmatrix}\\ =& -2e\begin{pmatrix}0 & L^{\uparrow}_{0,\mathrm{xy}} & 0\\ -L^{\uparrow}_{0,\mathrm{xy}} & 0 & 0\\ 0 & 0 & 0\end{pmatrix}\begin{pmatrix}E_{\mathrm{x}}\\E_{\mathrm{y}}\\E_{\mathrm{z}}\end{pmatrix} - 2e\begin{pmatrix}L^{\uparrow}_{0,\mathrm{xx}} & 0 & 0\\ 0 & L^{\uparrow}_{0,\mathrm{xx}} & 0\\ 0 & 0 & L^{\uparrow}_{0,\mathrm{zz}}\end{pmatrix}\begin{pmatrix}\nabla_{\mathrm{x}}\mu^{s}\\\nabla_{\mathrm{y}}\mu^{s}\\\nabla_{\mathrm{z}}\mu^{s}\end{pmatrix}\\ &-\frac{2}{T}\begin{pmatrix}0 & L^{\uparrow}_{1,\mathrm{xy}} & 0\\ -L^{\uparrow}_{1,\mathrm{xy}} & 0 & 0\\ 0 & 0 & 0\end{pmatrix}\begin{pmatrix}\nabla_{\mathrm{x}}T\\\nabla_{\mathrm{y}}T\\\nabla_{\mathrm{z}}T\end{pmatrix}. \end{aligned} \tag{2.299}$$

Solving this expression for $\boldsymbol{\nabla}\mu^s$ one has:

$$\begin{pmatrix} \nabla_\mathrm{x}\mu^s \\ \nabla_\mathrm{y}\mu^s \\ \nabla_\mathrm{z}\mu^s \end{pmatrix} = - \begin{pmatrix} 0 & \frac{L^\uparrow_{0,\mathrm{xy}}}{L^\uparrow_{0,\mathrm{xx}}} & 0 \\ -\frac{L^\uparrow_{0,\mathrm{xy}}}{L^\uparrow_{0,\mathrm{xx}}} & 0 & 0 \\ 0 & 0 & 0 \end{pmatrix} \begin{pmatrix} E_\mathrm{x} \\ E_\mathrm{y} \\ E_\mathrm{z} \end{pmatrix} - \frac{1}{eT} \begin{pmatrix} 0 & \frac{L^\uparrow_{1,\mathrm{xy}}}{L^\uparrow_{0,\mathrm{xx}}} & 0 \\ -\frac{L^\uparrow_{1,\mathrm{xy}}}{L^\uparrow_{0,\mathrm{xx}}} & 0 & 0 \\ 0 & 0 & 0 \end{pmatrix} \begin{pmatrix} \nabla_\mathrm{x}T \\ \nabla_\mathrm{y}T \\ \nabla_\mathrm{z}T \end{pmatrix} . \tag{2.300}$$

Inserting this result into Eq. (2.297) and solving finally for the electric field, one arrives at:

$$\begin{pmatrix} E_\mathrm{x} \\ E_\mathrm{y} \\ E_\mathrm{z} \end{pmatrix} = - \frac{1}{eT} \begin{pmatrix} \frac{L^\uparrow_{0,\mathrm{xx}}L^\uparrow_{1,\mathrm{xx}}+L^\uparrow_{0,\mathrm{xy}}L^\uparrow_{1,\mathrm{xy}}}{{L^\uparrow_{0,\mathrm{xx}}}^2+{L^\uparrow_{0,\mathrm{xy}}}^2} & 0 & 0 \\ 0 & \frac{L^\uparrow_{0,\mathrm{xx}}L^\uparrow_{1,\mathrm{xx}}+L^\uparrow_{0,\mathrm{xy}}L^\uparrow_{1,\mathrm{xy}}}{{L^\uparrow_{0,\mathrm{xx}}}^2+{L^\uparrow_{0,\mathrm{xy}}}^2} & 0 \\ 0 & 0 & \frac{L^\uparrow_{1,\mathrm{zz}}}{L^\uparrow_{0,\mathrm{zz}}} \end{pmatrix} \begin{pmatrix} \nabla_\mathrm{x}T \\ \nabla_\mathrm{y}T \\ \nabla_\mathrm{z}T \end{pmatrix} , \tag{2.301}$$

Obviously one obtains this way a second expression for the Seebeck coefficient $\underline{\boldsymbol{S}}$, that differs from the one given by Eq. (2.298). The first two diagonal elements contain now a product of two off-diagonal response coefficients, $L^\uparrow_{0,\mathrm{xy}}L^\uparrow_{1,\mathrm{xy}} = -L^\uparrow_{0,\mathrm{xy}}L^\uparrow_{1,\mathrm{yx}}$, which in combination give a longitudinal response. This has to be interpreted as a competition of the spin Nernst effect, creating (or trying to create) a spin accumulation transverse to the temperature gradient, and the inverse spin Hall effect transforming this gradient of spin polarisation into an electric field transverse to itself, which is again longitudinal to the temperature gradient. One might say that, without explicitly stating it, Tauber *et al.* [20] introduced the concept of the spin Nernst magneto-thermopower (SMT), that was employed for the observation of the spin Nernst effect in Ref. 21 (reprinted in Section 3.2). The boundary conditions for the spin current were controlled in experiment by rotating the magnetisation in a ferromagnetic insulator attached to the nonmagnet.

It should be noted that the tensor shape in Eq. (2.301) implies the symmetry of the cubic crystal to be broken, since the diagonal entries are not identical. This is due to the actual two dimensional situation one is looking at: the transverse (x and y) directions of the sample are finite, in order to allow for a spin accumulation, i.e., these dimensions are in the order of the spin diffusion length. In particular starting with the tensor shape in Eq. (2.282) the z direction is already assumed to be different from the x and y directions.

The resulting Seebeck tensor, that contains the additional "spin Nernst × inverse spin Hall effect"contribution, is identical to

$$\begin{aligned}\frac{1}{2}(\underline{\boldsymbol{S}}^{\uparrow}+\underline{\boldsymbol{S}}^{\downarrow})\boldsymbol{\nabla}T &= \frac{1}{2}\left[\begin{pmatrix} S^{\uparrow}_{\mathrm{xx}} & S^{\uparrow}_{\mathrm{xy}} & 0\\ -S^{\uparrow}_{\mathrm{xy}} & S^{\uparrow}_{\mathrm{xx}} & 0\\ 0 & 0 & S^{\uparrow}_{\mathrm{zz}}\end{pmatrix}+\begin{pmatrix} S^{\downarrow}_{\mathrm{xx}} & S^{\downarrow}_{\mathrm{xy}} & 0\\ -S^{\downarrow}_{\mathrm{xy}} & S^{\downarrow}_{\mathrm{xx}} & 0\\ 0 & 0 & S^{\downarrow}_{\mathrm{zz}}\end{pmatrix}\right]\boldsymbol{\nabla}T\\ =\frac{1}{2}(\underline{\boldsymbol{S}}^{\uparrow}+(\underline{\boldsymbol{S}}^{\uparrow})^{T})\boldsymbol{\nabla}T &= \frac{1}{2}\left[\begin{pmatrix} S^{\uparrow}_{\mathrm{xx}} & S^{\uparrow}_{\mathrm{xy}} & 0\\ -S^{\uparrow}_{\mathrm{xy}} & S^{\uparrow}_{\mathrm{xx}} & 0\\ 0 & 0 & S^{\uparrow}_{\mathrm{zz}}\end{pmatrix}+\begin{pmatrix} S^{\uparrow}_{\mathrm{xx}} & -S^{\uparrow}_{\mathrm{xy}} & 0\\ S^{\uparrow}_{\mathrm{xy}} & S^{\uparrow}_{\mathrm{xx}} & 0\\ 0 & 0 & S^{\uparrow}_{\mathrm{zz}}\end{pmatrix}\right]\boldsymbol{\nabla}T\\ &= \begin{pmatrix} S^{\uparrow}_{\mathrm{xx}} & 0 & 0\\ 0 & S^{\uparrow}_{\mathrm{xx}} & 0\\ 0 & 0 & S^{\uparrow}_{\mathrm{zz}}\end{pmatrix}\boldsymbol{\nabla}T=\underline{\boldsymbol{S}}\boldsymbol{\nabla}T\,. \end{aligned} \tag{2.302}$$

This expression contains only the diagonal elements of $\underline{\boldsymbol{S}}^{\uparrow}$,

$$S^{\uparrow}_{\mathrm{xx}}=-\frac{1}{eT}\frac{L^{\uparrow}_{0,\mathrm{xx}}L^{\uparrow}_{1,\mathrm{xx}}+L^{\uparrow}_{0,\mathrm{xy}}L^{\uparrow}_{1,\mathrm{xy}}}{{L^{\uparrow}_{0,\mathrm{xx}}}^{2}+{L^{\uparrow}_{0,\mathrm{xy}}}^{2}} \tag{2.303}$$

and

$$S^{\uparrow}_{\mathrm{zz}}=-\frac{1}{eT}\frac{L^{\uparrow}_{1,\mathrm{zz}}}{L^{\uparrow}_{0,\mathrm{zz}}}\,, \tag{2.304}$$

and corresponds to Eq. (8) of Ref. 20.

Analogously, a spin-polarised Seebeck coefficient $\underline{\boldsymbol{S}}^{s}$ for open spin-circuit conditions can be derived from Eq. (2.300) by inserting the r.h.s of Eq. (2.301), $-\frac{1}{eT}\underline{\boldsymbol{S}}\boldsymbol{\nabla}T$, for the electric field. This leads to

$$\boldsymbol{\nabla}\mu=\underline{\boldsymbol{S}}^{s}\boldsymbol{\nabla}T\,, \tag{2.305}$$

with the spin-polarised Seebeck coefficient $\underline{\boldsymbol{S}}^{s}=\frac{1}{2}(\underline{\boldsymbol{S}}^{\uparrow}-\underline{\boldsymbol{S}}^{\downarrow})$ given for non-magnetic materials as:

$$\underline{\boldsymbol{S}}^{s}=-\frac{1}{eT}\begin{pmatrix} 0 & \frac{L^{\uparrow}_{0,\mathrm{xy}}L^{\uparrow}_{1,\mathrm{xx}}-L^{\uparrow}_{0,\mathrm{xx}}L^{\uparrow}_{1,\mathrm{xy}}}{{L^{\uparrow}_{0,\mathrm{xx}}}^{2}+{L^{\uparrow}_{0,\mathrm{xy}}}^{2}} & 0\\ -\frac{L^{\uparrow}_{0,\mathrm{xy}}L^{\uparrow}_{1,\mathrm{xx}}-L^{\uparrow}_{0,\mathrm{xx}}L^{\uparrow}_{1,\mathrm{xy}}}{{L^{\uparrow}_{0,\mathrm{xx}}}^{2}+{L^{\uparrow}_{0,\mathrm{xy}}}^{2}} & 0 & 0\\ 0 & 0 & 0\end{pmatrix}\,. \tag{2.306}$$

In analogy to Eq. (2.302), this is identical to the off-diagonal elements of $\underline{\boldsymbol{S}}^{\uparrow}$ defined in Eq. (2.293) and corresponds to Eq. (10) of Ref. 20.

One might, for the sake of completeness, consider a case where a spin accumulation can build up in one direction (transverse w.r.t $\boldsymbol{\nabla}T$), while charge is flowing in the other (longitudinal w.r.t $\boldsymbol{\nabla}T$), i.e., open circuit conditions for the spin current and closed circuit conditions for the charge current. This is done by neglecting the effect of the electric field on the spin accumulation entering Eq. (2.300). This special

situation leads to a modified (reduced) spin-polarised Seebeck coefficient according to

$$\underline{\tilde{\boldsymbol{S}}}^{s} = \frac{\boldsymbol{\nabla}\mu^{s}}{\boldsymbol{\nabla}T} = -\frac{1}{eT}\begin{pmatrix} 0 & \frac{L^{\uparrow}_{1,\mathrm{xy}}}{L^{\uparrow}_{0,\mathrm{xx}}} & 0 \\ -\frac{L^{\uparrow}_{1,\mathrm{xy}}}{L^{\uparrow}_{0,\mathrm{xx}}} & 0 & 0 \\ 0 & 0 & 0 \end{pmatrix} . \tag{2.307}$$

Spincaloritronics in terms of spin-polarised response functions

In the following the formalism used in Refs. 322 and 266 will be outlined. As sketched in Section 2.3.1, with a proper formulation for the operators representing charge and spin transport at hand, the corresponding conductivity tensors can straightforwardly be expressed my means of Kubo's linear response formalism. At the same time group-theoretical considerations, see next section (2.3.4), allow without further assumptions to determine the shape of these tensors in an unambiguous way. Dealing for example with charge and spin transport induced by an electric field ($B = c$) or a temperature gradient ($B = q$) in a non-magnetic cubic system, one gets for the charge transport response functions $a = \sigma$ or L^{cc} and L^{cq}, respectively:

$$\underline{\boldsymbol{a}}^{cB} = \begin{pmatrix} a^{cB}_{\mathrm{xx}} & 0 & 0 \\ 0 & a^{cB}_{\mathrm{xx}} & 0 \\ 0 & 0 & a^{cB}_{\mathrm{xx}} \end{pmatrix} \tag{2.308}$$

and for the corresponding spin transport functions $a = \sigma^{\xi}$ or $\mathcal{L}^{\xi}$ with $\xi = \mathrm{z}$:

$$\underline{\boldsymbol{a}}^{sB} = \begin{pmatrix} 0 & a^{sB}_{\mathrm{xy}} & 0 \\ -a^{sB}_{\mathrm{xy}} & 0 & 0 \\ 0 & 0 & 0 \end{pmatrix} \tag{2.309}$$

The response functions L^{qq} connected to thermal transport have the same structure as a^{cB}, which will, as the relation between σ^{Ac}, $(L/\mathcal{L})^{Ac}$ and $(L/\mathcal{L})^{Aq}$, become obvious from Eq. (2.311) below. Heat transport via phonons will not be considered here, nor any other non-electronic transport mechanisms.

For the most general situation the set of relevant transport equations are summarised as

$$\begin{pmatrix} \mathbf{j} \\ \boldsymbol{J}^{s} \\ \mathbf{j}^{q} \end{pmatrix} = \begin{pmatrix} \underline{\boldsymbol{L}}^{cc} & \underline{\boldsymbol{\mathcal{L}}}^{cs} & \underline{\boldsymbol{L}}^{cq} \\ \underline{\boldsymbol{L}}^{sc} & \underline{\tilde{\boldsymbol{\mathcal{L}}}}^{ss} & \underline{\boldsymbol{\mathcal{L}}}^{sq} \\ \underline{\boldsymbol{L}}^{qc} & \underline{\boldsymbol{\mathcal{L}}}^{qs} & \underline{\boldsymbol{L}}^{qq} \end{pmatrix} \begin{pmatrix} -\boldsymbol{\nabla}\mu \\ \underline{\boldsymbol{F}}^{s} \\ -\frac{1}{T}\boldsymbol{\nabla}T \end{pmatrix} \tag{2.310}$$

with the corresponding transport coefficients to be determined by applying the generalised Mott relations

$$(\underline{\boldsymbol{L}}/\underline{\boldsymbol{\mathcal{L}}})^{(s/c)B(,\xi)}(T) = -\frac{1}{e}\int d\,E\; \underline{\boldsymbol{\sigma}}^{(s/c)c(,\xi)}(E)\left(-\frac{d\,f(E,T)}{d\,E}\right)(E - E_F)^{n} , \tag{2.311}$$

where $B = c$ if $n = 0$ and $B = q$ if $n = 1$. Obviously no assumptions concerning boundary conditions have been made so far, i.e., no specific experimental geometry is considered and the full symmetry of the three dimensional system is retained.

In Eq. (2.310) Onsager relations of the second kind connect the off-diagonal tensors when the role of response and force are interchanged, i.e. $\underline{\boldsymbol{\mathcal{L}}}^{sc} \leftrightarrow \underline{\boldsymbol{\mathcal{L}}}^{cs}$, $\underline{\boldsymbol{L}}^{cq} \leftrightarrow \underline{\boldsymbol{L}}^{qc}$ and $\underline{\boldsymbol{\mathcal{L}}}^{sq} \leftrightarrow \underline{\boldsymbol{\mathcal{L}}}^{qs}$. For the special case of a non-magnetic cubic system studied here,[38] they are $\underline{\boldsymbol{L}}^{cq} = (\underline{\boldsymbol{L}}^{qc})^T = \underline{\boldsymbol{L}}^{qc}$, $\underline{\boldsymbol{\mathcal{L}}}^{sc,\xi} = -(\underline{\boldsymbol{\mathcal{L}}}^{cs,\xi})^T = \underline{\boldsymbol{\mathcal{L}}}^{cs,\xi}$ and $\underline{\boldsymbol{\mathcal{L}}}^{sq,\xi} = -(\underline{\boldsymbol{\mathcal{L}}}^{qs,\xi})^T = \underline{\boldsymbol{\mathcal{L}}}^{qs,\xi}$ $\forall\ \xi \in \{\mathrm{x},\mathrm{y},\mathrm{z}\}$. This is because $\underline{\boldsymbol{\mathcal{L}}}^{cq}$ is diagonal and isotropic, the three sub-tensors of $\underline{\boldsymbol{\mathcal{L}}}^{sc,\xi}$ are purely anti-symmetric and contain only one independent element (the spin Hall conductivity), and the same holds true for $\underline{\boldsymbol{\mathcal{L}}}^{sq,\xi}$, as $\boldsymbol{j}$ and $\boldsymbol{j}^q$ transform identically. Here the coefficient $\mathcal{L}^{sq,z}_{\mathrm{xy}} = -\mathcal{L}^{sq,z}_{\mathrm{yx}}$ is of course connected to the spin Nernst conductivity.

Although the precise form of $\underline{\boldsymbol{F}}^s$ is not so clear, it certainly can be for example connected to the gradient of a spin accumulation. Also the mechanisms behind the corresponding responses described by the elements of $\underline{\boldsymbol{\mathcal{L}}}^{cs}$, $\underline{\tilde{\boldsymbol{\mathcal{L}}}}^{ss}$ and $\underline{\boldsymbol{\mathcal{L}}}^{qs}$ are a matter of debate. The first of the three is related to the inverse spin Hall effect, the third one suggests the existence of an inverse spin Nernst or "spin Ettingshausen effect". The fourth rank response tensor $\underline{\tilde{\boldsymbol{\mathcal{L}}}}^{ss}$ is the most enigmatic of them. It could for example describe the generation of a spin current by a spin accumulation, which is itself generated by, e.g., an electric field or a temperature gradient, via $\underline{\boldsymbol{\mathcal{L}}}^{sc}$ or $\underline{\boldsymbol{\mathcal{L}}}^{sq}$, respectively (spin Hall or Nernst effect). Most naively one could think of it in terms of spin relaxation. In the following, the diagonal sub-tensors of $\underline{\tilde{\boldsymbol{\mathcal{L}}}}^{ss}$ are assumed to be identical to the charge conductivity tensor.[39] This can be justified by considering the spin polarisation to be transported exclusively by the electronic subsystem, i.e., magnons for example are neglected. In fact only the zz sub-tensor is needed here and the polarisations will be assumed to be independent, i.e., no off-diagonal sub-tensors have to be considered. In the following we will accordingly only consider the case of $\xi = \mathrm{z}$ and drop the index altogether.

So far the fictitious field or *spin force* $\underline{\boldsymbol{F}}^s$ has not been considered explicitly as a source for any induced currents. Accordingly, the Seebeck tensor $\underline{\boldsymbol{S}}$ is simply obtained by setting $\boldsymbol{j}$ in the first line of Eq. (2.310) to zero, dropping $\underline{\boldsymbol{\mathcal{L}}}^{cs}$ and solving for the electric field. This way one obtains in analogy to Eq. (2.298) for non-magnetic system having cubic symmetry:

$$\begin{aligned}\mathbf{E} &= -\frac{1}{eT}\begin{pmatrix} L^{cc}_{\mathrm{xx}} & 0 & 0 \\ 0 & L^{cc}_{\mathrm{xx}} & 0 \\ 0 & 0 & L^{cc}_{\mathrm{xx}} \end{pmatrix}^{-1} \begin{pmatrix} L^{cq}_{\mathrm{xx}} & 0 & 0 \\ 0 & L^{cq}_{\mathrm{xx}} & 0 \\ 0 & 0 & L^{cq}_{\mathrm{xx}} \end{pmatrix} \boldsymbol{\nabla} T \\ &= -\frac{1}{eT}\begin{pmatrix} \frac{L^{cq}_{\mathrm{xx}}}{L^{cc}_{\mathrm{xx}}} & 0 & 0 \\ 0 & \frac{L^{cq}_{\mathrm{xx}}}{L^{cc}_{\mathrm{xx}}} & 0 \\ 0 & 0 & \frac{L^{cq}_{\mathrm{xx}}}{L^{cc}_{\mathrm{xx}}} \end{pmatrix} \boldsymbol{\nabla} T = \underline{\boldsymbol{S}} \boldsymbol{\nabla} T\ . \end{aligned} \tag{2.312}$$

The charge Seebeck tensor is obviously diagonal and isotropic *by construction*, in agreement with more general group-theoretical considerations [271] (See also Section 2.3.4 and Section 3.3). A spin-polarised Seebeck coefficient connected, e.g., to the spin-dependent Seebeck effect will be considered in the following.

[38] Magnetic Laue group $m\bar{3}m1'$ without external magnetic field, see Ref. 283 in Section 3.3.1.
[39] See also Eq. (1) of Ref. 24.

Comparison of the two formulations

The spin-projected formalism assumes that the total charge and the spin-polarisation current densities, $\boldsymbol{j}$ and $\boldsymbol{j}^s$, respectively, can be written as sum and difference of spin-projected current densities $\boldsymbol{j}^{\uparrow(\downarrow)}$, $\boldsymbol{j} = \boldsymbol{j}^{\uparrow} + \boldsymbol{j}^{\downarrow}$ and $\boldsymbol{j}^s = \boldsymbol{j}^{\uparrow} - \boldsymbol{j}^{\downarrow}$. Accepting this point of view allows connecting Eqs. (2.287) and (2.310) by starting from the definitions Eqs. (2.291) and (2.292),

$$\begin{pmatrix} 1 & 1 & 0 \\ 1 & -1 & 0 \\ 0 & 0 & 1 \end{pmatrix} \begin{pmatrix} \mathbf{j}^{\uparrow} \\ \mathbf{j}^{\downarrow} \\ \mathbf{j}^{q} \end{pmatrix} = \underline{\boldsymbol{M}} \begin{pmatrix} \mathbf{j}^{\uparrow} \\ \mathbf{j}^{\downarrow} \\ \mathbf{j}^{q} \end{pmatrix} = \begin{pmatrix} \mathbf{j} \\ \mathbf{j}^{s} \\ \mathbf{j}^{q} \end{pmatrix} \tag{2.313}$$

where $\mathbf{j}^{\mathbf{s}}$ corresponds to the third (z) column of $\underline{\boldsymbol{J}}^s$ in Eq. (2.310) and obviously $\boldsymbol{j} = \boldsymbol{j}^c$. Applying $\underline{\boldsymbol{M}}$ to the r.h.s. of Eq. (2.287) and inserting $\underline{\boldsymbol{I}}_3 = \underline{\boldsymbol{M}}^{-1}\underline{\boldsymbol{M}}$

$$\underline{\boldsymbol{M}} \begin{pmatrix} \underline{\boldsymbol{L}}_0^{\uparrow} & 0 & \underline{\boldsymbol{L}}_1^{\uparrow} \\ 0 & \underline{\boldsymbol{L}}_0^{\downarrow} & \underline{\boldsymbol{L}}_1^{\downarrow} \\ \underline{\boldsymbol{L}}_{1'}^{\uparrow} & \underline{\boldsymbol{L}}_{1'}^{\downarrow} & \underline{\boldsymbol{L}}_2^{\uparrow} + \underline{\boldsymbol{L}}_2^{\downarrow} \end{pmatrix} \begin{pmatrix} \boldsymbol{\nabla}\mu^{\uparrow} \\ \boldsymbol{\nabla}\mu^{\downarrow} \\ -\frac{1}{T}\boldsymbol{\nabla}T \end{pmatrix} \tag{2.314}$$

$$= \begin{pmatrix} \frac{\underline{\boldsymbol{L}}_0^{\uparrow}}{2} + \frac{\underline{\boldsymbol{L}}_0^{\downarrow}}{2} & \frac{\underline{\boldsymbol{L}}_0^{\uparrow}}{2} - \frac{\underline{\boldsymbol{L}}_0^{\downarrow}}{2} & \underline{\boldsymbol{L}}_1^{\uparrow} + \underline{\boldsymbol{L}}_1^{\downarrow} \\ \frac{\underline{\boldsymbol{L}}_0^{\uparrow}}{2} - \frac{\underline{\boldsymbol{L}}_0^{\downarrow}}{2} & \frac{\underline{\boldsymbol{L}}_0^{\uparrow}}{2} + \frac{\underline{\boldsymbol{L}}_0^{\downarrow}}{2} & \underline{\boldsymbol{L}}_1^{\uparrow} - \underline{\boldsymbol{L}}_1^{\downarrow} \\ \frac{\underline{\boldsymbol{L}}_{1'}^{\uparrow}}{2} + \frac{\underline{\boldsymbol{L}}_{1'}^{\downarrow}}{2} & \frac{\underline{\boldsymbol{L}}_{1'}^{\uparrow}}{2} - \frac{\underline{\boldsymbol{L}}_{1'}^{\downarrow}}{2} & \underline{\boldsymbol{L}}_2^{\uparrow} + \underline{\boldsymbol{L}}_2^{\downarrow} \end{pmatrix} \begin{pmatrix} 2e\boldsymbol{E} \\ 2e\boldsymbol{\nabla}\mu^{s} \\ -\frac{1}{T}\boldsymbol{\nabla}T \end{pmatrix} \tag{2.315}$$

where $2eE = \boldsymbol{\nabla}\mu^{\uparrow} + \boldsymbol{\nabla}\mu^{\downarrow}$ and $2e\boldsymbol{\nabla}\mu^s = \boldsymbol{\nabla}\mu^{\uparrow} - \boldsymbol{\nabla}\mu^{\downarrow} \equiv \boldsymbol{\nabla}(\mu^{\uparrow} - \mu^{\downarrow})$ is the force due to a possible spin accumulation. Note that the response coefficients representing the charge-charge coupling and the spin-spin coupling are indeed identical, as discussed above. The same applies to that describing spin-charge and charge-spin correlation as the tensors are fully anti-symmetric. The usual Onsager reciprocity also holds for the charge-heat/heat-charge and spin-heat/heat-spin pairs, due to Eqs. (2.284) and (2.289) as the former are sums and the latter differences.

Moving the factors 2 from the force vector in Eq. (2.314), i.e., the vector $(221)^T$, to the Onsager matrix of response tensors and writing this more compactly as

$$\begin{pmatrix} \underline{\boldsymbol{L}}_0^{+} & \underline{\boldsymbol{L}}_0^{-} & \underline{\boldsymbol{L}}_1^{+} \\ \underline{\boldsymbol{L}}_0^{-} & \underline{\boldsymbol{L}}_0^{+} & \underline{\boldsymbol{L}}_1^{-} \\ \underline{\boldsymbol{L}}_{1'}^{+} & \underline{\boldsymbol{L}}_{1'}^{-} & \underline{\boldsymbol{L}}_2^{+} \end{pmatrix}, \tag{2.316}$$

with

$$\underline{\boldsymbol{L}}_n^{\pm} = \begin{pmatrix} L_{n,\mathrm{xx}}^{\uparrow} \pm L_{n,\mathrm{xx}}^{\downarrow} & L_{n,\mathrm{xy}}^{\uparrow} \pm L_{n,\mathrm{xy}}^{\downarrow} & 0 \\ L_{n,\mathrm{yx}}^{\uparrow} \pm L_{n,\mathrm{yx}}^{\downarrow} & L_{n,\mathrm{xx}}^{\uparrow} \pm L_{n,\mathrm{xx}}^{\downarrow} & 0 \\ 0 & 0 & L_{n,\mathrm{zz}}^{\uparrow} \pm L_{0,\mathrm{zz}}^{\downarrow} \end{pmatrix} \tag{2.317}$$

and using Eq. (2.284) one gets for the full super-tensor

$$\begin{pmatrix} \begin{pmatrix} 2L^{\uparrow}_{0,\mathrm{xx}} & 0 & 0 \\ 0 & 2L^{\uparrow}_{0,\mathrm{xx}} & 0 \\ 0 & 0 & 2L^{\uparrow}_{0,\mathrm{zz}} \end{pmatrix} & \begin{pmatrix} 0 & 2L^{\uparrow}_{0,\mathrm{xy}} & 0 \\ -2L^{\uparrow}_{0,\mathrm{xy}} & 0 & 0 \\ 0 & 0 & 0 \end{pmatrix} & \begin{pmatrix} 2L^{\uparrow}_{1,\mathrm{xx}} & 0 & 0 \\ 0 & 2L^{\uparrow}_{1,\mathrm{xx}} & 0 \\ 0 & 0 & 2L^{\uparrow}_{1,\mathrm{zz}} \end{pmatrix} \\ \begin{pmatrix} 0 & 2L^{\uparrow}_{0,\mathrm{xy}} & 0 \\ -2L^{\uparrow}_{0,\mathrm{xy}} & 0 & 0 \\ 0 & 0 & 0 \end{pmatrix} & \begin{pmatrix} 2L^{\uparrow}_{0,\mathrm{xx}} & 0 & 0 \\ 0 & 2L^{\uparrow}_{0,\mathrm{xx}} & 0 \\ 0 & 0 & 2L^{\uparrow}_{0,\mathrm{zz}} \end{pmatrix} & \begin{pmatrix} 0 & 2L^{\uparrow}_{1,\mathrm{xy}} & 0 \\ -2L^{\uparrow}_{1,\mathrm{xy}} & 0 & 0 \\ 0 & 0 & 0 \end{pmatrix} \\ \begin{pmatrix} 2L^{\uparrow}_{1',\mathrm{xx}} & 0 & 0 \\ 0 & 2L^{\uparrow}_{1',\mathrm{xx}} & 0 \\ 0 & 0 & 2L^{\uparrow}_{1',\mathrm{zz}} \end{pmatrix} & \begin{pmatrix} 0 & 2L^{\uparrow}_{1',\mathrm{xy}} & 0 \\ -2L^{\uparrow}_{1',\mathrm{xy}} & 0 & 0 \\ 0 & 0 & 0 \end{pmatrix} & \begin{pmatrix} 2L^{\uparrow}_{2,\mathrm{xx}} & 0 & 0 \\ 0 & 2L^{\uparrow}_{2,\mathrm{xx}} & 0 \\ 0 & 0 & 2L^{\uparrow}_{2,\mathrm{zz}} \end{pmatrix} \end{pmatrix} \tag{2.318}$$

Writing Eq. (2.310) explicitly for the spin-polarised formulation used in version 1 of Ref. 322, again for the special case of a non-magnetic cubic system [283],

$$\begin{pmatrix} \mathbf{j} \\ \mathbf{J}^{\mathbf{s}} \\ \mathbf{j}^{q} \end{pmatrix} = \begin{pmatrix} \begin{pmatrix} L^{cc}_{\mathrm{xx}} & 0 & 0 \\ 0 & L^{cc}_{\mathrm{xx}} & 0 \\ 0 & 0 & L^{cc}_{\mathrm{xx}} \end{pmatrix} & \begin{pmatrix} 0 & \mathcal{L}^{cs}_{\mathrm{xy}} & 0 \\ -\mathcal{L}^{cs}_{\mathrm{xy}} & 0 & 0 \\ 0 & 0 & 0 \end{pmatrix} & \begin{pmatrix} L^{cq}_{\mathrm{xx}} & 0 & 0 \\ 0 & L^{cq}_{\mathrm{xx}} & 0 \\ 0 & 0 & L^{cq}_{\mathrm{xx}} \end{pmatrix} \\ \begin{pmatrix} 0 & \mathcal{L}^{sc}_{\mathrm{xy}} & 0 \\ -\mathcal{L}^{sc}_{\mathrm{xy}} & 0 & 0 \\ 0 & 0 & 0 \end{pmatrix} & \begin{pmatrix} \tilde{\mathcal{L}}^{ss}_{\mathrm{xx}} & 0 & 0 \\ 0 & \tilde{\mathcal{L}}^{ss}_{\mathrm{xx}} & 0 \\ 0 & 0 & \tilde{\mathcal{L}}^{ss}_{\mathrm{xx}} \end{pmatrix} & \begin{pmatrix} 0 & \mathcal{L}^{sq}_{\mathrm{xy}} & 0 \\ -\mathcal{L}^{sq}_{\mathrm{xy}} & 0 & 0 \\ 0 & 0 & 0 \end{pmatrix} \\ \begin{pmatrix} L^{qc}_{\mathrm{xx}} & 0 & 0 \\ 0 & L^{qc}_{\mathrm{xx}} & 0 \\ 0 & 0 & L^{qc}_{\mathrm{xx}} \end{pmatrix} & \begin{pmatrix} 0 & \mathcal{L}^{qs}_{\mathrm{xy}} & 0 \\ -\mathcal{L}^{qs}_{\mathrm{xy}} & 0 & 0 \\ 0 & 0 & 0 \end{pmatrix} & \begin{pmatrix} L^{qq}_{\mathrm{xx}} & 0 & 0 \\ 0 & L^{qq}_{\mathrm{xx}} & 0 \\ 0 & 0 & L^{qq}_{\mathrm{xx}} \end{pmatrix} \end{pmatrix} \begin{pmatrix} -\boldsymbol{\nabla}\mu \\ \boldsymbol{F}^{s} \\ -\frac{1}{T}\boldsymbol{\nabla}T \end{pmatrix} , \tag{2.319}$$

one can see the correspondence between the two formalisms. For a constant chemical potential μ_{c}, $-\boldsymbol{\nabla}\mu = -\boldsymbol{\nabla}(\mu_{\mathrm{c}} - e\phi) = e\boldsymbol{\nabla}\phi = e\mathbf{E}$ and identifying F^{s} with the spin accumulation in Eq. (2.297), or rather with $2e\boldsymbol{\nabla}\mu^{s}$, there is a one-to-one correspondence between Eq. (2.318) and the super-tensor in the above equation. All "↑"-elements appearing in the former are identical to the respective "↓"-quantities if longitudinal and equal in magnitude but different in sign if transverse transport is considered. For that reason they have to be multiplied by the factor 2 to obtain the coefficients appearing in Eq. (2.319). Applying the Onsager relations already discussed above, the reciprocal off-diagonal tensors are identical, i.e., $\underline{\boldsymbol{\mathcal{L}}}^{sc} = \underline{\boldsymbol{\mathcal{L}}}^{cs}$, $\underline{\boldsymbol{L}}^{cq} = \underline{\boldsymbol{L}}^{qc}$ and $\underline{\boldsymbol{L}}^{sq} = \underline{\boldsymbol{\mathcal{L}}}^{qs}$ for the situation considered here. The comparison with Eq. (2.318) furthermore suggests that the second-rank sub-tensor of $\underline{\tilde{\boldsymbol{\mathcal{L}}}}^{ss}$ for a spin current $\mathbf{J}^{\xi}$ and a "spin force" $\mathbf{F}^{\xi}$ with $\xi \in \{\mathrm{x}, \mathrm{y}, \mathrm{z}\}$ is identical to $\underline{\boldsymbol{L}}^{cc}$.

Starting from Eq. (2.319) and the considerations above, by setting the charge current $\boldsymbol{j}$ in the first line to $\mathbf{0}$ one has:

$$\begin{aligned}\begin{pmatrix}0\\0\\0\end{pmatrix} = &- e \begin{pmatrix} L^{cc}_{\mathrm{xx}} & 0 & 0 \\ 0 & L^{cc}_{\mathrm{xx}} & 0 \\ 0 & 0 & L^{cc}_{\mathrm{xx}} \end{pmatrix} \begin{pmatrix} E_{\mathrm{x}} \\ E_{\mathrm{y}} \\ E_{\mathrm{z}} \end{pmatrix} + \begin{pmatrix} 0 & \mathcal{L}^{sc}_{\mathrm{xy}} & 0 \\ -\mathcal{L}^{sc}_{\mathrm{xy}} & 0 & 0 \\ 0 & 0 & 0 \end{pmatrix} \begin{pmatrix} F^{\mathrm{z}}_{\mathrm{x}} \\ F^{\mathrm{z}}_{\mathrm{y}} \\ F^{\mathrm{z}}_{\mathrm{z}} \end{pmatrix} \\ &- \frac{1}{T} \begin{pmatrix} L^{cq}_{\mathrm{xx}} & 0 & 0 \\ 0 & L^{cq}_{\mathrm{xx}} & 0 \\ 0 & 0 & L^{cq}_{\mathrm{xx}} \end{pmatrix} \begin{pmatrix} \nabla_{\mathrm{x}} T \\ \nabla_{\mathrm{y}} T \\ \nabla_{\mathrm{z}} T \end{pmatrix} ,\end{aligned} \tag{2.320}$$

Doing the same with the spin current $\mathbf{J}^{\mathrm{z}}$

$$\begin{aligned}\begin{pmatrix}0\\0\\0\end{pmatrix} = &- e \begin{pmatrix} 0 & \mathcal{L}^{sc}_{\mathrm{xy}} & 0 \\ -\mathcal{L}^{sc}_{\mathrm{xy}} & 0 & 0 \\ 0 & 0 & 0 \end{pmatrix} \begin{pmatrix} E_{\mathrm{x}} \\ E_{\mathrm{y}} \\ E_{\mathrm{z}} \end{pmatrix} + \begin{pmatrix} L^{cc}_{\mathrm{xx}} & 0 & 0 \\ 0 & L^{cc}_{\mathrm{xx}} & 0 \\ 0 & 0 & L^{cc}_{\mathrm{xx}} \end{pmatrix} \begin{pmatrix} F^{\mathrm{z}}_{\mathrm{x}} \\ F^{\mathrm{z}}_{\mathrm{y}} \\ F^{\mathrm{z}}_{\mathrm{z}} \end{pmatrix} \\ &- \frac{1}{T} \begin{pmatrix} 0 & \mathcal{L}^{sq}_{\mathrm{xy}} & 0 \\ -\mathcal{L}^{sq}_{\mathrm{xy}} & 0 & 0 \\ 0 & 0 & 0 \end{pmatrix} \begin{pmatrix} \nabla_{\mathrm{x}} T \\ \nabla_{\mathrm{y}} T \\ \nabla_{\mathrm{z}} T \end{pmatrix} .\end{aligned} \tag{2.321}$$

Solving now for $\mathbf{F}^{\mathrm{z}}$,

$$\begin{aligned}\begin{pmatrix} F^{\mathrm{z}}_{\mathrm{x}} \\ F^{\mathrm{z}}_{\mathrm{y}} \\ F^{\mathrm{z}}_{\mathrm{z}} \end{pmatrix} = &\begin{pmatrix} L^{cc}_{\mathrm{xx}} & 0 & 0 \\ 0 & L^{cc}_{\mathrm{xx}} & 0 \\ 0 & 0 & L^{cc}_{\mathrm{xx}} \end{pmatrix}^{-1} \left[e \begin{pmatrix} 0 & \mathcal{L}^{sc}_{\mathrm{xy}} & 0 \\ -\mathcal{L}^{sc}_{\mathrm{xy}} & 0 & 0 \\ 0 & 0 & 0 \end{pmatrix} \begin{pmatrix} E_{\mathrm{x}} \\ E_{\mathrm{y}} \\ E_{\mathrm{z}} \end{pmatrix} \right. \\ &\left. + \frac{1}{T} \begin{pmatrix} 0 & \mathcal{L}^{sq}_{\mathrm{xy}} & 0 \\ -\mathcal{L}^{sq}_{\mathrm{xy}} & 0 & 0 \\ 0 & 0 & 0 \end{pmatrix} \begin{pmatrix} \nabla_{\mathrm{x}} T \\ \nabla_{\mathrm{y}} T \\ \nabla_{\mathrm{z}} T \end{pmatrix} \right] ,\end{aligned} \tag{2.322}$$

and inserting the result into Eq. (2.320) gives

$$\begin{aligned}\begin{pmatrix}0\\0\\0\end{pmatrix} = &- e \begin{pmatrix} L^{cc}_{\mathrm{xx}} & 0 & 0 \\ 0 & L^{cc}_{\mathrm{xx}} & 0 \\ 0 & 0 & L^{cc}_{\mathrm{xx}} \end{pmatrix} \begin{pmatrix} E_{\mathrm{x}} \\ E_{\mathrm{y}} \\ E_{\mathrm{z}} \end{pmatrix} + \begin{pmatrix} 0 & \mathcal{L}^{sc}_{\mathrm{xy}} & 0 \\ -\mathcal{L}^{sc}_{\mathrm{xy}} & 0 & 0 \\ 0 & 0 & 0 \end{pmatrix} \begin{pmatrix} L^{cc}_{\mathrm{xx}} & 0 & 0 \\ 0 & L^{cc}_{\mathrm{xx}} & 0 \\ 0 & 0 & L^{cc}_{\mathrm{xx}} \end{pmatrix}^{-1} \\ &\left[e \begin{pmatrix} 0 & \mathcal{L}^{sc}_{\mathrm{xy}} & 0 \\ -\mathcal{L}^{sc}_{\mathrm{xy}} & 0 & 0 \\ 0 & 0 & 0 \end{pmatrix} \begin{pmatrix} E_{\mathrm{x}} \\ E_{\mathrm{y}} \\ E_{\mathrm{z}} \end{pmatrix} + \frac{1}{T} \begin{pmatrix} 0 & \mathcal{L}^{sq}_{\mathrm{xy}} & 0 \\ -\mathcal{L}^{sq}_{\mathrm{xy}} & 0 & 0 \\ 0 & 0 & 0 \end{pmatrix} \begin{pmatrix} \nabla_{\mathrm{x}} T \\ \nabla_{\mathrm{y}} T \\ \nabla_{\mathrm{z}} T \end{pmatrix} \right] \\ &- \frac{1}{T} \begin{pmatrix} L^{cq}_{\mathrm{xx}} & 0 & 0 \\ 0 & L^{cq}_{\mathrm{xx}} & 0 \\ 0 & 0 & L^{cq}_{\mathrm{xx}} \end{pmatrix} \begin{pmatrix} \nabla_{\mathrm{x}} T \\ \nabla_{\mathrm{y}} T \\ \nabla_{\mathrm{z}} T \end{pmatrix} .\end{aligned} \tag{2.323}$$

Solving finally for the electric field,

$$\mathbf{E} = -\frac{1}{eT} \begin{pmatrix} \frac{L^{cc}_{\mathrm{xx}} L^{cq}_{\mathrm{xx}} + L^{sc}_{\mathrm{xy}} L^{sq}_{\mathrm{xy}}}{(L^{cc}_{\mathrm{xx}})^2 + (\mathcal{L}^{sc}_{\mathrm{xy}})^2} & 0 & 0 \\ 0 & \frac{L^{cc}_{\mathrm{xx}} L^{cq}_{\mathrm{xx}} + L^{sc}_{\mathrm{xy}} L^{sq}_{\mathrm{xy}}}{(L^{cc}_{\mathrm{xx}})^2 + (\mathcal{L}^{sc}_{\mathrm{xy}})^2} & 0 \\ 0 & 0 & \frac{L^{cq}_{\mathrm{xx}}}{L^{cc}_{\mathrm{xx}}} \end{pmatrix} \begin{pmatrix} \nabla_{\mathrm{x}} T \\ \nabla_{\mathrm{y}} T \\ \nabla_{\mathrm{z}} T \end{pmatrix} , \tag{2.324}$$

one obtains an expression for the Seebeck coefficient corresponding to Eq. (2.301). Correspondingly by inserting the r.h.s. of Eq. (2.324) for the electric field into Eq. (2.322),

$$\begin{aligned}\mathbf{F}^{\mathrm{z}} &= \frac{1}{T}\begin{pmatrix} 0 & \frac{L^{cc}_{\mathrm{xx}}\mathcal{L}^{sq}_{\mathrm{xy}}-\mathcal{L}^{sc}_{\mathrm{xy}}L^{cq}_{\mathrm{xx}}}{(L^{cc}_{\mathrm{xx}})^2+(L^{sc}_{\mathrm{xy}})^2} & 0 \\ -\frac{L^{cc}_{\mathrm{xx}}\mathcal{L}^{sq}_{\mathrm{xy}}-\mathcal{L}^{sc}_{\mathrm{xy}}L^{cq}_{\mathrm{xx}}}{(L^{cc}_{\mathrm{xx}})^2+(L^{sc}_{\mathrm{xy}})^2} & 0 & 0 \\ 0 & 0 & 0 \end{pmatrix}\begin{pmatrix}\nabla_{\mathrm{x}}T\\ \nabla_{\mathrm{y}}T\\ \nabla_{\mathrm{z}}T\end{pmatrix} \\ &= -\frac{1}{T}\begin{pmatrix} 0 & \frac{\mathcal{L}^{sc}_{\mathrm{xy}}L^{cq}_{\mathrm{xx}}-L^{cc}_{\mathrm{xx}}\mathcal{L}^{sq}_{\mathrm{xy}}}{(L^{cc}_{\mathrm{xx}})^2+(L^{sc}_{\mathrm{xy}})^2} & 0 \\ -\frac{\mathcal{L}^{sc}_{\mathrm{xy}}L^{cq}_{\mathrm{xx}}-L^{cc}_{\mathrm{xx}}\mathcal{L}^{sq}_{\mathrm{xy}}}{(L^{cc}_{\mathrm{xx}})^2+(L^{sc}_{\mathrm{xy}})^2} & 0 & 0 \\ 0 & 0 & 0 \end{pmatrix}\begin{pmatrix}\nabla_{\mathrm{x}}T\\ \nabla_{\mathrm{y}}T\\ \nabla_{\mathrm{z}}T\end{pmatrix}, \end{aligned} \tag{2.325}$$

one gets a formal expression describing a spin-polarised Seebeck effect corresponding to Eq. (2.306). The difference ($\frac{1}{e}$) in the prefactor in comparison to Eq. 2.306 comes about due to the imposed relation between fictitious field and the gradient of the spin-polarised chemical potential, $\mathbf{F}^{\mathrm{z}} = 2e\boldsymbol{\nabla}\mu^{s}$. A condensed version of the derivations of Eqs. (2.324) and (2.325) in compact notation can be found in Appendix A.3.

To summarise, based on the assumption that Mott's two-current model holds true also for thermally-driven spin transport, restricting to electrons as carriers of charge, spin, and heat, and demanding for the part of the spin-spin correlation relevant to the case under study to be adequately represented by the charge conductivity, the equivalence of spin-projected and spin-polarised thermoelectrics in non-magnetic systems could be shown. Most noteworthy is the fact that, while the former implicitly combines charge and spin transport, this has to be introduced in the latter by choosing the appropriate boundary conditions for charge and spin current. The clear advantage of the spin-polarised approach is certainly that it is much more general and can be applied without further modifications to magnetic scenarios. Due to its relativistic foundation it allows an unbiased description of spin-orbit-induced effects for arbitrary magnetic order.

As a final note, quite obviously in complete analogy to the above, when perturbation and response are reversed and one is in particular setting the heat and the spin current to zero, the obtained Peltier coefficient expressing the temperature difference induced by an applied electric field contains a term proportional to $\underline{\boldsymbol{\mathcal{L}}}^{qs}\underline{\boldsymbol{\mathcal{L}}}^{sc}$. For the same situation considered before, i.e., a non-magnetic cubic system adjacent to a spin current sink controlled by the magnetisation direction, this reciprocal to the spin Nernst magneto-thermopower (SMT) discussed in Ref. 21 could be used to observe the inverse spin Nernst effect or spin Ettingshausen effect (SEE). The mechanism of the spin Ettingshausen magneto-Peltier effect[40] is obviously exactly the inverse of the SMT: the spin current generated by the electric field via the spin Hall effect is, for open boundary conditions, converted into a heat current by the SEE. Of particular interest in such an experiment would be of course the possibility to prove the Onsager reciprocity between SNE and SEE and between SMT and SEMPE.

[40] It is impossible to resist suggesting the acronym SEMPE for it.

2.3.4 Space-time symmetry of linear response coefficients

Lars Onsager was awarded the Noble Prize in Chemistry in 1968 for his *Reciprocal Relations in Irreversible Processes*, sometimes called the fourth law of thermodynamics, that give surprisingly simple relations between coefficients for irreversible phenomena and their time-reversed counterparts [205, 206]. Originally strictly valid only for scalar quantities, they have been extended to anisotropic media [330] and to broken time-reversal symmetry in presence of a magnetic field [331, 332] or, equivalently, in a magnetic sample.[41]
A modern formulation of these extended relations, given by Hals and Brataas [52], is

$$L^{AB}(\boldsymbol{H},\boldsymbol{M}) = \epsilon_A\epsilon_B L^{BA}(-\boldsymbol{H},-\boldsymbol{M}) \tag{2.326}$$

with $\boldsymbol{H}$ the external magnetic field and $\boldsymbol{M}$ the internal magnetisation or spin configuration and $\epsilon_{A/B} = \pm 1$, depending on whether response and perturbation are time-reversal symmetric or anti-symmetric (i.e., even or odd under time-reversal). In Eq. (2.326) the superscripts AB (BA) indicate the order of perturbation, B (A), and response, A (B). For $B = A$, that is concerning the symmetry of a single response tensor as, e.g., that of the electrical conductivity, one speaks generally of *Onsager relations of the first kind*. While for $B \neq A$, i.e., the connection between two different phenomena with cause and effect interchanged, the expression is accordingly *Onsager relations of the second kind*.

From an entirely different perspective, namely a group-theoretical analysis of the transformation properties of the Kubo formula under the space-time symmetry of magnetic solids, Kleiner [271, 333, 334] derived what he called *generalised Onsager relations* that give the shape of thermogalvanomagnetic tensors (understood as electrical conductivity and thermo(magneto)electric power) for all 1651 magnetic space groups. His approach has been extended to response tensors involving three operators by Seemann *et al.* [283] and applied to spintronic and spincaloritronic [92, 283] as well as spinorbitronic phenomena [335, 336]. As the corresponding publications are reprinted in Section 3.3 (Refs. 283 and 92) and Section 3.5 (Refs. 335 and 336), in the following only a brief introduction and overview will be given, together with additional notes and observations made *in hindsight* or not extensively discussed in the published works.

Of course Kleiner was not the first to combine the restrictions due to spatial symmetry, Neumann's principle, with that due to time-reversal symmetry, first considered by Onsager. See for example Ref. 337 for a historical overview and a critical assessment of Kleiner's work. But as the author himself states, he was the first to treat them *on the same footing* [271]. Starting from the Kubo formula in Eq. (2.171),

$$\tau_{B_\mu A_\nu}(\omega,\boldsymbol{H}) = \int_0^\infty dt\, e^{-i\omega t} \int_0^\beta d\lambda\, \mathrm{Tr}\rho(\boldsymbol{H})\, A_\nu B_\mu(t + i\hbar\lambda;\boldsymbol{H}), \tag{2.327}$$

where A_ν represents a Cartesian component of the perturbation operator and B_μ correspondingly for the response (for further details see page 43 and Refs. 271, 338, 339, and 283), two expressions for the transformation due to unitary (pure spatial)

[41] See Refs. 208 and 209 for an extensive discussion.

and anti-unitary (including time-reversal) operations of the magnetic space group of the solid under consideration, u and a, respectively, are obtained:

$$\tau_{B_\mu A_\nu}(\omega, \boldsymbol{H}) = \sum_{\kappa\lambda} \tau_{B_\kappa A_\lambda}(\omega, \boldsymbol{H}_u) D^{(B)}(u)_{\kappa\mu} D^{(A)}(u)_{\lambda\nu} \tag{2.328}$$

and

$$\tau_{B_\mu A_\nu}(\omega, \boldsymbol{H}) = \sum_{\kappa\lambda} \tau_{A^\dagger_\lambda B^\dagger_\kappa}(\omega, \boldsymbol{H}_u) D^{(B)}(a)^*_{\kappa\mu} D^{(A)}(a)^*_{\lambda\nu} \,. \tag{2.329}$$

Here the $\underline{\boldsymbol{D}}^{(X)}(x)$ are the *co-representation matrices* of the symmetry operations $x \in \{u, a\}$ and the operators $X \in \{A, B\}$, and $\boldsymbol{H}_x$ is the transformed field. Equation (2.328) obviously connects elements of the same response tensor while Eq. (2.329) gives *generalised Onsager relations* between reciprocal or time-reversed phenomena. Applying these equations to all pairs of Cartesian components of the operators and going over all space-time symmetry operations of a magnetic space group[42], one obtains a set of linear relations between elements of $\underline{\boldsymbol{\tau}}$ and, in presence of time-reversal symmetry, between elements of $\underline{\boldsymbol{\tau}}$ and $\underline{\boldsymbol{\tau}}'$ (representing the reciprocal phenomenon). Solving these leads to the tensor shape, in the sense of which elements are non-zero and which (if any) are identical, and in addition to a possible connection between elements of $\underline{\boldsymbol{\tau}}$ and $\underline{\boldsymbol{\tau}}'$. Kleiner applied his prescription to the electrical conductivity tensor, that is the case of $\boldsymbol{B} = \boldsymbol{A} = \hat{\boldsymbol{j}}$, the current density operator, and for the case of $\boldsymbol{B} \neq \boldsymbol{A}$ with one of them being $\hat{\boldsymbol{j}}$ and the other $\hat{\boldsymbol{q}}$, the heat current density operator. Note that the precise form of the operators is irrelevant here, it is their transformation properties under time and space inversion that matters.

As stated before, the scheme can be applied to in principle any pair of operators. The case of $\boldsymbol{B}$ representing the magnetic torque operator $\hat{\boldsymbol{T}}$ and $\boldsymbol{A}$ the electric current density, leading to the so-called spin-orbit torque, has been discussed in Ref. 335, reprinted in this thesis in Section 3.5, the case of both operators being $\hat{\boldsymbol{T}}$ leading to the symmetry restrictions on the Gilbert damping tensor is discussed in Ref. 339. The so-called Edelstein effect can be described by a response operator $\hat{\boldsymbol{m}}$ for the magnetisation induced by an electric field represented by $\boldsymbol{A} = \hat{\boldsymbol{j}}$ and is the subject of Ref. 336, reprinted as well in Section 3.5. An extension of Kleiner's prescription to three operators has been worked out by Seemann *et al.* [283] and applied to the spin conductivity and its spincaloritronic analogues in Refs. 283 and 92, that can be found in Section 3.3. The results in Refs. 271 and 283 have been furthermore used for the discussion of spincaloritronic effects in Ref. 21 (reprinted in Section 3.2 on page 133), in the context of the anomalous Hall effect in compensated ferrimagnets in Ref. 340 (reprinted in Section 3.6 on page 279), as well as for the discussion of galvanomagnetic, thermomagnetoelectric, and thermomagnetic effects in Refs. 309 and 341 (reprinted in Section 3.1 on page 89 and 105, respectively) and for the discussion of transverse responses in non-collinear and non-coplanar antiferromagnets in Section 3.4.

Kleiner's prescription has been criticised by a number of authors, see for example Refs. 342, 343, 344, 337, and 345. In the latter three works it is in particular

[42] Their number can be significantly reduced depending on the nature of the operators and on the specific group.

emphasised that time reversal should in fact be replaced by magnetic reversal to obtain truly generalised Onsager relations between a system and its *magnetic companion* [344] (obtained by complete magnetic reversal, of the internal magnetic structure as well as of an external magnetic field, if present). This certainly might be useful when doing a projection to sub-lattices in collinear or Néel antiferromagnets [346], but to obtain the tensor forms for the whole system (or the individual sublattices) this is unnecessary. These space-time symmetry relations are what Kleiner called generalised Onsager relations, connecting observables of one and the same system. Moreover, it is questionable if comparing a system and its magnetic companion is of any use at all (except for the case just mentioned). Most importantly, in the absence of external fields the results of Kleiner [271] (and Ref. 283) and Butzal [344] (and Butzal and Birss [347]) agree, as do those of Železný *et al.* [346] and Ref. 335.
Moreover, the results obtained for groups of Kleiner's category (c) are precisely the tensor shapes for the two sub-lattices of a collinear antiferromagnet, i.e., the direct effect on one sub-lattice is identical to the inverse on the other. Taking as the simplest possible example again the electrical conductivity, that is in this sense self-inverse, the anti-symmetric off-diagonal elements of the two *ferromagnetic* sub-lattices cancel each other, leading to a vanishing anomalous Hall conductivity. The symmetry operation connecting the two sub-lattices of a Néel AFM is time reversal connected with a spatial operation, the former is exactly what connects the direct and inverse effects, the latter alone does not belong to the magnetic point group and thus has no effect on the tensor shapes. Accordingly the Edelstein polarisations or spin orbit torkances that act, in contrast to conductivities, locally on the magnetic moments of individual sub-lattices in antiferromagnets are described by the tensors for the direct and inverse effects [335, 346].

As a final note in this regard, the decomposition of linear response tensors into even and odd components w.r.t. the magnetisation direction or into symmetric and anti-symmetric parts, as done, e.g., already by Shtrikman and Thomas [348] as well as Kleiner [334] and that is thoroughly discussed in Ref. 345, will not be considered herein.

In order to introduce the anomalous Hall effect and related phenomena on a phenomenological basis, quite commonly the electrical conductivity tensor shape for a cubic ferromagnet is referred to [235, 349, 350],

$$\underline{\boldsymbol{\sigma}} = \begin{pmatrix} \sigma_{xx} & \sigma_{xy} & 0 \\ -\sigma_{xy} & \sigma_{xx} & 0 \\ 0 & 0 & \sigma_{zz} \end{pmatrix} , \tag{2.330}$$

defining the anomalous Hall conductivity as the off-diagonal anti-symmetric element $\sigma_{xy} = -\sigma_{yx}$. Often this is followed by the statement that this particular tensor shape is found for any magnetic material with a principal rotation axis larger than three-fold. Although this is not wrong as such, it is still highly misleading and probably has been the reason for the wide-spread belief that an anomalous Hall effect can only occur in materials with a finite global magnetisation, i.e., in ferro- or ferrimagnets. The quite recent prediction [351] and observation [352] of an AHE in non-collinear antiferromagnets has accordingly created quite a stir. In hindsight one is tempted to say that a look into the tables of, e.g., Kleiner [271] and considerations of possi-

ble spin structures in the magnetic Laue groups[43] 3, 4, 6, and ∞ of category (b) in Table 4 and $2'$, $2'2'2$, $32'$, $42'2'$, $62'2'$, and $\infty 2'$ of category (c) given in Table 6, could have been made earlier. These are the groups whose conductivity tensors exhibit off-diagonal anti-symmetric elements, i.e., that allow occurrence of the AHE. Mn_3Ir as discussed by Chen *et al.* [351] has the magnetic Laue group $32'$ and Mn_3Sn on which the experiments of Nakatsuji *et al.* [352] were performed belongs to $2'2'2$. Generally spoken, all materials within a subgroup of the limiting Curie group $\infty/mm'm'$ can exhibit a finite anomalous Hall conductivity. Although this is indeed exactly the symmetry criterion for the existence of a globally finite magnetisation, that itself is not required.

Another interesting observation that can be made on inspection of Kleiner's tables is that there obviously are cases ($\bar{3}1'$, $4/m1'$, $6/m1'$ in category (a) and $4'/m$, $4'/mm'm$, $6'/m'$ in category (c))[44] where the symmetry of $\underline{\boldsymbol{\sigma}}$ is higher than that of $\underline{\boldsymbol{\tau}}$. Here the applicability of the Mott formula, generalised or not, has to be reconsidered. The reason for this difference in tensor shapes is that for the electrical conductivity Eq. (2.329) imposes additional restriction on the tensor shape, while for the thermoelectric power Eq. (2.328) alone determines the shape and Eq. (2.329) connects $\underline{\boldsymbol{\tau}}$ and $\underline{\boldsymbol{\tau}}'$. This discrepancy does not apply to the Mott relations for the spin conductivity, leading to the spin Nernst effect or the spin-dependent Seebeck effect, or corresponding expressions for the spin-orbit torkance or the Edelstein response tensor, leading to the thermal SOT and the thermal Edelstein effect, respectively. In those cases the shapes of the tensors whose energy dependence gives rise to the thermal analogues are not determined by anti-unitary operations, as perturbation and response are represented by different operators and accordingly Eq. (2.329) and the corresponding expression for three operators connect reciprocal phenomena. As the electric current density operator is assumed to have the same symmetry as the heat current density operator, electric-field- and thermally-induced phenomena have accordingly the same tensor shapes. This should in principle apply of course as well to the heat conductivity, at least concerning the first term in Eq. (2.271), whereas the second one might also have to be reconsidered in light of its connection to the combination of direct and inverse thermoelectric effects.

Effects related to the Peltier tensor, as for example the anomalous Peltier effect (APE), that is the inverse to the ASE, or the anomalous Ettingshausen or second Nernst-Ettingshausen effect (AEE), as well as such related to the inverse spin conductivity tensor, i.e., the inverse spin Hall effect (ISHE) and an inverse of the longitudinal spin conductivity discussed in Ref. 92, and the reciprocals of SOT (ISOT) and Edelstein effect (IEE) could in principle be calculated from corresponding Kubo formulae interchanging the operators for perturbation and response. But due to the generalised Onsager relations given by Kleiner [271], Seemann *et al.* [283], Wimmer *et al.* [335], and Wimmer *et al.* [336], this is often[45] not necessary, since they can be

[43] Obtained from the magnetic point group either by removal of the improper part of all operations [271] or by adding spatial inversion [283], see Ref. 283 in section 3.3 and Appendix A.4 for details.

[44] One should note that the cases in (a) are exactly the MLGs where the results of Refs. 271 and 283 differ and that the case of $4'/mm'm$ in (c) is the result of a rotated coordinate system compared to the equivalent group $4'/mmm'$, see Appendix A.4.

[45] Not always, magnetic groups without any time-reversal symmetry as in category (b) in Kleiner's notation are an exception here.

expressed by the coefficients for the direct effects. Accordingly, the effects inverse to the related thermally-induced phenomena can be obtained from generalised Mott and generalised Onsager relations combined, giving access to, e.g., spincaloritronic effects as the inverse SNE or spin Ettingshausen effect, the spin-dependent Peltier effect, as well as the inverse thermal spin-orbit torque and the inverse thermal Edelstein effect.

Finally one could consider possible future extensions, such as mechanical, gravitational, acoustical, or optical effects, as long as they can be formulated as operator-operator correlation within Kubo's linear response formalism. Another extension of the scheme is its application to non-linear response tensors, as done for example by Huhne [353].

Chapter 3

Results

In this chapter results obtained using the methods outlined in the previous chapter are presented, in most cases in the form of reprints of published articles. Further, so far unpublished results are compiled in manuscripts to be submitted. Additional information related to the various sections is given in several appendices (A.2, A.3, A.4, and A.7). The order of the following sections and results is not chronological but rather sorted in a logical sequence going from fundamental aspects to more complex properties. At the same time a certain hierarchy is implied, according to the central topic of this thesis: Spincaloritronics.

With this in mind, the following order was chosen: The first section (3.1) is a collection of two published and one unpublished article on thermoelectrics in ferromagnetic transition metals and alloys. Supporting information can be found in Appendix A.2. The next section (3.2) features two published articles on the spin Nernst effect, a truly spincaloritronic transport phenomenon and as such can be seen to be at the heart of this thesis. Additional considerations on spin-dependent thermoelectrics and results on another spincaloritronic effect, the spin-dependent Seebeck effect, are collected in Appendices A.3 and A.2, respectively. Section 3.3 focuses on a more fundamental aspect of linear response theory, namely the space-time symmetry of the response tensors connecting perturbation and response. Two publications, one on the formalism and another focussing on one of its predictions are presented, additional information can be found in Appendix A.4. An application of the corresponding group-theoretical scheme, combined with first-principles calculations of transport and magneto-optic properties in non-collinear and non-coplanar magnetic systems is presented in Section 3.4 in the form of two unpublished manuscripts. The focus of Section 3.5 is on two intimately related effects in response to an electric field: the spin-orbit torque occurring in non-centrosymmetric magnetic systems and the inverse spin-galvanic or Edelstein effect that describes the spin-polarisation induced by an electric field in magnetic as well as non-magnetic materials without inversion symmetry. The impact of finite temperature effects on transport coefficients is the subject of Section 3.6, which presents a published article on the spin Hall effect in AuPt alloys and an unpublished manuscript on the anomalous Hall effect in a compensated ferrimagnetic Heusler alloy. Preceding each section a short introduction into and an overview over its content is given. In most cases additional remarks and errata are appended. Computational details can be found in Appendix A.7.

3.1 Thermogalvanomagnetics

The following section summarises results on thermoelectric transport in magnetic solids. Dealing with magnetic systems, which for the time being we will equate with finite net magnetisation as in ferro- or ferrimagnetism, one encounters additional transport anisotropies as compared to the case of non-magnetic solids. These so-called galvanomagnetic effects are the anisotropic magnetoresistance (AMR), reflecting the difference in resistivity parallel and perpendicular to the magnetisation, and the occurrence of a charge current perpendicular to both applied electric field and magnetisation, the anomalous Hall effect (AHE). These intrinsically spin-dependent phenomena have their thermogalvanomagnetic counterparts, the anisotropy of the Seebeck effect (ASE)[2] and the anomalous Nernst effect (ANE), that are as such spincaloritronic effects. The first publication in this section (3.1.1), Ref. 267, is a study of the concentration dependence of these four types of effects in the prototypical ferromagnetic alloy Co_xPd_{1-x}. Additional remarks and errata can be found on page 87. Another important aspect of thermoelectric transport in magnetic systems is the interaction of electrons with collective magnetic excitations, so-called magnons. The second publication (3.1.2), Ref. 309, was a collaborative experimental and theoretical effort within the SPP 1538 funded by the DFG aimed at identifying the signatures of electron-magnon and electron-phonon scattering in the electric, thermoelectric and thermal transport properties of CoFe alloys. The role of the first-principles calculations in this study was that of a *blank* reference, providing as accurate as possible data without the effect of inelastic scattering. A by far more detailed discussion of the concentration- and temperature dependence of the various effects is given in a draft manuscript in Section 3.1.3, including additional theoretical and computational details as well as unpublished results, in particular also for transverse transport effects.

[2] Alternative names for this phenomenon were already mentioned in the introduction (Chapter 1).

3.1.1 Published results on CoPd alloys

The following is a copy of the article *Galvanomagnetic and thermogalvanomagnetic transport effects in ferromagnetic fcc Co_xPd_{1-x} alloys from first principles* [267], reprinted (including Supplemental Material) with permission from

S. Wimmer, D. Ködderitzsch, and H. Ebert, Phys. Rev. B **89**, 161101(R) (2014).

RAPID COMMUNICATIONS

PHYSICAL REVIEW B **89**, 161101(R) (2014)

Galvanomagnetic and thermogalvanomagnetic transport effects in ferromagnetic fcc Co_xPd_{1-x} alloys from first principles

S. Wimmer,* D. Ködderitzsch, and H. Ebert

Department Chemie/Phys. Chemie, Ludwig-Maximilians-Universität München, Butenandtstrasse 11, 81377 München, Germany

(Received 11 November 2013; revised manuscript received 6 March 2014; published 2 April 2014)

The galvanomagnetic and thermogalvanomagnetic transport of the prototypical ferromagnetic transition-metal alloy system fcc Co_xPd_{1-x} has been investigated on the basis of Kubo's linear response formalism. The results for the full electric conductivity tensor allow discussing the spin-orbit-induced anisotropic magnetoresistance and the anomalous Hall effect. These are complemented by results for the corresponding thermogalvanomagnetic transport properties anisotropy of the Seebeck effect and anomalous Nernst effect. The relation between the respective response coefficients is discussed with the underlying electronic structure calculated relativistically within the Korringa-Kohn-Rostoker coherent potential approximation band structure method for disordered alloys.

DOI: 10.1103/PhysRevB.89.161101 PACS number(s): 71.15.Rf, 71.70.Ej, 72.15.Jf, 72.15.Qm

A ferromagnet subject to an external electric field and/or thermal gradient shows a plethora of interesting transport effects, with some of them already being exploited in technological applications. Depending on the direction of the magnetization such materials show a variation of the electric resistivity, denoted as anisotropic magnetoresistance (AMR). Furthermore the anomalous Hall effect (AHE) gives rise to components of the electric current transverse to the applied electric field. Both effects, present also in the absence of an external magnetic field, result from the relativistic coupling of spin and orbital degrees of freedom [spin-orbit coupling (SOC)].

The thermal counterparts to the AMR, the anisotropy of the Seebeck effect (ASE) and to the AHE, the anomalous Nernst effect (ANE) share the same origins. These anisotropic and anomalous effects pose challenges to a theoretical description starting from first principles, which is needed in order to give *material-specific* parameters. While the AMR and the closely related planar Hall effect have been extensively studied, there are relatively few experimental investigations on the ASE and planar Nernst effect (PNE) to be found in the literature [1–4], and, to our knowledge, so far only one first-principles study is available [5], which deals with the magnetic anisotropy of the transmission through a Cu|Co|Cu trilayer system and its enhancement due to the symmetry breaking at the Co|Cu interface. To a much greater extent investigations have been carried out on a closely related class of phenomena, namely the magneto-thermopower or -Seebeck effect and its variations (spin-dependent, tunneling, tunneling anisotropic) occurring in various types of heterostructures [6–9].

Concerning the AHE [10–13] and ANE [13,14], strong interest has arisen in recent years driven by progress in the understanding of the microscopic origins of transverse transport effects and by the (re)discovery of the spin Hall effect [15–17]. The latter also has its thermoelectric analog, the spin Nernst effect [18–20]. Disentangling the various contributions to the anomalous and spin Hall effects [21] has recently been supported by material-specific first-principles calculations. Apart from an intrinsic contribution, a pure band structure effect related to the Berry phase [14,22], there are extrinsic contributions due to scattering at impurities [11,12]. Usually those are related to skew or Mott scattering [23] and the side-jump mechanism [24] and are mainly discussed in the dilute limit. In recent years several first-principles calculations have been reported, dealing with the intrinsic parts of anomalous Hall conductivity (AHC) [25,26] and spin Hall conductivity (SHC) [27,28], a scattering-independent side-jump contribution to the AHE [26,29] and the skew scattering in the SHE [30,31]. To a lesser extent studies exist treating *all* contributions on equal footing on a first-principles level [31–34].

The thermally induced electron (and spin) transport, which is much less explored on a quantitative theoretical level than the responses to an electric field, has recently gained tremendous impetus giving rise to the new field of spin caloritronics [35]. Since there already exists a great deal of insight into the microscopic mechanisms responsible for longitudinal and transverse galvanomagnetic transport effects, and their thermal counterparts share the same origin—namely the spin-orbit interaction—one has an obvious starting point for detailed investigations of the latter. Concerning explicitly spin-dependent effects first-principles work has been done for the spin Nernst effect using the Boltzmann formalism [36] and Kubo linear response theory [37]. So far no clear-cut experimental verification of this phenomenon could be made, but there is substantial evidence [38]. For the symmetric part of the corresponding response tensor (see below) Slachter *et al.* [39] were able to show that indeed a spin-dependent Seebeck effect exists and later on the same group reported the observation of its reciprocal, the spin-dependent Peltier effect [40]. The interest in the implicitly spin-dependent phenomena (ASE/PNE [2–4] and ANE [3,41–43]) has been revived lately by the fact that in experiments on the recently discovered spin Seebeck effect (SSE) [44] its signal has to be disentangled from those of the aforementioned effects having the same symmetry [4,41,43,45].

It is therefore crucial to have a quantitative description of those effects at hand in order to be able to extract the true spin Seebeck signal. So far only a very few such investigations

*sebastian.wimmer@cup.uni-muenchen.de

RAPID COMMUNICATIONS

have been carried out, e.g., for the ANE [14,46], but to our knowledge not for the ASE/PNE and in particular not for disordered alloys. This Rapid Communication aims at filling this gap by presenting results for various galvanomagnetic and thermogalvanomagnetic properties (AMR, ASE, AHE, and ANE) of a prototypical ferromagnetic alloy, namely $Co_{1-x}Pd_x$. Using the concentration as an independent parameter allows varying electronic properties and the strength of the spin-orbit interaction.

Kubo's linear response formalism allows relating the electric current densities $\vec{j}^{\,c}$ to the gradients of the electrochemical potential μ and temperature T [47,48]:

$$\vec{j}^{\,c} = -L^{cc}\vec{\nabla}\mu - L^{cq}\vec{\nabla}T/T, \tag{1}$$

with the gradient of the electrochemical potential $\vec{\nabla}\mu = \vec{\nabla}\mu_c + e\vec{E}$, where μ_c is the chemical potential, $e = |e|$ the elementary charge and $\vec{E}$ the electric field. Furthermore $\vec{\nabla}T$ denotes the temperature gradient. All elements of the second rank response tensors L^{ij} will be considered as temperature dependent with the restriction to the electronic temperature T, i.e., the phononic and magnonic temperatures are neglected. The response tensors appearing in Eq. (1) can be calculated from the corresponding conductivities in the athermal limit (see Smrčka and Středa [49] or Jonson and Mahan [50]). For the electric field along ν, with $\mu,\nu \in \{x,y,z\}$ one has:

$$L^{cc}_{\mu\nu}(T) = -\frac{1}{e}\int dE\, \sigma^{cc}_{\mu\nu}(E) D(E,T), \tag{2}$$

with $D(E,T) = (-\frac{\partial f(E,T)}{\partial E})$, $f(E,T)$ the Fermi function, and the energy-dependent charge conductivity $\sigma^{cc}_{\mu\nu}(E)$, which is obtained by applying the Kubo-Středa formalism. In the zero temperature limit one has $-eL^{cc} \equiv \sigma^{cc}(E_F)$, with E_F being the Fermi energy.

Assuming Cartesian coordinates and the sample being a cubic collinear magnet with magnetization pointing in the z direction the conductivity tensor has the structure (all the following quantities are given for that particular symmetry of the system) [51]:

$$\sigma^{cc} = \begin{pmatrix} \sigma_{xx} & \sigma_{xy} & 0 \\ -\sigma_{xy} & \sigma_{xx} & 0 \\ 0 & 0 & \sigma_{zz} \end{pmatrix}. \tag{3}$$

The tensor for the residual resistivity is obtained by inversion of the conductivity tensor: $\rho = (\sigma^{cc})^{-1}$ and with the assumed symmetry restriction the isotropic resistivity is $\rho_{iso} = \mathrm{Tr}(\rho) = (2\rho_{xx} + \rho_{zz})/3$.

The anisotropic magnetoresistance (AMR), describing the resistance of the magnetic system dependent on the mutual angle of magnetization and current driving electric field is given by

$$\Delta\rho = \rho_{zz} - \rho_{xx} \tag{4}$$

and the so called AMR ratio by $\Delta\rho/\rho_{iso}$. Finally, the anomalous Hall conductivity is given by the off-diagonal element σ_{xy} in Eq. (3).

The transport coefficient $L^{cq}_{\mu\nu}(T)$ is expressed through the energy dependence of the electric conductivity $\sigma^{cc}_{\mu\nu}(E)$ as [49,50]:

$$L^{cq}_{\mu\nu}(T) = -\frac{1}{e}\int dE\, \sigma^{cc}_{\mu\nu}(E)\, D(E,T)\,(E - E_F). \tag{5}$$

Considering a thermal gradient $\vec{\nabla}T$ without an external electric field $\vec{E}$ the resulting electric current $\vec{j}^{\,c}$ vanishes when open-circuit conditions are imposed. Equation (1) implies that an internal electric field

$$\vec{E} = -\frac{1}{eT}(L^{cc})^{-1}L^{cq}\vec{\nabla}T = S\,\vec{\nabla}T \tag{6}$$

builds up in order to compensate the charge imbalance induced by $\vec{\nabla}T$, where S is the thermogalvanomagnetic tensor. It has been shown by various authors (cf., e.g., Ref. [50]) that the expression for S implied by Eq. (6) reduces to the original expression of Mott for $T \to 0$ K. Obviously, the resulting Seebeck effect connected with longitudinal transport is expressed by the diagonal elements of the tensor

$$S = \sigma^{-1}\alpha\ . \tag{7}$$

On the other hand the pure ANE—which is not restricted to the open-circuit condition—connected with transverse transport is represented in the following by the off-diagonal elements of the tensor α^{cq} (or L^{cq}). The chosen notation is in line with the conventional symbol $\alpha^{cq}_{\mu\nu} = -L^{cq}_{\mu\nu}/T$ for the Nernst [41,42,46] (or Peltier [52]) coefficient or conductivity.

To investigate the transport properties of the ferromagnetic fcc Co_xPd_{1-x}, seen as a prototype transition-metal alloy system, in a most detailed way its electronic structure has been determined in a first step by means of the fully relativistic version of the Korringa-Kohn-Rostoker (KKR) band structure method [53]. The corresponding calculations have been done self-consistently within the framework of local spin density functional theory (LSDA) with the substitutional disorder in the alloys accounted for by the coherent potential approximation (CPA). In a second step, the transport coefficients L^{cc} and L^{cq} were determined using Eqs. (2) and (5), respectively, on the basis of the Kubo-Středa formalism [31,32,54,55]. For the athermal limit Mott's classical formula for the thermopower to obtain S/T and α/T has been used. It should be noted that, whereas for determining the symmetric part of the conductivity tensor [see Eq. (3)] the Kubo-Greenwood approach is sufficient, for the calculation of the antisymmetric components a Kubo-Středa or Kubo-Bastin approach is needed.

Figure 1 shows the residual resistivity ρ_{iso} of Co_xPd_{1-x} as a function of the composition in comparison with experiment. As one notes, ρ_{iso} has a maximum at around 20% Co, which is more pronounced for the calculations as in experiment [56], for which it is probably not fully resolved. The strong deviation from the Nordheim rule, which implies a symmetric and parabolic dependence of ρ_{iso} on the concentration x, can be explained by details of the electronic structure (see below). A well-known property of the Co_xPd_{1-x} system is its rather high anisotropic magnetoresistance (AMR), which is one of the largest found in binary transition-metal alloys,

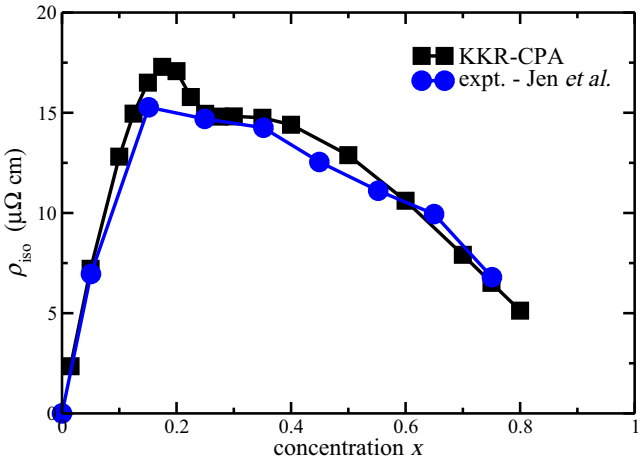

FIG. 1. (Color online) Calculated (squares) and experimental [56] (circles) isotropic residual resistivity ρ_{iso} of Co_xPd_{1-x} as a function of alloy composition.

although not as large as in Fe_xNi_{1-x} or Co_xNi_{1-x} alloys. The calculated AMR ratio is shown in Fig. 2 (top) together with experimental results [57]. Its steep rise between 0 and approximately 20–25 % Co is consistent with experiment. For higher Co concentrations the experimental value stays nearly constant over a large concentration range (approximately up to 70% Co), while the theoretical value drops. A possible reason for this discrepancy could be structural inhomogeneities of the investigated samples, e.g., caused by clustering.

The Seebeck coefficients S_{ii} for transport perpendicular (xx) and parallel (zz) to the magnetization are shown in terms of $-S_{ii}/T$ in Fig. 2 (bottom). As one notes these quantities show a very prominent maximum slightly above 20% Co and differ in particular in the region of the maximum. The corresponding anisotropy of the Seebeck effect (ASE) can be expressed in terms of the ratio:

$$\mathrm{ASE} = \frac{S_{xx} - S_{zz}}{\frac{2}{3}S_{xx} + \frac{1}{3}S_{zz}} = \frac{\Delta S_{ii}}{S_{\mathrm{iso}}}. \tag{8}$$

As one can see in Fig. 2 (bottom) the ASE ratio also shows a maximum at 20% Co, slightly lower than the AMR in the top figure, reaching nearly the value of 0.2. In contrast to the Seebeck coefficient itself, the ASE ratio still shows appreciable values away from the maximum region as well. Here one should note that so far relatively few experimental investigations on the ASE (or PNE) can be found in the literature [1,2,4,43]. Measurements on the diluted ferromagnetic semiconductor $Ga_{1-x}Mn_xAs$, for example, gave for $x = 0.039$ a value of around 6% at 6 K [2], which is clearly lower than the maximum value for Co_xPd_{1-x} found here.

The use of Mott's formula for the Seebeck coefficient implies an extrapolation $T \to 0$ K (athermal limit) leading to a constant value for $-S_{ii}/T$. Using instead the generalized Mott formula as given by Eq. (5) $S_{ii}(T)$ has to be calculated for each individual temperature T. Figure 3 shows for $Co_{0.2}Pd_{0.8}$ the Seebeck coefficients S_{xx} and S_{zz} as a function of the temperature. As one notes, there are clear deviations from the simple linear behavior expected from Mott's formula for higher temperatures. In addition, one finds that the individual temperature dependence of S_{xx} and S_{zz} leads to an appreciable temperature dependence of the ASE ratio with a broad

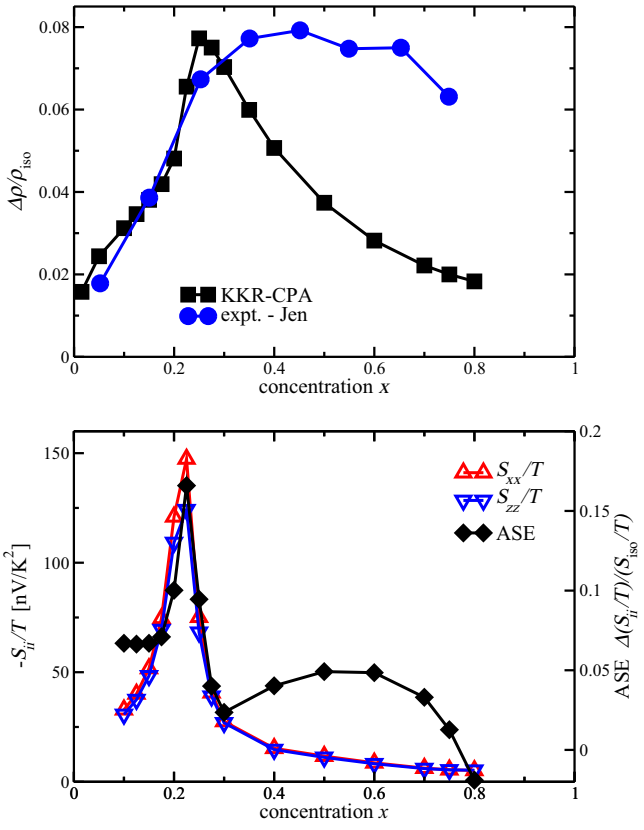

FIG. 2. (Color online) (Top) Calculated (squares) and experimental [57] (circles) AMR ratio $\Delta\rho/\rho_{iso}$ of Co_xPd_{1-x}. (Bottom) Calculated Seebeck coefficients in terms of $-S_{ii}/T$ for transport perpendicular (xx) and parallel (zz) to the magnetization for the athermal limit $T \to 0$ K. In addition the anisotropy of the Seebeck coefficient (ASE) calculated by Eq. (8) is given.

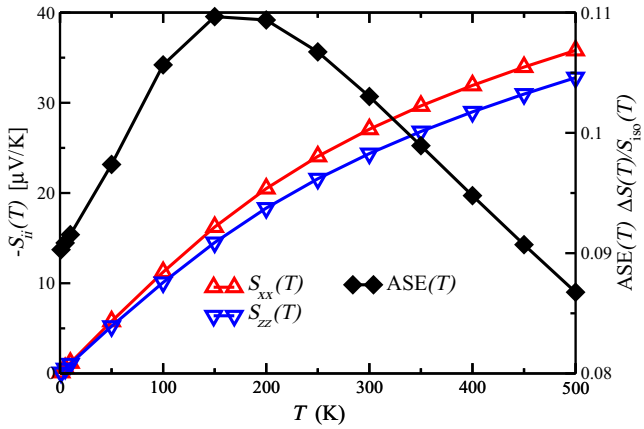

FIG. 3. (Color online) Temperature dependence of the calculated Seebeck coefficients S_{xx} and S_{zz} (triangles up and down, respectively) in $Co_{0.2}Pd_{0.8}$. In addition the corresponding anisotropy ratio ASE $= (S_{xx} - S_{zz})/(\frac{2}{3}S_{xx} + \frac{1}{3}S_{zz})$ is shown.

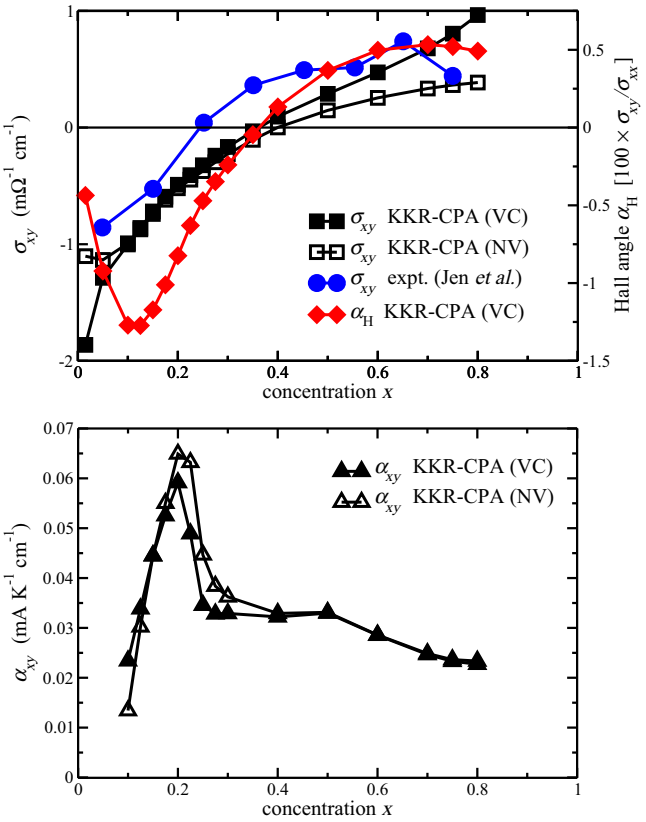

FIG. 4. (Color online) (Top) Calculated AHC (VC, full squares) together with its intrinsic contribution (NV, open squares) in comparison to low temperature experimental data [58] (circles). In addition the theoretical Hall angle $\alpha_{\mathrm{H}} = \sigma_{xy}/\sigma_{xx}$ is shown. (Bottom) Calculated ANC α_{xy} (VC, full triangles) together with its intrinsic contribution (NV, open triangles), in the athermal limit.

maximum around 150 K. (One should bear in mind that the influence of phonons and magnons is not accounted for in these calculations, which might not be negligible in this system. In fact the Curie temperature for the alloy with 20% Co is around 500 K [60].)

The calculated AHC σ_{xy} of $\mathrm{Co}_x\mathrm{Pd}_{1-x}$ for $T = 0$ K shown in Fig. 4 (top) is found in very satisfying agreement with the corresponding low-temperature experimental data [58]. In addition to the theoretical AHC that includes the so-called vertex corrections (VC) [13,54], results are given for which these were ignored (NV). The difference between these can be identified with the extrinsic contributions to σ_{xy} due to the skew scattering and side-jump mechanisms [21,32]. Obviously, there are pronounced extrinsic contributions in the Pd-rich as well as Co-rich regimes having different sign. This situation is very similar to that found for the spin Hall effect in nonmagnetic transition-metal alloys [31]. In addition the figure shows the Hall angle $\alpha_{\mathrm{H}} = \sigma_{xy}/\sigma_{xx}$ that—as the AHC σ_{xy}—shows a sign change at around 35% Co. This is followed by a very broad maximum around around 75% Co.

The anomalous Nernst conductivity (ANC) α_{xy} for $T \to 0$ corresponding to σ_{xy} is given in the bottom panel of Fig. 4. Again a very prominent maximum around 20% Co is found. As for the AHC, Fig. 4 (bottom) gives results for calculations including (VC) and excluding the vertex corrections. In contrast to σ_{xy}, these are relatively weak and remarkable only for the Pd-rich side of the system. Altogether the intrinsic contribution is dominant for all concentrations. As one notes from Fig. 4 there is no obvious direct relation between these transverse thermoelectric and electric transport coefficients α_{xy} and σ_{xy}, respectively (see below and Supplemental Material [59]).

The prominent maximum of the longitudinal transport quantities ρ_{iso} and $\Delta\rho/\rho_{\mathrm{iso}}$ shown in Figs. 1 and 2, respectively, can be understood by having a look at the variation of the electronic structure of $\mathrm{Co}_x\mathrm{Pd}_{1-x}$ with its composition (see Supplemental Material [59]). For the majority channel, the upper edges of the d-like bands at the X and W points in the Brillouin zone touch the Fermi level for around 20% Co. The latter in fact extends over almost the whole length of the Z direction connecting W and X. For the minority spin channel, on the other hand, the Fermi level crosses sp-like bands that have a steep slope leading to a very different conductivity for the two spin channels. The peculiar features of the electronic structure of $\mathrm{Co}_x\mathrm{Pd}_{1-x}$ and its concentration dependence clearly also determine the behavior of the more complex transport quantities S_{ii} (and the associated ASE), σ_{xy} and α_{xy}. Concerning the transverse AHC σ_{xy} one has to account in addition for the prominent role of the spin-orbit coupling that has a rather different strength for the two alloy partners.

As mentioned above, there is no simple relationship between the galvanomagnetic and their corresponding thermogalvanomagnetic quantities, as AMR and ASE and AHC and ANC, respectively. This has to be ascribed to the fact that σ_{xy} is determined by the electronic structure in the range $k_{\mathrm{B}}T$ around the Fermi energy E_{F}, while for α_{xy} the first-order weight $(E - E_{\mathrm{F}})$ enters in addition the corresponding calculation.

In summary, a first-principles description of the galvanomagnetic and thermogalvanomagnetic properties of the prototypical ferromagnetic transition-metal alloy system $\mathrm{Co}_x\mathrm{Pd}_{1-x}$ has been presented. The results are in satisfying agreement with corresponding available experimental results. The prominent features of the concentration dependence of the various transport properties could be related to characteristic features of the underlying electronic structure as well as to the prominent role of spin-orbit coupling. In particular for a concentration of 20% Co in Pd a rather high ASE of around 10% was found, exhibiting an interesting nonlinear temperature dependence. For longitudinal as well as transverse responses to electric field and temperature gradient, different concentration dependences were found, which clearly shows that there is no trivial relation between the two classes of phenomena. The pronounced sensitivity of the galvanomagnetic and, to an apparently even greater extent, thermogalvanomagnetic transport effects to the electronic structure obviously allows tuning them in a relatively wide range by varying the composition of a substitutional alloy system.

This work was supported financially by the Deutsche Forschungsgemeinschaft (DFG) via the priority programme SPP 1538 and the SFB 689.

[1] V. D. Ky, Phys. Stat. Sol. (b) **17**, K207 (1966).
[2] Y. Pu, E. Johnston-Halperin, D. D. Awschalom, and J. Shi, Phys. Rev. Lett. **97**, 036601 (2006).
[3] A. Slachter, F. L. Bakker, and B. J. van Wees, Phys. Rev. B **84**, 020412 (2011).
[4] A. D. Avery, M. R. Pufall, and B. L. Zink, Phys. Rev. B **86**, 184408 (2012).
[5] V. Popescu and P. Kratzer, Phys. Rev. B **88**, 104425 (2013).
[6] L. Gravier, S. Serrano-Guisan, F. Reuse, and J.-P. Ansermet, Phys. Rev. B **73**, 024419 (2006).
[7] M. Czerner, M. Bachmann, and C. Heiliger, Phys. Rev. B **83**, 132405 (2011).
[8] M. Walter *et al.*, Nature Mater. **10**, 742 (2011).
[9] Ts. Naydenova, P. Dürrenfeld, K. Tavakoli, N. Pégard, L. Ebel, K. Pappert, K. Brunner, C. Gould, and L. W. Molenkamp, Phys. Rev. Lett. **107**, 197201 (2011).
[10] R. Karplus and J. M. Luttinger, Phys. Rev. **95**, 1154 (1954).
[11] A. Crépieux and P. Bruno, Phys. Rev. B **64**, 014416 (2001).
[12] S. Onoda, N. Sugimoto, and N. Nagaosa, Phys. Rev. B **77**, 165103 (2008).
[13] N. A. Sinitsyn, J. Phys.: Cond. Mat. **20**, 023201 (2008).
[14] D. Xiao, Y. Yao, Z. Fang, and Q. Niu, Phys. Rev. Lett. **97**, 026603 (2006).
[15] M. Dyakonov and V. Perel, Phys. Lett. A **35**, 459 (1971).
[16] J. E. Hirsch, Phys. Rev. Lett. **83**, 1834 (1999).
[17] J. Sinova, D. Culcer, Q. Niu, N. A. Sinitsyn, T. Jungwirth, and A. H. MacDonald, Phys. Rev. Lett. **92**, 126603 (2004).
[18] S. G. Cheng, Y. Xing, Q. F. Sun, and X. C. Xie, Phys. Rev. B **78**, 045302 (2008).
[19] X. Liu and X. Xie, Solid State Commun. **150**, 471 (2010).
[20] Z. Ma, Solid State Commun. **150**, 510 (2010).
[21] N. Nagaosa, J. Sinova, S. Onoda, A. H. MacDonald, and N. P. Ong, Rev. Mod. Phys. **82**, 1539 (2010).
[22] M. Gradhand *et al.*, J. Phys.: Cond. Mat. **24**, 213202 (2012).
[23] J. Smit, Physica **21**, 877 (1955).
[24] L. Berger, Phys. Rev. B **2**, 4559 (1970).
[25] X. Wang, D. Vanderbilt, J. R. Yates, and I. Souza, Phys. Rev. B **76**, 195109 (2007).
[26] J. Weischenberg, F. Freimuth, J. Sinova, S. Blügel, and Y. Mokrousov, Phys. Rev. Lett. **107**, 106601 (2011).
[27] Y. Yao and Z. Fang, Phys. Rev. Lett. **95**, 156601 (2005).
[28] G. Y. Guo, S. Murakami, T.-W. Chen, and N. Nagaosa, Phys. Rev. Lett. **100**, 096401 (2008).
[29] A. A. Kovalev, J. Sinova, and Y. Tserkovnyak, Phys. Rev. Lett. **105**, 036601 (2010).
[30] M. Gradhand, D. V. Fedorov, P. Zahn, and I. Mertig, Phys. Rev. Lett. **104**, 186403 (2010).
[31] S. Lowitzer, M. Gradhand, D. Ködderitzsch, D. V. Fedorov, I. Mertig, and H. Ebert, Phys. Rev. Lett. **106**, 056601 (2011).
[32] S. Lowitzer, D. Ködderitzsch, and H. Ebert, Phys. Rev. Lett. **105**, 266604 (2010).
[33] I. Turek, J. Kudrnovský, and V. Drchal, Phys. Rev. B **86**, 014405 (2012).
[34] D. Ködderitzsch, K. Chadova, J. Minár, and H. Ebert, New J. Phys. **15**, 053009 (2013).
[35] G. E. Bauer, A. H. MacDonald, and S. Maekawa, Solid State Commun. **150**, 459 (2010).
[36] K. Tauber, M. Gradhand, D. V. Fedorov, and I. Mertig, Phys. Rev. Lett. **109**, 026601 (2012).
[37] S. Wimmer, D. Ködderitzsch, K. Chadova, and H. Ebert, Phys. Rev. B **88**, 201108(R) (2013).
[38] T. Seki, I. Sugai, Y. Hasegawa, S. Mitani, and K. Takanashi, Solid State Commun. **150**, 496 (2010).
[39] A. Slachter, F. L. Bakker, J.-P. Adam, and B. J. van Wees, Nature Phys. **6**, 879 (2010).
[40] J. Flipse, F. L. Bakker, A. Slachter, F. K. Dejene, and B. J. van Wees, Nature Nanotechnol. **7**, 166 (2012).
[41] Y. Pu, D. Chiba, F. Matsukura, H. Ohno, and J. Shi, Phys. Rev. Lett. **101**, 117208 (2008).
[42] S. Y. Huang, W. G. Wang, S. F. Lee, J. Kwo, and C. L. Chien, Phys. Rev. Lett. **107**, 216604 (2011).
[43] M. Schmid, S. Srichandan, D. Meier, T. Kuschel, J.-M. Schmalhorst, M. Vogel, G. Reiss, C. Strunk, and C. H. Back, Phys. Rev. Lett. **111**, 187201 (2013).
[44] K. Uchida *et al.*, Nature (London) **455**, 778 (2008).
[45] M. Weiler *et al.*, Phys. Rev. Lett. **108**, 106602 (2012).
[46] J. Weischenberg, F. Freimuth, S. Blügel, and Y. Mokrousov, Phys. Rev. B **87**, 060406 (2013).
[47] R. Kubo, J. Phys. Soc. Japan **12**, 570 (1957).
[48] J. M. Luttinger, Phys. Rev. **135**, A1505 (1964).
[49] L. Smrčka and P. Středa, J. Phys. C: Solid State Phys. **10**, 2153 (1977).
[50] M. Jonson and G. D. Mahan, Phys. Rev. B **21**, 4223 (1980).
[51] W. H. Kleiner, Phys. Rev. **142**, 318 (1966).
[52] H. Kontani, Phys. Rev. B **67**, 014408 (2003).
[53] H. Ebert, D. Ködderitzsch, and J. Minár, Rep. Prog. Phys. **74**, 096501 (2011).
[54] W. H. Butler, Phys. Rev. B **31**, 3260 (1985).
[55] J. Banhart, R. Bernstein, J. Voitländer, and P. Weinberger, Solid State Commun. **77**, 107 (1991).
[56] S. U. Jen, T. P. Chen, and S. A. Chang, J. Appl. Physics **70**, 5831 (1991).
[57] S. U. Jen, Phys. Rev. B **45**, 9819 (1992).
[58] S. U. Jen, B. L. Chao, and C. C. Liu, J. Appl. Physics **76**, 5782 (1994).
[59] See Supplemental Material at http://link.aps.org/supplemental/10.1103/PhysRevB.89.161101 for a discussion of the changes in the electronic structure of Co_xPd_{1-x} alloys around $x \approx 0.2$ and their implications for transport properties. Furthermore the connection between galvanomagnetic and thermogalvanomagnetic effetcs is illustrated by means of the energy dependence of the anomalous Hall conductivity and the temperature dependence of the anomalous Nernst conductivity.
[60] R. M. Bozorth, P. A. Wolff, D. D. Davis, V. B. Compton, and J. H. Wernick, Phys. Rev. **122**, 1157 (1961).

Supplemental Material to "Galvanomagnetic and thermogalvanomagnetic transport effects in ferromagnetic fcc Co_xPd_{1-x} alloys from first-principles"

S. Wimmer*, D. Ködderitzsch, and H. Ebert
Department Chemie/Phys. Chemie, Ludwig-Maximilians-Universität München, Butenandtstrasse 11, 81377 München, Germany
(Dated: March 21, 2014)

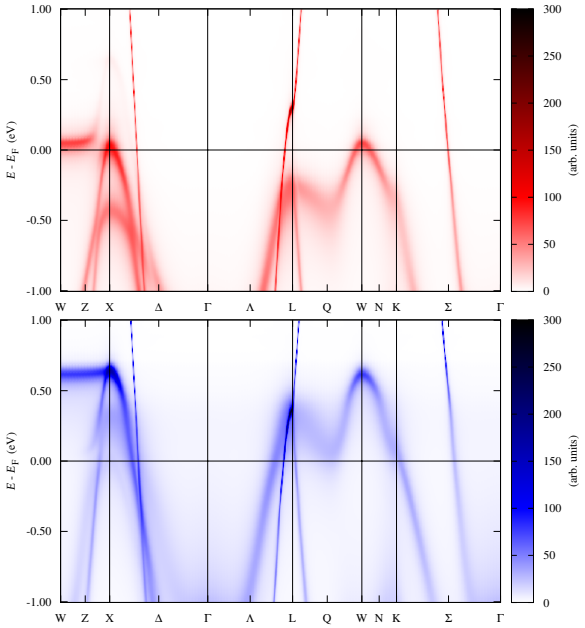

FIG. 1. BSF of $Co_{0.15}Pd_{0.85}$ for spin up (top) and down (bottom).

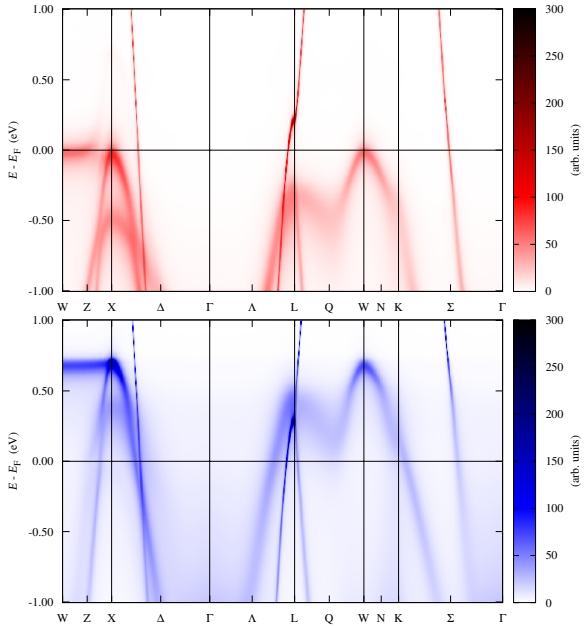

FIG. 2. BSF of $Co_{0.2}Pd_{0.8}$ for spin up (top) and down (bottom).

Electronic structure of Co_xPd_{1-x} alloys with $x \approx 0.2$

Many of the transport phenomena discussed in the main paper show characteristic features at a Cobalt concentration of or close 20 %. In order to understand this behavior the spin-dependent Bloch spectral functions (BSF) of three alloys containing 15, 20 and 25 % of Co were calculated. As visible from Figs. 1-3 the Fermi level rises with growing Co content and at around 20 % crosses the top of *d*-like bands of the majority channel at and between the X- and W-points of the Brillouin zone. In the minority channel the bands crossing the Fermi level are of *sp*-character having in contrast large slopes. This leads to very different conductivities and also energy dependencies of the conductivities for the two channels. From this the large AMR and, to some extent, also the ASE for Cobalt concentrations of around 20 % can be understood. The transverse transport properties anomalous Hall conductivity and anomalous Nernst conductivity certainly also are determined by subtle features of the band structure, but due to the more complex nature of the mechanisms behind them (intrinsic, side-jump and skew scattering contributions) one in addition has to take the role of spin-orbit coupling into account. On the basis of one single alloy system (as discussed here) a simple model at the moment is therefore not conceivable.

Energy dependence of the AHC and temperature dependence of the ANC

To illustrate the connection between galvanomagnetic and thermogalvanomagnetic effects in FIG. 4 the anomalous Hall conductivity of $Co_{0.2}Pd_{0.8}$ is shown as a function of energy at the top and the corresponding anomalous Nernst conductivity as a function of temperature, calculated from the former via Eq. (5) of the main paper, is shown at the bottom. Due to the energy dependence of the vertex corrections, which in this case have a larger impact at energies above the Fermi level, the ANC with and without vertex corrections show a different temperature dependence. Furthermore one observes a deviation from linearity of ANC(T) for higher temperatures, even more pronounced for the VC result. This traces back to Eq. (5) being a measure for the asymme-

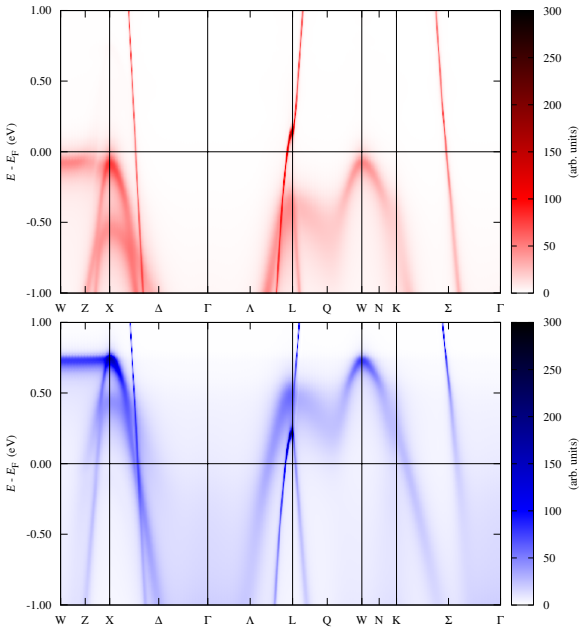

FIG. 3. BSF of $Co_{0.25}Pd_{0.75}$ for spin up (top) and down (bottom).

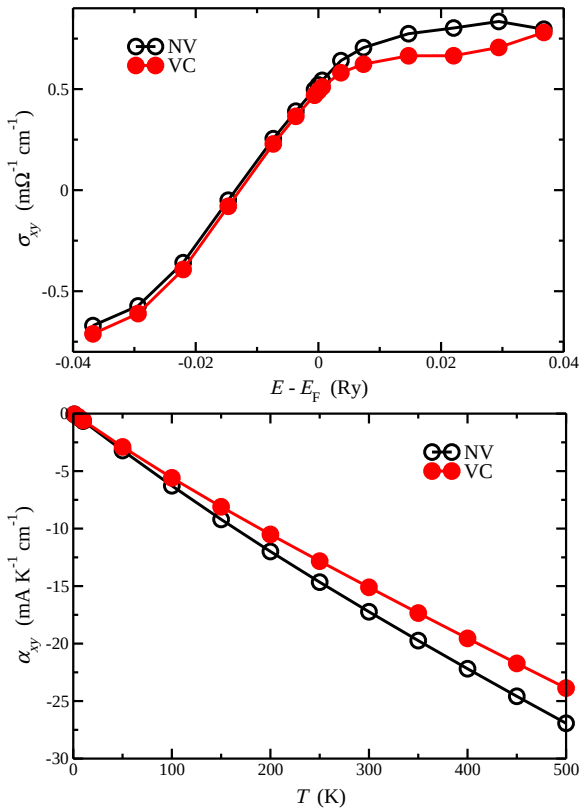

FIG. 4. Energy-dependent anomalous Hall conductivity (top) and temperature-dependent anomalous Nernst conductivity (bottom), calculated from the former by Eq. (5) of the main paper. For both quantities results with (VC, full squares) and without (NV, open circles) vertex corrections are shown.

try of the AHC(E) curve in a certain energy interval around E_F. With increasing width of this interval, the asymmetry becomes larger, and thus the deviation from linearity–which would be expected from Mott's classical formula for the thermopower

$$\begin{aligned} S &= \left.\frac{\pi^2 k_B^2 T}{3e}\,\frac{d\ln\sigma(E)}{dE}\right|_{E_F} \\ &= \left.\frac{\pi^2 k_B^2 T}{3e}\,\frac{1}{\sigma(E)}\,\frac{d\sigma(E)}{dE}\right|_{E_F} \\ &= \sigma^{-1}\alpha. \end{aligned} \tag{1}$$

The absolute value of the integral is smaller for the calculations including vertex corrections hence the ANC is as well smaller for the whole temperature range considered here.

* sebastian.wimmer@cup.uni-muenchen.de

Additional remarks and errata

- Kudrnovský *et al.* [354] could later show that the rather poor agreement between calculated and measured AMR data for intermediate concentrations in CoPd alloys (see Fig. 2, top panel, on page 82 of this thesis) can be traced back to the structural anisotropy due to $L1_0$ ordering near equiatomic composition. To which extent this affects also the anisotropy of the Seebeck effect is not settled, since to the best of the author's knowledge no experimental investigations on this property have been performed so far.

- The definition of the Seebeck coefficient S in terms of the thermoelectric conductivity α in Eq. (7) of Ref. 267 (page 81 herein) as well as Eq. (1) of the Supplemental Material (page 86 herein) is unfortunately inconsistent. Since S was defined as $-1/(eT)L^{cq}(L^{cc})^{-1}$ in Eq. (6), $\sigma = -eL^{cc}$ and $\alpha = -L^{cq}/T$, it should be $S = -\alpha\sigma^{-1}$.

- The caption of Fig. 4 in the Supplemental Material to Ref. 267 (page 86 herein) falsely states that results including vertex corrections (VC) are given as full squares rather than circles.

3.1.2 Published results on CoFe alloys

The following is a copy of the article *Magnon scattering in the transport coefficients of CoFe thin films* [309], reprinted (including Supplemental Material) with permission from

S. Srichandan, S. Wimmer, S. Pöllath, M. Kronseder, H. Ebert, C.H. Back, and C. Strunk, Phys. Rev. B **98**, 020406(R) (2018).

PHYSICAL REVIEW B **98**, 020406(R) (2018)

Rapid Communications

Magnon scattering in the transport coefficients of CoFe thin films

S. Srichandan,[1] S. Wimmer,[2] S. Pöllath,[1] M. Kronseder,[1] H. Ebert,[2] C. H. Back,[1] and C. Strunk[1]
[1]*Institute of Experimental and Applied Physics, University of Regensburg, D-93040 Regensburg, Germany*
[2]*Department of Chemistry, Physical Chemistry, Ludwig-Maximilians-Universität, D-81377 Munich, Germany*

(Received 5 January 2018; published 13 July 2018)

Resistivity ρ, thermopower $\mathcal{S}$, and thermal conductivity κ were measured simultaneously on a set of CoFe alloy films. Variation of the Co content x_{Co} allows for a systematic tuning of the Fermi level through the band structure, and the study of the interplay between electronic and magnetic contributions to the transport coefficients. While band-structure and magnon effects in ρ and κ are rather weak, they turn out to be very significant in $\mathcal{S}$. A decomposition of $\mathcal{S}$ into Mott and magnon drag contributions results in a systematic evolution between the two limiting cases of pure Fe and pure Co. At low temperatures, we find an interesting sign change of the curvature of $\mathcal{S}(T)$ that indicates a corresponding sign change of the magnon drag.

DOI: 10.1103/PhysRevB.98.020406

Spintronics [1,2] and more recently spin caloritronics [3,4] have sparked interest in the fundamental transport properties of ferromagnetic thin films since devices engineered from ultrathin ferromagnetic layer stacks have a potential for technological applications. While the measurement and interpretation of electrical transport parameters is rather straightforward, even for thin ferromagnetic films [5], the measurements and interpretation of their thermal, thermoelectric, and magnetothermoelectric counterparts is much more difficult. However, the optimization of spintronic and spin-caloritronic devices depends on the accurate knowledge of the various thermal transport parameters as well as the parameters governing the relaxation mechanisms for electrons, phonons, and magnons in thin-film ferromagnetic materials. Similarly, the exploitation of magnon transport in temperature gradients for the transmission and processing of information [6,7] depends on the understanding and quantitative knowledge of their thermoelectric and thermomagnetic properties.

So far only a few experiments have addressed the interplay of the magnetothermoelectric transport parameters using the modern toolbox of nanotechnology [8–15]; these were mainly focused on the prototypical ferromagnet permalloy while systematic investigations as a function of alloy composition are still lacking. On the theory side, significant progress has been made in the description of spin-dependent transport phenomena. The use of *ab initio* theory in combination with a realistic description of alloys [16–19] allows now for a fresh look at the transport properties of ferromagnetic alloys. Of particular interest is the prediction of Flebus *et al.* [20], who pointed out that besides the usual diffusion term in the thermoelectric power (TEP), two contributions compete in the *magnon drag*: one of hydrodynamic origin that drives majority carriers towards the cold side of the sample, and a second one in the opposite direction. The second contribution arises from the accumulation of spin Berry phase in a time-dependent magnetization texture [21], caused here by the thermally excited spin waves.

Experimental evidence for magnon drag effects in the TEP has been reported for elemental Fe [22] and Cr [23] bulk samples. Only very recently was the topic taken up again by Watzman *et al.* [24], who attributed an important contribution to the TEP and the Nernst coefficient of elemental Fe and Co to magnon scattering. Interestingly, the sign of the presumed magnon contribution to the TEP is opposite for both metals. Hence the natural questions arise, what is the reason for this sign change and what is the evolution of the TEP in CoFe alloys between the two elements. With varying composition, not only does the electron density, but also the phonon and magnon dispersion relations change. This affects all sources of scattering processes for the electrons and thus the temperature dependence of the transport coefficients. So far only the electric and spin transport in CoFe alloys were recently carefully studied, and the spin-wave damping parameters $\alpha(x_{\mathrm{Co}})$ measured [25,26].

Here, we investigate a series of CoFe alloy films on SiN_x-based suspended microcalorimeters. Simultaneous measurements of several transport coefficients, i.e., the resistivity $\rho(T)$, the TEP $\mathcal{S}(T)$, and the thermal conductivity $\kappa(T)$, are performed in a wide temperature range of 25–300 K on the very same films. In this way, we directly probe the variation of the spin-polarized band structure and the relevant scattering mechanisms with the Co content, and the evolution of magnon scattering in different observables. We find evidence for magnon scattering effects most clearly in the TEP. The magnon drag contribution $\mathcal{S}_{\mathrm{mag}}(T,x_{\mathrm{Co}}) \propto T^{3/2}$ systematically decreases with x_{Co}, and changes sign near $x_{\mathrm{Co}} \simeq 0.6$.

To fabricate the samples, (60–80)-nm-thick CoFe films are deposited as rectangles (116 μm × 60 μm) by molecular beam epitaxy in an ultrahigh vacuum chamber on 500-nm-thick SiN_x membranes [light blue in Fig. 1(b)] with an area of 500 μm × 500 μm. The film is examined using atomic force microscopy (AFM) for the determination of the surface roughness, by x-ray photoelectron spectroscopy for stoichiometry determination, and by electron diffraction for structural analysis. The crystal structure for $x_{\mathrm{Co}} = 0.3$ turns out to be bcc while for $x_{\mathrm{Co}} = 0.8$ we find a clear admixture of fcc precipitations, similar to the findings in Ref. [25].

Next, the contact leads and thermometers are patterned using e-beam lithography (EBL) and a deposition of 50 nm

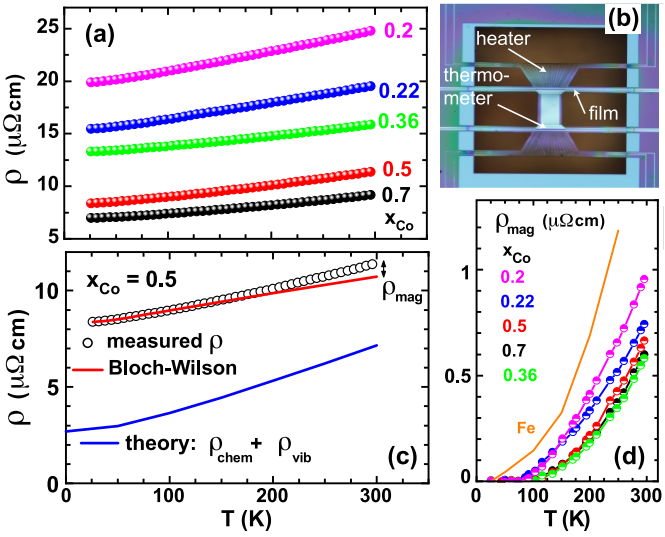

FIG. 1. (a) Resistivity $\rho(T)$ for several values of Co content x_{Co}. (b) Optical image of a typical device. (c) The phonon contribution to the resistivity for $x_{\mathrm{Co}} = 0.5$ (open circles) fitted to a Bloch-Wilson function for $T \leqslant 100$ K (red line). Double-headed arrow: Estimated magnon contribution to $\rho(T)$. Blue line: Calculated resistivity taking into account chemical disorder and lattice vibrations for $x_{\mathrm{Co}} = 0.5$ (see text). (d) Estimated ρ_{mag} for all samples (dots) vs temperature with ρ_{mag} for bulk Fe from Ref. [29] (orange line).

of Al. The thermometers are 100-μm-long and 1.5-μm-wide wires. The contact leads are also 1.5 μm wide. In a second EBL step, two symmetrically placed meander heater structures are patterned in a 40-nm-thick $Au_{60}Pd_{40}$ film. Finally, the parts of the membranes that do not support the metal structures [black area in Fig. 1(b)] are reactively etched using a CHF_3/O_2 plasma for 10 min, leaving a freely suspended SiN_x bridge. (More details on the film characterization and sample layout are given in the Supplemental Material [27].)

The measurements were performed in a helium flow cryostat in vacuum. Radiation losses are minimized by virtue of a radiation shield at the sample temperature. All resistances were measured in a four-terminal configuration. The TEP $\mathcal{S}(T)$ and the thermal conductance $K(T)$ were determined simultaneously by measuring the temperature difference ΔT between the ends of the bridge versus heater current such that $\Delta T/T < 0.01$. The corresponding thermovoltage V_{th} is measured using a nanovoltmeter and the TEP is extracted from the slope of $V_{\mathrm{th}}(\Delta T)$. The total thermal conductance $K = P_{\mathrm{H}}/\Delta T$ includes the thermal conductances K_{B} and K_{L} of the bridge and the lead sections, respectively. P_{H} is the heater power. In the absence of radiation or convection losses, the one-dimensional (1D) heat diffusion equation can be solved to find K_{B} and K_{L} independently [15,28]. K_{B} contains both K_{CoFe} and K_{SiN_x}. To determine K_{SiN}, we have prepared four devices with bare SiN_x. From the thermal conductance $K_{\mathrm{CoFe}} = K_{\mathrm{B}} - K_{\mathrm{SiN}_x}$ we calculate the thermal conductivity $\kappa_{\mathrm{CoFe}} = \kappa$ using the known dimensions of the film for all the samples with different compositions. The maximal uncertainty of κ resulting from the variance of K_{SiN} between the different SiN_x membranes is $\simeq$7.5 W/(K m).

In Fig. 1(a) the resistivity $\rho(T)$ of all five samples is plotted as a function of temperature. The resistivity is highest for $x_{\mathrm{Co}} = 0.20$ and decreases monotonically with the addition of Co. This decrease is mainly a consequence of the increase in electron number. In addition, at $x_{\mathrm{Co}} \simeq 0.2$, a d-like band crosses the Fermi surface, resulting in a maximal $\rho(x_{\mathrm{Co}})$ (for more details and a comparison with earlier experiments, see the Supplemental Material [27]).

Next, we evaluate the magnon contribution ρ_{mag} to $\Delta\rho(T)$. According to the analysis of Refs. [29,30], ρ_{mag} becomes sizable only above $T \simeq 100$ K. Hence, we first determine the phonon contribution by fitting the measured $\rho(T)$ to a Bloch-Wilson (BW) function [27] from 26 up to 100 K. An example is shown in Fig. 1(c) for $x_{\mathrm{Co}} = 0.5$. Extrapolating to 300 K, we can evaluate the magnon contribution $\rho_{\mathrm{mag}}(T)$ by subtracting the BW fit from the measured $\rho(T)$. The results are plotted in Fig. 1(d): $\rho_{\mathrm{mag}}(T)$ gradually decreases with increasing x_{Co} (with $x_{\mathrm{Co}} = 0.36$ being an outlier). The magnon contribution is at most 6.5% of ρ at room temperature for $x_{\mathrm{Co}} = 0.20$, corresponding to about 1/5 of the phonon contribution. The magnitude and temperature dependence of $\rho_{\mathrm{mag}}(T)$ are quite comparable to that of elemental Fe [29] [orange line in Fig. 1(d)]. The blue line in Fig. 1(c) shows a first-principles calculation of $\rho(T)$ for $x_{\mathrm{Co}} = 0.5$ within the Kubo formalism accounting for chemical disorder via the coherent-potential approximation (CPA) alloy theory and for thermal lattice vibrations via the alloy analogy model [16]. The calculation underestimates the absolute values and overestimates the slope of $\rho(T)$ both by a factor of $\simeq$2 as it does not include the considerable structural disorder.

Next, we present the results for the thermopower in Fig. 2(a), which constitutes our main result. At high temperatures, $\mathcal{S}(T)$ is negative and varies roughly linearly with temperature. Note that the approximately linear parts at $T > 100$ K do not extrapolate to $\mathcal{S} = 0$ at $T = 0$, as opposed to the expectation from the Mott law. At low temperatures $\mathcal{S}(T)$ is not linear. This implies that $\mathcal{S}(T)$ cannot be described by a Mott-like dependence alone, but additional nonlinear contributions have to be present. Moreover, the curvature clearly changes sign: It is positive for lower Co content, i.e., $x_{\mathrm{Co}} = 0.2$ and 0.22, but negative for $x_{\mathrm{Co}} = 0.7$ and 0.5. At the lowest temperatures, $\mathcal{S}(T, x_{\mathrm{Co}} = 0.7)$ becomes slightly positive.

By fitting the high-temperature part of $\mathcal{S}(T)$ to a Mott-like term linear in T, and a second term proportional to $T^{3/2}$, we can decompose the TEP according to

$$\mathcal{S}(T) = \mathcal{S}'_{\mathrm{Mott}} T + \mathcal{S}'_{\mathrm{mag}} T^{3/2} + \mathcal{S}_{\mathrm{res}}(T). \tag{1}$$

The coefficients $\mathcal{S}'_{\mathrm{Mott}}(x_{\mathrm{Co}})$ and $\mathcal{S}'_{\mathrm{mag}}(x_{\mathrm{Co}})$ describe the dependencies of the Mott-like part $\mathcal{S}_{\mathrm{Mott}}(T)$ and magnon drag contribution $\mathcal{S}_{\mathrm{mag}}(T)$ on x_{Co}. We have verified that these coefficients are robust against a change of the fit interval within 100–300 K. Below 100 K a much smaller residual contribution $\mathcal{S}_{\mathrm{res}}(T) \lesssim 1$ μV/K remains (see Supplemental Material [27]).

Figure 2(b) shows the Mott-like contribution that is proportional to T. The absolute values $|\mathcal{S}_{\mathrm{Mott}}(T)|$ decrease with increasing Co content, i.e., with increasing electron density, which is consistent with the corresponding trend seen in $\rho(T)$. The values of $\mathcal{S}'_{\mathrm{Mott}}$ contain a small contribution $\mathcal{S}'_{\mathrm{Mott,Al}} = 3.7$ nV/K^2 from the diffusion thermopower of the Al leads [31].

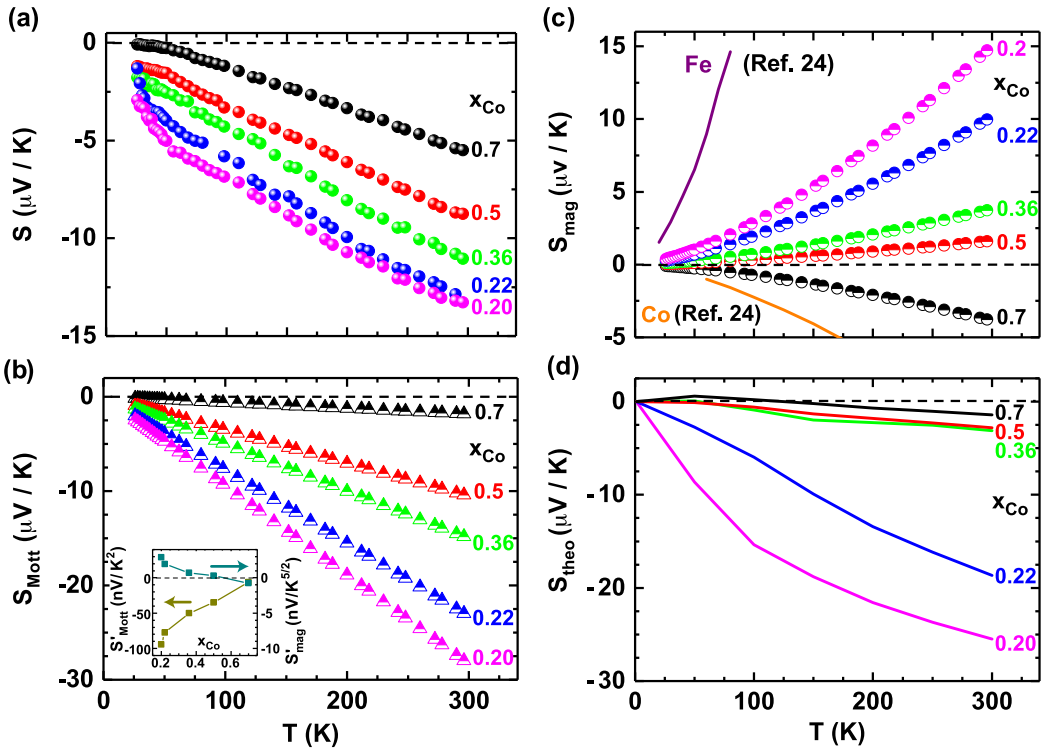

FIG. 2. (a) Measured thermopower vs temperature for all Co_xFe_{1-x} samples from 26 to 296 K, labeled on the right by at. % Co. (b) Mott-like contribution $\mathcal{S}_{\rm Mott}(T)$ (half-solid triangles) as a function of temperature. Inset: $\mathcal{S}_{\rm Mott}$ and $\mathcal{S}_{\rm mag}$ vs at. % Co at 296 K. (c) Magnon drag $\mathcal{S}_{\rm mag}(T) \propto T^{3/2}$ contribution (half-solid circles); literature values for bulk Co and Fe [24] are shown as lines. (d) Calculated thermopower taking into account chemical and vibrational disorder.

On the other hand, we find a substantial nonlinear contribution $\mathcal{S}_{\rm mag}(T)$ that increases proportionally to the magnon number and is as large as 13.5 μV/K at 296 K for the film with $x_{\rm Co} = 0.2$ [Fig. 2(c)]. The sign of the coefficient $\mathcal{S}'_{\rm mag}$ is positive for $x_{\rm Co} \lesssim 0.5$ and negative for $x_{\rm Co} = 0.7$ (inset). This is reflected in the sign change of $\mathcal{S}_{\rm mag}(T)$ from positive for the Fe-rich to negative for the Co-rich alloys, which agrees with $\mathcal{S}_{\rm mag}$ for the case of elemental Fe and Co [24] at these temperatures. The inset in Fig. 2(b) shows the evolution of the coefficients $\mathcal{S}'_{\rm Mott}$ and $\mathcal{S}'_{\rm mag}$ with $x_{\rm Co}$.

In ferromagnets, the magnon drag contribution to the TEP has a $T^{3/2}$ dependence at low T, provided that $T > \Delta_{\rm mag}/k_{\rm B}$ ($\Delta_{\rm mag}$ being the gap in the magnon dispersion relation), which reflects the variation of magnon density and specific heat with T. The magnon drag peak normally occurs at a temperature roughly one fifth to one half of the Curie temperature $T_{\rm C}$ of the material [22]. Due to the high $T_{\rm C}$ of the studied CoFe alloys the maximal magnon drag for our films is expected above the temperature range investigated here. The magnon damping in CoFe alloys is comparable to or even lower than those of the pure elements [26]. Hence, alloying does not lead to a substantial shortening of the magnon lifetime, and magnon drag can survive in the presence of disorder, in contrast to phonon drag [24].

The TEP can also be obtained from first-principles calculations [27]. The results are shown in Fig. 2(d). For the highest and lowest Co concentration the calculation can reproduce the size and systematics of the experimental data, but for intermediate concentrations it significantly underestimates both the measured TEP in Fig. 2(a) and the linear contribution to the TEP in Fig. 2(b). In this theory the curvature arises from the rapid variation of the energy-dependent conductivity when the d bands touch the Fermi energy around $x_{\rm Co} \simeq 0.2$ (see Supplemental Material for details [27]). At high temperatures, this requires one to go beyond the term linear in T in the Sommerfeld expansion. Taking into account also spin disorder further reduces $\mathcal{S}_{\rm theo}$. Given the significant curvature of the measured thermopower below 100 K, our experimental results cannot be explained by the diffusion contribution alone.

The computed suppression of $\mathcal{S}_{\rm theo}(x_{\rm Co} \lesssim 0.5)$ can, in part, be reverted by the presence of fcc precipitations with intrinsically larger absolute values of $\mathcal{S}_{\rm theo}$ and an opposite curvature [27,32]. The relevance of such precipitations is also corroborated by the behavior of the thermal conductivity (see below).

Most interesting is the sign change observed for $\mathcal{S}_{\rm mag}$ when $x_{\rm Co}$ is tuned from the Fe- to the Co-rich side. As already mentioned, recent theoretical work has calculated the spin-motive forces in presence of a magnetization texture [20]: (i) a Berry-phase contribution that drives the majority spins towards the hot end and is controlled by the adiabatic damping parameter β, and (ii) a hydrodynamic contribution that drives the majority spins towards the cold end and is controlled by the Gilbert damping α. A finite difference between majority- and minority-spin-motive force results in an electromotive force proportional to the magnon number (i.e., $\propto T^{3/2}$). The magnetic texture induced by a thermally excited magnon generates a magnon drag contribution to the TEP. The Gilbert damping $\alpha(x_{\rm Co})$ has been determined from ferromagnetic resonance experiments [26]. So far the analysis of our data using this strongly simplified model results in unphysically high values of

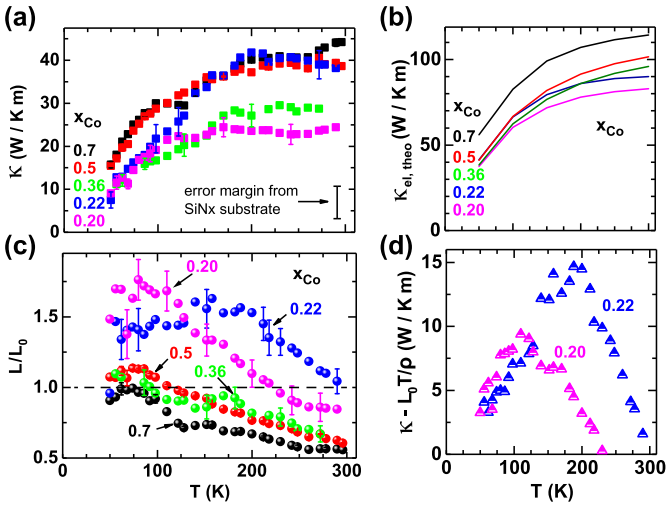

FIG. 3. (a) Measured thermal conductivity of the Co_xFe_{1-x} films. (b) Calculated electronic contribution to κ_{el} including elastic scattering on lattice vibrations. (c) Extracted Lorenz number L as a function of bath temperature. The horizontal line indicates the Sommerfeld value $L_0 = \pi^2/3 \cdot (k_B/e)^2$. (d) Positive deviations from the Wiedemann-Franz law using the measured resistivity of the films with low Co content.

β. On the other hand, the clear systematics that we observe calls for a more quantitative theoretical treatment of magnon drag.

Finally, we investigate the thermal conductivity κ in the films. As demonstrated in Fig. 3(a), $\kappa(T)$ increases with temperature and then saturates at high temperatures for all films. The individual curves are subjected to a $\pm 10\%$ random shift from the slightly varying background contribution of the different SiN_x membranes (see Supplemental Material [27]). The corresponding calculation of the electronic contribution $\kappa_{el}(T)$ including temperature-dependent vibrational disorder in Fig. 3(b) overall reproduces the systematics and the proportions for samples of different Co contents, with the exception that the monotonic increase of κ with x_{Co} observed in the calculated data is violated for $x_{Co} = 0.36$ at high T in our experiment. The absolute values of κ are overestimated by the very same factor of $\simeq 2$, by which the theory underestimates the electric resistivity in Fig. 1(c).

The Lorenz number $L(T) = \kappa(T)\rho(T)/T$ evaluated from the measured set of ρ and κ is shown in Fig. 3(c). We observe a significant violation of Wiedemann-Franz law (WFL, indicated by the horizontal line). Enhancement of L above L_0 is found for $x_{Co} = 0.22$, while L is smaller than L_0 for $x_{Co} = 0.7$ at all temperatures. For intermediate x_{Co}, $L > L_0$ at low T and vice versa at higher T. The positive deviation from WFL, i.e., $L > L_0$, is naturally explained by the contribution κ_{ph} from phonons to the thermal conductivity. In the investigated T regime the magnon contribution to κ is usually small compared to the phonon contribution [33]. Only in films without fcc precipitations ($x_{Co} = 0.2$ and 0.22) can one expect κ_{ph} to become significant, because such precipitations drastically shorten the phonon mean free path. Hence we estimate $\kappa_{ph} \simeq \kappa - TL_0/\rho$ [see Fig. 3(d); Supplemental Material [27]]; it shows clear maxima around 100 and 200 K, respectively, which resemble the well-known umklapp peak. They are shifted towards higher temperatures with respect to the phononic umklapp peak for pure Fe or Co.

The observed negative deviations from WFL can be explained by the gradual reduction of the phonon mean free path in films with $x_{Co} \gtrsim 0.36$. Besides suppressing κ_{ph}, the electronic contribution κ_{el} is known to be enhanced in the presence of inelastic ("vertical") scattering of electron with phonons [13,34], while these scattering events are not effective in the resistivity. In addition, it is known that $L < L_0$ for pure Co in this temperature range [35], and is thus in agreement with the behavior of $L(T)$ in Co-rich samples.

To summarize, simultaneous measurements of the electric, thermoelectric, and thermal transport coefficients performed on alloyed CoFe films have enabled us to understand the contribution from electrons, phonons, and magnons qualitatively and in part even quantitatively. In particular, the evolution of the thermopower indicates a possible interplay of diffusion and magnon drag contributions, the latter changing sign close to the center of the concentration range. A generalized Mott theory is also qualitatively consistent with the results. For the thermal conductivity a pronounced violation of the Wiedemann-Franz law is observed in structurally homogeneous samples with low Co content. A quantitative understanding of the observed systematic evolution of the thermoelectric power calls for a more elaborate theory.

The authors thank T. N. G. Meier for the XPS analysis, M. Zimmermann for AFM measurements, M. Vogel for COMSOL simulations, C. Sürgers for the x-ray characterization of the CoFe films, Y. Tserkovnyak and R. A. Duine for helpful comments on their theory, J. Zweck for support with the electron diffraction, and gratefully acknowledge financial support by the Deutsche Forschungsgemeinschaft (DFG) within the priority programme SpinCaT (SPP 1538) and the Bundesministerium für Bildung und Forschung (BMBF).

[1] I. Zutić, J. Fabian, and S. D. Sharma, Rev. Mod. Phys. **76**, 323 (2004).
[2] D. C. Ralph and M. D. Stiles, J. Magn. Magn. Mater. **320**, 1190 (2008).
[3] G. E. W. Bauer, A. H. MacDonald, and S. Maekawa, Solid State Commun. **150**, 459 (2010).
[4] S. R. Boona, R. C. Myers, and J. P. Heremans, Energy Environ. Sci. **7**, 885 (2014).
[5] *Spin Dependent Transport in Magnetic Nanostructures*, edited by S. Maekawa and T. Shinjo, Advances in Condensed Matter Science Vol. 3 (CRC Press, Boca Raton, FL, 2002).
[6] S. A. Nikitov *et al.*, Phys. Usp. **58**, 1002 (2015).
[7] L. J. Cornelisen, J. Liu, R. A. Duine, J. B. Youssef, and B. J. van Wees, Nat. Phys. **11**, 1022 (2015).
[8] D. W. Denlinger, E. N. Abarra, K. Allen, P. W. Rooney, M. T. Messer, S. K. Watson, and F. Hellman, Rev. Sci. Instrum. **65**, 946 (1994).
[9] A. Lopeandia, L. Cerdo, M. Clavaguera-Mora, L. R. Arana, K. Jensen, F. Munoz, and J. Rodriguez-Viejo, Rev. Sci. Instrum. **76**, 065104 (2005).
[10] M. N. Ou, T. J. Yang, S. R. Harutyunyan, Y. Y. Chen, C. D. Chen, and S. J. Lai, Appl. Phys. Lett. **92**, 063101 (2008).

[11] B. L. Zink, A. D. Avery, R. Sultan, D. Bassett, and M. R. Pufall, Solid State Commun. **150**, 514 (2010).

[12] D. W. Cooke, F. Hellman, J. R. Groves, B. M. Clemens, and S. Moyerman, Rev. Sci. Instrum. **82**, 023908 (2011).

[13] A. D. Avery, M. R. Pufall, and B. L. Zink, Phys. Rev. Lett. **109**, 196602 (2012).

[14] M. Schmid, S. Srichandan, D. Meier, T. Kuschel, J.-M. Schmalhorst, M. Vogel, G. Reiss, C. Strunk, and C. H. Back, Phys. Rev. Lett. **111**, 187201 (2013).

[15] R. Sultan, A. D. Avery, G. Stiehl, and B. L. Zink, J. Appl. Phys. **105**, 043501 (2009).

[16] H. Ebert, S. Mankovsky, K. Chadova, S. Polesya, J. Minár, and D. Ködderitzsch, Phys. Rev. B **91**, 165132 (2015).

[17] R. Kováčik, P. Mavropoulos, and S. Blügel, Phys. Rev. B **91**, 014421 (2015).

[18] M. Obstbaum, M. Decker, A. K. Greitner, M. Haertinger, T. N. G. Meier, M. Kronseder, K. Chadova, S. Wimmer, D. Ködderitzsch, H. Ebert, and C. H. Back, Phys. Rev. Lett. **117**, 167204 (2016).

[19] S. Meyer, Y.-T. Chen, S. Wimmer, M. Althammer, T. Wimmer, R. Schlitz, S. Geprägs, H. Huebl, D. Ködderitzsch, H. Ebert, G. E. W. Bauer, R. Gross, and S. T. B. Goennenwein, Nat. Mater. **16**, 977 (2017).

[20] B. Flebus, R. A. Duine, and Y. Tserkovnyak, Europhys. Lett. **115**, 57004 (2016).

[21] Y. Tserkovnyak and C. H. Wong, Phys. Rev. B **79**, 014402 (2009).

[22] F. J. Blatt, D. J. Flood, V. Rowe, P. A. Schroeder, and J. E. Cox, Phys. Rev. Lett. **18**, 395 (1967).

[23] A. L. Trego and A. R. Mackintosh, Phys. Rev. **166**, 495 (1968).

[24] S. J. Watzman, R. A. Duine, Y. Tserkovnyak, S. R. Boona, H. Jin, A. Prakash, Y. Zheng, and J. P. Heremans, Phys. Rev. B **94**, 144407 (2016).

[25] M. A. W. Schoen, J. Lucassen, H. T. Nembach, T. J. Silva, B. Koopmans, C. H. Back, and J. M. Shaw, Phys. Rev. B **95**, 134410 (2017).

[26] M. A. W. Schoen, J. Lucassen, H. T. Nembach, B. Koopmans, T. J. Silva, C. H. Back, and J. M. Shaw, Phys. Rev. B **95**, 134411 (2017).

[27] See Supplemental Material at http://link.aps.org/supplemental/10.1103/PhysRevB.98.020406 for more details on theory and experiment, which includes Refs. [36–70].

[28] P. Kim, L. Shi, A. Majumdar, and P. L. McEuen, Phys. Rev. Lett. **87**, 215502 (2001).

[29] B. Raquet, M. Viret, E. Sondergard, O. Cespedes, and R. Mamy, Phys. Rev. B **66**, 024433 (2002).

[30] M. V. Kamalakar, A. K. Raychaudhuri, X. Wei, J. Teng, and P. D. Prewett, Appl. Phys. Lett. **95**, 013112 (2009).

[31] R. P. Huebener, Phys. Rev. **171**, 634 (1968).

[32] In the fcc structure and for intermediate Co concentration the Fermi level is situated more closely above the step, while $\sigma(E)$ increases more strongly, when compared to the bcc structure. At elevated T the step contributes to $\mathcal{S}(T)$, resulting in an opposite curvature.

[33] D. T. Edmonds and R. G. Petersen, Phys. Rev. Lett. **2**, 499 (1959).

[34] T. M. Tritt, *Thermal Conductivity: Theory, Properties, and Applications* (Kluwer, New York, 2004).

[35] M. J. Laubitz and T. Matsumura, Can. J. Phys. **51**, 1247 (1973).

[36] International Centre of Diffraction Data, Powder Diffraction File 2, 48-1816 (http://www.icdd.com/); I. Baker, Thayer School of Engineering, Dartmouth College, 1997.

[37] International Centre of Diffraction Data, Powder Diffraction File 2, 15-0806 (http://www.icdd.com/); Natl. Bur. Stand. (U.S.) Monogr. **25**, 4, 10 (1966).

[38] P. P. Freitas and L. Berger, Phys. Rev. B **37**, 6079 (1988).

[39] M. Rubinstein, F. J. Rachford, W. W. Fuller, and G. A. Prinz, Phys. Rev. B **37**, 8689 (1988).

[40] J. W. C. De Vries, Thin Solid Films **167**, 25 (1988).

[41] N. W. Ashcroft and N. D. Mermin, *Solid State Physics* (Saunders College, New York, 1976).

[42] C. Ahn, K.-H. Shin, R. Loloee, J. Bass, and W. P. Pratt, Jr., J. Appl. Phys. **108**, 023908 (2010).

[43] H. Ebert, D. Ködderitzsch, and J. Minár, Rep. Prog. Phys. **74**, 096501 (2011).

[44] H. Ebert, J. Braun, D. Ködderitzsch, and S. Mankovsky, Phys. Rev. B **93**, 075145 (2016).

[45] H. Ebert *et al.*, The Munich SPR-KKR package, version 7.7, http://olymp.cup.uni-muenchen.de/ak/ebert/sprkkr (2017).

[46] P. Soven, Phys. Rev. **156**, 809 (1967).

[47] B. Velický, Phys. Rev. **184**, 614 (1969).

[48] B. Predel, *Phase Equilibria, Crystallographic and Thermodynamic Data of Binary Alloys: Ca-Cd-Co-Zr*, edited by O. Madelung, Landolt-Börnstein, New Series, Group IV Physical Chemistry, Vol. 5c (Springer, Berlin, 1993), Chap. Co-Fe (Cobalt-Iron), pp. 1–13.

[49] That is, not for the whole range between the pure metals as in Vegard's law.

[50] S. H. Vosko, L. Wilk, and M. Nusair, Can. J. Phys. **58**, 1200 (1980).

[51] O. K. Andersen, Phys. Rev. B **12**, 3060 (1975).

[52] R. Kubo, J. Phys. Soc. Jpn. **12**, 570 (1957).

[53] D. A. Greenwood, Proc. Phys. Soc. **71**, 585 (1958).

[54] L. Smrčka and P. Středa, J. Phys. C: Solid State Phys. **10**, 2153 (1977).

[55] W. H. Butler, Phys. Rev. B **31**, 3260 (1985).

[56] J. Banhart, R. Bernstein, J. Voitländer, and P. Weinberger, Solid State Commun. **77**, 107 (1991).

[57] J. Banhart, H. Ebert, P. Weinberger, and J. Voitländer, Phys. Rev. B **50**, 2104 (1994).

[58] S. Lowitzer, D. Ködderitzsch, and H. Ebert, Phys. Rev. B **82**, 140402(R) (2010).

[59] S. Lowitzer, M. Gradhand, D. Ködderitzsch, D. V. Fedorov, I. Mertig, and H. Ebert, Phys. Rev. Lett. **106**, 056601 (2011).

[60] A. Bastin, C. Lewiner, O. Betbeder-Matibet, and P. Nozieres, J. Phys. Chem. Solids **32**, 1811 (1971).

[61] A. Crépieux and P. Bruno, Phys. Rev. B **64**, 014416 (2001).

[62] D. Ködderitzsch, K. Chadova, and H. Ebert, Phys. Rev. B **92**, 184415 (2015).

[63] G. D. Mahan, *Many-Particle Physics*, 2nd ed. (Plenum, New York, 1993).

[64] M. Cutler and N. F. Mott, Phys. Rev. **181**, 1336 (1969).

[65] M. Jonson and G. D. Mahan, Phys. Rev. B **21**, 4223 (1980); **42**, 9350 (1990).

[66] S. Wimmer, D. Ködderitzsch, K. Chadova, and H. Ebert, Phys. Rev. B **88**, 201108(R) (2013).

[67] S. Wimmer, D. Ködderitzsch, and H. Ebert, Phys. Rev. B **89**, 161101(R) (2014).

[68] Y. Kakehashi and O. Hosohata, Phys. Rev. B **40**, 9080 (1989).

[69] W. H. Kleiner, Phys. Rev. **142**, 318 (1966).

[70] M. Seemann, D. Ködderitzsch, S. Wimmer, and H. Ebert, Phys. Rev. B **92**, 155138 (2015).

Supplementary Material for Magnon scattering in the transport coefficients of CoFe alloys

S. Srichandan[1], S. Wimmer[2], S. Pöllath[1], M. Kronseder[1], H. Ebert[2], C.H. Back[1], and C. Strunk[1]
[1] *Institute of Experimental and Applied Physics, University of Regensburg, D-93040, Germany and*
[2] *Department of Chemistry, Physical Chemistry, Ludwig-Maximilians University, Munich, D-81377, Germany*
(Dated: June 29, 2018)

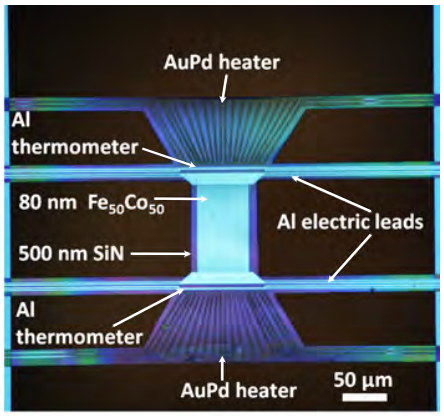

FIG. S1. Optical image of a typical device with an allocation of the different elements.

SCHEMATIC OF A TYPICAL DEVICE

Figure S1 shows an optical image of the central region of a typical suspended microcalorimeter for the measurement of the transport coefficients as seen from the top. The central rectangle constitutes the 80 nm thick $Co_{50}Fe_{50}$ film. The 40 nm thick $Au_{60}Pd_{40}$ meander heaters are placed onto trapezoidal islands at both ends of the bridge. Thermometers and electrical leads are made of 50 nm thick Al. The suspended 500 nm thick SiN membrane appears as purple background, while the etched regions are seen as dark empty areas.

STRUCTURAL CHARACTERIZATION

Electron diffraction at 300 keV in a transmission electron microscope (TEM) was employed for structural characterization of our films deposited on 30 nm thick SiN-membranes. The insets to Figs. S2(a,b) show diffraction patterns for two films with $x_{Co} = 0.3$ and 0.8. These compositions represent the two regimes, where pure bcc and mixed bcc/fcc phases are expected [25]. The observation of bright diffraction rings indicates the polycrystalline nature of our films. The radially integrated linescan (integrated intensity versus scattering vector $|\vec{k}|$ in nm^{-1}) corresponding to the inset in Fig. S2(a) is shown in the main figure. The labels near the peaks (marked by filled red circles) indicate the Miller indices *hkl* of the

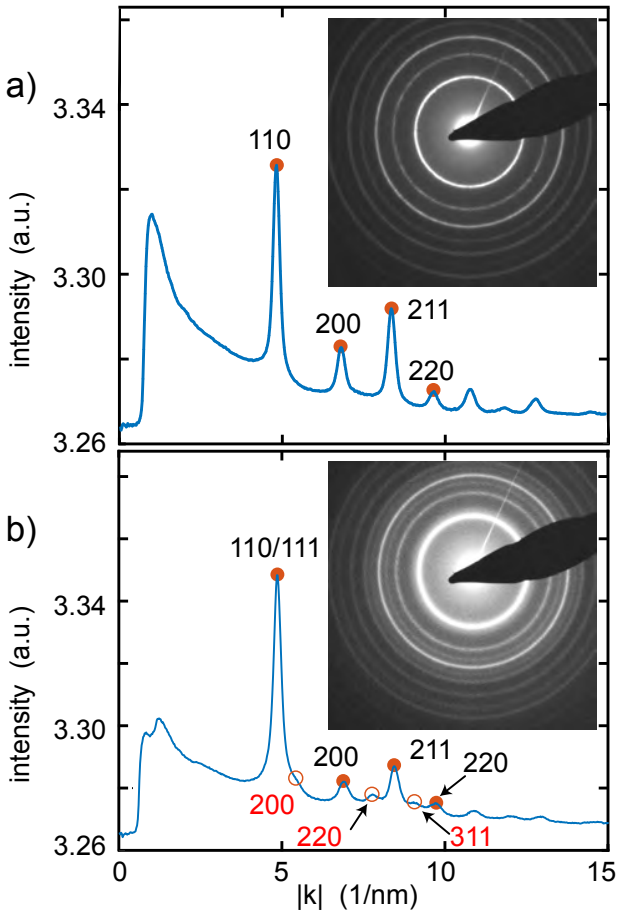

FIG. S2. (a) Electron diffraction pattern and radially integrated linescan of the $x_{Co} = 0.3$ film. (b) Electron diffraction pattern and radially integrated linescan of the $x_{Co} = 0.8$ film.

corresponding lattice planes. The measured sequence of peak spacings matches very well the expectations for a bcc lattice. No additional peaks are observed. The absolute values of $|\vec{k}|$ are listed for the first four peaks in table I. The absolute accuracy is limited by the knowledge of the precise distance between the sample and image planes in the TEM, but matches within a few percent with the literature values for $x_{Co} = 0.3$ [36].

In the inset to Fig. S2(b), additional and slightly fainter diffraction rings are observed for $x_{Co} = 0.8$, when compared to the inset to Fig. S2(a). In between the indexed bcc-peaks, the corresponding line scan (main fig-

Miller indices (hkl)	$Fe_{0.7}Co_{0.3}$	Ref. [36]	$Fe_{0.2}Co_{0.8}$	Ref. [37]
110 (bcc)	4.8	5	4.8	-
200 (bcc)	6.8	7	6.9	-
211 (bcc)	8.3	8.6	8.4	-
220 (bcc)	9.6	9.9	9.7	-
111 (fcc)	-	-	4.8	4.9
200 (fcc)	-	-	5.4	5.6
220 (fcc)	-	-	7.8	8
311 (fcc)	-	-	9.1	9.4

TABLE I. The miller indices and corresponding scattering vectors $|\vec{k}|$ (in nm^{-1} for films with $x_{Co} = 0.3$ and $x_{Co} = 0.8$ and literature values for $x_{Co} = 0.3$ [36] and fcc Co [37].

ure) displays several additional peaks marked by open circles. Their positions match very well the expected scattering vectors for a fcc lattice with a spacing of (111) planes identical to those of the (110) planes of a bcc lattice. The positions of the additional peaks are listed in table I and match very nicely those expected for a fcc Co [37]. Note that for bcc lattices only reflexes with $h + k + l$ =even are allowed, while for fcc lattices only those are allowed, where all indices are either even or odd.

Thus the diffraction patterns evidence that the film with $x_{Co} = 0.3$ exhibits pure bcc crystal structure, while the film with $x_{Co} = 0.8$ consists of mixed bcc and fcc crystallites. This is consistent with earlier observations for FeCo-films on a different substrate [25]. Our structural analysis corroborates our interpretation of Fig. 3(c) of the main text. There we linked the observed negative deviation of Lorenz number from the Sommerfeld value in case of Co_xFe_{1-x} thin films with $x_{Co} = 0.36, 0.5$ and 0.7 to enhanced inelastic electron and phonon scattering. The gradually increasing enhancement results from the increasing weight of fcc domains in crystal structure with increasing Co content in these films.

MORE DETAILS ABOUT THE RESISTIVITY

We decompose the total resistivity into a residual and a T-dependent part: $\rho = \rho_0 + \Delta\rho(T)$. In Figure S3 the residual resistivity $\rho_0(x_{Co})$ of all five samples at $T = 26\,K$ is plotted. It is maximal near $x_{Co} = 0.20$ then decreases monotonically with addition of Co. Our data are well in line with earlier data on bulk samples [38–40]. The solid green line has been calculated within the Kubo formalism accounting for chemical disorder via the CPA alloy theory (see Sec. below). It systematically underestimates our experimental data and for $x_{Co} < 0.4$ also those of Ref. 38.

Taking into account chemical disorder only, $\rho_0(x_{Co})$ is reproduced qualitatively by our model calculations. When compared to pure Fe and Co, but also to bulk alloy samples, the values of ρ_0 are significantly higher than expected for purely chemical disorder, i.e., a perfect bcc lattice with a random distribution of Fe and Co atom on the lattice sites. This indicates a rather high degree of additional structural disorder in our films. In order to test this assumption we performed an annealing test at 400 °C for 5 minutes with a film with $x_{Co} = 0.7$. The annealing led to a significant drop of ρ from 6.94 $\mu\Omega$ cm to 3.68 $\mu\Omega$ cm at 26 K [blue star in Fig. S3].

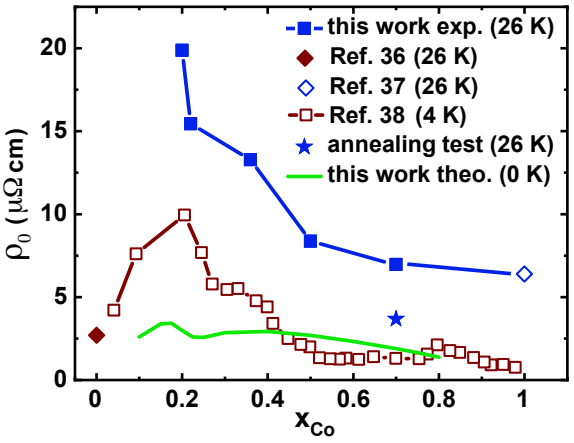

FIG. S3. Residual resistivity $\rho(x_{Co})$ from this work at 26 K (filled squares), after annealing (filled star), from literature (20 nm Fe at 26 K (filled diamond [38]), 53 nm Co (open diamond [39]), and bulk CoFe at 4.2 K (open squares [40]), and the calculated contribution of chemical disorder at 0 K (line).

Next we discuss the separation of phonon and magnon contributions to $\Delta\rho(T)$. According to the analysis of Ref. [29, 30] the magnon contribution ρ_{mag} becomes sizable only above $T \simeq 100\,K$. We first determine the phonon contribution by fitting the measured $\rho(T)$ to a Bloch-Wilson (BW) function

$$\Delta\rho_{phon}(T) = \alpha_{ep}\left(\frac{T}{\Theta_R}\right)^3 \int_0^{\Theta_R/T} \frac{x^3\,dx}{(e^x - 1)(1 - e^{-x})} \quad \text{(S1)}$$

from 26 K up to 100 K, where the magnon contribution is expected to be very small. The free parameters α_{ep} and Θ_R represent the electron-phonon coupling constant and a characteristic phonon temperature Θ_R, respectively. We extract $\Theta_R \simeq 260 - 280\,K$ from these fits, which is about 25% smaller than Θ_{Debye} of pure Fe or Co [41]. Such a discrepancy between the characteristic temperatures extracted from equilibrium and transport quantities is not surprising, as the Debye model characterizes the phonon spectrum only very roughly.

Figure S4 shows the results for films with 20, 22, 36 and 70 % Co. The disorder in our films is also reflected in the temperature dependence $\rho(296\,K) - \rho(26\,K)$; ρ changes by $2 \sim 5\,\mu\Omega$ cm between 26 and 296 K which is about

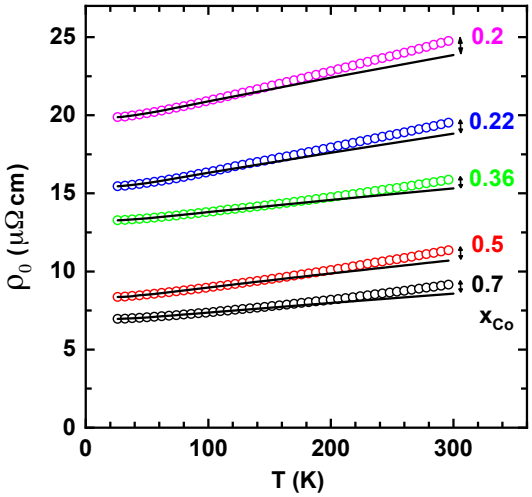

FIG. S4. Resistivity data and Bloch-Wilson fits (see main text) from 26 K to 100 K and extrapolated to 296 K (lines) on measured data (open circles) as a function of temperature for $x_{\mathrm{Co}} = 0.2, 0.22, 0.36, 0.5, 0.7$. ρ_{mag} is indicated as a double headed arrow at the highest temperature.

half of the values 6.2 $\mu\Omega$ cm and 10.4 $\mu\Omega$ cm for bulk Co and Fe, respectively. A similar reduction of the phonon resistivity in thin films has been observed earlier [42]. Extrapolating to 300 K we can evaluate the magnon contribution $\rho_{\mathrm{mag}}(T)$ (marked by double-headed arrows) by subtracting the BW-fit (lines) from the measured $\rho(T)$. The magnon contribution is at most 6.5% of ρ at room temperature for $x_{\mathrm{Co}} = 0.20$, and thus only a fraction of the phonon contribution.

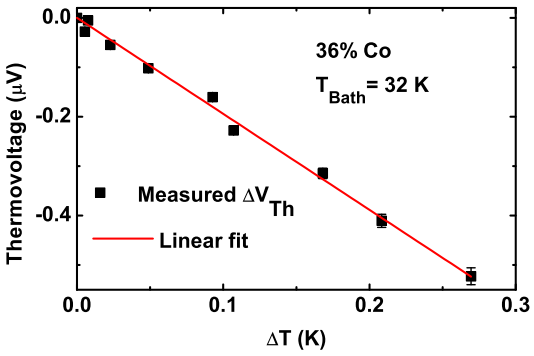

FIG. S5. Measured thermovoltage as a function of ΔT for a film with 36% Co at temperature of 32 K is shown as black squares and the red line represents the linear fit of the data with zero intercept.

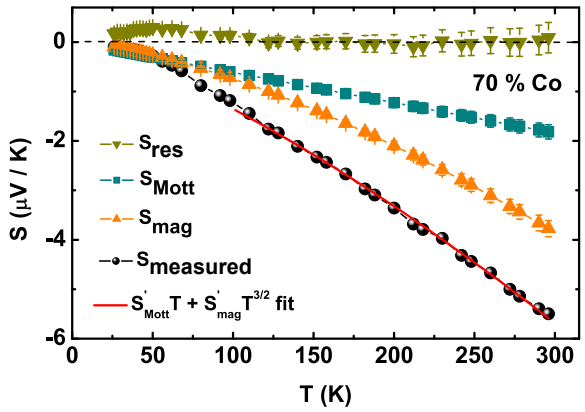

FIG. S6. Total measured thermopower (black dots) and corresponding fit function (red line) for a film with x_{Co}=0.7. The squares, triangles and the inverted triangles represent the S_{Mott}, S_{mag} and S_{Res} respectively.

DETAILS OF TEP MEASUREMENT

As explained in the main text, the thermopower is determined from the ratio of measured thermovoltage ΔV_{th} and the temperature difference of ΔT. In particular at lower bath temperatures T it is important to assure that ΔV_{th} depends linearly on ΔT. At a given base temperature, the thermovoltage ΔV_{th} and the temperature difference ΔT between the islands is measured for a series of applied heater powers. Figure S5 shows a typical plot of ΔV_{th} vs. ΔT at 32 K while maintaining ΔT smaller than $\simeq 1\%$ of the corresponding bath temperature.

The decomposition of the total thermopower into S_{Mott} and S_{mag} according to Eq. 2 has been explained in the main text. Fig. S6 is an illustration of such a decomposition for a film with x_{Co}=0.7. The measured data is shown as black dots to which Equation 2 is fitted as a red line in the temperature range above 100 K. The contributions $S_{\mathrm{Mott}} \propto T$ and $S_{\mathrm{mag}} \propto T^{3/2}$, are parameterized by the respective prefactors S'_{Mott} and S'_{mag}. The resulting individual contributions are shown as squares and triangles, respectively. Note that the curvature in the raw data occurs predominantly at low temperature. This evidences the necessity of a non-linear term in this regime, where the Sommerfeld expansion for the diffusion TEP is still valid.

In Figure S7 we show the small residual contribution to the TEP that remains after subtraction of the Mott-like and magnon drag contributions. For films in single bcc phase, i.e., films with x_{Co}=0.20 and 0.22, we find small dips are reminiscent of the phonon-drag effect. For films in mixed phase, the contribution from in-elastic scattering could produce such peaks. Additionally the diffusion thermopower of Al contacts is included in S_{res}, it is possible that residues of a phonon-drag peak in the thermopower of the Al leads provide a positive contribution

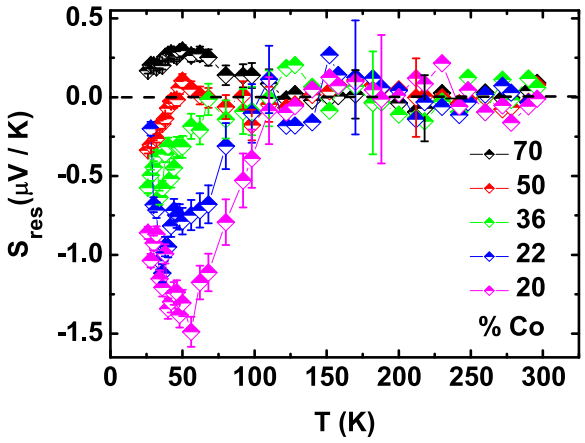

FIG. S7. Residual thermopower S_{res} after subtraction of the Mott- and magnon drag terms for all five Co_xFe_{1-x} films vs temperature from 50 K-296 K. The numbers at the right indicate Co concentration.

to the peak structures below 100 K.

THERMAL CONDUCTIVITY OF CoFe ALLOYS

Figure S8 shows the measured thermal conductivity κ of the five CoFe films as a function of temperature. For comparison we plot the electronic contribution to κ_{el} as calculated from the measured resistivity using the Wiedemann-Franz law: $\kappa_{el} = 2.45 \times 10^{-8}$ WΩ/K$^2\times$ T/ρ (lines in Fig. S8). Only for the films with lower Co concentrations (20% and 22%), the difference $\kappa - \kappa_{el}$ is positive (see Fig. 3(c) in the main text) and can be assigned to a phonon contribution (at lower T) or to a phonon/magnon scattering contribution (at higher T) to the thermal conductivity. The magnon contribution to κ

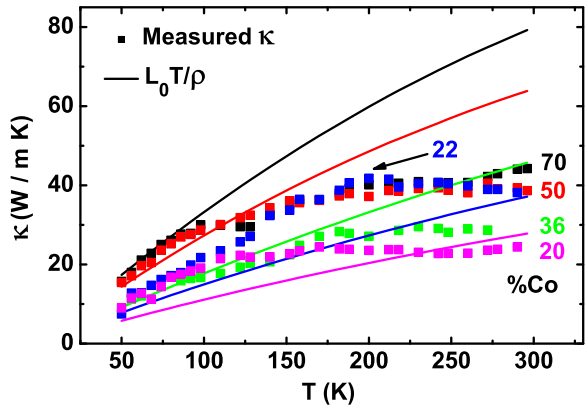

FIG. S8. Thermal conductivity κ for all five Co_xFe_{1-x} films vs temperature graph from 50 K-296 K is shown as squares. The numbers at the right indicate Co concentration. The lines represent the Wiedemann-Franz expectation value κ_e.

is usually visible below a few K only, when the phonon contribution is already negligible.

DETAILS OF THE FIRST-PRINCIPLES CALCULATIONS

The electronic structure of the bcc Co_xFe_{1-x} alloys has been determined using the spin-polarised relativistic Korringa-Kohn-Rostoker band structure method [43, 44] as implemented in the Munich SPR-KKR program package [45]. Chemical disorder is treated within the Coherent Potential Approximation (CPA) [46, 47]. For the entire concentration range considered here, the bcc structure has been assumed. At selected intermediate concentrations (30, 40, 50, 60, 70 at% Co) calculations have been performed for the fcc phase as well, assuming the same volume per atom as in the bcc structure of the same composition. Lattice parameters have been taken from literature [48] and interpolated appropriately for *intermediate* [49] concentrations. For the self-consistent determination of spin-polarised ground-state potentials the fully relativistic version of the program has been used. The exchange and correlation part is treated within the Local Spin-Density Approximation (LSDA) using the parametrisation of Vosko *et al.* [50]. All calculations were done in the Atomic Sphere Approximation (ASA) [51] for the potential shape.

The symmetric and antisymmetric parts of the electric conductivity tensor have been determined within Kubo's linear response framework using the Kubo-Greenwood and -Středa formulae, respectively [52–59]. These are derived in the athermal limit of the Kubo-Bastin equation [60, 61] and have been shown to yield numerically identical results for the type of systems treated here (cubic transition metals) in the limit $T \to 0$ [62]. Inclusion of the so-called vertex corrections (VC) [55, 63] is necessary to correct for improper averaging within the Coherent Potential Approximation (CPA) when dealing with products of Green's functions. For calculating electric, thermoelectric, and thermal transport properties at finite electronic temperatures, the generalized Mott formula [64**?** –67] and related expressions for the charge-charge (cc), charge-heat (cq), and heat-heat (qq) current correlation functions or response coefficients

$$L_{ij}^{cc}(T) = -\frac{1}{|e|}\int dE\, \sigma_{ij}^{cc}(E)\left(-\tfrac{\partial f(E,T)}{\partial E}\right) \quad \text{(S2)}$$

$$L_{ij}^{cq}(T) = -\frac{1}{|e|}\int dE\, \sigma_{ij}^{cc}(E)\left(-\tfrac{\partial f(E,T)}{\partial E}\right)(E - E_F) \quad \text{(S3)}$$

$$L_{ij}^{qq}(T) = -\frac{1}{|e|}\int dE\, \sigma_{ij}^{cc}(E)\left(-\tfrac{\partial f(E,T)}{\partial E}\right)(E - E_F)^2 \quad \text{(S4)}$$

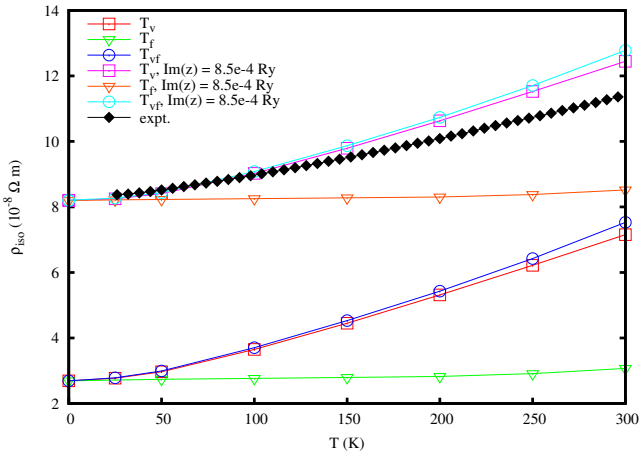

FIG. S9. Calculated isotropic resistivity $\rho_{\rm iso} = (2\rho_{\rm xx} + \rho_{\rm zz})/3$ in $Co_{0.50}Fe_{0.50}$ accounting for lattice disorder (T_v, red), transverse spin disorder (T_f, green), and both combined (T_{vf}, blue). In purple, orange and cyan corresponding results are shown including in addition an energy-independent finite imaginary part of the complex energy, $\Im(z) = 8.5 \cdot 10^{-4}$ Ry, mimicking structural disorder in the experiment, results of which are shown in black.

in terms of the energy-dependent electric conductivity $\sigma_{ij}^{cc}(E)$ have been used. Here T is the (electronic) temperature, entering via the Fermi-Dirac distribution $f(E,T)$, e is the elementary charge, and the integral over real energies E contains the product of the energy-dependent electrical conductivity $\sigma_{ij}^{cc}(E)$ with a kernel consisting of the (negative) energy derivative of $f(E,T)$ and a factor of $(E - E_{\rm F})^n$, where n equals the number of heat currents q involved and $E_{\rm F}$ is the Fermi energy. The Alloy Analogy Model [**?**] for temperature-induced vibrational and fluctuational disorder has been applied using calculated $M(T)$ data from Kakehashi and Hosohata [68] as input for the latter. For intermediate concentrations where results are not available in Ref. 68 linear interpolations between fits to

$$M(T)/M(0) = (1 - (T/T_{\rm C})^{\alpha})^{\beta} \qquad \text{(S5)}$$

have been performed.

CALCULATED RESISTIVITY INCLUDING VARIOUS SOURCES OF DISORDER

The isotropic residual resistivity $\rho_{\rm iso} = (2\rho_{\rm xx} + \rho_{\rm zz})/3$ is shown as a function of temperature for the exemplary case of $Co_{0.50}Fe_{0.50}$ in Fig. S9. Temperature is treated here on the level of the alloy-analogy model accounting for either lattice displacements only (red squares), transverse spin fluctuations only (green triangles), or both combined (blue circles). The total result including both sources of disorder simultaneously on the level of the Green function is obviously dominated by the vibrational disorder contribution and the two effects are nearly additive following Matthiessen's rule. As discussed in the main text, the as-prepared samples show a considerable amount of structural disorder. To compensate for this, a finite and constant imaginary part of the complex energy z was chosen for a quantitative agreement at low temperature with the experimental data shown as black diamonds. Corresponding results are given in magenta (T_v), orange (T_f), and cyan (T_{vf}). The finite imaginary part, corresponding to an additional decrease of the electronic lifetime, leads to an overall increase of the resistivity without major modification of the temperature dependence. Considering in addition the effect of a modified Fermi-Dirac statistics by means of Eq. S2 leads only to minor changes at higher T (not shown).

CALCULATED SEEBECK COEFFICIENT

The Seebeck or thermoelectric tensor, expressing the ratio of charge transport due to a temperature gradient versus that in response to an electric field, is obtained from Eqs. (S2) and (S3) as

$$\underline{\boldsymbol{S}} = -\tfrac{1}{eT}(\underline{\boldsymbol{L}}^{cc})^{-1}\underline{\boldsymbol{L}}^{cq} = \underline{\boldsymbol{\sigma}}^{-1}\underline{\boldsymbol{\alpha}} = \begin{pmatrix} S_{\rm xx} & S_{\rm xy} & 0 \\ -S_{\rm xy} & S_{\rm xx} & 0 \\ 0 & 0 & S_{\rm zz} \end{pmatrix}$$
$$= \begin{pmatrix} \frac{\sigma_{\rm xx}\alpha_{\rm xx}+\sigma_{\rm xy}\alpha_{\rm xy}}{\sigma_{\rm xx}^2+\sigma_{\rm xy}^2} & \frac{\sigma_{\rm xx}\alpha_{\rm xy}-\sigma_{\rm xy}\alpha_{\rm xx}}{\sigma_{\rm xx}^2+\sigma_{\rm xy}^2} & 0 \\ -\frac{\sigma_{\rm xx}\alpha_{\rm xy}-\sigma_{\rm xy}\alpha_{\rm xx}}{\sigma_{\rm xx}^2+\sigma_{\rm xy}^2} & \frac{\sigma_{\rm xx}\alpha_{\rm xx}+\sigma_{\rm xy}\alpha_{\rm xy}}{\sigma_{\rm xx}^2+\sigma_{\rm xy}^2} & 0 \\ 0 & 0 & \frac{\alpha_{\rm zz}}{\sigma_{\rm zz}} \end{pmatrix}, \qquad \text{(S6)}$$

where $\underline{\boldsymbol{\sigma}} = -e\underline{\boldsymbol{L}}^{cc}$ is the electrical conductivity tensor and $\underline{\boldsymbol{\alpha}} = -\frac{1}{T}\underline{\boldsymbol{L}}^{cq}$ is the Nernst conductivity tensor. In the limit of $T \to 0\,$K the energy integrals in Eqs. (S2) and (S3) transform via the Sommerfeld expansion into the well-known Mott formula.

When comparing to experimental results the isotropic value $S_{\rm iso} = \frac{2}{3}S_{\rm xx} + \frac{1}{3}S_{\rm zz}$, i.e., one third of the tensor in Eq. (S6) is used. Neglecting off-diagonal contributions as in $S_{ii} = -\frac{1}{eT}L_{ii}^{cq}/L_{ii}^{cc}$ leads however, for the systems and conditions considered in this work, only to minor differences, since $L_{ij}^{AB} << L_{ii}^{AB}$ holds for both $\underline{\boldsymbol{L}}^{cc}$ and $\underline{\boldsymbol{L}}^{cq}$. Additional contributions arising from direct and inverse spin Nernst and Hall effects, such as the spin Nernst magnetothermopower [**?**], are neglected in this work due to their vanishingly small size.

Figure S10 shows results for bcc Co_xFe_{1-x} with $x =$ 0.20, 0.22, 0.36, 0.50, and 0.70 accounting for chemical disorder only (T_{el}), including, by means of the alloy-analogy model, the effect of lattice displacements alone (T_v) or in combination with transverse spin fluctuations (T_{vf}). The effect of the additional temperature-dependent disorder apparently leads to a reduction of

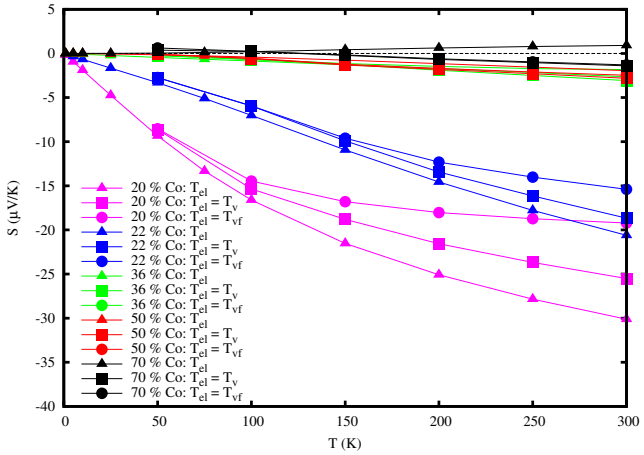

FIG. S10. Calculated thermoelectric power for bcc Co_xFe_{1-x} treating temperature either only on the level of the Fermi-Dirac distribution (*electronic temperature*, T_{el}, triangles), including in addition vibrational disorder (T_v, squares), and including both, vibrational and spin-fluctuation disorder (T_{vf}, circles).

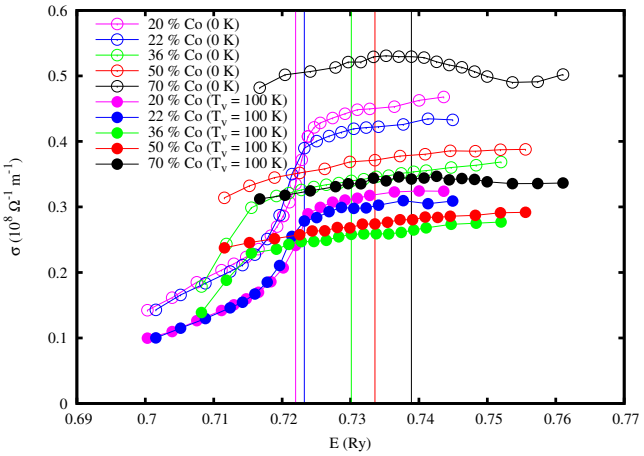

FIG. S11. Energy dependence of the conductivity of bcc Co_xFe_{1-x} at zero temperature (empty symbols) and $T_v = 100\,\mathrm{K}$ (full symbols). The vertical lines indicate the positions of the respective Fermi levels at $T = 0\,\mathrm{K}$.

the TEP for low Co content (as well as to an increased curvature), to minor enhancement for intermediate x_{Co} (0.36 and 0.50), and to sign change for $x_{\mathrm{Co}} = 0.70$. The importance of spin disorder decreases with increasing Co content, consistent with the decrease of the Curie temperature and simultaneous increase of the slope of the $M(T)$ curves [68] entering the calculations as input.

ENERGY-DEPENDENT CONDUCTIVITY

The theoretical results for the energy-dependent conductivity are shown in Fig. S11 taking account the chemical disorder only (0 K) and including vibrational disorder corresponding to a temperature of $T_v = 100,\mathrm{K}$. At higher T the rather sharp step in $\sigma(E)$ qualitatively explains the rather large values of the Mott-like contribution to the TEP at low x_{Co}. The step width is comparable to the temperature so that the leading term in the Sommerfeld expansion is not sufficient to calculate the TEP – at higher temperatures this leads to a curvature in the T-dependence of Fig. 2d in the main manuscript. The temperature dependent contributions of vibrational and spin disorder (not shown) tend to smear the step, in addition to a reduced overall magnitude. On the other hand, $\sigma(E)$ is rather flat on the high energy side, which leads to much lower values of the TEP than observed in the experiment for the Mott-like contribution.

THERMOELECTRIC POWER IN THE FCC PHASE

This discrepancy may result from fcc precipitations which appear at higher x_{Co} in the characterization. Such precipitation are also consistent with the low phonon contribution in the thermal conductivity. For this reason we also calculated the TEP for the fcc structure. The results are plotted in Fig. S12, and show that for the fcc lattice structure significantly larger values of the TEP are found and that the curvature is opposite to that in the bcc-structure for low Co concentrations. Thus the competition between the contributions from both structures may explain the observed evolution of the TEP with Co-

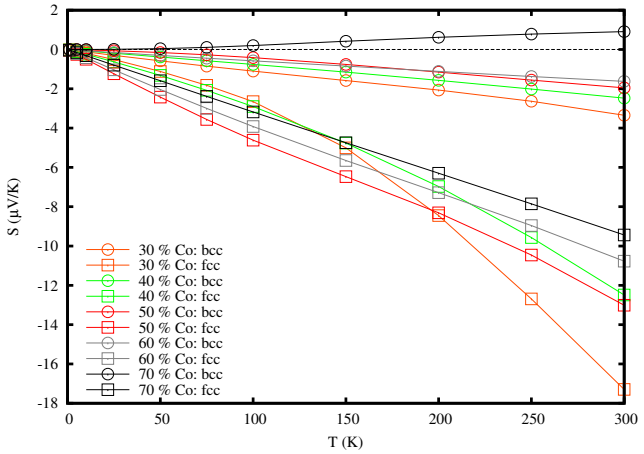

FIG. S12. Calculated electronic contribution to the Seebeck coefficient in bulk bcc and fcc Co_xFe_{1-x} for $x = 0.30$, 0.40, 0.50, 0.60, and 0.70.

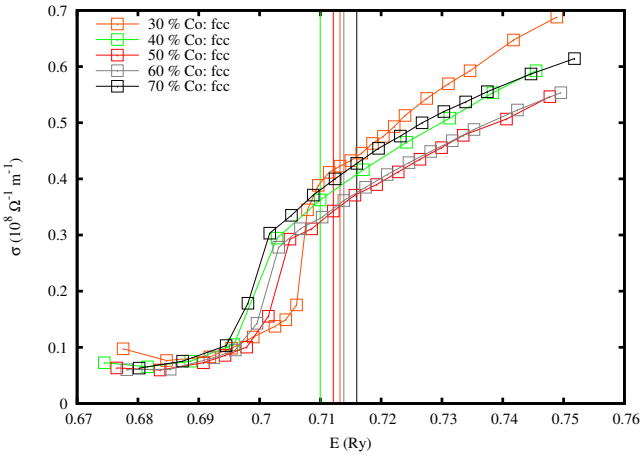

FIG. S13. Energy dependence of the conductivity of fcc Co_xFe_{1-x} at zero temperature. The vertical lines indicate the positions of the respective Fermi levels.

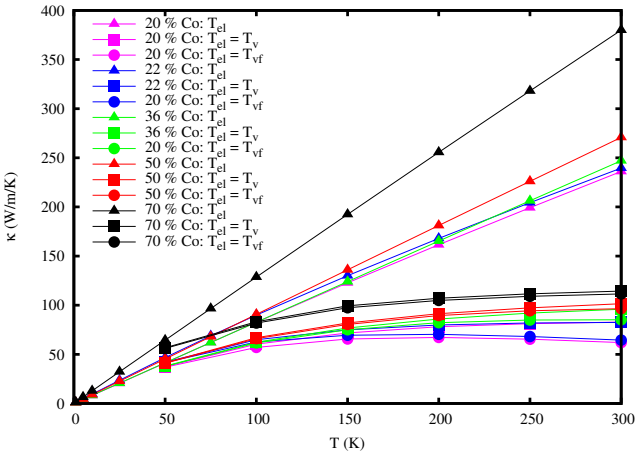

FIG. S14. Calculated electronic contribution to the thermal conductivity for bcc Co_xFe_{1-x} treating temperature either only on the level of the Fermi-Dirac distribution (*electronic temperature*, T_{el}, triangles), including in addition vibrational disorder (T_v, squares), and including both, vibrational and spin-fluctuation disorder (T_{vf}, circles).

content at high temperatures.

The underlying energy-dependent electrical conductivities are shown in Fig S13 for $T = 0\,\mathrm{K}$, the Fermi levels are again indicated by the vertical lines of corresponding color. The major differences compared to the bcc curves in Fig. S11 are the pronounced, approximately linear increase of σ in the vicinity of the Fermi level and its relative position with respect to the step in the conductivity. The former leads to the larger Seebeck coefficient in the fcc phase for all concentrations and the latter to the negative curvature of $Co_{0.3}Fe_{0.7}$ and $Co_{0.4}Fe_{0.6}$. For these two alloys with increasing temperature the step is close enough to E_F to be included in the interval for the energy integration of Eq. S3 and therefore its strong asymmetry enhances the TEP.

CALCULATED THERMAL CONDUCTIVITY

The electronic contribution to the thermal conductivity κ can be calculated, assuming only elastic scattering at impurities, from the energy dependence of the electrical conductivity using a generalized Mott-like expression [65**?**]. In Fig. S14 results are shown for the temperature-dependent isotropic thermal conductivity,

$$\kappa_{\mathrm{iso}} = \frac{2}{3}\kappa_{\mathrm{xx}} + \frac{1}{3}\kappa_{\mathrm{zz}} \tag{S7}$$

$$\text{with } \kappa_{ii} = \frac{1}{T}\left[\underline{\boldsymbol{L}}^{qq} - \frac{\underline{\boldsymbol{L}}^{cq}\underline{\boldsymbol{L}}^{qc}}{\underline{\boldsymbol{L}}^{cc}}\right]_{ii} \tag{S8}$$

$$\approx \frac{1}{T}\left(L_{ii}^{qq} - \frac{(L_{ii}^{cq})^2}{L_{ii}^{cc}}\right) \tag{S9}$$

with the charge-charge, charge-heat, and heat-heat current response functions of Eqs. S2-S4 and exploiting the symmetry relations [69, 70] $\underline{\boldsymbol{L}}^{qc} = \underline{\boldsymbol{L}}^{cq}$ and $L_{ij}^{AB} = -L_{ji}^{AB}$ as well as the observation $L_{ij}^{AB} << L_{ii}^{AB}$. In the last line of Eq. S7 the contribution from off-diagonal tensor elements is neglected, the exact form of $\underline{\boldsymbol{\kappa}}$ in $4/mm'm'$ reads

$$\kappa_{\mathrm{xx}} = \kappa_{yy} = \frac{1}{T}\left[L_{\mathrm{xx}}^{qq} - \left(\frac{L_{\mathrm{xx}}^{cc}((L_{\mathrm{xx}}^{cq})^2-(L_{\mathrm{xy}}^{cq})^2)}{(L_{\mathrm{xx}}^{cc})^2+(L_{\mathrm{xy}}^{cc})^2} + \frac{2L_{\mathrm{xy}}^{cc}L_{\mathrm{xx}}^{cq}L_{\mathrm{xy}}^{cq}}{(L_{\mathrm{xx}}^{cc})^2+(L_{\mathrm{xy}}^{cc})^2}\right)\right] \tag{S10}$$

$$\kappa_{\mathrm{xy}} = -\kappa_{yx} = \frac{1}{T}\left[L_{\mathrm{xy}}^{qq} - \left(\frac{L_{\mathrm{xy}}^{cc}((L_{\mathrm{xy}}^{cq})^2-(L_{\mathrm{xx}}^{cq})^2)}{(L_{\mathrm{xx}}^{cc})^2+(L_{\mathrm{xy}}^{cc})^2} + \frac{2L_{\mathrm{xx}}^{cc}L_{\mathrm{xy}}^{cq}L_{\mathrm{xx}}^{cq}}{(L_{\mathrm{xx}}^{cc})^2+(L_{\mathrm{xy}}^{cc})^2}\right)\right] \tag{S11}$$

$$\kappa_{\mathrm{zz}} = \frac{1}{T}\left[L_{\mathrm{zz}}^{qq} - \frac{(L_{\mathrm{zz}}^{cq})^2}{L_{\mathrm{zz}}^{cc}}\right], \tag{S12}$$

leading to negligibly small corrections in case of conductive metals. The temperature dependence of the results accounting only for the electronic temperature is fairly linear and, with increasing iron content the curves fall almost on top of each other. In particular for high temperatures κ is strongly reduced by lattice displacements and spin fluctuations as additional sources of disorder, the effect of the latter being again of minor importance.

BAND STRUCTURE OF BCC Co_xFe_{1-x} ALLOYS

The transport phenomena discussed in this work show characteristic features at Co concentrations of $\sim 20\,\mathrm{at\%}$. To elucidate the composition dependence of the transport coefficients discussed in this work, the spin-projected Bloch spectral function (BSF) of the bcc alloys and their clean limits have been calculated (1st and 4th column in

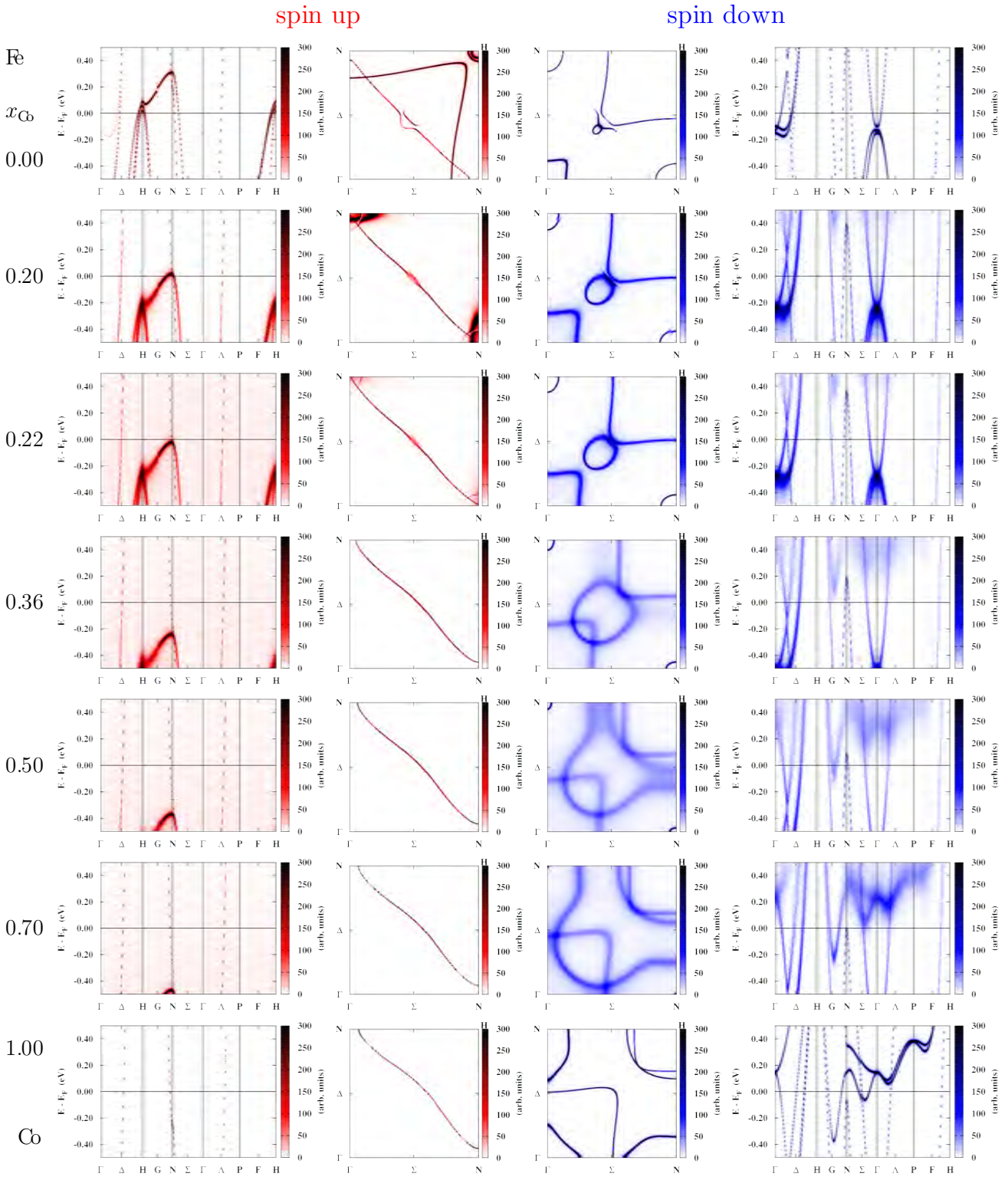

FIG. S15. Spin-projected band structure (Bloch spectral function, BSF) in bcc Co_xFe_{1-x} for, from top to bottom, $x_{Co} = 0$, 0.20, 0.22, 0.36, 0.50, 0.70, and 1 (*hypothetical* bcc Co), for majority spin up (left two columns, red) and minority spin down (right two columns, blue). The first and fourth columns show the energy-dependence along high-symmetry lines in the Brillouin zone between -0.5 and 0.5 eV around the Fermi level while the second and third columns depict constant-energy isosurfaces in the $\Gamma - N - H$ plane at $E = E_F$.

Fig. S15). Since the electronic contributions to the linear response properties are intimately (but not trivially) connected to the band structure, one can expect to infer a qualitative explanation for some of the concentration-dependent characteristics. As visible in Fig. S15, the overall shape of the bands is very different for the two spin channels (majority "spin-up", left two columns, in red and minority "spin-down", right two columns, in blue) and so is the extent as well as the $\vec{k}$-space position of broadening effects on the band structure. The Fermi level rises from top to bottom with growing Co content (as Fe has one electron less than Co) and at around 22 % crosses the top of *d*-like bands of the majority channel (left) at the N point of the Brillouin zone (2^{nd} and 3^{rd} column in Fig. S15). This qualitatively explains the maximum of the resistivity in this concentration range, because the Fermi level is located in flat and broadened regions. For the energy dependence of the conductivity this results in the pronounced step discussed above, giving rise to distinct magnitudes and temperature dependencies for different concentrations. In the minority channel (right two columns) the bands crossing the Fermi level are predominantly of *sp*-character having large slopes for small cobalt concentration ($x > 0.4$). At 40 % Co, the Fermi level cuts through the bottom of a parabolic band in between H and N point. This should qualitatively explain the additional resistivity peak at $x = 0.4$. The avoided crossing at $\sim 1/4$ of the distance between Γ and H point could be connected to the local minimum around 25 % cobalt content, where it is passing through E_{F}.

[1] I. Zutić, J. Fabian and S. D. Sharma Rev. Mod. Phys. **76**, 323 (2004).

[2] D. C. Ralph and M. D. Stiles J. Magn. Magn. Mater. **320**, 1190-1216 (2008).

[3] G.E.W. Bauer, A. H. MacDonald and S. Maekawa Sol. Stat. Commun. **150**, 459 (2010).

[4] S. R. Boona, Vlaminck, R. C. Myers and J. P. Heremans Energy Environ. Sci. **7**, 885 (2014).

[5] S. Maekawa and T. Shinjo, Adv. Cond. Mat. Sci. **3** (CRC press LLC 2002).

[6] S. A. Nikitov, *et al.*, Physics-Uspekhi **58** , 10 (2015).

[7] L.J. Cornelisen, J. Liu, R.A. Duine, J.B. Youssef, and B.J. van Wees, Nat. Phys. **11**, 1022 (2015).

[8] D. W. Denlinger, E. N. Abarra, K. Allen, P. W. Rooney, M. T. Messer, S. K.Watson and F. Hellman, Rev. Sci. Instrum. **65**, 946 (1994).

[9] A. Lopeandia, L. Cerdo, M. Clavaguera-Mora, L. R. Arana, K. Jensen, F. Munoz, and J. Rodriguez-Viejo, Rev. Sci. Instrum. **76**, 065104 (2005).

[10] M.N. Ou, T.J. Yang, S.R. Harutyunyan, Y.Y. Chen, C.D. Chen, S.J. Lai, Appl. Phys. Lett. **92**, 063101 (2008).

[11] B.L. Zink, A.D. Avery, Rubina Sultan, D. Bassett, M.R. Pufall, Solid State Commun. **150**, 514 (2010).

[12] D.W. Cooke, F. Hellman, J.R. Groves, B.M. Clemens, S. Moyerman, Rev. Sci. Instrum. **82**, 023908 (2011).

[13] A. D. Avery, M. R. Pufall, and B. L. Zink, Phys. Rev. Lett. **109**, 196602 (2012).

[14] M. Schmid, S. Srichandan, D. Meier, T. Kuschel, J.-M. Schmalhorst, M. Vogel, G. Reiss, C. Strunk, and C. H. Back, Phys. Rev. Lett. **111** 187201 (2013).

[15] R. Sultan, A. D. Avery, G. Stiehl, and B. L. Zink J. Appl. Phys. **105**, 043501 (2009).

[16] H. Ebert, S. Mankovsky, K. Chadova, S. Polesya, J. Minár, and D. Ködderitzsch, Phys. Rev. B **91**, 165132 (2015).

[17] R. Kováčik, P. Mavropoulos, and S. Blügel, Phys. Rev. B **91**, 014421 (2015).

[18] M. Obstbaum, M. Decker, A. K. Greitner, M. Haertinger, T. N. G. Meier, M. Kronseder, K. Chadova, S. Wimmer, D. Ködderitzsch, H. Ebert, and C. H. Back, Phys. Rev. Lett. **117**, 167204 (2016).

[19] S. Meyer, Y.-T. Chen, S. Wimmer, M. Althammer, T. Wimmer, R. Schlitz, S. Geprägs, H. Huebl, D. Ködderitzsch, H. Ebert, G. E. W. Bauer, R. Gross, and S. T. B. Goennenwein, Nat. Mater. **16**, 977 (2017).

[20] B. Flebus, R. A. Duine, Y. Tserkovnyak, Europhys. Lett. **115**, 57004 (2016).

[21] Y. Tserkovnyak, C. H. Wong, Phys. Rev. B **79**, 014402 (2009).

[22] F. J. Blatt, D. J. Flood, V. Rowe, P. A. Schroeder and J. E. Cox Phys. Rev. Lett. **18** 395 (1967).

[23] A. L. Trego, A. R. Mackintosh, Phys. Rev. **166**, 495 (1968).

[24] S. J. Watzman, R. A. Duine, Y. Tserkovnyak, S. R. Boona, H. Jin, A. Prakash, Y. Zheng and J. P. Heremans, Phys. Rev. B **94**, 144407 (2016).

[25] M. A. W. Schoen, J. Lucassen, H. T. Nembach, T. J. Silva, B. Koopmans, C. H. Back, J. M. Shaw, Phys. Rev. B **95**, 134410 (2017).

[26] M. A. W. Schoen, J. Lucassen, H. T. Nembach, B. Koopmans, T. J. Silva, C. H. Back, J. M. Shaw, Phys. Rev. B **95**, 134411 (2017).

[27] Supplementary Material at [XXX] for more details on theory and experiment.

[28] P. Kim, L. Shi, A. Majumdar and P. L. McEuen, Phys. Rev. Lett. **87** 215502 (2001).

[29] B. Raquet, M. Viret, E. Sondergard, O. Cespedes and R. Mamy, Phys. Rev. B **66**, 024433 (2002).

[30] M. V. Kamalakar, A. K. Raychaudhuri, X. Wei, J. Teng and P. D. Prewett, Appl. Phys. Lett. **95**, 013112 (2009).

[31] R. P. Huebener, Phys. Rev. **171**, 634 (1968).

[32] In the fcc structure and for intermediate Co concentration the Fermi level is situated more closely above the step, while $\sigma(E)$ increases more strongly, when compared to the bcc-structure. At elevated T the step contributes to $\mathcal{S}(\mathcal{T})$, resulting in an opposite curvature.

[33] D. T. Edmonds, R. G. Petersen, Phys. Rev. Lett. **2**, 499 (1959).

[34] T.M. Tritt, Thermal Conductivity: Theory, Properties, and Applications, Kluwer, New York, (2004).

[35] M. J. Laubitz and T. Matsumura, Canadian J.Phys. **51**, 1247 (1973).

[36] International Centre of Diffraction Data, Powder Diffraction File 2, 48-1816 (http://www.icdd.com/); I. Baker, Thayer School of Engineering, Dartmouth College, NH, USA, ICDD Grant-in-Aid (1997).

[37] International Centre of Diffraction Data, Powder Diffraction File 2, 15-0806 (http://www.icdd.com/); Natl. Bur. Stand. (U.S.) Monogr. **25**, 4, 10 (1966).

[38] P. P. Freitas and L. Berger, Phys. Rev. B **37**, 6079 (1988).
[39] M. Rubinstein, F. J. Rachford, W. W. Fuller and G. A. Prinz, Phys. Rev. B **37**, 8689 (1988).
[40] J. W. C. De Vries, Thin Solid Films **167**, 25 (1988).
[41] N. W. Ashcroft and N. D. Mermin, *Solid State Physics*, (Saunders College, New York 1976).
[42] C. Ahn, K.-H. Shin, R. Loloee, J. Bass, and W. P. Pratt, Jr., J. Appl. Phys. **108** 023908 (2010).
[43] H. Ebert, D. Ködderitzsch, and J. Minár, Rep. Prog. Phys. **74**, 096501 (2011).
[44] H. Ebert, J. Braun, D. Ködderitzsch, and S. Mankovsky, Phys. Rev. B **93**, 075145 (2016).
[45] *The Munich SPR-KKR package* vers. 7.7, H. Ebert *et al.*, http://olymp.cup.uni-muenchen.de/ak/ebert/SPRKKR (2017).
[46] P. Soven, Phys. Rev. **156**, 809 (1967).
[47] B. Velický, Phys. Rev. **184**, 614 (1969).
[48] B. Predel, "Landolt-Börnstein - Group IV Physical Chemistry," (Springer Berlin Heidelberg, Berlin, Heidelberg, 1993), Chap. Co-Fe (Cobalt-Iron), pp. 1–13.
[49] That is, not for the whole range between the pure metals as in Vegard's law.
[50] S. H. Vosko, L. Wilk, and M. Nusair, Can. J. Phys. **58**, 1200 (1980).
[51] O. K. Andersen, Phys. Rev. B **12**, 3060 (1975).
[52] R. Kubo, J. Phys. Soc. Japan **12**, 570 (1957).
[53] D. A. Greenwood, Proc. Phys. Soc. **71**, 585 (1958).
[54] L. Smrčka and P. Středa, J. Phys. C: Solid State Phys. **10**, 2153 (1977).
[55] W. H. Butler, Phys. Rev. B **31**, 3260 (1985).
[56] J. Banhart, R. Bernstein, J. Voitländer, and P. Weinberger, Solid State Commun. **77**, 107 (1991).
[57] J. Banhart, H. Ebert, P. Weinberger, and J. Voitländer, Phys. Rev. B **50**, 2104 (1994).
[58] S. Lowitzer, D. Ködderitzsch, and H. Ebert, Phys. Rev. B **82**, 140402(R) (2010).
[59] S. Lowitzer, M. Gradhand, D. Ködderitzsch, D. V. Fedorov, I. Mertig, and H. Ebert, Phys. Rev. Lett. **106**, 056601 (2011).
[60] A. Bastin, C. Lewiner, O. Betbeder-Matibet, and P. Nozieres, J. Phys. Chem. Solids **32**, 1811 (1971).
[61] A. Crépieux and P. Bruno, Phys. Rev. B **64**, 014416 (2001).
[62] D. Ködderitzsch, K. Chadova, and H. Ebert, Phys. Rev. B **92**, 184415 (2015).
[63] G. D. Mahan, *Many-Particle Physics, 2nd ed.*, Physics of Solids and Liquids (Plenum Press, New York, 1993).
[64] M. Cutler and N. F. Mott, Phys. Rev. **181**, 1336 (1969).
[65] M. Jonson and G. D. Mahan, Phys. Rev. B **21**, 4223 (1980); Phys. Rev. B **42**, 9350 (1990).
[66] S. Wimmer, D. Ködderitzsch, K. Chadova, and H. Ebert, Phys. Rev. B **88**, 201108(R) (2013).
[67] S. Wimmer, D. Ködderitzsch, and H. Ebert, Phys. Rev. B **89**, 161101(R) (2014).
[68] Y. Kakehashi and O. Hosohata, Phys. Rev. B **40**, 9080 (1989).
[69] W. H. Kleiner, Phys. Rev. **142**, 318 (1966).
[70] M. Seemann, D. Ködderitzsch, S. Wimmer, and H. Ebert, Phys. Rev. B **92**, 155138 (2015).

3.1.3 Additional results on CoFe alloys

The following is an unpublished manuscript on the electric, thermal, and thermoelectric transport properties of CoFe alloys, providing more details and additional theoretical results than what is published in Ref. 309 (3.1.2).

Galvanomagnetic, thermogalvanomagnetic, and thermal transport properties of ferromagnetic bcc Fe_xCo_{1-x} bulk-alloys from first principles

S. Wimmer[1],* S. Mankovsky[1], S. Srichandan[2], M. Kronseder[2], C.H. Back[2], C. Strunk[2], and H. Ebert[1]
[1] *Department of Chemistry, Physical Chemistry, Ludwig-Maximilians-Universität, D-81377 Munich, Germany and*
[2] *Institute of Experimental and Applied Physics, University of Regensburg, D-93040 Regensburg, Germany*

The ferromagnetic alloy system bcc Fe_xCo_{1-x} constitutes, due to its mutual miscibility over a wide range of composition, an important test system for the study of transport phenomena in response to electric fields and temperature gradients. A recent investigation by Srichandan *et al.*[1] has focused on the impact of inelastic scattering processes, in particular electron-magnon scattering, on electrical resistivity, Seebeck coefficient, and thermal conductivity. Here we present an extension to this investigation, focusing on the composition- and temperature dependence of these coefficients together with a detailed discussion on the basis of the underlying electronic structure, give results for the pure limits bcc Fe and hcp Co in comparison to recent experiments by Watzmann *et al.*[2] and for transverse response properties such as anomalous Hall and Nernst effect as well as the electronic contribution to thermal Hall or Righi-Leduc effect.

I. INTRODUCTION

The galvanomagnetic, thermogalvanomagnetic, and thermal transport properties of bcc Fe_xCo_{1-x} alloys have been investigated by performing first-principles band structure and subsequent linear response transport calculations. For this the Korringa-Kohn-Rostoker multiple scattering Green function formalism in conjunction with Kubo's linear response formalism as implemented in the Munich SPR-KKR package has been used. Temperature-dependent response coefficients such as resistivity, Seebeck coefficient, and the electronic part of the thermal conductivity have been obtained from an implementation of the generalized Mott expressions following Jonson and Mahan[3]. Effects beyond the simplistic "electronic temperature" connected with the temperature dependence of the Fermi-Dirac distribution have been accounted for using the so-called alloy-analogy model (AAM) based on the Coherent Potential Approximation (CPA). This work has been triggered by recent experimental research on the transport properties of Fe_xCo_{1-x} films at the University of Regensburg and was in part published in Ref. 1. Here we provide additional theoretical details of the transport calculations and present an extended study of the concentration and in particular temperature dependence of the various response coefficients. In addition results on the antisymmetric tensor elements of the electric, thermoelectric as well as the electronic part of the thermal conductivity are presented.

II. METHODS

The electronic structure of the bcc Fe_xCo_{1-x} alloys has been determined using the spin-polarised relativistic Korringa-Kohn-Rostoker band structure method[4,5] as implemented in the Munich SPR-KKR program package.[6] Chemical disorder has been treated within the Coherent Potential Approximation (CPA).[7,8] For the whole concentration range considered here, from 20 to 85 % Fe content, the bcc structure has been assumed. The corresponding lattice parameters have been taken from the literature[9] and interpolated appropriately for *intermediate*[10] concentrations. For the self-consistent determination of spin-polarized ground-state potentials the fully relativistic version of the program has been used. The exchange and correlation part is treated within the Local Spin-Density Approximation (LSDA) using the parametrization of Vosko *et al.*[11]. All calculations were done in the Atomic Sphere Approximation (ASA).[12]

The symmetric and antisymmetric parts of the electric conductivity tensor have been determined within Kubo's linear response framework using the Kubo-Greenwood and -Středa formulae, respectively.[13–20] These are derived in the athermal limit of the so-called Kubo-Bastin equation[21,22] and have been shown to yield numerically identical results for the type of systems treated here (cubic transition metals) in the limit $T \to 0$.[23] Inclusion of the so-called vertex corrections (VC)[16,24] is necessary to achieve a proper averaging within the Coherent Potential Approximation (CPA) when dealing with products of Green functions. For calculating electric, thermoelectric, and thermal transport properties at finite electronic temperatures, the generalized Mott formula[3,25–27] and related expressions for the charge-charge (cc), charge-heat (cq), and heat-heat (qq) current correlation functions or response coefficients

$$L_{ij}^{cc}(T) = -\frac{1}{|e|}\int dE\, \sigma_{ij}^{cc}(E)\left(-\tfrac{\partial f(E,T)}{\partial E}\right) \quad (1)$$

$$L_{ij}^{cq}(T) = -\frac{1}{|e|}\int dE\, \sigma_{ij}^{cc}(E)\left(-\tfrac{\partial f(E,T)}{\partial E}\right)(E-E_{\mathrm{F}}) \quad (2)$$

$$L_{ij}^{qq}(T) = -\frac{1}{|e|}\int dE\, \sigma_{ij}^{cc}(E)\left(-\tfrac{\partial f(E,T)}{\partial E}\right)(E-E_{\mathrm{F}})^2 \quad (3)$$

in terms of the energy-dependent electric conductivity $\sigma_{ij}^{cc}(E)$ have been used. Here T is the (electronic) temperature, entering via the Fermi-Dirac distribution function $f(E,T)$, e is the elementary charge, and the integral over real energies E contains the product of the energy-dependent electrical conductivity $\sigma_{ij}^{cc}(E)$ with a kernel consisting of the (negative) energy derivative of $f(E,T)$ and a factor of $(E-E_{\rm F})^n$, where n equals the number of heat currents q involved and $E_{\rm F}$ is the Fermi energy. The Alloy Analogy Model[28] for temperature-induced vibrational and fluctuational disorder has been applied using calculated $M(T)$ data from Kakehashi and Hosohata[29] as input for the latter. For intermediate concentrations where results are not available in Ref. 29 linear interpolations between fits to

$$M(T)/M(0) = (1-(T/T_{\rm C})^{\alpha})^{\beta} \qquad (4)$$

have been performed.

III. TRANSPORT PROPERTIES

A. Residual resistivity and anisotropic magnetoresistance

Figure 1 shows results for the isotropic residual resistivity $\rho_{\rm iso}$ (top) and the anisotropic magnetoresistance (bottom) as a function of the Fe content x in bcc Fe_xCo_{1-x}. As visible in the upper panel the calculated residual resistivity (black squares) appears to follow the Nordheim rule[33] up to about $x = 0.75$, apart from a slight shift of the maximum to $x = 0.6$, but then shows a maximum at $x \approx 0.85$. This behavior can be qualitatively explained by details of the band structure (see Section IV below). It is in reasonably good qualitative agreement with the experimental results of Freitas and Berger[31] (full blue circles), except for the local minimum we observe at $x \approx 0.75$ Fe content. A corresponding feature appears to be present in the experimental data at $x \approx 0.7$ as well. Quantitatively, theory and experiment agree well for $x < 0.6$, the absolute values around the resistivity maximum are considerably underestimated by the calculations. The same applies to theoretical results obtained by Turek and coworkers[30] using a fully relativistic implementation of the Kubo-Bastin equation[21,34] within the TB-LMTO-CPA method, shown in full red squares. Although these data around the maximum are rather scarce, it seems that the agreement with experiment concerning magnitude and position of the maximum is slightly better in their case.[35] Note that here also a small local minimum exists around $x \approx 0.7$. Comparison of the results of the present work ex- and including vertex corrections (NV and VC, open and full black squares) reveals that these are small and negative throughout the whole range of concentrations considered.

In the lower panel the anisotropic magnetoresistance (AMR) defined as $\Delta\rho/\rho_{\rm iso}$ with $\Delta\rho$ being the difference in (residual) resistivity parallel ($\rho_{\rm zz}$) and perpendicular ($\rho_{\rm xx}$) to the magnetization direction (z) is shown. Again results obtained within this work (full black squares) is

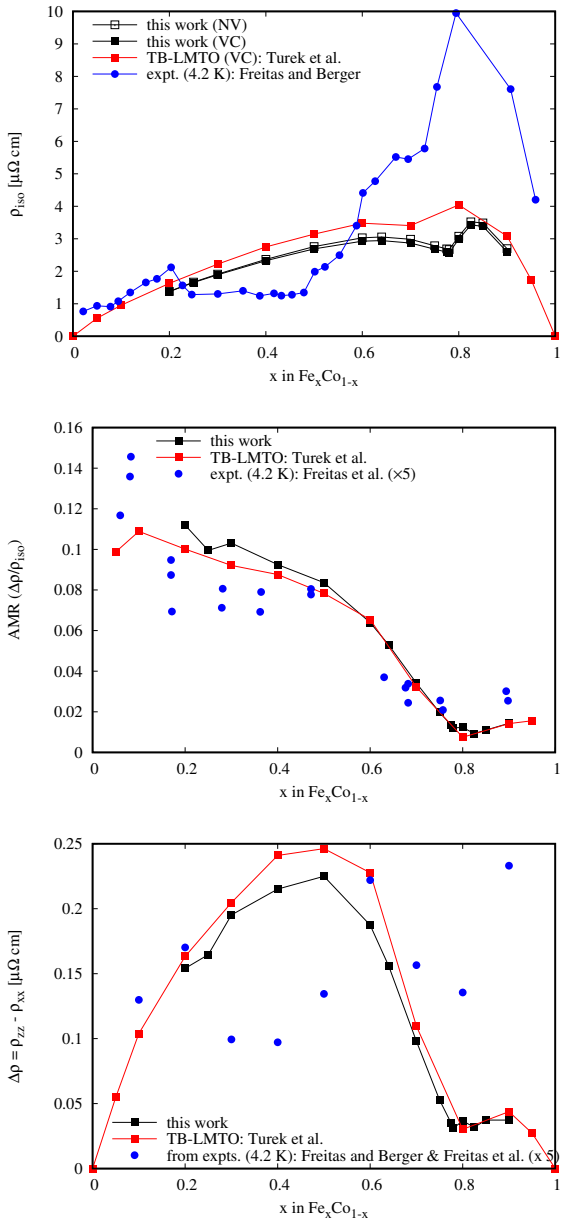

FIG. 1. Top: Composition dependence of the residual resistivity ex- (NV) and including vertex corrections (VC) compared to TB-LMTO-CPA results by Turek *et al.*[30] and experimental low-temperature data by Freitas and Berger[31]. Center: The anisotropic magnetoresistance (AMR) $\Delta\rho/\rho_{\rm iso}$ as a function of Fe content x, in comparison to TB-LMTO-CPA results by Turek *et al.*[30] and experimental low-temperature data by Freitas *et al.*[32]. Note that the latter have been scaled by a factor of five. Bottom: Resistivity anisotropy $\Delta\rho = \rho_{\rm zz} - \rho_{\rm xx}$ compared to theoretical results by Turek *et al.*[30] and experimental data by Freitas *et al.*[32] and Freitas and Berger[31], which are again scaled by 5.

compared to TB-LMTO data by Turek and coworkers[36] and experimental low-temperature measurements by Freitas *et al.*[32]. The latter have been scaled by a factor of five to facilitate comparison of the concentration dependence. Since the order of magnitude of the residual resistivity ρ_{iso} is comparable in theory and experiment, as visible in the upper panel of Fig. 1, this deviation is due to a smaller magnetic anisotropy of the resistivity in experiment, possibly caused by inhomogeneities of the sample leading to incomplete alignment of magnetic domains. Starting from about $\Delta\rho/\rho_{\mathrm{iso}} = 0.13$ at $x = 0.2$ the AMR monotonously decreases with increasing Fe content, mostly due to the increase of ρ_{iso}. The absolute difference $\Delta\rho$ (not shown) exhibits a maximum right in the middle of the concentration range. This behavior of the AMR is in qualitative and quantitative accordance with the theoretical findings by Turek *et al.*[36] and in qualitative agreement with the experimental findings by Freitas *et al.*[32].

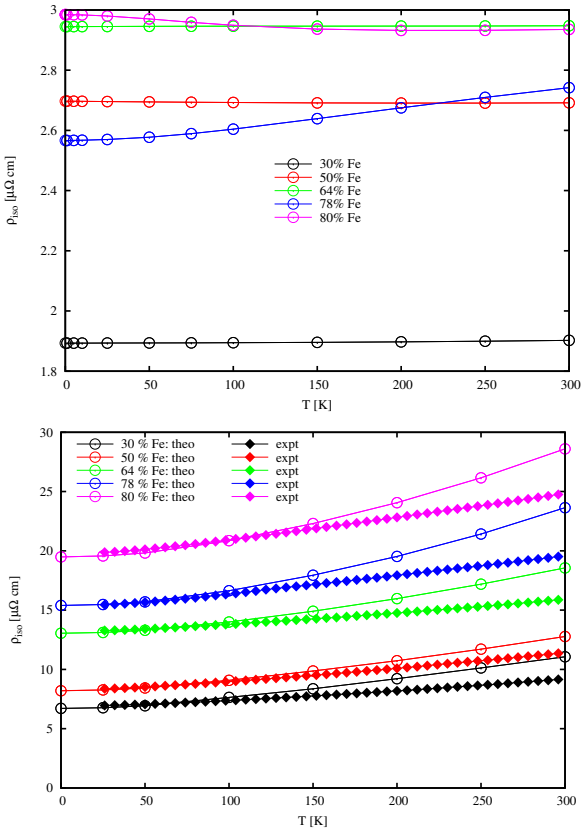

FIG. 2. Top: Calculated T_{el}-dependent isotropic resistivity for alloys with Fe contents $x = 0.3$, 0.5, 0.64, 0.78, and 0.8. Bottom: Results including the effect of lattice displacements, spin fluctuations and a finite imaginary part of the energy in comparison to measured $\rho(T)$ data.

The top panel of Fig. 2 shows the dependence of the isotropic resistivity ρ_{iso} on temperature in the range of 0–300 K for for Fe contents of $x = 0.3$, 0.5, 0.64, 0.78, and 0.8. The temperature dependence is described using Eq. (1) to account for the effect of the temperature on the occupation of states via the Fermi-Dirac distribution function ("electronic temperature" T_{el}). As can be seen, this effect is negligibly small since all curves are more or less constant, with slight deviations for $x = 0.78$ (ρ increasing with T) and 0.8 (ρ decreasing with T). This result is of course quite unintuitive and in fact unphysical. Hence (as expected), a more sophisticated treatment of finite-temperature effects, in particular lattice vibrations and spin fluctuations is called for.

The experimental results for T between $\sim$ 25 and 300 K are given in the bottom panel as full diamonds. In comparison to the theoretical T_{el}-data shown in the upper upper panel, the experimental curves have first of all a larger offset at 0 K (i.e., the residual resistivity). This can be primarily ascribed to additional scattering at grain boundaries, defects, and possibly also the film geometry. Their temperature dependence is in addition more pronounced, which certainly has to be attributed to the simplified treatment of finite temperatures in theory, as discussed in the preceding paragraph. All experimental curves show an almost linear T-dependence essentially in parallel to each other, largest deviations occur for the alloy containing 78 % Fe. The theoretical results in the lower panel of Fig. 2 were obtained by considering the additional disorder due to lattice vibrations and (transverse) spin fluctuations employing the alloy analogy model[28] which transfers the mean field approach of the CPA alloy theory to finite temperature effects. The $M(T)$ data serving as an input for the treatment of fluctuational disorder were taken from calculations by Kakehashi and Hosohata[29] using the finite-temperature theory of local-environment effects. Moreover a finite and constant imaginary part of the energy $\mathrm{Im}(E)$ was employed to account for the structural disorder of the samples. This was chosen such as to reproduce the low-temperature behavior of the experimental curves. As can be seen, the inclusion of finite temperature effects leads to an improved agreement with experiment concerning the temperature dependence. However the rate of increase is overestimated, apparently proportional to the increase of the overall magnitude with rising Fe content. This has to be ascribed to the contributions from inelastic scattering at phonons and possibly magnons, as discussed in detail in Ref. 1.

Figure 3 gives a detailed account of the influence of lattice vibrations and/or spin fluctuations on the temperature dependence of the resistivity for the alloy $Fe_{0.5}Co_{0.5}$. The former are determined by the average Debye temperature of the alloy and the latter by the Weiss field evaluated from the temperature dependence of the atom-resolved magnetization, which can be taken either from experiment, from Monte-Carlo simulations based on the Heisenberg model, or, as in the upper panel, from RDLM calculations.[28,37,38]

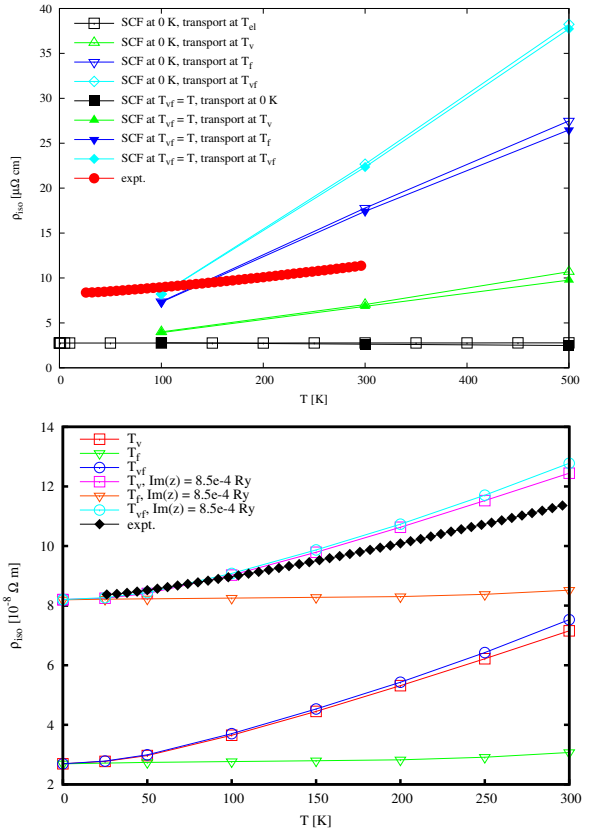

FIG. 3. Top: Temperature-dependent ρ_{iso} of $Fe_{0.5}Co_{0.5}$ for T_{el}, T_{v}, T_{f}, and T_{vf} with $M(T)$ data from RDLM. Results for the latter three are shown in addition with the alloy analogy model applied during the SCF calculation as well (always T_{vf}). Bottom: Corresponding results for SCF at $T = 0\,\mathrm{K}$ and magnetization data from Kakehashi and Hosohata[29]. In addition the effect of a finite imaginary part of the energy $\mathrm{Im}(z)$ is shown, added to account for structural disorder.

The resistivity for a given (finite) temperature has been calculated within this approach using the self-consistent potential obtained for the same temperature via RDLM calculations (full symbols) as well as for $T = 0\,\mathrm{K}$ (open symbols, except for black). In the first case the electronic structure calculations allow taking into account the modification of the local exchange field due to the thermally-induced magnetic disorder in the system. For subsequent electronic transport calculations this can be regarded as a contribution of longitudinal spin fluctuations. The latter approach of applying the AAM to transport calculations based on potentials for $T = 0\,\mathrm{K}$ can only account for the effect of transverse spin fluctuations.

The temperature-dependent resistivity without making use of the AAM in the transport calculations is shown in black, open symbols stand again for the results from Fig. 2 ($T_{\mathrm{el}} = T$), while the full symbols represent RDLM potentials and transport for $T = 0\,\mathrm{K}$. As can be seen, the effect of the additional temperature-induced disorder on the potentials is negligible for the resistivity. The green triangles represent resistivities calculated accounting only for lattice vibrations, once based on the potential for $T = 0\,\mathrm{K}$ (open symbols) and once for RDLM potentials (full symbols). Again the influence of the finite-T potentials is small, but the AAM-transport calculations give significantly different and qualitatively (as a function of T) as well as quantitatively somewhat more satisfying results when comparing to the experimental results shown as red full circles. Accounting only for the influence of fluctuational disorder (blue up-side-down triangles), the agreement with experiment at 100 K is considerably improved. Unfortunately, the increase in resistivity with temperature is much more pronounced as compared to the results for T_{v} and apparently even grossly overestimated at higher temperatures. This can be related to the overestimation of the decay of $M(T)$ with temperature in the RDLM calculations.[38] Taking both random lattice displacements and tilted moments into account (cyan diamonds), obviously the resistivity is largest and for $T = 100\,\mathrm{K}$ (accidentally) agrees well with experiment. As for fluctuational disorder only, the increase with temperature is exaggerated.

For all three temperatures considered here, the results taking both vibrational and fluctuational disorder into account is seemingly following Matthiessen's rule.[39] This behavior, i.e., that the effects of vibrations and spin fluctuations on the resistivity add up as expected for independent sources of scattering, is in fact rather seldomly found in this type of calculations.[28] This, as well as the almost perfectly linear temperature dependence of all curves shown here, might be attributed to the large chemical disorder present in the $Fe_{0.5}Co_{0.5}$ alloy, effectively reducing vibrations and fluctuations to uncorrelated additional sources of disorder.

The bottom panel of Fig. 3 shows in comparison results using only the potential for $T = 0\,\mathrm{K}$ and taking the $M(T)$ data from Ref. 29. Obviously the dominant source for scattering responsible for the temperature dependence of ρ seems to be the lattice vibrations (T_v), whereas the spin fluctuations alone (T_f) are almost negligible in this temperature range. Note, that the magnetization at 300 K is reduced by 10^{-3} relative to the value at $T = 0\,\mathrm{K}$. Considering both effects at the same time gives a slight increase of ρ, again in good agreement with Matthiessen's rule. The dominant source of scattering responsible for the absolute magnitude of $\rho(T)$ however is the structural disorder mimicked here by a finite imaginary part of the energy as discussed above. Under the assumption that this should be essentially temperature independent, the remaining disagreement with experiment leaves room for inelastic processes as electron-phonon and electron-magnon scattering.

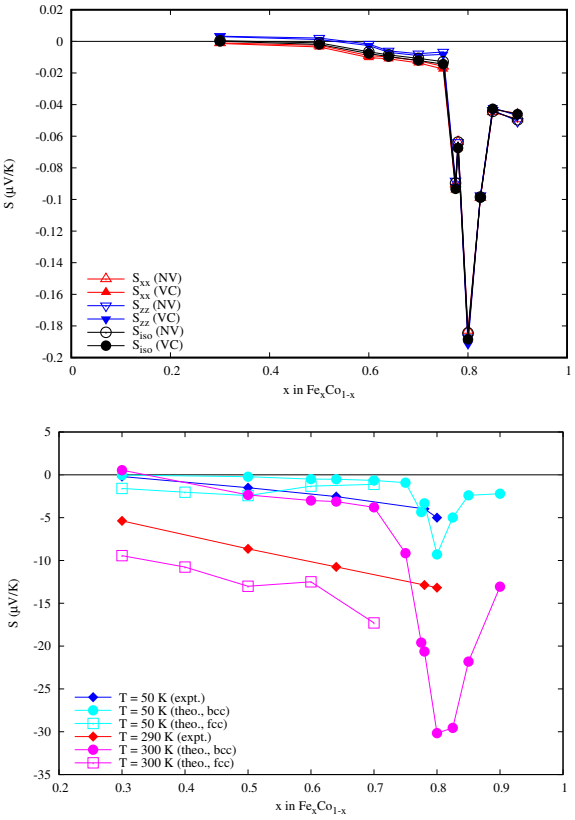

FIG. 4. Top: Seebeck coefficient in the athermal limit ($T_{\rm el} = 1\,$K) as a function of Fe content x. Results ex- (NV) and including vertex correction (VC) for the tensor elements perpendicular (S_{xx}) and parallel (S_{zz}) to the magnetization direction as well as for the isotropic value are shown. for Bottom: Experimental and theoretical results for the isotropic Seebeck coefficient $S_{\rm iso}$ as a function of Fe content for temperatures of 50 K (experiment: blue diamonds, theory (bcc): cyan circles, theory (fcc): cyan squares) and ∼300 K (experiment: red diamonds, theo. (bcc): magenta circles, theo. (fcc): magenta squares).

B. Seebeck coefficient

Turning now to the thermoelectric properties of bcc Fe_xCo_{1-x} alloys, that are expressed by the Seebeck coefficient S. It relates the electrical response to a temperature gradient, the Nernst conductivity or Peltier coefficient (tensor) $\underline{\boldsymbol{\alpha}} = -\frac{1}{T}\underline{\boldsymbol{L}}^{cq}$ in terms of the charge-heat response given by Eq. (2), to that caused by an external electric field, the conductivity (tensor) $\underline{\boldsymbol{\sigma}} = -e\underline{\boldsymbol{L}}^{cc}$ in terms of the charge-charge response in Eq. (1), as in $\underline{\boldsymbol{S}} = -\underline{\boldsymbol{\sigma}}^{-1}\underline{\boldsymbol{\alpha}}$. Fig. 4 (top) depicts the concentration dependence of the Seebeck coefficients perpendicular (S_{xx}, red symbols) and parallel (S_{zz}, blue symbols) to the magnetization along z

$$\underline{\boldsymbol{S}} = -\frac{1}{eT}(\underline{\boldsymbol{L}}^{cc})^{-1}\underline{\boldsymbol{L}}^{cq} = -\underline{\boldsymbol{\sigma}}^{-1}\underline{\boldsymbol{\alpha}} = \begin{pmatrix} S_{xx} & S_{xy} & 0 \\ -S_{xy} & S_{xx} & 0 \\ 0 & 0 & S_{zz} \end{pmatrix}$$
$$= -\begin{pmatrix} \frac{\sigma_{xx}\alpha_{xx}+\sigma_{xy}\alpha_{xy}}{\sigma_{xx}^2+\sigma_{xy}^2} & \frac{\sigma_{xx}\alpha_{xy}-\sigma_{xy}\alpha_{xx}}{\sigma_{xx}^2+\sigma_{xy}^2} & 0 \\ -\frac{\sigma_{xx}\alpha_{xy}-\sigma_{xy}\alpha_{xx}}{\sigma_{xx}^2+\sigma_{xy}^2} & \frac{\sigma_{xx}\alpha_{xx}+\sigma_{xy}\alpha_{xy}}{\sigma_{xx}^2+\sigma_{xy}^2} & 0 \\ 0 & 0 & \frac{\alpha_{zz}}{\sigma_{zz}} \end{pmatrix} \quad (5)$$

as a function of Fe content x in the bcc alloys Fe_xCo_{1-x}.[40] These as well as the isotropic values $S_{\rm iso} = \frac{2}{3}S_{xx} + \frac{1}{3}S_{zz}$ are given for the athermal limit ("classical" Mott formula or generalized Mott for $T \to 0$)[33]. The anisotropy of the Seebeck coefficient is apparently rather small and S_{xx} as well as S_{zz}, and therefore $S_{\rm iso}$, show a very similar concentration dependence. Starting from the Co-rich side S has a very small and positive value of $\sim 10^{-4}\,a\mu V/K$. In fact S_{xx} is perpendicular to the magnetization is negative while the parallel S_{zz} is slightly larger and positive, making their sum (incl. VC) therefore very close to zero. Increasing the Fe content there is a sign change at around $x = 0.35$, at first sight consistent with the different sign of S in bulk bcc Fe and hcp Co[2,41]. This will be discussed in Sec. III E and IV. In the middle of the concentration range the absolute values slowly increase until at $x \approx 0.75$ a sharp peak sets on with an extremal value of almost $-0.2\ \mu V/$K at $x = 0.8$. Increasing the Fe content further S drops again fast in magnitude, staying negative over the remainder of the investigated concentration range. For all concentrations Over the whole range the importance of the vertex corrections is, as already observed for the residual resistivities, rather small.

Upon increasing the temperature, the isotropic Seebeck coefficient increases quite significantly, as visible in the lower panel of Fig. 4, where calculated (full circles) and measured values (squares) are shown for 50 K (cyan: theo., blue: expt.) and 300 K (magenta: theo., red: expt.). The theoretical values are in quite good qualitative and quantitative agreement with the experimental data for the lower temperature, except for the features at $x = 0.7$. For the higher temperature the theoretical values still show a sign change at around 0.35, then follow the almost linear trend of the experimental results up to 0.7, but with considerably smaller absolute values. The steep decrease at x around 0.7 is still visible in the calculated but not in the measured Seebeck coefficient. It appears that an enhancement of the purely diffusive Seebeck values due to temperature-related effects not accounted for in the calculations is taking place, and that the peculiar behavior around $x = 0.7$ is again most likely related to band structure effects that are unstable against additional thermally-induced disorder.

Fig. 5 (top) shows the temperature dependence of $S_{\rm iso}$ for alloys Fe_xCo_{1-x} with $x = 0.2 - 0.8$ calculated from the generalized Mott formula, Eqs. (5,1,2), accounting only for the electronic temperature. As observed before, alloys with Fe contents < 0.3 have positive Seebeck coef-

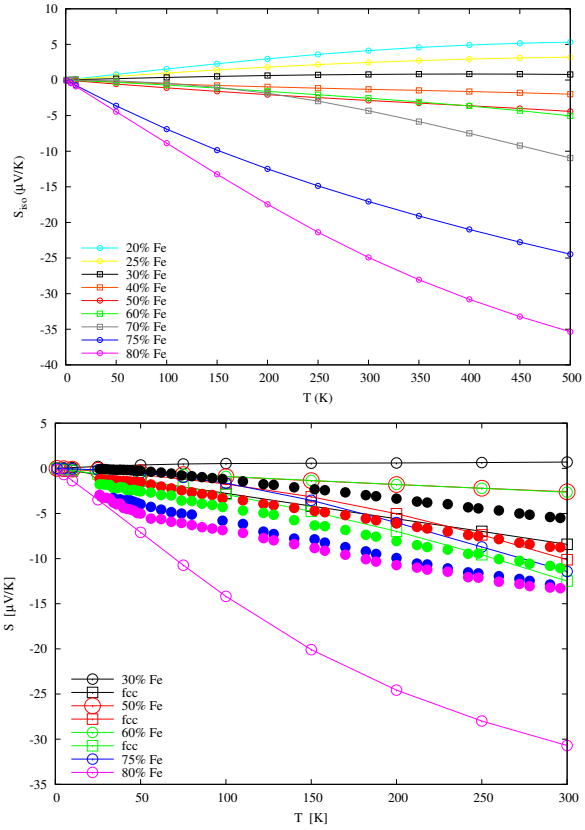

FIG. 5. Top: Calculated temperature dependence of $S_{\rm iso}$ for bcc alloys with iron content $x = 0.2$ to 0.8. Only the electronic temperature is accounted for (see text). Bottom: Comparison to experimental $S(T)$ curves for $x = 0.3$, 0.5, 0.64, 0.78, and 0.8. In addition to theoretical results for the bcc structure also such for fcc

ficients, which are increasing throughout the whole temperature range considered here. In contrast the alloys with $x > 0.3$ have monotonously decreasing negative values. For all alloys there are more or less pronounced deviations from the classical Mott formula (Sommerfeld approximation), particularly obvious at higher temperatures, which leads in some cases ($x = 0.5, 0.6$, and 0.7) to intersections of the curves. The two alloys $Fe_{0.75}Co_{0.25}$ and $Fe_{0.8}Co_{0.2}$ show considerably larger values of S than the rest, especially the difference between $x = 0.7$ and 0.75 is striking. The bottom panel shows the experimentally observed temperature dependence of alloys containing $x = 0.3, 0.5, 0.64, 0.78$, and 0.8 in comparison to calculated $S(T)$ curves for bcc as well as fcc alloys. For the latter the same volume per atom as in the former has been assumed.

All measured Seebeck coefficients are negative, including those of the alloy with $x = 0.3$, and they all show a rather linear T-dependence at higher but some deviations from linearity at lower temperatures. No unsystematic temperature- or concentration dependence as in the theoretical results for bcc structures can be observed. As noted above, the absolute values are larger in experiment, except for the two alloys $Fe_{0.75}Co_{0.25}$ and $Fe_{0.8}Co_{0.2}$ at $T \geq 50\,\mathrm{K}$. For low to intermediate Fe concentrations where fcc precipitations are likely[1], these could in part explain discrepancies between experiment and theory, as they lead to a sign change for $x = 0.3$ as well as to an increase in magnitude. Including the effect of finite temperatures via the alloy-analogy model for thermally-induced lattice vibrations and spin fluctuations leads to an appreciable improvement of the agreement with experiment as discussed in Ref. 1 In particular the magnitude of S at higher temperature is reduced for alloys with large Fe content while for low concentration a complete sign change can be observed.

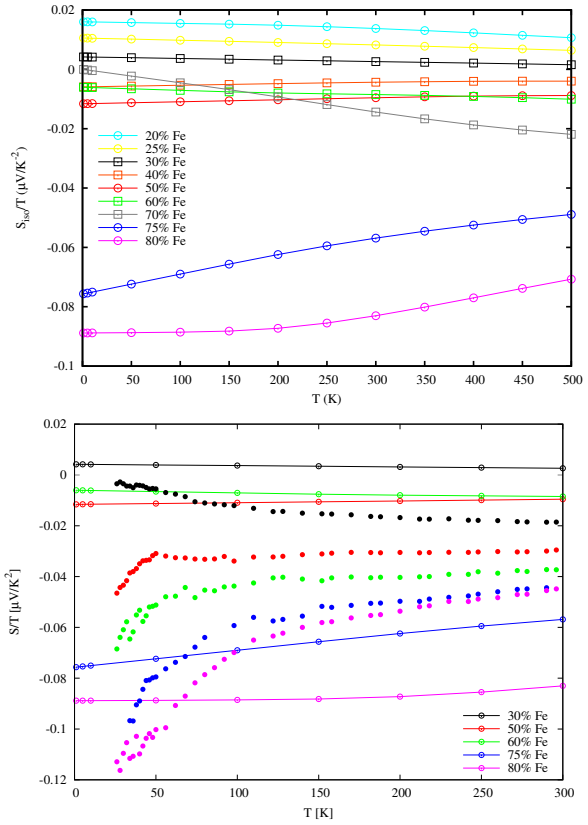

FIG. 6. Top: Ratio of $S_{\rm iso}$ and temperature T as a function of T for alloys from $x = 0.2$ to 0.8, as before $T = T_{\rm el}$. Bottom: Comparison to the experimental S/T ratio for 30, 50, 64, 78, and 80 % Fe content.

To illustrate the deviation from the classical Mott formula more clearly, in Fig. 6 the ratio of isotropic Seebeck coefficient $S_{\rm iso}$ and temperature T is given as a function of the latter. The calculated values for concentrations $\leq 60\,\%$ Fe (top) behave quite "Mott-like", i.e., they remain constant over the whole temperature range. Larger deviations are (again) visible for, in particular, $x = 0.7$ and 0.75 but also 0.8. Although only for high temperatures ($> 200\,\mathrm{K}$) in case of the latter. Quite

interestingly, the deviations for $x = 0.7$ and 0.75 have opposite signs. The experimental S/T-ratios (bottom) instead show rather pronounced non-linear behavior at low T for all concentrations. For $x = 0.78$ and 0.8 these persist the longest with increasing temperature, for the intermediate concentrations $x = 0.5$ and 0.64 already starting from $T \approx 50\,\mathrm{K}$ a linear relation is found. Interestingly, only for $x = 0.3$ one observes a positive deviation while all other alloys show larger, more negative values at low temperatures than expected from the Mott relation. Since these pronounced features at low temperature do not appear in the calculated $S(T)/T$ curves it seems probable that they are caused by vibrational and fluctuational disorder or rather electron-phonon and electron-magnon coupling of some form, that depends on a) the type and b) the extent of substitutional disorder.

C. Thermal conductivity and Wiedemann-Franz law

The electronic contribution to the thermal conductivity κ can be calculated, assuming only elastic scattering at impurities, from the energy dependence of the electrical conductivity using a generalized Mott-like formula[3,25]. In the top panel of Fig. 7 results for the temperature-dependent isotropic thermal conductivity,

$$\kappa_{\mathrm{iso}} = \frac{2}{3}\kappa_{\mathrm{xx}} + \frac{1}{3}\kappa_{\mathrm{zz}} \tag{6}$$

are shown for alloys with Fe concentrations corresponding to experiment. Here the individual terms are determined from the relations

$$\kappa_{ii} = \frac{1}{T}\left[\underline{\boldsymbol{L}}^{qq} - \frac{\underline{\boldsymbol{L}}^{cq}\underline{\boldsymbol{L}}^{qc}}{\underline{\boldsymbol{L}}^{cc}}\right]_{ii} \tag{7}$$

$$\approx \frac{1}{T}\left(L_{ii}^{qq} - \frac{(L_{ii}^{cq})^2}{L_{ii}^{cc}}\right) \tag{8}$$

with the charge-charge, charge-heat, and heat-heat current response functions of Eqs. (1-3) and exploiting the symmetry relations[42,43] $\underline{\boldsymbol{L}}^{qc} = \underline{\boldsymbol{L}}^{cq}$ and $L_{ij}^{AB} = -L_{ji}^{AB}$ as well as the observation $L_{ij}^{AB} << L_{ii}^{AB}$. In the second line of Eq. 7 the contribution from off-diagonal tensor elements is neglected, the exact form of $\underline{\boldsymbol{\kappa}}$ in systems with $4/mm'm'$ symmetry reads

$$\kappa_{xx} = \kappa_{yy} = \frac{1}{T}\left[L_{xx}^{qq} - \left(\frac{L_{xx}^{cc}((L_{xx}^{cq})^2 - (L_{xy}^{cq})^2)}{(L_{xx}^{cc})^2 + (L_{xy}^{cc})^2} + \frac{2L_{xy}^{cc}L_{xx}^{cq}L_{xy}^{cq}}{(L_{xx}^{cc})^2 + (L_{xy}^{cc})^2}\right)\right] \tag{9}$$

$$\kappa_{xy} = -\kappa_{yx} = \frac{1}{T}\left[L_{xy}^{qq} - \left(\frac{L_{xy}^{cc}((L_{xy}^{cq})^2 - (L_{xx}^{cq})^2)}{(L_{xx}^{cc})^2 + (L_{xy}^{cc})^2} + \frac{2L_{xx}^{cc}L_{xy}^{cq}L_{xx}^{cq}}{(L_{xx}^{cc})^2 + (L_{xy}^{cc})^2}\right)\right] \tag{10}$$

$$\kappa_{zz} = \frac{1}{T}\left[L_{zz}^{qq} - \frac{(L_{zz}^{cq})^2}{L_{zz}^{cc}}\right], \tag{11}$$

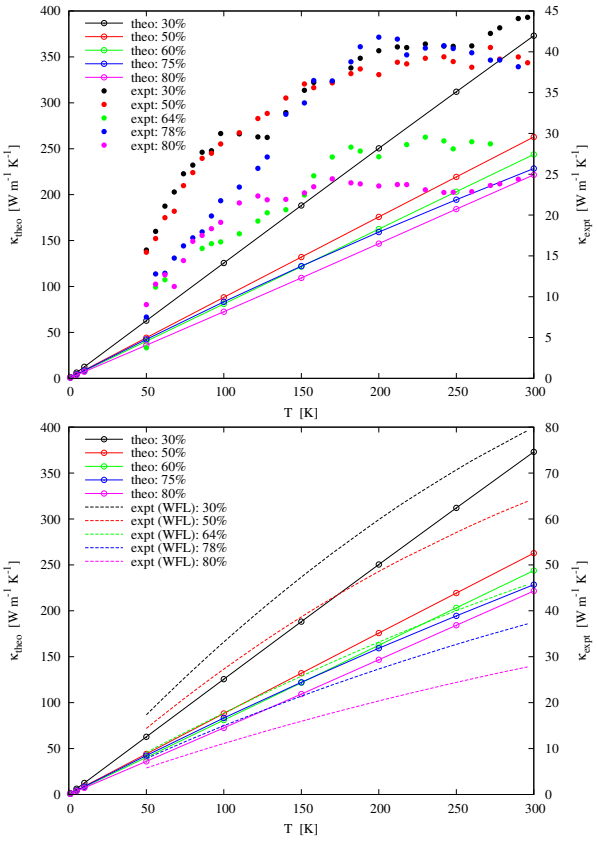

FIG. 7. Top: T_{el}-dependence of the calculated isotropic thermal conductivity κ_{iso} for $\mathrm{Fe}_x\mathrm{Co}_{1-x}$ alloys with $x = 0.3$, 0.5, 0.6, 0.75, and 0.8 (open circles, left axis), compared to experimental results (full circles, right axis). Bottom: Comparison to experimental results for $\kappa(T)$ calculated from the temperature-dependent resistivities via the Wiedemann-Franz law (see text).

leading to negligibly small corrections in case of conductive metals (see also discussion below). As seen in Fig. (7) the temperature dependence is fairly linear and, with increasing Fe content the curves fall almost on top of each other. The experimentally obtained results for $\kappa(T)$ are given for the concentrations as before by full circles. The correspondingly colored dashed lines are obtained from the temperature dependence of the measured resistivities using the Wiedemann-Franz law, i.e., via $\kappa(T) = \frac{1}{\rho(T)}L_0T$ using the free-electron-gas value of the Lorenz number $L_0 = \frac{\pi^2}{3}(\frac{k_B}{e})^2$. Obviously, the Wiedemann-Franz law is quite significantly violated for all alloys at higher temperatures ($> 100\,\mathrm{K}$). The qualitative and, for $x = 0.3$, 0.5, and 0.64 also quantitative agreement at low T (50–100 K) hints to the fact that the thermal conductivity is dominated by the electronic contribution and that its temperature dependence is dominated by the energy dependence of impurity scattering at low temperatures. For high temperatures κ appears to be strongly reduced by lattice distortions and

spin fluctuations as additional sources of disorder. Note that it is at first sight rather puzzling that, while the temperature dependence of the Seebeck coefficient was more "Mott-like" at higher T, the thermal conductivity κ behaves instead more "Wiedemann-Franz-like" at low T. This seems to be due to the different power n of energy terms $(E - E_{\rm F})^n$ entering the respective generalized Mott expressions (see Eqs.(2) and (3). The coefficients L_{ij}^{cq} and L_{ij}^{qc} are linear in $(E - E_F)$, therefore probe the asymmetry of $\sigma_{ij}(E)$ in the vicinity of E_F, while L_{ij}^{qq}, the (usually) dominant contribution to κ_{ij}, is quadratic in the energy $(E - E_F)^2$ and therefore related to the variance of $\sigma_{ij}(E)$. As can be seen from the above equations, in fact κ contains contributions from L_{ij}^{cq} and L_{ij}^{qc} as well, which are however of minor importance in conductive metals where these terms are a) small, b) appear as a product, and c) are weighted by a large L_{ij}^{cc} (essentially the conductivity). Comparing the magnitude of theoretical and experimental values for the thermal conductivity, the overestimation (roughly by a factor of five) of the calculated results can again most certainly be attributed to an underestimation of scattering due to disorder (see Fig. 2 and corresponding discussion). Inclusion of thermal lattice vibrations and spin fluctuations leads to a far better agreement with experiment concerning magnitude as well as temperature dependence.[1]

Fig. 8 shows the calculated (top) and experimental (bottom) values of the Lorenz function in dependence of the electronic temperature. For the theoretical results of the isotropic values

$$L_{\rm iso} = \frac{2}{3}L_{\rm xx} + \frac{1}{3}L_{\rm zz} \tag{12}$$

the relations

$$L_{ii} = \frac{1}{T^2}\left[\frac{\underline{\boldsymbol{L}}^{cc}\underline{\boldsymbol{L}}^{qq} - \underline{\boldsymbol{L}}^{cq}\underline{\boldsymbol{L}}^{qc}}{(\underline{\boldsymbol{L}}^{cc})^2}\right]_{ii} \tag{13}$$

$$\approx \frac{1}{T^2}\left(\frac{L_{ii}^{cc}L_{ii}^{qq} - (L_{ii}^{cq})^2}{(L_{ii}^{cc})^2}\right), \tag{14}$$

have been applied. In the last step again the same assumptions as for the thermal conductivity have been used. The exact expressions for the non-zero elements of the Lorenz function tensor,

$$\begin{aligned} L_{xx} = L_{yy} = {} & \tfrac{1}{T^2}\left[\tfrac{-2(2L_{xx}^{cq}L_{xy}^{cq} - L_{xy}^{cc}L_{xx}^{qq} - L_{xx}^{cc}L_{xy}^{qq})L_{xx}^{cc}L_{xy}^{cc}}{(L_{xx}^{cc})^4 + 2(L_{xx}^{cc})^2(L_{xy}^{cc})^2 + (L_{xy}^{cc})^4}\right. \\ & \left. - \tfrac{((L_{xx}^{cc})^2 - (L_{xy}^{cc})^2)((L_{xx}^{cq})^2 - (L_{xy}^{cq})^2 - L_{xx}^{cc}L_{xx}^{qq} + L_{xy}^{cc}L_{xy}^{qq})}{(L_{xx}^{cc})^4 + 2(L_{xx}^{cc})^2(L_{xy}^{cc})^2 + (L_{xy}^{cc})^4}\right] \end{aligned} \tag{15}$$

$$\begin{aligned} L_{xy} = -L_{yx} = {} & \tfrac{1}{T^2}\left[\tfrac{-2((L_{xx}^{cq})^2 - (L_{xy}^{cq})^2 - L_{xx}^{cc}L_{xx}^{qq} + L_{xy}^{cc}L_{xy}^{qq})L_{xx}^{cc}L_{xy}^{cc}}{(L_{xx}^{cc})^4 + 2(L_{xx}^{cc})^2(L_{xy}^{cc})^2 + (L_{xy}^{cc})^4}\right. \\ & \left. + \tfrac{((L_{xx}^{cc})^2 - (L_{xy}^{cc})^2)(2L_{xx}^{cq}L_{xy}^{cq} - L_{xy}^{cc}L_{xx}^{qq} - L_{xx}^{cc}L_{xy}^{qq})}{(L_{xx}^{cc})^4 + 2(L_{xx}^{cc})^2(L_{xy}^{cc})^2 + (L_{xy}^{cc})^4}\right] \end{aligned} \tag{16}$$

$$L_{zz} = \tfrac{1}{T^2}\left[L_{zz}^{qq} - \tfrac{(L_{zz}^{cq})^2}{L_{zz}^{cc}}\right], \tag{17}$$

however lead again to only negligibly small numerical differences compared to the approximate values. The theoretical values are, apart from the special cases already mentioned ($Fe_{0.70}Co_{0.30}$ and $Fe_{0.75}Co_{0.25}$), rather close to the hypothetical value L_0 (thin black line). Although at higher temperatures deviations occur for all alloys. Note, that all alloys converge more or less exactly to a single value for $T \to 0$, which differs slightly from the ideal value L_0. The experimentally obtained Lorenz functions are given in the lower panel. It is immediately obvious that deviations from the Wiedemann-Franz law are much more pronounced here for all alloys. Interestingly for the alloys with $x = 0.3$, 0.5, and 0.64 this applies to high temperatures whereas for $x = 0.78$ and 0.8 agreement at low T is worse. Going beyond the simplified treatment of temperature via the Fermi distribution of the electrons alone, that is, including again the effect of lattice displacements and spin fluctuations, leads, as expected from a WFL-conform description by Mott-like expressions, only to minor modifications of L (not shown). These are most prominent yet again for high (low) Fe (Co) content.

D. Transverse transport

All response tensors considered here, electric, thermoelectric, and thermal, share the same well-known shape[42,43]

$$\underline{\boldsymbol{\chi}} = \begin{pmatrix} \chi_{xx} & \chi_{xy} & 0 \\ -\chi_{xy} & \chi_{xx} & 0 \\ 0 & 0 & \chi_{zz} \end{pmatrix} \tag{18}$$

for a cubic ferromagnet with magnetization along the z axis. The anisotropy of the resistivity has been considered already above (Fig. 1), while the anisotropy of the Seebeck coefficient is visible in the top panel of Fig. 4 (not discussed). Furthermore the electronic part of the

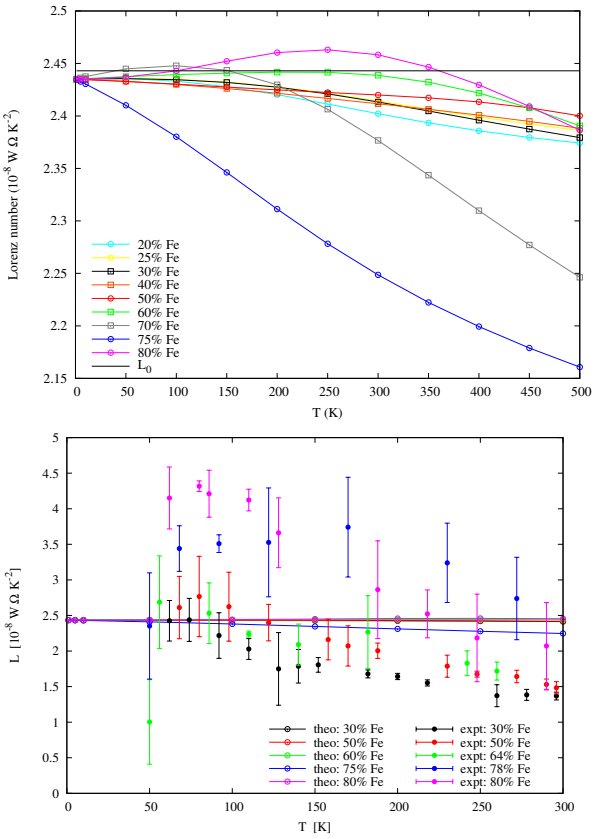

FIG. 8. Top: Temperature ($T_{\rm el}$) dependence of the isotropic Lorenz function $L_{\rm iso} = \frac{\kappa_{\rm iso}}{\sigma_{\rm iso} T}$, neglecting off-diagonal contributions (see text). The thin horizontal line marks the free-electron-gas value of $L_0 = \frac{\pi^2}{3}(\frac{k_B}{e})^2$. Bottom: Comparison to experimental results for $L(T)$ in alloys with Fe content of $x = 0.3$, 0.5, 0.64, 0.78, and 0.80 (full circles with error bars).

thermal conductivity also depends on the relative orientation of the magnetization (not shown). Results for the antisymmetric part of the three response tensors are shown in Fig. 9. In the top panel the residual anomalous Hall conductivity (AHC) σ_{yx} (open black squares, axis to the right) is plotted as a function of Fe concentration. It exhibits a pronounced concentration dependence, decreasing with increasing Fe content until a minimum at $x = 0.7$ and steeply rising again to a local maximum at 0.8, then decreasing once more. The anomalous Hall angle $\theta_{AH} = \sigma_{yx}/\sigma_{xx}$ in red shows an even more pronounced variation with concentration due to the additional structure of the longitudinal conductivity σ_{xx}, in particular around $x = 0.75$. This leads to a maximum of θ_{AH} for $x = 0.8$ of ∼0.0025 or 0.25 %.

In the central panel of Fig. 9 results for the thermoelectric analogue to the anomalous Hall conductivity, the anomalous Nernst conductivity (ANC) α_{yx} are given as a function of (electronic) temperature. The ANC is the antisymmetric off-diagonal element of the Nernst conductivity or Peltier tensor $\underline{\boldsymbol{\alpha}}$, usually defined

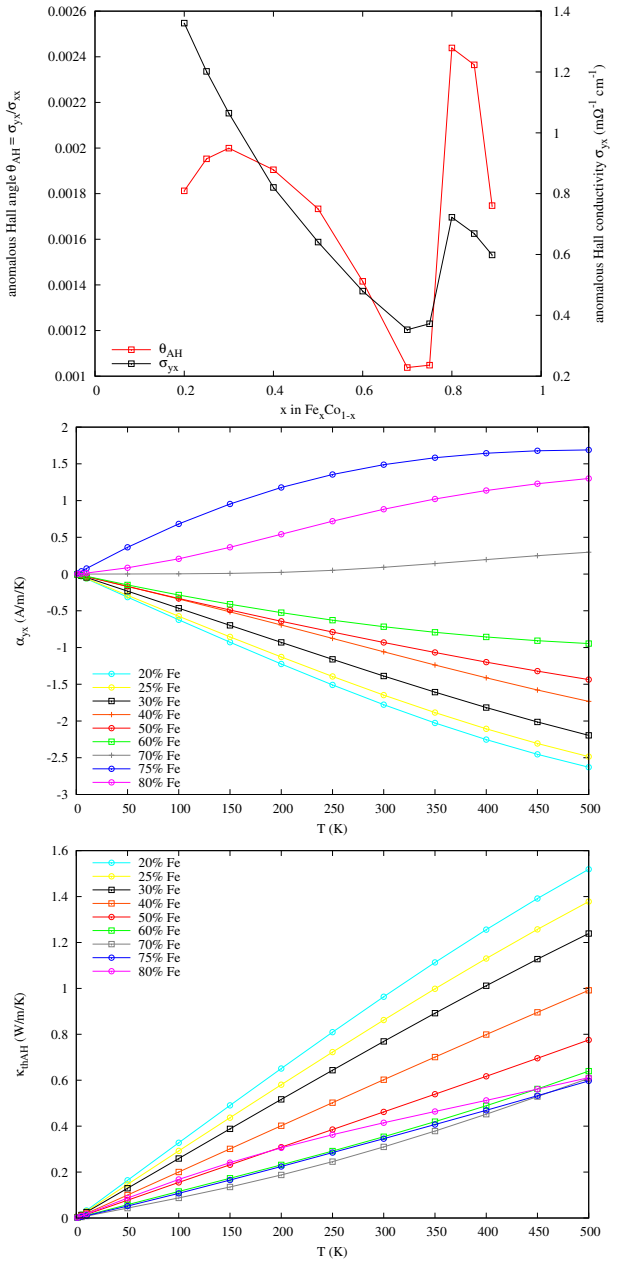

FIG. 9. Top: Anomalous Hall angle $\theta_{AH} = \sigma_{yx}/\sigma_{xx}$ (red open squares, left y axis) and anomalous Hall conductivity σ_{yx} (black open squares, right y axis) as a function of Fe content. Results were obtained in the athermal limit ($T = 0\,$K). Middle: $T_{\rm el}$-dependence of the anomalous Nernst conductivity α_{yx} for alloys with x between 0.2 and 0.8. Bottom: $T_{\rm el}$-dependence of the transverse antisymmetric thermal conductivity $\kappa_{yx} = -\kappa_{xy} = \kappa_{thAH}$ related to the anomalous thermal Hall or Righi-Leduc effect.

via $\underline{\boldsymbol{S}} = -\underline{\boldsymbol{\sigma}}^{-1}\underline{\boldsymbol{\alpha}}$. These data suggest that there should be a sign change observable depending on the Fe concentration x at ∼0.7, even more pronounced at high temperatures. Assuming that phonon- or magnon contributions

to the anomalous Nernst conductivity will most likely be suppressed at elevated temperatures, this should in principle be accessible experimentally.

Finally, the temperature dependence of the off-diagonal antisymmetric element of the electronic thermal conductivity tensor $\underline{\boldsymbol{\kappa}}$ connected to the (electronic contribution to the) thermal Hall or Righi-Leduc effect is shown in the bottom panel of Fig. 9. Again only the approximated values according to Eq. (6) are shown, but as for the isotropic value the influence of the additional contributions in Eq. (9) have been confirmed to be marginal. All alloys show the same sign and a similar, linear temperature dependence of κ_{yx}, in fact very much resembling that of the isotropic value κ_{iso} in Fig. 7. The absolute values are decreasing with increasing Fe content. Slight deviations from this behavior are once more found for $x = 0.75$ and 0.8, in the latter case already at low temperatures. Again this quantity should be measurable in concentrated alloys at elevated temperatures (to distinguish from phonon- and magnon-related effects), although the absolute values are more than two orders of magnitude smaller than the isotropic values.

All three transverse antisymmetric transport properties certainly are affected by scattering at phonons and magnons. This has been again investigated employing the alloy analogy model to account for the elastic contributions. As can be seen in Figure 10 (top) for the anomalous Hall conductivity σ_{yx} finite temperature induced disorder leads to a significant reduction. The rate of decrease with temperature appears to be proportional to the residual value, it amounts to more than 50 % for 70 % Co content, about 30-40 % for 20 and 50 % Co and ∼25 % for 22 and 36 % Co. The lattice vibrations are again the dominating effect, for low Co content at high temperature the spin fluctuations however are appreciable as well. The anomalous Nernst conductivity α_{yx} in the middle panel behaves rather similar concerning the impact of thermal effects. For all concentrations but 20 % Co these lead to a decrease of the AHC as compared to the results for T_{el}. The sign remains unaffected in the temperature range considered, for higher Co contents at $T > 300$ K a sign change might take place. The thermal Hall effect in the bottom panel of Fig. 10 shows again a pronounced decrease when considering lattice vibrations and spin fluctuations, the temperature dependence is modified as well, suggesting a saturation at $T > 300$ K. In fact this is very much alike the observations made for the longitudinal thermal conductivity in Ref. 1.

In all three cases it might be necessary to go beyond the presently employed Kubo-Středa formula to properly account for the contribution of Fermi sea terms to the intrinsic conductivities by means of the Kubo-Bastin formalism.[23] This is far beyond the scope of the present and therefore left for future work.

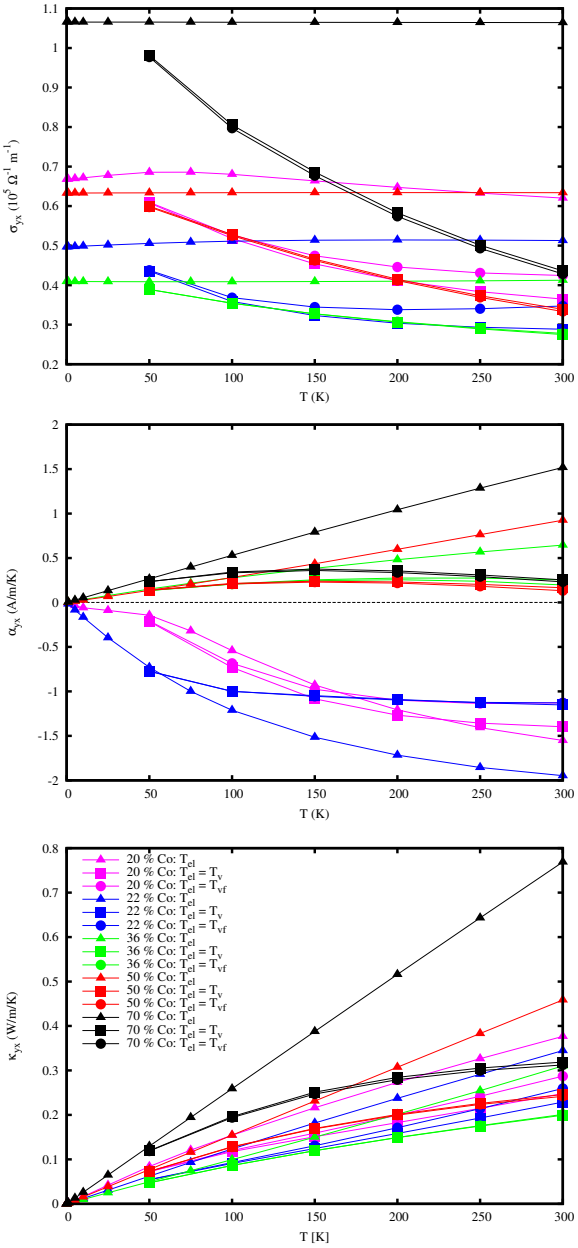

FIG. 10. Anomalous Hall conductivity σ_{yx} (top), anomalous Nernst conductivity α_{yx} (center), and transverse antisymmetric thermal conductivity κ_{yx} (bottom) as functions of temperature for alloys with $x = 0.3$, 0.5, 0.64, 0.78, and 0.8. Results accounting for the electronic temperature alone (T_{el}), including the effect of thermally-induced lattice vibrations $T_{\mathrm{el}} = T_{\mathrm{v}}$ as well as in addition spin fluctuations $T_{\mathrm{el}} = T_{\mathrm{vf}}$ are shown.

E. Results for pure hcp Co and bcc Fe

So far only concentrated $\mathrm{Fe}_x\mathrm{Co}_{1-x}$ alloys have been considered but it is of course a natural question if their properties are continuously varying between the pure limits of cobalt and iron. A recent study by Watzmann *et*

al.[2] was dealing with the electric, thermoelectric, and thermal transport properties of Fe, Co, and Ni, focusing on the magnon-drag contribution to the thermopower. In order to suppress the effect of phonons porous and/or polycrystalline samples have been chosen. Comparison with single crystalline samples revealed, by absence of a characteristic phonon-drag peak at low temperature, that the mean-free path of the phonons could be sufficiently reduced this way.

Figure 11 shows a comparison of first-principles results for the Seebeck coefficient with experimental data from Ref. 2. As can be seen in the top panel for hcp Co the agreement with experiment for all theoretical results is acceptable concerning the temperature dependence while the absolute values are almost one order of magnitude too low. The results in black include only the effect of an electronic temperature T_{el}, the underlying conductivities were calculated in the athermal limit by adding a small imaginary part to the energy. This corresponds to a constant relaxation time that enters nominator and denominator of the generalized Mott formula and drops out, the two curves for $\mathrm{Im}(E) = 10^{-3}$ and 10^{-4} accordingly fall on top of each other. Inclusion of lattice vibrations (T_v, red symbols) and in addition spin fluctuations (T_{vf}, blue symbols) further reduces the absolute value of S but does not lead to a major modification of the variation with T.

For bcc Fe in the central panel the situation is significantly different: Already the results for T_{el} deviate strongly from experiment, inclusion of non-electronic thermal effects even changes the sign of S. Under the assumption that the main difference between theoretical and experimental results for the polycrystalline sample is the inelastic electron-magnon scattering contribution, this suggests that is significant not only for the magnitude but also for the sign of S.

The bottom panel of Fig. 11 shows the energy-dependent conductivities of bcc Fe and hcp Co, calculated in the limit $T \to 0$. From these curves one can immediately read of the difference in sign of the thermopower for $T = T_{el}$ in hcp Co and bcc Fe.

The electronic contribution to the thermal conductivity κ was calculated under the same conditions as described above for the thermopower. The corresponding results for κ are shown in Fig. 12. It should be noted that the above-mentioned *relaxation time approximation* does not hold here, as κ contains contributions of unbalanced fractions of L coefficients (see Eq. (6)). The by far dominating one is of course from the $\underline{\boldsymbol{L}}^{qq}$ tensor. For Co shown in the top panel the results for smaller imaginary part and $T = T_{el}$ quite nicely reproduce the low temperature behavior of the experiment on the ingot while for larger imaginary part match those of the porous sample. In both cases however already below 50 K the deviations become significant. Upon inclusion of thermal effects the calculations agree quite well with the high temperature data for the ingot. For bcc Fe quite similar observations can be made, although here both samples behave much more alike.

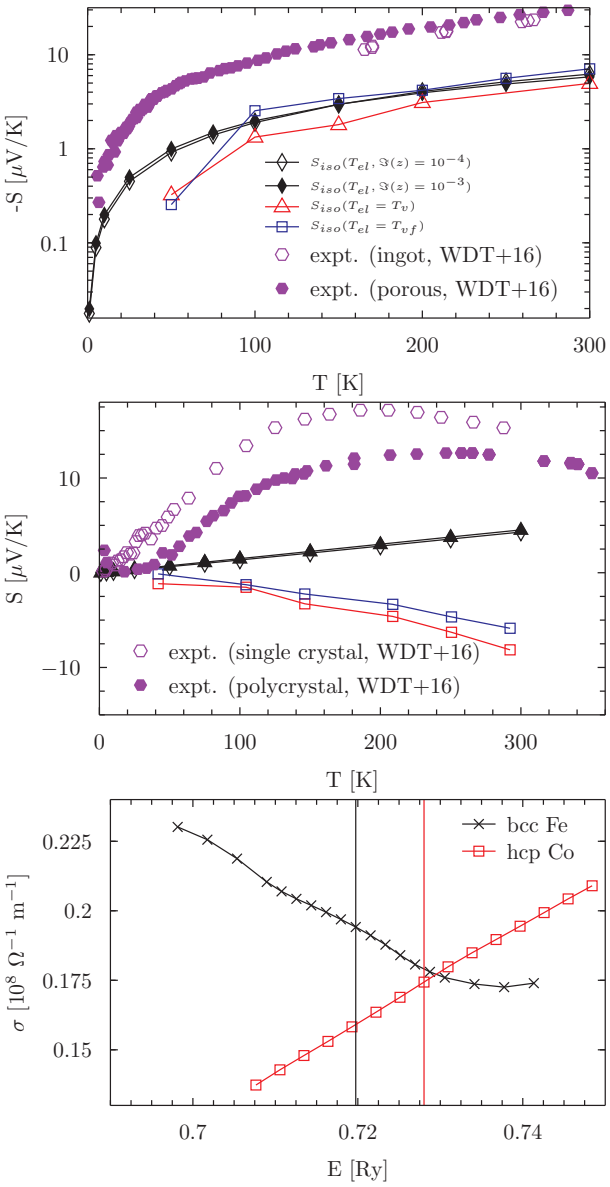

FIG. 11. Top: Temperature dependence of the Seebeck coefficient in hcp Co accounting for electronic temperature, T_{el}, only (black open diamonds: for $\eta = 10^{-4}$ Ry, black full diamonds: for $\eta = 10^{-3}$ Ry), including in addition the effect of thermal lattice vibrations, $T_{el} = T_v$ (red triangles), and including furthermore temperature-induced spin fluctuations, $T_{el} = T_{vf}$ (blue squares). Experimental results obtained by Watzmann *et al.*[2] are given as magenta open (ingot) and full (porous sample) hexagons. Center: Corresponding results for bcc Fe. Bottom: Energy dependence of the electrical conductivity in elemental bcc Fe (black crosses) and hcp Co (red squares) calculated in the presence of an imaginary part of the complex energy of $\mathrm{Im}(z) = \mathrm{Im}(E + i\eta) = \eta = 10^{-3}$ Ry. The vertical lines mark the respective Fermi levels.

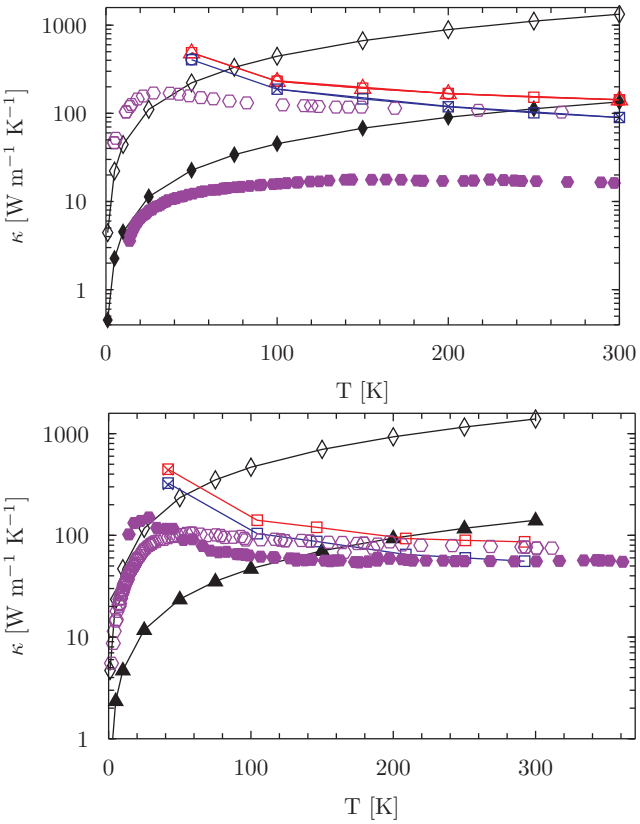

FIG. 12. Temperature dependence of the electronic contribution to the thermal conductivity in hcp Co (top) and bcc Fe (bottom) in comparison to experimental data by Watzmann *et al.*[2]. The use of colors and symbols is the same as in Fig. 11.

IV. ELECTRONIC STRUCTURE AS A FUNCTION OF IRON CONTENT

Most of the transport phenomena discussed in the previous sections show characteristic features at Fe concentrations between $x = 0.6$ and 0.85. In order to understand this behavior the spin-dependent Bloch spectral functions (BSF) of alloys containing $x = 0.3$, 0.4, 0.5, 0.6, 0.7, 0.75, 0.8, and 0.85 were calculated. Since the linear response properties are intimately connected to the band structure –although within Kubo linear response theory not as transparent as in the Boltzmann approach– and its energy dependence in case of the Mott relations, it is hoped that an at least qualitative picture of some of the concentration-dependent features in the measured and calculated properties can be deduced.

As visible from Fig. 13 the overall shape of the bands is very different in the two spin channels (majority "spin-up", left column, in red and minority "spin-down", right column, in blue) and so is the extent as well as the $\boldsymbol{k}$-space position of broadening effects on the band structure. The Fermi level sinks with growing Fe content (as Fe has one electron less than Co, see also Fig. 14 below) and at around $x = 0.80$ crosses the top of the d-like bands of the majority channel (left) at the N point of the Brillouin zone. This qualitatively explains the maximum of the resistivity in this concentration range, because the Fermi level is located in regions where the Bloch spectral function is flat and broadened. In the minority channel (right) the bands crossing the Fermi level are predominantly of sp-character having large slopes for large Fe concentrations ($x > 0.6$). At $x = 0.6$ the Fermi level cuts through the bottom of a parabolic band in-between the H and the N point. This qualitatively explains the additional resistivity peak at $x = 0.6$. The avoided crossing between the Γ and the H point could be connected to the local minimum around $x = 0.75$.

For the electronic contribution to the Seebeck coefficient the energy dependence of the band structure is crucial, as it is calculated directly from the energy-dependent conductivity. Due to the additional energy factor $(E-E_\mathrm{F})$ in the integral of Eq. (2) it is the asymmetry of $\sigma(E)$ that determines both its sign and magnitude, together with a normalization by the conductivity itself. Increasing the electronic temperature leads by means of the Fermi distribution to an increasing number of states contributing to transport and hence a larger energy range in which the asymmetry is probed. A change in concentration is most importantly reflected in the position of the Fermi level, as stated above, and accordingly it determines the relevant energy window. Moreover it leads to a change in the extent of broadening of energy bands and which bands are affected. The most obvious example for this interplay is again the region around $x = 0.8$ where not only the resistivity maximum lies but also the change in $\sigma(E)$ is most pronounced. Accordingly the Seebeck coefficient is largest here as well. The negative sign is caused by the positive slope of $\sigma(E)$ (see supplemental material of Ref. 1) leading in the Mott-limit to a positive derivative w.r.t. the energy or more generally a positive thermoelectric conductivity α. As the conductivity is positive, the minus sign leads to $S < 0$. A more detailed discussion is given in Ref. 1, in particular in the supplemental material.

An interesting point to mention here is, that although the Seebeck coefficient changes sign as a function of Fe concentration x (see Fig. 5), going from positive values at low x to negative at large x, this is in obvious contradiction to the results for elemental Co and Fe in Fig. 11 (top and center, respectively). There are several important factors underlying this behavior. Firstly, starting from bcc Fe the Fermi level lies in hole-like bands with positive curvature leading to a decrease of conductivity with energy, see Fig. 11 (bottom), causing S to be positive (Fig. 11 (center, black symbols)). For $x = 0.85$ at the bottom of Fig. 13 the Fermi energy is, as previously discussed, situated in a flat d-like band. As discussed in detail in Ref. 1 there is a sharp step-like increase in con-

13

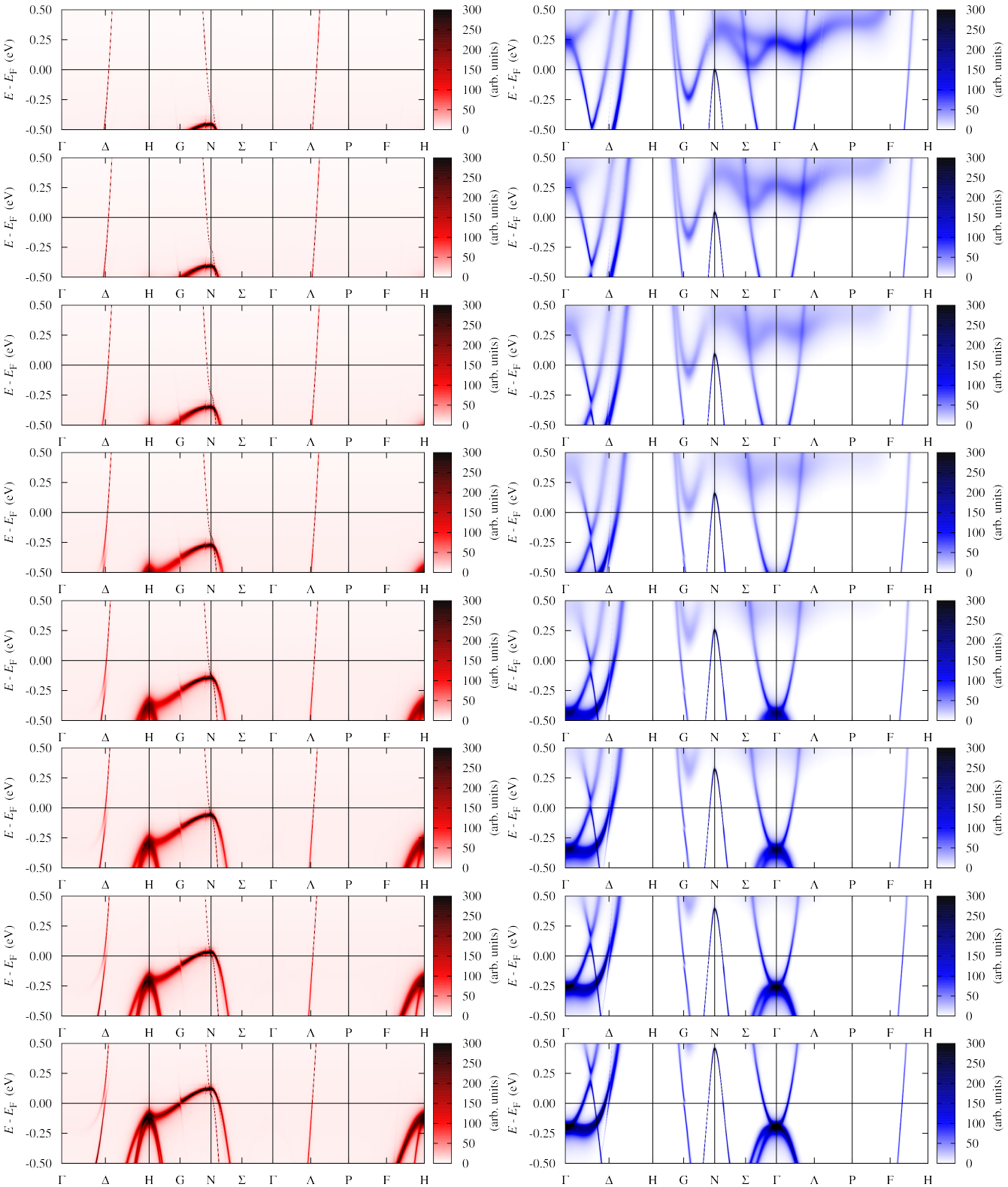

FIG. 13. Band structure (Bloch spectral function, BSF) of bcc Fe_xCo_{1-x} for, from top to bottom, $x = 0.3$, 0.4, 0.5, 0.6, 0.7, 0.75, 0.8, and 0.85 for majority spin up (left) and minority spin down (right).

ductivity when going from closely below the Fermi level to energies slightly above. This leads to the large and negative Seebeck coefficient for high Fe content. Upon increasing the Co concentration, that is going from bottom to top in Fig. 13, as already mentioned the Fermi level shifts upwards due to the increasing number of electrons, away from the step in $\sigma(E)$. This leads to a reduction of $|S|$. At the same time the importance of minority spin carriers increases whose bands become increasingly broadened (see right column of Fig. 13). There is a competition between increasing slope of the bands towards higher energies for both spin channels and the Fermi level approaching a flat and broadened d-like band in the minority spin channel, leading to a modest decrease of conductivity with energy and in turn to a small positive Seebeck coefficient for $x < 0.3$. Finally for pure hcp Co the Fermi level lies in regions of bands with predominantly positive curvature, resulting in a positive slope of $\sigma(E)$ (Fig. 11 bottom) and accordingly a negative Seebeck coefficient (Fig. 11 top, black symbols).

The transverse transport properties anomalous Hall conductivity, anomalous Nernst conductivity, and anomalous (electronic) thermal Hall conductivity or anomalous Righi-Leduc coefficient and their concentration dependence certainly also are determined by subtle features of the band structure. Due to the more complex nature of the mechanisms behind them (intrinsic, side-jump and skew scattering contributions) one in addition has to take the decisive role of spin-orbit coupling into account, as it is done here by using a fully relativistic approach. This makes a direct comparison of Bloch spectral function and transverse transport properties next to impossible.

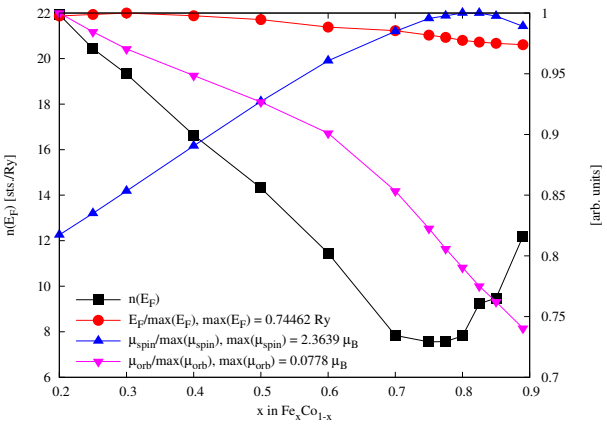

FIG. 14. Density of states at the Fermi level $n(E_\mathrm{F})$ (full black squares, left y axis), and normalized Fermi level E_F, spin- and orbital magnetic moments, μ_{spin} and μ_{orb}, (full red circles, full blue triangles, and full magenta up-side-down triangles; all right y axis) as a function of Fe content.

As visible in Fig. 14, the density of states at the Fermi level decreases upon increasing the Fe content until a minimum at $x = 0.75$ is reached, from which on $n(E_\mathrm{F})$ increases again. The Fermi level itself decreases from a flat maximum at $x = 0.3$ onwards. As it has been argued by Ebert *et al.*[44] for the composition dependence of the Gilbert damping parameter α in bcc $\mathrm{Fe}_x\mathrm{Co}_{1-x}$,[45] the resistivity seems to be dominated by the electronic structure at the Fermi level. To a fair extent this seems to apply even directly to the density of states, as one would in fact expect from a simple Drude picture of the resistivity. Guessing from the magnitude of the spin-magnetic moment as a function of concentration, the effect of spin fluctuations might be more pronounced at higher Fe concentrations.

V. CONCLUSIONS

To summarize, we have presented first-principles linear response calculations of the galvanomagnetic, thermogalvanomagnetic, and thermal transport properties of bulk bcc $\mathrm{Fe}_x\mathrm{Co}_{1-x}$ alloys. The current study is an extension to a joint experimental and theoretical investigation on *Magnon scattering in the transport coefficients of CoFe alloys* by Srichandan *et al.*.[1] Residual resistivity and anisotropic magnetoresistance were found in fair accordance with experimental low-temperature data. The temperature dependence of the isotropic resistivity was found to depend significantly on the treatment of non-electronic thermal effects such as lattice vibrations and spin fluctuations. In comparison to experiment a considerable amount of structural disorder prevented quantitative agreement. The electronic contribution to the Seebeck coefficient could be shown to compare reasonably well with experimental data already on the level of the generalized Mott formula treating temperature only via a modified Fermi-Dirac distribution function. In particular the concentration dependence found in experiment could be reproduced. Even without considering inelastic scattering on phonons and magnons a deviation from the classical Mott behavior was observed and could be traced back to pronounced changes of the band structure around the Fermi level. The thermal conductivity accordingly does deviate from the Wiedemann-Franz law as well, in case of high Fe content even the Lorenz function shows a considerable variation with temperature. The antisymmetric transport properties anomalous Hall and Nernst effect were found to exhibit a strong concentration dependence with distinct features again at high Fe content around $x = 0.7 - 0.8$. For the AHE a minimum is found in this regime whereas the ANE even changes sign. The electronic contribution to the thermal Hall effect as a function of temperature behaves in contrast very similar to the isotropic thermal conductivity, its absolute values are however much lower. Finally a direct comparison to experimental data on the Seebeck coefficient and the thermal conductivity in elemental bcc Fe and hcp Co obtained by Watzmann *et al.*[2] was made,

supporting the suggested relevance of inelastic scattering process on magnitude and even sign of the Seebeck coefficient. The thermal conductivity was found to be in reasonable quantitative agreement at elevated temperatures employing the alloy analogy model for the description of elastic scattering on lattice vibrations and spin fluctuations.

Future work is planned to achieve a more realistic treatment of structural disorder and sample geometry and to extend the investigations to explicitly spin-dependent spintronic and spincaloritronic transport phenomena such as spin Hall and spin Nernst effect as well as the spin-dependent Seebeck effect.

* sebastian.wimmer@cup.uni-muenchen.de

[1] S. Srichandan, S. Wimmer, M. Kronseder, H. Ebert, C. H. Back, and C. Strunk, ArXiv e-prints (2018), arXiv:1802.01038 [cond-mat.mes-hall].

[2] S. J. Watzman, R. A. Duine, Y. Tserkovnyak, S. R. Boona, H. Jin, A. Prakash, Y. Zheng, and J. P. Heremans, Phys. Rev. B **94**, 144407 (2016).

[3] M. Jonson and G. D. Mahan, Phys. Rev. B **21**, 4223 (1980).

[4] H. Ebert, D. Ködderitzsch, and J. Minár, Rep. Prog. Phys. **74**, 096501 (2011).

[5] H. Ebert, J. Braun, D. Ködderitzsch, and S. Mankovsky, Phys. Rev. B **93**, 075145 (2016).

[6] *The Munich SPR-KKR package*, H. Ebert *et al.* `http://olymp.cup.uni-muenchen.de/ak/ebert/SPRKKR`.

[7] P. Soven, Phys. Rev. **156**, 809 (1967).

[8] B. Velický, Phys. Rev. **184**, 614 (1969).

[9] B. Predel, "Landolt-Börnstein - Group IV Physical Chemistry," (Springer Berlin Heidelberg, Berlin, Heidelberg, 1993) Chap. Co-Fe (Cobalt-Iron), pp. 1–13.

[10] That is, not for the whole range between the pure metals as in Vegard's law.

[11] S. H. Vosko, L. Wilk, and M. Nusair, Can. J. Phys. **58**, 1200 (1980).

[12] O. K. Andersen, Phys. Rev. B **12**, 3060 (1975).

[13] R. Kubo, J. Phys. Soc. Japan **12**, 570 (1957).

[14] D. A. Greenwood, Proc. Phys. Soc. **71**, 585 (1958).

[15] L. Smrčka and P. Středa, J. Phys. C: Solid State Phys. **10**, 2153 (1977).

[16] W. H. Butler, Phys. Rev. B **31**, 3260 (1985).

[17] J. Banhart, R. Bernstein, J. Voitländer, and P. Weinberger, Solid State Commun. **77**, 107 (1991).

[18] J. Banhart, H. Ebert, P. Weinberger, and J. Voitländer, Phys. Rev. B **50**, 2104 (1994).

[19] S. Lowitzer, D. Ködderitzsch, and H. Ebert, Phys. Rev. B **82**, 140402(R) (2010).

[20] S. Lowitzer, M. Gradhand, D. Ködderitzsch, D. V. Fedorov, I. Mertig, and H. Ebert, Phys. Rev. Lett. **106**, 056601 (2011).

[21] A. Bastin, C. Lewiner, O. Betbeder-Matibet, and P. Nozieres, J. Phys. Chem. Solids **32**, 1811 (1971).

[22] A. Crépieux and P. Bruno, Phys. Rev. B **64**, 014416 (2001).

[23] D. Ködderitzsch, K. Chadova, and H. Ebert, Phys. Rev. B **92**, 184415 (2015).

[24] G. D. Mahan, *Many-particle physics, 2nd ed.*, Physics of Solids and Liquids (Plenum Press, New York, 1993).

[25] M. Jonson and G. D. Mahan, Phys. Rev. B **42**, 9350 (1990).

[26] S. Wimmer, D. Ködderitzsch, K. Chadova, and H. Ebert, Phys. Rev. B **88**, 201108(R) (2013).

[27] S. Wimmer, D. Ködderitzsch, and H. Ebert, Phys. Rev. B **89**, 161101(R) (2014).

[28] H. Ebert, S. Mankovsky, K. Chadova, S. Polesya, J. Minár, and D. Ködderitzsch, Phys. Rev. B **91**, 165132 (2015).

[29] Y. Kakehashi and O. Hosohata, Phys. Rev. B **40**, 9080 (1989).

[30] I. Turek, private communication.

[31] P. P. Freitas and L. Berger, Phys. Rev. B **37**, 6079 (1988).

[32] P. P. Freitas, L. Berger, and J. F. Silvain, J. Appl. Phys. **61**, 4385 (1987).

[33] N. F. Mott and H. Jones, *The Theory of the Properties of Metals and Alloys* (Oxford University Press (Clarendon Press, Oxford, England), 1936).

[34] I. Turek, J. Kudrnovský, and V. Drchal, Phys. Rev. B **89**, 064405 (2014).

[35] The first aspect might be in part related to a difference in lattice constants, the second could be simply due to a less dense sampling of concentrations.

[36] I. Turek, Phys. Rev. B **93**, 245114 (2016).

[37] J. B. Staunton, S. Ostanin, S. S. A. Razee, B. L. Gyorffy, L. Szunyogh, B. Ginatempo, and E. Bruno, Phys. Rev. Lett. **93**, 257204 (2004).

[38] J. B. Staunton, L. Szunyogh, A. Buruzs, B. L. Gyorffy, S. Ostanin, and L. Udvardi, Phys. Rev. B **74**, 144411 (2006).

[39] A. Matthiessen and C. Vogt, Philosophical Transactions of the Royal Society of London **154**, 167 (1864).

[40] Contributions from the combination of spin Nernst and inverse spin Hall effects, as discussed in Ref. 46, are neglected in this work due to their vanishingly small size.

[41] A. D. Avery, R. Sultan, D. Bassett, D. Wei, and B. L. Zink, Phys. Rev. B **83**, 100401 (2011).

[42] W. H. Kleiner, Phys. Rev. **142**, 318 (1966).

[43] M. Seemann, D. Ködderitzsch, S. Wimmer, and H. Ebert, Phys. Rev. B **92**, 155138 (2015).

[44] H. Ebert, S. Mankovsky, D. Ködderitzsch, and P. J. Kelly, Phys. Rev. Lett. **107**, 066603 (2011).

[45] On the basis that magnetic moments and spin-orbit coupling strength would not differ too much for the two elements, which seems to be reasonably well justified for the former (20 % and 25 % variation within the investigated concentration range for μ_{spin} and μ_{orb}, respectively.).

[46] S. Meyer, Y.-T. Chen, S. Wimmer, M. Althammer, T. Wimmer, R. Schlitz, S. Geprägs, H. Huebl, D. Ködderitzsch, H. Ebert, G. E. W. Bauer, R. Gross, and S. T. B. Goennenwein, Nat. Mater. **16**, 977 (2017).

3.2 Spincaloritronics

At the heart of spin caloric transport or spincaloritronics is the occurrence of spin currents due to temperature gradients, induced either macroscopically by heating and/or cooling opposite ends of a conductor or by local heating with a laser. The most promising spincalor(itron)ic effects that could be exploited in an application are the Spin Seebeck effect (SSE) mentioned in the introduction, the spin-dependent Seebeck (SDSE) and the spin Nernst effect (SNE). While the first phenomenon will not be discussed here and the second only in passing, the spin Nernst effect is the central issue of the following. As in the SSE, the SNE can be used to generate a pure spin current in a non-magnetic system.[3] From its theoretical prediction [324, 358, 359], soon followed by first-principles calculations [20], it took only a few years until its experimental verification in Pt [21] and W [360]. Both experimental results could a little later be confirmed independently [361].

In the following two publications will be presented. The first one [266] verified the predictions of the spin-projected formalism of Ref. 20 for dilute copper alloys using a spin-polarised relativistic formulation. It furthermore gave an extensive comparison of spin Hall and spin Nernst conductivities, in particular concerning their decomposition into intrinsic and extrinsic contributions, and extended the discussion to the concentrated regime in Au_xCu_{1-x} alloys. Moreover, it had two important additional aspects: First, a large spin Hall angle close to equiatomic composition was found in the calculations that later on could be indeed observed in experiment [362]. Second, ensuing discussions with D. Fedorov (MLU Halle) on spin-projected vs. spin-polarised approaches (see Section 2.3.3.1 and Appendix A.3) lead to first considerations on the mechanism underlying the so-called spin Nernst magneto-thermopower (SMT) from a first-principles perspective. Of course only the bulk contribution had been considered at that time. An erratum to Ref. 266 can be found on page 131.

The second publication, Ref. 21, was a collaborative effort between experimental and theoretical groups, with the later ones applying model as well as first-principles methods, that resulted in the first experimental observation of the spin Nernst effect. The above-mentioned SMT, derived from the nowadays established concept of the spin Hall magnetoresistance (SMR) (see Refs. 363 and 364 and references therein), was employed to measure indirectly the spin current generated by the SNE via the inverse spin Hall effect. The interpretation of the experimental results was supported by finite-temperature linear response calculations which could confirm both, relative sign and magnitude of (inverse) spin Hall effect and spin Nernst effect. Additional details on the experimental aspects can be found in Ref. 365.

[3] Other sources of such currents are, e.g., the spin Hall effect, lateral spin valves [355, 356], spin pumping [46], and the photo-spin-voltaic effect [357].

3.2.1 Published results on the spin Nernst effect in Cu alloys

The following is a copy of the article *First-principles linear response description of the spin Nernst effect* [266], reprinted (including Supplemental Material) with permission from

S. Wimmer, D. Ködderitzsch, K. Chadova, and H. Ebert, Phys. Rev. B **88**, 201108(R) (2013).

RAPID COMMUNICATIONS

PHYSICAL REVIEW B **88**, 201108(R) (2013)

First-principles linear response description of the spin Nernst effect

S. Wimmer,* D. Ködderitzsch, K. Chadova, and H. Ebert

Department Chemie/Phys. Chemie, Ludwig-Maximilians-Universität München, Butenandtstrasse 11, 81377 München, Germany

(Received 17 May 2013; published 19 November 2013)

A first-principles description of the spin Nernst effect, denoting the occurrence of a transverse spin current due to a temperature gradient, is presented. The approach, based on an extension to the Kubo-Středa equation for spin transport, supplies in particular the formal basis for investigations of diluted as well as concentrated alloys. Results for corresponding applications to the alloy system Au_xCu_{1-x} give the intrinsic and extrinsic contributions to the relevant transport coefficients. Using scaling laws allows in addition splitting the extrinsic contribution into its skew scattering and side-jump parts.

DOI: 10.1103/PhysRevB.88.201108 PACS number(s): 72.25.Ba, 71.15.Rf, 72.15.Jf, 72.15.Qm

In recent years, transverse transport phenomena have moved into the focus of many studies, the enormous interest being of twofold origin: first, due to their promising potential use in applications; second, because of the intriguing underlying physics—the delicate and nontrivial entanglement of the electrons' spin and orbital degrees of freedom due to relativistic effects. Prominent examples for these are the anomalous Hall effect (AHE) in magnetically ordered solids[1–3] and the spin Hall effect (SHE) occurring in nonmagnetic solids.[4–6] While these transverse charge (AHE) and spin (SHE) transport phenomena are connected with an electric field $\vec{E}$ applied to a sample, corresponding phenomena can also be induced by a temperature gradient $\vec{\nabla}T$, giving rise to the anomalous Nernst (ANE)[7,8] and spin Nernst (SNE)[9–11] effects.

Spin-orbit interaction is the ultimate origin of all the aforementioned transverse transport phenomena, and different mechanisms giving contributions to the transverse conductivities have been identified. For pure systems they consist of an intrinsic contribution that can be connected to the so-called Berry curvature,[7,12,13] as has been demonstrated by various first-principles investigations on the AHE[14–16] as well as the SHE.[17–19] It has been suggested that for pure systems the intrinsic contribution has to be complemented by a concentration-independent side-jump contribution, which is meant to account for inevitable impurities. Corresponding first-principles work has been done for the AHE[16] and ANE.[20] For diluted alloys skew or Mott scattering and the side-jump mechanisms have been identified as additional extrinsic contributions.[1,2] Recently, model calculations on the basis of Friedel's impurity model have demonstrated for the SHE of $5d$-transition metals diluted in Cu that both contributions may be of the same order of magnitude.[21] Corresponding first-principles work on the SHE[22] as well as the SNE[23,24] has been done using the Boltzmann formalism that gives so far access to the skew scattering contribution only. As an alternative to this, the Kubo-Středa formalism, which is applicable to pure systems as well as diluted and concentrated alloys, has been used to deal with the AHE[25,26] and the SHE.[27] In the case of concentrated alloys, a decomposition into intrinsic and extrinsic contributions to the transport coefficients has been suggested[25,27] on the basis of their relation to the so-called vertex corrections[1,28,29] (which correspond to the scattering-in term of the Boltzmann equation) and the scaling laws connecting transverse and longitudinal transport coefficients.[1,2] This approach led for diluted alloys to contributions due to the skew scattering mechanism in full agreement with results based on the Boltzmann formalism.[27]

Among the various transport phenomena, the SNE has so far been considered only by a relatively few authors.[9–11,23,30–32] Only recently, the first calculations from first principles for the skew scattering contribution have been performed for diluted alloys.[23] As suggested by previous work,[33] the concept of a spin-projected conductivity has been used for this. As demonstrated in this Rapid Communication, this simplifying concept[34] can be avoided by working throughout with the spin current density and its related transport coefficients. This, together with a fully relativistic first-principles band structure scheme, allows to include all spin-flip transitions.[35] Finally, as demonstrated below, the extension of the Kubo-Středa formalism for spin transport leads to a first-principles description of the SNE that accounts for all possible contributions and that can be applied to pure as well as disordered systems. Furthermore, it supplies a proper basis to deal with nonmagnetic solids, as done here, but also to discuss thermally induced spin transport in magnetic solids.

Kubo's linear response formalism allows to relate the electric and heat current densities, $\vec{j}^c$ and $\vec{j}^q$, respectively, to the gradients of the electrochemical potential μ and temperature T.[36,37] These standard relations may be extended to include an induced spin current density J^s and can formally be written (see, e.g., Ref. 33)

$$\vec{j}^c = -L^{cc}\vec{\nabla}\mu - L^{cq}\vec{\nabla}T/T, \tag{1}$$

$$\vec{j}^q = -L^{qc}\vec{\nabla}\mu - L^{qq}\vec{\nabla}T/T, \tag{2}$$

$$J^s = -\mathcal{L}^{sc}\vec{\nabla}\mu - \mathcal{L}^{sq}\vec{\nabla}T/T, \tag{3}$$

with the gradient of the electrochemical potential $\vec{\nabla}\mu = \vec{\nabla}\mu_c + e\vec{E}$, where μ_c is the chemical potential,[38] $e = |e|$ the elementary charge, $\vec{E}$ the electric field, and $\vec{\nabla}T$ denotes the temperature gradient. Here, the L^{ij} and J^s are tensors of second rank and $\mathcal{L}^{ij}$ denote tensors of third rank. In the following we will consider only the response to the vector fields $\vec{E}$ and $\vec{\nabla}T$. All elements of the response tensors will be considered as temperature dependent with the restriction to the electronic temperature T. In addition T which appears in the forces is interpreted as the average sample temperature and not as a microscopic $T(\vec{r})$ due to the temperature gradient, assuming that we are in the regime of linear response. Furthermore only the carrier diffusion contribution to the thermoelectric

effects will be considered; collective phenomena such as the phonon-drag effect are not accounted for.

The response tensors appearing in Eqs. (1) and (2) can be calculated from the corresponding conductivities in the athermal limit, as was demonstrated, e.g., by Smrčka and Středa[39] or Jonson and Mahan.[40] Extending existing approaches employing a spin-projection scheme in the spirit of Mott's two-current model and avoiding the use of spin-dependent electrochemical potentials,[23,33] the present relativistic formulation leads to analogous expressions for the spin response coefficients. In particular, the underlying spin conductivity σ^{sc} ($\equiv -e\mathcal{L}^{sc}$ for $T \to 0$ K) may be calculated by an expression analogous to the Kubo-Středa formula for σ^{cc} ($\equiv -eL^{cc}$ for $T \to 0$ K).[27,41] Numerical checks against the Kubo-Bastin formula[42] proved this to be justified for the metallic systems considered here. Therefore it is possible to use the concept of an energy-dependent conductivity $\sigma^{sc}(E)$ providing the basis for calculating the response to $\vec{\nabla}T$ following the conventional scheme. For the spin-polarization axis along ξ, the spin current along μ, and the electric field along ν, with $\mu(\nu,\xi) \in \{x,y,z\}$, one obtains

$$\mathcal{L}^{sc,\xi}_{\mu\nu}(T) = -\frac{1}{e}\int dE\, \sigma^{sc,\xi}_{\mu\nu}(E) D(E,T), \tag{4}$$

with $D(E,T) = -\frac{\partial f(E,T)}{\partial E}$, $f(E,T)$ the Fermi function, and the energy-dependent spin conductivity $\sigma^{sc,\xi}_{\mu\nu}(E)$, which is obtained by applying the Kubo-Středa formalism in the framework of KKR-CPA,[25,27,29,43] using a relativistic spin current density operator.[27,44]

In analogy to the connection between the transport coefficient $L^{cq}_{\mu\nu}(T)$ and the energy-dependent electrical conductivity $\sigma^{cc}_{\mu\nu}(E)$,[40] the temperature-dependent spin transport coefficient $\mathcal{L}^{sq,\xi}_{\mu\nu}(T)$ is expressed in terms of the energy-dependent spin conductivity $\sigma^{sc,\xi}_{\mu\nu}(E)$:

$$\mathcal{L}^{sq,\xi}_{\mu\nu}(T) = -\frac{1}{e}\int dE\, \sigma^{sc,\xi}_{\mu\nu}(E)\, D(E,T)\,(E - E_F), \tag{5}$$

with E_F the Fermi energy.

Considering a thermal gradient $\vec{\nabla}T$ without an external electric field $\vec{E}$, the resulting electric current density $\vec{j}^c$ vanishes when open-circuit conditions are imposed. Equation (1) implies that an internal electric field

$$\vec{E} = -\frac{1}{eT}(L^{cc})^{-1} L^{cq}\vec{\nabla}T = S\,\vec{\nabla}T \tag{6}$$

builds up in order to compensate the charge imbalance induced by $\vec{\nabla}T$, where S is the thermo(magneto)electric tensor. Equations (4), (5), and (6) are in their combination sometimes called the generalized Mott formula for the thermopower (e.g., Refs. 20 and 45) and it has been shown by various authors (e.g., Ref. 40) that this expression reduces to the original expression of Mott for $T \to 0$ K. Using Eq. (3) together with Eq. (6) a spin-polarized current as a response to a temperature gradient is obtained under the aforementioned conditions for the charge current:

$$J^s = \mathcal{L}^{sc}(-e\vec{E}) + \mathcal{L}^{sq}(-\vec{\nabla}T/T) = \alpha^{scq}\,\vec{\nabla}T, \tag{7}$$

with the third-rank tensor

$$\begin{aligned}\alpha^{scq} &= -e\mathcal{L}^{sc}S - \mathcal{L}^{sq}/T \\ &= \mathcal{L}^{sc}(L^{cc})^{-1}L^{cq}/T - \mathcal{L}^{sq}/T,\end{aligned} \tag{8}$$

with notation chosen to be in line with the conventional symbol $\alpha^{cq}_{\mu\nu} = -L^{cq}_{\mu\nu}/T$ for the Nernst[20,46,47] (or Peltier[48]) coefficient or conductivity. In the following $\alpha^{sq,\xi}_{\mu\nu} = -\mathcal{L}^{sq,\xi}_{\mu\nu}/T$ will be used accordingly for the spin Nernst conductivity.

Obviously, the properties of the tensors appearing in Eq. (8) allow to decide in a most general way whether a thermal gradient may give rise to longitudinal and/or transverse spin currents. To investigate the symmetry properties of the tensor $\mathcal{L}^{sc}$ we have extended the symmetry scheme of Kleiner[49] in an appropriate way and applied it to $\sigma^{sc}(E)$.[50] For nonmagnetic cubic solids as considered here one obtains for spin-polarization along $\xi = z$

$$\sigma^{sc,z} = \begin{pmatrix} 0 & \sigma^z_{xy} & 0 \\ -\sigma^z_{xy} & 0 & 0 \\ 0 & 0 & 0 \end{pmatrix}, \tag{9}$$

which by virtue of Eqs. (4) and (5) leads to the same structure for $\mathcal{L}^{sc,\xi}$ and $\mathcal{L}^{sq,\xi}$, respectively. Cyclic permutations of the indices μ, ν, and ξ do not change the value of $\sigma^{\xi}_{\mu\nu}$, while anticyclic permutations reverse its sign. It should be mentioned that the structure of $\sigma^{\xi}_{\mu\nu}$ given by Eq. (9) is obtained accounting only for the spatial symmetry operations of the cubic point group. Inclusion of time-reversal symmetry does not give further restriction to the shape of the tensor σ^{sc} but introduces Onsager relations among tensors of response coefficients when response and force are interchanged.

As for the situation considered here (nonmagnetic, cubic) the conductivity tensor σ^{cc} (derived from L^{cc}) is diagonal and isotropic, a temperature gradient cannot create a longitudinal spin current. However, for the transverse components with respect to the polarization axis in $\xi = z$ one finds for example in the open electrical circuit case the nonvanishing term

$$\alpha^{scq,z}_{yx} = -e\mathcal{L}^{sc,z}_{yx}S_{xx} - \frac{1}{T}\mathcal{L}^{sq,z}_{yx} \tag{10}$$

$$= \alpha^{sc,z}_{yx} + \alpha^{sq,z}_{yx}, \tag{11}$$

consisting of the "electrical" and "thermal" contributions, $\alpha^{sc,z}_{yx}$ and $\alpha^{sq,z}_{yx}$, respectively.[51]

The second term of Eq. (10) represents the energy dependence of the spin-polarized transverse (spin Hall) conductivity in the vicinity of the Fermi level weighted with the asymmetrical occupation of states due to the temperature gradient [see Eq. (5)]. The first term, which is caused by zero charge current conditions, couples the thermoelectric effect in the direction of the temperature gradient via the generated charge imbalance (or internal electric field) to a transverse spin current. In the linear response regime this can be equivalently interpreted as an additional charge current (balancing the effect of $\vec{\nabla}T$) with a transverse (spin) component at the mean temperature of the sample or the action of the internal field on two heat currents (mediated by electrons) with opposite directions and hence on their off-diagonal spin-dependent components (as described in the second term without the field).

TABLE I. Longitudinal charge (σ_{xx}) and transverse spin (σ^z_{yx}) conductivities (in $\mu\Omega^{-1}$ cm^{-1}) at the Fermi energy, longitudinal charge Seebeck coefficient S_{xx} (in μV/K), and both contributions to $\alpha^{scq,z}_{yx}$, $\alpha^{sc,z}_{yx} = \sigma^z_{yx}(T)S_{xx}(T)$ and the conventional spin Nernst conductivity $\alpha^{sq,z}_{yx}$ (in A K^{-1} m^{-1}), always for $T = 300$ K, for the diluted alloys $Cu_{0.99}M_{0.01}$ with M = Ti, Au, Bi. Comparison is made to experimental data for the electrical conductivity (Ref. 53) and for all quantities to the Boltzmann results of Tauber *et al.* (Ref. 23).

	$\sigma_{xx}(E_F)$			$\sigma^z_{yx}(E_F)$		σ^z_{yx}(300 K)	S_{xx}(300 K)		$\alpha^{sc,z}_{yx}$(300 K)		$\alpha^{sq,z}_{yx}$(300 K)	
M	Exp.	Boltz.	Kubo	Boltz.	Kubo	(this work)	Boltz.	Kubo	Boltz.	Kubo	Boltz.	Kubo
Ti	0.12	0.09	0.08	3.24×10^{-4}	4.28×10^{-4}	4.29×10^{-4}	5.83	5.72	0.19	0.25	0.43	0.50
Au	1.92	2.64	2.28	2.67×10^{-2}	2.11×10^{-2}	2.11×10^{-2}	0.08	1.41	0.21	2.98	−15.1	−28.4
Bi	0.20	0.23	0.19	2.02×10^{-2}	2.05×10^{-2}	2.05×10^{-2}	−1.49	−1.02	−3.01	−2.10	−2.01	−0.20

A fully relativistic implementation of the Korringa-Kohn-Rostoker (KKR) band structure method[52] is used to determine the electronic structure of the various investigated systems self-consistently with disorder in the alloys accounted for by the coherent potential approximation (CPA). In a second step, the transport coefficients L^{cc}, L^{cq}, $\mathcal{L}^{sc}$, and $\mathcal{L}^{sq}$ are determined using the Kubo-Středa formalism together with Eqs. (4) and (5). For the athermal limit we use Mott's classical formula for the thermopower to obtain S/T and α/T.

Table I gives for the three diluted alloys $Cu_{0.99}M_{0.01}$ with M = Ti, Au, and Bi the resulting longitudinal conductivity σ_{xx} that is found in good agreement with experiment[53] as well as theoretical data obtained by Tauber *et al.*[23] using the Boltzmann formalism. Also the transverse spin conductivity σ^z_{yx} (for $T = 0$ and 300 K) and spin Nernst conductivity $\alpha^{sq,z}_{yx}$ obtained via the Boltzmann[23] and Kubo-Středa formalisms are found in fairly good agreement. Furthermore, the "electrical" contribution to $\alpha^{scq,z}_{yx}$, $\alpha^{sc,z}_{yx}(T) = -e\mathcal{L}^{sc,z}_{yx}(T)S_{xx}(T)$ is given for $T = 300$ K. The large discrepancy between the Kubo-Středa and Boltzmann result for M = Au for this quantity are mostly related to the strong deviations in S_{xx}, which is shown in the table as well. Possible sources for the deviations seen in Table I are discussed in the Supplemental Material.[50]

The transverse conductivities given in Table I reflect that these are induced by spin-orbit coupling (SOC) and accordingly most pronounced for the diluted Au and Bi systems. In fact, a model study for $Cu_{0.99}M_{0.01}$ with M being one of the heavy elements from Lu to At for which the SOC of Cu and the element M has been manipulated clearly showed that σ^z_{yx} is primarily caused by the SOC of the element M (see Supplemental Material[50]). However, along the series M = Lu to At the electronic structure of M at the Fermi energy E_F is dominated by d states for the transition-metal elements and by p states for the later elements. In addition, the SOC strength of the d electrons showing a maximum at M = Tl is weaker than for the p electrons. As a consequence, there is a crossover of the dominance of d to p states for σ^z_{yx} around M = Pt when going through the periodic table. The spin Hall conductivity is found to be maximal at M = Hg. As Eq. (5) connects σ^z_{yx} and α^z_{yx} the latter transport quantity could be expected to show a similar behavior along the series. However, as Table I clearly shows there is no strict one-to-one correspondence between σ^z_{yx} and $\alpha^{sq,z}_{yx}$ as for M = Au and Bi the values for the first quantity are nearly identical while those for the latter differ by two orders of magnitude. The different behavior of σ^z_{yx} and $\alpha^{sq,z}_{yx}$ is obviously caused by the fact that the latter is not only determined by the electronic structure at the Fermi energy E_F but by its variation around E_F (see below). A detailed discussion of the deviations between the two theoretical approaches for the spin Nernst conductivity is given in the Supplemental Material.[50]

In contrast to the Boltzmann approach,[22] the Kubo-Středa formalism can be applied straightforwardly to concentrated alloys. Figure 1 shows results for the residual resistivity ρ, i.e., the inverse of the longitudinal conductivity σ_{xx} for the energy $E = E_F$. Evaluating the equation with (VC) and without (NV) vertex corrections shows that these give only a minor reduction of ρ of a few percent for this system. Including finite-temperature effects in analogy to the expression in Eq. (4) gives rise to a negligibly small increase of ρ when going from 0 to 5 K. These results are in fairly good agreement with the experimental data for $T = 4$ K and show in particular the nearly parabolic concentration dependence.

As the extrinsic contributions to the transverse spin Hall conductivity σ^z_{yx} can be ascribed to the vertex corrections[27] its intrinsic part ($\sigma^{z\,\mathrm{intr}}_{yx}$) is obtained by ignoring these within the calculations. As Fig. 2 shows, $\sigma^{z\,\mathrm{intr}}_{yx}$ is rather small and increases nearly linearly with concentration when going from Cu to Au, obviously reflecting the increase of the average SOC strength. Including the vertex corrections leads to strong—apparently diverging—extrinsic contributions in the low-concentration regimes (x close to 0 or 1, respectively).

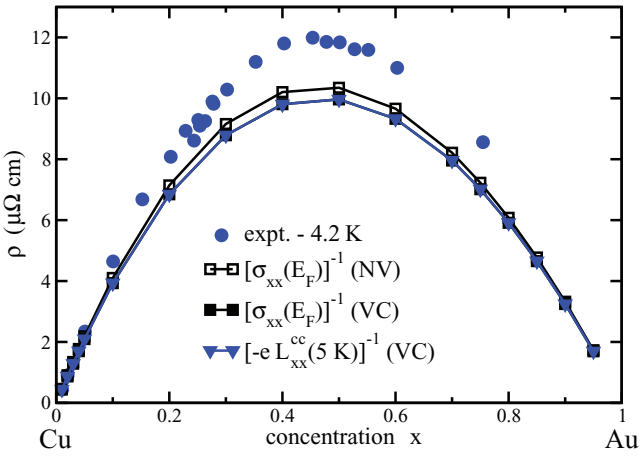

FIG. 1. (Color online) Longitudinal residual resistivity $\rho = [\sigma_{xx}(E_F)]^{-1}$ in Au_xCu_{1-x} calculated with (VC) and without (NV) vertex corrections for $T = 0$ K. In addition the resistivity $\rho = [-eL^{cc}_{xx}]^{-1}$ for $T = 5$ K obtained by an expression analogous to Eq. (4) is shown.

RAPID COMMUNICATIONS

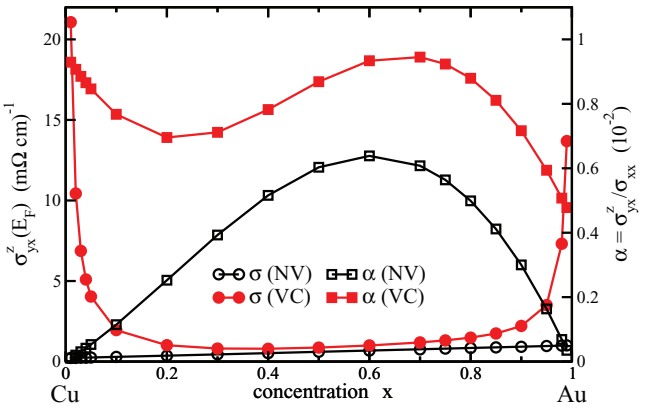

FIG. 2. (Color online) Spin Hall conductivity σ^z_{yx} and spin Hall angle $\alpha = \sigma^z_{yx}/\sigma_{xx}$ of Au_xCu_{1-x} calculated with (VC) and without (NV) vertex corrections for $T = 0$ K. In both cases σ_{xx} contains the vertex corrections.

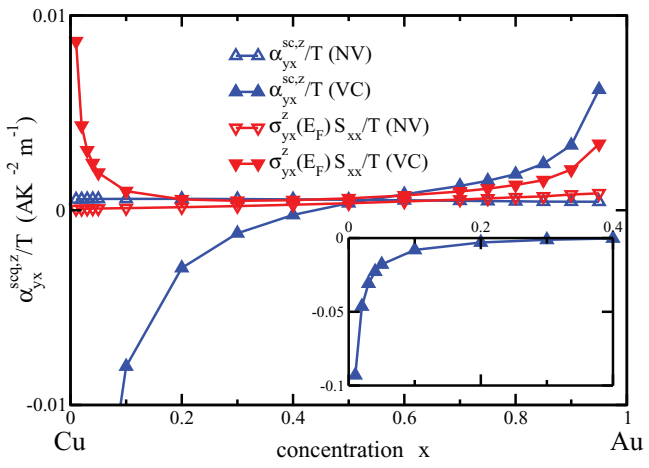

FIG. 3. (Color online) Components of the total spin Nernst conductivity (for $T \to 0$) in Au_xCu_{1-x}, excluding and including the vertex corrections.

In contrast to this behavior, the spin Hall ratio $\alpha = \sigma^z_{yx}/\sigma_{xx}$, which is most relevant for applications, shows a rather smooth and simple behavior. Taking only the intrinsic part of the spin Hall conductivity the ratio $\sigma^{z\,\mathrm{intr}}_{yx}/\sigma_{xx}$ goes to 0 in the limit $x \to 0$ and $x \to 1$, respectively, while the full ratio $\sigma^z_{yx}/\sigma_{xx}$ stays finite also in these limits. Making use of the different scaling behavior[1,2] of the extrinsic contributions to σ^z_{yx} ($\sigma^{z\,\mathrm{extr}}_{yx}$) one finds that the side-jump part of $\sigma^{z\,\mathrm{extr}}_{yx}$ is as $\sigma^{z\,\mathrm{intr}}_{yx}$ quite small and weakly concentration dependent but opposite in sign. As a consequence, the skew scattering part of $\sigma^{z\,\mathrm{extr}}_{yx}$ dominates by far in the low-concentration regimes (see Supplemental Material[50]).

The electrical and thermal contributions to the total spin Nernst conductivity divided by T, $\alpha^{sc,z}_{yx}/T$, and $\alpha^{sq,z}_{yx}/T$, respectively, for Au_xCu_{1-x} are shown in Fig. 3. As one notes, the intrinsic contributions obtained by ignoring the vertex corrections (NV) are quite small and vary nearly linearly with concentration for both terms. Including the vertex corrections, the concentration dependence of the electrical contribution $\alpha^{sc,z}_{yx}/T$ is obviously following that of the spin Hall conductivity σ^z_{yx} with a diverging behavior in the low-concentration regimes [see Eq. (10) and Fig. 2]. The thermal contribution $\alpha^{sq,z}_{yx}/T$ also shows a diverging behavior but with opposite sign for $x \to 0$ and $x \to 1$. This clearly demonstrates that there is no simple one-to-one correspondence between the spin Hall conductivity σ^z_{yx} and $\alpha^{sq,z}_{yx}/T$ as one can already expect from Eq. (5).

Making again use of the connection of the vertex corrections to the extrinsic contributions to the spin conductivity and of the scaling laws, one finds—similarly to the SHE—only small and linearly varying intrinsic contributions to the SNE. Also the extrinsic contribution, namely once again the skew scattering part, is prevailing in the dilute-concentration regimes of Au_xCu_{1-x} (see Supplemental Material[50]).

In summary, a first-principles description of the spin Nernst effect has been presented that is based on the Kubo-Středa formalism. It is demonstrated that the concept of a spin-projected conductivity can be avoided allowing in particular an unambiguous symmetry analysis for the various transport coefficients involved. Numerical implementation of the scheme using the KKR-CPA method led to satisfying agreement with previous results for diluted alloys obtained using the Boltzmann formalism. In addition, the first application of the approach presented to diluted and concentrated alloys allowed accessing all contributions to the SNE. For the investigated alloy system Au_xCu_{1-x} the extrinsic skew scattering contribution was found to dominate in the low-concentration regimes of the system.

This work was supported financially by the Deutsche Forschungsgemeinschaft (DFG) via the priority program SPP 1538 and the SFB 689. Discussions with D. Fedorov, M. Gradhand, K. Tauber, and I. Mertig are gratefully acknowledged.

*sebastian.wimmer@cup.uni-muenchen.de

[1] A. Crépieux and P. Bruno, Phys. Rev. B **64**, 014416 (2001).
[2] S. Onoda, N. Sugimoto, and N. Nagaosa, Phys. Rev. B **77**, 165103 (2008).
[3] N. Nagaosa, J. Sinova, S. Onoda, A. H. MacDonald, and N. P. Ong, Rev. Mod. Phys. **82**, 1539 (2010).
[4] M. I. Dyakonov and V. I. Perel, Phys. Lett. A **35**, 459 (1971).
[5] J. E. Hirsch, Phys. Rev. Lett. **83**, 1834 (1999).
[6] J. Sinova, D. Culcer, Q. Niu, N. A. Sinitsyn, T. Jungwirth, and A. H. MacDonald, Phys. Rev. Lett. **92**, 126603 (2004).
[7] D. Xiao, Y. Yao, Z. Fang, and Q. Niu, Phys. Rev. Lett. **97**, 026603 (2006).
[8] N. A. Sinitsyn, J. Phys.: Condens. Matter **20**, 023201 (2008).
[9] S. G. Cheng, Y. Xing, Q. F. Sun, and X. C. Xie, Phys. Rev. B **78**, 045302 (2008).
[10] X. Liu and X. Xie, Solid State Commun. **150**, 471 (2010).
[11] Z. Ma, Solid State Commun. **150**, 510 (2010).

[12]D. Xiao, J. Shi, and Q. Niu, Phys. Rev. Lett. **95**, 137204 (2005).

[13]M. Gradhand *et al.*, J. Phys.: Condens. Matter **24**, 213202 (2012).

[14]X. Wang, D. Vanderbilt, J. R. Yates, and I. Souza, Phys. Rev. B **76**, 195109 (2007).

[15]E. Roman, Y. Mokrousov, and I. Souza, Phys. Rev. Lett. **103**, 097203 (2009).

[16]J. Weischenberg, F. Freimuth, J. Sinova, S. Blügel, and Y. Mokrousov, Phys. Rev. Lett. **107**, 106601 (2011).

[17]Y. Yao and Z. Fang, Phys. Rev. Lett. **95**, 156601 (2005).

[18]G. Y. Guo, S. Murakami, T.-W. Chen, and N. Nagaosa, Phys. Rev. Lett. **100**, 096401 (2008).

[19]F. Freimuth, S. Blügel, and Y. Mokrousov, Phys. Rev. Lett. **105**, 246602 (2010).

[20]J. Weischenberg, F. Freimuth, S. Blügel, and Y. Mokrousov, Phys. Rev. B **87**, 060406 (2013).

[21]A. Fert and P. M. Levy, Phys. Rev. Lett. **106**, 157208 (2011).

[22]M. Gradhand, D. V. Fedorov, P. Zahn, and I. Mertig, Phys. Rev. Lett. **104**, 186403 (2010).

[23]K. Tauber, M. Gradhand, D. V. Fedorov, and I. Mertig, Phys. Rev. Lett. **109**, 026601 (2012).

[24]K. Tauber, D. V. Fedorov, M. Gradhand, and I. Mertig, Phys. Rev. B **87**, 161114 (2013).

[25]S. Lowitzer, D. Ködderitzsch, and H. Ebert, Phys. Rev. Lett. **105**, 266604 (2010).

[26]I. Turek, J. Kudrnovský, and V. Drchal, Phys. Rev. B **86**, 014405 (2012).

[27]S. Lowitzer, M. Gradhand, D. Ködderitzsch, D. V. Fedorov, I. Mertig, and H. Ebert, Phys. Rev. Lett. **106**, 056601 (2011).

[28]B. Velický, Phys. Rev. **184**, 614 (1969).

[29]W. H. Butler, Phys. Rev. B **31**, 3260 (1985).

[30]T. Seki, I. Sugai, Y. Hasegawa, S. Mitani, and K. Takanashi, Solid State Commun. **150**, 496 (2010).

[31]A. Dyrdał and J. Barnaś, J. Phys.: Condens. Matter **24**, 275302 (2012).

[32]H. Akera and H. Suzuura, Phys. Rev. B **87**, 075301 (2013).

[33]G. E. W. Bauer, E. Saitoh, and B. J. van Wees, Nat. Mater. **11**, 391 (2012).

[34]That even leads to artificial off-diagonal contributions to the longitudinal Seebeck effect in a nonmagnetic crystal, as in Eq. (8) of Ref. 23.

[35]S. Lowitzer, D. Ködderitzsch, and H. Ebert, Phys. Rev. B **82**, 140402(R) (2010).

[36]R. Kubo, J. Phys. Soc. Jpn. **12**, 570 (1957).

[37]J. M. Luttinger, Phys. Rev. **135**, A1505 (1964).

[38]Assumed to be constant (Ref. 40).

[39]L. Smrčka and P. Středa, J. Phys. C: Solid State Phys. **10**, 2153 (1977).

[40]M. Jonson and G. D. Mahan, Phys. Rev. B **21**, 4223 (1980).

[41]S. Lowitzer, Ph.D. thesis, Ludwig-Maximilians-Universität München, 2010, http://edoc.ub.uni-muenchen.de/12218.

[42]K. Chadova, H. Ebert, and D. Ködderitzsch (unpublished).

[43]J. Banhart, R. Bernstein, J. Voitländer, and P. Weinberger, Solid State Commun. **77**, 107 (1991).

[44]A. Vernes, B. L. Györffy, and P. Weinberger, Phys. Rev. B **76**, 012408 (2007).

[45]Y. M. Zuev, W. Chang, and P. Kim, Phys. Rev. Lett. **102**, 096807 (2009).

[46]S. Y. Huang, W. G. Wang, S. F. Lee, J. Kwo, and C. L. Chien, Phys. Rev. Lett. **107**, 216604 (2011).

[47]Y. Pu, D. Chiba, F. Matsukura, H. Ohno, and J. Shi, Phys. Rev. Lett. **101**, 117208 (2008).

[48]H. Kontani, Phys. Rev. B **67**, 014408 (2003).

[49]W. H. Kleiner, Phys. Rev. **142**, 318 (1966).

[50]See Supplemental Material at http://link.aps.org/supplemental/10.1103/PhysRevB.88.201108 for a general note on symmetry considerations for spin-dependent response tensors; a detailed comparison to results of previous work[23] regarding Seebeck coefficient, energy dependence of longitudinal charge and transverse spin Hall conductivities for 1% Ti, Au and Bi in copper and temperature dependence of the two contributions to the spin Nernst conductivity; additional results for the full series of 5*d* and 6*p* impurties in copper, including an investigation on the origins of the trends observed. This comprises a model study on the effect of the spin-orbit coupling and results & discussion for spin-orbit coupling strength and density of states at the Fermi level for the series; and a decomposition of spin Hall and spin Nernst conductivity on the Cu-rich side of Au_xCu_{1-x} into intrinsic, side-jump and skew scattering contributions.

[51]The two terms in Eq. (10) have been denoted σ_{SN}^{E} and σ_{SN}^{T} (Ref. 23) or σ_{TE}^{SH} and σ_{TM}^{SH} (Ref. 11) in previous work. The latter author termed the sum thermo-spin Hall conductivity and its constituents thermoelectric spin Hall and thermal spin Hall conductivity.

[52]H. Ebert, D. Ködderitzsch, and J. Minár, Rep. Prog. Phys. **74**, 096501 (2011).

[53]J. Bass, *Electrical Resistivity of Pure Metals and Alloys*, Landolt-Bornstein New Series, Group III, Part (a), Vol. 15 (Springer, New York, 1982).

Supplement

S. Wimmer, D. Ködderitzsch, K. Chadova and H. Ebert
Department Chemie/Phys. Chemie, Ludwig-Maximilians-Universität München, Germany
(Dated: August 23, 2013)

Symmetry considerations

Kleiner [1] introduced a very flexible scheme to investigate the symmetry relations for arbitrary response functions with the perturbation represented by a vector operator. We extended this scheme for the case that the response is given by a combination of two vector operators. For the spin current density considered here care has to be taken furthermore for the fact that one operator is an axial and the other one a polar vectorial quantity. With this accounted for the structure of the spin conductivity as well as spin Nernst conductivity tensors are determined applying the restrictions imposed by the cubic point group. Any other lattice symmetry can be treated in the same way. In addition, application to magnetically ordered systems runs completely analogously.

More detailed comparison to previous results

In Table I results for several transport properties are compared to those obtained by Boltzmann transport theory in the work by Tauber et al. [2]. The following Fig. 1 shows the comparison for the charge Seebeck coefficient S_{xx} [3] in more detail, namely its temperature dependence. As a function of temperature all three systems

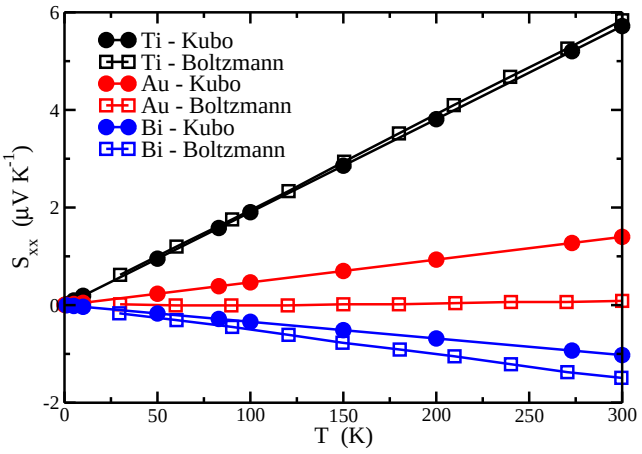

FIG. 1. (Color online) Temperature dependence of the charge Seebeck coefficient S_{xx} in $Cu_{0.99}Ti_{0.01}$, $Cu_{0.99}Au_{0.01}$, and $Cu_{0.99}Bi_{0.01}$ obtained within Kubo and Boltzmann [2] transport theory.

show a linear increase in magnitude, reflecting the basically linear behavior of the underlying $\sigma_{xx}(E)$ in the considered energy interval, as can be seen from Fig. 2. The different sign of the Seebeck coefficient in $Cu_{0.99}Bi_{0.01}$ directly traces back to the increase of the longitudinal conductivity as a function of energy in the vicinity of the Fermi level, as opposed to decreasing $\sigma_{xx}(E)$ for $Cu_{0.99}Ti_{0.01}$ and $Cu_{0.99}Au_{0.01}$.

A corresponding comparison is shown in Fig. 3 for the total spin Nernst conductivity as well as its individual, electrical and thermal, contributions. Again the temperature dependence is approximately linear for all contributions and all three systems. The differences in the constitution of the total spin Nernst conductivity, i.e. the relative magnitudes and signs of the two terms $\alpha_{yx}^{sc,z}$ and $\alpha_{yx}^{sq,z}$ found in Ref. [2] are reproduced. Just as for the Seebeck coefficient, magnitude, sign and temperature dependence of the spin Nernst conductivity (SNC) can be already qualitatively estimated from the $\sigma(E)$ curves in Fig. 2. Note that for $Cu_{0.99}Bi_{0.01}$ the deviation from linearity is the most prominent, which results in a moderately non-linear T-dependence of $\alpha_{yx}^{sq,z}$ (nearly invisible in Fig. 3, bottom).

Results for both quantities show very good agreement for $Cu_{0.99}Ti_{0.01}$ but pronounced deviations for the two other systems containing heavy elements. For $Cu_{0.99}Au_{0.01}$ this concerns mostly the longitudinal Seebeck coefficient but also transverse transport properties while for $Cu_{0.99}Bi_{0.01}$ the spin Nernst conductivities, especially their thermal contributions, deviate. This could possibly be ascribed to the neglect of spin-flip contributions by Tauber et al. [2], that indeed are expected to increase with the atomic number. But particularly for longitudinal transport coefficients in $Cu_{0.99}Au_{0.01}$ they could be ruled out to be of significance [4]. Another possible source for the discrepancies is the the fact that the Kubo-Středa formalism used here gives the full conductivities including in particular the intrinsic as well as the extrinsic side-jump contributions. These are given explicitly for Cu(Au) in the dilute limit below and can be shown to be too small to serve as an explanation. Furthermore, as the two approaches for determining the electronic structure of the alloy differ insofar as here the CPA is used whereas in Ref. [2] an embedded cluster method has been employed, differences in the response coefficients are to be expected. In particular, the energy dependence of the conductivities around the Fermi energy seems to be very sensitive. Another possible explanation for the discrepancies is the description of the spin

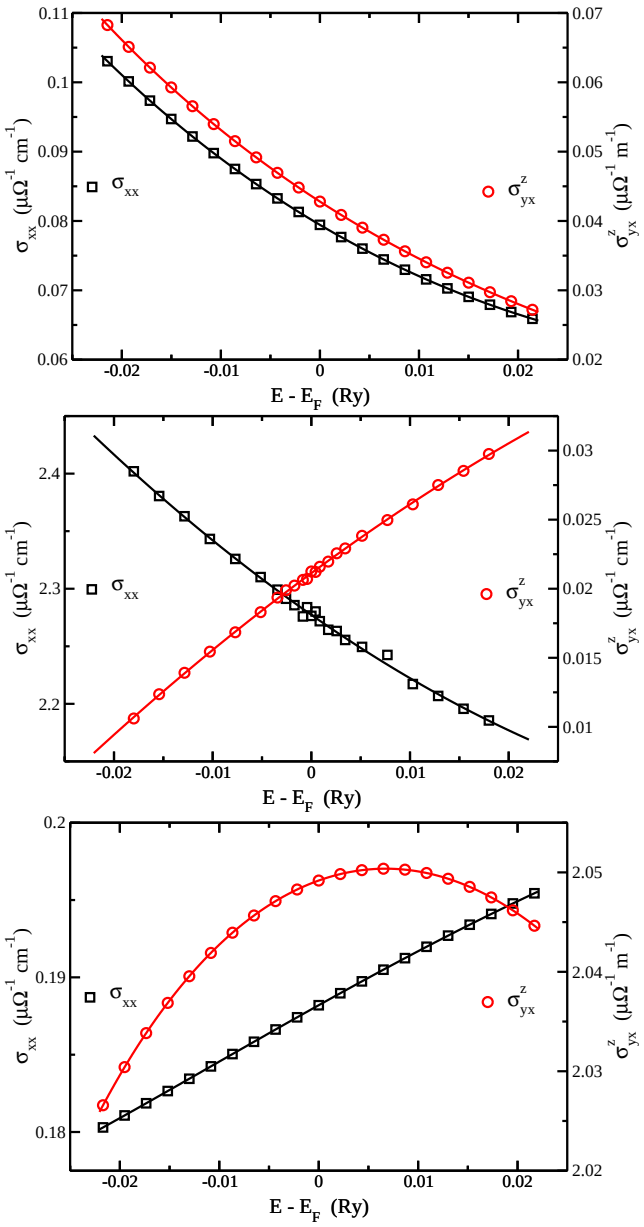

FIG. 2. (Color online) Energy dependence of the longitudinal charge and the transverse spin Hall conductivity, σ_{xx} and σ^z_{yx} respectively for (from top to bottom) $Cu_{0.99}Ti_{0.01}$, $Cu_{0.99}Au_{0.01}$, and $Cu_{0.99}Bi_{0.01}$.

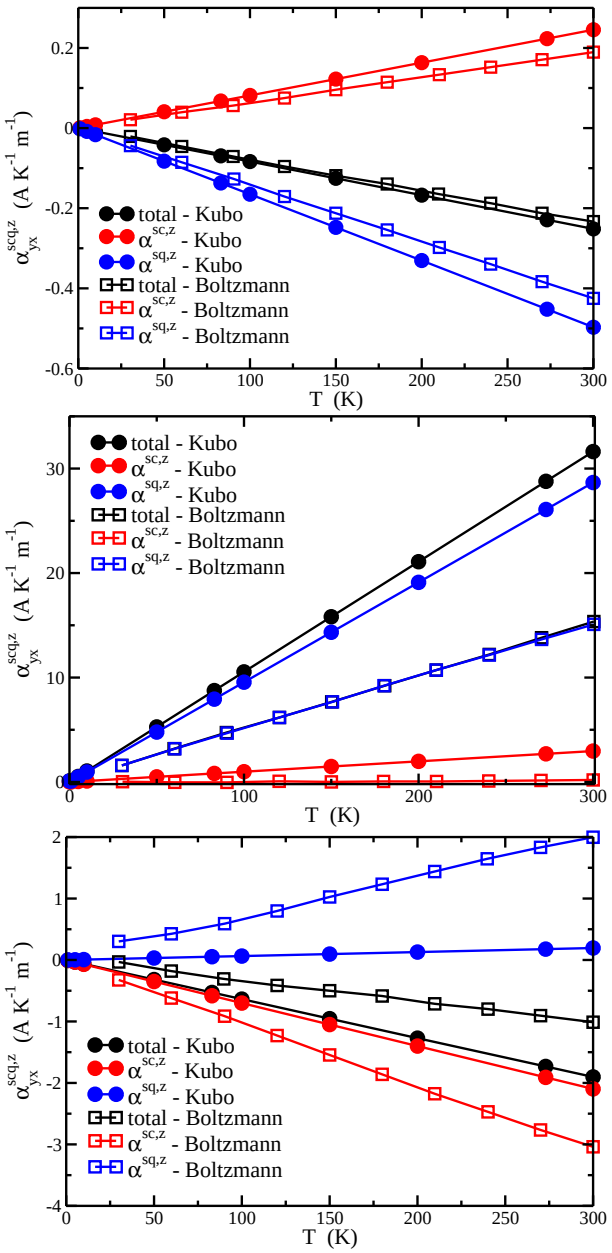

FIG. 3. (Color online) Temperature dependence of the spin-dependent Nernst conductivity and its constituents for, from top to bottom, in $Cu_{0.99}Ti_{0.01}$, $Cu_{0.99}Au_{0.01}$, and $Cu_{0.99}Bi_{0.01}$ obtained within Kubo and Boltzmann [2] transport theory.

current density, on the one hand by the use of the four-component polarization operator [5] and on the other hand via the spin polarization of the Bloch states as outlined in Ref. [6]. Still in all cases the overall agreement concerning magnitude, sign and temperature dependence is satisfactory.

Results for diluted Cu-alloy series

The discussion presented on the results of $Cu_{0.99}Au_{0.01}$ and $Cu_{0.99}Bi_{0.01}$ is supported by an additional study of the spin Hall conductivity for diluted Cu-M alloys. The underlying principles and the used formalism are outlined in Ref. 7. Suppressing the spin-orbit coupling on the host element Cu hardly changes the spin Hall con-

ductivity as shown in Fig. 4. Applying the manipulation

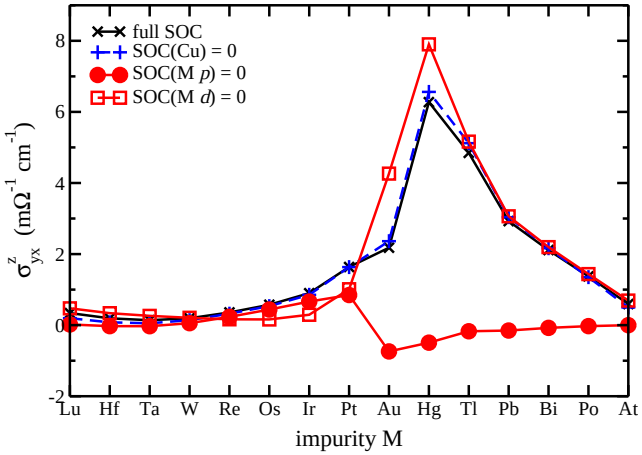

FIG. 4. (Color online) Spin Hall conductivities obtained for manipulated spin-orbit coupling (SOC) strength in $Cu_{0.99}M_{0.01}$.

for the heavy element M on the other hand leads to a strong variation of the spin Hall conductivity (SHC), in particular for elements around Hg. For this impurity the spin Hall conductivity with full spin-orbit coupling has the largest value. Performing the manipulation individually on the *p*- and *d*-channels shows that the relative importance of the *p*-channel increases drastically starting from M = Au.[8] Up to M = Hg also the SOC of the *d*-channel contributes considerably, for Au and Hg as impurities it even diminishes the SHC. The corresponding spin-orbit coupling strength for the elements M (see Fig. 5) is found to be minimal in the *p*-channel at M = Hg, shifted by one to higher atomic numbers, at Tl, the *d*-channel has its maximum. Furthermore the density of states at the Fermi energy shows a crossover of the dominance of *d*- to *p*-states between M = Au and Hg when going from light to heavy elements, as depicted in Fig. 6. All this does not yet provide a full explanation of the behavior of the SHC as a function of impurity type, it only hints, by highlighting the necessary ingredients, on the route one has to take in order to understand the underlying mechanisms in more detail.

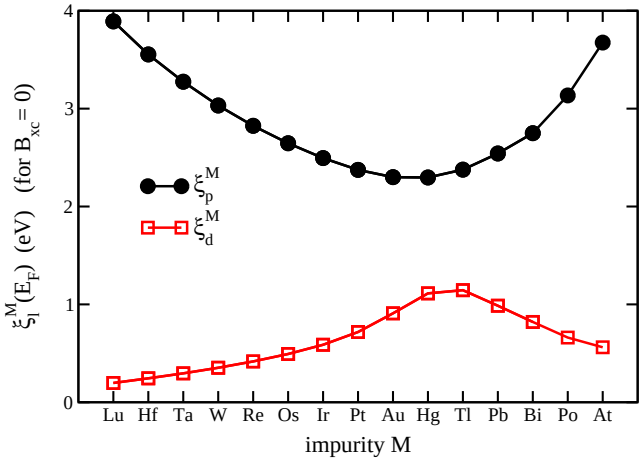

FIG. 5. (Color online) Spin-orbit coupling strength of impurity M from Lu to At in $Cu_{0.99}M_{0.01}$

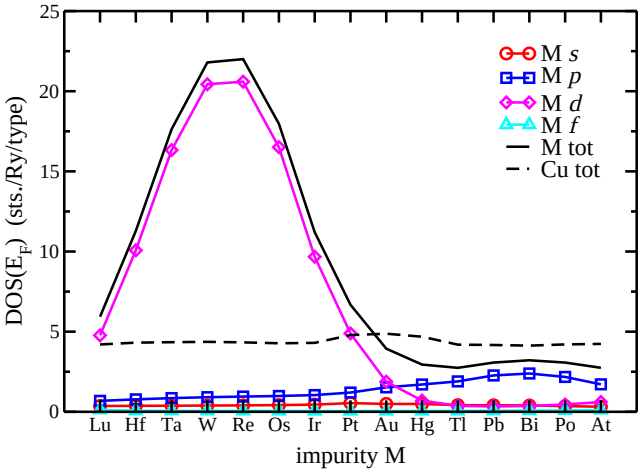

FIG. 6. (Color online) Density of states (DOS) at the Fermi energy for impurity M from Lu to At and Cu in $Cu_{0.99}M_{0.01}$. For the former elements the contributions of the *l*-channels up to *f* are given in addition.

Decomposition of spin Hall and spin Nernst conductivity

Making use of the connection of the vertex corrections to the extrinsic contributions to the spin Hall and spin Nernst conductivities these have been split accordingly into their intrinsic and extrinsic parts. For the intrinsic contributions (calculated excluding vertex corrections) in both cases a linear variation with the concentration is found, as shown in Fig. 7.

Using the scaling behavior [9, 10] of the extrinsic contribution due to the skew scattering and side-jump mechanisms w.r.t. to the longitudinal conductivity a corresponding decomposition has been made in addition. Fig. 7 shows that the side-jump contributions for both quantities are in the same order of magnitude as the intrinsic one and also vary only slightly with concentration. The skew scattering contribution, on the other hand, gives rise to the diverging behavior of both SHC and SNC when approaching the dilute limit.

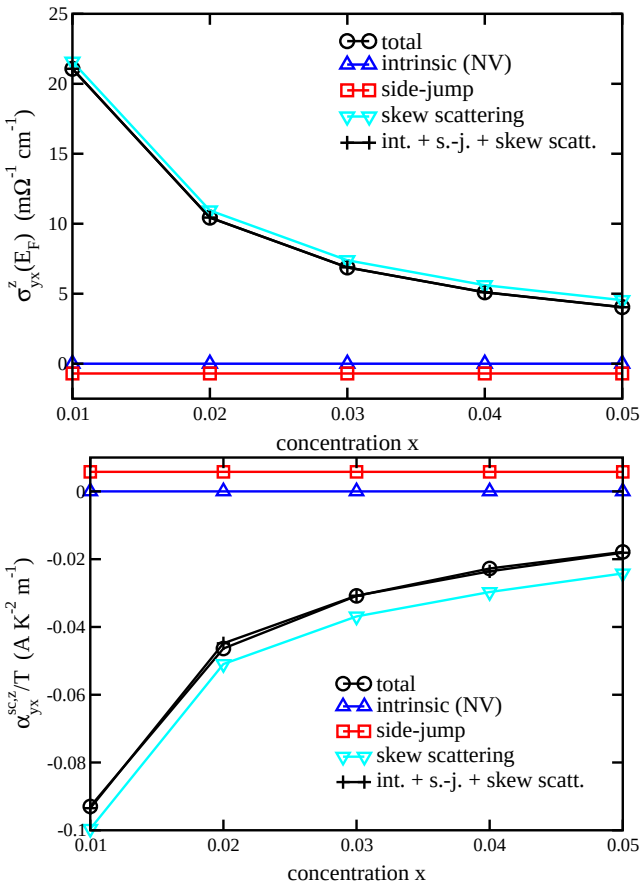

FIG. 7. (Color online) Decomposition (and reassembly) of the spin Hall (top) and spin Nernst conductivity (bottom) on the Cu-rich side of Au_xCu_{1-x} into intrinsic and extrinsic (skew scattering and side-jump) contributions.

[1] W. H. Kleiner, Phys. Rev. **142**, 318 (1966).

[2] K. Tauber, M. Gradhand, D. V. Fedorov, and I. Mertig, Phys. Rev. Lett. **109**, 026601 (2012).

[3] Which in our case has no contributions from transverse response coefficients, unlike Eq. (8) of Ref. [2], since both L^{cc} and L^{cq} in Eq. (6) are diagonal for nonmagnetic cubic crystals. Note that those artificial contributions could be shown to be negligibly small.

[4] K. Tauber, D. Fedorov, and I. Mertig, private communication.

[5] V. Bargmann and E. P. Wigner, Proc. Natl. Acad. Sci. U.S.A. **34**, 211 (1948).

[6] M. Gradhand, D. V. Fedorov, P. Zahn, and I. Mertig, Phys. Rev. Lett. **104**, 186403 (2010).

[7] H. Ebert, H. Freyer, A. Vernes, and G.-Y. Guo, Phys. Rev. B **53**, 7721 (1996).

[8] Interestingly, also for the elements at the beginning of the series, M = Lu to W, neglecting ξ_p^M drastically reduces the SHC.

[9] A. Crépieux and P. Bruno, Phys. Rev. B **64**, 014416 (2001).

[10] S. Onoda, N. Sugimoto, and N. Nagaosa, Phys. Rev. B **77**, 165103 (2008).

Errata

- The first two curves in Fig. 3 on page 4 of Ref. 266 (page 125 herein) should be labelled $\alpha_{yx}^{s\mathbf{q},z}/T$ (NV/VC), as the thermal contribution to $\alpha_{yx}^{scq,z}/T$ is shown.
- Likewise the axis label of the bottom panel of Fig. 7 on page 4 of the Supplemental Material to Ref. 266 (page 130 herein), should read $\alpha_{yx}^{s\mathbf{q},z}/T$ ($\mathrm{AK^{-2}m^{-1}}$).

3.2.2 Published results on the spin Nernst magneto-thermopower

The following is a preprint copy of the article "Observation of the spin Nernst effect" [21], reprinted (including Supplementary Information) from

S. Meyer, Y.-T. Chen, S. Wimmer, M. Althammer, T. Wimmer, R. Schlitz, S. Geprägs, H. Huebl, D. Ködderitzsch, H. Ebert, G.E.W. Bauer, R. Gross, and S.T.B. Goennenwein, arXiv:1607.02277 [cond-mat.mtrl-sci] (2016), published in Nat. Mater. **16**, 977 (2017).

Observation of the spin Nernst effect

S. Meyer[1,2], Y.-T. Chen[3,4], S. Wimmer[5], M. Althammer[1], T. Wimmer[1,2], R. Schlitz[1,6,7], S. Geprägs[1], H. Huebl[1,2,8], D. Ködderitzsch[5], H. Ebert[5], G.E.W. Bauer[3,9,10], R. Gross[1,2,8] and S.T.B. Goennenwein[1,2,6,7,8]

1. *Walther-Meißner-Institut, Bayerische Akademie der Wissenschaften, Walther-Meißner-Straße 8, 85748 Garching, Germany*
2. *Physik-Department, Technische Universität München, 85748 Garching, Germany*
3. *Kavli Institute of NanoScience, Delft University of Technology, Lorentzweg 1, 2628 CJ Delft, The Netherlands*
4. *RIKEN Center for Emergent Matter Science (CEMS), 2-1 Hirosawa, Wako, Saitama 351-0198, Japan*
5. *Department Chemie, Physikalische Chemie, Universität München, Butenandtstraße 5-13, 81377 München, Germany*
6. *present address: Institut für Festkörperphysik, Technische Universität Dresden, 01062 Dresden, Germany*
7. *present address: Center for Transport and Devices of Emergent Materials, Technische Universität Dresden, 01062 Dresden, Germany*
8. *Nanosystems Initiative Munich (NIM), Schellingstraße 4, 80799 München, Germany*
9. *Institute for Materials Research, Tohoku University, Sendai, Miyagi 980-8577, Japan*
10. *WPI Advanced Institute for Materials Research, Tohoku University, Sendai 980-8577, Japan*

June 2, 2017

The observation of the spin Hall effect [1, 2, 3] triggered intense research on pure spin current transport [4]. With the spin Hall effect [1, 2, 5, 6], the spin Seebeck effect [7, 8, 9], and the spin Peltier effect [10, 11] already observed, our picture of pure spin current transport is almost complete. The only missing piece is the spin Nernst (-Ettingshausen) effect, that so far has only been discussed on theoretical grounds [12, 13, 14, 15]. Here, we report the observation of the spin Nernst effect. By applying a longitudinal temperature gradient, we generate a pure transverse spin current in a Pt thin film. For readout, we exploit the magnetization-orientation-dependent spin transfer to an adjacent yttrium iron garnet layer, converting the spin Nernst current in Pt into a controlled change of the longitudinal and transverse thermopower voltage. Our experiments show that the spin Nernst and the spin Hall effect in Pt are of comparable magnitude, but differ in sign, as corroborated by first-principles calculations.

1 Main letter

Transverse transport is a key aspect of charge and/or spin motion in the solid state. In the charge channel, the Hall effect [16] and the Nernst effect [17] sketched in Fig. 1 (a), (b) enshrine transverse charge motion due to a gradient in the longitudinal potential imposed by an electric or thermal stimulus, respectively. Since the magnitude of the Hall charge current $\mathbf{j}_\mathrm{c}^\mathrm{Hall} \propto \theta_\mathrm{H}\, \mathbf{j}_\mathrm{c} \times \mathbf{H}$ (parameterized by the Hall angle θ_H, the applied charge current $\mathbf{j}_\mathrm{c}$ and the external magnetic field $\mathbf{H}$) is governed by the density of mobile charge carriers in simple metals and semiconductors, Hall effect experiments quickly became a standard tool for material characterization. As sketched in Fig. 1(b), the transverse Nernst charge current $\mathbf{j}_\mathrm{c}^\mathrm{Nernst} \propto \theta_\mathrm{N} \nabla T \times \mathbf{H}$ is driven by a temperature gradient ∇T or the corresponding heat current $\mathbf{j}_\mathrm{h} = -\kappa \nabla T$, where κ is the thermal conductivity and θ_N the Nernst angle.

While first experiments in the spirit of the spin Hall effect have been conducted in the 1970s [18] , only recently, electrically driven transverse *spin* transport in the form of the spin Hall effect (SHE) [19, 20] resulted in a new paradigm for spin-electronic device design [3, 21, 4]. The SHE refers to a transverse pure spin current $\mathbf{j}_\mathrm{s}^\mathrm{SH} \propto \theta_\mathrm{SH}\, \mathbf{j}_\mathrm{c} \times \mathbf{s}$ driven by a charge current density $\mathbf{j}_\mathrm{c}$, see Fig. 1(c). The spin Hall angle θ_SH characterizes the charge-to-spin conversion efficiency [4, 22]. Analogous to the Nernst effect, the spin Nernst effect (SNE) describes a transverse pure spin current $\mathbf{j}_\mathrm{s}^\mathrm{SN} \propto \theta_\mathrm{SN}\, \mathbf{j}_\mathrm{h} \times \mathbf{s}$ arising from a longitudinal

temperature gradient, cf. Fig. 1(d). Here, θ_{SN} is the spin Nernst angle [12, 13, 14, 15]. In linear response and Sommerfeld approximation:

$$\begin{pmatrix} \mathbf{j}_{\mathrm{c}} \\ \mathbf{j}_{\mathrm{h}} \\ \mathbf{j}_{\mathrm{s,i}} \end{pmatrix} = \sigma \begin{pmatrix} 1 & ST & \theta_{\mathrm{SH}}\mathbf{i}\times \\ ST & L_0T^2 & ST\theta_{\mathrm{SN}}\mathbf{i}\times \\ \theta_{\mathrm{SH}}\mathbf{i}\times & ST\theta_{\mathrm{SN}}\mathbf{i}\times & 1 \end{pmatrix} \begin{pmatrix} \nabla\mu_0/e \\ -\nabla T/T \\ \nabla\boldsymbol{\mu}_{\mathrm{si}}/(2e) \end{pmatrix}, \quad (1)$$

where the gradients of the electrochemical potential μ_0, T and spin accumulation $\boldsymbol{\mu}_{si}$ are connected via a tensor to $\mathbf{j}_{\mathrm{c}}$, $\mathbf{j}_{\mathrm{h}}$ and the pure spin current $\mathbf{j}_{\mathrm{s,i}}$ (with spin polarization $\mathbf{s}$ and $i \in \{\mathrm{x}, \mathrm{y}, \mathrm{z}\}$). The response tensor contains the electrical conductivity σ, the Seebeck coefficient S, the Lorenz constant L_0 and the spin Hall (Nernst) angle θ_{SH} (θ_{SN}) (for more details see SI). In spite of its fundamental importance for the understanding of pure spin current transport, the SNE has remained a theoretical conjecture.

In this Letter, we report direct experimental evidence for the spin Nernst effect in platinum. In order to quantify the spin Nernst spin current, we modulate the transverse spin current transport boundary conditions and detect the spin accumulation induced by the spin Nernst effect (SNE) in the charge channel, via the inverse spin Hall effect (ISHE) [6]. In model calculations, we show that the combined action of SNE and ISHE results in a thermopower along (and normal to) the applied temperature gradient. This spin Nernst magneto-thermopower (SMT) is present in any electrical conductor with spin orbit coupling, but usually cannot be discerned from the conventional Seebeck effect, since it has the same symmetry. However, by selectively changing the spin transport boundary conditions, the SMT can be quantitatively extracted and analyzed.

The concept is illustrated in Fig. 2(a-d). A paramagnetic metal film is exposed to a temperature gradient $\nabla T || -\mathbf{x}$. Through the Seebeck effect, a thermopower arises along $\mathbf{x}$. Furthermore, because of the SNE, a transverse spin current $\mathbf{j}_{\mathrm{s}}^{\mathrm{SN}}$ is flowing along $\mathbf{z}$ with spin polarization along $\mathbf{y}$, resulting in a spin accumulation at the metal film boundaries, as sketched in Fig. 2(a). The ensuing spin accumulation in turn drives a diffusive spin current $\mathbf{j}_{\mathrm{s}}^{\mathrm{b}}$. In the steady state, the spin current back flow $\mathbf{j}_{\mathrm{s}}^{\mathrm{b}} = -\mathbf{j}_{\mathrm{s}}^{\mathrm{SN}}$ exactly balances the spin Nernst spin current, such that the net transverse spin current flow vanishes. Through the ISHE, both $\mathbf{j}_{\mathrm{s}}^{\mathrm{b}}$ and $\mathbf{j}_{\mathrm{s}}^{\mathrm{SN}}$ are accompanied by inverse spin Hall charge currents (cf. Fig. 2(b)). Since the latter are of equal magnitude but opposite in sign, they cancel. In that case the charge current vanishes and thereby the SMT. In contrast, when the transverse spin transport is short-circuited, the spins can not accumulate at the interface [Fig. 2(c)], such that $\mathbf{j}_{\mathrm{s}}^{\mathrm{b}}$ is suppressed. As a consequence, only $\mathbf{j}_{\mathrm{s}}^{\mathrm{SN}}$ drives an ISHE charge current that leads to a

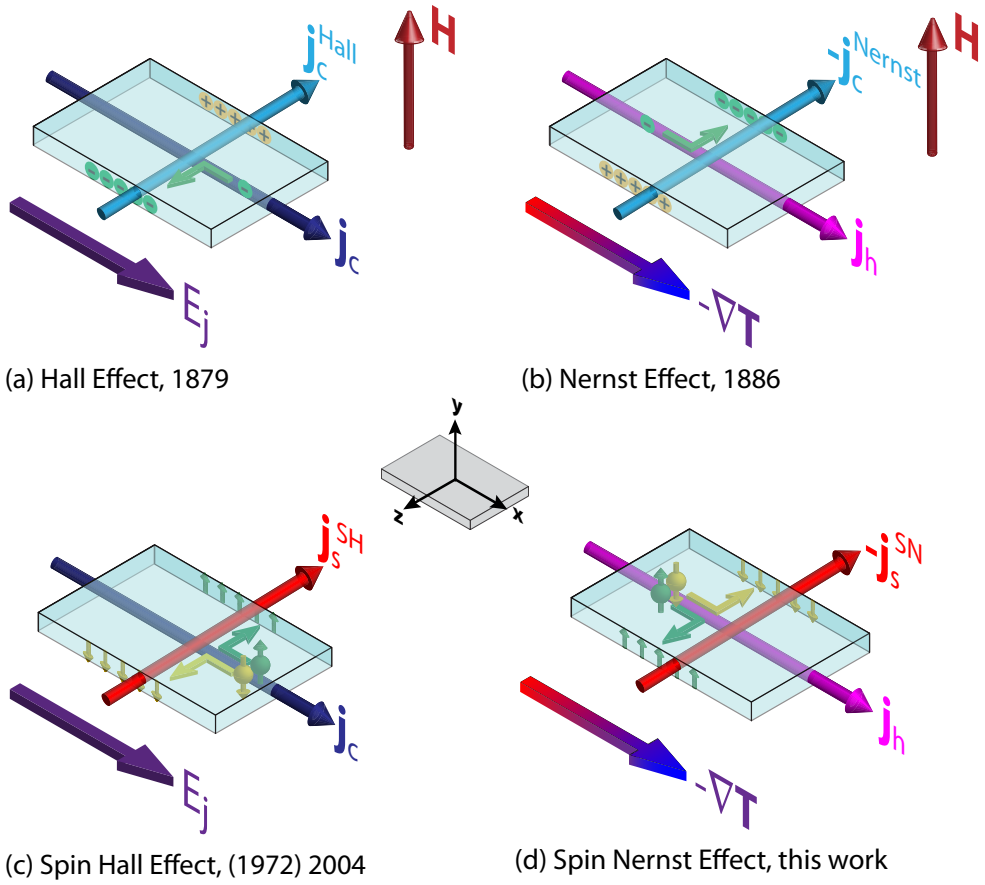

Figure 1: ***Charge and spin-related electric and thermal effects.*** *(a) In the Hall effect, a transverse charge current density* $\mathbf{j}_c^{Hall}$ *arises when a magnetic field* $\mathbf{H}$ *and a charge current density* $\mathbf{j}_c$ *are applied normal to each other.* ***(b)*** *The Nernst effect is the thermal analogue of the Hall effect. The electric effects are shown for negative charge carriers (electrons), translating into negative Hall and Nernst angles.* ***(c)*** *In the spin Hall effect, a transverse spin current density* $\mathbf{j}_s^{SH}$ *perpendicular to the charge current density* $\mathbf{j}_c$ *is generated due to spin orbit coupling.* ***(d)*** *A transverse spin current density* $\mathbf{j}_s^{SN}$ *is also generated by a longitudinal temperature gradient. This effect has been named spin Nernst effect and is experimentally demonstrated here. The spin effects are shown for negative spin Hall and spin Nernst angles.*

net charge current $\mathbf{j}_c^{\mathrm{ISHE,SN}}$ along $\mathbf{x}$, i.e., along the direction of the thermal bias [cf. Fig. 2(d)]. The combination of spin Nernst and inverse spin Hall effects thereby induces a thermopower along the temperature gradient with a magnitude depending on the transverse spin current boundary conditions. This SMT can be distinguished from the conventional Seebeck effect when modulating the transverse spin current boundary conditions by the spin transfer torque (STT) at the ferromagnetic insulator/normal metal (FMI/N) interface [23, 24]. The STT depends on the orientation of the magnetization $\mathbf{M}$ in the

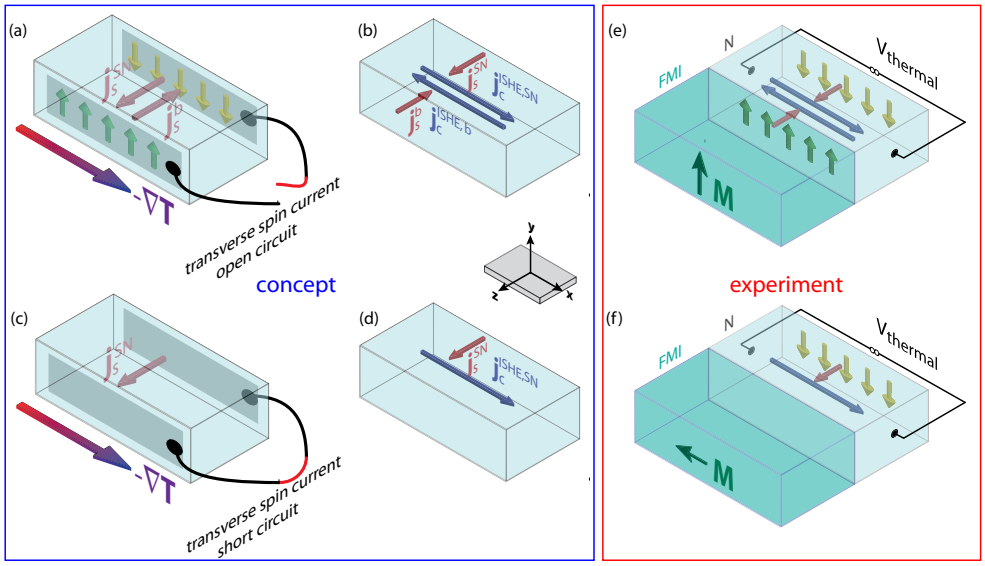

Figure 2: ***Boundary conditions for the spin Nernst magneto-thermopower (SMT)****: **(a)**: A temperature gradient ∇T along $-\mathbf{x}$ evokes a spin current density $\mathbf{j}_s^{\mathrm{SN}}$ along $\mathbf{z}$, leading to a spin-dependent chemical potential along $\mathbf{z}$. Open circuit boundary conditions depicted in **(a)** block the transverse spin current, generating a spin current back flow $\mathbf{j}_s^{\mathrm{b}} = -\mathbf{j}_s^{\mathrm{SN}}$. **(b)** Both spin current densities $\mathbf{j}_s^{\mathrm{SN}}$ and $\mathbf{j}_s^{\mathrm{b}}$ give rise to charge current densities $\mathbf{j}_c^{\mathrm{ISHE,SN}}$ and $\mathbf{j}_c^{\mathrm{ISHE,b}}$ parallel and antiparallel to $\mathbf{x}$. **(c)** Short-circuiting the spin transport along $\mathbf{z}$ suppresses the spin-dependent chemical potential and $\mathbf{j}_s^{\mathrm{back}}$. **(d)** The absence of $\mathbf{j}_s^{\mathrm{back}}$ enhances the net charge current. **(e,f)** We utilize an insulating ferrimagnet (FMI) attached to the metal layer (N) to switch between open (no spin transfer torque, panel **(e)**) and short-circuit (finite spin transfer torque, panel **(f)**) boundary conditions by the FMI magnetization orientation $\mathbf{M}$.*

magnetic insulator. When $\mathbf{s}$ and $\mathbf{M}$ are collinear (either parallel or antiparallel), the STT vanishes. This situation corresponds to open transverse spin transport

boundary conditions [cf. Fig. 2(e)]. In contrast, when **s** and **M** enclose a finite angle, the STT is finite, becoming maximal for **s** orthogonal to **M** [short-circuit boundary conditions, Fig. 2(f)]. We control the transverse spin current boundary conditions by systematically changing the orientation of the magnetization in the FMI layer, and record the ensuing spin Nernst driven changes in the thermopower, i.e., the SMT. The phenomenology of the SMT is similar to the recently established spin Hall magnetoresistance (SMR) [25, 26].
We model the SMT, by the spin diffusion equation in the metal with quantum mechanical boundary conditions at the ferromagnet, as detailed in the SI. The (longitudinal) thermopower V_{thermal} can be expressed in terms of an effective Seebeck coefficient as:

$$\frac{V_{\mathrm{thermal}}}{l} = -[S + \Delta S_0 + \Delta S_1(1 - m_{\mathrm{y}}^2)]\partial_x T \tag{2}$$

with

$$\frac{\Delta S_1}{S} = -\theta_{\mathrm{SN}}\theta_{\mathrm{SH}}\frac{\lambda}{t_{\mathrm{N}}}\mathrm{Re}\frac{2\lambda G \tanh^2(\frac{t_{\mathrm{N}}}{2\lambda})}{\sigma + 2\lambda G \coth(\frac{t_{\mathrm{N}}}{\lambda})}. \tag{3}$$

Here, t_{N}, σ and λ are the thickness, electrical conductivity, and spin diffusion length of the N film, respectively, G the spin mixing conductance of the FMI/N interface, l the sample length and $m_{\mathrm{y}} = \mathbf{M}\cdot\mathbf{y}/|\mathbf{M}|$. The t_{N}-dependence of $\Delta S_1/S$ in Eq. (3) is identical to that of the SMR [27].

The sample is a yttrium iron garnet ($Y_3Fe_5O_{12}$, YIG)|Pt bilayer [28] patterned into a Hall bar as shown in Fig. 3(a). An additional YIG|Pt strip extending in **y** direction serves as an on-chip heater. We heat one side of the sample by applying a constant electric power of 286 mW to the on-chip heater and connect the other end of the sample to a heat sink. This generates a temperature difference $\Delta T = T_{\mathrm{hot}} - T_{\mathrm{cold}} = 18.0\,\mathrm{K}$ between the two ends of the Hall bar as measured by on-chip resistive thermometry (see SI), while the dip stick is kept at $T_{\mathrm{base}} = 220\,\mathrm{K}$; the average sample temperature for these heater settings amounts to $T_{\mathrm{sample}} \approx 255\,\mathrm{K}$(see SI).
The external magnetic field of $\mu_0 H = 1\,\mathrm{T}$ is much larger than the demagnetization and anisotropy fields of YIG, such that $\mathbf{M} \parallel \mathbf{H}$. Then, $\mathbf{H}||\mathbf{y}$ corresponds to $\mathbf{M}||\mathbf{s}$ and thus open boundary conditions (no spin current flow across the interface), while for $\mathbf{H}||\mathbf{x}$ and $\mathbf{H}||\mathbf{z}$ the ferrimagnet represents an efficient spin current sink resulting in maximum spin current flow across the interface. The thermopower $V_{\mathrm{thermal}} = (\tilde{S} + \Delta S_1)\Delta T$ measured along **x** [cf. Fig. 3(b)] contains the conventional Seebeck effect of the Pt Hall bar with the Seebeck coefficient $\tilde{S}$ (for details see SI). For Pt, $\tilde{S} < 0$, such that the corresponding thermopower is negative. By rotating **H** and therefore the magnetization **M** of the YIG within

the film plane from $\alpha = 0°$ ($\mathbf{H} \parallel \mathbf{x}$) to $\alpha = 90°$($\mathbf{H} \parallel \mathbf{y}$), the spin current boundary conditions are switched from short-circuit (finite transverse spin current) to open circuit (vanishing transverse spin current) conditions. The thermopower therefore shows a characteristic modulation as expressed by Eq. (2).

Our measurements confirm this expectation: For open boundary conditions, $V_{\mathrm{thermal}} = -66.225\,\mu\mathrm{V}$ is about $\Delta V_{\mathrm{thermal}} = 100\,\mathrm{nV}$ larger than for short-circuit conditions, with a relative signal amplitude of $|\Delta V_{\mathrm{thermal}}/V_{\mathrm{thermal}}| = (1.5 \pm 0.3) \times 10^{-3}$, see Fig. 3(e). We reproduced this behavior for full 360° rotations of the applied field in the sample plane spanned by $\mathbf{x}$ and $\mathbf{y}$, leading to a $\sin^2\alpha$ behavior of V_{thermal} with minima for short-circuit boundary conditions ($\alpha = 0°, 180°$), and maxima for open boundary conditions ($\alpha = 90°, 270°$). We can also switch the boundary conditions by rotating the magnetic field in the (normal) plane spanned by $\mathbf{y}$ and $\mathbf{z}$, see Fig. 3(f). Starting at $\beta = 0°$ from $\mathbf{H} \parallel \mathbf{y}$ (open boundary conditions), the thermal voltage decreases while rotating $\mathbf{H}$ towards $\mathbf{z}$ ($\beta = 90°$, short-circuit boundary conditions) and the minimal and maximal levels of V_{thermal} coincide with the ones obtained in the first geometry. Rotating $\mathbf{H}$ out-of-plane perpendicular to $\mathbf{y}$ [Fig. 3(g)], the signal is almost constant and coincides with the lower signal levels observed for the other rotation planes. This is exactly the behavior expected from Eq. (2), since $\mathbf{H} \perp \mathbf{s}$ is fulfilled for every magnetization orientation in this rotation geometry, causing a maximum spin Nernst spin current flow. Also the observed transverse thermopower agrees very well with theory (see SI, Fig. 6). Spurious effects can be ruled out by their symmetries. For example, a spin Seebeck voltage arising from ∇T along $\mathbf{z}$ would result in a $\sin(\alpha)$ [$\cos(\beta)$] dependence of V_{thermal} in the ($\mathbf{x}$,$\mathbf{y}$) [($\mathbf{y}$,$\mathbf{z}$)] rotation plane, which is not observed (see also SI). Control experiments conducted on a GGG/Pt sample exhibit no SMT signature (see SI). Using $\lambda = 1.5\,\mathrm{nm}$, $\theta_{\mathrm{SH}} = 0.11$ and $\mathrm{Re}(G) = 4 \times 10^{14}\,\Omega^{-1}\mathrm{m}^{-2}$ [29] in Eq. (3), the observed $\Delta V_{\mathrm{thermal}}/V_{\mathrm{thermal}} = -1.5 \times 10^{-3}$ corresponds to a spin Nernst angle of $\theta_{\mathrm{SN}} = -0.20$ for Pt. Our first-principles calculations for the spin transport in bulk Pt confirm the relative sign and suggest $\theta_{\mathrm{SH}}/\theta_{\mathrm{SN}} = -0.6$ at T_{sample}(see SI). This is in fair agreement with $\theta_{\mathrm{SH}}/\theta_{\mathrm{SN}}(\mathrm{exp.}) = -0.5$. For different heating powers between 100 mW and 286 mW as well as for two different magnetic field values $\mu_0 H = 0.5\,\mathrm{T}$ and 1 T, we obtain identical SNE signatures. The relative amplitude of the modulation of the thermal voltage does not depend on both heating power and external magnetic field, as expected (see SI). Note that the observed field dependence excludes interference by the spin Seebeck effect [7, 8, 9].

In summary, we report an SMT signal in Pt|YIG hybrids proportional to an in-plane temperature gradient that reveals the spin Nernst effect in Pt, thereby opening a new strategy for the thermal generation of spin currents. The spin

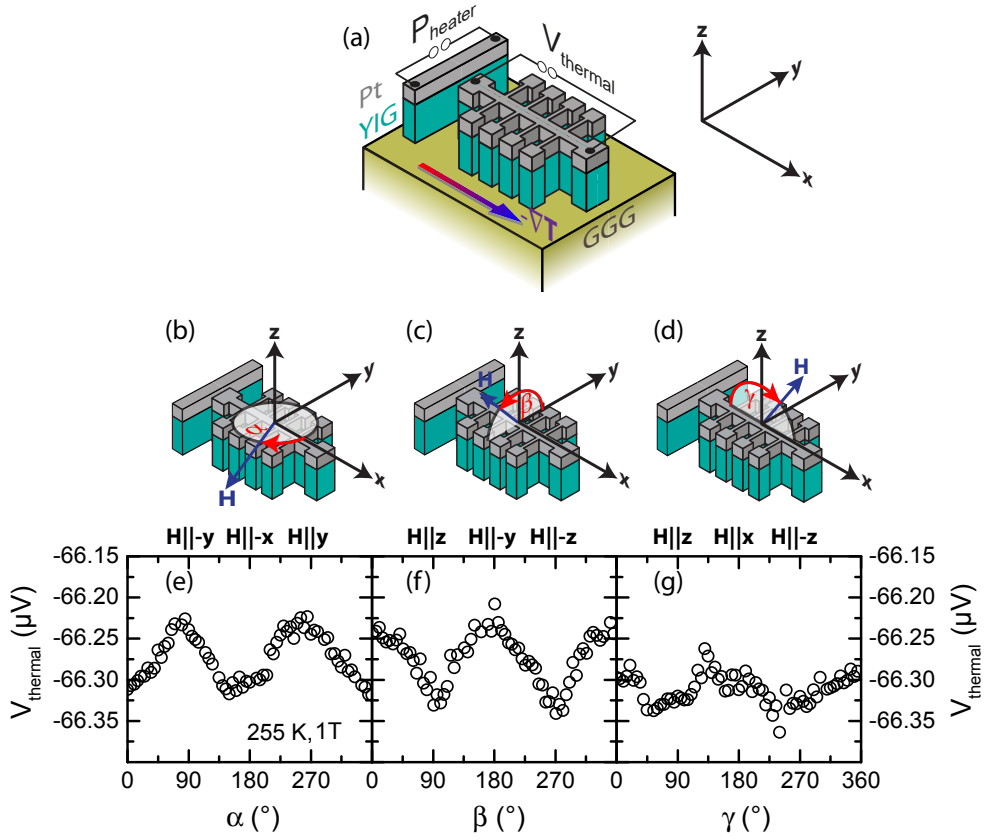

Figure 3: ***(a)*** *Setup of the SMT experiments. A YIG|Pt ($t_F = 40\,\mathrm{nm}/t_N = 4.1\,\mathrm{nm}$) thin film is patterned into a Hall bar (width $w = 250\,\mu\mathrm{m}$, length $l = 3150\,\mu\mathrm{m}$). An additional heater strip is defined along* $\mathbf{y}$*, $d = 250\,\mu\mathrm{m}$ beyond the top of the Hall bar. By applying an electric current with power P_{heater} to the heater strip, one end of the Hall bar is hotter than the other end that is connected to a heat sink provided by the sample holder (see supplementary information for details), leading to a temperature gradient $-\nabla T$ along* $\mathbf{x}$*.* ***(b)-(d)*** *The magnetization vector* $\mathbf{M}$ *of the YIG layer is rotated by an external magnetic field $\mu_0 H = 1\,\mathrm{T}$ in three different rotation planes spanned by (*$\mathbf{x}$*,* $\mathbf{y}$*) (panel* ***(b)****), (*$\mathbf{y}$*,* $\mathbf{z}$*)(panel* ***(c)****) and (*$\mathbf{x}$*,* $\mathbf{z}$*)(panel* ***(d)****). The measured thermal voltage V_{thermal} for all three geometries and $P_{\mathrm{heater}} = 286\,\mathrm{mW}$ (or $\Delta T = 18.0\,\mathrm{K}$ along the Hall bar, corresponding to $T_{\mathrm{sample}} \approx 255\,\mathrm{K}$) is depicted in panels* ***(e)*** *for the (*$\mathbf{x}$*,* $\mathbf{y}$*)-plane,* ***(f)*** *for the (*$\mathbf{y}$*,* $\mathbf{z}$*)-plane and* ***(g)*** *for the (*$\mathbf{x}$*,* $\mathbf{z}$*)-plane.*

Nernst and spin Hall angles are of equal magnitude in Pt but of opposite sign, as corroborated by first principle calculations. With the observation of the spin Nernst effect, the "zoo" of magneto-thermo-galvanic effects is complete. We anticipate that this spin Nernst magneto-thermopower can help in the optimization of spintronic devices harvesting ubiquitous temperature gradients e.g. from Joule heating hot spots. *Note added*: While writing this manuscript, we became aware of an additional experiment on the spin Nernst effect in metallic multilayers. [30]

2 Methods summary

In our experiments, an yttrium iron garnet ($Y_3Fe_5O_{12}$, YIG) thin film was epitaxially grown on a (111)-oriented gadolinium gallium garnet ($Gd_3Ga_5O_{12}$, GGG) substrate by pulsed laser deposition, covered in-situ with Pt by electron beam evaporation [28]. The YIG film is a an insulating ferrimagnet with a saturation magnetization of 120 kA/m. The Pt layer is polycrystalline with a resistivity of 430 nΩm at room temperature. The thicknesses of the YIG and Pt layers were determined by x-ray reflectometry as $t_F = (40 \pm 2)$ nm and $t_N = (4.1 \pm 0.2)$ nm, respectively. The $5 \times 5\,mm^2$ sample is patterned into a Hall bar with an additional heating strip as shown in Fig. 3(a). For temperature differences $\Delta T \leq 18.0$ K between both ends of the Hall bar, the voltage signal $V_{thermal}$ is measured while rotating a magnetic field of constant magnitude $\mu_0 H = 1$T in different planes. $\mu_0 H$ is much larger than the saturation field of YIG to ensure the alignment of the magnetization **M** of the FMI parallel to the external field even in the presence of magnetic and shape anisotropies. More details on the experimental methods are given in the SI.

3 Acknowledgments

S.M., M.A., S.G., H.H., R.G. and S.T.B.G. thank Andreas Erb for the preparation of the stoichiometric YIG target, Thomas Brenninger for technical support, and Nynke Vlietstra for the non-local sample preparation. Y.-T.C. and G.E.W.B. acknowledge funding by the FOM (Stichting voor Fundamenteel Onderzoek der Materie), EU- ICT-7 "INSPIN", and Grant-in-Aid for Scientific Research (Grant Nos. 25247056, 25220910, 26103006). S.W. thanks Sebastian TÃűlle and Ulrich Eckern for helpful discussions. All authors acknowledge funding via the DFG Priority program 1538 "Spin-Caloric Transport" (Projects GO 944/4, BA 2954/2 and EB 154/25).

4 Author Contributions

S.M., R.S., T.W. designed the sample layout and carried out the experiments. S.M., Y.-T.C., G.E.W.B., R.G. and S.T.B.G. developed the explanation of the SMT effect. S.G. supervised the sample growth. Y.-T.C. and G.E.W.B. developed the theoretical framework and S.W., D.K. and H.E. performed first-principles calculations of the relevant spin-caloric transport coefficients. S.T.B.G. supervised the experiments. The manuscript was written by S.M., M.A. and S.T.B.G. All authors discussed and participated in writing the manuscript under

the guidance of S.M. and G.E.W.B.

5 Affiliations

Walther-Meißner-Institut, Bayerische Akademie der Wissenschaften, Walther-Meißner-Straße 8, 85748 Garching, Germany
Sibylle Meyer, Matthias Althammer, Stephan Geprägs, Hans Huebl, Rudolf Gross and Sebastian T. B. Goennenwein
Physik-Department, Technische Universität München, 85748 Garching, Germany
Sibylle Meyer, Hans Huebl, Rudolf Gross and Sebastian T.B. Goennenwein
Kavli Institute of NanoScience, Delft University of Technology, Lorentzweg 1, 2628 CJ Delft, The Netherlands
Yan-Ting Chen and Gerrit E. W. Bauer
RIKEN Center for Emergent Matter Science (CEMS), 2-1 Hirosawa, Wako, Saitama 351-0198, Japan
Yan-Ting Chen
Department Chemie, Physikalische Chemie, Universität München, Butenandtstraße 5-13, 81377 München, Germany
Sebastian Wimmer, Diemo Ködderitzsch and Hubert Ebert
Nanosystems Initiative Munich (NIM), Schellingstraße 4, 80799 München, Germany
Hans Huebl, Rudolf Gross and Sebastian T. B. Goennenwein
Institute for Materials Research, Tohoku University, Sendai, Miyagi 980-8577, Japan
Gerrit E. W. Bauer
WPI Advanced Institute for Materials Research, Tohoku University, Sendai 980-8577, Japan
Gerrit E. W. Bauer

6 Competing Interests Statement

The authors declare that they have no competing financial interests. Supplementary information accompanies this paper online.

7 Corresponding author

Correspondence and requests for materials should be addressed to S.T.B.G.

References

[1] Kato, Y. K., Myers, R. C., Gossard, A. C., and Awschalom, D. D. *Science* **306**, 1910(2004).

[2] Wunderlich, J., Kaestner, B., Sinova, J., and Jungwirth, T. *Physical Review Letters* **94**, 047204 (2005).

[3] Wunderlich, J., Park, B.-G., Irvine, A. C., Zârbo, L. P., Rozkotová, E., Nemec, P., Novák, V., Sinova, J., and Jungwirth, T. *Science* **330**, 1801 (2010).

[4] Sinova, J., Valenzuela, S. O., Wunderlich, J., Back, C. H., and Jungwirth, T. *Review of Modern Physics* **87**, 1213 (2015).

[5] Valenzuela, S. O. and Tinkham, M. *Nature* **442**, 176 (2006).

[6] Saitoh, E., Ueda, M., Miyajima, H., and Tatara, G. *Applied Physics Letters* **88**, 182509 (2006).

[7] Uchida, K., Takahashi, S., Harii, K., Ieda, J., Koshibae, W., Ando, K., Maekawa, S., and Saitoh, E. *Nature* **455**, 778 (2008).

[8] Jaworski, C. M., Yang, J., Mack, S., Awschalom, D. D., Heremans, J. P., and Myers, R. C. *Nature Materials* **9**, 898 (2010).

[9] Uchida, K., Adachi, H., Ota, T., Nakayama, H., Maekawa, S., and Saitoh, E. *Applied Physics Letters* **97**, 172505 (2010).

[10] Flipse, J., Bakker, F. L., Slachter, A., Dejene, F. K., and van Wees, B. J. *Nature Nanotechnology* **7**, 166 (2012).

[11] Flipse, J., Dejene, F. K., Wagenaar, D., Bauer, G. E. W., Ben Youssef, J., and van Wees, B. J. *Physical Review Letters* **113**, 027601 (2014).

[12] Cheng, S., Xing, Y., Sun, Q., and Xie, X. C. *Physical Review B* **78**, 045302 (2008).

[13] Liu, X. and Xie, X. *Solid State Communications* **150**, 471 (2010).

[14] Tauber, K., Gradhand, M., Fedorov, D. V., and Mertig, I. *Physical Review Letters* **109**, 026601 (2012).

[15] Wimmer, S., Ködderitzsch, D., Chadova, K., and Ebert, H. *Physical Review B* **88**, 201108 (2013).

[16] Hall, E. *American Journal of Mathematics* **2**, 286 (1879).

[17] Von Ettingshausen, A. and Nernst, W. *Annalen der Physik und Chemie* **265**, 343 (1886).

[18] Chazalviel, J. N. and Solomon, I. *Physical Review Letters* **29**(25), 1676 (1972).

[19] D'akonov, M. I. and Perel, V. I. *JETP Letters* **13**, 467 (1971).

[20] Hirsch, J. E. *Physical Review Letters* **83**, 1834 (1999).

[21] Betthausen, C., Dollinger, T., Saarikoski, H., Kolkovsky, V., Karczewski, G., Wojtowicz, T., Richter, K., and Weiss, D. *Science* **337**, 324 (2012).

[22] Hoffmann, A. *Magnetics, IEEE Transactions on* **49**, 5172 (2013).

[23] Ralph, D. C. and Stiles, M. D. *Journal of Magnetism and Magnetic Materials* **320**, 1190 (2008).

[24] Brataas, A., Bauer, G. E., and Kelly, P. J. *Physics Reports* **427**, 157 (2006).

[25] Nakayama, H., Althammer, M., Chen, Y.-T., Uchida, K., Kajiwara, Y., Kikuchi, D., Ohtani, T., Geprägs, S., Opel, M., Takahashi, S., Gross, R., Bauer, G. E. W., Goennenwein, S. T. B., and Saitoh, E. *Physical Review Letters* **110**, 206601 (2013).

[26] Vlietstra, N., Shan, J., Castel, V., Ben Youssef, J., Bauer, G. E. W., and van Wees, B. J. *Applied Physics Letters* **103**, 032401 (2013).

[27] Chen, Y.-T., Takahashi, S., Nakayama, H., Althammer, M., Goennenwein, S. T. B., Saitoh, E., and Bauer, G. E. W. *Physical Review B* **87**, 144411 (2013).

[28] Althammer, M., Meyer, S., Nakayama, H., Schreier, M., Altmannshofer, S., Weiler, M., Huebl, H., Geprägs, S., Opel, M., Gross, R., Meier, D., Klewe, C., Kuschel, T., Schmalhorst, J.-M., Reiss, G., Shen, L., Gupta, A., Chen, Y.-T., Bauer, G. E. W., Saitoh, E., and Goennenwein, S. T. B. *Physical Review B* **87**, 224401 (2013).

[29] Meyer, S., Althammer, M., Geprägs, S., Opel, M., Gross, R., and Goennenwein, S. T. B. *Applied Physics Letters* **104**, 242411 (2014).

[30] Sheng, P., Sakuraba, Y., Takahashi, S., Mitani, S., and Hayashi, M. *Scientific Reports* **7**, 40586 (2017).

Observation of the spin Nernst effect (Supplementary Information)

***S. Meyer*[1,2], *Y.-T. Chen*[3,4], *S. Wimmer*[5], *M. Althammer*[1], *T. Wimmer*[1,2], *R. Schlitz*[1,6,7], *S. Geprägs*[1], *H. Huebl*[1,2,8], *D. Ködderitzsch*[5], *H. Ebert*[5], *G.E.W. Bauer*[3,9,10], *R. Gross*[1,2,8] and *S.T.B. Goennenwein*[1,2,6,7,8]**

1. *Walther-Meißner-Institut, Bayerische Akademie der Wissenschaften, Walther-Meißner-Straße 8, 85748 Garching, Germany*
2. *Physik-Department, Technische Universität München, 85748 Garching, Germany*
3. *Kavli Institute of NanoScience, Delft University of Technology, Lorentzweg 1, 2628 CJ Delft, The Netherlands*
4. *RIKEN Center for Emergent Matter Science (CEMS), 2-1 Hirosawa, Wako, Saitama 351-0198, Japan*
5. *Department Chemie, Physikalische Chemie, Universität München, Butenandtstraße 5-13, 81377 München, Germany*
6. *present address: Institut für Festkörperphysik, Technische Universität Dresden, 01062 Dresden, Germany*
7. *present address: Center for Transport and Devices of Emergent Materials, Technische Universität Dresden, 01062 Dresden, Germany*
8. *Nanosystems Initiative Munich (NIM), Schellingstraße 4, 80799 München, Germany*
9. *Institute for Materials Research, Tohoku University, Sendai, Miyagi 980-8577, Japan*
10. *WPI Advanced Institute for Materials Research, Tohoku University, Sendai 980-8577, Japan*

May 24, 2017

1 Supplementary Information (SI)

1.1 Theory of the spin Nernst magnetothermopower

Here we present a theoretical analysis of the SMT effect in N|FMI bilayer systems in terms of a non-equilibrium proximity effect caused by the simultaneous action of the spin Nernst effect (SNE) and the inverse spin Hall effect (ISHE). This effect scales like the product of the spin Hall and spin Nernst angle, and is modulated by the magnetization direction in YIG via the spin transfer at the N|FMI interface. Our explanation is a generalization of that of the spin Hall magnetoresistance [1, 2], and is based on the spin-diffusion approximation in the N layer in the presence of spin-orbit interaction [3] and quantum mechanical boundary conditions at the interface in terms of the spin-mixing conductance [4, 5].

We consider a N|FMI bilayer homogeneous in the x-y plane ($z = 0$ defines the interface), and calculate the spin accumulation, spin currents and finally the measured charge currents that are compared with the experimental SMT. We also find that the imaginary part of the spin-mixing conductance generates an anomalous Nernst effect (ANE) (that appears to be too small to be observable, however).

The spin current density in the weakly relativistic limit

$$\mathbf{j}_\mathrm{s} = -en\frac{<\mathbf{v}\times\boldsymbol{\sigma}+\boldsymbol{\sigma}\times\mathbf{v}>}{2} = (\mathbf{j}_{\mathrm{s,x}},\mathbf{j}_{\mathrm{s,y}},\mathbf{j}_{\mathrm{s,z}})^\mathrm{T} = (\mathbf{j}_\mathrm{s}^\mathrm{x},\mathbf{j}_\mathrm{s}^\mathrm{y},\mathbf{j}_\mathrm{s}^\mathrm{z}) \qquad (1)$$

is a second-order tensor (in units of the charge current density $\mathbf{j}_\mathrm{c} = -en < \mathbf{v} >$), where $-e$ ($e > 0$) is the electron charge, n is the density of the electrons, $\mathbf{v}$ is the velocity operator, $\boldsymbol{\sigma}$ is the vector of Pauli spin matrices, and $< ... >$ denotes the thermodynamic expectation value for a non-equilibrium state. The row vectors $\mathbf{j}_{\mathrm{s,i}} = -en < \mathbf{v}\times\sigma_\mathrm{i}+\sigma_\mathrm{i}\times\mathbf{v} > /2$ are the spin current densities polarized in the $\mathbf{i}$ direction, while the column vectors $\mathbf{j}_\mathrm{s}^\mathrm{j} = -en < v_\mathrm{j}\times\boldsymbol{\sigma}+\boldsymbol{\sigma}\times v_\mathrm{j} > /2$ denote the spin current densities with polarization η flowing in the $\mathbf{j}$ direction. On the other hand, the heat current reads $\mathbf{j}_\mathrm{h} = n < (E - E_\mathrm{F})\mathbf{v} >$, where E stands for the energy of the particle, E_F represents the Fermi energy. Ohm's Law for metals with spin-orbit interactions can be summarized by the relation between thermodynamic driving forces and currents that reflects the Onsager

reciprocity by the symmetry of the response matrix [2, 3]

$$\begin{pmatrix} \mathbf{j}_{\mathrm{c}} \\ \mathbf{j}_{\mathrm{h}} \\ \mathbf{j}_{\mathrm{s,x}} \\ \mathbf{j}_{\mathrm{s,y}} \\ \mathbf{j}_{\mathrm{s,z}} \end{pmatrix} = \sigma \begin{pmatrix} 1 & ST & \theta_{\mathrm{SH}}\mathbf{x}\times & \theta_{\mathrm{SH}}\mathbf{y}\times & \theta_{\mathrm{SH}}\mathbf{z}\times \\ ST & L_0T^2 & ST\theta_{\mathrm{SN}}\mathbf{x}\times & ST\theta_{\mathrm{SN}}\mathbf{y}\times & ST\theta_{\mathrm{SN}}\mathbf{z}\times \\ \theta_{\mathrm{SH}}\mathbf{x}\times & ST\theta_{\mathrm{SN}}\mathbf{x}\times & 1 & 0 & 0 \\ \theta_{\mathrm{SH}}\mathbf{y}\times & ST\theta_{\mathrm{SN}}\mathbf{y}\times & 0 & 1 & 0 \\ \theta_{\mathrm{SH}}\mathbf{z}\times & ST\theta_{\mathrm{SN}}\mathbf{z}\times & 0 & 0 & 1 \end{pmatrix} \begin{pmatrix} \nabla\mu_0/e \\ -\nabla T/T \\ \nabla\mu_{\mathrm{sx}}/(2e) \\ \nabla\mu_{\mathrm{sy}}/(2e) \\ \nabla\mu_{\mathrm{sz}}/(2e) \end{pmatrix} \tag{2}$$

where $\boldsymbol{\mu}_{\mathrm{s}} = (\mu_{\mathrm{sx}}, \mu_{\mathrm{sy}}, \mu_{\mathrm{sz}})^T - \mu_0\mathbf{1}$ is the spin accumulation, i.e. the spin-dependent chemical potential relative to the electrochemical potential μ_0, σ is the electrical conductivity, $S = -eL_0T\partial_E(\ln(\sigma))|_{E_F}$ is the Seebeck coefficient, $L_0 = (\pi^2/3)(k_{\mathrm{B}}/e)^2$ is the Lorenz number with k_{B} the Boltzmann constant, θ_{SH} (θ_{SN}) is the spin Hall (Nernst) angle, and $\times$ denotes the vector cross product operating on the driving forces. The spin Hall (Nernst) effect [6, 7] is represented by the lower non-diagonal elements that generate the spin currents in the presence of an applied electric field (temperature gradient), while the inverse spin Hall (Nernst) effect is governed by elements above the diagonal that connect the gradients of the spin accumulations to the charge (heat) current density. The Mott relations, expressing the response to a temperature gradient in terms of the energy derivative of the electric response (as done above for the Seebeck coefficient), are the leading terms in the Sommerfeld expansion of the linear response coefficients given by Eqns. (20) and (21). They are exact in the limit of sufficiently low temperatures. Deviations from the Mott relations at elevated temperatures can be parameterized by a temperature-dependent effective Lorenz number. The ab-initio calculations detailed below, however, do not make use of the Sommerfeld approximation. In this study, we focus on the charge current generated by an external temperature gradient and thus the driving force is chosen to be a temperature gradient in the $\mathbf{x}$ direction $\nabla T = \mathbf{x}\partial_x T$ which drives a charge current $j_{c0}\mathbf{x} = -\sigma S\partial_x T\mathbf{x}$ via the Seebeck effect.

The spin accumulation μ_{s} is obtained from the spin-diffusion equation in the normal metal

$$\nabla^2\boldsymbol{\mu}_{\mathrm{s}} = \frac{\boldsymbol{\mu}_{\mathrm{s}}}{\lambda^2} \tag{3}$$

where the spin-diffusion length $\lambda = \sqrt{D\tau_{\mathrm{sf}}}$ is expressed in terms of the charge diffusion constant D and spin-flip relaxation time τ_{sf} [8]. For films with thickness t_{N} in the $\mathbf{z}$ direction,

$$\boldsymbol{\mu}_{\mathrm{s}}(z) = \mathbf{A}e^{-z/\lambda} + \mathbf{B}e^{z/\lambda} \tag{4}$$

where the constant column vectors $\mathbf{A}$ and $\mathbf{B}$ are determined by the boundary

conditions at the interfaces. According to Eq. (2), the spin current in N consists of diffusion and spin Nernst drift contributions. Since our system is homogeneous in the x-y plane, we focus on the spin current density flowing in the **z** direction,

$$\mathbf{j}_{\mathrm{s}}^{\mathrm{z}}(z) = \frac{\sigma}{2e}\partial_z \boldsymbol{\mu}_{\mathrm{s}} - j_{\mathrm{s0}}^{\mathrm{SN}}\mathbf{y}, \tag{5}$$

where $j_{\mathrm{s0}}^{\mathrm{SN}} = -\theta_{\mathrm{SN}}\sigma S\partial_x T$ is the bare spin Nernst current, i.e., the spin current generated directly by the SNE. The boundary conditions require that $\mathbf{j}_{\mathrm{s}}^{\mathrm{z}}$ is continuous at the interfaces $z = t_{\mathrm{N}}$ and $z = 0$. The spin current at a vacuum (V) interface vanishes, $\mathbf{j}_{\mathrm{s}}(V) = 0$. The spin current density $\mathbf{j}_{\mathrm{s}}^{(\mathrm{F})}$ at a magnetic interface is governed by the spin accumulation and spin-mixing conductance:[4]

$$e\mathbf{j}_{\mathrm{s}}^{(\mathrm{F})}(\mathbf{m}) = G_{\mathrm{r}}\mathbf{m}\times(\mathbf{m}\times\boldsymbol{\mu}_{\mathrm{s}}) + G_{\mathrm{i}}(\mathbf{m}\times\boldsymbol{\mu}_{\mathrm{s}}) \tag{6}$$

where $\mathbf{m} = (m_x, m_y, m_z)^T$ is a unit vector along the magnetization and $G = G_{\mathrm{r}} + \imath G_{\mathrm{i}}$ the complex spin-mixing interface conductance per unit area and $\imath = \sqrt{-1}$. The imaginary part G_{i} can be interpreted as an effective exchange field acting on the spin accumulation. A positive current in Eq. (6) corresponds to up spins flowing from the FMI towards N. With these boundary conditions we determine the coefficients **A** and **B**, which leads to the spin accumulation in the bilayer system

$$\boldsymbol{\mu}_{\mathrm{s}}(z) = \mathbf{y}\mu_s^0\frac{\sinh\frac{2z-t_{\mathrm{N}}}{2\lambda}}{\sinh\frac{t_{\mathrm{N}}}{2\lambda}} - \mathbf{j}_{\mathrm{s}}^{(\mathrm{F})}(\mathbf{m})\frac{2e\lambda}{\sigma}\frac{\cosh\frac{z-t_{\mathrm{N}}}{\lambda}}{\sinh\frac{t_{\mathrm{N}}}{\lambda}} \tag{7}$$

where $\mu_s^0 = (2e\lambda/\sigma)\mathbf{j}_{\mathrm{s0}}^{\mathrm{SN}}\tanh(t_{\mathrm{N}}/2\lambda)$ is the spin accumulation at the interface in the absence of spin transfer, i.e., when $G = 0$. Following Ref. [2], the spin accumulation reads

$$\begin{aligned}\frac{\boldsymbol{\mu}_{\mathrm{s}}(z)}{\mu_{\mathrm{s}}^0} &= \mathbf{y}\frac{\sinh\frac{2z-t_{\mathrm{N}}}{2\lambda}}{\sinh\frac{t_{\mathrm{N}}}{2\lambda}} \\ &\quad - \left[\mathbf{m}\times(\mathbf{m}\times\mathbf{y})\mathrm{Re} + (\mathbf{m}\times\mathbf{y})\mathrm{Im}\right]\frac{2\lambda G}{\sigma + 2\lambda G\coth\frac{t_{\mathrm{N}}}{\lambda}}\frac{\cosh\frac{z-t_{\mathrm{N}}}{\lambda}}{\sinh\frac{t_{\mathrm{N}}}{\lambda}}\end{aligned} \tag{8}$$

which leads to the distributed spin current in the N

$$\frac{\mathbf{j}_{\mathrm{s}}^{z}(z)}{j_{\mathrm{s0}}^{\mathrm{SN}}} = \mathbf{y}\frac{\cosh\frac{2z-t_{\mathrm{N}}}{2\lambda} - \cosh\frac{t_{\mathrm{N}}}{2\lambda}}{\cosh\frac{t_{\mathrm{N}}}{2\lambda}} - [\mathbf{m}\times(\mathbf{m}\times\mathbf{y})\mathrm{Re} + (\mathbf{m}\times\mathbf{y})\mathrm{Im}]\,\frac{2\lambda G\tanh\frac{t_{\mathrm{N}}}{2\lambda}}{\sigma + 2\lambda G\coth\frac{t_{\mathrm{N}}}{\lambda}}\frac{\sinh\frac{z-t_{\mathrm{N}}}{\lambda}}{\sinh\frac{t_{\mathrm{N}}}{\lambda}} \tag{9}$$

The ISHE drives a charge current in the x-y plane by the diffusion spin current component flowing along the **z** direction. The total longitudinal (along **x**) and transverse or Hall (along **y**) charge currents become

$$\frac{\mathbf{j}_{\mathrm{c,long}}(z)}{j_{\mathrm{c0}}} = 1 + \theta_{\mathrm{SH}}\theta_{\mathrm{SN}}\left[\frac{\cosh\frac{2z-t_{\mathrm{N}}}{2\lambda}}{\cosh\frac{t_{\mathrm{N}}}{2\lambda}} + (1-m_y^2)\mathrm{Re}\frac{2\lambda G\tanh\frac{t_{\mathrm{N}}}{2\lambda}}{\sigma + 2\lambda G\coth\frac{t_{\mathrm{N}}}{\lambda}}\frac{\sinh\frac{z-t_{\mathrm{N}}}{\lambda}}{\sinh\frac{t_{\mathrm{N}}}{\lambda}}\right] \tag{10}$$

$$\frac{\mathbf{j}_{\mathrm{c,trans}}(z)}{j_{\mathrm{c0}}} = \theta_{\mathrm{SH}}\theta_{\mathrm{SN}}(m_x m_y\mathrm{Re} - m_z\mathrm{Im})\frac{2\lambda G\tanh\frac{t_{\mathrm{N}}}{2\lambda}}{\sigma + 2\lambda G\coth\frac{t_{\mathrm{N}}}{\lambda}}\frac{\sinh\frac{z-t_{\mathrm{N}}}{\lambda}}{\sinh\frac{t_{\mathrm{N}}}{\lambda}} \tag{11}$$

For an open-circuit configuration for the charge current, the observable in the experiment (thermal voltage) is expressed as an electric field $\mathbf{E}_{\mathrm{th}} = E_{\mathrm{th,x}}\mathbf{x} + E_{\mathrm{th,y}}\mathbf{y}$ which compensates $j_{\mathrm{c,long}}$ and $j_{\mathrm{c,trans}}$:

$$E_{\mathrm{th,x}} = \left[1 + \theta_{\mathrm{SH}}\theta_{\mathrm{SN}}\left[\frac{\cosh\frac{2z-t_{\mathrm{N}}}{2\lambda}}{\cosh\frac{t_{\mathrm{N}}}{2\lambda}} + (1-m_y^2)\mathrm{Re}\frac{2\lambda G\tanh\frac{t_{\mathrm{N}}}{2\lambda}}{\sigma + 2\lambda G\coth\frac{t_{\mathrm{N}}}{\lambda}}\frac{\sinh\frac{z-t_{\mathrm{N}}}{\lambda}}{\sinh\frac{t_{\mathrm{N}}}{\lambda}}\right]\right] S\partial_x T$$

$$E_{\mathrm{th,y}} = \theta_{\mathrm{SH}}\theta_{\mathrm{SN}}(m_x m_y\mathrm{Re} - m_z\mathrm{Im})\frac{2\lambda G\tanh\frac{t_{\mathrm{N}}}{2\lambda}}{\sigma + 2\lambda G\coth\frac{t_{\mathrm{N}}}{\lambda}}\frac{\sinh\frac{z-t_{\mathrm{N}}}{\lambda}}{\sinh\frac{t_{\mathrm{N}}}{\lambda}} S\partial_x T. \tag{12}$$

Averaging the electric field components along **x** and **y** over the film thickness z, we obtain

$$\overline{E_{\mathrm{th,x}}} = [S + \Delta S_0 + \Delta S_1(1-m_{\mathrm{y}}^2)]\partial_x T \tag{13}$$

$$\overline{E_{\mathrm{th,y}}} = (\Delta S_1 m_x m_y - \Delta S_2 m_z)\partial_x T \tag{14}$$

which includes

$$\Delta S_0 = S\theta_{\mathrm{SH}}\theta_{\mathrm{SN}}\frac{2\lambda}{t_{\mathrm{N}}}\tanh\frac{t_{\mathrm{N}}}{2\lambda} \tag{15}$$

$$\Delta S_1 = -S\theta_{\mathrm{SH}}\theta_{\mathrm{SN}}\frac{\lambda}{t_{\mathrm{N}}}\mathrm{Re}\frac{2\lambda G\tanh^2\frac{t_{\mathrm{N}}}{2\lambda}}{\sigma + 2\lambda G\coth\frac{t_{\mathrm{N}}}{\lambda}} \tag{16}$$

$$\Delta S_2 = -S\theta_{\mathrm{SH}}\theta_{\mathrm{SN}}\frac{\lambda}{t_{\mathrm{N}}}\mathrm{Im}\frac{2\lambda G\tanh^2\frac{t_{\mathrm{N}}}{2\lambda}}{\sigma + 2\lambda G\coth\frac{t_{\mathrm{N}}}{\lambda}} \tag{17}$$

ΔS_1 (caused mainly by G_r) contributes to the SMT, while ΔS_2 (caused mainly by G_i) contributes only when there is a magnetization component normal to the plane (anomalous Nernst effect).
The voltages detected in our experiments are linked to the electric field components in Eq. (13) via

$$V_{\mathrm{thermal}} = -\int \overline{E_{\mathrm{th,x}}}(\mathbf{x})d\mathbf{x} \tag{18}$$

Thus, the spin current generated by the SNE generates additional contributions ΔS_0 and ΔS_1 to the Seebeck coefficient. For longitudinal thermopower measurements, we therefore expect a magnetization orientation dependent contribution to S and thus to the thermopower voltage V_{thermal} proportional to $\Delta S_1(1-m_{\mathrm{y}}^2)$. This is caused by the spin transport across the N|FMI interface described mainly by G_r. Comparing Eq. (13) with the longitudinal SMR (cf. Ref. [2]), we find the same magnetization orientation dependence proportional to m_{y}^2. We thus expect that the SMT has a similar fingerprint as the SMR, with modulations in V_{thermal} when the magnetization of the FMI (the YIG) is rotated in planes spanned by $\mathbf{x}$ and $\mathbf{y}$ as well as in planes spanned by $\mathbf{z}$ and $\mathbf{y}$, while we expect no modulations in V_{thermal} when the magnetization of the FMI is rotated in ($\mathbf{x}$,$\mathbf{z}$) plane.

1.2 First principles description of the spin Nernst effect

In an independent theoretical effort, we derive the magnitude of the spin Hall and the spin Nernst angles in bulk platinum from first principles. Assuming a constant chemical potential and considering both an electric field $\mathbf{E}$ and a temperature gradient ∇T as generating forces for a spin-polarized current

$$J^{\mathrm{s}} = -e\mathcal{L}^{\mathrm{sc}}\mathbf{E} - \mathcal{L}^{\mathrm{sq}}\nabla T/T \tag{19}$$

the tensors $\mathcal{L}^{\mathrm{sc}}$ and $\mathcal{L}^{\mathrm{sq}}$ describe the response of the system under investigation. For a spin-polarization axis along $\mathbf{i}$, the spin current along $\mathbf{j}$, and the electric field along $\mathbf{k}$, with $\mathrm{i(j,k)} \in \{\mathrm{x,y,z}\}$, one obtains for the former

$$\mathcal{L}_{\mathrm{jk}}^{\mathrm{sc,i}}(T) = -\frac{1}{e}\int dE\,\sigma_{\mathrm{jk}}^{\mathrm{sc,i}}(E)D(E,E_F,T)\ , \tag{20}$$

with $D(E,E_F,T) = \left(-\frac{\partial f(E,E_F,T)}{\partial E}\right)$, $f(E,E_F,T)$ the Fermi function, E_F the Fermi energy (or chemical potential of the electrons at $T = 0\,\mathrm{K}$), and the

energy-dependent spin conductivity $\sigma^{\mathrm{sc,i}}_{\mathrm{jk}}(E)$ at T. The latter is obtained by applying the Kubo-Bastin linear response formalism and an appropriate form of the spin current density operator [9, 10] in combination with the relativistic KKR (Korringa-Kohn-Rostocker) band structure method [11, 12, 13] and the alloy analogy model [14] to account for thermally-induced structural disorder.

In analogy to the relation between the transport coefficient $L^{\mathrm{cq}}_{\mathrm{jk}}(T)$ and the energy-dependent electrical conductivity $\sigma^{\mathrm{cc}}_{\mathrm{jk}}(E)$ [15], the temperature-dependent spin transport coefficient $\mathcal{L}^{\mathrm{sq,i}}_{\mathrm{jk}}(T)$ is expressed in terms of the energy-dependent spin conductivity $\sigma^{\mathrm{sc,i}}_{\mathrm{jk}}(E)$:

$$\mathcal{L}^{\mathrm{sq,i}}_{\mathrm{jk}}(T) = -\frac{1}{e}\int dE\, \sigma^{\mathrm{sc,i}}_{\mathrm{jk}}(E)\, D(E, E_F, T)\, (E - E_F)\ . \tag{21}$$

Considering a temperature gradient ∇T without an external electric field $\mathbf{E}$, the electric current density

$$\mathbf{j}^{\mathrm{c}} = -eL^{\mathrm{cc}}\mathbf{E} - L^{\mathrm{cq}}\nabla T/T \tag{22}$$

vanishes when open-circuit conditions are imposed. Equation (22) implies that an internal electric field

$$\mathbf{E} \;=\; -\frac{1}{eT}(L^{\mathrm{cc}})^{-1}L^{\mathrm{cq}}\nabla T = S\,\nabla T \tag{23}$$

compensates the charge imbalance induced by ∇T, where S is the thermo-(magneto-) electric tensor. The ratios $\mathcal{L}^{\mathrm{sc,i}}_{\mathrm{jk}}/L^{\mathrm{cc}}_{\mathrm{kk}} = \theta_{\mathrm{SH}}$, i.e. the spin Hall angle (θ_{SH}), and $\mathcal{L}^{\mathrm{sq,i}}_{\mathrm{jk}}/L^{\mathrm{cq}}_{\mathrm{kk}} = \theta_{\mathrm{SN}}$, i.e. the corresponding spin Nernst angle (θ_{SN}), express the efficiency of conversion of a longitudinal charge current density into a transverse spin current density, generated by an electric field or a temperature gradient, respectively (see Eq. (2)). Since the conversion of the **y**-polarized spin current along **z**, generated by the SNE, back into an electric field along **x** is expressed by the inverse spin Hall conductivity $\sigma'^{,\mathrm{y}}_{\mathrm{xz}} = \sigma^{\mathrm{y}}_{\mathrm{xz}} = -\sigma^{\mathrm{y}}_{\mathrm{zx}}$ (See Ref. [16]), the relevant (inverse) spin Hall angle θ_{SH} is the ratio $\mathcal{L}^{\mathrm{sc,y}}_{\mathrm{xz}}/\mathcal{L}^{\mathrm{cc}}_{\mathrm{xx}} = -\mathcal{L}^{\mathrm{sc,y}}_{\mathrm{zx}}/\mathcal{L}^{\mathrm{cc}}_{\mathrm{xx}}$. The spin Nernst angle θ_{SN} is given by $\mathcal{L}^{\mathrm{sq,y}}_{\mathrm{zx}}/\mathcal{L}^{\mathrm{cq}}_{\mathrm{xx}}$. Using Eq. (23) and the expressions for the electrical and thermoelectrical conductivities in terms of Eqs. (20) and (21), σ_{xx} ($\sigma^{\mathrm{y}}_{\mathrm{zx}}$) $= -eL^{\mathrm{cc}}_{\mathrm{xx}}$ ($-e\mathcal{L}^{\mathrm{sc,y}}_{\mathrm{zx}}$) and α_{xx} ($\alpha^{\mathrm{y}}_{\mathrm{zx}}$) $= -\frac{1}{T}L^{\mathrm{cq}}_{\mathrm{xx}}$ ($-\frac{1}{T}\mathcal{L}^{\mathrm{sq,y}}_{\mathrm{zx}}$), their (temperature-dependent) ratio can be written as

$$\frac{\theta_{\mathrm{SH}}}{\theta_{\mathrm{SN}}}(T) = \frac{-\sigma^{\mathrm{y}}_{\mathrm{zx}}(T)}{\sigma_{\mathrm{xx}}(T)}\frac{\alpha_{\mathrm{xx}}(T)}{\alpha^{\mathrm{y}}_{\mathrm{zx}}(T)} = +S_{\mathrm{xx}}(T)\frac{\sigma^{\mathrm{y}}_{\mathrm{zx}}(T)}{\alpha^{\mathrm{y}}_{\mathrm{zx}}(T)}\ . \tag{24}$$

Following the notation of the previous section, σ_{xx} corresponds to σ in Eq. (2), $-\sigma^{y}_{zx}$ to $\theta_{SH}\sigma$, α_{xx} to $-\sigma S$ and α^{y}_{zx} to $-\theta_{SN}\sigma S$. The energy-dependent conductivities entering Eqs. (20) and (21) and the corresponding expressions for the longitudinal transport coefficients were calculated for a set of energy points E around E_F for each temperature T accounting for the effect of uncorrelated lattice displacements via the alloy analogy model [13].

Figure 1 shows the calculated values of $\sigma_{xx}(E)$ (top) and $\sigma^{y}_{zx}(E)$ (bottom) for $T = 200\,\mathrm{K}$ (blue pluses), $250\,\mathrm{K}$ (black triangles), and $300\,\mathrm{K}$ (red squares). The temperature-dependent Seebeck coefficient, spin Hall conductivity and spin Nernst conductivity subsequently obtained from these are shown in Fig. (2) at the top left, top right and bottom left, respectively.

They were calculated using the fitted $\sigma(E)$ curves from Fig. 1 in the integrands of Eqs. (20) and (21), i.e. without making use of the Sommerfeld approximation, which would lead to the Mott relations for the Seebeck coefficient and spin Nernst conductivity. Finally, the ratio of the spin Hall and the spin Nernst angle, expressed by the above quantities as in Eq. (24), is shown as a function of temperature in Fig. (2), bottom right. As can be seen, for the conventions and definitions chosen here, the two angles have opposite signs for the whole temperature range considered here and θ_{SN} is larger than θ_{SH} for $T > 210$ K.

1.3 Experimental methods

The sample used in this study is a YIG|Pt thin film heterostructure. YIG hereby stands for Yttrium Iron Garnet ($Y_3Fe_5O_{12}$). The 40 nm thick YIG layer was epitaxially grown on a 500 μm thick, single crystalline, (111)-oriented Gadolinium Gallium Garnet (GGG, $Gd_3Ga_5O_{12}$) substrate via pulsed laser deposition using a stoichiometric targets [17]. The deposition was carried out in an oxygen atmosphere of 25 μbar, with a laser energy density of $2\,\mathrm{J/cm^2}$ at the target, and a substrate temperature of 550 °C. The YIG layer is capped in-situ, without breaking the vacuum, with a 4.1 nm thick Pt layer via electron beam evaporation at room temperature. The thicknesses of the YIG and Pt layer were determined by high-resolution X-ray reflectometry (HR-XRR) to $t_F = (40 \pm 2)\,\mathrm{nm}$ and $t_N = (4.1 \pm 0.2)\,\mathrm{nm}$, respectively. High-resolution X-ray diffraction (HR-XRD) measurements confirmed the polycrystallinity of the Pt thin film and revealed no secondary phases.

After pre-characterization, the sample was patterned into a Hall bar structure with the additional on-chip heater strip as sketched in Fig. 3(a) via optical lithography and Ar ion beam milling. The Hall bar has a width of $w = 250\,\mu$m, a length of $l = 3150\,\mu$m and a contact separation of $s = 625\,\mu$m, the heating strip along $\mathbf{y}$ is $w_h = 250\,\mu$m wide and $l_h = 1175\,\mu$m long, the distance between

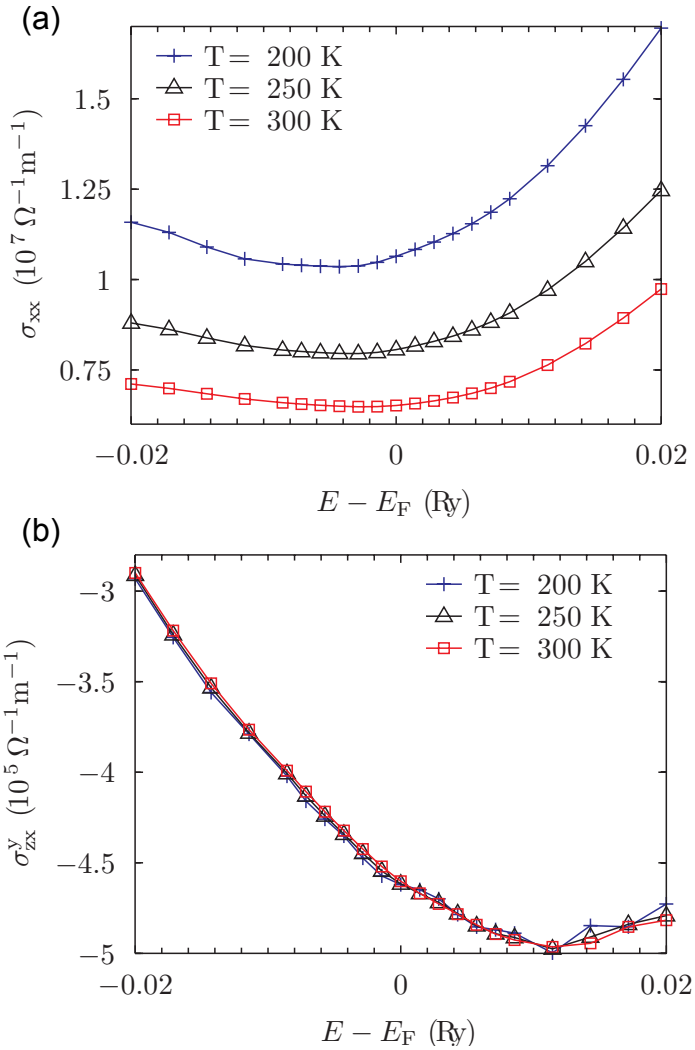

Figure 1: *Energy dependence of longitudinal charge (a) and transverse spin-polarized conductivity (b), $\sigma_{xx}(E)$ and $\sigma^y_{zx}(E)$, respectively. Calculations were performed at fixed temperatures $T = 200 - 300\,\mathrm{K}$ in steps of $10\,\mathrm{K}$ using the alloy analogy model. Only the results for $200\,\mathrm{K}$ (blue pluses), $250\,\mathrm{K}$ (black triangles), and $300\,\mathrm{K}$ (red squares) are shown here.*

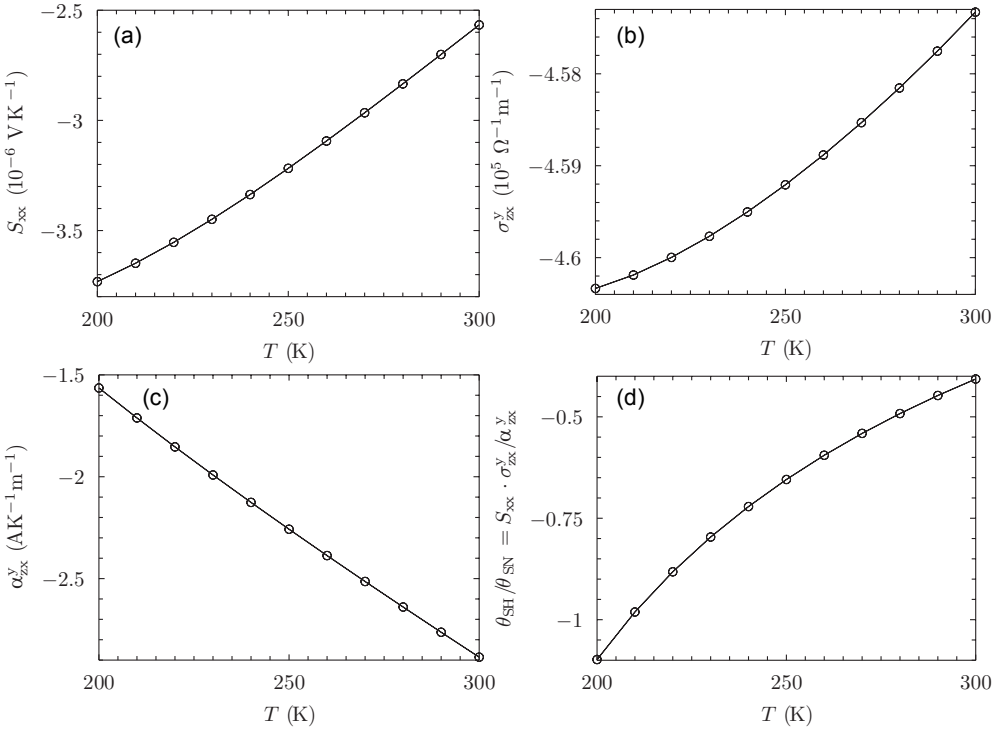

Figure 2: *Temperature dependence of* ***(a)*** *the Seebeck coefficient* S_{xx}*,* ***(b)*** *the spin Hall conductivity* σ^{y}_{zx}*,* ***(c)*** *the spin Nernst conductivity,* α^{y}_{zx}*, and* ***(d)*** *of the ratio* θ_{SH}/θ_{SN} *as defined in Eq. (24).*

Hall bar and heating strip is $d = 250\,\mu$m. The sample is mounted onto a massive copper sample holder with one end, using GE 7031 thermally conductive varnish. The other end of the sample (with the heater strip) is connected to a Vespel block, again with GE varnish. In this way, the sample is thermally anchored to the sample holder on one end, and can be heated on the other, thermally 'isolated' end attached to the Vespel. All bonding pads at the Hall bar as well as the heater strip were connected to a printed circuit connector board with 30 μm thick Al wires via wedge bonding. The bonded sample is mounted on a dedicated magnet cryostat dipstick. This dipstick is enclosed in an evacuated steel jacket, such that the sample resides in vacuum. A pressure of $(5 \pm 1) \times 10^{-6}$ mbar within the sample space was kept constant during the experiments.

Our Oxford Instruments 3D vector magnet cryostat, equipped with a variable temperature insert (VTI), allows to apply magnetic fields $\leq 2\,$T in any desired orientation to the sample, while at the same time adjusting the VTI temperature

in the range $2\,\mathrm{K} \leq T \leq 300\,\mathrm{K}$. In all magneto-transport experiments discussed here, we used external magnetic field magnitudes $\mu_0 H_{\mathrm{ext}} \geq 500\,\mathrm{mT}$, which exceed the saturation magnetization $\mu_0 M_{\mathrm{Sat}}^{\mathrm{F}} \approx 170\,\mathrm{mT}$ of our YIG thin films at room temperature by at least about 3 times [18]. Thus, the magnetization vector $\mathbf{M}$ of the YIG layer is always aligned parallel to $\mu_0 \mathbf{H}_{\mathrm{ext}}$.

On-chip thermometry

The base temperature of the sample holder (to which the cold end of the sample is anchored) was set to 220 K and stabilized using the PID feedback loop of a LakeShore LS340 temperature controller. Using the on-chip thermometry described below, we found that the temperature was stable within fluctuations of $\Delta T_{\mathrm{base}} = 3\,\mathrm{mK}$ (given by the temperature fluctuations displayed by the temperature controller) after a thermalization time of six hours. By applying heating currents of up to 20 mA to the heater strip next to the Hall bar by means of an Agilent B2900A Precision Source Measure Unit, corresponding to heating powers up to 286 mW, we created a temperature gradient along the Hall bar direction $\mathbf{x}$. The temperature profile along the Hall bar was determined by resistive thermometry (see Fig. 3) along two transverse Hall bar contact pairs separated by a distance of $l_1 = 2500\,\mu\mathrm{m}$ using two Keithley K2400 Source Measure Units and currents of $10\,\mu\mathrm{A}$ [cf. Fig. 3(a)]. In order to calibrate our 'on-chip Pt temperature sensors', we first stabilized the sample (viz the sample holder) temperature to 220 K (no heating current applied to the on-chip heater strip) and measured $R_{1,2}(T)$ at either end of the Hall bar while sweeping the sample temperature with 1 K/min up to 270 K using the temperature control of the dipstick just described. These resistance vs. temperature curves, shown in Fig. 3 (c) are used as calibration curves. After that, we again cooled the sample down to the base temperature of 220 K and determined $R_{1,2}(P_{\mathrm{heater}})$ while applying different heating powers up to 286 mW [cf. Fig. 3 (b)]. Comparing $R_{1,2}(P_{\mathrm{heat}})$ with the calibration curves taken before allow to recalculate the local sample temperature, such that a temperature profile of the sample with an experimental error of $\Delta T_{\mathrm{local}} \approx 0.4\,\mathrm{K}$ [see Fig. 3 (d)] is established. Please note that the error of $\Delta T_{\mathrm{local}} \approx 0.4\,\mathrm{K}$ is determined at the platinum strips by resistive thermometry , while the fluctuation $\Delta T_{\mathrm{base}} = 3\,\mathrm{mK}$ of the heat bath was determined by a Cernox temperature sensor at the sample holder.

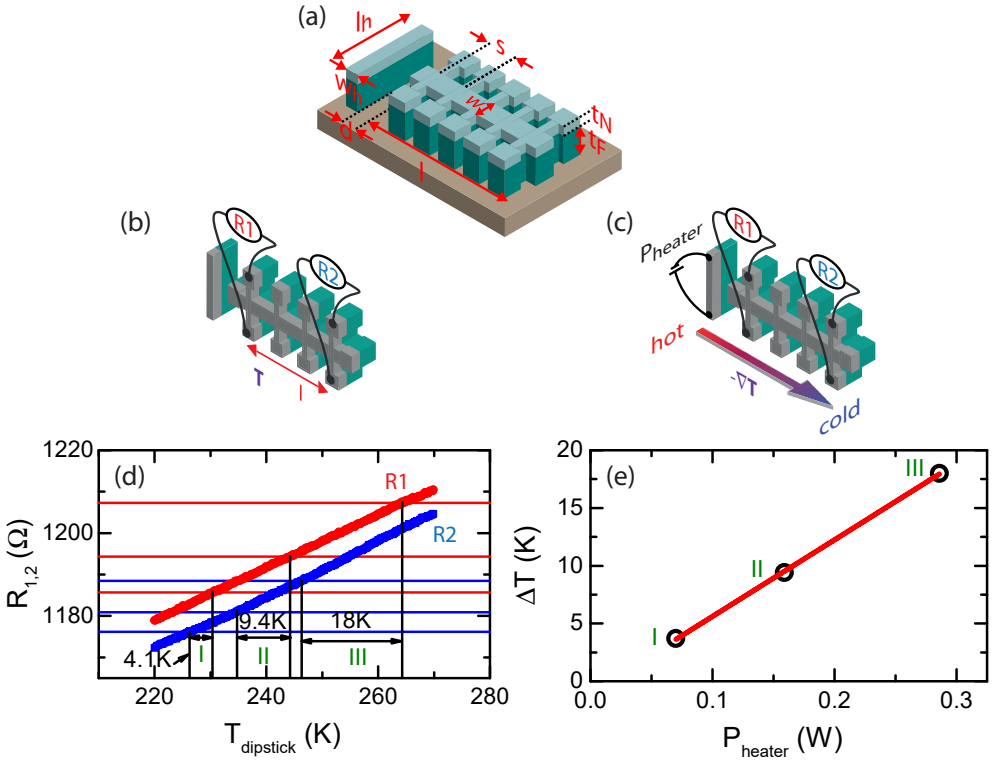

Figure 3: ***(a)*** *Experimental setup for SMT experiments. A YIG|Pt ($t_F = 40\,\mathrm{nm}/t_N = 4.1\,\mathrm{nm}$) thin film sample is patterned into a Hall bar geometry (width $w = 250\,\mu\mathrm{m}$, length $l = 3150\,\mu\mathrm{m}$). An additional heater strip (width $w_h = 250\,\mu\mathrm{m}$, length $l_h = 1175\,\mu\mathrm{m}$) is defined along* $\mathbf{y}$*, separated by $d = 250\,\mu\mathrm{m}$ beyond the top of the Hall bar.* ***(b,c)*** *Concept of the resistive thermometry: In a first step* ***(b)****, the resistance vs. temperature curves $R_1(T)$ and $R_2(T)$ along two transverse contact pairs are measured, while no power is applied to the heater. Here, the sample temperature is homogeneous and given by the dipstick temperature T_{dipstick}. $R_1(T)$ and $R_2(T)$ serve as calibration curves for the thermometry. Afterwards* ***(c)****, the dipstick temperature is kept constant ($T_{\mathrm{base}} = 220\,\mathrm{K}$) while the electric power P_{heater} at the on-chip heater is increased stepwise. R_1 and R_2 are now taken as a function of P_{heater}. Panel* ***(d)*** *shows both the calibration curves $R_1(T)$ and $R_2(T)$ and the heater dependent resistance values (horizontal lines). From those calibration curves, the local temperatures can be calculated as a function of P_{heater}. Here, we show three different heater powers (I) $P_{\mathrm{heater}} = 70\,\mathrm{mW}$, (II) $P_{\mathrm{heater}} = 159\,\mathrm{mW}$ and (III) $P_{\mathrm{heater}} = 286\,\mathrm{mW}$. The extracted temperature differences ΔT along the Hall bar as a function of P_{heater} are shown in* ***(e)****.*

Power scaling

We find a linear dependence of the temperature difference along the Hall bar on the applied heating power. Accordingly, we expect an almost linear scaling between thermopower and applied heater power [19]. The maximum generated temperature difference between the contacts separated by the distance l_1 was found to be 18.0 K for $P_{\mathrm{heater}} = 286\,\mathrm{mW}$. In Fig. 4, we show the thermopower voltage taken along the Hall bar direction for different, constant heating currents applied to the on-chip heater. Although the presence of a magnetic field usually is not required for the determination of the thermoelectric voltages, we applied a magnetic field of 1 T along $\mathbf{x}$ in theses experiments, in order to orient the magnetization of the YIG film and thus induce a reproducible contribution from the SMT. As evident from Fig. 4, we find an increase in the absolute value of V_{thermal} with increasing I_{heater}, as expected for a thermopower effect from $V_{\mathrm{therm}} = S\Delta T$. For the highest heater current applied, we extract $S = -3.7\mu\mathrm{V/K}$ using $\Delta T = 18.0\,\mathrm{K}$. With respect to the average sample temperature $\bar{T} = (T_{\mathrm{hot}} - T_{\mathrm{cold}})/2 = 255.4\,\mathrm{K}$ extracted from the resistive thermometry shown above, S is in excellent agreement with the literature value for Pt, $S(260\,\mathrm{K}) = -3.8\mu\mathrm{V/K}$ [19].

Power modulation

To generate large temperature differences along the Hall bar, we use the on-chip heating strip consisting of the same YIG|Pt hybrid structure as the Hall bar. Since the YIG|Pt heterostructure shows spin Hall magnetoresistance (SMR) (i.e., a magnetization-orientation dependent resistance), a modulation of the heating power $P_{\mathrm{heater}} = R_{\mathrm{heater}} \times I^2_{\mathrm{heater}}$ with magnetization orientation must be taken into account. We measured the magnitude of the SMR effect in our sample to be $\Delta\rho_1/\rho_0 = (1.0 \pm 0.1) \times 10^{-3}$ at $T_{\mathrm{base}} = 220\,\mathrm{K}$ with $P_{\mathrm{heater}} = 286\,\mathrm{mW}$ applied to the heating strip. To avoid a SMR-based modulation of the heater power in our magnetization-orientation dependent thermopower measurements, we use a closed-loop control to adjust the applied heater current depending on magnetization orientation, such as to provide a constant heater power of $P_{\mathrm{heater}} = 286.30\,\mathrm{mW}$. Using this method, the applied heater power is stabilized with fluctuations smaller than 0.04 mW, see Fig. 5.

1.4 Fingerprint of the SMT

For SMT experiments, we remove all current sources from the Hall bar ($I_{\mathrm{q}} = 0$) and thermalize the sample to $T_{\mathrm{base}} = 220\,\mathrm{K}$. In order to apply a temperature

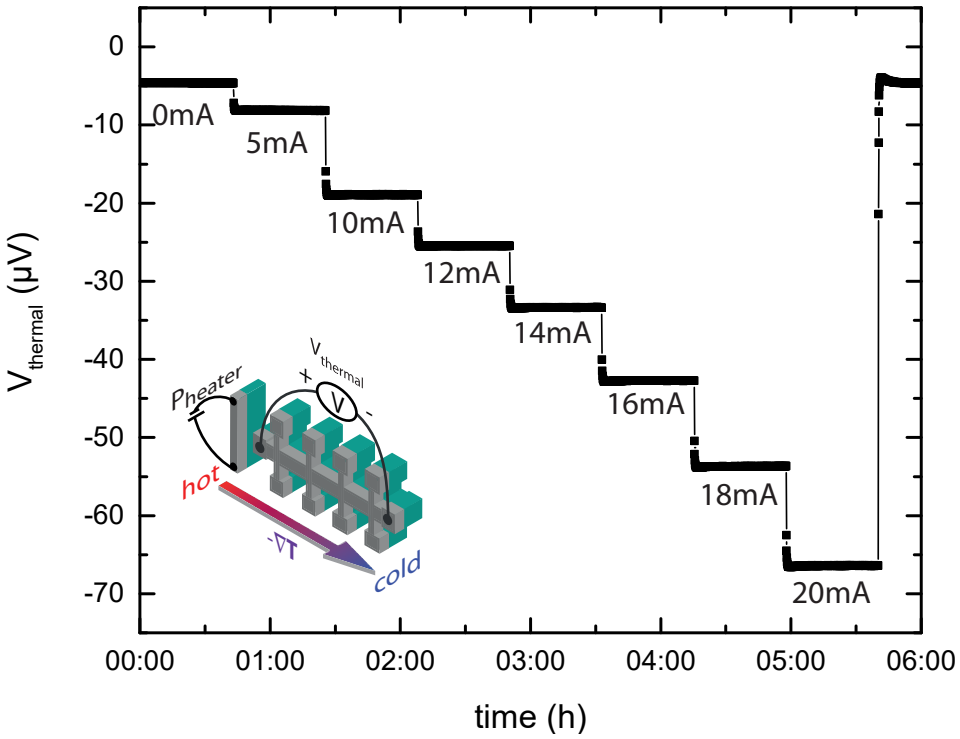

Figure 4: *Longitudinal thermal voltage* V_{thermal} *taken for a stepwise increase of currents applied to the heater strip.* 20 mA *correspond to* $P_{\mathrm{heater}} = 286\,\mathrm{mW}$.

gradient along $\mathbf{x}$ as a driving force, we bias the on-chip heater with the appropriate, magnetization orientation-dependent heater current, such that a constant heater power of $P_{\mathrm{heater}} = 286\,\mathrm{mW}$ independent of the magnetic field orientation is applied. We rotate a constant external magnetic field $\mu_0\mathbf{H}$ in the three orthogonal planes defined by $\mathbf{x}$, $\mathbf{y}$, and $\mathbf{z}$ and detect the longitudinal and transverse ($V_{\mathrm{thermal,trans}}$) voltages with an Agilent 34420A nanovoltmeter. We use a digital filter to detect the signal and average over 100 power line cycles using internal filter functions. We define the longitudinal $E_{\mathrm{thermal}} = -V_{\mathrm{thermal}}/l_{\mathrm{long}}$ and transverse $E_{\mathrm{thermal,trans}} = -V_{\mathrm{thermal,trans}}/l_{\mathrm{trans}}$ electric fields, where l_{long} and l_{trans} are the edge-to-edge separations of the contacts (Al-wire bonds) used for measuring V_{thermal} and $V_{\mathrm{thermal,trans}}$, respectively.

Figure 6 shows the evolution of E_{thermal} and $E_{\mathrm{thermal,trans}}$ as a function of the magnetization orientation while rotating the external magnetic field $\mu_0 H = 1\,\mathrm{T}$ and 0.5 T in in-plane (ip, $(\mathbf{x},\mathbf{y})$-plane, panels d, g, j, and m), out-of-plane perpendicular $\mathbf{x}$ (oopx, $(\mathbf{y},\mathbf{z})$-plane, panels e, h, k, and n) and out-of-plane

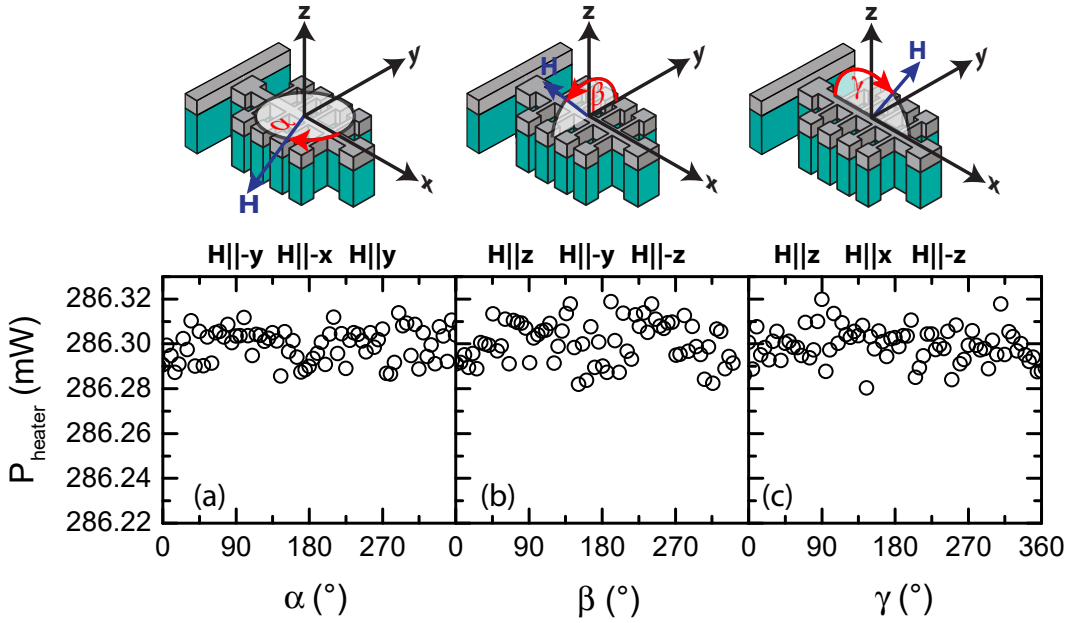

Figure 5: *Heater power P_{heater} as a function of the YIG magnetization orientation in* ***(a)*** *ip,* ***(b)*** *oopx and* ***(c)*** *oopy configuration for $\mu_0 H = 1\,\text{T}$. During this measurement, we modulated the current I_{heater} applied to the on-chip heater to keep the heating power constant.*

perpendicular **y** (oopy, (**x**, **z**)-plane, panel f, i, l, and o) configuration. For the ip data of $E_{\text{thermal}}(1\text{ T})$ [cf. Fig. 6(d),(j)], we find a $\sin^2\alpha$ dependence with $\Delta E_{\text{thermal}}(1\text{ T}) \approx -30\,\mu\text{V/m}$, $\Delta E_{\text{thermal}}(0.5\text{ T}) \approx -28\,\mu\text{V/m}$ on top of the thermopower signal given by the Seebeck effect of Pt. This modulation is smallest for $\mathbf{H} \parallel \mathbf{x}$ and $\mathbf{H} \parallel -\mathbf{x}$, and largest for $\mathbf{H} \parallel \mathbf{y}$ and $\mathbf{H} \parallel -\mathbf{y}$.

In the oopx rotation geometry [cf. Fig. 6(e),(k)], we find a similar, $\cos^2\beta$ modulation on top of the thermopower signal with an amplitude $\Delta E_{\text{thermal}}(1\text{ T}) \approx -31\,\mu\text{V/m}$ and $\Delta E_{\text{thermal}}(0.5\text{ T}) \approx -29\,\mu\text{V/m}$. Again, a maximum is recorded for $\mathbf{H} \parallel \mathbf{y}$ and $\mathbf{H} \parallel -\mathbf{y}$ and the signal level coincides in good approximation with the one found for the ip rotation. For this oopx geometry, the minima are located at $\mathbf{H} \parallel \mathbf{z}$ and $\mathbf{H} \parallel -\mathbf{z}$ and the voltage level for $\mathbf{H} \parallel \mathbf{z}$ is in good agreement with the signal detected at $\mathbf{H} \parallel \mathbf{x}$ in ip rotations.

For the oopy rotation [cf. Fig. 6(f),(l)], however, we find no angular dependence of E_{thermal} within the noise level of our voltage measurement.

For the transverse thermopower signal $E_{\text{therm,trans}}$, we observe for the ip rotation plane a $\cos\alpha \sin\alpha$-dependence with a modulation amplitude $\Delta E_{\text{thermal,trans}}(1\text{ T}) \approx -$

$40\,\mu$V/m and $\Delta E_{\text{thermal}}(0.5\text{ T}) \approx -39\,\mu$V/m, in good agreement with the modulation amplitude $\Delta E_{\text{thermal}}$ observed for the longitudinal thermopower and Eqs. (13),(14). As discussed in more detail below, the experimental data can be consistently fitted using one single value for $\Delta E_{\text{thermal}}$ and $\Delta E_{\text{thermal,trans}}$ (E_1 in Eqs. (25) and (26)). The additional magnetic field orientation independent background in $E_{\text{therm,trans}}$ can be attributed to a spurious longitudinal Seebeck signal caused by a small misalignment ($\approx 25\,\mu$m) of the two voltage probes on the Hall bar.

For the oopx and oopy rotation $E_{\text{therm,trans}}$ exhibits a sine dependence, that is dominated by the ordinary Nernst effect of Pt. A more detailed investigation of the field dependence of the modulation amplitude can identify the spin Nernst contributions in the spirit of Ref. [17].

The data sets shown in Fig. 6 and Fig. 3 in the main text can be understood in terms of the spin Nernst magneto-thermopower: In our geometry, the temperature gradient along $\mathbf{x}$ induces a spin Nernst spin current along $\mathbf{z}$ with spin polarization $\mathbf{s} \parallel \mathbf{y}$. Thus, $\mathbf{H} \parallel \mathbf{y}$ and $\mathbf{H} \parallel -\mathbf{y}$ correspond to the spin current open circuit boundary condition, since a spin transfer towards the YIG is prohibited for $\mathbf{H} \parallel \mathbf{s} \parallel \mathbf{y}$. On the other hand, both $\mathbf{H} \parallel \pm\mathbf{x}$ and $\mathbf{H} \parallel \pm\mathbf{z}$ correspond to perfect spin current short-circuit boundary conditions since they allow for a spin transfer. We compare the measurements with Eqs. (13),(14) in the theory section, by the red lines in Fig. 6 that represent a simulation for E_{therm} and $E_{\text{therm,trans}}$ based on the following set of equations:

$$E_{\text{therm}} = E_0 - E_1 m_{\text{y}}^2, \tag{25}$$

$$E_{\text{therm,trans}} = E_{\text{off}} + E_1 m_x m_y - E_2 m_z, \tag{26}$$

and assuming that the magnetization $\mathbf{m}$ is always aligned parallel with the external applied magnetic field $\mathbf{H}$. The field-independent parameters $E_0 = 25.51$ mV/m, $E_1 = 42\ \mu$V/m, $E_{\text{off}} = 620\ \mu$V/m, $E_2 = 42\ \mu$V/m lead to an excellent agreement within the noise limit, such that the experimental set of data can completely be understood in the theoretical framework provided by the spin Nernst magnetothermopower. These findings thus leave little room for alternative explanations. We note that for the parameter E_2 a more systematic investigation in the spirit of Ref. [17] will be necessary to separate Spin Nernst contributions from additional effects like the ordinary Nernst effect.

Spurious effects can be ruled out by the observed angular dependence of the thermopower voltages. For example, ∇T along $\mathbf{z}$ drives a pure spin current along $\mathbf{z}$ with the spin polarization parallel to the magnetization direction of the YIG by the longitudinal spin Seebeck effect [20]. The inverse spin Hall

effect in Pt would generate a $\sin(\alpha)$ and $\cos(\beta)$ modulation of E_{therm} in the $(\mathbf{x},\mathbf{y})$ and $(\mathbf{y},\mathbf{z})$ rotation planes, while for $E_{\mathrm{therm,trans}}$ a $\cos(\alpha)$ and $\cos(\gamma)$ modulation would be present for the $(\mathbf{x},\mathbf{y})$ and $(\mathbf{x},\mathbf{z})$ rotation planes. This is not consistent with the observed angular dependence in the experiment. A temperature gradient along $\mathbf{y}$ would lead to a pure spin current flowing along $\mathbf{z}$ with the spin polarization parallel to the magnetization direction of the YIG because of the transversal spin Seebeck effect [21, 22]. The inverse spin Hall effect in Pt would then generate a $\sin(\alpha)$ and $\cos(\beta)$ modulation of E_{therm} and a $\cos(\alpha)$ and $\cos(\gamma)$ modulation of $E_{\mathrm{therm,trans}}$ in the $(\mathbf{x},\mathbf{y})$, $(\mathbf{y},\mathbf{z})$ and $(\mathbf{x},\mathbf{y})$, $(\mathbf{x},\mathbf{z})$ rotation planes, respectively, which is contradicted by the observations. Moreover, a magnon current driven by ∇T along $\mathbf{x}$ could lead to a pure spin current along $\mathbf{z}$ with a spin polarization parallel to $\mathbf{m}$ of YIG due to the magnon Hall effect [23]. Due to the inverse spin Hall effect in Pt this spin current will lead to a $\sin(\alpha)$ dependence of the longitudinal and a $\cos(\alpha)$ dependence of the transverse thermopower voltage in the $(\mathbf{x},\mathbf{y})$ rotation plane. We do not observe such a modulation in our experiments. Taken together, spurious effects such as the ones mentioned above can be ruled out as the cause for the observed angular dependence of the thermopower signals.

1.5 Power and field dependence

On the same sample, we repeated the angle dependent magneto-thermopower measurements for different heating powers between 100 mW and 286 mW resulting in temperature differences between 7.7 K and 18.0 K along the Hall bar as well as for two different magnetic field strengths (0.5 T and 1 T). To extract the modulation amplitudes $\Delta V_{\mathrm{thermal}}$ and ratios $\Delta V_{\mathrm{thermal}}/V_{\mathrm{thermal}}$ from our experimental data, we performed $\cos^2\delta$ fits.

We observe an increase in the absolute value of the modulation voltage $\Delta V_{\mathrm{thermal}}$ with increasing P_{heater} in ip and oopx rotations. This is shown in Fig. 7(d) and (e) for two different magnetic field magnitudes. For both 0.5 T (red triangles) and 1 T (black squares), $\Delta V_{\mathrm{thermal}}$ increases with increasing P_{heater} and the difference between the 0.5 T and 1 T data points is within the experimental error of ± 5 nV given by the thermal stability of the nanovoltmeters. As the SMT can be interpreted as a modulation on the thermal voltage due to a spin current flow across the YIG|Pt interface, the relative amplitude of the modulation of the longitudinal voltage is expected to be independent of both heating power P_{heater} and external magnetic field strength $\mu_0 H$, as long as a thermally driven spin current is generated. We find that, within the experimental error, the ratio is almost constant as a function of P_{heater} and $\mu_0 H$ for ip and oopx, $\Delta V_{\mathrm{thermal}}/V_{\mathrm{thermal}} \approx 1.2 \times 10^{-3}$. For the temperature range

studied here (the average sample temperature rises with increasing P_{heater}, see Fig. 3), θ_{SH} is known to be almost independent of temperature [24]. Considering $\Delta V_{\mathrm{thermal}}/V_{\mathrm{thermal}} \approx$ const., which is proportional to $\theta_{\mathrm{SH}}\theta_{\mathrm{SN}}$, the data in Fig. 7(d) and (e) suggest that the temperature dependence of the spin Nernst angle θ_{SN} is rather weak.
The power dependence of the oopy signal is depicted in Fig. 7(f). As stated by Eq. (13), we expect a constant SMT signal as a function of the magnetization orientation in this geometry. While $\Delta V_{\mathrm{thermal}}$ scales with P_{heater} [cf. Fig. 7(d, e)] for ip and oopx rotations, we find that the modulation amplitude observed in oopy is almost constant [$\Delta V_{\mathrm{thermal}}^{\mathrm{oopy}} \approx -25\,\mathrm{nV}$, cf. Fig. 7(f)].Thus, the origin of the modulation in oopy rotations is not related to the spin Nernst magneto-thermopower. However, this power independence can not be explained by the interpretation of $\Delta V_{\mathrm{thermal}}^{\mathrm{oopy}}$ with a non-vanishing $\mathbf{y}$ component of ∇T. Additionally, $\Delta V_{\mathrm{thermal}}^{\mathrm{oopy}}$ seems to increase with increasing magnetic field strength. The decrease of $\Delta V_{\mathrm{thermal}}^{\mathrm{oopy}}(P_{\mathrm{heater}})$ also results in a negative power dependence of the voltage ratio $\Delta V_{\mathrm{thermal}}^{\mathrm{oopy}}/V_{\mathrm{thermal}}$. With increasing heater power, the voltage modulation in oopy decreases slightly. This again is at odds with the results found for ip and oopx rotations. In conclusion, due to the absence of a power dependence, the modulation of the thermal voltage in oopy rotations can neither be attributed to the SMT concept for $\nabla T \cdot \mathbf{y} \neq 0$, nor to parasitic thermopower effects.

1.6 Calculation of the spin Nernst angle

Now, we utilize the theory of Sec. 1.1 to extract the heat to spin conversion efficiency for Pt, i.e. the spin Nernst angle θ_{SN}. To this end, we calculate the relative thermopower ratio between open and short-circuit spin current boundary conditions,

$$\frac{\Delta V_{\mathrm{thermal}}}{V_{\mathrm{thermal}}} = \frac{V_{\mathrm{thermal}}(\mathbf{H} \parallel \mathbf{y}, \mathrm{open}) - V_{\mathrm{thermal}}(\mathbf{H} \perp \mathbf{y}, \mathrm{short})}{V_{\mathrm{thermal}}(\mathbf{H} \parallel \mathbf{y}, \mathrm{open})}. \tag{27}$$

Via Eq. (13), the definitions of $V_{\mathrm{thermal}}(\mathbf{H} \parallel \mathbf{y}, \mathrm{open})$ and $V_{\mathrm{thermal}}(\mathbf{H} \perp \mathbf{y}, \mathrm{short})$ read

$$V_{\mathrm{thermal}}(\mathbf{H} \parallel \mathbf{y}, \mathrm{open}) = -\left(S + \Delta S_0\right) \Delta T \tag{28}$$

and

$$V_{\mathrm{thermal}}(\mathbf{H} \perp \mathbf{y}, \mathrm{short}) = -\left(S + \Delta S_0 + \Delta S_1\right) \Delta T \tag{29}$$

with $\Delta T = T_{\mathrm{hot}} - T_{\mathrm{cold}} > 0$. Thus, $\Delta V_{\mathrm{thermal}}/V_{\mathrm{thermal}}$ corresponds to $-\Delta S_1/\tilde{S}$ with $\tilde{S} = S + \Delta S_0$.
We find $\Delta V_{\mathrm{thermal}}/V_{\mathrm{thermal}} = -100\,\mathrm{nV}/66.225\,\mu\mathrm{V} = -1.5 \times 10^{-3}$ from the raw

data taken at 1 T in the oopx plane shown in Fig. 3(f) in the main text. Based on Eq. (16), we calculate the spin Nernst angle θ_{SN} via

$$\theta_{\mathrm{SN}} \approx -\frac{\Delta S_1}{S}\frac{t_{\mathrm{N}}}{\theta_{\mathrm{SH}}\lambda}\frac{\sigma_{\mathrm{N}} + 2\lambda G_r \coth\frac{t_{\mathrm{N}}}{\lambda}}{2\lambda G_r \tanh^2\frac{t_{\mathrm{N}}}{2\lambda}}. \tag{30}$$

We use $G_r = 4.0 \times 10^{14}\,\Omega^{-1}\mathrm{m}^{-2}$, $\lambda = 1.5\,\mathrm{nm}$ and $\theta_{\mathrm{SH}} = 0.11$ determined in Ref. [24] for YIG|Pt hybrids at $T = 250\mathrm{K}$ comparable to $\bar{T} = 255\mathrm{K}$ used in our thermopower measurements for this sample. With these parameters, we obtain $\theta_{\mathrm{SN}} = -0.20$ from Eq. (30).

It seems surprising that we are able to confirm the sign of the spin Nernst angle by transport experiments. Since SMR depends on the square of the spin Hall angle and cannot be used to measure its sign. Similarly, the SMT depends on the product of θ_{SN} and θ_{SH}, so from these data alone we cannot conclude that $\theta_{\mathrm{SN}} < 0$. We come to our conclusion only because spin pumping measurements conclusively find a positive spin Hall angle in Pt [25]. We note that from a physical point of view $\theta_{\mathrm{SN}} < 0$ is not problematic at all. For $S < 0$, $\theta_{\mathrm{SN}} < 0$ corresponds to $\alpha^{\mathrm{y}}_{\mathrm{zx}} > 0$, i.e. the spin Nernst conductivity is positive. For $\theta_{\mathrm{SH}} > 0$, one finds $\sigma^{\mathrm{y}}_{\mathrm{xz}} > 0$ and accordingly due to Onsager symmetry $\sigma^{\mathrm{y}}_{\mathrm{zx}} < 0$. In the Sommerfeld limit ($T \to 0$) this implies that the spin Hall conductivity $\sigma^{\mathrm{y}}_{\mathrm{zx}}$ and its energy derivative at the Fermi energy, which is proportional to $\alpha^{\mathrm{y}}_{\mathrm{zx}}$, have the same sign, as θ_{SH} represents the inverse spin Hall conductivity $\sigma^{\mathrm{y}}_{\mathrm{xz}} = -\sigma^{\mathrm{y}}_{\mathrm{zx}}$ and θ_{SN} the (direct) spin Nernst conductivity $\alpha^{\mathrm{y}}_{\mathrm{zx}}$. Indeed, our first-principles calculations of the ratio between θ_{SH} and θ_{SN} find $\theta_{\mathrm{SH}}/\theta_{\mathrm{SN}} \approx -0.6$ at 250 K [see Sec. 1.2 and Fig. 2(d)]. This beautifully agrees with the ratio $\theta_{\mathrm{SH}}/\theta_{\mathrm{SN}} \approx -0.5$ found in our experiments.

1.7 Control Experiments

In the spirit of recent magnon-mediated magnetoresistance experiments [26, 27, 28, 29, 30, 31, 32], we conducted further control experiments to exclude spurious signals leading to the observed SMT. We investigated two samples: a GGG/YIG/Pt, and a GGG/Pt heterostructure. The GGG/YIG/Pt heterostructure was fabricated starting from a single crystalline (111) oriented GGG substrate onto which a 2 μm thick YIG film was deposited by liquid-phase epitaxy. After cleaning in a piranha solution, a 10 nm thick Pt film was deposited on the YIG film by electron beam evaporation [33]. For the second sample, we used a bare single crystalline (111) oriented GGG substrate, which also was cleaned in a piranha solution and then covered with a 5.8 nm

thick Pt film by electron beam evaporation. Subsequently, the Pt films on both samples were patterned into thin stripes using electron beam lithography and Argon ion beam milling, as described in more detail e.g. in Refs. [27, 28]. As sketched in Fig. 8(a), for the GGG/YIG/Pt heterostructure, the Pt strips had a width of $w_{N1} = 0.5$ μm and length of $l_{N1} = 148$ μm, both strips being separated by $d_{N1} = 1.6$ μm. For the GGG/Pt sample (see Fig. 8(b)), the strip dimensions were $w_{N2} = 1$ μm, $l_{N2} = 148$ μm, and $d_{N2} = 2.6$ μm. Both samples were mounted into the very same superconducting 3D-vector magnet cryostat, that was also used for the SMT experiments discussed in the main text, and cooled down to a sample temperature of $T_{base} = 220$ K. For both samples a constant DC electrical current I_{drive} was applied to one strip by a Keithley 2400 current source, while the voltage V_{nl} across the other strip was recorded using a Keithley 2182A Nanovoltmeter. As detailed in [34, 26, 27], I_{drive}, on one hand, generates a local thermal gradient owing to the Joule heating power P_{heater} associated with the charge current flow. The presence of this thermal gradient induces non-local thermopower voltages in the second Pt strip. On the other hand, when a magnetic insulator is located beneath the Pt strip, a non-equilibrium magnon population is injected into the magnet by virtue of the spin Hall spin accumulation. Magnon diffusion to the second Pt contact results in a non-local Ohmic voltage signal in the second strip, also called magnon-mediated magnetoresistance. We separate the non-local thermal and resistive contributions to V_{nl} by current reversal [35]: for each data point, the current polarity applied to the first strip is changed from positive ($+I_{drive}$) to negative ($-I_{drive}$) and the voltage signals $V_{nl}(+I)$ and $V_{nl}(-I)$ are recorded for the two different bias current polarities. The thermal voltage is then extracted as $V_{nl,therm} = (V_{nl}(+I) + V_{nl}(-I))/2$, which is even with respect to current reversal. The MMR signal corresponds to $V_{nl,MMR} = (V_{nl}(+I) - V_{nl}(-I))/2$. In the following, we concentrate on the thermal signal. We carried out SMT measurements for both samples with similar heater power and thermal gradients being present along $\mathbf{x}$. While the exact magnitude of the thermal gradient is difficult to quantify (the detector contact is very close to the "heater" and rather wide ($w \approx d$), such that it cannot be used for reasonable spatially resolved Pt thermometry), we find in SMT experiments in the oopy configuration that the ordinary Nernst signal recorded across the detector contact in the two samples is the same (to within 20 %).

In Fig. 8(c) we show the results obtained for the GGG/YIG/Pt sample for an external magnetic field of 1 T rotated in the $\mathbf{x} - \mathbf{y}$ plane and a heater power of 8.68 mW ($I = 1$ mA). $V_{nl,therm}$ exhibits a clear $\cos(\alpha)$ dependence, which we attribute to a commonly observed spin Seebeck contribution due to a local thermal gradient along $\mathbf{z}$ [26, 29]. We fit the data with a cosine function for

both clockwise and counterclockwise rotations and extract an amplitude of 19.3 μV for the spin Seebeck signal. Subtracting the fitted $\cos\alpha$ function from the data we obtain the thermal voltage signal $\Delta V_{\mathrm{nl,therm}}$ plotted in Fig. 8(e). This signal exhibits the same angular dependence as the transverse spin Nernst thermopower signal in Fig. 6(g). We thus attribute this signal again to the SMT. Here, the modulation amplitude $\Delta V_{\mathrm{nl,therm}}$ is 0.15 μV, which corresponds to an electric field of 1 mV/m. This signal is much larger than the SMT signal observed in standard SMT experiments because the small spacing between heater and detector strip implies a much larger in-plane temperature gradient.

Repeating the thermopower experiments on the GGG/Pt sample, again using an external magnetic field of 1 T and a heater power of 12.2 mW, we obtain the results compiled in Fig. 8(d). For the GGG/Pt we do *not* observe any angular dependence of $V_{\mathrm{nl,therm}}$ for the ip geometry as expected considering that no SSE should be present in the absence of a magnetic insulator layer (for the oopx and oopy geometry we observe the ordinary Nernst effect of the Pt, as mentioned above). We subtract a (already small) constant voltage offset of 0.655 μV from $V_{\mathrm{nl,therm}}$ to obtain a $\Delta V_{\mathrm{nl,therm}}$. The result of this procedure is shown in Fig. 8(f) (on the same scale as for Fig. 8(e)). Again, there is no systematic angular dependence for $\Delta V_{\mathrm{nl,therm}}$ in the GGG/Pt sample. This shows that the presence of a magnetic insulator layer (YIG layer) is mandatory for the SMT to arise, as expected in the SNE picture proposed in the main manuscript. This control experiment thus further corroborates the notion that the SMT observed in YIG/Pt heterostructures indeed originates from the spin Nernst effect.

Taken together, the results compiled in Fig. 8 demonstrate that the SMT signal is only observed in YIG/Pt heterostructures while it is absent if only a GGG/Pt bilayer is used. Thus, these results further confirm our model predictions for the SMT and provide additional evidence for our first experimental observation of the spin Nernst effect. Moreover, these results show that the SMT is observable in non-local sample geometries, which broadens its appeal and relevance.

References

[1] Nakayama, H., Althammer, M., Chen, Y.-T., Uchida, K., Kajiwara, Y., Kikuchi, D., Ohtani, T., Geprägs, S., Opel, M., Takahashi, S., Gross, R., Bauer, G. E. W., Goennenwein, S. T. B., and Saitoh, E. *Physical Review Letters* **110**, 206601 (2013).

[2] Chen, Y.-T., Takahashi, S., Nakayama, H., Althammer, M., Goennenwein, S. T. B., Saitoh, E., and Bauer, G. E. W. *Physical Review B* **87**, 144411 (2013).

[3] Takahashi, S., Imamura, H., and Maekawa, S. In *Concepts in Spin electronics,* Maekawa, S., editor, 343. Oxford University Press, New York (2006).

[4] Brataas, A., Bauer, G. E., and Kelly, P. J. *Physics Reports* **427**, 157 (2006).

[5] Jia, X., Liu, K., Xia, K., and Bauer, G. E. W. *Europhysics Letters* **96**, 17005 (2011).

[6] Borge, J., Gorini, C., and Raimondi, R. *Physical Review B* **87**,085309 (2013).

[7] Tölle, S., Gorini, C., and Eckern, U. *Physical Review B* **90**, 235117 (2014).

[8] Valet, T. and Fert, A. *Physical Review B* **48**, 7099 (1993).

[9] Vernes, A., Györffy, B. L., and Weinberger, P. *Physical Review B* **76**, 012408 (2007).

[10] Lowitzer, S., Gradhand, M., Ködderitzsch, D., Fedorov, D. V., Mertig, I., and Ebert, H. *Physical Review Letters* **106**, 056601 (2011).

[11] Butler, W. H. *Physical Review B* **31**, 3260 (1985).

[12] Banhart, J., Bernstein, R., Voitländer, J., and Weinberger, P. *Solid State Communications* **77**, 107 (1991).

[13] Ködderitzsch, D., Chadova, K., and Ebert, H. *Physical Review B* **92**, 184415 (2015).

[14] Ebert, H., Mankovsky, S., Chadova, K., Polesya, S., Minár, J., and Ködderitzsch, D. *Physical Review B* **91**,165132 (2015).

[15] Jonson, M. and Mahan, G. D. *Physical Review B* **21**, 4223 (1980).

[16] Seemann, M., Ködderitzsch, D., Wimmer, S., and Ebert, H. *Physical Review B* **92**, 155138 (2015).

[17] Althammer, M., Meyer, S., Nakayama, H., Schreier, M., Altmannshofer, S., Weiler, M., Huebl, H., Geprägs, S., Opel, M., Gross, R., Meier, D., Klewe, C., Kuschel, T., Schmalhorst, J.-M., Reiss, G., Shen, L., Gupta, A., Chen, Y.-T., Bauer, G. E. W., Saitoh, E., and Goennenwein, S. T. B. *Physical Review B* **87**, 224401 (2013).

[18] Geprägs, S., Meyer, S., Altmannshofer, S., Opel, M., Wilhelm, F., Rogalev, A., Gross, R., and Goennenwein, S. T. B. *Applied Physics Letters* **101**, 262407 (2012).

[19] Moore, J. P. and Graves, R. S. *Journal of Applied Physics* **44**, 1174 (1973).

[20] Uchida, K., Adachi, H., Ota, T., Nakayama, H., Maekawa, S., and Saitoh, E. *Applied Physics Letters* **97**, 172505 (2010).

[21] Uchida, K., Takahashi, S., Harii, K., Ieda, J., Koshibae, W., Ando, K., Maekawa, S., and Saitoh, E. *Nature* **455**, 778 (2008).

[22] Jaworski, C. M., Yang, J., Mack, S., Awschalom, D. D., Heremans, J. P., and Myers, R. C. *Nature Materials* **9**, 898 (2010).

[23] Onose, Y., Ideue, T., Katsura, H., Shiomi, Y., Nagaosa, N., and Tokura, Y. *Science* **329**, 297 (2010).

[24] Meyer, S., Althammer, M., Geprägs, S., Opel, M., Gross, R., and Goennenwein, S. T. B. *Applied Physics Letters* **104**, 242411 (2014).

[25] Czeschka, F. D., Dreher, L., Brandt, M. S., Weiler, M., Althammer, M., Imort, I.-M., Reiss, G., Thomas, A., Schoch, W., Limmer, W., Huebl, H., Gross, R., and Goennenwein, S. T. B. *Physical Review Letters* **107**, 046601 (2011).

[26] Cornelissen, L. J., Liu, J., Duine, R. A., Youssef, J. B., and van Wees, B. J. *Nature Physics* **11**, 1022 (2015).

[27] Goennenwein, S. T. B., Schlitz, R., Pernpeintner, M., Ganzhorn, K., Althammer, M., Gross, R., and Huebl, H. *Applied Physics Letters* **107**, 172405 (2015).

[28] Ganzhorn, K., Klingler, S., Wimmer, T., Geprägs, S., Gross, R., Huebl, H., and Goennenwein, S. T. B. *Applied Physics Letters* **109**, 022405 (2016).

[29] Cornelissen, L. J., Peters, K. J. H., Bauer, G. E. W., Duine, R. A., and van Wees, B. J. *Physical Review B* **94**,014412 (2016).

[30] Vélez, S., Bedoya-Pinto, A., Yan, W., Hueso, L. E., and Casanova, F. *Physical Review B* **94**,174405 (2016).

[31] Wu, H., Wan, C. H., Zhang, X., Yuan, Z. H., Zhang, Q. T., Qin, J. Y., Wei, H. X., Han, X. F., and Zhang, S. *Physical Review B* **93**,060403 (2016).

[32] Li, J., Xu, Y., Aldosary, M., Tang, C., Lin, Z., Zhang, S., Lake, R., and Shi, J. *Nature Communications* **7**, 10858 (2016).

[33] Pütter, S., Geprägs, S., Schlitz, R., Althammer, M., Erb, A., Gross, R., and Goennenwein, S. T. B. *Applied Physics Letters* **110**, 012403 (2017).

[34] Roschewsky, N., Schreier, M., Kamra, A., Schade, F., Ganzhorn, K., Meyer, S., Huebl, H., Geprägs, S., Gross, R., and Goennenwein, S. T. B. *Applied Physics Letters* **104**, 202410 (2014).

[35] Schreier, M., Roschewsky, N., Dobler, E., Meyer, S., Huebl, H., Gross, R., and Goennenwein, S. T. B. *Applied Physics Letters* **103**), 242404 (2013).

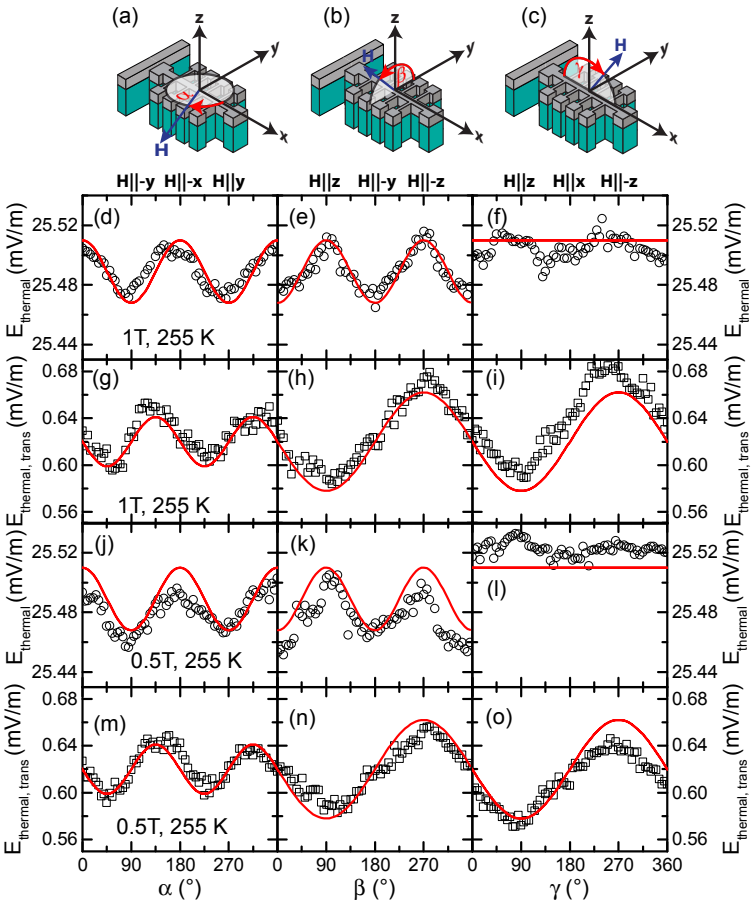

Figure 6: ***(a)-(c)*** *The magnetization vector* **M** *of the YIG layer is rotated by an external magnetic field in the three different rotation planes spanned by (***x***,* **y***) (panel* ***(a)****), (***y***,* **z***)(panel* ***(b)****) and (***x***,* **z***)(panel* ***(c)****). The measured thermal electric field* E_{thermal} *(black circles) for all three geometries and* $P_{\mathrm{heater}} = 286\,\mathrm{mW}$ *(or* $\Delta T = 18.0\,\mathrm{K}$ *along the Hall bar) is depicted in panels* ***(d),(j)*** *for the (***x***,* **y***)-plane,* ***(e),(k)*** *for the (***y***,* **z***)-plane and* ***(f),(l)*** *for the (***x***,* **z***)-plane, for* $\mu_0 H = 1$ T *and* $\mu_0 H = 0.5$ T*, respectively. The transverse electric field* $E_{\mathrm{thermal,trans}}$ *(black squares) for all three geometries is displayed in panels* ***(g),(m)*** *for the (***x***,* **y***)-plane,* ***(h),(n)*** *for the (***y***,* **z***)-plane and* ***(i),(o)*** *for the (***x***,* **z***)-plane, for* $\mu_0 H = 1$ T *and* $\mu_0 H = 0.5$ T*, respectively. The average sample temperature during these measurements was* 255 K*. Red lines in the graphs are calculations based on our spin Nernst thermopower model via Eqs. (25),(26).*

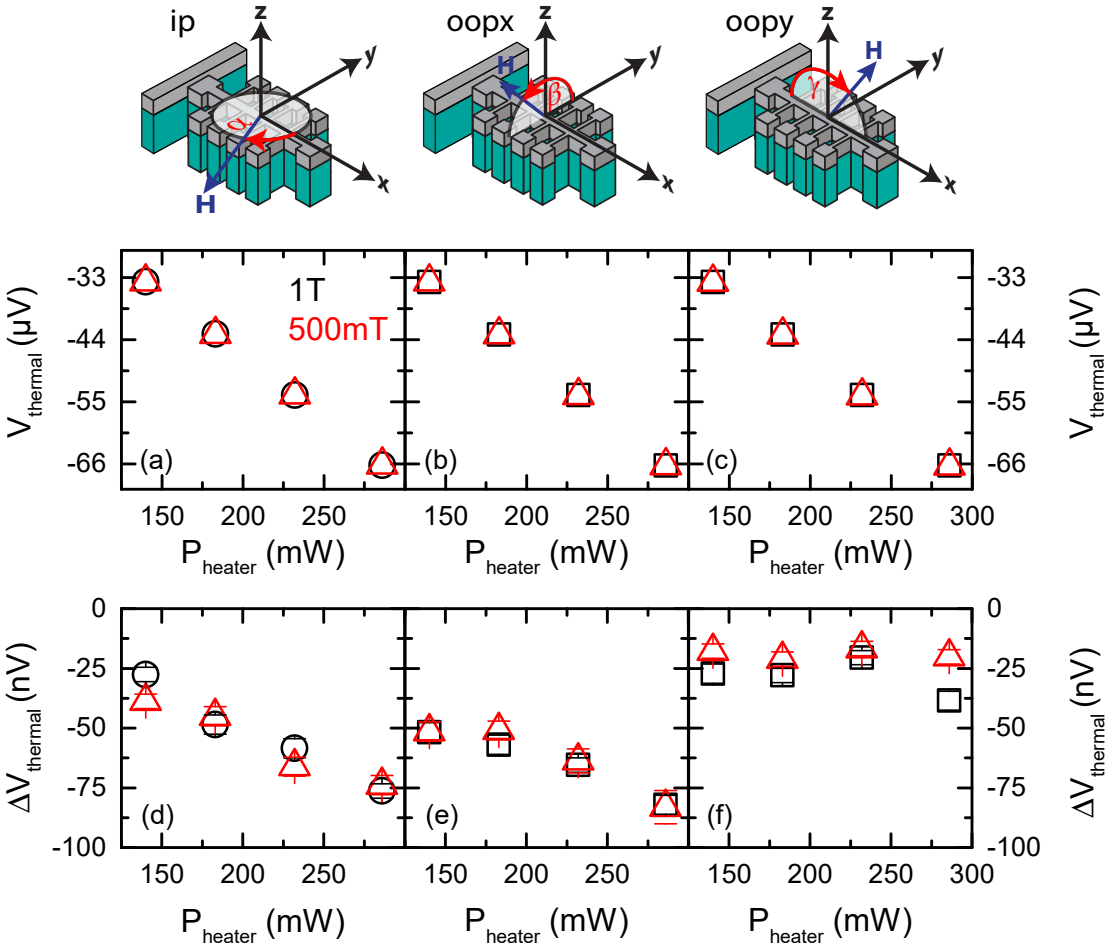

Figure 7: ***(a-c)*** *Power dependence of the thermal voltage* V_{thermal} *and* ***(d-f)*** *the voltage modulation amplitude* $\Delta V_{\mathrm{thermal}}$ *for ip (left column), oopx (middle) and oopy rotations (right column) at a base temperature of* $T = 220\,\mathrm{K}$ *and magnetic field strength of* $0.5\,\mathrm{T}$ *(red triangles) and* $1\,\mathrm{T}$ *(black squares), respectively.*

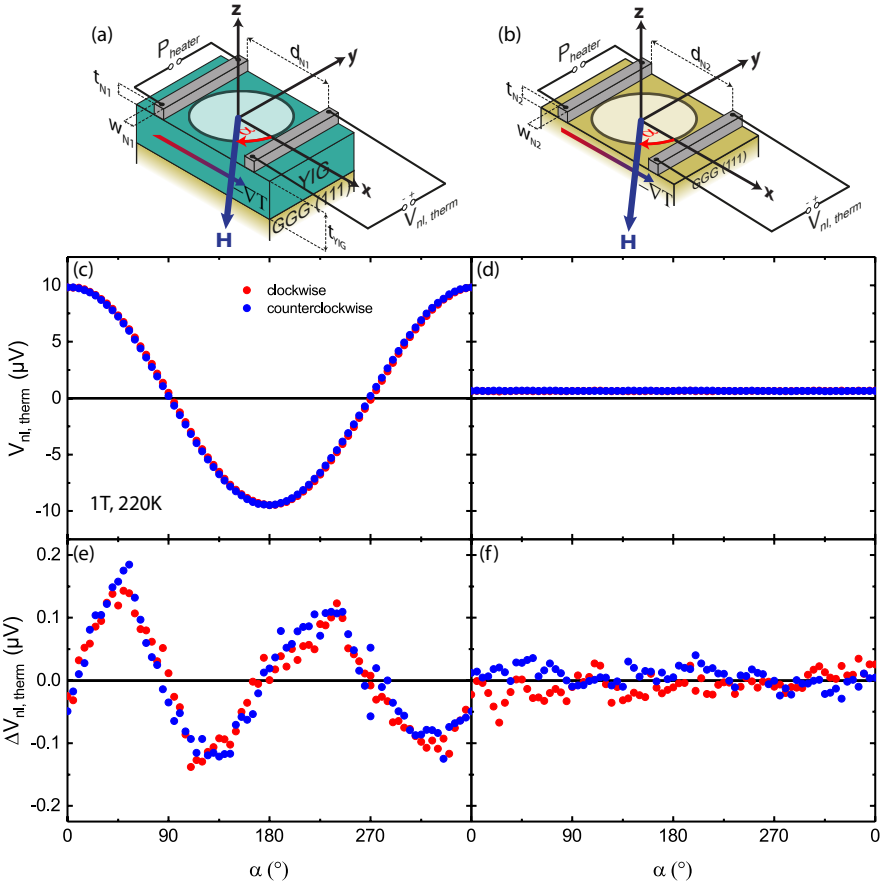

Figure 8: *Non-local thermopower signals for GGG/YIG/Pt and GGG/Pt samples.* ***(a)*** *sample sketch for the GGG/YIG/Pt heterostructure, with two Pt strips (t_{N1} = 10 nm, w_{N1} = 0.5 μm) separated by d_{N1} = 1.6 μm.* ***(b)*** *GGG/Pt control sample with two Pt strips (t_{N2} = 5.8 nm, w_{N2} = 1 μm) separated by d_{N2} = 2.6 μm.* ***(c)*** *Thermal voltage obtained for the GGG/YIG/Pt sample in the ip configuration. A sinusoidal signal is observed, which originates from the longitudinal spin Seebeck signal due to an out-of-plane temperature gradient.* ***(d)*** *Absence of an ip angular dependence of the thermal voltage in the GGG/Pt control sample.* ***(e)*** *Thermal voltage signal for the GGG/YIG/Pt sample after subtracting the spin Seebeck signal, which confirms the transverse spin Nernst magnetothermopower symmetry.* ***(f)*** *Thermal voltage signal for the GGG/Pt control sample shows* no angular dependence *even after subtraction of a constant voltage offset.*

3.3 Space-time symmetry of response tensors

As outlined in Section 2.3, most phenomena relevant to the field of spintronics can be described by a linear response coefficient, that in turn can be expressed and calculated within the framework of Kubo's linear response formalism. Obviously, the shape of the corresponding tensor of response coefficients, in particular the presence of non-vanishing elements, decides wether a phenomenon occurs or not. As demonstrated by Kleiner [271] in the 1960-ies, for the electrical and heat transport tensors, their shape is uniquely determined by the magnetic space group of a material. The concept of Kleiner has been extended to deal with more complex situations relevant for spintronics and spincaloritronics. In a first application of the formalism the focus was on the spin-conductivity tensor that allows in particular a description of the spin Hall effect. The extended formalism, comparison to established results for electric and thermoelectric transport, and the tensor shapes for direct and inverse spin-conductivity for all magnetic Laue groups is presented in Ref. 283. Later applications were devoted to the spin-orbit torque (SOT) and the Edelstein effect (EE) and their corresponding response tensors. These will be the subject of one of the following sections (Section 3.5). Inspection of the tables giving the shape of the spin-conductivity tensor for all magnetic Laue groups, the possibility of a longitudinal spin-polarised current in non-magnetic solids emerged. This group-theoretical prediction could be independently verified by subsequent numerical investigations, detailed in Ref. 92, that demonstrated that the possible longitudinal spin current occuring in low-symmetric materials may be in the same order of magnitude as the transversal spin current due to the spin Hall effect. Errata and additional considerations to Refs. 283 and 92 can be found on page 187 and 197, respectively.

3.3.1 Published results on the symmetry of response tensors

The following is a copy of the article *Symmetry-imposed shape of linear response tensors* [283], reprinted with permission from

M. Seemann, D. Ködderitzsch, S. Wimmer, and H. Ebert, Phys. Rev. B **92**, 155138 (2015).

PHYSICAL REVIEW B **92**, 155138 (2015)

Symmetry-imposed shape of linear response tensors

M. Seemann, D. Ködderitzsch,* S. Wimmer,† and H. Ebert
Department Chemie/Phys. Chemie, Ludwig-Maximilians-Universität München, Germany
(Received 17 July 2015; published 23 October 2015)

A scheme suggested in the literature to determine the symmetry-imposed shape of linear response tensors is revised and extended to allow for the treatment of more complex situations. The extended scheme is applied to discuss the shape of the spin conductivity tensor for all magnetic space groups. This allows in particular investigating the character of longitudinal as well as transverse spin transport for arbitrary crystal structure and magnetic order that give rise, e.g., to the spin Hall, Nernst, and the spin-dependent Seebeck effects.

DOI: 10.1103/PhysRevB.92.155138 PACS number(s): 75.76.+j, 61.50.Ah, 72.15.Jf, 72.25.Ba

I. INTRODUCTION

The shape of a linear response tensor is of central importance as it decides whether a physical phenomenon may occur and what anisotropy may be expected for a solid with given crystal symmetry and magnetic order. A prominent and common example for this is the anomalous Hall effect in ferromagnetic solids, which is connected with the nonzero antisymmetric contributions to the electrical conductivity tensor. Accordingly, several schemes were suggested in the past to predict the shape of linear response tensors on the basis of group-theoretical arguments (for a corresponding review see for example Ref. [1]). Among the various schemes suggested, that of Kleiner [2–4] seems to be most convincing as it is starting from the expression for linear response tensors as given by Kubo's linear response formalism and as it uses only the behavior of the involved operators under the appropriate space and time transformations of the relevant magnetic space group. A further appealing feature of Kleiner's scheme is that it does not make use of Onsager's relations but allows deriving them in a most general way.

Kleiner's scheme was originally derived having response quantities in mind that are connected with the perturbation as well as the observable represented by the components of a single vector operator. A more general starting point is adopted in this contribution to allow the treatment of situations involving three operators. As a first simple application the tensors representing the charge and heat transport in response to an electric field and thermal gradient are considered. As a more complex transport quantity the corresponding spin conductivity is considered for all magnetic space groups. Among other things this allows the discussion of the transverse spin transport as occurring for the spin Hall [5,6] and spin Nernst [7,8] effects. In particular, it is demonstrated that these effects may be discussed without use of spin-projected conductivities [8,9].

II. SYMMETRY OF RESPONSE FUNCTIONS

Within Kubo's linear response formalism, the change of the expectation value of an observable $\hat{B}_i$ due to a time-dependent perturbation $\hat{A}_j$ can be expressed by the corresponding response function [10]

$$\tau_{\hat{B}_i\hat{A}_j}(\omega,\mathbf{H}) = \int_0^\infty dt\, e^{-i\omega t} \int_0^\beta d\lambda\, \mathrm{Tr}[\rho(\mathbf{H})\hat{A}_j\hat{B}_i(t+i\hbar\lambda;\mathbf{H})]. \quad (1)$$

Here $\rho(\mathbf{H}) = e^{-\beta\hat{H}(\mathbf{H})}/\mathrm{Tr}(e^{-\beta\hat{H}(\mathbf{H})})$ is the density operator for the unperturbed system, the operators $\hat{B}_i$ and $\hat{A}_j$ in the Heisenberg picture are assumed to be the Cartesian components of a corresponding vector operator, and $\mathbf{H}$ is an external magnetic field.

Equation (1) was used by Kleiner [2] as the starting point to investigate the symmetry of the tensors $\underline{\boldsymbol{\tau}}$ that describe the charge and heat transport due to an electric field or thermal gradient. Kleiner's scheme, however, is quite general and can be easily extended to deal with more complex situations. In the following, Kleiner's scheme will be adopted to the case when the observable is represented by an operator product of the form $\hat{B}_i\hat{C}_j$, again with the operators $\hat{C}_i$, $\hat{B}_j$, and $\hat{A}_k$ being the Cartesian components of a vector operator. In this case the corresponding response function is obviously given by

$$\tau_{(\hat{B}_i\hat{C}_j)\hat{A}_k}(\omega,\mathbf{H}) = \int_0^\infty dt\, e^{-i\omega t} \int_0^\beta d\lambda\, \mathrm{Tr} \times [\rho(\mathbf{H})\hat{A}_k\hat{B}_i(t+i\hbar\lambda;\mathbf{H})\hat{C}_j(t+i\hbar\lambda;\mathbf{H})], \quad (2)$$

where by using the parentheses in the symbol $\tau_{(\hat{B}_i\hat{C}_j)\hat{A}_k}$ it is made clear that it is the observable and not the perturbation that consists of a product of two operators. The shape of the response tensor $\underline{\boldsymbol{\tau}}$ in Eq. (2), i.e., the occurrence and degeneracy of nonzero elements, has to reflect the symmetry of the investigated solid. This shape can be found by considering the impact of a symmetry operation of the corresponding space group on Eq. (2), as this will lead to an equation connecting the elements of $\underline{\boldsymbol{\tau}}$ or possibly of a complementary tensor $\underline{\boldsymbol{\tau}}'$ (see below). Collecting the restrictions imposed by all symmetry operations the shape of $\underline{\boldsymbol{\tau}}$ is obtained. In this context it is important to note that the magnetic structure of the system, if present, has to be considered. In this case, the set of symmetry operations contains unitary pure spatial (u), but also antiunitary symmetry operations (a).

*diemo.koedderitzsch@cup.uni-muenchen.de
†sebastian.wimmer@cup.uni-muenchen.de

The general transformation properties of the operators $\hat{\mathbf{X}} \in \{\hat{\mathbf{A}},\hat{\mathbf{B}},\hat{\mathbf{C}}\}$ in Eq. (2) under unitary (u) and antiunitary symmetry operations (a) can be written as

$$u\hat{X}_i u^{-1} = \sum_j \hat{X}_j D^{(\hat{\mathbf{X}})}(u)_{ji}, \tag{3}$$

$$a\hat{X}_i a^{-1} = \sum_j \hat{X}_j D^{(\hat{\mathbf{X}})}(a)_{ji}, \tag{4}$$

where $\underline{\mathbf{D}}^{(\hat{\mathbf{X}})}(u)$ and $\underline{\mathbf{D}}^{(\hat{\mathbf{X}})}(a)$ are the representation matrices corresponding to the operator $\hat{\mathbf{X}}$ and operation u or a, respectively. The group properties are reflected by the following relations:

$$\underline{\mathbf{D}}(uu') = \underline{\mathbf{D}}(u)\,\underline{\mathbf{D}}(u'), \tag{5}$$

$$\underline{\mathbf{D}}(aa') = \underline{\mathbf{D}}(a)\,\underline{\mathbf{D}}(a')^*. \tag{6}$$

For all unitary operations u the expression under the trace in Eq. (2) can be reformulated by cyclic permutation and by inserting the factor $u^{-1}u = 1$:

$$\begin{aligned}\mathrm{Tr}[e^{-\beta\hat{H}(\mathbf{H})}\hat{A}_k\hat{B}_i(t+i\hbar\lambda;\mathbf{H})\hat{C}_j(t+i\hbar\lambda;\mathbf{H})] &= \mathrm{Tr}\left[u^{-1}ue^{-\beta\hat{H}(\mathbf{H})}u^{-1}u\hat{A}_ku^{-1}u\hat{B}_j(t+i\hbar\lambda,\mathbf{H})u^{-1}uC_i(t+i\hbar\lambda;\mathbf{H})\right]\\ &= \mathrm{Tr}\left[(ue^{-\beta\hat{H}(\mathbf{H})}u^{-1})(u\hat{A}_ku^{-1})(u\hat{B}_i(t+i\hbar\lambda,\mathbf{H})u^{-1})(u\hat{C}_j(t+i\hbar\lambda,\mathbf{H})u^{-1})\right].\end{aligned} \tag{7}$$

The four expressions grouped in parentheses can now be dealt with separately. The term containing $\hat{A}_k$ can be rewritten using Eq. (3). For the term containing $\hat{B}_j$ one has accordingly

$$u\hat{B}_i(t+i\hbar\lambda,\mathbf{H})u^{-1} = \sum_m \hat{B}_m(t+i\hbar\lambda,\mathbf{H}_u)D^{(\hat{\mathbf{B}})}(u)_{mi}, \tag{8}$$

with $\mathbf{H}_u$ the transformed field

$$u\hat{H}(\mathbf{H})u^{-1} = \hat{H}(\mathbf{H}_u) \tag{9}$$

connected with the operation u. For the term containing $C_j(t+i\hbar\lambda,\mathbf{H})$ an analogous expression is obtained. Inserting these relations into Eq. (7) one obtains

$$\begin{aligned}&\mathrm{Tr}\left[e^{-\beta\hat{H}(\mathbf{H})}\hat{A}_k\hat{B}_i(t+i\hbar\lambda,\mathbf{H})\hat{C}_j(t+i\hbar\lambda,\mathbf{H})\right]\\ &\quad= \sum_{lmn}\mathrm{Tr}\left[e^{-\beta\hat{H}(\mathbf{H}_u)}\hat{A}_l\hat{B}_m(t+i\hbar\lambda,\mathbf{H}_u)\hat{C}_n(t+i\hbar\lambda,\mathbf{H}_u)D^{(\hat{\mathbf{A}})}(u)_{lk}\,D^{(\hat{\mathbf{B}})}(u)_{mi}\,D^{(\hat{\mathbf{C}})}(u)_{nj}\right].\end{aligned} \tag{10}$$

This equation must hold for any operators $\hat{A}_k$, $\hat{B}_j$, and $\hat{C}_i$, i.e., also in the special case $\hat{A}_k = \hat{B}_j = \hat{C}_i = \mathbb{1}$, leading to

$$\mathrm{Tr}(e^{-\beta\hat{H}(\mathbf{H})}) = \mathrm{Tr}(e^{-\beta\hat{H}(\mathbf{H}_u)}). \tag{11}$$

Inserting the two last equations into Eq. (2) for the general transport coefficients, one obtains the transformation behavior of $\underline{\boldsymbol{\tau}}$ under a unitary symmetry operation u:

$$\tau_{(\hat{B}_i\hat{C}_j)\hat{A}_k}(\omega,\mathbf{H}) = \sum_{lmn}\tau_{(\hat{B}_m\hat{C}_n)\hat{A}_l}(\omega,\mathbf{H}_u)D^{(\hat{\mathbf{A}})}(u)_{lk}\,D^{(\hat{\mathbf{B}})}(u)_{mi}\,D^{(\hat{\mathbf{C}})}(u)_{nj}. \tag{12}$$

A similar procedure can be applied for antiunitary operators a that contain the time-reversal T, i.e., that can be decomposed as $a = vT$ with v a unitary operator describing a pure spatial operation. For antiunitary operators cyclic permutation under the trace does not hold, but one may use the relation

$$\mathrm{Tr}(aa') = [\mathrm{Tr}(a'a)]^*. \tag{13}$$

This expression can be used to transform Eq. (2) in a similar way as done for Eq. (7) leading to

$$\begin{aligned}&\mathrm{Tr}\left[e^{-\beta\hat{H}(\mathbf{H})}\hat{A}_k\hat{B}_i(t+i\hbar\lambda,\mathbf{H})\hat{C}_j(t+i\hbar\lambda,\mathbf{H})\right] = \mathrm{Tr}\left[a^{-1}ae^{-\beta\hat{H}(\mathbf{H})}a^{-1}a\hat{A}_ka^{-1}a\hat{B}_i(t+i\hbar\lambda,\mathbf{H})a^{-1}a\hat{C}_j(t+i\hbar\lambda,\mathbf{H})\right]\\ &\quad= \left\{\mathrm{Tr}\left[(ae^{-\beta\hat{H}(\mathbf{H})}a^{-1})(a\hat{A}_ka^{-1})(a\hat{B}_i(t+i\hbar\lambda,\mathbf{H})a^{-1})(a\hat{C}_j(t+i\hbar\lambda,\mathbf{H})a^{-1})\right]\right\}^*.\end{aligned} \tag{14}$$

Of the four expressions in parentheses, the second one is directly given by Eq. (4), while the first one can be rewritten by introducing $\mathbf{H}_a$ via the definition

$$a\hat{H}(\mathbf{H})a^{-1} = \hat{H}(\mathbf{H}_a). \tag{15}$$

Expressing the last two terms according to

$$a\hat{B}_i(t+i\hbar\lambda,\mathbf{H})a^{-1} = \sum_m \hat{B}_m(-t+i\hbar\lambda,\mathbf{H})D^{(\hat{\mathbf{B}})}(a)_{mi}, \tag{16}$$

which follows directly from the fact that a contains the time-reversal operation, and inserting these expressions into Eq. (14) one arrives at

$$\mathrm{Tr}\left[e^{-\beta\hat{H}(\mathbf{H})}\hat{A}_k\hat{B}_i(t+i\hbar\lambda,\mathbf{H})\hat{C}_j(t+i\hbar\lambda,\mathbf{H})\right]=\sum_{lmn}\mathrm{Tr}\left[e^{-\beta\hat{H}(\mathbf{H}_a)}\hat{A}_l\hat{B}_m(-t+i\hbar\lambda,\mathbf{H}_a)\hat{C}_n(-t+i\hbar\lambda,\mathbf{H}_a)\right]^* D^{(\hat{\mathbf{A}})}(a)^*_{lk}$$
$$\times D^{(\hat{\mathbf{B}})}(a)^*_{mi}\,D^{(\hat{\mathbf{C}})}(a)^*_{nj}. \tag{17}$$

Using the relation [11]

$$\mathrm{Tr}[e^{-\beta\hat{H}}\hat{\mathbf{A}}\hat{\mathbf{B}}(\tau)\hat{\mathbf{C}}(\tau)]=\mathrm{Tr}[e^{-\beta\hat{H}}\hat{A}(-\tau)\hat{\mathbf{B}}\hat{\mathbf{C}}] \tag{18}$$

one arrives at an expression that is completely analogous to Eq. (10):

$$\mathrm{Tr}\left[e^{-\beta\hat{H}(\mathbf{H})}\hat{A}_k\hat{B}_i(t+i\hbar\lambda,\mathbf{H})\hat{C}_j(t+i\hbar\lambda,\mathbf{H})\right]=\sum_{lmn}\mathrm{Tr}\left[e^{-\beta\hat{H}(\mathbf{H}_a)}\hat{C}^\dagger_n\hat{B}^\dagger_m\hat{A}^\dagger_l(t+i\hbar\lambda,\mathbf{H}_a)D^{(\hat{\mathbf{A}})}(a)^*_{lk}\,D^{(\hat{\mathbf{B}})}(a)^*_{mi}\,D^{(\hat{\mathbf{C}})}(a)^*_{nj}\right], \tag{19}$$

where

$$(\mathrm{Tr}\,L)^*=\mathrm{Tr}(L^\dagger), \tag{20}$$

with L being a linear operator was used. Again, this equation must also hold for the special case $\hat{\mathbf{A}}=\hat{\mathbf{B}}=\hat{\mathbf{C}}=\mathbb{1}$, thus

$$\mathrm{Tr}(e^{-\beta\hat{H}(\mathbf{H})})=\mathrm{Tr}(e^{-\beta\hat{H}(\mathbf{H}_a)}). \tag{21}$$

Finally, inserting all these relations one obtains the transformation behavior for $\underline{\boldsymbol{\tau}}$ as

$$\tau_{(\hat{B}_i\hat{C}_j)\hat{A}_k}(\omega,\mathbf{H})=\sum_{lmn}\tau_{\hat{A}^\dagger_l(\hat{C}^\dagger_n\hat{B}^\dagger_m)}(\omega,\mathbf{H}_a)D^{(\hat{\mathbf{A}})}(a)^*_{lk}\,D^{(\hat{\mathbf{B}})}(a)^*_{mi}\,D^{(\hat{\mathbf{C}})}(a)^*_{nj}, \tag{22}$$

which is the counter part of Eq. (12), but for antiunitary operators a.

It is important to note that in general the tensors $\tau_{(\hat{B}_i\hat{C}_j)\hat{A}_k}$ and $\tau_{\hat{A}^\dagger_k(\hat{B}^\dagger_i\hat{C}^\dagger_j)}$ are different objects representing different response functions which are only interrelated by Eq. (22). Accordingly, the symbols $\underline{\boldsymbol{\tau}}$ and $\underline{\boldsymbol{\tau}}'$ will be used below to distinguish them. Obviously the two tensors $\underline{\boldsymbol{\tau}}$ and $\underline{\boldsymbol{\tau}}'$ coincide only if all operators and their adjoined ones are the same, i.e., $\hat{A}_i=\hat{B}_i$ and so on.

Equations (12) and (22) relate the elements of the tensor $\underline{\boldsymbol{\tau}}$ with all the elements of $\underline{\boldsymbol{\tau}}$ and $\underline{\boldsymbol{\tau}}'$, respectively. As mentioned above, these relations impose for each symmetry operation restrictions on the shape of $\underline{\boldsymbol{\tau}}$ that determine which elements have to be zero and which are degenerate. However, to find the final shape of $\underline{\boldsymbol{\tau}}$ it is not necessary to derive restrictions for all symmetry operations of the relevant space group. Instead, it is sufficient to use only a generating set of symmetry operations [2]. Finally, as was stressed by Kleiner [2], for the application of Eqs. (12) and (22) it is not necessary to know the explicit form of the operators $\hat{A}_i$, $\hat{B}_j$, and $\hat{C}_k$, but only their behavior under a symmetry operation expressed by Eqs. (3) and (4).

III. APPLICATIONS

A. Symmetry operations and magnetic Laue groups

For a periodic solid, the corresponding unitary symmetry operations u can be represented by the Seitz symbol [12]

$$u=\{R\mid t\}, \tag{23}$$

where R describes a (proper or improper) rotation and t describes a translation. The application of this symmetry operation on a three-dimensional vector $\mathbf{v}$ is defined as

$$u\,\mathbf{v}=\underline{\mathbf{D}}(R)\,\mathbf{v}+\mathbf{t}, \tag{24}$$

where $\underline{\mathbf{D}}(R)$ is the three-dimensional matrix representation of the rotation R and $\mathbf{t}$ is a three-dimensional translation vector. For an antiunitary symmetry operation a, the time-reversal operation T has to be considered in addition to the spatial symmetry operations. It can be included in the Seitz symbol according to

$$a=\{R\mid t\}\,T. \tag{25}$$

The transformation properties of a vector $\mathbf{v}$ under a depend now on its behavior under space inversion and time reversal. A vector that reverses its orientation under space inversion is called a spatial vector (or polar vector), if it stays unaltered it is called a pseudovector or axial vector.

Generally, the transformation of a vector field $\mathbf{v}(\mathbf{r})$ under an arbitrary symmetry operation s is given accordingly by

$$s\,\mathbf{v}(\mathbf{r})=\pm\underline{\mathbf{D}}(R)\,\mathbf{v}(s^{-1}\mathbf{r}), \tag{26}$$

where the sign is determined by the behavior of $\mathbf{v}(\mathbf{r})$ under time-reversal T that may by part of s. On the other hand, a pseudovector field $\mathbf{v}(\mathbf{r})$ transforms as

$$s\,\mathbf{v}(\mathbf{r})=\pm\det\left(\underline{\mathbf{D}}(R)\right)\underline{\mathbf{D}}(R)\,\mathbf{v}(s^{-1}\mathbf{r}). \tag{27}$$

An example for this is the magnetic field $\mathbf{H}$. As $\mathbf{H}$ changes sign under time reversal, the minus sign in Eq. (27) applies. In particular one has

$$I\,\mathbf{H}=+\mathbf{H}, \tag{28}$$

$$T\,\mathbf{H}=-\mathbf{H}, \tag{29}$$

for the application of space inversion I and time reversal T. In the following we will use in parallel the symbols $\bar{1}$ and $1'$ for I and T, respectively.

TABLE I. Magnetic point groups of category (a) and their corresponding magnetic Laue group. In parentheses the magnetic Laue group according to its old definition used by Kleiner [2] is given (see text). Because equivalent magnetic point group and Laue group symbols have not been removed (see text) there are 62 and 12 instead of 53 and 11, respectively, entries.

Magnetic point group	Magnetic Laue group
$11', \bar{1}', \bar{1}1'$	$\bar{1}1'$ $(1')$
$21', m1', 2/m1', 2'/m, 2/m'$	$2/m1'$ $(21')$
$2221', mm21', m'mm,$	
$mmm1', m'm'm'$	$mmm1'$ $(2221')$
$41', \bar{4}1', 4/m', 4/m1', 4'/m'$	$4/m1'$ $(41')$
$4221', 4mm1', \bar{4}2m1',$	
$\bar{4}m21', 4/m'mm, 4'/m'm'm,$	
$4/mmm1', 4'/m'mm', 4/m'm'm'$	$4/mmm1'$ $(42221')$
$31', \bar{3}', \bar{3}1'$	$\bar{3}1'$ $(3')$
$3121', 31m1', \bar{3}'1m, \bar{3}'1m', \bar{3}1m1'$	$\bar{3}1m1'$ $(3'2)$
$3211', 3m11', \bar{3}'m1, \bar{3}'m'1, \bar{3}m11'$	$\bar{3}m11'$ $(3'2)$
$61', \bar{6}1', 6'/m, 6/m', 6/m1'$	$6/m1'$ $(61')$
$6221', 6mm1', \bar{6}m21',$	
$\bar{6}2m1', 6/m'mm, 6'/mm'm,$	
$6'/mmm', 6/mmm1', 6/m'm'm'$	$6/mmm1'$ $(6221')$
$231', m'\bar{3}', m\bar{3}1'$	$m\bar{3}1'$ $(23')$
$4321', \bar{4}3m1', m'\bar{3}'m, m'\bar{3}'m', m\bar{3}m1'$	$m\bar{3}m1'$ $(43'2)$

Taking into account the time-reversal operation, the full symmetry of a periodic solid is represented by its magnetic space group $\mathcal{G}$ that combines all symmetry operations of the type given in Eqs. (23) and (25). Altogether there are 1651 magnetic space groups that fall into three categories [13]:

(a) $\mathcal{G}$ contains the time-reversal operation T as an element,

(b) $\mathcal{G}$ does not contain T at all, neither as a separate element nor in a combination,

(c) $\mathcal{G}$ contains T only in combination with another symmetry element.

Only nonmagnetic solids possess one of the 230 space groups of category (a), while magnetically ordered solids belong either to category (b) or (c). Category (b) consists of 230 space groups, isomorphic to the nonmagnetic space groups, and category (c) combines the remaining 1191 space groups.

Since the operators $\hat{\mathbf{X}}$ appearing in Eqs. (12) and (22) are translational invariant, it is sufficient to consider only the corresponding magnetic point group operations instead of all elements of the magnetic space group. If the operators representing perturbation and response behave identically under space inversion, as it is, e.g., the case for the electrical conductivity (see below), it is possible to restrict the consideration further to the corresponding magnetic Laue group of a solid that is generated by adding the inversion operation I to the crystallographic magnetic point group. This conventional definition [14] deviates from the older one used by Kleiner [2] that derives the Laue group from the corresponding crystallographic point group by removing from each improper rotation $R = P_R I$ its improper part I. For this reason we list in Tables I–III all magnetic point groups of the three categories together with their corresponding magnetic Laue group. The symbol in parentheses gives in addition the magnetic Laue group as used by Kleiner [2].

TABLE II. Magnetic point groups of category (b) and their corresponding magnetic Laue group. In parentheses the magnetic Laue group according to its old definition used by Kleiner [2] is given (see text). Because equivalent magnetic point group and Laue group symbols have not been removed (see text) there are 37 and 12 instead of 32 and 11, respectively, entries.

Magnetic point group	Magnetic Laue group
$1, \bar{1}$	$\bar{1}$ (1)
$2, m, 2/m$	$2/m$ (2)
$222, mm2, mmm$	mmm (222)
$4, \bar{4}, 4/m$	$4/m$ (4)
$422, 4mm, \bar{4}2m, \bar{4}m2, 4/mmm$	$4/mmm$ (422)
$3, \bar{3}$	$\bar{3}$ (3)
$312, 31m, \bar{3}1m$	$\bar{3}1m$ (32)
$321, 3m1, \bar{3}m1$	$\bar{3}m1$ (32)
$6, \bar{6}, 6/m$	$6/m$ (6)
$622, 6mm, \bar{6}m2, \bar{6}2m, 6/mmm$	$6/mmm$ (622)
$23, m\bar{3}$	$m\bar{3}$ (23)
$432, \bar{4}3m, m\bar{3}m$	$m\bar{3}m$ (432)

Deriving the symbols for the magnetic point and Laue groups from those for the magnetic space groups, one may be led in some cases to two symbols that differ only concerning the sequence of the second and third generators (one of these might be a dummy 1). As this depends on the chosen coordinate system and because the shape of the response tensor may depend on this choice, both symbols are listed although being

TABLE III. Magnetic point groups of category (c) and their corresponding magnetic Laue group. In parentheses the magnetic Laue group according to its old definition used by Kleiner [2] is given (see text). Because equivalent magnetic point group and Laue group symbols have not been removed (see text) there are 52 and 13 instead of 37 and 10, respectively, entries.

Magnetic point group	Magnetic Laue group
$2', m', 2'/m'$	$2'/m'$ $(2')$
$2'2'2, m'm2', m'm'2, m'm'm$	$m'm'm$ $(2'2'2)$
$4', \bar{4}', 4'/m$	$4'/m$ $(4')$
$4'2'2, 4'm'm, \bar{4}'2'm,$	
$\bar{4}'m'2, 4'/mm'm$	$4'/mm'm$ $(4'22')$
$4'22', 4'mm', \bar{4}'2m',$	
$\bar{4}'m2', 4'/mmm'$	$4'/mmm'$ $(4'22')$
$42'2', 4m'm', \bar{4}2'm',$	
$\bar{4}m'2', 4/mm'm'$	$4/mm'm'$ $(42'2')$
$312', 31m', \bar{3}1m'$	$\bar{3}1m'$ $(32')$
$32'1, 3m'1, \bar{3}m'1$	$\bar{3}m'1$ $(32')$
$6', \bar{6}', 6'/m'$	$6'/m'$ $(6')$
$6'2'2, 6'm'm, \bar{6}'m'2,$	
$\bar{6}'2'm, 6'/m'm'm$	$6'/m'm'm$ $(6'22')$
$6'22', 6'mm', \bar{6}'m2',$	
$\bar{6}'2m', 6'/m'mm'$	$6'/m'mm'$ $(6'22')$
$62'2', 6m'm', \bar{6}m'2',$	
$\bar{6}2'm', 6/mm'm'$	$6/mm'm'$ $(62'2')$
$4'32', \bar{4}'3m', m\bar{3}m'$	$m\bar{3}m'$ $(4'32')$

completely equivalent. This applies to $\bar{3}1m1'$ and $\bar{3}m11'$ of category (a), $\bar{3}1m$ and $\bar{3}m1$ of category (b), and $4'/mm'm$ and $4'/mmm'$, $\bar{3}1m'$ and $\bar{3}m'1$, as well as $6'/m'm'm$ and $6'/m'mm'$ of category (c). Furthermore, it should be noted that for the magnetic Laue groups $2/m1'$ of category (a), $2/m$ of category (b), and $2'/m'$ of category (c), the coordinate system has been chosen according to *cell choice 1* of space group $2/m$ as documented in the *International Tables for Crystallography* [15].

B. Thermoelectric coefficients

Within linear response theory, the induced electric current density $\mathbf{j}$ and the heat current density $\mathbf{q}$ are given by [2]

$$\begin{pmatrix}\mathbf{j}\\ \mathbf{q}\end{pmatrix}=\begin{pmatrix}|e|\underline{\mathbf{L}}_{11} & |e|\underline{\mathbf{L}}_{12}\\ -\underline{\mathbf{L}}_{21} & -\underline{\mathbf{L}}_{22}\end{pmatrix}\begin{pmatrix}\nabla\mu\\ \frac{1}{T}\nabla T\end{pmatrix}, \tag{30}$$

with $e=|e|$ the elementary charge and the electrochemical potential μ which is related to the chemical potential μ_c and the electric potential φ via

$$\mu=\mu_c-|e|\varphi. \tag{31}$$

As explicitly demonstrated by Kleiner [2] as well as below, the coefficients $\underline{\mathbf{L}}_{ij}$ satisfy Onsager relations of the form

$$\underline{\mathbf{L}}_{11}(\mathbf{H})=\underline{\mathbf{L}}_{11}(-\mathbf{H}), \tag{32}$$

$$\underline{\mathbf{L}}_{22}(\mathbf{H})=\underline{\mathbf{L}}_{22}(-\mathbf{H}), \tag{33}$$

$$\underline{\mathbf{L}}_{12}(\mathbf{H})=\underline{\mathbf{L}}_{21}^{T}(-\mathbf{H}). \tag{34}$$

Identifying the operators $\hat{A}_i$ and $\hat{B}_i$ with one of the components of the electric current density operator $\hat{\mathbf{j}}$ and the heat current density operator $\hat{\mathbf{q}}$ and setting $\hat{C}_i=1$, Eqs. (12) and (22) reduce to the expressions given by Kleiner to investigate the symmetry properties of the thermoelectric coefficients $\underline{\mathbf{L}}_{ij}$. His derivation will be repeated here in a modified way as we use the conventional definition for the Laue group and as the results will be used later on.

Expressing the electric current density operator $\hat{\mathbf{j}}=-|e|\hat{\mathbf{v}}$ as a product of the electronic charge $-|e|$ and the velocity operator $\hat{\mathbf{v}}$ one can see that $\hat{\mathbf{j}}$ transforms as a vector that changes sign under time-reversal T and space inversion I:

$$I\ \hat{j}_i=-\hat{j}_i, \tag{35}$$

$$T\ \hat{j}_i=-\hat{j}_i. \tag{36}$$

The same relations apply for the heat current density operator $\hat{q}_i$ [2,16]. The corresponding 3×3 matrix representation for a unitary operator $u=\{R|t\}$ and an antiunitary operator $a=\{R|t\}T$ to be used in Eqs. (12) and (22) is

$$\underline{\mathbf{D}}^{(\hat{\mathbf{j}})}(u)=\underline{\mathbf{D}}^{(\hat{\mathbf{q}})}(u)=\ \underline{\mathbf{D}}(R), \tag{37}$$

$$\underline{\mathbf{D}}^{(\hat{\mathbf{j}})}(a)=\underline{\mathbf{D}}^{(\hat{\mathbf{q}})}(a)=-\underline{\mathbf{D}}(R). \tag{38}$$

Equations (12) and (22) (with $\hat{C}_i=1$) can be brought into a more convenient form by replacing every $\underline{\mathbf{D}}(R)$ by $\underline{\mathbf{D}}(R^{-1})$ and $\mathbf{H}$ by $\mathbf{H}_{u^{-1}}$ or $\mathbf{H}_{a^{-1}}$, respectively. Thus, Eq. (12) for unitary operators u simplifies to

$$\tau_{\hat{B}_i\hat{A}_j}(\omega,\mathbf{H}(R))=\sum_{kl}\tau_{\hat{B}_k\hat{A}_l}(\omega,\mathbf{H})\ D(R)_{ki}\ D(R)_{lj} \tag{39}$$

and Eq. (22) for antiunitary operators a to

$$\tau_{\hat{B}_i\hat{A}_j}(\omega,-\mathbf{H}(R))=\sum_{kl}\tau_{\hat{A}_l\hat{B}_k}(\omega,\mathbf{H})\ D(R)_{ki}\ D(R)_{lj}, \tag{40}$$

where

$$\mathbf{H}(R)_i=\sum_j D(P_R)_{ij}H_j. \tag{41}$$

Here we used the fact that the matrices $\underline{\mathbf{D}}(R)$ are real and that $\mathbf{H}$ is a pseudovector. A further simplification can be achieved by splitting R in a proper rotation P_R and the space inversion I, if it is contained in R. Explicitly, this means that $R=P_R$ if R is a proper rotation and $R=P_RI$ if R is an improper rotation. For proper rotations one has $\det(\underline{\mathbf{D}}(R))=+1$ while for improper rotations $\det(\underline{\mathbf{D}}(R))=-1$ holds. Because the space inversion amounts to a simple multiplication with $-\mathbb{1}_3$, this splitting can be expressed by

$$\underline{\mathbf{D}}(R)=\det(\underline{\mathbf{D}}(R))\,\underline{\mathbf{D}}(P_R). \tag{42}$$

Since the matrix $\underline{\mathbf{D}}(R)$ appears twice in Eqs. (39) and (40), the two factors $\det(\underline{\mathbf{D}}(R))$ compensate each other, regardless whether R is a proper or an improper rotation. Thus, the final equation for the unitary operators is

$$\tau_{\hat{B}_i\hat{A}_j}(\omega,\mathbf{H})=\sum_{kl}\tau_{\hat{B}_k\hat{A}_l}(\omega,\mathbf{H})D(P_R)_{ki}D(P_R)_{lj}, \tag{43}$$

and for antiunitary operators

$$\tau_{\hat{B}_i\hat{A}_j}(\omega,-\mathbf{H})=\sum_{kl}\tau_{\hat{A}_l\hat{B}_k}(\omega,\mathbf{H})D(P_R)_{ki}D(P_R)_{lj}. \tag{44}$$

This splitting of R enables one to consider the symmetry property of the thermogalvanic coefficients of a solid on the basis of its magnetic Laue group instead of its magnetic point group. This applies whether the conventional definition of the Laue group (see Sec. III A) is applied or that used by Kleiner [2]. In the latter case the removal of the ineffective inversion I happens already when constructing the Laue group. In the former case, one may add improper rotations $R=P_RI$, where again I is ineffective and P_R is an element of both groups. Working only with the magnetic Laue group has the obvious advantage that less cases have to be considered (see Tables I–III) as there are only 32 magnetic Laue groups, while there are 122 different crystallographic magnetic point groups.

On the basis of Eqs. (43) and (44) it is now rather straightforward to give explicit forms for the response tensors $\underline{\mathbf{L}}_{ij}$ in Eq. (30). For this purpose the abbreviations $\tau_{ij}=\tau_{\hat{A}_i\hat{B}_j}$, $\tau'_{ij}=\tau_{\hat{B}_i\hat{A}_j}$, and $\sigma_{ij}=\tau_{\hat{A}_i\hat{A}_j}$ will be used, where $\hat{\mathbf{A}}$ and $\hat{\mathbf{B}}$ can stand for $\hat{\mathbf{j}}$ or $\hat{\mathbf{q}}$. Accordingly, $\underline{\boldsymbol{\tau}}$ and $\underline{\boldsymbol{\tau}}'$ represent either $\underline{\mathbf{L}}_{12}$ or $\underline{\mathbf{L}}_{21}$ or the other way around, and $\underline{\boldsymbol{\sigma}}$ represents $\underline{\mathbf{L}}_{11}$ or $\underline{\mathbf{L}}_{22}$, respectively, which obviously have to have the same structure. It is interesting to note that Eq. (44) can lead to restrictions on the tensor elements in addition to those imposed by Eq. (43). These hold even for the tensors of type $\underline{\boldsymbol{\tau}}'$.

In the case of a magnetically ordered solid having a magnetic space group of category (b) the restrictions to the

TABLE IV. Tensor forms for magnetic Laue groups of category (a).

Magnetic Laue group	$\underline{\boldsymbol{\tau}}'$	$\underline{\boldsymbol{\sigma}}$
$\bar{1}1'$	$\begin{pmatrix} \tau_{xx} & \tau_{yx} & \tau_{zx} \\ \tau_{xy} & \tau_{yy} & \tau_{zy} \\ \tau_{xz} & \tau_{yz} & \tau_{zz} \end{pmatrix}$	$\begin{pmatrix} \sigma_{xx} & \sigma_{xy} & \sigma_{xz} \\ \sigma_{xy} & \sigma_{yy} & \sigma_{yz} \\ \sigma_{xz} & \sigma_{yz} & \sigma_{zz} \end{pmatrix}$
$2/m1'$	$\begin{pmatrix} \tau_{xx} & 0 & \tau_{zx} \\ 0 & \tau_{yy} & 0 \\ \tau_{xz} & 0 & \tau_{zz} \end{pmatrix}$	$\begin{pmatrix} \sigma_{xx} & 0 & \sigma_{xz} \\ 0 & \sigma_{yy} & 0 \\ \sigma_{xz} & 0 & \sigma_{zz} \end{pmatrix}$
$mmm1'$	$\begin{pmatrix} \tau_{xx} & 0 & 0 \\ 0 & \tau_{yy} & 0 \\ 0 & 0 & \tau_{zz} \end{pmatrix}$	$\begin{pmatrix} \sigma_{xx} & 0 & 0 \\ 0 & \sigma_{yy} & 0 \\ 0 & 0 & \sigma_{zz} \end{pmatrix}$
$\bar{3}1',4/m1',$ $6/m1'$	$\begin{pmatrix} \tau_{xx} & -\tau_{xy} & 0 \\ \tau_{xy} & \tau_{xx} & 0 \\ 0 & 0 & \tau_{zz} \end{pmatrix}$	$\begin{pmatrix} \sigma_{xx} & 0 & 0 \\ 0 & \sigma_{xx} & 0 \\ 0 & 0 & \sigma_{zz} \end{pmatrix}$
$\bar{3}1m1', \bar{3}m11',$ $4/mmm1', 6/mmm1'$	$\begin{pmatrix} \tau_{xx} & 0 & 0 \\ 0 & \tau_{xx} & 0 \\ 0 & 0 & \tau_{zz} \end{pmatrix}$	$\begin{pmatrix} \sigma_{xx} & 0 & 0 \\ 0 & \sigma_{xx} & 0 \\ 0 & 0 & \sigma_{zz} \end{pmatrix}$
$m\bar{3}1', m\bar{3}m1'$	$\begin{pmatrix} \tau_{xx} & 0 & 0 \\ 0 & \tau_{xx} & 0 \\ 0 & 0 & \tau_{xx} \end{pmatrix}$	$\begin{pmatrix} \sigma_{xx} & 0 & 0 \\ 0 & \sigma_{xx} & 0 \\ 0 & 0 & \sigma_{xx} \end{pmatrix}$

shape of the thermogalvanic tensors result only from the application of Eq. (43) as there are no antiunitary operations. As a consequence, all tensors $\underline{\boldsymbol{\sigma}}$, $\underline{\boldsymbol{\tau}}$, and $\underline{\boldsymbol{\tau}}'$ have the same shape. Accordingly, only the shape of $\underline{\boldsymbol{\tau}}$ is given in Table V, that is in full agreement with Kleiner's Table IV [2].

For magnetic space groups belonging to category (a) or category (c) Eq. (44) has to be applied in addition to Eq. (43). In general, this leads to different symmetry restrictions for the tensors of type $\underline{\boldsymbol{\tau}}'$ and $\underline{\boldsymbol{\sigma}}$. The resulting shape of the tensors for category (a) is given in Table IV. These results agree with those given by Kleiner's Table V [2], apart from those for the Laue groups $\bar{3}1'$, $4/m1'$, and $6/m1'$. Since the magnetic Laue groups in category (a) differ from those in (b) only by the time-reversal $1'$ as an element of its own, the tensor shapes in Table IV

TABLE V. Tensor forms for magnetic Laue groups of category (b).

Magnetic Laue group	$\underline{\boldsymbol{\tau}}$
$\bar{1}$	$\begin{pmatrix} \tau_{xx} & \tau_{xy} & \tau_{xz} \\ \tau_{yx} & \tau_{yy} & \tau_{yz} \\ \tau_{zx} & \tau_{zy} & \tau_{zz} \end{pmatrix}$
$2/m$	$\begin{pmatrix} \tau_{xx} & 0 & \tau_{xz} \\ 0 & \tau_{yy} & 0 \\ \tau_{zx} & 0 & \tau_{zz} \end{pmatrix}$
mmm	$\begin{pmatrix} \tau_{xx} & 0 & 0 \\ 0 & \tau_{yy} & 0 \\ 0 & 0 & \tau_{zz} \end{pmatrix}$
$\bar{3}, 4/m, 6/m$	$\begin{pmatrix} \tau_{xx} & \tau_{xy} & 0 \\ -\tau_{xy} & \tau_{xx} & 0 \\ 0 & 0 & \tau_{zz} \end{pmatrix}$
$\bar{3}1m, \bar{3}m1, 4/mmm, 6/mmm$	$\begin{pmatrix} \tau_{xx} & 0 & 0 \\ 0 & \tau_{xx} & 0 \\ 0 & 0 & \tau_{zz} \end{pmatrix}$
$m\bar{3}, m\bar{3}m$	$\begin{pmatrix} \tau_{xx} & 0 & 0 \\ 0 & \tau_{xx} & 0 \\ 0 & 0 & \tau_{xx} \end{pmatrix}$

TABLE VI. Tensor forms for magnetic Laue groups of category (c). The tensor forms for the groups $4'/mm'm$ and $4'/mmm'$ are related to each other by a rotation of the coordinate system around the principal (z) axis by $\pi/4$.

Magnetic Laue group	$\underline{\boldsymbol{\tau}}'$	$\underline{\boldsymbol{\sigma}}$
$2'/m'$	$\begin{pmatrix} \tau_{xx} & -\tau_{yx} & \tau_{zx} \\ -\tau_{xy} & \tau_{yy} & -\tau_{zy} \\ \tau_{xz} & -\tau_{yz} & \tau_{zz} \end{pmatrix}$	$\begin{pmatrix} \sigma_{xx} & \sigma_{xy} & \sigma_{xz} \\ -\sigma_{xy} & \sigma_{yy} & \sigma_{yz} \\ \sigma_{xz} & -\sigma_{yz} & \sigma_{zz} \end{pmatrix}$
$m'm'm$	$\begin{pmatrix} \tau_{xx} & -\tau_{yx} & 0 \\ -\tau_{xy} & \tau_{yy} & 0 \\ 0 & 0 & \tau_{zz} \end{pmatrix}$	$\begin{pmatrix} \sigma_{xx} & \sigma_{xy} & 0 \\ -\sigma_{xy} & \sigma_{yy} & 0 \\ 0 & 0 & \sigma_{zz} \end{pmatrix}$
$4'/m$	$\begin{pmatrix} \tau_{yy} & -\tau_{xy} & 0 \\ -\tau_{yx} & \tau_{xx} & 0 \\ 0 & 0 & \tau_{zz} \end{pmatrix}$	$\begin{pmatrix} \sigma_{xx} & 0 & 0 \\ 0 & \sigma_{xx} & 0 \\ 0 & 0 & \sigma_{zz} \end{pmatrix}$
$4'/mm'm$	$\begin{pmatrix} \tau_{xx} & -\tau_{xy} & 0 \\ -\tau_{xy} & \tau_{xx} & 0 \\ 0 & 0 & \tau_{zz} \end{pmatrix}$	$\begin{pmatrix} \sigma_{xx} & 0 & 0 \\ 0 & \sigma_{xx} & 0 \\ 0 & 0 & \sigma_{zz} \end{pmatrix}$
$4'/mmm'$	$\begin{pmatrix} \tau_{yy} & 0 & 0 \\ 0 & \tau_{xx} & 0 \\ 0 & 0 & \tau_{zz} \end{pmatrix}$	$\begin{pmatrix} \sigma_{xx} & 0 & 0 \\ 0 & \sigma_{xx} & 0 \\ 0 & 0 & \sigma_{zz} \end{pmatrix}$
$\bar{3}1m', \bar{3}m'1,$ $4/mm'm',$ $6/mm'm'$	$\begin{pmatrix} \tau_{xx} & \tau_{xy} & 0 \\ -\tau_{xy} & \tau_{xx} & 0 \\ 0 & 0 & \tau_{zz} \end{pmatrix}$	$\begin{pmatrix} \sigma_{xx} & \sigma_{xy} & 0 \\ -\sigma_{xy} & \sigma_{xx} & 0 \\ 0 & 0 & \sigma_{zz} \end{pmatrix}$
$6'/m'$	$\begin{pmatrix} \tau_{xx} & -\tau_{xy} & 0 \\ \tau_{xy} & \tau_{xx} & 0 \\ 0 & 0 & \tau_{zz} \end{pmatrix}$	$\begin{pmatrix} \sigma_{xx} & 0 & 0 \\ 0 & \sigma_{xx} & 0 \\ 0 & 0 & \sigma_{zz} \end{pmatrix}$
$6'/m'm'm,$ $6'/m'mm'$	$\begin{pmatrix} \tau_{xx} & 0 & 0 \\ 0 & \tau_{xx} & 0 \\ 0 & 0 & \tau_{zz} \end{pmatrix}$	$\begin{pmatrix} \sigma_{xx} & 0 & 0 \\ 0 & \sigma_{xx} & 0 \\ 0 & 0 & \sigma_{zz} \end{pmatrix}$
$m\bar{3}m'$	$\begin{pmatrix} \tau_{xx} & 0 & 0 \\ 0 & \tau_{xx} & 0 \\ 0 & 0 & \tau_{xx} \end{pmatrix}$	$\begin{pmatrix} \sigma_{xx} & 0 & 0 \\ 0 & \sigma_{xx} & 0 \\ 0 & 0 & \sigma_{xx} \end{pmatrix}$

alternatively can be deduced from those in Table V simply by considering in addition the effect of $1'$. In case of $\underline{\boldsymbol{\sigma}}$ this can lead to additional restrictions (degeneracies and zero elements) since in this case the antiunitary time reversal connects $\underline{\boldsymbol{\sigma}}$ with itself according to its definition given above. For the thermoelectric tensor on the other hand, this just states the usual Onsager relations as expressed by $\tau'_{ij}(\mathbf{H}) = \tau_{ji}(-\mathbf{H})$ [see Eq. (34)]. Table VI gives the results for category (c) that are in full agreement with those given by Kleiner's Table VI [2]. Obviously the results presented in Tables IV–VI fulfill the Onsager relations given by Eqs. (32) to (34) that are not postulated *a priori*.

Kleiner's scheme was applied here to derive the shape of the tensors representing homogeneous bulk systems. However, it may also be applied to investigate the symmetry restrictions on the so-called layer-resolved conductivity tensor $\underline{\boldsymbol{\sigma}}^{IJ}$ with I and J labeling atomic layers of a two-dimensional periodic system [17]. This concept may be used for example in the context of electrical transport in layered GMR systems [18,19] or magneto-optical properties of surface systems [20,21]. Another extension of Kleiner's scheme is the discussion of nonlinear effects [17].

C. Shape of the spin conductivity tensor

Spin transport as reflected for example by the spin Hall effect is usually described by use of the spin conductivity σ_{ij}^{k}

that gives the current density along direction i for the spin polarization with respect to the k axis induced by an electrical field along the j axis. Within a single-particle description of the electronic structure the Kubo formalism leads for σ_{ij}^{k} to an expression analogous to the Kubo-Bastin equation [22] for the electrical conductivity [23,24]:

$$\sigma_{ij}^{k} = \frac{i\hbar}{V}\int_{-\infty}^{\infty} dE\; f(E)\,\mathrm{Tr}\left\langle \hat{J}_i^k \frac{dG^+(E)}{dE}\,\hat{j}_j\,\delta(E-\hat{H}) - \hat{J}_i^k\,\delta(E-\hat{H})\,\hat{j}_j\,\frac{dG^-}{dE}\right\rangle_c. \tag{45}$$

Here $\hat{H}$ is the Hamiltonian of the system, $G^+(E)$ and $G^-(E)$ are the corresponding retarded and advanced Green functions, and $\hat{j}_j$ is the ordinary electrical current density operator. A straightforward definition for the spin current density operator $\hat{J}_i^k = \frac{1}{2}\{\hat{v}_i,\sigma_k\}$ consists in the anticommutator of the conventional velocity operator $\hat{v}_i$ and the Pauli spin matrix σ_k [25]. As the spin conductivity is caused by spin-orbit coupling a coherent relativistic implementation of Eq. (45) seems to be more appropriate. This implies that the electrical current density operator $\hat{j}_j = -|e|c\alpha_j$ is expressed in terms of the 4×4 Dirac α matrices [26]. A corresponding expression for the spin current density operator $\hat{J}_i^k = \hat{\mathcal{T}}_k\hat{j}_i$ was suggested by Vernes *et al.* [27] that involves the spatial part $\hat{\mathcal{T}}_k$ of the spin polarization operator introduced by Bargmann and Wigner [28]:

$$\hat{\mathcal{T}}_k = \beta\Sigma_k - \tfrac{1}{mc}\gamma_5\Pi_k. \tag{46}$$

Here β, γ_5, Σ_k are again standard 4×4 Dirac matrices, m is the electron mass, and Π_k stands for the kinetic momentum [26]. In fact this approach was adopted by Lowitzer *et al.* [23,24] when dealing with the spin Hall effect of disordered alloys. However, as mentioned above, for an investigation of the shape of a response tensor the explicit expressions for the involved operators are not relevant but only their behavior under symmetry operations. Both definitions of $\hat{J}_i^k$ given above consist of a combination of the current density operator $\hat{j}_i$ with an operator that represents the spin polarization of an electron. In contrast to $\hat{j}_i$ [see Eq. (38)], the latter one (e.g., $\hat{\mathcal{T}}_k$) transforms as a pseudovector which changes sign under time reversal. Accordingly, one has for the transformation matrices

$$\underline{\mathbf{D}}^{(\hat{\mathcal{T}}_k)}(u) = \det(R)\underline{\mathbf{D}}(R), \tag{47}$$

$$\underline{\mathbf{D}}^{(\hat{\mathcal{T}}_k)}(a) = -\det(R)\underline{\mathbf{D}}(R), \tag{48}$$

corresponding to Eqs. (5) and (6).

Identifying now $\hat{A}_i = \hat{j}_j$, $\hat{B}_j = \hat{j}_i$, and $\hat{C}_k = \hat{\mathcal{T}}_k$ in Eqs. (12) and (22) one finds the behavior of σ_{ij}^k under unitary transformations

$$\sigma_{ij}^{k} = \sum_{lmn}\det(R)\;D(R)_{li}\;D(R)_{mj}\;D(R)_{nk}\;\sigma_{lm}^{n}, \tag{49}$$

and under antiunitary transformations

$$\sigma_{ij}^{k} = -\sum_{lmn}\det(R)\;D(R)_{li}\;D(R)_{mj}\;D(R)_{nk}\;\sigma_{lm}^{\prime n}, \tag{50}$$

respectively. In analogy to the treatment of thermoelectric coefficients presented above one may again split the rotation R into its proper part P_R and, if present, improper part as given in Eq. (42). The resulting equation for unitary transformations is then

$$\sigma_{ij}^{k} = \sum_{lmn} D(P_R)_{li}\;D(P_R)_{mj}\;D(P_R)_{nk}\;\det(R)^4\;\sigma_{lm}^{n} \tag{51}$$

$$= \sum_{lmn} D(P_R)_{li}\;D(P_R)_{mj}\;D(P_R)_{nk}\;\sigma_{lm}^{n} \tag{52}$$

and

$$\sigma_{ij}^{k} = -\sum_{lmn} D(P_R)_{li}\;D(P_R)_{mj}\;D(P_R)_{nk}\;\sigma_{lm}^{\prime n} \tag{53}$$

for antiunitary transformations, respectively. As a consequence, as found for the thermoelectric coefficients by Kleiner [2] also for the spin conductivity tensor it is sufficient to consider the magnetic Laue group of the solid.

Using Eqs. (52) and (53) the shape of the inverse spin conductivity tensor was determined with the results given in the left column of Tables VII–IX for magnetic Laue group of categories (a)–(c).

It should be noted that these tables for the spin conductivity and its inverse effect can be seen as an equivalent to the generalized Onsager relations derived by Kleiner for the thermogalvanic transport tensors $\underline{\boldsymbol{\tau}}$ and $\underline{\boldsymbol{\tau}}'$. In particular, they give the shape of the tensors $\underline{\boldsymbol{\sigma}}'^{k}$ representing the Onsager reciprocal quantity, e.g., the inverse spin Hall effect (ISHE) as counterpart to the spin Hall effect (SHE), as discussed for instance by Shi *et al.* [25].

Because $\hat{\mathbf{j}}$ and $\hat{\mathbf{q}}$ have the same transformation properties and because the tensors $\tau_{(\hat{B}_i\hat{C}_j)\hat{A}_k}$ and $\tau_{\hat{A}_l^\dagger(\hat{B}_m^\dagger C_n^\dagger)}$ in Eq. (22) are different objects in both cases, the tensor shapes for tensors describing the connection between spin currents and heat currents have exactly the same shape as those tabulated in the left column of Tables VII, VIII, and IX.

For convenience, it is possible to alter the notation of these symmetry-restricted matrices in such a way that the symmetry of the spin conductivity tensor is easier to recognize at first sight. This is achieved by removing the time-reversal operator $1'$ from every antiunitary operation (or by omitting it if it appears on its own). However, this reduction leads to the loss of the specific meaning, i.e., the generalized Onsager relations, contained in the tensors $\underline{\boldsymbol{\sigma}}'^{k}$. The reduced tensors are tabulated for categories (a), (b), and (c) in the right column of Tables VII, VIII, and IX, respectively.

As discussed in the context of the charge and heat current in response to an electric field the corresponding operators $\hat{j}_i$ and $\hat{q}_i$ have the same symmetry properties. As a consequence the tensors $\underline{\mathbf{L}}_{11}$ and $\underline{\mathbf{L}}_{22}$ in Eq. (30) have the same shape given by $\underline{\boldsymbol{\sigma}}$ in Tables IV–VI. For the same reason the tensor representing the spin current induced by a thermal gradient has the same shape as that connected with an electric field with both given by the right column of Tables VII–IX.

One of the major benefits of Tables VII–IX is obviously the prediction of all possible linear response spin transport phenomena induced by an electric field or a thermal gradient for any solid based on its magnetic space group. The occurrence of antisymmetric off-diagonal elements in the tensor $\underline{\boldsymbol{\sigma}}^{k}$ ($k = x,y,z$) in Table VII implies that the transverse spin Hall effect is, in principle, allowed by symmetry in any paramagnetic

TABLE VII. Polarization tensor forms and reduced polarization tensor forms for magnetic Laue groups of category (a). The tensor forms for the groups $\bar{3}1m1'$ and $\bar{3}m11'$ are related to each other by a rotation of the coordinate system around the principal (z) axis by $\pi/2$.

Magnetic Laue group	$\underline{\boldsymbol{\sigma}}'^{x}$	$\underline{\boldsymbol{\sigma}}'^{y}$	$\underline{\boldsymbol{\sigma}}'^{z}$	$\underline{\boldsymbol{\sigma}}^{x}$	$\underline{\boldsymbol{\sigma}}^{y}$	$\underline{\boldsymbol{\sigma}}^{z}$
$\bar{1}1'$	$\begin{pmatrix} -\sigma^x_{xx} & -\sigma^x_{xy} & -\sigma^x_{xz} \\ -\sigma^y_{xx} & -\sigma^y_{xy} & -\sigma^y_{xz} \\ -\sigma^z_{xx} & -\sigma^z_{xy} & -\sigma^z_{xz} \end{pmatrix}$	$\begin{pmatrix} -\sigma^x_{yx} & -\sigma^x_{yy} & -\sigma^x_{yz} \\ -\sigma^y_{yx} & -\sigma^y_{yy} & -\sigma^y_{yz} \\ -\sigma^z_{yx} & -\sigma^z_{yy} & -\sigma^z_{yz} \end{pmatrix}$	$\begin{pmatrix} -\sigma^x_{zx} & -\sigma^x_{zy} & -\sigma^x_{zz} \\ -\sigma^y_{zx} & -\sigma^y_{zy} & -\sigma^y_{zz} \\ -\sigma^z_{zx} & -\sigma^z_{zy} & -\sigma^z_{zz} \end{pmatrix}$	$\begin{pmatrix} \sigma^x_{xx} & \sigma^x_{xy} & \sigma^x_{xz} \\ \sigma^x_{yx} & \sigma^x_{yy} & \sigma^x_{yz} \\ \sigma^x_{zx} & \sigma^x_{zy} & \sigma^x_{zz} \end{pmatrix}$	$\begin{pmatrix} \sigma^y_{xx} & \sigma^y_{xy} & \sigma^y_{xz} \\ \sigma^y_{yx} & \sigma^y_{yy} & \sigma^y_{yz} \\ \sigma^y_{zx} & \sigma^y_{zy} & \sigma^y_{zz} \end{pmatrix}$	$\begin{pmatrix} \sigma^z_{xx} & \sigma^z_{xy} & \sigma^z_{xz} \\ \sigma^z_{yx} & \sigma^z_{yy} & \sigma^z_{yz} \\ \sigma^z_{zx} & \sigma^z_{zy} & \sigma^z_{zz} \end{pmatrix}$
$2/m1'$	$\begin{pmatrix} 0 & -\sigma^x_{xy} & 0 \\ -\sigma^y_{xx} & 0 & -\sigma^y_{xz} \\ 0 & -\sigma^z_{xy} & 0 \end{pmatrix}$	$\begin{pmatrix} -\sigma^x_{yx} & 0 & -\sigma^x_{yz} \\ 0 & -\sigma^y_{yy} & 0 \\ -\sigma^z_{yx} & 0 & -\sigma^z_{yz} \end{pmatrix}$	$\begin{pmatrix} 0 & -\sigma^x_{zy} & 0 \\ -\sigma^y_{zx} & 0 & -\sigma^y_{zz} \\ 0 & -\sigma^z_{zy} & 0 \end{pmatrix}$	$\begin{pmatrix} 0 & \sigma^x_{xy} & 0 \\ \sigma^x_{yx} & 0 & \sigma^x_{yz} \\ 0 & \sigma^x_{zy} & 0 \end{pmatrix}$	$\begin{pmatrix} \sigma^y_{xx} & 0 & \sigma^y_{xz} \\ 0 & \sigma^y_{yy} & 0 \\ \sigma^y_{zx} & 0 & \sigma^y_{zz} \end{pmatrix}$	$\begin{pmatrix} 0 & \sigma^z_{xy} & 0 \\ \sigma^z_{yx} & 0 & \sigma^z_{yz} \\ 0 & \sigma^z_{zy} & 0 \end{pmatrix}$
$mmm1'$	$\begin{pmatrix} 0 & 0 & 0 \\ 0 & 0 & -\sigma^y_{xz} \\ 0 & -\sigma^z_{xy} & 0 \end{pmatrix}$	$\begin{pmatrix} 0 & 0 & -\sigma^x_{yz} \\ 0 & 0 & 0 \\ -\sigma^z_{yx} & 0 & 0 \end{pmatrix}$	$\begin{pmatrix} 0 & -\sigma^x_{zy} & 0 \\ -\sigma^y_{zx} & 0 & 0 \\ 0 & 0 & 0 \end{pmatrix}$	$\begin{pmatrix} 0 & 0 & 0 \\ 0 & 0 & \sigma^x_{yz} \\ 0 & \sigma^x_{zy} & 0 \end{pmatrix}$	$\begin{pmatrix} 0 & 0 & \sigma^y_{xz} \\ 0 & 0 & 0 \\ \sigma^y_{zx} & 0 & 0 \end{pmatrix}$	$\begin{pmatrix} 0 & \sigma^z_{xy} & 0 \\ \sigma^z_{yx} & 0 & 0 \\ 0 & 0 & 0 \end{pmatrix}$
$4/m1', 6/m1'$	$\begin{pmatrix} 0 & 0 & -\sigma^x_{xz} \\ 0 & 0 & -\sigma^y_{xz} \\ -\sigma^z_{xx} & -\sigma^z_{xy} & 0 \end{pmatrix}$	$\begin{pmatrix} 0 & 0 & \sigma^y_{xz} \\ 0 & 0 & -\sigma^x_{xz} \\ \sigma^z_{xy} & -\sigma^z_{xx} & 0 \end{pmatrix}$	$\begin{pmatrix} -\sigma^x_{zx} & \sigma^y_{zx} & 0 \\ -\sigma^y_{zx} & -\sigma^x_{zx} & 0 \\ 0 & 0 & -\sigma^z_{zz} \end{pmatrix}$	$\begin{pmatrix} 0 & 0 & \sigma^x_{xz} \\ 0 & 0 & -\sigma^y_{xz} \\ \sigma^x_{zx} & -\sigma^y_{zx} & 0 \end{pmatrix}$	$\begin{pmatrix} 0 & 0 & \sigma^y_{xz} \\ 0 & 0 & \sigma^x_{xz} \\ \sigma^y_{zx} & \sigma^x_{zx} & 0 \end{pmatrix}$	$\begin{pmatrix} \sigma^z_{xx} & -\sigma^z_{xy} & 0 \\ -\sigma^z_{xy} & \sigma^z_{xx} & 0 \\ 0 & 0 & 0 \end{pmatrix}$
$4/mmm1', 6/mmm1'$	$\begin{pmatrix} 0 & 0 & 0 \\ 0 & 0 & -\sigma^y_{xz} \\ 0 & -\sigma^z_{xy} & 0 \end{pmatrix}$	$\begin{pmatrix} 0 & 0 & \sigma^y_{xz} \\ 0 & 0 & 0 \\ \sigma^z_{xy} & 0 & 0 \end{pmatrix}$	$\begin{pmatrix} 0 & \sigma^y_{zx} & 0 \\ -\sigma^y_{zx} & 0 & 0 \\ 0 & 0 & 0 \end{pmatrix}$	$\begin{pmatrix} 0 & 0 & 0 \\ 0 & 0 & -\sigma^y_{xz} \\ 0 & -\sigma^y_{zx} & 0 \end{pmatrix}$	$\begin{pmatrix} 0 & 0 & \sigma^y_{xz} \\ 0 & 0 & 0 \\ \sigma^y_{zx} & 0 & 0 \end{pmatrix}$	$\begin{pmatrix} 0 & \sigma^z_{xy} & 0 \\ -\sigma^z_{xy} & 0 & 0 \\ 0 & 0 & 0 \end{pmatrix}$
$\bar{3}1'$	$\begin{pmatrix} -\sigma^x_{xx} & -\sigma^y_{xx} & -\sigma^x_{xz} \\ -\sigma^y_{xx} & \sigma^x_{xx} & -\sigma^y_{xz} \\ -\sigma^z_{xx} & -\sigma^z_{xy} & 0 \end{pmatrix}$	$\begin{pmatrix} -\sigma^y_{xx} & \sigma^x_{xx} & \sigma^y_{xz} \\ \sigma^x_{xx} & \sigma^y_{xx} & -\sigma^x_{xz} \\ \sigma^z_{xy} & -\sigma^z_{xx} & 0 \end{pmatrix}$	$\begin{pmatrix} -\sigma^x_{zx} & \sigma^y_{zx} & 0 \\ -\sigma^y_{zx} & -\sigma^x_{zx} & 0 \\ 0 & 0 & -\sigma^z_{zz} \end{pmatrix}$	$\begin{pmatrix} \sigma^x_{xx} & \sigma^y_{xx} & \sigma^x_{xz} \\ \sigma^y_{xx} & -\sigma^x_{xx} & -\sigma^y_{xz} \\ \sigma^x_{zx} & -\sigma^y_{zx} & 0 \end{pmatrix}$	$\begin{pmatrix} 0 & -\sigma^x_{xx} & \sigma^y_{xz} \\ -\sigma^x_{xx} & 0 & \sigma^x_{xz} \\ \sigma^y_{zx} & \sigma^x_{zx} & 0 \end{pmatrix}$	$\begin{pmatrix} \sigma^z_{xx} & \sigma^z_{xy} & 0 \\ \sigma^z_{xy} & -\sigma^z_{xx} & 0 \\ 0 & 0 & 0 \end{pmatrix}$
$\bar{3}1m1'$	$\begin{pmatrix} -\sigma^x_{xx} & 0 & 0 \\ 0 & \sigma^x_{xx} & -\sigma^y_{xz} \\ 0 & -\sigma^z_{xy} & 0 \end{pmatrix}$	$\begin{pmatrix} 0 & \sigma^x_{xx} & \sigma^y_{xz} \\ \sigma^x_{xx} & 0 & 0 \\ \sigma^z_{xy} & 0 & 0 \end{pmatrix}$	$\begin{pmatrix} 0 & \sigma^y_{zx} & 0 \\ -\sigma^y_{zx} & 0 & 0 \\ 0 & 0 & 0 \end{pmatrix}$	$\begin{pmatrix} \sigma^x_{xx} & 0 & 0 \\ 0 & -\sigma^x_{xx} & -\sigma^y_{xz} \\ 0 & -\sigma^y_{zx} & 0 \end{pmatrix}$	$\begin{pmatrix} 0 & -\sigma^x_{xx} & \sigma^y_{xz} \\ -\sigma^x_{xx} & 0 & 0 \\ \sigma^y_{zx} & 0 & 0 \end{pmatrix}$	$\begin{pmatrix} 0 & \sigma^z_{xy} & 0 \\ -\sigma^z_{xy} & 0 & 0 \\ 0 & 0 & 0 \end{pmatrix}$
$\bar{3}m11'$	$\begin{pmatrix} 0 & -\sigma^y_{xx} & 0 \\ -\sigma^y_{xx} & 0 & -\sigma^y_{xz} \\ 0 & -\sigma^z_{xy} & 0 \end{pmatrix}$	$\begin{pmatrix} -\sigma^y_{xx} & 0 & \sigma^y_{xz} \\ 0 & \sigma^y_{xx} & 0 \\ \sigma^z_{xy} & 0 & 0 \end{pmatrix}$	$\begin{pmatrix} 0 & \sigma^y_{zx} & 0 \\ -\sigma^y_{zx} & 0 & 0 \\ 0 & 0 & 0 \end{pmatrix}$	$\begin{pmatrix} 0 & \sigma^y_{xx} & 0 \\ \sigma^y_{xx} & 0 & -\sigma^y_{xz} \\ 0 & -\sigma^y_{zx} & 0 \end{pmatrix}$	$\begin{pmatrix} \sigma^y_{xx} & 0 & \sigma^y_{xz} \\ 0 & -\sigma^y_{xx} & 0 \\ \sigma^y_{zx} & 0 & 0 \end{pmatrix}$	$\begin{pmatrix} 0 & \sigma^z_{xy} & 0 \\ -\sigma^z_{xy} & 0 & 0 \\ 0 & 0 & 0 \end{pmatrix}$
$m\bar{3}1'$	$\begin{pmatrix} 0 & 0 & 0 \\ 0 & 0 & -\sigma^y_{xz} \\ 0 & -\sigma^z_{xy} & 0 \end{pmatrix}$	$\begin{pmatrix} 0 & 0 & -\sigma^x_{xz} \\ 0 & 0 & 0 \\ -\sigma^y_{xz} & 0 & 0 \end{pmatrix}$	$\begin{pmatrix} 0 & -\sigma^x_{xy} & 0 \\ -\sigma^y_{xz} & 0 & 0 \\ 0 & 0 & 0 \end{pmatrix}$	$\begin{pmatrix} 0 & 0 & 0 \\ 0 & 0 & \sigma^x_{xz} \\ 0 & \sigma^x_{xz} & 0 \end{pmatrix}$	$\begin{pmatrix} 0 & 0 & \sigma^y_{xz} \\ 0 & 0 & 0 \\ \sigma^y_{xz} & 0 & 0 \end{pmatrix}$	$\begin{pmatrix} 0 & \sigma^z_{xy} & 0 \\ \sigma^z_{xy} & 0 & 0 \\ 0 & 0 & 0 \end{pmatrix}$
$m\bar{3}m1'$	$\begin{pmatrix} 0 & 0 & 0 \\ 0 & 0 & \sigma^z_{xy} \\ 0 & -\sigma^z_{xy} & 0 \end{pmatrix}$	$\begin{pmatrix} 0 & 0 & -\sigma^z_{xy} \\ 0 & 0 & 0 \\ -\sigma^z_{xy} & 0 & 0 \end{pmatrix}$	$\begin{pmatrix} 0 & \sigma^z_{xy} & 0 \\ -\sigma^z_{xy} & 0 & 0 \\ 0 & 0 & 0 \end{pmatrix}$	$\begin{pmatrix} 0 & 0 & 0 \\ 0 & 0 & \sigma^z_{xy} \\ 0 & \sigma^z_{xy} & 0 \end{pmatrix}$	$\begin{pmatrix} 0 & 0 & \sigma^z_{xy} \\ 0 & 0 & 0 \\ \sigma^z_{xy} & 0 & 0 \end{pmatrix}$	$\begin{pmatrix} 0 & \sigma^z_{xy} & 0 \\ \sigma^z_{xy} & 0 & 0 \\ 0 & 0 & 0 \end{pmatrix}$

TABLE VIII. Polarization tensor forms and (identical) reduced polarization tensor forms for magnetic Laue groups of category (b). The tensor forms for the groups $\bar{3}1m$ and $\bar{3}m1$ are related to each other by a rotation of the coordinate system around the principal (z) axis by $\pi/2$.

Magnetic Laue group	$\underline{\boldsymbol{\sigma}}^{/x}$	$\underline{\boldsymbol{\sigma}}^{/y}$	$\underline{\boldsymbol{\sigma}}^{/z}$	$\underline{\boldsymbol{\sigma}}^{x}$	$\underline{\boldsymbol{\sigma}}^{y}$	$\underline{\boldsymbol{\sigma}}^{z}$
$\bar{1}$	$\begin{pmatrix} \sigma^x_{xx} & \sigma^x_{xy} & \sigma^x_{xz} \\ \sigma^x_{yx} & \sigma^x_{yy} & \sigma^x_{yz} \\ \sigma^x_{zx} & \sigma^x_{zy} & \sigma^x_{zz} \end{pmatrix}$	$\begin{pmatrix} \sigma^y_{xx} & \sigma^y_{xy} & \sigma^y_{xz} \\ \sigma^y_{yx} & \sigma^y_{yy} & \sigma^y_{yz} \\ \sigma^y_{zx} & \sigma^y_{zy} & \sigma^y_{zz} \end{pmatrix}$	$\begin{pmatrix} \sigma^z_{xx} & \sigma^z_{xy} & \sigma^z_{xz} \\ \sigma^z_{yx} & \sigma^z_{yy} & \sigma^z_{yz} \\ \sigma^z_{zx} & \sigma^z_{zy} & \sigma^z_{zz} \end{pmatrix}$	$\begin{pmatrix} \sigma^x_{xx} & \sigma^x_{xy} & \sigma^x_{xz} \\ \sigma^x_{yx} & \sigma^x_{yy} & \sigma^x_{yz} \\ \sigma^x_{zx} & \sigma^x_{zy} & \sigma^x_{zz} \end{pmatrix}$	$\begin{pmatrix} \sigma^y_{xx} & \sigma^y_{xy} & \sigma^y_{xz} \\ \sigma^y_{yx} & \sigma^y_{yy} & \sigma^y_{yz} \\ \sigma^y_{zx} & \sigma^y_{zy} & \sigma^y_{zz} \end{pmatrix}$	$\begin{pmatrix} \sigma^z_{xx} & \sigma^z_{xy} & \sigma^z_{xz} \\ \sigma^z_{yx} & \sigma^z_{yy} & \sigma^z_{yz} \\ \sigma^z_{zx} & \sigma^z_{zy} & \sigma^z_{zz} \end{pmatrix}$
$2/m$	$\begin{pmatrix} 0 & \sigma^x_{xy} & 0 \\ \sigma^x_{yx} & 0 & \sigma^x_{yz} \\ 0 & \sigma^x_{zy} & 0 \end{pmatrix}$	$\begin{pmatrix} 0 & \sigma^y_{xy} & 0 \\ \sigma^y_{yx} & 0 & \sigma^y_{yz} \\ 0 & \sigma^y_{zy} & 0 \end{pmatrix}$	$\begin{pmatrix} 0 & \sigma^z_{xy} & 0 \\ \sigma^z_{yx} & 0 & \sigma^z_{yz} \\ 0 & \sigma^z_{zy} & 0 \end{pmatrix}$	$\begin{pmatrix} 0 & \sigma^x_{xy} & 0 \\ \sigma^x_{yx} & 0 & \sigma^x_{yz} \\ 0 & \sigma^x_{zy} & 0 \end{pmatrix}$	$\begin{pmatrix} \sigma^y_{xx} & 0 & \sigma^y_{xz} \\ 0 & \sigma^y_{yy} & 0 \\ \sigma^y_{zx} & 0 & \sigma^y_{zz} \end{pmatrix}$	$\begin{pmatrix} 0 & \sigma^z_{xy} & 0 \\ \sigma^z_{yx} & 0 & \sigma^z_{yz} \\ 0 & \sigma^z_{zy} & 0 \end{pmatrix}$
mmm	$\begin{pmatrix} 0 & 0 & 0 \\ 0 & 0 & \sigma^x_{yz} \\ 0 & \sigma^x_{zy} & 0 \end{pmatrix}$	$\begin{pmatrix} 0 & 0 & \sigma^y_{xz} \\ 0 & 0 & 0 \\ \sigma^y_{zx} & 0 & 0 \end{pmatrix}$	$\begin{pmatrix} 0 & \sigma^z_{xy} & 0 \\ \sigma^z_{yx} & 0 & 0 \\ 0 & 0 & 0 \end{pmatrix}$	$\begin{pmatrix} 0 & 0 & 0 \\ 0 & 0 & \sigma^x_{yz} \\ 0 & \sigma^x_{zy} & 0 \end{pmatrix}$	$\begin{pmatrix} 0 & 0 & \sigma^y_{xz} \\ 0 & 0 & 0 \\ \sigma^y_{zx} & 0 & 0 \end{pmatrix}$	$\begin{pmatrix} 0 & \sigma^z_{xy} & 0 \\ \sigma^z_{yx} & 0 & 0 \\ 0 & 0 & 0 \end{pmatrix}$
$4/m$, $6/m$	$\begin{pmatrix} 0 & 0 & \sigma^x_{xz} \\ 0 & 0 & -\sigma^x_{yz} \\ \sigma^x_{zx} & -\sigma^x_{zy} & 0 \end{pmatrix}$	$\begin{pmatrix} 0 & 0 & \sigma^y_{xz} \\ 0 & 0 & \sigma^y_{yz} \\ \sigma^y_{zx} & \sigma^y_{zy} & 0 \end{pmatrix}$	$\begin{pmatrix} 0 & \sigma^z_{xy} & 0 \\ \sigma^z_{yx} & 0 & 0 \\ 0 & 0 & 0 \end{pmatrix}$	$\begin{pmatrix} 0 & 0 & \sigma^x_{xz} \\ 0 & 0 & -\sigma^x_{yz} \\ \sigma^x_{zx} & -\sigma^x_{zy} & 0 \end{pmatrix}$	$\begin{pmatrix} 0 & 0 & \sigma^y_{xz} \\ 0 & 0 & \sigma^y_{yz} \\ \sigma^y_{zx} & \sigma^y_{zy} & 0 \end{pmatrix}$	$\begin{pmatrix} 0 & \sigma^z_{xy} & 0 \\ \sigma^z_{yx} & 0 & 0 \\ 0 & 0 & 0 \end{pmatrix}$
$4/mmm$, $6/mmm$	$\begin{pmatrix} 0 & 0 & 0 \\ 0 & 0 & -\sigma^y_{xz} \\ 0 & -\sigma^y_{zx} & 0 \end{pmatrix}$	$\begin{pmatrix} 0 & 0 & \sigma^y_{xz} \\ 0 & 0 & 0 \\ \sigma^y_{zx} & 0 & 0 \end{pmatrix}$	$\begin{pmatrix} 0 & \sigma^z_{xy} & 0 \\ -\sigma^z_{xy} & 0 & 0 \\ 0 & 0 & 0 \end{pmatrix}$	$\begin{pmatrix} 0 & 0 & 0 \\ 0 & 0 & -\sigma^y_{xz} \\ 0 & -\sigma^y_{zx} & 0 \end{pmatrix}$	$\begin{pmatrix} 0 & 0 & \sigma^y_{xz} \\ 0 & 0 & 0 \\ \sigma^y_{zx} & 0 & 0 \end{pmatrix}$	$\begin{pmatrix} 0 & \sigma^z_{xy} & 0 \\ -\sigma^z_{xy} & 0 & 0 \\ 0 & 0 & 0 \end{pmatrix}$
$\bar{3}$	$\begin{pmatrix} \sigma^x_{xx} & \sigma^x_{xy} & \sigma^x_{xz} \\ \sigma^y_{xx} & \sigma^y_{xy} & \sigma^y_{xz} \\ \sigma^x_{zx} & \sigma^x_{zy} & 0 \end{pmatrix}$	$\begin{pmatrix} \sigma^y_{xx} & -\sigma^x_{xx} & \sigma^y_{xz} \\ -\sigma^x_{xx} & -\sigma^y_{xx} & \sigma^x_{xz} \\ \sigma^y_{zx} & \sigma^x_{zx} & 0 \end{pmatrix}$	$\begin{pmatrix} \sigma^z_{xx} & \sigma^z_{xy} & 0 \\ \sigma^z_{yx} & \sigma^z_{yy} & 0 \\ 0 & 0 & \sigma^z_{zz} \end{pmatrix}$	$\begin{pmatrix} \sigma^x_{xx} & \sigma^x_{xy} & \sigma^x_{xz} \\ \sigma^y_{xx} & \sigma^y_{xy} & \sigma^y_{xz} \\ \sigma^x_{zx} & \sigma^x_{zy} & 0 \end{pmatrix}$	$\begin{pmatrix} \sigma^y_{xx} & -\sigma^x_{xx} & \sigma^y_{xz} \\ -\sigma^x_{xx} & -\sigma^y_{xx} & \sigma^x_{xz} \\ \sigma^y_{zx} & \sigma^x_{zx} & 0 \end{pmatrix}$	$\begin{pmatrix} \sigma^z_{xx} & \sigma^z_{xy} & 0 \\ \sigma^z_{yx} & \sigma^z_{yy} & 0 \\ 0 & 0 & \sigma^z_{zz} \end{pmatrix}$
$\bar{3}1m$	$\begin{pmatrix} \sigma^x_{xx} & 0 & 0 \\ 0 & -\sigma^x_{xx} & -\sigma^y_{xz} \\ 0 & -\sigma^y_{zx} & 0 \end{pmatrix}$	$\begin{pmatrix} 0 & -\sigma^x_{xx} & \sigma^y_{xz} \\ -\sigma^x_{xx} & 0 & 0 \\ \sigma^y_{zx} & 0 & 0 \end{pmatrix}$	$\begin{pmatrix} 0 & \sigma^z_{xy} & 0 \\ -\sigma^z_{xy} & 0 & 0 \\ 0 & 0 & 0 \end{pmatrix}$	$\begin{pmatrix} \sigma^x_{xx} & 0 & 0 \\ 0 & -\sigma^x_{xx} & -\sigma^y_{xz} \\ 0 & -\sigma^y_{zx} & 0 \end{pmatrix}$	$\begin{pmatrix} 0 & -\sigma^x_{xx} & \sigma^y_{xz} \\ -\sigma^x_{xx} & 0 & 0 \\ \sigma^y_{zx} & 0 & 0 \end{pmatrix}$	$\begin{pmatrix} 0 & \sigma^z_{xy} & 0 \\ -\sigma^z_{xy} & 0 & 0 \\ 0 & 0 & 0 \end{pmatrix}$
$\bar{3}m1$	$\begin{pmatrix} 0 & \sigma^y_{xx} & 0 \\ \sigma^y_{xx} & 0 & -\sigma^y_{xz} \\ 0 & -\sigma^y_{zx} & 0 \end{pmatrix}$	$\begin{pmatrix} \sigma^y_{xx} & 0 & \sigma^y_{xz} \\ 0 & -\sigma^y_{xx} & 0 \\ \sigma^y_{zx} & 0 & 0 \end{pmatrix}$	$\begin{pmatrix} 0 & \sigma^z_{xy} & 0 \\ -\sigma^z_{xy} & 0 & 0 \\ 0 & 0 & 0 \end{pmatrix}$	$\begin{pmatrix} 0 & \sigma^y_{xx} & 0 \\ \sigma^y_{xx} & 0 & -\sigma^y_{xz} \\ 0 & -\sigma^y_{zx} & 0 \end{pmatrix}$	$\begin{pmatrix} \sigma^y_{xx} & 0 & \sigma^y_{xz} \\ 0 & -\sigma^y_{xx} & 0 \\ \sigma^y_{zx} & 0 & 0 \end{pmatrix}$	$\begin{pmatrix} 0 & \sigma^z_{xy} & 0 \\ -\sigma^z_{xy} & 0 & 0 \\ 0 & 0 & 0 \end{pmatrix}$
$m\bar{3}$	$\begin{pmatrix} 0 & 0 & 0 \\ 0 & 0 & \sigma^z_{xy} \\ 0 & \sigma^y_{xz} & 0 \end{pmatrix}$	$\begin{pmatrix} 0 & 0 & \sigma^y_{xz} \\ 0 & 0 & 0 \\ \sigma^z_{xy} & 0 & 0 \end{pmatrix}$	$\begin{pmatrix} 0 & \sigma^z_{xy} & 0 \\ \sigma^y_{xz} & 0 & 0 \\ 0 & 0 & 0 \end{pmatrix}$	$\begin{pmatrix} 0 & 0 & 0 \\ 0 & 0 & \sigma^z_{xy} \\ 0 & \sigma^y_{xz} & 0 \end{pmatrix}$	$\begin{pmatrix} 0 & 0 & \sigma^y_{xz} \\ 0 & 0 & 0 \\ \sigma^z_{xy} & 0 & 0 \end{pmatrix}$	$\begin{pmatrix} 0 & \sigma^z_{xy} & 0 \\ \sigma^y_{xz} & 0 & 0 \\ 0 & 0 & 0 \end{pmatrix}$
$m\bar{3}m$	$\begin{pmatrix} 0 & 0 & 0 \\ 0 & 0 & \sigma^z_{xy} \\ 0 & -\sigma^z_{xy} & 0 \end{pmatrix}$	$\begin{pmatrix} 0 & 0 & -\sigma^z_{xy} \\ 0 & 0 & 0 \\ \sigma^z_{xy} & 0 & 0 \end{pmatrix}$	$\begin{pmatrix} 0 & \sigma^z_{xy} & 0 \\ -\sigma^z_{xy} & 0 & 0 \\ 0 & 0 & 0 \end{pmatrix}$	$\begin{pmatrix} 0 & 0 & 0 \\ 0 & 0 & \sigma^z_{xy} \\ 0 & -\sigma^z_{xy} & 0 \end{pmatrix}$	$\begin{pmatrix} 0 & 0 & -\sigma^z_{xy} \\ 0 & 0 & 0 \\ \sigma^z_{xy} & 0 & 0 \end{pmatrix}$	$\begin{pmatrix} 0 & \sigma^z_{xy} & 0 \\ -\sigma^z_{xy} & 0 & 0 \\ 0 & 0 & 0 \end{pmatrix}$

TABLE IX. Polarization tensor forms and reduced polarization tensor forms for magnetic Laue groups of category (c). Note that the reduced tensor forms for the groups $m'm'm$ and $4'/m$ as well as for the groups $\bar{3}1m'$, $\bar{3}m'1$, and $6'/m'$ are identical. Moreover those of $4'/mm'm$ and $4'/mmm'$, of $\bar{3}1m'$ and $\bar{3}m'1$, as well as of $6'/m'm'm$ and $6'/m'mm'$ are (pairwise) related to each other by a rotation of the coordinate system around the principal (z) axis by $\pi/4$, $\pi/2$, and $\pi/2$, respectively.

Magnetic Laue group	$\underline{\sigma}'^x$	$\underline{\sigma}'^y$	$\underline{\sigma}'^z$	$\underline{\sigma}^x$	$\underline{\sigma}^y$	$\underline{\sigma}^z$
$2'/m'$	$\begin{pmatrix} \sigma^x_{xx} & -\sigma^x_{xy} & \sigma^x_{xz} \\ -\sigma^y_{xx} & \sigma^y_{xy} & -\sigma^y_{xz} \\ \sigma^z_{xx} & -\sigma^z_{xy} & \sigma^z_{xz} \end{pmatrix}$	$\begin{pmatrix} -\sigma^x_{yx} & \sigma^x_{yy} & -\sigma^x_{yz} \\ \sigma^y_{yx} & -\sigma^y_{yy} & \sigma^y_{yz} \\ -\sigma^z_{yx} & \sigma^z_{yy} & -\sigma^z_{yz} \end{pmatrix}$	$\begin{pmatrix} \sigma^x_{zx} & -\sigma^x_{zy} & -\sigma^x_{zz} \\ -\sigma^y_{zx} & \sigma^y_{zy} & -\sigma^y_{zz} \\ \sigma^z_{zx} & -\sigma^z_{zy} & \sigma^z_{zz} \end{pmatrix}$	$\begin{pmatrix} \sigma^x_{xx} & \sigma^x_{xy} & \sigma^x_{xz} \\ \sigma^x_{yx} & \sigma^x_{yy} & \sigma^x_{yz} \\ \sigma^x_{zx} & \sigma^x_{zy} & \sigma^x_{zz} \end{pmatrix}$	$\begin{pmatrix} \sigma^y_{xx} & \sigma^y_{xy} & \sigma^y_{xz} \\ \sigma^y_{yx} & \sigma^y_{yy} & \sigma^y_{yz} \\ \sigma^y_{zx} & \sigma^y_{zy} & \sigma^y_{zz} \end{pmatrix}$	$\begin{pmatrix} \sigma^z_{xx} & \sigma^z_{xy} & \sigma^z_{xz} \\ \sigma^z_{yx} & \sigma^z_{yy} & \sigma^z_{yz} \\ \sigma^z_{zx} & \sigma^z_{zy} & \sigma^z_{zz} \end{pmatrix}$
$m'm'm$	$\begin{pmatrix} 0 & 0 & \sigma^x_{xz} \\ 0 & 0 & -\sigma^y_{xz} \\ \sigma^z_{xx} & -\sigma^z_{xy} & 0 \end{pmatrix}$	$\begin{pmatrix} 0 & 0 & -\sigma^x_{yz} \\ 0 & 0 & \sigma^y_{yz} \\ -\sigma^z_{yx} & \sigma^z_{yy} & 0 \end{pmatrix}$	$\begin{pmatrix} \sigma^x_{zx} & -\sigma^x_{zy} & 0 \\ -\sigma^y_{zx} & \sigma^y_{zy} & 0 \\ 0 & 0 & \sigma^z_{zz} \end{pmatrix}$	$\begin{pmatrix} 0 & 0 & \sigma^x_{xz} \\ 0 & 0 & \sigma^x_{yz} \\ \sigma^x_{zx} & \sigma^x_{zy} & 0 \end{pmatrix}$	$\begin{pmatrix} 0 & 0 & \sigma^y_{xz} \\ 0 & 0 & \sigma^y_{yz} \\ \sigma^y_{zx} & \sigma^y_{zy} & 0 \end{pmatrix}$	$\begin{pmatrix} \sigma^z_{xx} & \sigma^z_{xy} & 0 \\ \sigma^z_{yx} & \sigma^z_{yy} & 0 \\ 0 & 0 & \sigma^z_{zz} \end{pmatrix}$
$4'/m$	$\begin{pmatrix} 0 & 0 & -\sigma^y_{xz} \\ 0 & 0 & \sigma^x_{yz} \\ -\sigma^z_{yy} & \sigma^z_{yx} & 0 \end{pmatrix}$	$\begin{pmatrix} 0 & 0 & \sigma^y_{xz} \\ 0 & 0 & -\sigma^x_{xz} \\ \sigma^z_{xy} & -\sigma^z_{xx} & 0 \end{pmatrix}$	$\begin{pmatrix} -\sigma^y_{zy} & \sigma^y_{zx} & 0 \\ \sigma^x_{zy} & -\sigma^x_{zx} & 0 \\ 0 & 0 & -\sigma^z_{zz} \end{pmatrix}$	$\begin{pmatrix} 0 & 0 & \sigma^x_{xz} \\ 0 & 0 & \sigma^x_{yz} \\ \sigma^x_{zx} & \sigma^x_{zy} & 0 \end{pmatrix}$	$\begin{pmatrix} 0 & 0 & \sigma^y_{xz} \\ 0 & 0 & \sigma^y_{yz} \\ \sigma^y_{zx} & \sigma^y_{zy} & 0 \end{pmatrix}$	$\begin{pmatrix} \sigma^z_{xx} & \sigma^z_{xy} & 0 \\ \sigma^z_{yx} & \sigma^z_{yy} & 0 \\ 0 & 0 & \sigma^z_{zz} \end{pmatrix}$
$4'/mm'm$	$\begin{pmatrix} 0 & 0 & \sigma^x_{xz} \\ 0 & 0 & -\sigma^y_{xz} \\ \sigma^z_{xx} & -\sigma^z_{xy} & 0 \end{pmatrix}$	$\begin{pmatrix} 0 & 0 & \sigma^y_{xz} \\ 0 & 0 & -\sigma^x_{xz} \\ \sigma^z_{xy} & -\sigma^z_{xx} & 0 \end{pmatrix}$	$\begin{pmatrix} \sigma^x_{zx} & -\sigma^y_{zx} & 0 \\ -\sigma^x_{zy} & \sigma^y_{zy} & 0 \\ 0 & 0 & 0 \end{pmatrix}$	$\begin{pmatrix} 0 & 0 & \sigma^x_{xz} \\ 0 & 0 & -\sigma^y_{xz} \\ \sigma^x_{zx} & -\sigma^y_{zx} & 0 \end{pmatrix}$	$\begin{pmatrix} 0 & 0 & \sigma^y_{xz} \\ 0 & 0 & -\sigma^x_{xz} \\ \sigma^y_{zx} & -\sigma^x_{zx} & 0 \end{pmatrix}$	$\begin{pmatrix} \sigma^z_{xx} & -\sigma^z_{xy} & 0 \\ -\sigma^z_{yx} & \sigma^z_{yy} & 0 \\ 0 & 0 & \sigma^z_{zz} \end{pmatrix}$
$4'/mmm'$	$\begin{pmatrix} 0 & 0 & 0 \\ 0 & 0 & \sigma^x_{yz} \\ 0 & \sigma^y_{yz} & 0 \end{pmatrix}$	$\begin{pmatrix} 0 & 0 & \sigma^y_{xz} \\ 0 & 0 & 0 \\ \sigma^z_{xy} & 0 & 0 \end{pmatrix}$	$\begin{pmatrix} 0 & \sigma^y_{zx} & 0 \\ \sigma^x_{zy} & 0 & 0 \\ 0 & 0 & 0 \end{pmatrix}$	$\begin{pmatrix} 0 & 0 & 0 \\ 0 & 0 & \sigma^x_{yz} \\ 0 & \sigma^x_{zy} & 0 \end{pmatrix}$	$\begin{pmatrix} 0 & 0 & \sigma^y_{xz} \\ 0 & 0 & 0 \\ \sigma^y_{zx} & 0 & 0 \end{pmatrix}$	$\begin{pmatrix} 0 & \sigma^z_{xy} & 0 \\ \sigma^z_{yx} & 0 & 0 \\ 0 & 0 & 0 \end{pmatrix}$
$4/mm'm'$, $6/mm'm'$	$\begin{pmatrix} 0 & 0 & \sigma^x_{xz} \\ 0 & 0 & -\sigma^y_{xz} \\ \sigma^z_{xx} & -\sigma^z_{xy} & 0 \end{pmatrix}$	$\begin{pmatrix} 0 & 0 & \sigma^y_{xz} \\ 0 & 0 & \sigma^x_{xz} \\ \sigma^z_{xy} & \sigma^z_{xx} & 0 \end{pmatrix}$	$\begin{pmatrix} \sigma^x_{zx} & \sigma^y_{zx} & 0 \\ -\sigma^x_{zy} & \sigma^x_{zx} & 0 \\ 0 & 0 & \sigma^z_{zz} \end{pmatrix}$	$\begin{pmatrix} 0 & 0 & \sigma^x_{xz} \\ 0 & 0 & -\sigma^y_{xz} \\ \sigma^x_{zx} & -\sigma^y_{zx} & 0 \end{pmatrix}$	$\begin{pmatrix} 0 & 0 & \sigma^y_{xz} \\ 0 & 0 & \sigma^x_{xz} \\ \sigma^y_{zx} & \sigma^x_{zx} & 0 \end{pmatrix}$	$\begin{pmatrix} \sigma^z_{xx} & -\sigma^z_{xy} & 0 \\ -\sigma^z_{yx} & \sigma^z_{yy} & 0 \\ 0 & 0 & \sigma^z_{zz} \end{pmatrix}$
$\bar{3}1m'$	$\begin{pmatrix} -\sigma^x_{xx} & \sigma^y_{xx} & \sigma^x_{xz} \\ \sigma^y_{xx} & \sigma^x_{xx} & -\sigma^y_{xz} \\ \sigma^z_{xx} & -\sigma^z_{xy} & 0 \end{pmatrix}$	$\begin{pmatrix} \sigma^y_{xx} & \sigma^x_{xx} & \sigma^y_{xz} \\ \sigma^x_{xx} & -\sigma^y_{xx} & \sigma^x_{xz} \\ \sigma^z_{xy} & \sigma^z_{xx} & 0 \end{pmatrix}$	$\begin{pmatrix} \sigma^x_{zx} & \sigma^y_{zx} & 0 \\ -\sigma^x_{zy} & \sigma^x_{zx} & 0 \\ 0 & 0 & \sigma^z_{zz} \end{pmatrix}$	$\begin{pmatrix} \sigma^x_{xx} & \sigma^y_{xx} & \sigma^x_{xz} \\ \sigma^y_{xx} & -\sigma^x_{xx} & -\sigma^y_{xz} \\ \sigma^x_{zx} & -\sigma^y_{zx} & 0 \end{pmatrix}$	$\begin{pmatrix} \sigma^y_{xx} & -\sigma^x_{xx} & \sigma^y_{xz} \\ -\sigma^x_{xx} & -\sigma^y_{xx} & \sigma^x_{xz} \\ \sigma^y_{zx} & \sigma^x_{zx} & 0 \end{pmatrix}$	$\begin{pmatrix} \sigma^z_{xx} & \sigma^z_{xy} & 0 \\ \sigma^z_{yx} & \sigma^z_{xx} & 0 \\ 0 & 0 & \sigma^z_{zz} \end{pmatrix}$
$\bar{3}m'1$	$\begin{pmatrix} \sigma^x_{xx} & -\sigma^y_{xx} & \sigma^x_{xz} \\ -\sigma^y_{xx} & -\sigma^x_{xx} & -\sigma^y_{xz} \\ \sigma^z_{xx} & -\sigma^z_{xy} & 0 \end{pmatrix}$	$\begin{pmatrix} -\sigma^y_{xx} & -\sigma^x_{xx} & \sigma^y_{xz} \\ -\sigma^x_{xx} & \sigma^y_{xx} & \sigma^x_{xz} \\ \sigma^z_{xy} & \sigma^z_{xx} & 0 \end{pmatrix}$	$\begin{pmatrix} \sigma^x_{zx} & -\sigma^y_{zx} & 0 \\ -\sigma^x_{zy} & \sigma^x_{zx} & 0 \\ 0 & 0 & \sigma^z_{zz} \end{pmatrix}$	$\begin{pmatrix} \sigma^x_{xx} & \sigma^y_{xx} & \sigma^x_{xz} \\ \sigma^y_{xx} & -\sigma^x_{xx} & -\sigma^y_{xz} \\ \sigma^x_{zx} & -\sigma^y_{zx} & 0 \end{pmatrix}$	$\begin{pmatrix} \sigma^y_{xx} & -\sigma^x_{xx} & \sigma^y_{xz} \\ -\sigma^x_{xx} & -\sigma^y_{xx} & \sigma^x_{xz} \\ \sigma^y_{zx} & \sigma^x_{zx} & 0 \end{pmatrix}$	$\begin{pmatrix} \sigma^z_{xx} & \sigma^z_{xy} & 0 \\ \sigma^z_{yx} & \sigma^z_{xx} & 0 \\ 0 & 0 & \sigma^z_{zz} \end{pmatrix}$
$6'/m'$	$\begin{pmatrix} \sigma^x_{xx} & \sigma^y_{xx} & -\sigma^x_{xz} \\ \sigma^y_{xx} & -\sigma^x_{xx} & -\sigma^y_{xz} \\ -\sigma^z_{xx} & -\sigma^z_{xy} & 0 \end{pmatrix}$	$\begin{pmatrix} \sigma^y_{xx} & -\sigma^x_{xx} & \sigma^y_{xz} \\ -\sigma^x_{xx} & -\sigma^y_{xx} & -\sigma^x_{xz} \\ \sigma^z_{xy} & -\sigma^z_{xx} & 0 \end{pmatrix}$	$\begin{pmatrix} -\sigma^x_{zx} & \sigma^y_{zx} & 0 \\ \sigma^x_{zy} & -\sigma^y_{zx} & 0 \\ 0 & 0 & -\sigma^z_{zz} \end{pmatrix}$	$\begin{pmatrix} \sigma^x_{xx} & \sigma^y_{xx} & \sigma^x_{xz} \\ \sigma^y_{xx} & -\sigma^x_{xx} & -\sigma^y_{xz} \\ \sigma^x_{zx} & -\sigma^y_{zx} & 0 \end{pmatrix}$	$\begin{pmatrix} \sigma^y_{xx} & -\sigma^x_{xx} & \sigma^y_{xz} \\ -\sigma^x_{xx} & -\sigma^y_{xx} & \sigma^x_{xz} \\ \sigma^y_{zx} & \sigma^x_{zx} & 0 \end{pmatrix}$	$\begin{pmatrix} \sigma^z_{xx} & \sigma^z_{xy} & 0 \\ \sigma^z_{yx} & \sigma^z_{xx} & 0 \\ 0 & 0 & \sigma^z_{zz} \end{pmatrix}$
$6'/m'm'm$	$\begin{pmatrix} \sigma^x_{xx} & 0 & 0 \\ 0 & -\sigma^x_{xx} & -\sigma^y_{xz} \\ 0 & -\sigma^z_{xy} & 0 \end{pmatrix}$	$\begin{pmatrix} 0 & -\sigma^x_{xx} & 0 \\ -\sigma^x_{xx} & 0 & 0 \\ 0 & 0 & 0 \end{pmatrix}$	$\begin{pmatrix} 0 & \sigma^y_{zx} & 0 \\ \sigma^y_{zx} & 0 & 0 \\ 0 & 0 & 0 \end{pmatrix}$	$\begin{pmatrix} \sigma^x_{xx} & 0 & 0 \\ 0 & -\sigma^x_{xx} & -\sigma^y_{xz} \\ 0 & -\sigma^y_{zx} & 0 \end{pmatrix}$	$\begin{pmatrix} 0 & -\sigma^x_{xx} & 0 \\ -\sigma^x_{xx} & 0 & 0 \\ 0 & 0 & 0 \end{pmatrix}$	$\begin{pmatrix} 0 & \sigma^z_{xy} & 0 \\ \sigma^z_{yx} & 0 & 0 \\ 0 & 0 & 0 \end{pmatrix}$
$6'/m'mm'$	$\begin{pmatrix} 0 & \sigma^y_{xx} & 0 \\ \sigma^y_{xx} & 0 & -\sigma^y_{xz} \\ 0 & -\sigma^z_{xy} & 0 \end{pmatrix}$	$\begin{pmatrix} \sigma^y_{xx} & 0 & \sigma^y_{xz} \\ 0 & -\sigma^y_{xx} & 0 \\ \sigma^z_{xy} & 0 & 0 \end{pmatrix}$	$\begin{pmatrix} 0 & \sigma^y_{zx} & 0 \\ \sigma^y_{zx} & 0 & 0 \\ 0 & 0 & 0 \end{pmatrix}$	$\begin{pmatrix} 0 & \sigma^y_{xx} & 0 \\ \sigma^y_{xx} & 0 & -\sigma^y_{xz} \\ 0 & -\sigma^y_{zx} & 0 \end{pmatrix}$	$\begin{pmatrix} \sigma^y_{xx} & 0 & \sigma^y_{xz} \\ 0 & -\sigma^y_{xx} & 0 \\ \sigma^y_{zx} & 0 & 0 \end{pmatrix}$	$\begin{pmatrix} 0 & \sigma^z_{xy} & 0 \\ \sigma^z_{yx} & 0 & 0 \\ 0 & 0 & 0 \end{pmatrix}$
$m\bar{3}m'$	$\begin{pmatrix} 0 & 0 & 0 \\ 0 & 0 & \sigma^z_{xy} \\ 0 & \sigma^y_{xz} & 0 \end{pmatrix}$	$\begin{pmatrix} 0 & 0 & \sigma^y_{xz} \\ 0 & 0 & 0 \\ \sigma^z_{xy} & 0 & 0 \end{pmatrix}$	$\begin{pmatrix} 0 & \sigma^z_{xy} & 0 \\ \sigma^y_{xz} & 0 & 0 \\ 0 & 0 & 0 \end{pmatrix}$	$\begin{pmatrix} 0 & 0 & 0 \\ 0 & 0 & \sigma^x_{yz} \\ 0 & \sigma^y_{xz} & 0 \end{pmatrix}$	$\begin{pmatrix} 0 & 0 & \sigma^y_{xz} \\ 0 & 0 & 0 \\ \sigma^z_{xy} & 0 & 0 \end{pmatrix}$	$\begin{pmatrix} 0 & \sigma^z_{xy} & 0 \\ \sigma^y_{xz} & 0 & 0 \\ 0 & 0 & 0 \end{pmatrix}$

solid. However, one has to stress that in case of the magnetic Laue groups $\bar{1}$, $2/m$, and $mmm1'$ the shape of the tensor is not purely antisymmetric. The same is true for a ferromagnetic solid according to Tables VIII and IX, i.e., the spin Hall and Nernst effects are symmetry allowed in any magnetic solid as well (again not all cases show purely antisymmetric elements). Considering as an example a ferromagnetic cubic solid with the magnetic Laue group $4/mm'm'$ (e.g., bcc-Fe or fcc-Ni with the magnetization along the z direction) its spin conductivity tensor is very different from the form of its nonmagnetic counterpart with $m\bar{3}m1'$. For the nonmagnetic case only the elements σ_{ij}^{k} with $i \neq j \neq k \neq i$ are nonzero. In addition, these are the same for a cyclic permutation of (i,j,k) and change the sign for an anticyclic one. For the ferromagnetic case additional off-diagonal elements may appear, with the degeneracies depending on the spin projection component k, and the tensors are no longer purely antisymmetric. In particular one notes that there are diagonal elements that imply the occurrence of a longitudinal spin current induced by an electric field that in general will depend on whether the electric field is along (σ_{zz}^{z}) or perpendicular ($\sigma_{xx}^{z} = \sigma_{yy}^{z}$) the magnetization. These tensor elements are obviously responsible for the occurrence of the spin-dependent Seebeck effect [29]. Interestingly, for a nonmagnetic solid there are several magnetic space groups that also imply a nonvanishing diagonal tensor element σ_{ii}^{k}, i.e., a longitudinal current along the direction of the applied electric field or thermal gradient. This was demonstrated recently by corresponding numerical work on nonmagnetic $(Au_{1-x}Pt_x)_4Sc$ showing that the longitudinal spin conductivity can be comparable in magnitude to the transverse spin Hall conductivity [30].

D. Implementation

The symmetry restrictions imposed on the thermogalvanic tensors by Eqs. (43) and (44) as well as on the spin conductivity tensor by Eqs. (52) and (53), respectively, were determined by means of a Python script that is based on the *Computational Crystallography Toolbox*, *cctbx* [31]. Although this library provides support only for the nonmagnetic crystallographic operations, it is also of great value when dealing with magnetic solids. To determine the magnetic space group of a solid all possible magnetic space groups are simply scanned through and checked which fits to the system under investigation. The corresponding symmetry operations are taken from the magnetic space group data file `magnetic_data.txt` [13,32]. Once the magnetic point group has been found, the u and a operators needed for an application of Eqs. (43) and (44) or Eqs. (52) and (53), respectively, are fixed. Going through all elements of the magnetic point group leads to a set of connecting equations between the tensor elements which can then be solved to get the shape of the tensor. For these symbolic calculations the *SymPy* library [33] is used. Although in principle the generators of a magnetic point group are sufficient to obtain all symmetry restrictions, it turned out to be more convenient to apply all symmetry operations since the *cctbx* library and the magnetic space group tables do not provide a set of generators.

Finally, it should be mentioned that the results for the spin conductivity tensor $\underline{\boldsymbol{\sigma}}^{z}$ for the spin polarization along the z axis have been checked against the output of the SPRKKR program package [34] that allows calculating this tensor on the basis of the relativistic Kubo formalism [35]. For all investigated magnetic Laue groups of categories (a) ($\bar{1}1'$, $mm1'$, $2/m1'$, $4/m1'$, $4/mmm1'$, $6/mmm1'$, $m\bar{3}m1'$), (b) ($4/m$), and (c) ($2'/m'$, $m'm'm$, $4/mm'm'$, $\bar{3}m'1$, $6/mm'm'$) the numerical results for $\underline{\boldsymbol{\sigma}}^{z}$ were found to be completely in line with the analytical predictions given in Tables VII–IX.

IV. SUMMARY

Kleiner's scheme to determine the shape of a linear response tensor has been extended to deal with more complex situations. The resulting set of equations has been used to revise the shape of the electric charge and heat conductivity tensors for all magnetic space groups. It was demonstrated that for this only the magnetic Laue group of a solid is relevant. This also holds for the spin conductivity tensor that is used among other to discuss the longitudinal spin-dependent Seebeck effect as well as the transverse spin Hall and Nernst effects. Results for all magnetic space groups are presented in an easily accessible way, by giving in addition to the tensors $\underline{\boldsymbol{\sigma}}'^{k}$ containing the generalized Onsager relations also the reduced tensor forms $\underline{\boldsymbol{\sigma}}^{k}$. Furthermore, the axis conventions of the space groups are preserved when constructing the magnetic Laue groups and therefore, although redundant, the tensor forms are given in both coordinate systems whenever there is an ambiguity. Interestingly, several magnetic Laue groups for nonmagnetic solids were identified that should show a new longitudinal spin transport phenomenon [30]. Finally, it should be stressed that the scheme presented here can be applied straightforwardly to any other response function. Examples relevant for spintronics and related fields are the response tensors representing spin-orbit torque, Gilbert damping, or the Edelstein effect [36].

ACKNOWLEDGMENTS

This work was supported financially by the Deutsche Forschungsgemeinschaft (DFG) via the priority program SPP 1538 and the SFB 689.

[1] H. Grimmer, General relations for transport properties in magnetically ordered crystals, Acta Crystallogr. Sect. A **49**, 763 (1993).

[2] W. H. Kleiner, Space-Time Symmetry of Transport Coefficients, Phys. Rev. **142**, 318 (1966).

[3] W. H. Kleiner, Space-Time Symmetry Restrictions on Transport Coefficients. II. Two Theories Compared, Phys. Rev. **153**, 726 (1967).

[4] W. H. Kleiner, Space-Time Symmetry Restrictions on Transport Coefficients. III. Thermogalvanomagnetic Coefficients, Phys. Rev. **182**, 705 (1969).

[5] M. Dyakonov and V. Perel, Current-induced spin orientation of electrons in semiconductors, Phys. Lett. A **35**, 459 (1971).

[6] Y. K. Kato, R. C. Myers, A. C. Gossard, and D. D. Awschalom, Observation of the spin Hall effect in semiconductors, Science **306**, 1910 (2004).

[7] Z. Ma, Spin Hall effect generated by a temperature gradient and heat current in a two-dimensional electron gas, Solid State Commun. **150**, 510 (2010).

[8] K. Tauber, M. Gradhand, D. V. Fedorov, and I. Mertig, Extrinsic Spin Nernst Effect from First Principles, Phys. Rev. Lett. **109**, 026601 (2012).

[9] S. Wimmer, D. Ködderitzsch, K. Chadova, and H. Ebert, First-principles linear response description of the spin Nernst effect, Phys. Rev. B **88**, 201108(R) (2013).

[10] G. D. Mahan, *Many-Particle Physics*, Physics of Solids and Liquids (Springer, New York, 2000).

[11] R. Kubo, M. Toda, and N. Hashitsume, *Statistical Physics II: Nonequilibrium Statistical Mechanics*, Springer Series in Solid-State Sciences (Springer, New York, 1998).

[12] D. B. Litvin and V. Kopský, Seitz notation for symmetry operations of space groups, Acta Crystallogr. Sect. A **67**, 415 (2011).

[13] D. B. Litvin, Magnetic space-group types, Acta Crystallogr. Sect. A **57**, 729 (2001).

[14] W. Borchardt-Ott, *Crystallography: An Introduction*, 3rd ed. (Springer, Berlin, 2012), Chap. 13.4.

[15] *International Tables for Crystallography, Volume A: Space Group Symmetry* (Springer, New York, 2002).

[16] M. Jonson and G. D. Mahan, Mott's formula for the thermopower and the Wiedemann-Franz law, Phys. Rev. B **21**, 4223 (1980).

[17] T. Huhne, Magneto–optical Kerr effect of multilayer and surface layer systems, Ph.D. thesis, Ludwig-Maximilians-Universität München, 2001.

[18] W. H. Butler, X.-G. Zhang, D. M. C. Nicholson, and J. M. MacLaren, First-principles calculations of electrical conductivity and giant magnetoresistance of Co|Cu|Co spin valves, Phys. Rev. B **52**, 13399 (1995).

[19] P. Weinberger, V. Drchal, J. Kudrnovský, I. Turek, H. Herper, L. Szunyogh, and C. Sommers, Aspects of magnetotunnelling drawn from *ab-initio*-type calculations, Philos. Mag. **82**, 1027 (2002).

[20] T. Huhne and H. Ebert, Magneto-optical properties of ultra-thin surface layer systems, Europhys. Lett. **59**, 612 (2002).

[21] A. Vernes, L. Szunyogh, L. Udvardi, and P. Weinberger, Layer-resolved optical conductivity of Co|Pt multilayers, J. Magn. Magn. Mater. **240**, 215 (2002).

[22] A. Bastin, C. Lewiner, O. Betbeder-matibet, and P. Nozieres, Quantum oscillations of the Hall effect of a fermion gas with random impurity scattering, J. Phys. Chem. Solids **32**, 1811 (1971).

[23] S. Lowitzer, Relativistic electronic transport theory - The spin Hall effect and related phenomena, Ph.D. thesis, Ludwig-Maximilians-Universität München, 2010.

[24] S. Lowitzer, M. Gradhand, D. Ködderitzsch, D. V. Fedorov, I. Mertig, and H. Ebert, Extrinsic and Intrinsic Contributions to the Spin Hall Effect of Alloys, Phys. Rev. Lett. **106**, 056601 (2011).

[25] J. Shi, P. Zhang, D. Xiao, and Q. Niu, Proper Definition of Spin Current in Spin-Orbit Coupled Systems, Phys. Rev. Lett. **96**, 076604 (2006).

[26] M. E. Rose, *Relativistic Electron Theory* (Wiley, New York, 1961).

[27] A. Vernes, B. L. Györffy, and P. Weinberger, Spin currents, spin-transfer torque, and spin-Hall effects in relativistic quantum mechanics, Phys. Rev. B **76**, 012408 (2007).

[28] V. Bargmann and E. P. Wigner, Group theoretical discussion of relativistic wave equations, Proc. Natl. Acad. Sci. USA **34**, 211 (1948).

[29] A. Slachter, F. L. Bakker, J.-P. Adam, and B. J. van Wees, Thermally driven spin injection from a ferromagnet into a non-magnetic metal, Nat. Phys. **6**, 879 (2010).

[30] S. Wimmer, M. Seemann, K. Chadova, D. Ködderitzsch, and H. Ebert, Spin-orbit-induced longitudinal spin-polarized currents in nonmagnetic solids, Phys. Rev. B **92**, 041101(R) (2015).

[31] R. W. Grosse-Kunstleve, N. K. Sauter, N. W. Moriarty, and P. D. Adams, The *computational crystallography toolbox*: crystallographic algorithms in a reusable software framework, J. Appl. Crystallogr. **35**, 126 (2002).

[32] H. T. Stokes, D. M. Hatch, and B. J. Campbell, Isotropy software suite, http://stokes.byu.edu/iso/magnetic_data.txt (2013).

[33] SymPy Development Team, *SymPy: Python Library for Symbolic Mathematics*, https://www.sympy.org (2013).

[34] H. Ebert *et al.*, The Munich SPR-KKR package, version 6.3, http://olymp.cup.uni-muenchen.de/ak/ebert/SPRKKR (2012).

[35] H. Ebert, D. Ködderitzsch, and J. Minár, Calculating condensed matter properties using the KKR-Green's function method–recent developments and applications, Rep. Prog. Phys. **74**, 096501 (2011).

[36] M. Seemann, D. Ködderitzsch, S. Wimmer, S. Mankovsky, and H. Ebert (unpublished).

Errata and additional considerations

- On the r.h.s. of Eq. (18) on page 3 of Ref. 283 (page 177 herein), the vector operator $\hat{A}(-\tau)$ should read $\hat{\mathbf{A}}(-\tau)$, i.e., boldface instead of italic.

- On page 3 of Ref. 283 (page 177 herein), right column, the sentence around Eq. (26) should end "...that may **be** part of *s*."

- On page 5 of Ref. 283 (page 179 herein), the Onsager relations expressed in Eqs. (32)-(34) are only valid for *non-magnetic* systems. Hence the sentence preceding these should read "As explicitly demonstrated by Kleiner [2] as well as below, **in non-magnetic solids** the coefficients $\underline{\boldsymbol{L}}_{ij}$ satisfy Onsager relations of the form..."
  Accordingly, on page 6 (page 180 herein) the last sentence of the paragraph below TABLE VI should be "Obviously **only** the results presented in Table **IV** fulfil the Onsager relations given by Eqs. (32) to (34) that are not postulated *a priori*. **For magnetic systems different relations hold, termed *generalised Onsager relations* by Kleiner. For category (b) these state that $\underline{\boldsymbol{\sigma}}$, $\underline{\boldsymbol{\tau}}$, and $\underline{\boldsymbol{\tau}}'$ have the same shape, but the latter two are unconnected. For magnetic Laue groups in (c), the relation of $\underline{\boldsymbol{\tau}}$, and $\underline{\boldsymbol{\tau}}'$ depends on which spatial operations have to be connected with time reversal to be a symmetry operation of the group.**"

- In Table VIII on page 9 of Ref. 283 (page 183 herein), all tensor elements in the first three columns should be primed. There is no connection between $\underline{\boldsymbol{\sigma}}^k$ and $\underline{\boldsymbol{\sigma}}'^k$, since there are no anti-unitary operations in groups of category (b).

- Note that according to TABLE IV on page 6 of Ref. 283 (page 180 herein), in *non-magnetic* solids with a (magnetic) Laue group of $\bar{3}(1')$, $4/m(1')$, or $6/m(1')$ one should be able to observe an *anomalous* Nernst and Ettingshausen effects. These are exactly the three Laue groups for which the tensor forms differ from Kleiner [271].

3.3.2 Published results on longitudinal spin transport in nonmagnets

The following is a copy of the article *Spin-orbit-induced longitudinal spin-polarized currents in non-magnetic solids* [92], reprinted (including Supplemental Material) with permission from

S. Wimmer, M. Seemann, K. Chadova, D. Ködderitzsch, and H. Ebert, Phys. Rev. B **92**, 041101(R) (2015).

RAPID COMMUNICATIONS

PHYSICAL REVIEW B **92**, 041101(R) (2015)

Spin-orbit-induced longitudinal spin-polarized currents in nonmagnetic solids

S. Wimmer,* M. Seemann, K. Chadova, D. Ködderitzsch,† and H. Ebert

Department Chemie/Physikalische Chemie, Ludwig-Maximilians-Universität München, Butenandtstrasse 11, 81377 München, Germany

(Received 26 November 2014; revised manuscript received 9 June 2015; published 2 July 2015)

For certain nonmagnetic solids with low symmetry the occurrence of spin-polarized longitudinal currents is predicted. These arise due to an interplay of spin-orbit interaction and the particular crystal symmetry. This result is derived using a group-theoretical scheme that allows investigating the symmetry properties of any linear response tensor relevant to the field of spintronics. For the spin conductivity tensor it is shown that only the magnetic Laue group has to be considered in this context. Within the introduced general scheme also the spin Hall and additional related transverse effects emerge without making reference to the two-current model. Numerical studies confirm these findings and demonstrate for $(Au_{1-x}Pt_x)_4Sc$ that the longitudinal spin conductivity may be on the same order of magnitude as the conventional transverse one. The presented formalism only relies on the magnetic space group and therefore is universally applicable to any type of magnetic order.

DOI: 10.1103/PhysRevB.92.041101 PACS number(s): 72.25.Ba, 61.50.Ah, 71.15.Rf, 72.15.Qm

The discovery of the spin Hall effect [1–3] (SHE) with its particular feature of converting a longitudinal charge current into a transverse spin current has sparked numerous studies that finally led to a deep understanding of many effects that are spin-orbit induced. Among them are the enigmatic anomalous Hall effect (AHE) that shares the same origin as the SHE and many new phenomena emerging from a coupling of spin, charge, and orbital degrees of freedom in electric fields as well as temperature gradients. Examples of these are the Edelstein effect (EE [4,5]) and the spincaloritronic pendants to the SHE and AHE, namely the spin and anomalous Nernst effects (SNE [6,7], ANE [8,9]), respectively. Many models have been formulated that aim to capture particular contributions to theses effects. For instance, the concept of the semiclassical Berry phase that can be determined on the basis of the band structure of perfect crystalline systems is connected to so called intrinsic contributions [10–12]. Extrinsic contributions arising from scattering at impurities in nonperfect systems can, for example, be obtained from diagrammatic methods [13] or Boltzmann transport theory [14].

The aforementioned transport phenomena and their different contributions being linear in the driving fields should, in principle, be described using the fundamental Kubo formula for the corresponding response function [15],

$$\tau_{ij}(\omega) = \int_0^\infty dt e^{-i\omega t} \int_0^\beta d\lambda \, \mathrm{Tr}[\rho \hat{A}_j \hat{B}_i(t + i\hbar\lambda)] \,. \qquad (1)$$

The effects then emerge from the characteristics of the underlying Hamiltonian, the pair of chosen operators for perturbation ($\hat{A}_j$) and observable ($\hat{B}_i$), and the symmetry of the system. Due to the intractability of the problem to exactly solve the Kubo formula for a realistic system in practice one has to resort to approximations and/or models. However, irrespective of this problem one can still analyze the transformation properties of response tensors $\underline{\boldsymbol{\tau}}$ determined by the Kubo formula to make statements about which effects are in principle allowed, i.e., which nonvanishing tensor elements may occur given a particular transformation property of the operators appearing in Eq. (1). This route has been followed by Kleiner [15,16], who demonstrated that the occurrence of the AHE is predicted by such a space-time symmetry analysis. Furthermore, considering in addition heat currents he derived general Onsager reciprocity relations.

Here, by extending this approach and applying it in the context of spin current operators [17] we demonstrate that in certain nonmagnetic low-symmetry systems an electric field can induce a *longitudinal* spin-polarized current [18] that has hitherto evaded perception, and complements the transverse spin Hall effect. Furthermore two additional transverse effects are found which differ from the SHE by the direction of polarization. The results of the group-theoretical analysis are independently verified for an alloy bulk system performing relativistic first-principles Kubo-type transport calculations. The presented formalism is furthermore very general, because (i) it allows identifying nontrivial response phenomena as nonzero elements in respective response tensors, as, e.g., the AHE, (ii) it applies to both magnetic and nonmagnetic systems, and (iii) it is free of the notion of a two-current model often used as an approximation in discussing spintronic phenomena; instead it is based on the concept of spin (polarization) current densities.

The material-specific features of any transport property may be discussed on the basis of the corresponding response function tensor $\underline{\boldsymbol{\tau}}$. Concerning this, the shape of the tensor $\underline{\boldsymbol{\tau}}$, i.e., the occurrence and degeneracy of nonzero elements, reflecting the symmetry of the investigated solid, is obviously of central importance. To find, in particular, the shape of the spin conductivity tensor, Kleiner's scheme [15] to deal with the symmetry properties of ordinary transport tensors has been extended to the case when the response observable is represented by an arbitrary operator product of the form $(\hat{B}_i \hat{C}_j)$ while an operator $\hat{A}_k$ represents the perturbation and the operators $\hat{A}_k$, $\hat{B}_j$, and $\hat{C}_i$ are seen as the Cartesian components of vector operators. Within Kubo's linear response formalism the corresponding frequency-(ω)-dependent response function is then given by

$$\tau_{(\hat{B}_i \hat{C}_j)\hat{A}_k}(\omega, \mathbf{H}) = \int_0^\infty dt \, e^{-i\omega t} \int_0^\beta d\lambda \, \mathrm{Tr}[\rho(\mathbf{H}) \hat{A}_k \times \hat{B}_i(t + i\hbar\lambda; \mathbf{H}) \hat{C}_j(t + i\hbar\lambda; \mathbf{H})], \qquad (2)$$

*sebastian.wimmer@cup.uni-muenchen.de
†diemo.koedderitzsch@cup.uni-muenchen.de

RAPID COMMUNICATIONS

TABLE I. Electrical ($\underline{\boldsymbol{\sigma}}$) and spin ($\underline{\boldsymbol{\sigma}}^k$) conductivity tensor forms for the magnetic Laue groups discussed in the text [18,19]. Below each group symbol an example for a material is given in parentheses.

Magnetic Laue Group	$\underline{\boldsymbol{\sigma}}$	$\underline{\boldsymbol{\sigma}}^{\mathrm{x}}$	$\underline{\boldsymbol{\sigma}}^{\mathrm{y}}$	$\underline{\boldsymbol{\sigma}}^{\mathrm{z}}$
$m\bar{3}m1'$ (fcc-Pt)	$\begin{pmatrix}\sigma_{xx} & 0 & 0\\ 0 & \sigma_{xx} & 0\\ 0 & 0 & \sigma_{xx}\end{pmatrix}$	$\begin{pmatrix}0 & 0 & 0\\ 0 & 0 & \sigma^x_{yz}\\ 0 & -\sigma^x_{yz} & 0\end{pmatrix}$	$\begin{pmatrix}0 & 0 & -\sigma^x_{yz}\\ 0 & 0 & 0\\ \sigma^x_{yz} & 0 & 0\end{pmatrix}$	$\begin{pmatrix}0 & \sigma^x_{yz} & 0\\ -\sigma^x_{yz} & 0 & 0\\ 0 & 0 & 0\end{pmatrix}$
$4/mm'm'$ (fcc-Fe_xNi_{1-x})	$\begin{pmatrix}\sigma_{xx} & \sigma_{xy} & 0\\ -\sigma_{xy} & \sigma_{xx} & 0\\ 0 & 0 & \sigma_{zz}\end{pmatrix}$	$\begin{pmatrix}0 & 0 & \sigma^x_{xz}\\ 0 & 0 & \sigma^x_{yz}\\ \sigma^x_{zx} & \sigma^x_{zy} & 0\end{pmatrix}$	$\begin{pmatrix}0 & 0 & -\sigma^x_{yz}\\ 0 & 0 & \sigma^x_{xz}\\ -\sigma^x_{zy} & \sigma^x_{zx} & 0\end{pmatrix}$	$\begin{pmatrix}\sigma^z_{xx} & \sigma^z_{xy} & 0\\ -\sigma^z_{xy} & \sigma^z_{xx} & 0\\ 0 & 0 & \sigma^z_{zz}\end{pmatrix}$
$4/m1'$ (Au_4Sc)	$\begin{pmatrix}\sigma_{xx} & 0 & 0\\ 0 & \sigma_{xx} & 0\\ 0 & 0 & \sigma_{zz}\end{pmatrix}$	$\begin{pmatrix}0 & 0 & \sigma^x_{xz}\\ 0 & 0 & \sigma^x_{yz}\\ \sigma^x_{zx} & \sigma^x_{zy} & 0\end{pmatrix}$	$\begin{pmatrix}0 & 0 & -\sigma^x_{yz}\\ 0 & 0 & \sigma^x_{xz}\\ -\sigma^x_{zy} & \sigma^x_{zx} & 0\end{pmatrix}$	$\begin{pmatrix}\sigma^z_{xx} & \sigma^z_{xy} & 0\\ -\sigma^z_{xy} & \sigma^z_{xx} & 0\\ 0 & 0 & \sigma^z_{zz}\end{pmatrix}$
$2/m1'$ (Pt_3Ge)	$\begin{pmatrix}\sigma_{xx} & \sigma_{xy} & 0\\ \sigma_{xy} & \sigma_{yy} & 0\\ 0 & 0 & \sigma_{zz}\end{pmatrix}$	$\begin{pmatrix}0 & 0 & \sigma^x_{xz}\\ 0 & 0 & \sigma^x_{yz}\\ \sigma^x_{zx} & \sigma^x_{zy} & 0\end{pmatrix}$	$\begin{pmatrix}0 & 0 & \sigma^y_{xz}\\ 0 & 0 & \sigma^y_{yz}\\ \sigma^y_{zx} & \sigma^y_{zy} & 0\end{pmatrix}$	$\begin{pmatrix}\sigma^z_{xx} & \sigma^z_{xy} & 0\\ \sigma^z_{yx} & \sigma^z_{yy} & 0\\ 0 & 0 & \sigma^z_{zz}\end{pmatrix}$

where as usual [15] ρ stands for the density operator, $\beta = 1/k_BT$ with k_B the Boltzmann constant, T is the temperature, and $\mathbf{H}$ is a magnetic field that might be present.

The shape of $\underline{\boldsymbol{\tau}}$ can be found by considering the impact of a symmetry operation of the space group of the solid on Eq. (2), as this will lead to equations connecting elements of $\underline{\boldsymbol{\tau}}$. Collecting the restrictions imposed by all symmetry operations the shape of $\underline{\boldsymbol{\tau}}$ is obtained. In this context it is important to note that the relevant space group of the considered system may contain not only unitary pure spatial (u) but also antiunitary symmetry operations (a) that involve time reversal.

The transformation properties of the operators $X = A_i$, B_i, or C_i in Eq. (2) under symmetry operations can be expressed in terms of the corresponding Wigner D-matrices [15] $\underline{\mathbf{D}}^{(\hat{X})}(u)$ and $\underline{\mathbf{D}}^{(\hat{X})}(a)$ belonging to the operator $\hat{X}$ and the operation u or a, respectively. Starting from Eq. (2) and making use of these transformation relations one gets the transformation behavior of $\underline{\boldsymbol{\tau}}$ under a unitary (u) or antiunitary (a) symmetry operation, respectively [19]:

$$\tau_{(\hat{B}_i\hat{C}_j)\hat{A}_k}(\omega,\mathbf{H}) = \sum_{lmn} \tau_{(\hat{B}_m\hat{C}_n)\hat{A}_l}(\omega,\mathbf{H}_u) \times D^{(\hat{A})}(u)_{lk}\, D^{(\hat{B})}(u)_{mi}\, D^{(\hat{C})}(u)_{nj}, \quad (3)$$

$$\tau_{(\hat{B}_i\hat{C}_j)\hat{A}_k}(\omega,\mathbf{H}) = \sum_{lmn} \tau_{\hat{A}^\dagger_l(\hat{B}^\dagger_m\hat{C}^\dagger_n)}(\omega,\mathbf{H}_a) \times D^{(\hat{A})}(a)^*_{lk}\, D^{(\hat{B})}(a)^*_{mi}\, D^{(\hat{C})}(a)^*_{nj}. \quad (4)$$

It should be noted that in general the tensors $\tau_{(\hat{B}_i\hat{C}_j)\hat{A}_k}$ and $\tau_{\hat{A}^\dagger_k(\hat{B}^\dagger_i\hat{C}^\dagger_j)}$ are different objects representing different response functions which are only interrelated by Eq. (4). It nevertheless imposes restrictions on the shape of $\tau_{(\hat{B}_i\hat{C}_j)\hat{A}_k}$ giving rise to (generalized) Onsager relations.

Assuming $\hat{C}_i = 1$ and $\hat{B}_i = \hat{A}_i = \hat{j}_i$ with $\hat{j}_i$ the current density operator $\underline{\boldsymbol{\tau}}$ corresponds to the ordinary electrical conductivity tensor $\underline{\boldsymbol{\sigma}}$. Using the behavior of $\hat{j}_i$ under symmetry operations [15], it turns out that only the magnetic Laue group of the system has to be considered, that is generated by adding the (space) inversion operation I to the crystallographic magnetic point group [20]. The resulting shape of the conductivity tensor $\underline{\boldsymbol{\sigma}}$ is given in Table I for four different magnetic Laue groups [19].

When considering the spin conductivity tensor its elements σ^k_{ij} give the current density along direction i for the spin polarization with respect to the k axis induced by an electrical field along the j axis. In this case the perturbing electric field is still represented by $\hat{A}_i = \hat{j}_i$ while the induced spin current density is represented by the corresponding operator $\hat{J}^k_i = (\hat{B}_i\hat{C}_k)$. As the explicit definition of $\hat{J}^k_i$ is not relevant for the following, but only its symmetry properties, the frequently used nonrelativistic definition $\hat{J}^k_i = \frac{1}{2}\{\hat{v}_i,\sigma_k\}$ may be used that consists of a combination of the Pauli spin matrix σ_k and the conventional velocity operator $\hat{v}_i$ [21]. Alternatively, one may use the relativistic definition of the spin current operator $\hat{J}^k_i = \hat{\mathcal{T}}_k\hat{j}_i$ as suggested by Vernes *et al.* [22] that involves the spatial part $\hat{\mathcal{T}}_k$ of the spin polarization operator [23].

Expressing the transformation behavior of $\hat{J}^k_i$ in terms of the Wigner matrices allows deducing the shape of the corresponding spin conductivity tensor on the basis of Eqs. (3) and (4). As for the electrical conductivity it turns out again that one has to consider only the magnetic Laue group; i.e., there are only 37 different cases. Table I gives for the four cases considered here the shape of the various subtensors $\underline{\boldsymbol{\sigma}}^k$, where k specifies the component of the spin polarization.

Considering a nonmagnetic metal with fcc or bcc structure ($m\bar{3}m1'$) Kleiner's scheme naturally leads to an isotropic electrical conductivity tensor $\underline{\boldsymbol{\sigma}}$. The extension to deal with the spin conductivity tensor sketched above gives in this case only a few nonvanishing elements that are associated with the SHE and are symmetry related according to $\sigma^{\mathrm{x}}_{\mathrm{yz}} = \sigma^{\mathrm{y}}_{\mathrm{zx}} = \sigma^{\mathrm{z}}_{\mathrm{xy}} = -\sigma^{\mathrm{x}}_{\mathrm{zy}} = -\sigma^{\mathrm{y}}_{\mathrm{xz}} = -\sigma^{\mathrm{z}}_{\mathrm{yx}}$; i.e., cyclic permutation of the indices gives no change while anticyclic permutation changes the sign. In contrast to other derivations, there is obviously no need to artificially introduce a spin-projected conductivity or to make reference to the conductivity tensor of a spin-polarized solid. For a ferromagnetic metal with fcc or bcc structure ($4/mm'm'$) with the magnetization along the z direction, the well-known shape of the conductivity tensor $\underline{\boldsymbol{\sigma}}$ is obtained that reflects the anomalous Hall effect (σ_{xy}) as well as the magnetoresistance anisotropy ($\sigma_{xx} \neq \sigma_{zz}$) with the symmetry relations $\sigma_{xy} = -\sigma_{yx}$ and $\sigma_{xx} = \sigma_{yy}$. The

RAPID COMMUNICATIONS

spin conductivity tensor $\underline{\sigma}^z$ shows as for the nonmagnetic case antisymmetric off-diagonal elements that represent the transverse spin conductivity. This implies the occurrence of the spin Hall effect in ferromagnets that was investigated recently for diluted alloys [24]. For polarization along the x and y axes, however, different although still interrelated elements appear as compared to the nonmagnetic case since fewer symmetry relations survive in the presence of a spontaneous magnetization. Additionally, in contrast to the nonmagnetic case also a longitudinal spin-polarized conductivity (σ^z_{ii}) occurs in a ferromagnet, that for example gives rise to the spin-dependent Seebeck effect [25]. A simple explanation for the corresponding longitudinal spin transport would be based on Mott's two-current model assuming different conductivities for the two spin channels. However, it is well known that spin-orbit interaction leads to a hybridization of the spin channels and influences even the longitudinal conductivity of a ferromagnet this way [26]. Accordingly, it cannot be ruled out that the longitudinal tensor elements σ^z_{ii} are not only reflecting the spontaneous spin magnetization of the material but are to some extent due to spin-orbit coupling.

Indeed the scheme presented above leads for nonmagnetic systems having low symmetry not only to off-diagonal elements reflecting transverse spin conductivity, i.e., the SHE, but also to diagonal elements reflecting longitudinal spin transport, that was not observed so far. For the two magnetic Laue groups $4/m1'$ and $2/m1'$ for nonmagnetic solids considered in Table I, a 4- and 2-fold, resp., rotation axis is present. As a consequence longitudinal spin currents show up only with spin polarization along this principal axis of rotation.

To verify the results of our group-theoretical approach independently we calculated the full spin conductivity tensor for solids having different structures corresponding to different magnetic Laue groups. This work employs a computational scheme that has been used before for numerical studies on the SHE in nonmagnetic transition metal alloys [27]. Performing these calculations without making use of symmetry led numerically to a spin conductivity tensor that was always fully in line with the analytical group-theoretical results concerning the shape and degeneracies of the tensor.

To get a first estimate of the order of magnitude of the longitudinal spin-polarized conductivity in nonmagnets, calculations have been done for the system $(Au_{1-x}Pt_x)_4Sc$ having the magnetic Laue group $4/m1'$ for varying Pt concentration x. Figure 1 (top) shows the corresponding electrical conductivity that is, in agreement with Table I, diagonal and slightly anisotropic; i.e., $\sigma_{xx} = \sigma_{yy} \approx \sigma_{zz}$.

Furthermore, the conductivities σ_{ii} are strongly asymmetric with respect to the concentration x when replacing Au with prominent sp character at the Fermi level by Pt with dominant d character. Furthermore, one notes a relatively strong impact of the vertex corrections on the Au-rich side of the system ($x \approx 0$) while these are much less important on the Au-poor side ($x \approx 1$). This observation is well known from binary transition metal alloys, such as $Cu_{1-x}Pt_x$ [28] or $Ag_{1-x}Pd_x$ [29], where the dominance of sp character changes to d character when x is varied from 0 to 1.

The transverse spin conductivity σ^x_{ij} is shown in the middle panel of Fig. 1 for x polarization of the spin. As Table I shows going from $m\bar{3}m1'$ to $4/m1'$ symmetry the relation

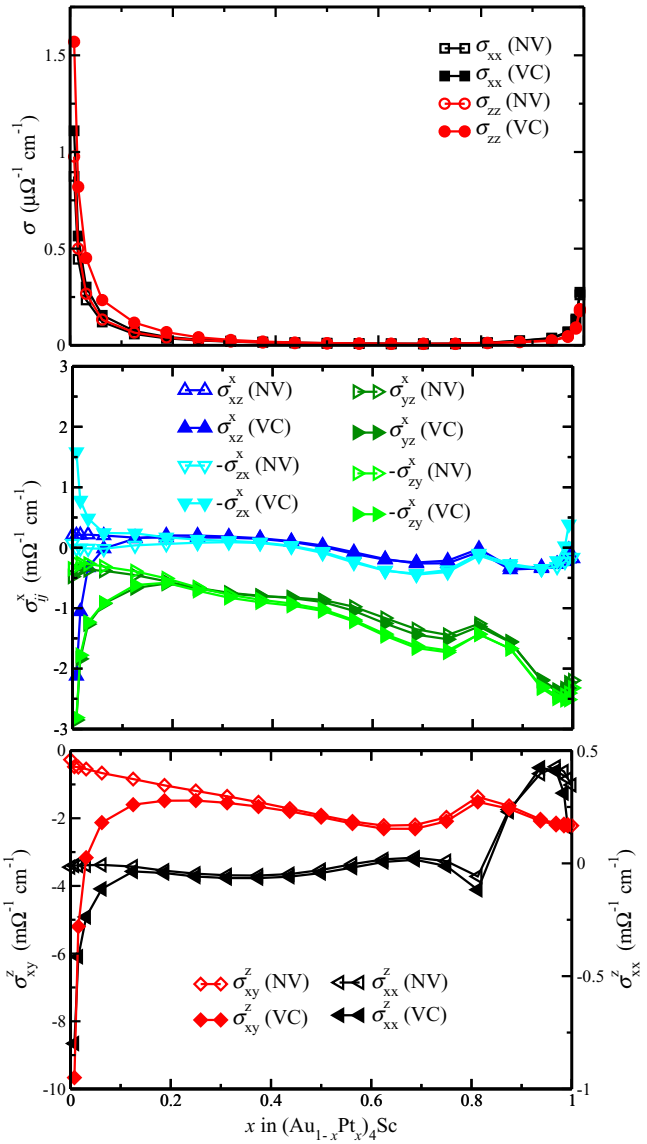

FIG. 1. (Color online) Top: Longitudinal conductivity σ_{ii} for $(Au_{1-x}Pt_x)_4Sc$ as a function of the concentration x calculated without (NV) and with (VC) the vertex corrections. Middle: Transverse spin conductivities σ^x_{ij}. Bottom: Transverse and longitudinal spin conductivity σ^z_{xy} and σ^z_{xx}, respectively.

$\sigma^x_{yz} = -\sigma^x_{zy}$ disappears; i.e., the corresponding subtensor is not antisymmetric anymore. A symmetric component, which is by definition not present in the ordinary SHE, indeed can be seen in Fig. 1 (middle) although the deviations are not very pronounced. In line one finds (except for $x \to 0$) for the additional nonzero tensor elements $\sigma^x_{xz} \approx -\sigma^x_{zx}$. The first coefficient relates a spin current j^x_x polarized in the direction of motion to an electric field E_z, whereas σ^x_{zx} describes a spin current j^x_z transverse, but with the spin polarization parallel to the driving electric field E_x. To our knowledge the corresponding effects have not been considered so far. Interestingly, both elements occur simultaneously for a given magnetic Laue group or both are absent. However, compared to the spin-Hall-like elements σ^x_{yz} and σ^x_{zy} they are smaller. For

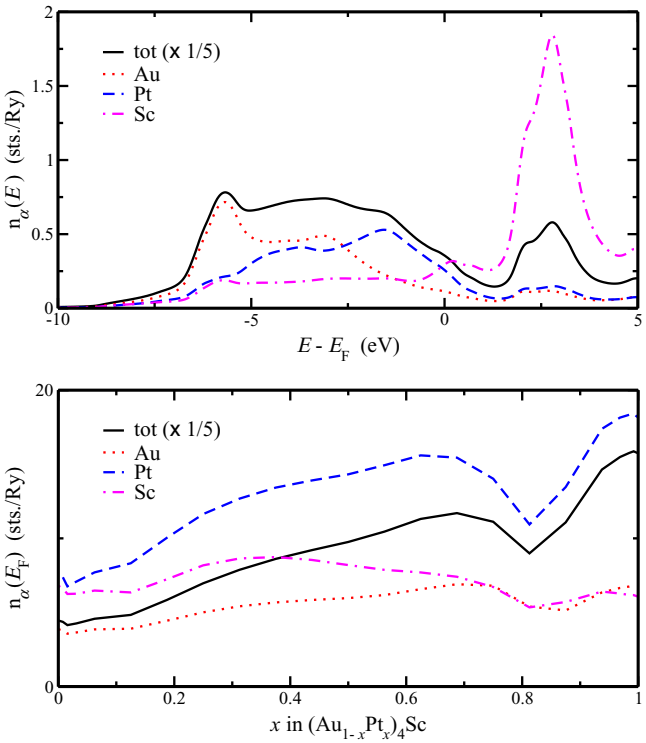

FIG. 2. (Color online) Top: Energy-dependent component-(α)-resolved DOS $n_\alpha(E)$ for $(Au_{0.5}Pt_{0.5})_4Sc$. Bottom: Component-resolved DOS $n_\alpha(E_F)$ at the Fermi energy E_F for $(Au_{1-x}Pt_x)_4Sc$ as a function of the concentration x.

y polarization of the spin the corresponding tensor elements are uniquely related to those for x polarization according to Table I and for this reason not given here. The tensor elements σ^z_{ij} for z polarization are given in the lower panel of Fig. 1. In line with Table I they obey the symmetry relation $\sigma^z_{xy} = -\sigma^z_{yx}$ (i.e., describing the pure SHE) and differ from σ^x_{yz}. This difference however is, except again for $x \to 0$, not very pronounced. In particular, σ^x_{yz} and σ^z_{xy} show a similar variation with concentration x that differs clearly from that of the longitudinal spin conductivity σ^z_{xx} shown as well in Fig. 1 (bottom). Although this new type of tensor element is overall somewhat smaller in magnitude than the dominating transverse elements it has nevertheless the same order of magnitude, especially in the Au-rich regime, and for that reason it should be possible to determine it experimentally.

As can be seen in Fig. 1 the curves for the spin conductivity tensor elements σ^k_{ij} as function of the concentration x are much more structured than the electrical conductivity σ_{ii}; i.e., they are much more strongly affected by the variation of the electronic structure with composition. In particular the spin conductivities σ^k_{ij} show pronounced peaks or dips for $x \approx 0.8$. This behavior can be related to the variation of the density of states (DOS) with x as can be seen from Fig. 2. The figure shows the component-resolved DOS $n_\alpha(E)$ as a function of the energy E for $(Au_{0.5}Pt_{0.5})_4Sc$ (top) and at the Fermi energy E_F for $(Au_{1-x}Pt_x)_4Sc$ as a function of the concentration x (bottom). As mentioned above, at the Fermi energy the partial DOS $n_{Au}(E_F)$ of Au is dominated by sp states while that of Pt has dominant d character. The pronounced dip of the Pt DOS $n_{Pt}(E_F)$ at $x \approx 0.8$ is apparently responsible for the prominent features in the spin conductivity curves shown in Fig. 1 (middle and bottom panels). As mentioned before, for the longitudinal conductivity σ_{ii} inclusion of the vertex corrections has primarily an impact at the Au-rich side of the system. The same behavior is found for the transverse (σ^k_{ij}) as well as the longitudinal (σ^z_{ii}) spin conductivity components. For the transverse spin Hall conductivity it could be demonstrated that the contribution connected with the vertex corrections corresponds to the so-called extrinsic contribution that is primarily caused by the skew scattering mechanism [24,27]. The very similar dependence of σ^k_{ij} and σ^z_{ii} on the vertex corrections suggests that this applies also for the longitudinal spin conductivity.

In summary, a group-theoretical scheme has been presented that allows determining the shape of response tensors relevant for the field of spintronics. Application to the spin conductivity tensor gave a sound and model-independent explanation for the occurrence of the transverse tensor elements responsible for the spin Hall effect and two additional, closely related effects. In addition it was found that for low symmetry longitudinal elements show up in addition even for nonmagnetic solids that were not considered before. Independent numerical investigations confirmed these results and demonstrated for $(Au_{1-x}Pt_x)_4Sc$ that the longitudinal spin conductivity may be on the same order of magnitude as the transverse one. It should be noted that the discussion of the spin conductivity tensor was referring to the dc limit $\omega = 0$. However, the tensor forms given in Table I also hold for finite frequencies, implying the occurrence of the ac counterparts to the discussed effects. In addition, the formalism is applicable to numerous other linear response phenomena as, e.g., the AHE, anisotropic magnetoresistance (AMR), the Edelstein effect [4,5], Gilbert damping [30], spin-orbit torques [31], etc. Furthermore, using the fact that the operators for electrical and heat currents share the same transformation properties the presented formalism can be applied to spincaloritronic phenomena as well.

This work was supported financially by the Deutsche Forschungsgemeinschaft (DFG) under the priority program SPP 1538 (Spin Caloric Transport) and the SFB 689 (Spinphänomene in reduzierten Dimensionen). Discussions with Ch. Back and H. Hübl are gratefully acknowledged.

[1] M. Dyakonov and V. Perel, Phys. Lett. A **35**, 459 (1971).
[2] J. E. Hirsch, Phys. Rev. Lett. **83**, 1834 (1999).
[3] J. Sinova, D. Culcer, Q. Niu, N. A. Sinitsyn, T. Jungwirth, and A. H. MacDonald, Phys. Rev. Lett. **92**, 126603 (2004).
[4] A. G. Aronov and Y. B. Lyanda-Geller, Zh. Eksp. Teor. Fiz. **50**, 398 (1989) [JETP Lett. **50**, 431 (1989)].
[5] V. M. Edelstein, Solid State Commun. **73**, 233 (1990).
[6] K. Tauber, M. Gradhand, D. V. Fedorov, and I. Mertig, Phys. Rev. Lett. **109**, 026601 (2012).

[7] S. Wimmer, D. Ködderitzsch, K. Chadova, and H. Ebert, Phys. Rev. B **88**, 201108 (2013).
[8] J. Weischenberg, F. Freimuth, S. Blügel, and Y. Mokrousov, Phys. Rev. B **87**, 060406 (2013).
[9] S. Wimmer, D. Ködderitzsch, and H. Ebert, Phys. Rev. B **89**, 161101 (2014).
[10] Z. Fang *et al.*, Science **302**, 92 (2003).
[11] Y. Yao and Z. Fang, Phys. Rev. Lett. **95**, 156601 (2005).
[12] N. Nagaosa, J. Sinova, S. Onoda, A. H. MacDonald, and N. P. Ong, Rev. Mod. Phys. **82**, 1539 (2010).
[13] N. A. Sinitsyn, J. Phys.: Condens. Matter **20**, 023201 (2008).
[14] M. Gradhand, D. V. Fedorov, P. Zahn, and I. Mertig, Phys. Rev. Lett. **104**, 186403 (2010).
[15] W. H. Kleiner, Phys. Rev. **142**, 318 (1966).
[16] W. H. Kleiner, Phys. Rev. **153**, 726 (1967).
[17] More precisely, one should use the expression *spin polarization current density operator*, but we keep the abbreviated term also in the relativistic context.
[18] M. Seemann, D. Ködderitzsch, S. Wimmer, and H. Ebert (unpublished).
[19] See Supplemental Material at http://link.aps.org/supplemental/10.1103/PhysRevB.92.041101 for a sketch of the derivation of Eq. (3), notes on the application of Eqs. (3) and (4) to the spin-polarized conductivity tensor, including results for all possible magnetic Laue groups of nonmagnetic solids, and details of the first-principles approach used.
[20] In contrast to Kleiner we adopt here the definition of a Laue group that is in general use nowadays.
[21] J. Shi, P. Zhang, D. Xiao, and Q. Niu, Phys. Rev. Lett. **96**, 076604 (2006).
[22] A. Vernes, B. L. Györffy, and P. Weinberger, Phys. Rev. B **76**, 012408 (2007).
[23] V. Bargmann and E. P. Wigner, Proc. Natl. Acad. Sci. USA **34**, 211 (1948).
[24] B. Zimmermann *et al.*, Phys. Rev. B **90**, 220403 (2014).
[25] A. Slachter, F. L. Bakker, J.-P. Adam, and B. J. van Wees, Nat. Phys. **6**, 879 (2010).
[26] J. Banhart, H. Ebert, and A. Vernes, Phys. Rev. B **56**, 10165 (1997).
[27] S. Lowitzer, M. Gradhand, D. Ködderitzsch, D. V. Fedorov, I. Mertig, and H. Ebert, Phys. Rev. Lett. **106**, 056601 (2011).
[28] J. Banhart, H. Ebert, P. Weinberger, and J. Voitländer, Phys. Rev. B **50**, 2104 (1994).
[29] P. R. Tulip, J. B. Staunton, S. Lowitzer, D. Ködderitzsch, and H. Ebert, Phys. Rev. B **77**, 165116 (2008).
[30] H. Ebert, S. Mankovsky, D. Ködderitzsch, and P. J. Kelly, Phys. Rev. Lett. **107**, 066603 (2011).
[31] K. Garello *et al.*, Nat. Nanotechnol. **8**, 587 (2013).

Spin-orbit-induced longitudinal spin-polarized currents in nonmagnetic solids

SUPPLEMENTAL MATERIAL

S. Wimmer,* M. Seemann, K. Chadova, D. Ködderitzsch,† and H. Ebert
Department Chemie/Phys. Chemie, Ludwig-Maximilians-Universität München, Butenandtstrasse 11, 81377 München, Germany
(Dated: 19th June 2015)

I. DERIVATION OF EQ. (3)

In the following we sketch the derivation of the transformation relation Eq. (3) in the manuscript of a response function τ under a unitary symmetry operation u. For Eq. (4) in the manuscript referring to an antiunitary symmetry operation a the derivation is similar.

Within Kubo's linear response formalism[1], the change of the expectation value of an observable represented by an operator product of the form $\hat{B}_i\hat{C}_j$ due to a time-dependent perturbation $\hat{A}_j$ (with the operators $\hat{C}_i$, $\hat{B}_j$, and $\hat{A}_k$ being the Cartesian components of a vector operator) can be expressed by the corresponding response function:

$$\tau_{(\hat{B}_i\hat{C}_j)\hat{A}_k}(\omega,\mathbf{H}) = \int_0^\infty \mathrm{d}t\, \mathrm{e}^{-\mathrm{i}\omega t} \int_0^\beta \mathrm{d}\lambda\, \mathrm{Tr}\left(\rho(\mathbf{H})\hat{A}_k\hat{B}_i(t+\mathrm{i}\hbar\lambda;\mathbf{H})\hat{C}_j(t+\mathrm{i}\hbar\lambda;\mathbf{H})\right), \tag{1}$$

with $\rho(\mathbf{H}) = \mathrm{e}^{-\beta\hat{H}(\mathbf{H})}/\mathrm{Tr}(\mathrm{e}^{-\beta\hat{H}(\mathbf{H})})$ being the density operator for the unperturbed system and $\mathbf{H}$ an external magnetic field.

The expression under the trace in Eq. (1) can be reformulated by cyclic permutation and by inserting the factor $u^{-1}u = 1$:

$$\begin{aligned}\mathrm{Tr}\left(\mathrm{e}^{-\beta\hat{H}(\mathbf{H})}\hat{A}_k\hat{B}_i(t+\mathrm{i}\hbar\lambda;\mathbf{H})\hat{C}_j(t+\mathrm{i}\hbar\lambda;\mathbf{H})\right) &= \mathrm{Tr}\left(u^{-1}u\mathrm{e}^{-\beta\hat{H}(\mathbf{H})}u^{-1}u\hat{A}_ku^{-1}u\hat{B}_j(t+\mathrm{i}\hbar\lambda,\mathbf{H})u^{-1}uC_i(t+\mathrm{i}\hbar\lambda;\mathbf{H})\right)\\ &= \mathrm{Tr}\left[\left(u\mathrm{e}^{-\beta\hat{H}(\mathbf{H})}u^{-1}\right)\left(u\hat{A}_ku^{-1}\right)\left(u\hat{B}_i(t+\mathrm{i}\hbar\lambda,\mathbf{H})u^{-1}\right)\left(u\hat{C}_j(t+\mathrm{i}\hbar\lambda,\mathbf{H})u^{-1}\right)\right]. \end{aligned}\tag{2}$$

The four expressions grouped in parenthesis can be dealt with separately. The term containing $\hat{A}_k$ can be rewritten using the general transformation properties of the operators $X_i = A_i$, B_i or C_i in Eq. (1) under a unitary symmetry operation u:

$$u\hat{X}_iu^{-1} = \sum_j \hat{X}_j D^{(\hat{X})}(u)_{ji}\,, \tag{3}$$

where $\underline{\mathbf{D}}^{(\hat{X})}(u)$ are the Wigner D-matrices corresponding to the operator $\hat{X}$ and operation u. For the term containing $\hat{B}_j$ one has accordingly :

$$u\hat{B}_i(t+\mathrm{i}\hbar\lambda,\mathbf{H})u^{-1} = \sum_m \hat{B}_m(t+\mathrm{i}\hbar\lambda,\mathbf{H}_u)\, D^{(\hat{B})}(u)_{mi} \tag{4}$$

with $\mathbf{H}_u$ the transformed field

$$u\hat{H}(\mathbf{H})u^{-1} = \hat{H}(\mathbf{H}_u) \tag{5}$$

connected with the operation u. For the term containing $C_j(t+\mathrm{i}\hbar\lambda,\mathbf{H})$ an analogous expression is obtained. Inserting these relations into Eq. (2) one arrives at:

$$\begin{aligned}\mathrm{Tr}\left(\mathrm{e}^{-\beta\hat{H}(\mathbf{H})}\hat{A}_k\hat{B}_i(t+\mathrm{i}\hbar\lambda,\mathbf{H})\hat{C}_j(t+\mathrm{i}\hbar\lambda,\mathbf{H})\right) = \sum_{lmn}\mathrm{Tr}\Big(&\mathrm{e}^{-\beta\hat{H}(\mathbf{H}_u)}\hat{A}_l\hat{B}_m(t+\mathrm{i}\hbar\lambda,\mathbf{H}_u)\hat{C}_n(t+\mathrm{i}\hbar\lambda,\mathbf{H}_u)\\ &D^{(\hat{A})}(u)_{lk}\, D^{(\hat{B})}(u)_{mi}\, D^{(\hat{C})}(u)_{nj}\Big).\end{aligned}\tag{6}$$

This equation must hold for any operators $\hat{A}_k$, $\hat{B}_j$ and $\hat{C}_i$, i.e. also in the special case $\hat{A}_k = \hat{B}_j = \hat{C}_i = \mathbb{1}$, leading

to:

$$\mathrm{Tr}\left(\mathrm{e}^{-\beta\hat{H}(\mathbf{H})}\right) = \mathrm{Tr}\left(\mathrm{e}^{-\beta\hat{H}(\mathbf{H}_u)}\right) . \qquad (7)$$

Inserting the two last equations into Eq. (1) for the general transport coefficients, one obtains the transformation behavior of $\underline{\tau}$ under a unitary symmetry operation u:

$$\tau_{(\hat{B}_i\hat{C}_j)\hat{A}_k}(\omega,\mathbf{H}) = \sum_{lmn} \tau_{(\hat{B}_m\hat{C}_n)\hat{A}_l}(\omega,\mathbf{H}_u) \; D^{(\hat{A})}(u)_{lk}\, D^{(\hat{B})}(u)_{mi}\, D^{(\hat{C})}(u)_{nj} \qquad (8)$$

II. APPLICATION OF EQ. (3) AND EQ. (4) TO THE SPIN CONDUCTIVITY TENSOR

Spin transport may be expressed in terms of the spin conductivity tensor σ_{ij}^k that gives the current density along direction i for the spin polarization with respect to the k axis induced by an electrical field along the j axis. A straightforward but sufficient definition for the central spin current density operator $\hat{J}_i^k = \frac{1}{2}\{\hat{v}_i, \sigma_k\}$ consists in a combination of the Pauli spin matrix σ_k and the conventional velocity operator $\hat{v}_i$[2] (for an alternative definition see e.g. Vernes *et al.*[3]).

Eq. (3) has now to be considered individually for each of the various operators occurring in Eq. (1). For the present context it is important to note that, in contrast to the current density operator $\hat{j}_i = |e|\hat{v}_i$, $\hat{J}_i^k$ transforms as a pseudo-vector which changes sign under time reversal. Identifying $\hat{A}_j = \hat{j}_j$, $\hat{B}_i = \hat{j}_i$ and $\hat{C}_k = \hat{\sigma}_k$ in Eq. (8) one finds the behavior of σ_{ij}^k under unitary transformations

$$\sigma_{ij}^k = \sum_{lmn} \det(R)\, D(R)_{li}\, D(R)_{mj}\, D(R)_{nk}\, \sigma_{lm}^n \qquad (9)$$

and an analogous expression for antiunitary symmetry operations.

Eq. (9) and its counterpart connected with antiunitary symmetry operations can be used to deduce the shape of the spin conductivity tensor σ_{ij}^k for any solid on the basis of its magnetic space group. Similar to the case of the electrical conductivity tensor only the magnetic Laue group has to be considered for this purpose, i.e. there are only 37 different cases. Table I gives the corresponding results for the case of a nonmagnetic solid for which time inversion symmetry (1') is present. Complementary results for the remaining magnetic Laue groups of magnetic solids have been obtained as well (to be published).

III. NOTE ON FIRST-PRINCIPLES APPROACH

To verify the results of our group-theoretical approach independently we calculated the full spin conductivity tensor for solids having different structures corresponding to different magnetic Laue groups. This work employs a computational scheme that has been used before for numerical studies on the SHE in nonmagnetic transition metal alloys[4]. In brief, a single-particle description of the electronic structure within the framework of density functional theory was adopted. Spin-orbit coupling was accounted for by the use of a fully relativistic version of the Korringa-Kohn-Rostoker (KKR) Green function band structure method. This approach allowed in addition dealing with disordered systems making use of the CPA (Coherent Potential Approximation) alloy theory[5]. Performing these calculations without making use of symmetry led numerically to a spin conductivity tensor that was always fully in line with the analytical group-theoretical results concerning the shape and degeneracies of the tensor.

magnetic Laue group	$\underline{\boldsymbol{\sigma}}^{\mathrm{x}}$	$\underline{\boldsymbol{\sigma}}^{\mathrm{y}}$	$\underline{\boldsymbol{\sigma}}^{\mathrm{z}}$
$\bar{1}1'$	$\begin{pmatrix} \sigma_{xx}^x & \sigma_{xy}^x & \sigma_{xz}^x \\ \sigma_{yx}^x & \sigma_{yy}^x & \sigma_{yz}^x \\ \sigma_{zx}^x & \sigma_{zy}^x & \sigma_{zz}^x \end{pmatrix}$	$\begin{pmatrix} \sigma_{xx}^y & \sigma_{xy}^y & \sigma_{xz}^y \\ \sigma_{yx}^y & \sigma_{yy}^y & \sigma_{yz}^y \\ \sigma_{zx}^y & \sigma_{zy}^y & \sigma_{zz}^y \end{pmatrix}$	$\begin{pmatrix} \sigma_{xx}^z & \sigma_{xy}^z & \sigma_{xz}^z \\ \sigma_{yx}^z & \sigma_{yy}^z & \sigma_{yz}^z \\ \sigma_{zx}^z & \sigma_{zy}^z & \sigma_{zz}^z \end{pmatrix}$
$2/m1'$	$\begin{pmatrix} 0 & 0 & \sigma_{xz}^x \\ 0 & 0 & \sigma_{yz}^x \\ \sigma_{zx}^x & \sigma_{zy}^x & 0 \end{pmatrix}$	$\begin{pmatrix} 0 & 0 & \sigma_{xz}^y \\ 0 & 0 & \sigma_{yz}^y \\ \sigma_{zx}^y & \sigma_{zy}^y & 0 \end{pmatrix}$	$\begin{pmatrix} \sigma_{xx}^z & \sigma_{xy}^z & 0 \\ \sigma_{yx}^z & \sigma_{yy}^z & 0 \\ 0 & 0 & \sigma_{zz}^z \end{pmatrix}$
$mmm1'$	$\begin{pmatrix} 0 & 0 & 0 \\ 0 & 0 & \sigma_{yz}^x \\ 0 & \sigma_{zy}^x & 0 \end{pmatrix}$	$\begin{pmatrix} 0 & 0 & \sigma_{xz}^y \\ 0 & 0 & 0 \\ \sigma_{zx}^y & 0 & 0 \end{pmatrix}$	$\begin{pmatrix} 0 & \sigma_{xy}^z & 0 \\ \sigma_{yx}^z & 0 & 0 \\ 0 & 0 & 0 \end{pmatrix}$
$4/m1'$, $6/m1'$	$\begin{pmatrix} 0 & 0 & \sigma_{xz}^x \\ 0 & 0 & -\sigma_{xz}^y \\ \sigma_{zx}^x & -\sigma_{zx}^y & 0 \end{pmatrix}$	$\begin{pmatrix} 0 & 0 & \sigma_{xz}^y \\ 0 & 0 & \sigma_{xz}^x \\ \sigma_{zx}^y & \sigma_{zx}^x & 0 \end{pmatrix}$	$\begin{pmatrix} \sigma_{xx}^z & \sigma_{xy}^z & 0 \\ -\sigma_{xy}^z & \sigma_{xx}^z & 0 \\ 0 & 0 & \sigma_{zz}^z \end{pmatrix}$
$4/mmm1'$, $6/mmm1'$	$\begin{pmatrix} 0 & 0 & 0 \\ 0 & 0 & -\sigma_{xz}^y \\ 0 & -\sigma_{zx}^y & 0 \end{pmatrix}$	$\begin{pmatrix} 0 & 0 & \sigma_{xz}^y \\ 0 & 0 & 0 \\ \sigma_{zx}^y & 0 & 0 \end{pmatrix}$	$\begin{pmatrix} 0 & \sigma_{xy}^z & 0 \\ -\sigma_{xy}^z & 0 & 0 \\ 0 & 0 & 0 \end{pmatrix}$
$\bar{3}1'$	$\begin{pmatrix} \sigma_{xx}^x & \sigma_{xx}^y & \sigma_{xz}^x \\ \sigma_{xx}^y & -\sigma_{xx}^x & -\sigma_{xz}^y \\ \sigma_{zx}^x & -\sigma_{zx}^y & 0 \end{pmatrix}$	$\begin{pmatrix} \sigma_{xx}^y & -\sigma_{xx}^x & \sigma_{xz}^y \\ -\sigma_{xx}^x & -\sigma_{xx}^y & \sigma_{xz}^x \\ \sigma_{zx}^y & \sigma_{zx}^x & 0 \end{pmatrix}$	$\begin{pmatrix} \sigma_{xx}^z & \sigma_{xy}^z & 0 \\ -\sigma_{xy}^z & \sigma_{xx}^z & 0 \\ 0 & 0 & \sigma_{zz}^z \end{pmatrix}$
$\bar{3}1m1'$	$\begin{pmatrix} \sigma_{xx}^x & 0 & 0 \\ 0 & -\sigma_{xx}^x & -\sigma_{xz}^y \\ 0 & -\sigma_{zx}^y & 0 \end{pmatrix}$	$\begin{pmatrix} 0 & -\sigma_{xx}^x & \sigma_{xz}^y \\ -\sigma_{xx}^x & 0 & 0 \\ \sigma_{zx}^y & 0 & 0 \end{pmatrix}$	$\begin{pmatrix} 0 & \sigma_{xy}^z & 0 \\ -\sigma_{xy}^z & 0 & 0 \\ 0 & 0 & 0 \end{pmatrix}$
$\bar{3}m11'$	$\begin{pmatrix} 0 & \sigma_{xx}^y & 0 \\ \sigma_{xx}^y & 0 & -\sigma_{xz}^y \\ 0 & -\sigma_{zx}^y & 0 \end{pmatrix}$	$\begin{pmatrix} \sigma_{xx}^y & 0 & \sigma_{xz}^y \\ 0 & -\sigma_{xx}^y & 0 \\ \sigma_{zx}^y & 0 & 0 \end{pmatrix}$	$\begin{pmatrix} 0 & \sigma_{xy}^z & 0 \\ -\sigma_{xy}^z & 0 & 0 \\ 0 & 0 & 0 \end{pmatrix}$
$m\bar{3}1'$	$\begin{pmatrix} 0 & 0 & 0 \\ 0 & 0 & \sigma_{xy}^z \\ 0 & \sigma_{xz}^y & 0 \end{pmatrix}$	$\begin{pmatrix} 0 & 0 & \sigma_{xz}^y \\ 0 & 0 & 0 \\ \sigma_{xy}^z & 0 & 0 \end{pmatrix}$	$\begin{pmatrix} 0 & \sigma_{xy}^z & 0 \\ \sigma_{xz}^y & 0 & 0 \\ 0 & 0 & 0 \end{pmatrix}$
$m\bar{3}m1'$	$\begin{pmatrix} 0 & 0 & 0 \\ 0 & 0 & \sigma_{xy}^z \\ 0 & -\sigma_{xy}^z & 0 \end{pmatrix}$	$\begin{pmatrix} 0 & 0 & -\sigma_{xy}^z \\ 0 & 0 & 0 \\ \sigma_{xy}^z & 0 & 0 \end{pmatrix}$	$\begin{pmatrix} 0 & \sigma_{xy}^z & 0 \\ -\sigma_{xy}^z & 0 & 0 \\ 0 & 0 & 0 \end{pmatrix}$

Table I: Shape of the spin conductivity tensor σ_{ij}^k for the magnetic Laue groups of nonmagnetic solids.

3

* sebastian.wimmer@cup.uni-muenchen.de
† diemo.koedderitzsch@cup.uni-muenchen.de

[1] G. D. Mahan, *Many-particle physics*, Physics of Solids and Liquids (Springer, New York, 2000).
[2] J. Shi, P. Zhang, D. Xiao, and Q. Niu, Phys. Rev. Lett. **96**, 076604 (2006).
[3] A. Vernes, B. L. Györffy, and P. Weinberger, Phys. Rev. B **76**, 012408 (2007).
[4] S. Lowitzer, M. Gradhand, D. Ködderitzsch, D. V. Fedorov, I. Mertig, and H. Ebert, Phys. Rev. Lett. **106**, 056601 (2011).
[5] H. Ebert, D. Ködderitzsch, and J. Minár, Rep. Prog. Phys. **74**, 096501 (2011).

Additional considerations

- Upon inspection of Table I on page 2 of the Supplemental Material to Ref. 92 (page 195 herein) one notices that it is in fact more common, on the level of magnetic Laue groups, that a non-magnetic solid can exhibit the longitudinal spin transport effect (6 groups[4]) opposed to have it symmetry-forbidden (5 groups). This does of course not account for a) the number of magnetic point groups that have the same magnetic Laue group, b) the number of magnetic space groups with the same magnetic point group, and c) the abundance of naturally occurring or synthesisable materials with the corresponding magnetic space groups. It is however possible to give a simple criterion for the symmetry-allowed occurrence of a longitudinal spin conductivity tensor element in nonmagnets: the absence of *mutually perpendicular*[5] mirror planes. In $mmm1'$, $4/mmm1'$ & $6/mmm1'$, $m\bar{3}1'$, and $m\bar{3}m1'$ there are such mirror planes (always three of them), hence no longitudinal spin transport is possible. For the remaining magnetic Laue groups, $\bar{1}1'$, $2/m1'$, $4/m1'$ & $6/m1'$, $\bar{3}1'$, $\bar{3}1m1'$ ($\bar{3}m11'$), it is.

- The tensor shapes given in Table I on page 2 of the Supplemental Material to Ref. 92 (page 195 herein) have been reprinted in Table VII on page 8 (page 182 herein) of Ref. 283 (last three columns), together with the shapes for the tensors $\underline{\boldsymbol{\sigma}}'^{k}$ containing in addition the (generalised) Onsager relations between $\underline{\boldsymbol{\sigma}}'^{k}$ and $\underline{\boldsymbol{\sigma}}^{k}$.

[4] Note that $\bar{3}1m1'$ and $\bar{3}m11'$ just differ by a rotation of the coordinate system, see Ref. 283 in Section 3.3.1.

[5] $\bar{3}1m1'$ ($\bar{3}m11'$) has three vertical mirror planes, which naturally are not perpendicular to each other.

3.4 Transverse response properties of non-collinear antiferromagnets

In the following two manuscripts will be presented that deal with, in particular, anti-symmetric response properties of cubic and hexagonal Mn_3X compounds. Starting from group-theoretical considerations the occurrence of the anomalous Hall and related effects in spite of absence of a globally finite magnetisation will be discussed in Ref. 366. This is followed by results on the magneto-optic Kerr effect (MOKE) and the X-ray circular magnetic dichroism (XMCD) in Mn_3Ir, both of which are connected to the frequency-dependent (optical) anti-symmetric conductivity. Moreover the concentration dependence of the anomalous Hall and spin Hall effects in $Mn_3Ir_{1-x}Pt_x$ and $Mn_3Pt_{1-x}Rh_x$ alloys will be investigated. The hexagonal Heusler compound Mn_3Ge will be considered in addition, concerning its transport and magneto-optical properties in the spin-compensated state, but moreover an extensive study of the chirality-induced or *topological* contributions to various response properties will be presented in Ref. 367. By rotating the magnetic moments out of the Kagome planes a chiral and non-coplanar spin configuration is obtained, that gives rise to a so-called emergent electromagnetic field which leads to intrinsic anti-symmetric contributions to anomalous and spin Hall effects, as well as to spin-orbit torque and Edelstein polarisation. To prove that these effects are not induced by spin-orbit coupling, the limit of vanishing SOC is investigated in locally and globally chiral magnetic as well as antiferromagnetic structures.

3.4.1 Cubic and hexagonal Mn_3X (X = Ir,Ge)

The following is an unpublished manuscript on the occurrence of transverse antisymmetric elements of the frequency-dependent conductivity tensor in the noncollinear antiferromagnets cubic Mn_3Ir and hexagonal Mn_3Ge. In addition to spacetime symmetry considerations, first-principles calculations of the anomalous and spin Hall effects, the magneto-optical Kerr effect, and the X-ray magnetic circular dichroism will be presented.

Magneto-optic and transverse transport properties of non-collinear antiferromagnets

Sebastian Wimmer,[1,*] Ján Minár,[2] Sergiy Mankovsky,[1] Alexander N. Yaresko,[3] and Hubert Ebert[1]

[1] *Department Chemie, Physikalische Chemie, Universität München, Butenandtstr. 5-13, 81377 München, Germany*
[2] *University of West Bohemia, Pilsen, Czech Republic*
[3] *Max-Planck-Institute for Solid State Research, Heisenbergstrasse 1, 70569 Stuttgart, Germany*

Previous studies on the anomalous Hall effect in coplanar non-collinear antiferromagnets are revisited and extended to magneto-optic properties, namely magneto-optic Kerr effect (MOKE) and X-ray magnetic dichroism (XMCD). Starting from group-theoretical considerations the frequency-dependent conductivity tensor shapes for various actual and hypothetical spin configurations in cubic and hexagonal Mn_3X compounds are determined. Calculated MOKE and X-ray dichroism spectra are used to confirm these findings and to give estimates of the size of the effects. For Mn_3IrPt and Mn_3PtRh alloys the concentration dependence of the anomalous and spin Hall conductivity is studied in addition.

I. INTRODUCTION

The anomalous Hall effect (AHE) in magnetically ordered materials is usually considered to scale with the corresponding magnetization.[1–4] The same applies to the magneto-optical Kerr effect[5,6] (MOKE) that is used in particular to monitor the magnetization dynamics.[7,8] While the linear relationship of the AHE and the MOKE with the magnetization appears plausible, there seems to be no strict formal justification given for this in the literature apart from numerical studies based on *ab initio* calculations.[9] Nevertheless, a sum rule has been derived that relates the integrated off-diagonal optical conductivity to the orbital magnetic moment of the material.[10,11] The magnetic circular dichroism in X-ray absorption (XMCD) is very closely related to the MOKE.[12] To make full use of this local magnetic probe several authors have derived the so-called XMCD sum rules[13–15] that allow for example to deduce from the integrated $L_{2,3}$-spectra of 3d-transition metals their spin and orbital magnetic moments. In line with the sum rules an angular dependency according to $\cos(\hat{m} \cdot \hat{q})$ is assumed, where $\hat{m}$ and $\hat{q}$ are the orientation of the local moment probed by XMCD and that of the incident X-ray beam. This simple relation implies in particular that in spin-compensated antiferromagnetic systems the XMCD should vanish. For such systems information on the local magnetic moment can nevertheless be obtained by exploiting the linear magnetic X-ray dichroism (XMLD) for which two spectra with linear polarization parallel and perpendicular to the local magnetization are recorded.[16]

In contrast to this situation, Chen *et al.*[17] pointed out that perfect spin-compensation in an antiferromagnet is not a sufficient criterion for the AHE to be absent. In fact these authors give symmetry arguments that the AHE can indeed occur for example in spin-compensated non-collinear antiferromagnets as Mn_3Ir that is commonly employed in spin-valve devices. Numerical work by Chen *et al.* for Mn_3Ir gives in fact a rather large anomalous Hall conductivity, comparable in size to the values for Fe, Co, and Ni. Kübler and Felser[18] numerically confirmed the results of Chen *et al.* and investigated in addition the non-collinear antiferromagnetic hexagonal compounds Mn_3Ge and Mn_3Sn considering various coplanar and non-coplanar triangular magnetic configurations. Also in this case several spin-compensated configurations were identified that were predicted to exhibit an AHE. These predictions recently could indeed be experimentally verified in Mn_3Sn[19] and Mn_3Ge[20,21].

Here one should stress that the occurrence of off-diagonal anti-symmetric conductivity tensor elements has been unambiguously determined much earlier. In particular Kleiner[22] gave the space-time symmetry-restricted tensor forms for the electrical conductivity in all magnetic solids based on the transformation properties of the corresponding Kubo formula under the symmetry operations of the relevant magnetic group. These results in particular do not rest on the assumption of collinear magnetic order or a finite magnetization. Moreover, they apply to the frequency-dependent or optical conductivity just as well and therefore state the presence of MOKE as well as XMCD signals concomitant with the AHC. The former has been studied in chiral cuprates based on tight-binding model calculations of the Berry curvature[23] and, using first-principles methods, in cubic Mn_3Ir-type compounds[24]. The symmetry criteria for the presence of the spin Hall effect (SHE) have recently been given by the present authors[25], extending the approach by Kleiner[22] to more complex situations. The SHE in non-collinear antiferromagnets is currently the subject of intensive theoretical efforts[26–29] and has been observed in experiments on Mn_3Ir[30] via its contribution to the so-called spin-orbit torque. Due to the identical transformation properties of electronic charge and heat current operators[22,25] the occurrence of AHE and SHE imply the existence of corresponding thermally-induced effects, the anomalous and spin Nernst effects. These have been studied in hexagonal Mn_3X using the Berry curvature approach and a Mott-like formula.[31] The anomalous Nernst effect has recently been observed experimentally in Mn_3Sn.[32] Of particular current interest in the thriving field of non-collinear magnetism is the occurrence of chirality-induced or so-called *topological* effects arising from the emergent electromagnetic field created by a non-trivial real- or reciprocal-space texture.[33] This will

be the subject of another contribution.[34]

In the following we present a theoretical study on the transverse transport and optical properties of non-collinear coplanar antiferromagnets. The next section (II) gives a brief overview on the theoretical framework and methods applied. The major part of this contribution is devoted to results for the cubic prototype system Mn_3Ir in section III and a number of possible magnetic configurations of hexagonal Mn_3Ge in section IV.

II. THEORETICAL FRAMEWORK

A. Magnetic symmetry and shape of the conductivity tensor

For the specific case of Mn_3Ir the occurrence of a non-vanishing AHE was predicted by Chen *et al.*[17] by explicitly considering Kagome-type sub-lattices occupied by Mn-atoms with triangular antiferromagnetic order (see below) in combination with a suitable model Hamiltonian. A more general scheme to search for a finite AHE in spin-compensated systems is to use Kleiner's tables that give among others the shape of the frequency dependent conductivity tensor $\boldsymbol{\sigma}(\omega)$ for any material.[22] These tables were constructed by starting from Kubo's linear response formalism and making use of the behavior of the current density operator under all symmetry operations of the relevant magnetic space group. It turns out that only the magnetic Laue group of a material has to be known to fix unambiguously the shape of $\boldsymbol{\sigma}(\omega)$. Unfortunately, Kleiner[22] used an old definition for the Laue group that is obtained by removing the inversion from all improper symmetry operations of the magnetic point group leading to the magnetic Laue Group $32'$ in the case of Mn_3Ir.[22] With the (magnetic) Laue group defined[35] to be the (magnetic) point group artificially extended by the inversion one is led to the magnetic Laue group $\bar{3}m'$ instead. Kleiner's tables have been updated recently by Seemann *et al.*[25] to account in particular for the revised definition of the magnetic Laue group.

Having determined the magnetic Laue group of a solid, for this the program FINDSYM[36,37] was used here, the specific shape of its conductivity tensor $\boldsymbol{\sigma}(\omega)$ can be read from these tables. The presence of an anti-symmetric part for the off-diagonal tensor elements in particular indicates the simultaneous occurrence of the AHE, the MOKE as well as the XMCD (see below).

B. First-principles calculations of the anomalous Hall effect, the magneto-optical Kerr effect and the X-ray magnetic dichroism

The qualitative investigations on the occurrence of the AHE, the MOKE and XMCD of various materials presented below, had been complemented by corresponding numerical work. The underlying electronic structure calculations have been done within the framework of relativistic spin density functional theory with the corresponding Dirac Hamiltonian given by:[38]

$$\mathcal{H}_{\rm D} = c\boldsymbol{\alpha}\cdot\vec{p} + \beta mc^2 + V(\vec{r}) + \beta\Sigma_z B(\vec{r})\ . \qquad (1)$$

Here all quantities have their usual meaning[39], with the spin-averaged and spin-dependent exchange correlation contributions $\bar{V}_{\rm xc}(\vec{r})$ and $B_{\rm eff}(\vec{r})$, respectively, to the effective potential $V(\vec{r})$ set up using the parametrization of Vosko *et al.*[40]. To deal with the resulting four-component Dirac equation the spin-polarized relativistic (SPR) formulations of the Korringa-Kohn-Rostoker (KKR)[41,42] and linear-muffin-tin-orbital (LMTO)[43–45] methods have been used. With the electronic Green Function $G^+(\vec{r},\vec{r}',E)$ supplied by the SPR-KKR method the dc-conductivity tensor $\boldsymbol{\sigma}$ has been evaluated on the basis of the Kubo-Středa equation:[46]

$$\begin{aligned}\sigma_{\rm xy} = \frac{\hbar}{4\pi N\Omega}{\rm Trace}\,\big\langle \hat{j}_{\rm x}(G^+ - G^-)\hat{j}_{\rm y}G^- \\ -\hat{j}_{\rm x}G^+\hat{j}_{\rm y}(G^+ - G^-)\big\rangle_{\rm c} \\ +\frac{e}{4\pi i N\Omega}{\rm Trace}\,\big\langle (G^+ - G^-)(\hat{r}_{\rm x}\hat{j}_{\rm y} - \hat{r}_{\rm y}\hat{j}_{\rm x})\big\rangle_{\rm c}\ . \qquad (2)\end{aligned}$$

See for example Ref. 47 concerning the implementation of this expression.

The optical conductivity tensor $\boldsymbol{\sigma}(\omega)$ for finite frequencies, on the other hand, has been determined using the SPR-LMTO method and the standard expression for the absorptive part of the diagonal and off-diagonal tensor elements, $\sigma^1_{\lambda\lambda}(\omega)$ and $\sigma^2_{\lambda\lambda'}(\omega)$, respectively:[12,48,49]

$$\sigma^1_{\lambda\lambda}(\omega) = \frac{\pi e^2}{\hbar\omega m^2 V}\sum_{\substack{j'\vec{k}\,\text{occ.}\\ j\vec{k}\,\text{unocc.}}} |\Pi^\lambda_{jj'}|^2\delta(\omega-\omega_{jj'}) \qquad (3)$$

$$\sigma^2_{\lambda\lambda'}(\omega) = \frac{\pi e^2}{\hbar\omega m^2 V}\sum_{\substack{j'\vec{k}\,\text{occ.}\\ j\vec{k}\,\text{unocc.}}} \Im\left(\Pi^\lambda_{j'j}\Pi^{\lambda'}_{jj'}\right)\delta(\omega-\Pi^\lambda_{j'j}) \qquad (4)$$

with the matrix elements $\Pi^\lambda_{j'j} = \langle\phi_{j'\vec{k}}|\mathcal{H}_\lambda|\phi_{j\vec{k}}\rangle$ of the Bloch states $|\phi_{j\vec{k}}\rangle$ and their energy difference $\omega_{jj'} = E_{j\vec{k}} - E_{j'\vec{k}}$. The dispersive part was determined in a second step by means of a Kramers-Kronig transformation. With the full tensor $\boldsymbol{\sigma}(\omega)$ available, the Kerr rotation angle $\theta_{\rm K}$ was obtained from the standard expression:[12,49]

$$\theta_{\rm K} \simeq \Re\left(\frac{\sigma_{\rm xy}(\omega)}{\sigma_{\rm xx}(\omega)\sqrt{1-\frac{4\pi i}{\omega}\sigma_{\rm xx}(\omega)}}\right)\ , \qquad (5)$$

that clearly shows that the Kerr rotation – as the Kerr ellipticity – is connected one-to-one with the off-diagonal element $\sigma_{\rm xy}(\omega)$ of the conductivity tensor.

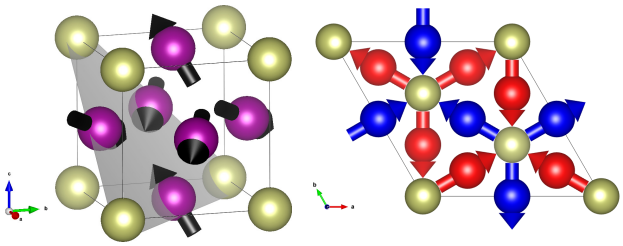

FIG. 1. Left: Cubic unit cell of Mn_3Ir in the triangular antiferromagnetic structure. Ir atoms are colored in gold (light gray), Mn atoms in purple (dark gray). Black arrows indicate the direction of the magnetic moments on the Mn sites, the gray-shaded surface marks the (111) plane. Right: View along [111] on the Kagome planes, Mn atoms and moments in alternating layers are colored in red and blue.[51]

Finally, the X-ray absorption coefficients $\mu_\lambda(\omega)$ for polarization λ have been calculated using the SPR-KKR Green function method on the basis of the expression:[12,50]

$$\mu_\lambda(\omega) \propto \sum_{i\,\mathrm{occ}} \langle \Phi_i | \mathcal{H}_\lambda^\dagger \, \Im G^+(E_i+\hbar\omega)\, \mathcal{H}_\lambda | \Phi_i \rangle \, \theta(E_i+\hbar\omega-E_\mathrm{F}) \;, \tag{6}$$

where the functions Φ_i represent the probed core states i at energy E_i and E_F is the Fermi energy.

The corresponding XMCD signal $\Delta\mu(\omega) = \frac{1}{2}(\mu_+(\omega) - \mu_-(\omega))$ is defined as the difference in absorption for left and right circularly polarized radiation. Expressing the absorption coefficient $\mu_\lambda(\omega)$ in terms of the absorptive part of the corresponding conductivity tensor element:[12]

$$\mu_\lambda(\omega) = \frac{4\pi}{c}\sigma^1_\lambda(\omega) \;, \tag{7}$$

with σ_λ given by

$$\sigma_\pm(\omega) = \sqrt{1/2}\,(\sigma_{\mathrm{xx}}(\omega) \pm i\sigma_{\mathrm{xy}}(\omega)) \;, \tag{8}$$

one sees immediately that the occurrence of the off-diagonal element $\sigma_{\mathrm{xy}}(\omega)$ implies the occurrence of a XMCD signal $\Delta\mu(\omega)$.

III. CUBIC Mn_3Ir

The structure and magnetic configuration of Mn_3Ir is given in Fig. 1 showing a non-collinear antiferromagnetic spin arrangement. The Mn moments are lying in the $\{111\}$ planes of the underlying Cu_3Au ($L1_2$) lattice and are oriented along the $\langle 112\rangle$ directions, forming a Kagome lattice of corner-sharing triangles. Calculated values for spin and orbital moments are given in Table I. Obviously, the magnetic moment of the Mn atoms is dominated by the spin contribution. For Ir on the other hand the very small induced moment is primarily due to its orbital part.

The magnetic structure leads to the magnetic space group $R\bar{3}m'$ that has to be considered instead of the space group $Pm\bar{3}m$ (221) of the Cu_3Au structure. The magnetic point group corresponding to $R\bar{3}m'$ is $\bar{3}m'$ and independent of the definition used for the magnetic Laue group, this implies the following shape of the conductivity tensor:

	$\mu_\mathrm{spin}(\mu_\mathrm{B})$	$\mu_\mathrm{orb.}(\mu_\mathrm{B})$	$\hat{\mu}$
Mn	2.849	0.066	$\langle 112\rangle$
Ir	-0.001	-0.033	[111]
tot.	-0.001	-0.033	[111]

TABLE I. Spin and orbital magnetic moments of Mn_3Ir, atomic type-resolved as well as total values are given in units of μ_B. Their directions are given in the last column.

$$\underline{\boldsymbol{\sigma}}(\omega) = \begin{pmatrix} \sigma_{xx}(\omega) & \sigma_{xy}(\omega) & 0 \\ -\sigma_{xy}(\omega) & \sigma_{xx}(\omega) & 0 \\ 0 & 0 & \sigma_{zz}(\omega) \end{pmatrix} . \tag{9}$$

Here the indices refer to a coordinate system that is conform with the symmetry of the system having the z-axis along the conventional [111]-direction of the cubic Cu_3Au ($L1_2$) lattice, while the x- and y-axes lie in the (111)-plane.

Obviously, $\boldsymbol{\sigma}(\omega)$ has exactly the same shape as any fcc or bcc ferromagnetic material with the magnetization along the z-axis that coincides with the [001]-direction.[12] This implies that any gyro-magnetic and magneto-optical phenomena occurring for this well-known situation will also be present for the non-collinear antiferromagnet Mn_3Ir. For the corresponding spin conductivity tensor shapes see Ref. 25.

A. Anomalous and spin Hall effect

In the DC-limit ($\omega = 0$) the conductivity tensor $\boldsymbol{\sigma}(\omega)$ given by Eq. (9) becomes real. For pure systems the diagonal elements representing longitudinal conductivity diverge for $T = 0$ K, while the off-diagonal anomalous Hall conductivity (AHC) $\sigma_{\mathrm{xy}} = -\sigma_{\mathrm{yx}}$ stays finite. Chen *et al.*[17] calculated the AHC using an expression in terms of the Berry curvature. Their result $\sigma_\mathrm{AH} = 218\,\Omega^{-1}cm^{-1}$ is comparable in size with that for the ferromagnets Fe, Co, and Ni. In the present work the Kubo-Středa linear response formalism[46,47,52] was used, that for pure systems is completely equivalent to the Berry curvature approach.

The values obtained for the intrinsic anomalous and spin Hall conductivities at $T = 0\,\mathrm{K}$ in pure Mn_3X with X = Ir, Pt, and Rh using the Kubo-Středa formula are collected in Table II. For the AHC in Mn_3Ir reasonable agreement with previous results by Chen *et al.*[17] (|218| S/m) and Zhang *et al.*[27] (-312 S/m) is achieved. The clear trend of increasing AHC as well as SHC with atomic number is however in disagreement with the findings of the latter authors.

Figure 2 shows results for the concentration dependence of the AHC in $Mn_3Ir_{1-x}Pt_x$ (top) as well as for

	AHC	SHC
Mn_3Rh	-85	-125
Mn_3Ir	-280	-230
Mn_3Pt	-360	-250

TABLE II. Anomalous and spin Hall conductivities, AHC $= \sigma_{xy}$ and SHC $= \sigma^z_{xy}$, respectively, for pure cubic Mn_3X compounds with $X =$ Rh, Ir, and Pt in units of [S/m]. The z direction corresponds to the [111] direction perpendicular to the Kagome planes. Results are obtained using the Kubo-Středa formula.

AHC and SHC in $Mn_3Rh_{1-x}Pt_x$ (middle and bottom, respectively). While for σ_{xy} in $Mn_3Ir_{1-x}Pt_x$ the usual divergence of the values including vertex corrections is found, followed by a non-trivial concentration dependence, in $Mn_3Rh_{1-x}Pt_x$ the impact of these is large for the whole investigated range. The spin Hall conductivity in this system behaves very similar to its charge counterpart. The fact that both conductivities without vertex corrections (NV) do not clearly converge towards the intrinsic values when approaching the dilute limits $x \to 0/1$ still has to be clarified. For AHC and SHC in $Mn_3Rh_{1-x}Pt_x$ an almost linear increase with increasing concentration of the heavier alloy partner Pt can be observed, the intrinsic contribution (NV) in particular for the AHC however appears to behave again non-trivially for intermediate concentrations.

B. Magneto-optical Kerr effect (MOKE)

For finite frequencies the absorptive part of the corresponding optical conductivity tensor $\boldsymbol{\sigma}(\omega)$ has been calculated in the energy regime $\hbar\omega = 0 - 10$ eV using the fully relativistic LMTO band structure method.[43–45] Figure 3 (top) shows the corresponding real parts of the optical conductivity, $\sigma^1_{ii}(\omega)$. A reasonable qualitative agreement with earlier theoretical work by Feng *et al.*[24] is achieved. The small difference between $\sigma^1_{xx}(\omega) = \sigma^1_{yy}(\omega)$ and $\sigma^1_{zz}(\omega)$ obviously reflects the anisotropy of the system due to the underlying lattice structure as well as the magnetic ordering. Accordingly it will give rise to corresponding magneto-optical phenomena.[12] As a reference, Fig. 3 (top) gives also corresponding results for ferromagnetic bcc-Fe. In this case the anisotropy, i.e., the difference between $\sigma^1_{xx}(\omega)$ and $\sigma^1_{zz}(\omega)$, is only due to the magnetic ordering. As it is much less pronounced than for Mn_3Ir only $\sigma^1_{xx}(\omega)$ is given.

Figure 3 (middle) shows the imaginary part of the off-diagonal transverse optical conductivity, σ^2_{xy}, that is the counterpart to the AHC and that in particular gives rise to the polar Kerr rotation. Interestingly, σ^2_{xy} for Mn_3Ir is in the same order of magnitude as for ferromagnetic Fe. Accordingly one finds θ_{K} of Mn_3Ir and Fe to be comparable in magnitude (see bottom panel of Fig. 3). Again reasonable qualitative agreement with Ref. 24 is obtained.

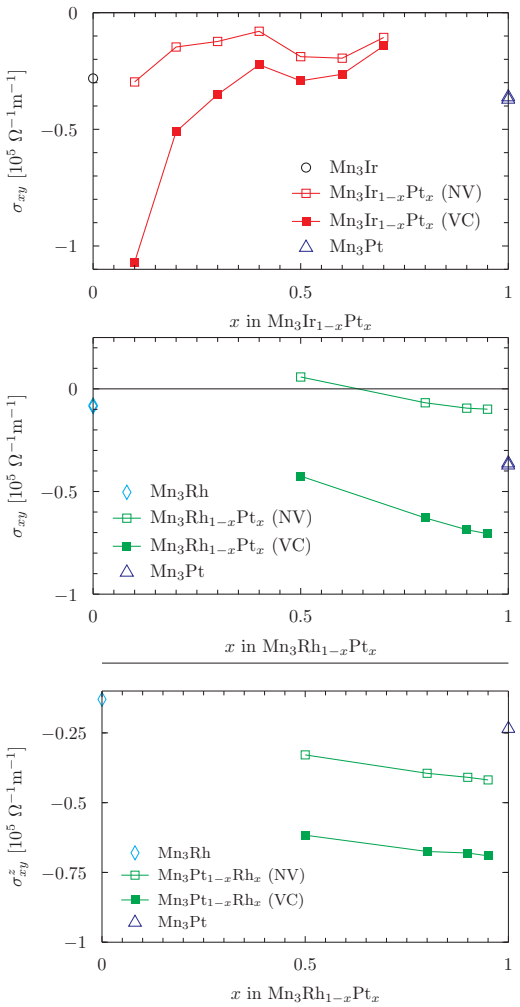

FIG. 2. Anomalous Hall conductivity of $Mn_3Ir_{1-x}Pt_x$ (top) and $Mn_3Rh_{1-x}Pt_x$ (middle) as well as spin Hall conductivity of $Mn_3Rh_{1-x}Pt_x$ alloys (bottom) as a function of concentration x. Open symbols are results excluding vertex corrections (NV) and filled symbols such including them (VC), see text for details. The intrinsic values of the pure compounds are shown in addition. All results were obtained using the Kubo-Středa formula.

C. X-ray absorption spectroscopy

Fig. 4 (upper panel) shows results of calculations for the X-ray absorption coefficient $\bar{\mu} = \frac{1}{2}(\mu_+ + \mu_-)$ at the Mn $L_{2,3}$-edges for polarization-averaged radiation. These spectra show the typical $L_{2,3}$-edges of a 3d transition metal shifted against each other by the spin-orbit splitting of the 2p core states. The two curves shown have been obtained for the radiation wave vector $\vec{q}_{\mathrm{rad}}$ along the [111]-direction and along the direction $\hat{m}_{\mathrm{Mn}}$ of the magnetic moment of one of the three equivalent Mn-atoms

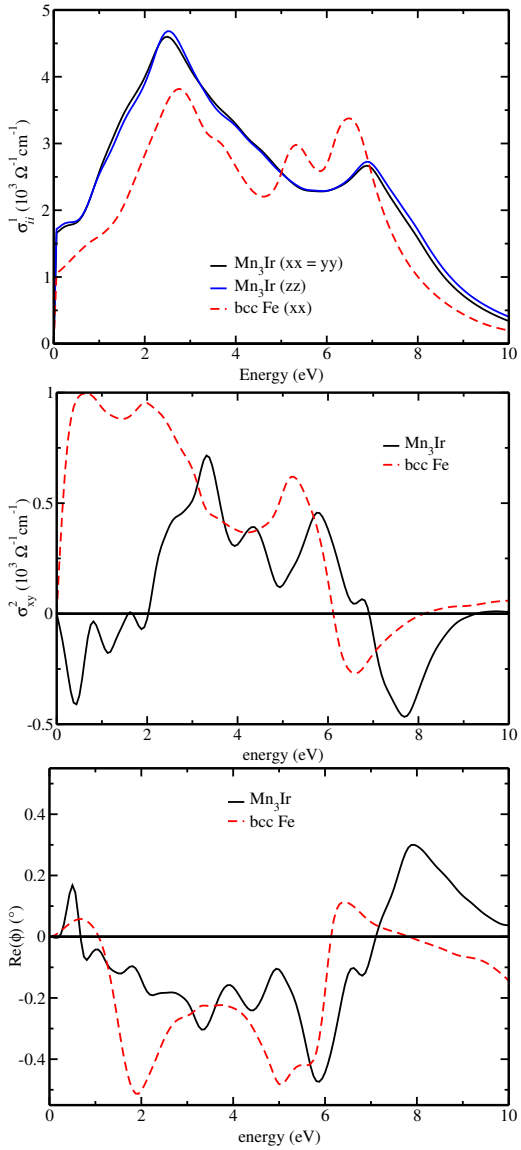

FIG. 3. Absorptive part of the optical conductivity tensor elements σ^1_{xx}, σ^1_{zz} (top) and σ^2_{xy} (middle) of Mn_3Ir (full lines) together with the Kerr rotation angle θ_K (bottom). In addition, corresponding results for ferromagnetic bcc-Fe are given (dashed lines).

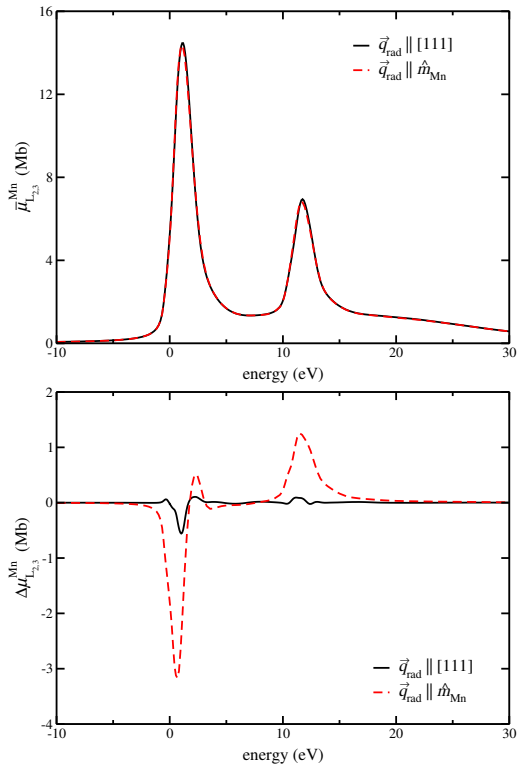

FIG. 4. Total absorption coefficient $\bar{\mu}$ at the $L_{2,3}$-edge of a single Mn atom of non-collinear antiferromagnetic Mn_3Ir (top) and corresponding circular dichroism spectra $\Delta\mu$ (bottom), both for incidence $\vec{q}_{rad}$ perpendicular (along [111]) and polar w.r.t. the magnetization direction.

in the unit cell. Similar to σ^1_{xx} and σ^1_{zz} in the optical regime discussed above the difference is quite small, i.e. only a weak anisotropy occurs. The lower panel of Fig. 4 gives the corresponding XMCD curves $\Delta\mu$. For the polar geometry $\vec{q}_{rad} \parallel \hat{m}_{Mn}$ with the artificial restriction to one of the Mn sites the highest XMCD signal can be expected. Indeed for the L_3-edge about 20 % is found for the ratio $\Delta\mu/\bar{\mu}$. This is the typical order of magnitude found in ferromagnetic transition metals.[12] Considering instead the geometry $\vec{q}_{rad} \parallel [111]$ with the X-ray beam perpendicular to the Mn magnetic moments, no XMCD signal is expected following the standard arguments.[12] In contrast to this, Fig. 4 (lower panel) clearly shows that there is indeed a finite XMCD present as one had to expect on the basis of Eqs. (7), (8) and (9). In addition one has to emphasize that the individual XMCD for the three Mn sites are identical, i.e. they do not compensate each other as in the case of $\vec{q}_{rad} \parallel \hat{m}_{Mn}$ but add up. Comparing the two XMCD spectra in Fig. 4 one notes that $\Delta\mu$ for $\vec{q}_{rad} \parallel [111]$ is very similar in shape to that for $\vec{q}_{rad} \parallel \hat{m}_{Mn}$ but about one order of magnitude smaller in amplitude. Nevertheless, this implies that it should be possible to detect this XMCD signal in experiment provided one domain dominates in the regime exposed to the X-ray beam (see also comment by Chen *et al.*[17]).

In the top panel of Figure 5 the difference in total absorption $\Delta\bar{\mu} = \bar{\mu}_i - \bar{\mu}_j$ with $\bar{\mu}_i = \frac{1}{2}(\mu_{i,+} + \mu_{i,-})$ for incidence along pairs of high symmetry directions ($i, j =$ x, y, z) and along intermediate directions ($i =$ xy, xz, yz) compared to the corresponding linear combinations of x, y, z is shown. Note that in contrast to the conventional X-ray magnetic linear dichroism, here the polarization of the incoming light is not rotated. The Cartesian directions x and y were chosen to be in the (111) plane

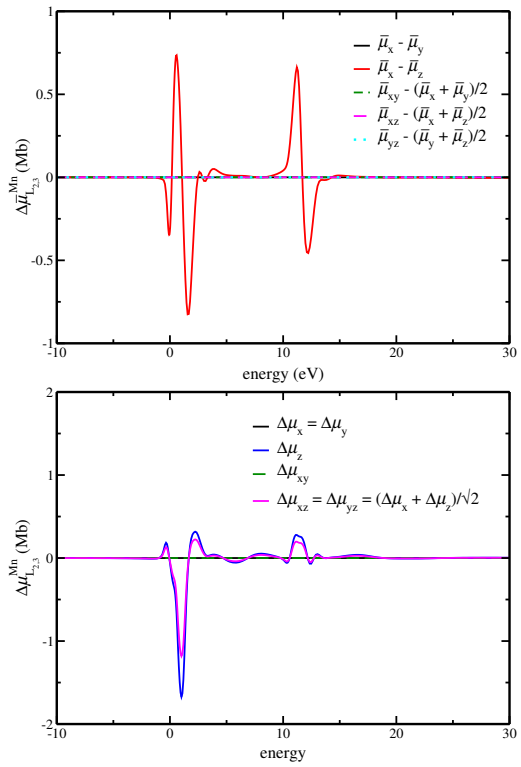

FIG. 5. Top: Differential polarization-averaged X-ray absorption spectra $\Delta\bar{\mu}$ comparing incidence along high-symmetry directions in Mn_3Ir. Bottom: X-ray magnetic circular dichroism (XMCD) spectra $\Delta\mu$ in Mn_3Ir for incidence along the same directions as in the top panel.

(indicated in gray in Figure 1), i.e., corresponding to the crystallographic directions $[11\bar{2}]$ (x) and $[\bar{1}10]$ (y), while z is parallel to the [111] direction (the space diagonal of the cubic unit cell shown in Fig. 1). As can be seen, the absorption is isotropic in the (111) plane ($\bar{\mu}_x = \bar{\mu}_y$), but different for incidence perpendicular to it, i.e., along the [111] direction ($\bar{\mu}_z \neq \bar{\mu}_x$). This agrees with the diagonal of the tensor in Eq. (9), since the first two elements are identical, $\sigma_{xx} = \sigma_{yy}$, and different from the third (σ_{zz}). Furthermore the absorption for intermediate directions (xy, xz and yz) can be described by a linear combination of the absorption coefficients along Cartesian axes, such as e.g. $\bar{\mu}_{xz} = \frac{1}{2}(\bar{\mu}_x + \bar{\mu}_z)$, i.e., no symmetric off-diagonal elements are present in the absorption tensor. In the lower panel of Figure 5 the circular dichroism for several directions of incidence is compared. Again the results are in agreement with the tensor shape of Eq. (9), inasmuch that the only linearly independent non-zero anti-symmetric tensor element is $\Delta\mu_z$, corresponding to $\sigma_{xy} = -\sigma_{yx}$.

IV. HEXAGONAL Mn_3Ge

A. Magnetic structure and symmetry

The hexagonal Mn_3Ge compound crystallizes, as its siblings Mn_3Sn and Mn_3Ga, in the $D0_{19}$ structure with space group $P6_3/mmc$ (194). The non-magnetic unit cell is shown in Fig. 6 and will be labeled NM in the following. The Mn atoms on the Wyckoff positions $6h$ in the {0001} planes colored in magenta (dark gray) form triangular, so-called Kagome lattices, stacked alternatingly along the [0001] (z) direction. Ge atoms occupying the Wyckoff positions $2h$ are colored in light gray.

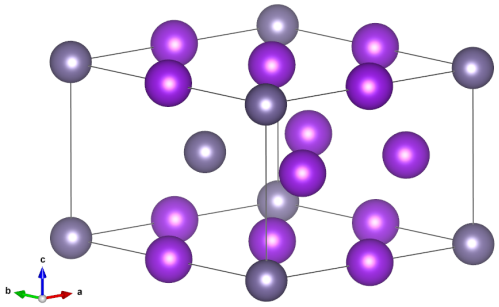

FIG. 6. Non-magnetic unit cell of Mn_3Ge in space group $P6_3/mmc$ (194). Mn atoms on the Wyckoff positions $6h$ are colored in magenta (dark grey) and Ge atoms (Wyckoff positions $2h$) are colored in light gray.[51]

A number of non-collinear but coplanar antiferromagnetic alignments of the moments in the two Kagome sublattices have been discussed for Mn_3Ge and related compounds in the literature.[18,53–57] These are collected in Figure 7 together with further, hypothetical spin compensated structures.

The structure AFM0 has the same spin arrangement in both Kagome planes with the Mn moments pointing alternatingly towards the center of the corner-sharing triangles or away from it. The two sub-lattices are connected by a 6_3 operation, i.e., a rotation around [0001] (z) by 60° combined with a translation along z by half of the corresponding lattice constant. This leads to a bipartite, globally chiral lattice with the non-magnetic Laue group $6/mmm1'$. It corresponds to Fig. 3(a) of Ref. 57. The structures AFM1-4 have been discussed by Kübler and Felser[18], see Figs. 2, 3(a), 3(b), and 5 therein. The structure AFM3 is reported to be obtained by a self-consistent calculation starting from AFM2. An anomalous Hall effect has been predicted for AFM3 and AFM4 by these authors, as well as for an additional non-coplanar structure which will not be discussed herein. The structures AFM5 and AFM6 are obtained from AFM0 by rotating all moments in the Kagome planes by 30°, counterclockwise and clockwise, respectively. AFM7, AFM8, and AFM10 are hypothetical structures. AFM9 is obtained from AFM0

7

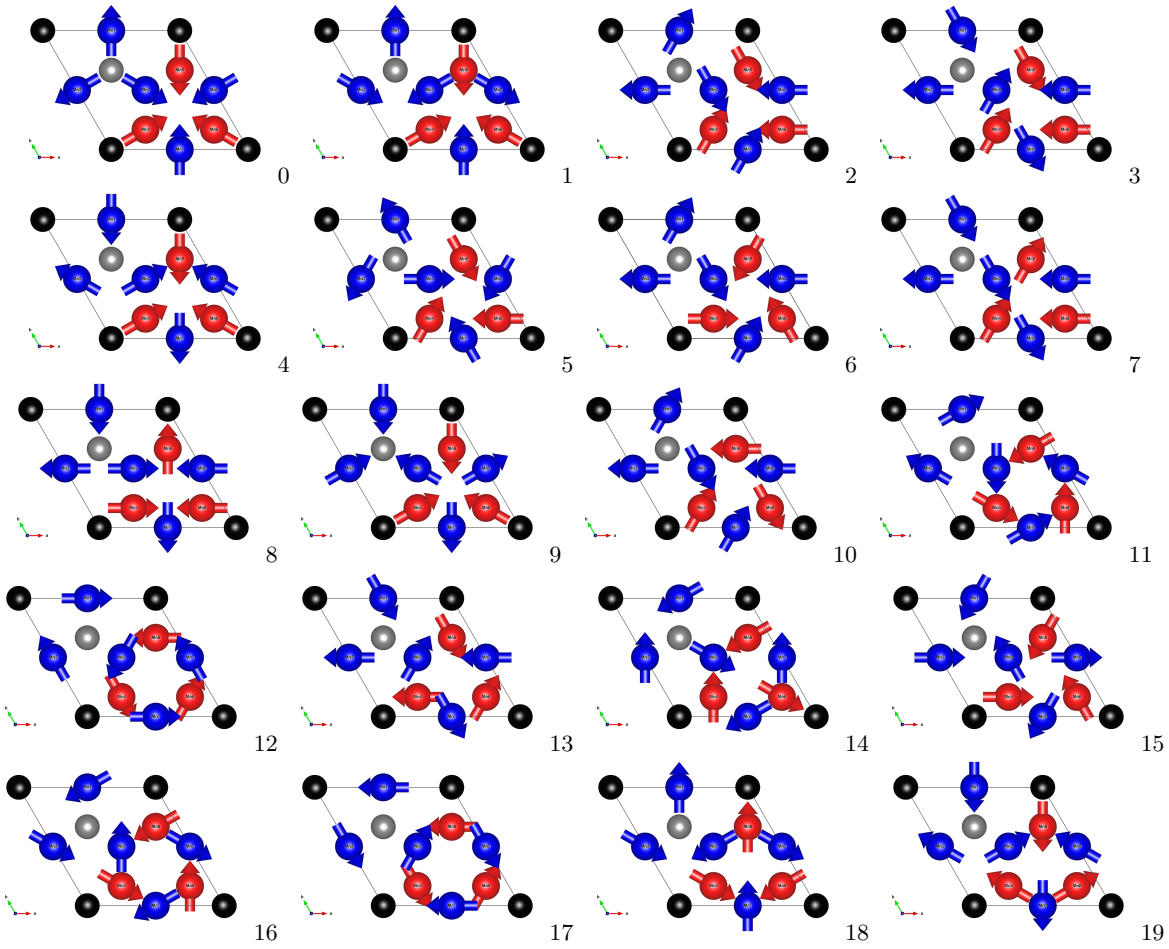

FIG. 7. Antiferromagnetic structures of Mn_3Ge, AFMi with $i = 0...19$, discussed in this contribution.[51]

by reversing the moments in one Kagome layer (here the one in blue), leading to opposite chirality in the two planes and global inversion symmetry. The sub-lattices are connected by $6'_3$, i.e., a screw rotation in combination with time reversal. It corresponds to Fig. 3(b) of Ref. 57. The structures AFM11 and AFM12 are 60° and 90° clockwise rotations of all moments in AFM0. AFM13 and AFM14 have been proposed in Ref. 20, the first experimental verification of an anomalous Hall effect in Mn_3Ge. AFM13 should furthermore correspond to the magnetic structure of Mn_3Sn in Ref. 19, the very first reported observation of the AHE in a non-collinear antiferromagnet of the hexagonal Mn_3X Heusler type. In AFM15, AFM16, and AFM17 the moments are 30°, 60°, and 90° clockwise rotated from AFM9. Finally, AFM18 and AFM19 are proposed in Refs. 21, 27–29, and 58, the latter of the two has been reported by Zhang *et al.*[57] to be the most stable for Mn_3X (X = Ga, Sn, Ge) based on DFT calculations. One should stress here again, that all of the above magnetic structures are coplanar and fully spin-compensated, i.e., no weak ferromagnetism[59] due to an out-of-plane rotation is taken into account here.

The magnetic space and Laue groups corresponding to the structures in Figs. 6 and 7 as well as of a ferromagnetic alignment of the Mn moments along the [0001] direction are given in Table III. For convenience also the magnetic Laue group following the definition of Kleiner[22] is given in parentheses. As can be seen, a number of structures have the same magnetic space group and moreover a number of these lead to the same magnetic Laue groups.

The corresponding symmetry-restricted tensor shapes are:[22,25]

$$\underline{\sigma}^{\mathrm{NM}} = \begin{pmatrix} \sigma_{xx} & 0 & 0 \\ 0 & \sigma_{xx} & 0 \\ 0 & 0 & \sigma_{zz} \end{pmatrix} \tag{10}$$

$$\underline{\sigma}^{\mathrm{FM}} = \begin{pmatrix} \sigma_{xx} & \sigma_{xy} & 0 \\ -\sigma_{xy} & \sigma_{xx} & 0 \\ 0 & 0 & \sigma_{zz} \end{pmatrix} \tag{11}$$

label	magn. space group	magn. Laue group
NM	$P6_3/mmc$	$6/mmm1'$ $(6221')$
FM	$P6_3/mm'c'$	$6/mm'm'$ $(62'2')$
AFM0	$P6_3/m'm'c'$	$6/mmm1'$ $(6221')$
AFM1	$Am'm'2$	$m'm'm$ $(2'2'2)$
AFM2	$P\bar{6}'2c'$	$6'/m'mm'$ $(6'22')$
AFM3	Pm'	$2'/m'$ $(2')$
AFM4	$Am'm'2$	$m'm'm$ $(2'2'2)$
AFM5	$P6_3/m'$	$6/m1'$ $(61')$
AFM6	$P6_3/m'$	$6/m1'$ $(61')$
AFM7	$Am'a'2$	$m'm'm$ $(2'2'2)$
AFM8	$Cm'c'm'$	$mmm1'$ $(2221')$
AFM9	$P6_3'/m'm'c$	$6'/m'm'm$ $(6'22')$
AFM10	Pm'	$2'/m'$ $(2')$
AFM11	$P6_3/m'$	$6/m1'$ $(61')$
AFM12	$P6_3/m'mc$	$6/mmm1'$ $(6221')$
AFM13	$Cmc'm'$	$mm'm'$ $(2'2'2)$
AFM14	$Cm'cm'$	$m'mm'$ $(2'22')$
AFM15	$P6_3'/m'$	$6'/m'$ $(6')$
AFM16	$P6_3'/m'$	$6'/m'$ $(6')$
AFM17	$P6_3'/m'mc'$	$6'/m'mm'$ $(6'22')$
AFM18	$Cm'cm'$	$m'mm'$ $(2'22')$
AFM19	$Cm'cm'$	$m'mm'$ $(2'22')$

TABLE III. Magnetic space and Laue groups of the magnetic structures shown in Fig. 7, as well as of the non-magnetic unit cell in Fig. 6 (NM) and a ferromagnetic structure (FM) with all moments along the [0001] direction. The magnetic Laue groups are given following the definition introduced by the present authors[25] as well as the one used by Kleiner[22] (in parentheses). The conventional setting concerning the sequence of generators is used for the space groups and carried over to point and Laue groups.[60]

$$\underline{\sigma}^{\mathrm{AFM0,2,5,6,9,11,12,15,16,17}} = \begin{pmatrix} \sigma_{xx} & 0 & 0 \\ 0 & \sigma_{xx} & 0 \\ 0 & 0 & \sigma_{zz} \end{pmatrix} \quad (12)$$

$$\underline{\sigma}^{\mathrm{AFM1,4,13,18,19}} = \begin{pmatrix} \sigma_{xx} & 0 & \sigma_{xz} \\ 0 & \sigma_{yy} & 0 \\ -\sigma_{xz} & 0 & \sigma_{zz} \end{pmatrix} \quad (13)$$

$$\underline{\sigma}^{\mathrm{AFM3,10}} = \begin{pmatrix} \sigma_{xx} & \sigma_{xy} & \sigma_{xz} \\ \sigma_{xy} & \sigma_{yy} & \sigma_{yz} \\ -\sigma_{xz} & -\sigma_{yz} & \sigma_{zz} \end{pmatrix} \quad (14)$$

$$\underline{\sigma}^{\mathrm{AFM7,AFM14}} = \begin{pmatrix} \sigma_{xx} & 0 & 0 \\ 0 & \sigma_{yy} & \sigma_{xz} \\ 0 & -\sigma_{xz} & \sigma_{zz} \end{pmatrix} \quad (15)$$

$$\underline{\sigma}^{\mathrm{AFM8}} = \begin{pmatrix} \sigma_{xx} & 0 & 0 \\ 0 & \sigma_{yy} & 0 \\ 0 & 0 & \sigma_{zz} \end{pmatrix} . \quad (16)$$

In fact, for the twenty actual and hypothetical structures in Fig. 7 obviously only four different tensor shapes are found: a) The non-magnetic shape of Eq. (10) with the crystallographic anisotropy $\sigma_{xx} = \sigma_{yy} \neq \sigma_{zz}$ that applies for a number of antiferromagnetic structures [see Eq. (12)], b) the ferromagnetic shape of Eq. (11) with an additional off-diagonal anti-symmetric element representing the AHE. This is found again for five antiferromagnetic structures in Eq. (13) and two others in Eq. (15), only with different principal axes, c) the full tensor with two anomalous Hall conductivities in Eq. (14), and finally d) the diagonal fully anisotropic form of AFM8 in Eq. (16). Note that all configurations assumed in experimental (AFM13[19,20], AFM14[20,21], AFM18/19[21]) as well as theoretical (AFM1-4[18], AFM18/19[27–29,58]) investigations on the anomalous Hall effect in hexagonal Mn_3X compounds are found to exhibit at least one off-diagonal anti-symmetric element of $\underline{\boldsymbol{\sigma}}$, with the exception of AFM1 for which no AHE is predicted in Ref. 18.

Corresponding tensor forms for direct and inverse spin conductivity can be found in Ref. 25, those for the spin-orbit torkance and the Edelstein polarization in chiral structures are given in Refs. 61 and 62, respectively.

B. X-ray absorption spectroscopy

The tensor shapes presented above were confirmed for selected representative cases using first-principles calculations of X-ray absorption spectra for circularly polarized light. Figures 8-11 show for the structures AFM1-4 the difference in polarization-averaged spectra, $\Delta\bar{\mu}$, along high-symmetry (Cartesian and intermediate) directions in the top panels and the corresponding spectra giving the difference in absorption for left and right circularly polarized X-rays, the XMCD signals, in the bottom panels. As stated above (see section III C), a finite $\Delta\bar{\mu}$ signal in the upper panels of Figs. 8-11 indicates an anisotropy in the symmetric part of the optical conductivity tensor, i.e., a difference on the diagonal and/or presence of symmetric contributions to off-diagonal elements. For the XMCD spectra in the lower panel a finite signal $\Delta\mu$ along a Cartesian direction i confirms the presence of anti-symmetric off-diagonal elements of $\underline{\boldsymbol{\sigma}}(\omega)$ with indices $j, k \neq i$. Moreover, an XMCD for incidence along intermediate directions $\langle 110 \rangle$ is in all cases, if present, found to be a linear combination of the corresponding signals for incidence along the Cartesian axes. Taken together, in all four cases the predicted tensor shapes are confirmed.

V. CONCLUSIONS

Based on general and model-independent symmetry arguments for the occurrence of galvano-magnetic and magneto-optical phenomena in materials with arbitrary magnetic order, the implications of in particular off-diagonal anti-symmetric elements of the frequency-dependent conductivity tensor in the coplanar non-

9

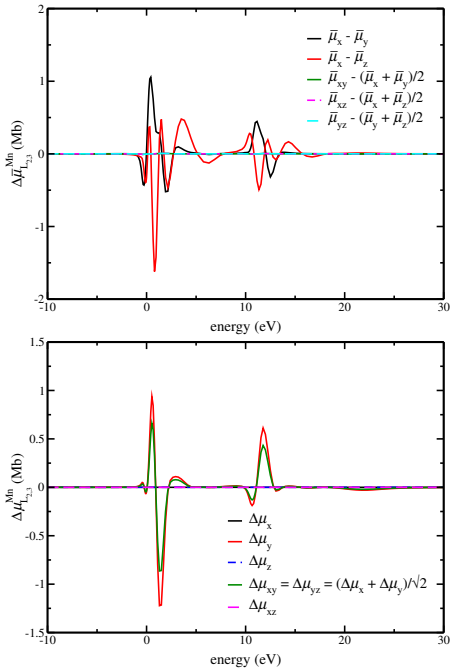

FIG. 8. Top: Differential polarization-averaged X-ray absorption spectra $\Delta\bar{\mu}$ comparing incidence along high-symmetry directions in Mn_3Ge with AFM1 magnetic structure (see Fig. 7). Bottom: Corresponding X-ray magnetic circular dichroism (XMCD) spectra $\Delta\mu$.

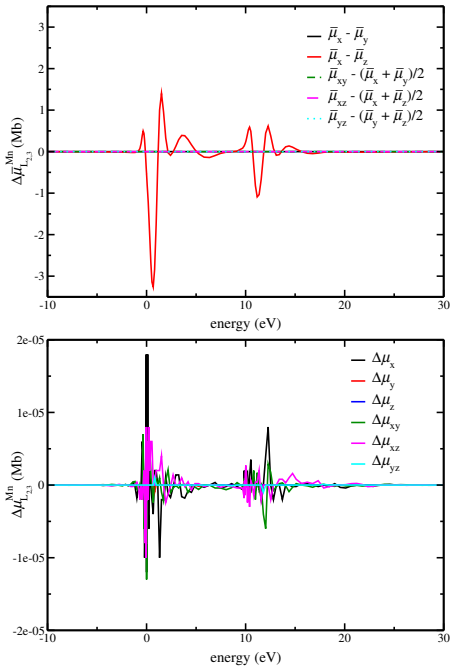

FIG. 9. Top: Differential polarization-averaged X-ray absorption spectra $\Delta\bar{\mu}$ comparing incidence along high-symmetry directions in Mn_3Ge with AFM2 magnetic structure (see Fig. 7). Bottom: Corresponding X-ray magnetic circular dichroism (XMCD) spectra $\Delta\mu$.

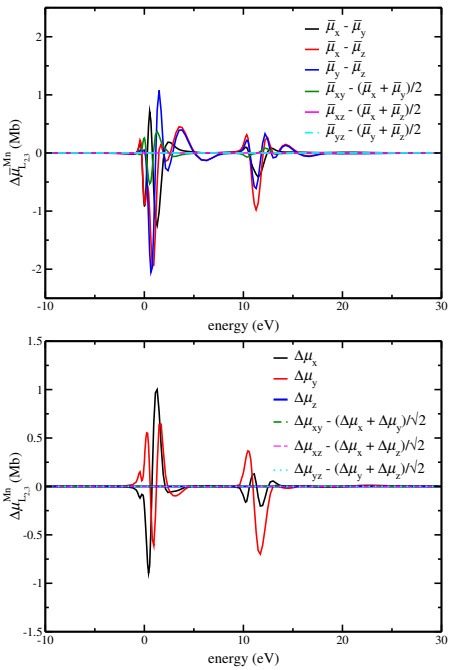

FIG. 10. Top: Differential polarization-averaged X-ray absorption spectra $\Delta\bar{\mu}$ comparing incidence along high-symmetry directions in Mn_3Ge with AFM3 magnetic structure (see Fig. 7). Bottom: Corresponding X-ray magnetic circular dichroism (XMCD) spectra $\Delta\mu$.

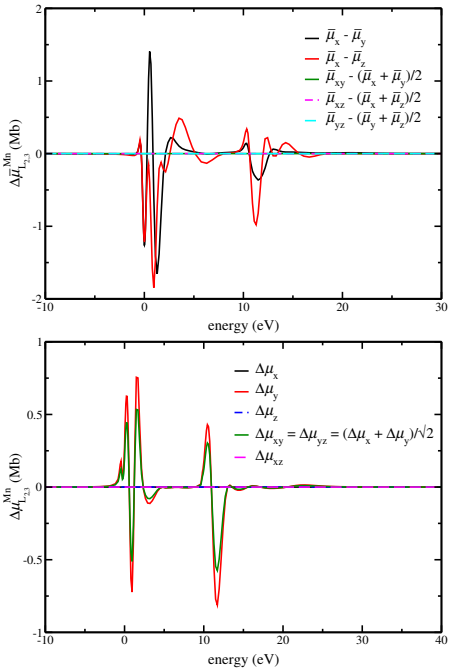

FIG. 11. Top: Differential polarization-averaged X-ray absorption spectra $\Delta\bar{\mu}$ comparing incidence along high-symmetry directions in Mn_3Ge with AFM4 magnetic structure (see Fig. 7). Bottom: Corresponding X-ray magnetic circular dichroism (XMCD) spectra $\Delta\mu$.

collinear antiferromagnets Mn_3X with X = Ir and Ge have been investigated. For the cubic Mn_3Ir-type compound the results of first-principles Kubo linear response calculations of the anomalous and spin Hall conductivities could be shown to be in reasonable agreement with previous findings. In addition the concentration dependence of the anomalous and spin Hall effects in substitutionally disordered alloys is found to be non-trivial in particular concerning the AHE. A clear increase of the intrinsic values for both, AHE and SHE, with increasing atomic number in the pure compounds Mn_3Rh, Mn_3Ir, and Mn_3Pt is however in agreement with expectations concerning the relevance of spin-orbit coupling. The magneto-optical properties of pure Mn_3Ir are again found to be in agreement with the shape of the optical conductivity tensor as well as with previous theoretical work. Comparison with corresponding results for the diagonal and off-diagonal optical conductivities in bcc Fe moreover shows that the magneto-optical Kerr effect is of similar magnitude in both. Calculated polarization-averaged X-ray absorption and magnetic circular dichroism spectra confirm expectation concerning their symmetry and in addition the size of the XMCD signal suggests the possibility of experimental confirmation. For the hexagonal Heusler compound Mn_3Ge a number of proposed as well as additional hypothetical spin-compensated non-collinear configurations has been studied w.r.t. to magnetic symmetry and consequent electrical conductivity tensor shape. The occurrence of at least one independent anomalous Hall conductivity can be confirmed for all magnetic structures usually assumed in the experimental and theoretical literature. For selected representative cases the tensor shapes have been confirmed by X-ray absorption spectroscopy calculations. The implications of a non-coplanar spin texture in chiral and achiral magnetic structures of Mn_3Ge on the linear response properties will be discussed in a separate contribution.[34]

ACKNOWLEDGMENTS

Financial support by the DFG via SFB 1277 (*Emergente relativistische Effekte in der Kondensierten Materie*) is gratefully acknowledged.

* sebastian.wimmer@cup.uni-muenchen.de

[1] E. M. Pugh and N. Rostoker, Rev. Mod. Phys. **25**, 151 (1953).
[2] Y. Yao, L. Kleinman, A. H. MacDonald, J. Sinova, T. Jungwirth, D.-s. Wang, E. Wang, and Q. Niu, Phys. Rev. Lett. **92**, 037204 (2004).
[3] C. Zeng, Y. Yao, Q. Niu, and H. H. Weitering, Phys. Rev. Lett. **96**, 037204 (2006).
[4] N. Nagaosa, J. Sinova, S. Onoda, A. H. MacDonald, and N. P. Ong, Rev. Mod. Phys. **82**, 1539 (2010).
[5] J. Kerr, Philosophical Magazine Series 5 **5**, 161 (1878).
[6] P. N. Argyres, Phys. Rev. **97**, 334 (1955).
[7] E. Beaurepaire, J.-C. Merle, A. Daunois, and J.-Y. Bigot, Phys. Rev. Lett. **76**, 4250 (1996).
[8] G. Woltersdorf, O. Mosendz, B. Heinrich, and C. H. Back, Phys. Rev. Lett. **99**, 246603 (2007).
[9] H. Toyosaki, T. Fukumura, Y. Yamada, and M. Kawasaki, Appl. Phys. Lett. **86**, 182503 (2005).
[10] H. Hasegawa and R. Howard, J. Phys. Chem. Sol. **21**, 179 (1961).
[11] D. Y. Smith, Phys. Rev. B **13**, 5303 (1976).
[12] H. Ebert, Rep. Prog. Phys. **59**, 1665 (1996).
[13] J. L. Erskine and E. A. Stern, Phys. Rev. B **12**, 5016 (1975).
[14] B. T. Thole, P. Carra, F. Sette, and G. van der Laan, Phys. Rev. Lett. **68**, 1943 (1992).
[15] P. Carra, B. T. Thole, M. Altarelli, and X. Wang, Phys. Rev. Lett. **70**, 694 (1993).
[16] P. Carra, H. König, B. Thole, and M. Altarelli, Physica B: Condensed Matter **192**, 182 (1993).
[17] H. Chen, Q. Niu, and A. H. MacDonald, Phys. Rev. Lett. **112**, 017205 (2014).
[18] J. Kübler and C. Felser, EPL (Europhysics Letters) **108**, 67001 (2014).
[19] S. Nakatsuji, N. Kiyohara, and T. Higo, Nature **527**, 212 (2015).
[20] N. Kiyohara, T. Tomita, and S. Nakatsuji, Phys. Rev. Applied **5**, 064009 (2016).
[21] A. K. Nayak, J. E. Fischer, Y. Sun, B. Yan, J. Karel, A. C. Komarek, C. Shekhar, N. Kumar, W. Schnelle, J. Kübler, C. Felser, and S. S. P. Parkin, Sci. Adv. **2**, e1501870 (2016).
[22] W. H. Kleiner, Phys. Rev. **142**, 318 (1966).
[23] J. Orenstein and J. E. Moore, Phys. Rev. B **87**, 165110 (2013).
[24] W. Feng, G.-Y. Guo, J. Zhou, Y. Yao, and Q. Niu, Phys. Rev. B **92**, 144426 (2015).
[25] M. Seemann, D. Ködderitzsch, S. Wimmer, and H. Ebert, Phys. Rev. B **92**, 155138 (2015).
[26] O. Gomonay, Phys. Rev. B **91**, 144421 (2015).
[27] Y. Zhang, Y. Sun, H. Yang, J. Železný, S. P. P. Parkin, C. Felser, and B. Yan, Phys. Rev. B **95**, 075128 (2017).
[28] J. Železný, Y. Zhang, C. Felser, and B. Yan, Phys. Rev. Lett. **119**, 187204 (2017).
[29] Y. Zhang, J. Zelezny, Y. Sun, J. van den Brink, and B. Yan, ArXiv e-prints (2017), arXiv:1704.03917 [cond-mat.mtrl-sci].
[30] W. Zhang, W. Han, S.-H. Yang, Y. Sun, Y. Zhang, B. Yan, and S. S. P. Parkin, Sci. Adv. **2**, e1600759 (2016).
[31] G.-Y. Guo and T.-C. Wang, Phys. Rev. B **96**, 224415 (2017).
[32] M. Ikhlas, T. Tomita, T. Koretsune, M.-T. Suzuki, D. Nishio-Hamane, R. Arita, Y. Otani, and S. Nakatsuji, Nat. Phys. **13**, 1085 (2017).
[33] N. Nagaosa and Y. Tokura, Nature Nanotechnology **8**, 899 (2013).
[34] S. Wimmer, S. Mankovsky, and H. Ebert, "Chirality-induced linear response properties in non-coplanar

Mn_3Ge," unpublished (2018).
[35] W. Borchardt-Ott, *Crystallography: An Introduction*, 3rd ed. (Springer-Verlag Berlin Heidelberg, 2012) Chap. 13.4.
[36] H. T. Stokes, D. M. Hatch, and B. J. Campbell, ISOTROPY Software Suite, `iso.byu.edu`.
[37] H. T. Stokes and D. M. Hatch, J. Appl. Crystallogr, **38**, 237 (2005).
[38] A. H. MacDonald and S. H. Vosko, J. Phys. C: Solid State Phys. **12**, 2977 (1979).
[39] M. E. Rose, *Relativistic Electron Theory* (John Wiley & Sons, Inc. - New York, London, 1961).
[40] S. H. Vosko, L. Wilk, and M. Nusair, Can. J. Phys. **58**, 1200 (1980).
[41] H. Ebert, J. Braun, D. Ködderitzsch, and S. Mankovsky, Phys. Rev. B **93**, 075145 (2016).
[42] *The Munich SPR-KKR package*, H. Ebert *et al.* `http://olymp.cup.uni-muenchen.de/ak/ebert/SPRKKR`.
[43] H. Ebert, Phys. Rev. B **38**, 9390 (1988).
[44] A. Y. Perlov, A. N. Yaresko, and V. N. Antonov, "PY-LMTO, A Spin-polarized Relativistic Linear Muffin-tin Orbitals Package for Electronic Structure Calculations," (unpublished).
[45] V. Antonov, B. Harmon, and A. Yaresko, *Electronic Structure and Magneto-Optical Properties of Solids* (Springer Netherlands, 2004).
[46] P. Středa, J. Phys. C: Solid State Phys. **15**, L717 (1982).
[47] D. Ködderitzsch, K. Chadova, and H. Ebert, Phys. Rev. B **92**, 184415 (2015).
[48] C. S. Wang and J. Callaway, Phys. Rev. B **9**, 4897 (1974).
[49] V. N. Antonov, A. N. Yaresko, A. Y. Perlov, and V. V. Nemoshkalenko, Low Temp. Phys. **25**, 387 (1999).
[50] H. Ebert, D. Ködderitzsch, and J. Minár, Rep. Prog. Phys. **74**, 096501 (2011).
[51] This figure has been created using the software VESTA[63].
[52] S. Lowitzer, D. Ködderitzsch, and H. Ebert, Phys. Rev. Lett. **105**, 266604 (2010).
[53] E. Krén and G. Kádár, Solid State Commun. **8**, 1653 (1970).
[54] T. Nagamiya, S. Tomiyoshi, and Y. Yamaguchi, Solid State Commun. **42**, 385 (1982).
[55] S. Tomiyoshi and Y. Yamaguchi, J. Phys. Soc. Japan **51**, 2478 (1982).
[56] S. Tomiyoshi, Y. Yamaguchi, and T. Nagamiya, J. Magn. Magn. Materials **31-34**, 629 (1983).
[57] D. Zhang, B. Yan, S.-C. Wu, J. Kübler, G. Kreiner, S. S. P. Parkin, and C. Felser, J. Phys.: Cond. Mat. **25**, 206006 (2013).
[58] H. Yang, Y. Sun, Y. Zhang, W.-J. Shi, S. S. P. Parkin, and B. Yan, New J. Phys. **19**, 015008 (2017).
[59] L. M. Sandratskii and J. Kübler, Phys. Rev. Lett. **76**, 4963 (1996).
[60] *International Tables for Crystallography, Volume A: Space Group Symmetry* (Springer, 2002).
[61] S. Wimmer, K. Chadova, M. Seemann, D. Ködderitzsch, and H. Ebert, Phys. Rev. B **94**, 054415 (2016).
[62] S. Wimmer, K. Chadova, and H. Ebert, "Symmetry and magnitude of the direct and inverse Edelstein effect: A KKR-CPA-Kubo approach," unpublished (2018).
[63] K. Momma and F. Izumi, J. Appl. Crystallogr. **44**, 1272 (2011).

3.4.2 Chirality-induced phenomena in hexagonal Mn_3Ge

The following is an unpublished manuscript on the effect of non-coplanar spin textures on the linear response properties of hexagonal Mn_3Ge. First-principles calculations of anomalous and spin Hall conductivity as well as spin-orbit torkance and Edelstein polarisation in the non-relativistic limit demonstrate the relevance of chirality-induced or topological contributions. Space-time symmetry aspects, orbital magnetism, and X-ray magnetic dichroism are discussed in addition.

Chirality-induced linear response properties in non-coplanar Mn_3Ge

Sebastian Wimmer,[1,*] Sergiy Mankovsky,[1] and Hubert Ebert[1]

[1] *Department Chemie, Physikalische Chemie, Universität München, Butenandtstr. 5-13, 81377 München, Germany*

Taking the non-collinear antiferromagnetic hexagonal Heusler compound Mn_3Ge as a precursor, the contributions to linear response phenomena arising solely from the chiral coplanar and non-coplanar spin configurations are investigated. Orbital moments, X-ray absorption, anomalous and spin Hall effects, as well as corresponding spin-orbit torques and Edelstein polarizations are studied depending on a continuous variation of the polar angle relative to the Kagome planes of corner-sharing triangles between the non-collinear antiferromagnetic and the ferromagnetic limits. By scaling the speed of light from the relativistic Dirac case to the non-relativistic limit the chirality-induced or topological contributions can be identified in the absence of spin-orbit coupling.

I. INTRODUCTION

Chiral magnetic order, its origins and consequences, continues to be a fascinating area of current solid state science.[1–5] Particularly intriguing is the occurrence of mesoscopic quasiparticles formed by a continuously varying non-coplanar spin texture with defined topology, so-called Skyrmions.[6–8] Their properties, creation, as well as detection and manipulation is a very active field of research,[9–14] motivated by potential future applicability in magnetic storage.[15–18] Electric-field-induced transport plays an important role in this context, as corresponding charge and spin currents can be utilized to detect and manipulate Skyrmions[15,16,19] and Antiskyrmions.[20] Due to the non-coplanar spin texture a so-called emergent electromagnetic field arises, that leads to chirality-induced or *topological*, in the sense of arising from the real-space topology of the spin configuration, contributions to phenomena commonly associated with spin-orbit coupling. The most fundamental of them are the occurrence of topological orbital moments[21–26] and of the related topological Hall effect.[27–34] A corresponding spin Hall effect arising from the real-space topology of the spin texture[35] is of particular interest in antiferromagnetic skyrmions, where the THE vanishes.[36]

A second heavily investigated type of chiral magnetic order is that of bulk antiferromagnets with non-collinear spin arrangements. The anomalous Hall effect (AHE) has been studied extensively in such compounds both theoretically[21,31,37–39] and experimentally.[40–46] Its relation to the magneto-optic Kerr effect of chiral magnets[47,48] and the X-ray circular dichroism[25,49], both connected to the optical conductivity tensor, suggests an alternative, magneto-optical approach to non-collinear magnetic order. Of particular relevance to the field are the hexagonal Heusler compounds Mn_3X with X =Ga, Ge, and Sn, in which the AHE has recently been confirmed experimentally.[42–44] Its spin-polarized counterpart, the spin Hall effect (SHE), in these and other non-collinear antiferromagnets also stimulated theoretical efforts[39,50–52] and has been measured in the achiral cubic system Mn_3Ir.[53,54] In Ref. 54 it has been furthermore shown, that the SHE contributes to the so-called spin-orbit torque (SOT), the current-induced magnetic torque that can be utilized to efficiently switch the magnetization. Thermally-induced analogues to the AHE and SHE, the anomalous and spin Nernst effects have been studied in Mn_3X (X = Sn, Ge, Ga) from first principles using the Berry curvature approach and a Mott-like formula.[55] The anomalous Nernst effect could in fact be measured recently in Mn_3Sn.[56]

The merger of these two fields, *topological antiferromagnetic spintronics*[57] aims at exploring the potential of topologically protected quasiparticles with non-trivial real- or momentum-space topology. This work presents a first-principles study on the chirality-induced or topological contributions to orbital moments, X-ray absorption spectra, anomalous and spin Hall effect, as well as to spin-orbit torques and the closely related Edelstein effect (EE). Two coplanar non-collinear antiferromagnetic spin structures in Mn_3Ge, one chiral and the other achiral, will be used as basis for investigations on the impact of non-coplanarity by rotating the magnetic moments out of the Kagome planes. Scaling the speed of light allows assessing the topological contributions to the various effects in absence of spin-orbit coupling. This will be accompanied by analysis of the corresponding symmetry-restricted response tensor shapes.

The article is organized as follows: In section II the underlying methods used for obtaining the results in section III will be outlined. The crystallographic and magnetic structures will be discussed in section III A, including the corresponding symmetry-restricted tensor shapes for electrical and spin conductivity as well as spin-orbit torkance and Edelstein polarization. Topological orbital moments and their signatures in X-ray absorption spectra are the subjects of sections III B and III C, respectively. The chirality-induced contributions to anomalous and spin Hall effect will be discussed in section III D, corresponding results for the spin-orbit torque and the Edelstein effect will be presented in section III E. Finally, hypothetical non-coplanar antiferromagnets will be investigated in section III F. A brief summary and outlook will be made at the end (IV), additional information can be found in the Appendix A.

II. METHODS

The space-time symmetry analysis of the linear response tensors for charge[58,59] and spin conductivity[59], spin-orbit torque[60] and Edelstein polarization[61] performed in this work is based on the magnetic space group determined using the software FINDSYM[62,63]. The electronic structure as well as subsequent Kubo linear response[64–68] and X-ray absorption spectroscopy[69] calculations are performed with the fully relativistic SPR-KKR program package[70] within the framework of the local spin density approximation (LSDA). For the calculation of electric-field induced response properties the Kubo-Středa[71] formula has been used throughout. To study the impact of the spin texture in absence of spin-orbit coupling, the non-relativistic limit of the Dirac formalism has been explored by scaling the speed of light.

III. RESULTS

A. Magnetic structure and symmetry

The hexagonal Mn_3Ge compound crystallizes, as its siblings Mn_3Sn and Mn_3Ga, in the $D0_{19}$ structure with space group $P6_3/mmc$. The non-magnetic unit cell is shown in Fig. 1 and will be labeled NM in the following. The Mn atoms on the Wyckoff positions $6h$ in the $\{0001\}$ planes colored in magenta (dark gray) form triangular, so-called Kagome lattices, stacked alternatingly along the [0001] (z) direction. Ge atoms occupying the Wyckoff positions $2h$ are colored in light gray. Figure 2 shows

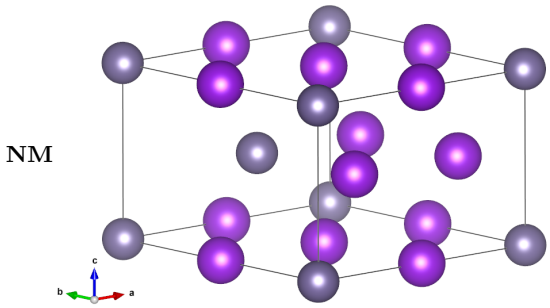

FIG. 1. Hexagonal unit cell of Mn_3Ge with space group $P6_3/mmc$ (labeled NM in the following). The Mn atoms on the Wyckoff positions $6h$ are colored in magenta (dark gray) and Ge atoms (Wyckoff positions $2h$) are colored in light gray.[72]

the situation of a field-aligned ferromagnetic structure with all moments (only shown on Mn) oriented along the [0001] or z direction (c axis of the unit cell). The corresponding magnetic space group is $P6_3/mm'c'$. This structure will be labeled FM in the following.

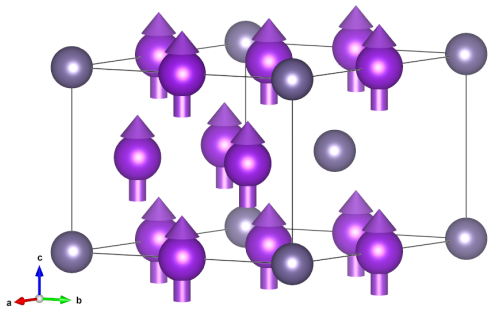

FIG. 2. Unit cell of hexagonal ferromagnetic (FM) Mn_3Ge with magnetic space group $P6_3/mm'c'$. Use of colors as in Fig. 1, magnetic moments on Mn sites are indicated as vectors.[72]

A number of non-collinear but coplanar antiferromagnetic alignments of the moments have been discussed for Mn_3Ge and related compounds in the literature (cf. Ref. 73 and references therein). Recently an overview on actual and hypothetical spin-compensated configurations has been given by the present authors.[49] Two of these structures discussed therein, both hypothetical, are shown in Fig. 3. The one in the upper panel, labeled ncAFM0, has the moments in the two alternating Kagome planes, indicated by different colors (red and blue), pointing towards the center of the triangles formed by the Mn atoms. The two magnetic sub-lattices are connected, e.g., by a 6_3 screw rotation about an axis going through the center of both triangles, but also by inversion half-way along this direction followed by time reversal. Reversing all moments in one layer (here blue), one obtains the structure ncAFM9 shown in the bottom panel. Here the operation connecting the two sub-lattices involves an additional time-reversal ($6_3'$), leading to a centrosymmetric or achiral structure with an inversion center half-way along c. Both structures will serve as references for the investigations on the consequences of non-coplanarity of the Mn moments in this article.

Rotation of the moments out of both Kagome planes by the same polar angle θ between the [0001] direction and the $\{0001\}$ planes leads for $\theta = 45°$ to the non-coplanar spin arrangements depicted in Fig. 4. The one in the upper panel, ncpM0 derived from ncAFM0, is obviously still chiral. The structure derived from ncAFM9, labeled ncpM9 and shown in the lower panel of Fig. 4 accordingly remains achiral, the inversion center connecting the two sub-lattices is indicated as an orange dot.

The main aim of the present work is the numerical study of chirality-induced or *topological* effects in transport and related properties. While the individual Kagome sub-lattices in the antiferromagnetic structures just discussed are chiral, as they have a finite vector spin chirality $\vec{S}_i \times \vec{S}_j + \vec{S}_j \times \vec{S}_k + \vec{S}_k \times \vec{S}_i$, the anomalous Hall conductivity arising from this is vanishing globally.

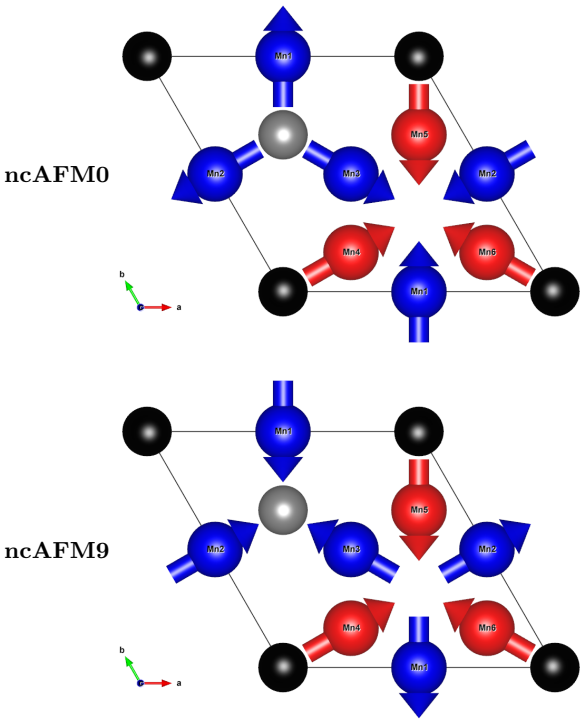

FIG. 3. Non-collinear antiferromagnetic reference structures of Mn_3Ge, ncAFM0 (top) and ncAFM9 (bottom). The coplanar Mn atoms in alternating Kagome planes are colored red and blue. The achiral structure ncAFM9 in the lower panel is obtained from ncAFM0 by reversing all moments in one plane (blue).[72]

This can be unambiguously derived from the space-time symmetry properties of the current-current correlation function in terms of the Kubo formula for the electrical conductivity.[58] The transformation under all symmetry operations of the so-called magnetic Laue group (see Ref. 59 for its definition used here) is sufficient to give the symmetry restricted tensor shape. The magnetic space and Laue groups for all spin configurations discussed in this work are given in Table. I. For convenience the Laue group is given also according to the definition of Kleiner[58].

The electrical conductivity tensor shapes derived from this are as follows:[58,59]

$$\underline{\boldsymbol{\sigma}}^{\mathrm{NM}} = \begin{pmatrix} \sigma_{xx} & 0 & 0 \\ 0 & \sigma_{xx} & 0 \\ 0 & 0 & \sigma_{zz} \end{pmatrix} = \underline{\sigma}^{\mathrm{ncAFM0,9}} = \underline{\sigma}^{\mathrm{ncpAFM0,9}} \tag{1}$$

$$\underline{\boldsymbol{\sigma}}^{\mathrm{FM}} = \begin{pmatrix} \sigma_{xx} & \sigma_{xy} & 0 \\ -\sigma_{xy} & \sigma_{xx} & 0 \\ 0 & 0 & \sigma_{zz} \end{pmatrix} = \underline{\sigma}^{\mathrm{ncpM0,9}} . \tag{2}$$

As stated above, the non-collinear coplanar antiferromagnetic structures in Fig. 3 have the same conductivity tensor shape as the non-magnetic one. This applies as well to the non-coplanar antiferromagnetic structures that will be discussed in Section III F. The non-coplanar magnetic structures of Fig. 4 have the same shape of $\underline{\boldsymbol{\sigma}}$ as the ferromagnetic (FM) case. However, as will be shown below, a chirality-induced contribution to the anomalous Hall conductivity $\sigma_{xy} = -\sigma_{yx}$ can be identified here.

The corresponding spin conductivity tensor shapes for

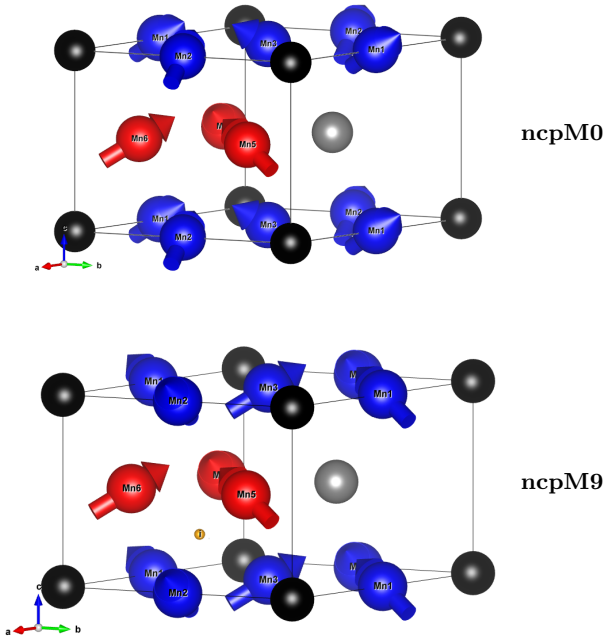

FIG. 4. Non-coplanar magnetic structures of Mn_3Ge derived from ncAFM0 and ncAFM9 (see Fig. 3) by rotating the moments out of the Kagome planes by $\theta = 45°$. While the one in top panel, labeled ncpM0, is chiral, the structure ncpM9 in the bottom panel has an inversion center that is indicated as an orange dot.[72]

label	MSG	MPG	MLG
NM	$P6_3/mmc1'$	$6/mmm1'$	$6/mmm1'$ $(6221')$
FM	$P6_3/mm'c'$	$6/mm'm'$	$6/mm'm'$ $(62'2')$
ncAFM0	$P6_3/m'm'c'$	$6/m'm'm'$	$6/mmm1'$ $(6221')$
ncAFM9	$P6_3'/m'm'c$	$6'/m'm'm$	$6'/m'm'm$ $(6'22')$
ncpM0	$P6_3m'c'$	$6m'm'$	$6/mm'm'$ $(62'2')$
ncpM9	$P\bar{3}m'1$	$\bar{3}m'1$	$\bar{3}m'1$ $(32')$
ncpAFM0	$P\bar{3}'1m'$	$\bar{3}'1m'$	$\bar{3}1m1'$ $(3'2)$
ncpAFM9	$P6_3'm'c$	$6'm'm$	$6'/m'm'm$ $(6'2'2)$

TABLE I. Magnetic space (MSG), point (MPG) and Laue groups (MLG) of the magnetic structures shown in Figs. 3 and 4, the Laue groups are given following the standard definition used by Seemann *et al.*[59] as well as the one used by Kleiner[58] (in parentheses). The conventional setting concerning the sequence of generators is used for the space groups and carried over to the point and Laue groups.[74]

polarization along the z or [0001] direction are:[59]

$$\underline{\boldsymbol{\sigma}}^{z,\mathrm{NM}} = \begin{pmatrix} 0 & \sigma^z_{xy} & 0 \\ -\sigma^z_{xy} & 0 & \\ 0 & 0 & 0 \end{pmatrix} = \underline{\sigma}^{z,\mathrm{ncAFM0,9}} = \underline{\sigma}^{z,\mathrm{ncpAFM0,9}} \tag{3}$$

$$\underline{\boldsymbol{\sigma}}^{z,\mathrm{FM}} = \begin{pmatrix} \sigma^z_{xx} & \sigma^z_{xy} & 0 \\ -\sigma^z_{xy} & \sigma^z_{xx} & 0 \\ 0 & 0 & \sigma^z_{zz} \end{pmatrix} = \underline{\sigma}^{z,\mathrm{ncpM0,9}} . \tag{4}$$

The antiferromagnetic structures, regardless whether coplanar or non-coplanar, chiral or achiral, all show only one independent non-zero element, the spin Hall conductivity $\sigma^z_{xy} = -\sigma^z_{yx}$ as in the non-magnetic case. Note however, that the tensors for the other two polarization directions differ for the structures ncAFM9, ncpAFM0, and ncpAFM9 (see Ref. 59). The non-coplanar magnetic structures have the same shape for $\underline{\boldsymbol{\sigma}}^z$ as the ferromagnetic one. While ncpM0 has the same magnetic Laue group ($6/mm'm'$) and accordingly the same shapes for all $\underline{\boldsymbol{\sigma}}^k$ as the FM structure, the other two polarizations, x and y, behave again differently for ncpM9. Also here a sizable chirality-induced contribution will be shown to exist.

The Edelstein polarization tensor shapes for the non-centrosymmetric spin configurations ncAFM0, ncpM0, ncpAFM0, and ncpAFM9 are as follows:[61]

$$\underline{\boldsymbol{p}}^{\mathrm{ncAFM0}} = \begin{pmatrix} p_{xx} & 0 & 0 \\ 0 & p_{xx} & 0 \\ 0 & 0 & p_{zz} \end{pmatrix} \tag{5}$$

$$\underline{\boldsymbol{p}}^{\mathrm{ncpM0}} = \begin{pmatrix} p_{xx} & p_{xy} & 0 \\ -p_{xy} & p_{xx} & 0 \\ 0 & 0 & p_{zz} \end{pmatrix} \tag{6}$$

$$\underline{\boldsymbol{p}}^{\mathrm{ncpAFM0}} = \begin{pmatrix} p_{xx} & 0 & 0 \\ 0 & p_{xx} & 0 \\ 0 & 0 & p_{zz} \end{pmatrix} \tag{7}$$

$$\underline{\boldsymbol{p}}^{\mathrm{ncpAFM9}} = \begin{pmatrix} 0 & p_{xy} & 0 \\ -p_{xy} & 0 & 0 \\ 0 & 0 & 0 \end{pmatrix} . \tag{8}$$

Finally, the shapes of the spin-orbit torkance tensors $\underline{\boldsymbol{t}}$ are identical to the ones given for $\underline{\boldsymbol{p}}$ in Eqs. (5)-(8).[60] Note that for these two response properties the tensor shape is determined by the magnetic point group and not by the magnetic Laue group.

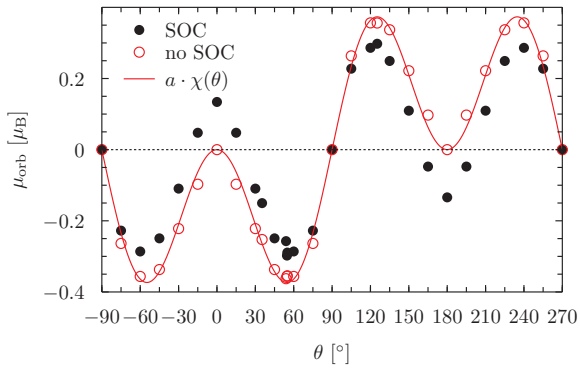

FIG. 5. Orbital moment as a function of polar angle θ in the non-coplanar chiral magnet ncpM0. Results including spin-orbit coupling (SOC) are shown as full (black) circles, those for vanishing SOC are given as open (red) circles. A fit of the latter to the scalar spin chirality $\chi(\theta)$ (see text) is shown as solid (red) line.

B. Orbital moments

The occurrence of chirality-induced orbital moments in non-coplanar spin arrangements has been predicted already quite some time ago.[21,22] First-principles calculations in, e.g., atomic-scale spin lattices[23,24], tri-atomic clusters of ferromagnetic $3d$-elements on a surface[25], and bulk γ-FeMn[26] could verify these in the limit of vanishing spin-orbit coupling. The (non-)coplanarity between three spins can be expressed compactly by the so-called scalar spin chirality $\chi_{ijk} = \vec{S}_i \cdot (\vec{S}_j \times \vec{S}_k)$. If the volume of the parallelepiped spanned by the three vectors is non-zero, they obviously are non-coplanar. In Figure 5 the orbital moment[75] is shown for ncpM0 as a function of the polar angle θ between the [0001] direction and the $\{0001\}$ planes. In case of vanishing spin-orbit coupling (no SOC, red open circles) the orbital moment can indeed be fairly well fitted with a function $\propto \cos(\theta)\sin^2(\theta)$. The zeros of this function correspond to the ferromagnetic state ($\theta = 0°, 180°$) and the non-collinear antiferromagnetic state ($\theta = -90°, 90°, 270°$). The extremal values are found for integer multiples of $\theta = \arccos(1/\sqrt{3}) \approx 54.7356°$, i.e., for the *magic angle*. Note, that the total energy shows a sharp peak here, indicating a pronounced instability.

Figure 6 shows spin and orbital moments for the structure ncpM9 as a function of polar angle θ, again with and without spin-orbit coupling. For the spin moment (black squares) spin-orbit coupling is, as to be expected, of negligible relevance. The orbital moment (red circles) again has a large chirality-induced component, whose angular dependence however does not appear to be simply proportional to the scalar spin chirality. While the even symmetry about $\theta = 0°$ and the odd symmetry around $\theta = 90°$ is obeyed, the behavior in-between seems to be more complicated. Note that, despite the global inversion symmetry connecting the two Kagome sub-lattices,

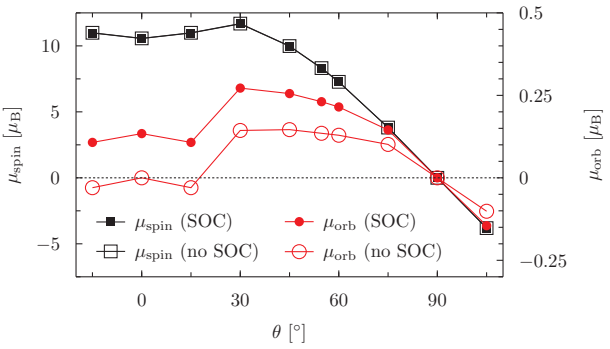

FIG. 6. Spin and orbital moment as a function of polar angle θ in the non-coplanar achiral magnet ncpM9. Results including spin-orbit coupling (SOC) are shown as full symbols, those for vanishing SOC are given as open symbols.

these have, as in the case of ncpM0, the same finite scalar spin chirality.

C. X-ray absorption spectra

X-ray absorption spectroscopy has a long and successful history concerning its application as a local probe to magnetic systems. In particular the so-called XMCD sum rules[76–78] allow for example to deduce from the integrated $L_{2,3}$-spectra of 3d-transition metals their spin and orbital magnetic moments. In line with the sum rules an angular dependence according to $\cos(\hat{m}\cdot\hat{q})$ is normally assumed, where $\hat{m}$ and $\hat{q}$ are the orientation of the local moment probed by XMCD and of the X-ray beam. This simple relation implies that in spin-compensated antiferromagnetic systems the XMCD should vanish. However, both XMCD[49] as well as the magneto-optic Kerr effect (MOKE)[37,47] are in fact, due to their relation to the frequency-dependent conductivity tensor,[69] expected to be observable in any magnetic structure that allows for a finite anomalous Hall conductivity.

In order to elucidate whether also the chirality-induced orbital moment discussed in Section III B can be deduced from X-ray absorption as suggested by Dos Santos Dias *et al.*[25], we perform first-principles calculations of XAS spectra as a function of polar angle θ. The XMCD signals in the non-coplanar magnetic structure ncpM0 in- and excluding spin-orbit coupling is shown in Figure 7 in the top and bottom panels, respectively. The absorption for incidence along the [0001] direction is calculated for the $L_{2,3}$-edge of Mn and summed over all sites of the unit cell. Suppressing spin-orbit coupling obviously leads to a degeneracy of the $2p$ initial states, accordingly only one edge is visible in the lower panel, that however indeed shows an XMCD signal. In both cases the strength of the signal is decreasing with increasing θ and anti-symmetric w.r.t. reversal of the global z component of the magnetization. The same applies to the XMCD spectra for the

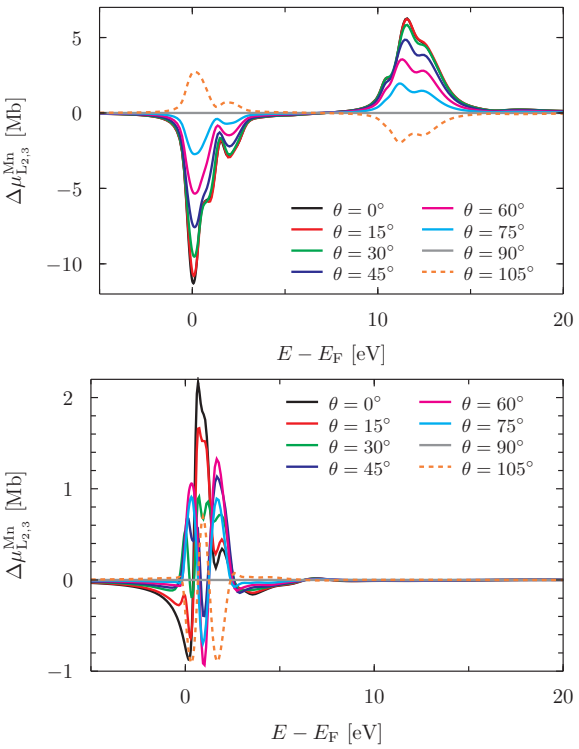

FIG. 7. X-ray magnetic circular dichroism (XMCD) spectra $\Delta\mu^{\rm Mn}_{\rm L_{2,3}}$ at the Mn $L_{2,3}$-edge in the non-coplanar chiral magnetic structure ncpM0 with (top) and without (bottom) inclusion of spin-orbit coupling (SOC). The polar angle θ gives the tilt of the moments w.r.t. the [0001] direction.

achiral structure ncpM9 in Fig. 8. Here the fine structure at the L_2-edge is slightly different from that in ncpM0 for the fully relativistic spectra in the top panel and quite so for the non-relativistic ones in the bottom panel.

As the XMCD signal is determined by both spin and orbital magnetic moment, in order to assess the chirality-induced contribution to the latter by X-ray absorption spectroscopy a clear-cut decomposition is desirable. Since the standard XMCD sum rules cannot be applied here and their generalization to non-collinear magnetic order is still on open issue, an approximate scheme following the proposal in Ref. 25 as been employed. Figures 9 and 10 show the difference between the average XAS and the XMCD signals for the field-aligned (ferromagnetic, FM, $\theta = 0°$) limit and the non-collinear structures with $\theta \neq 0°$ in ncpM0 and ncpM9, respectively. As stated above, this follows the proposed protocol of Dos Santos Dias *et al.*,[25] devised for magneto-optic experiments in skyrmionic systems. A remaining obstacle is however the assessment of the spin-moment-induced contribution for which a linear and spin texture-independent relation to the polar angle has been assumed by these authors. Obviously an unambiguous separation into spin- and orbital as well as spin-orbit- and chirality-induced contributions is duly needed. Note that due to the simplified assump-

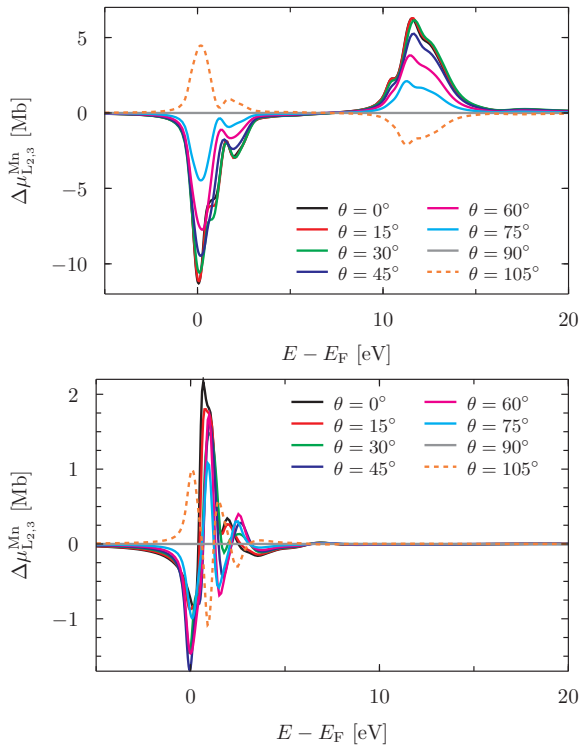

FIG. 8. X-ray magnetic circular dichroism (XMCD) spectra $\Delta\mu^{\mathrm{Mn}}_{\mathrm{L}_{2,3}}$ at the Mn $\mathrm{L}_{2,3}$-edge in the non-coplanar achiral magnetic structure ncpM9 with (top) and without (bottom) inclusion of spin-orbit coupling (SOC). The polar angle θ gives the tilt of the moments w.r.t. the [0001] direction.

tion of a collinear arrangement of moments the standard XMCD rules certainly have to be revised in order to make full use of the proposed procedure.

D. Transport results: (T)AHE and (T)SHE

The anomalous Hall conductivity σ_{xy} is shown as a function of θ in the top panel of Figure 11 for ncpM0. As can be seen both AHC and the chirality-induced or topological contribution σ^T_{xy} obtained in the non-relativistic limit $c_0/c \to 0$ (see Appendix A) are anti-symmetric or odd w.r.t. magnetization reversal around $\theta = 90°$. The chirality-induced component is clearly not simply proportional to the scalar spin chirality (see Fig. 5), similar to the observation made by Hanke *et al.*[26] in γ-FeMn. The largest values for σ^T_{xy} are for example found for $\theta = 60°$ and 120° and not for the magic angle. In addition we observe two sign changes between the coplanar antiferromagnetic structure ($\theta = 90°$) and the ferromagnetic states at $\theta = 0°$ and 180°. In these limits σ^T_{xy} vanishes and the AHC is purely spin-orbit-induced. Note, that the calculations were performed at a finite temperature $T = 300\,\mathrm{K}$ represented by uncorrelated lattice displacements via the so-called alloy analogy

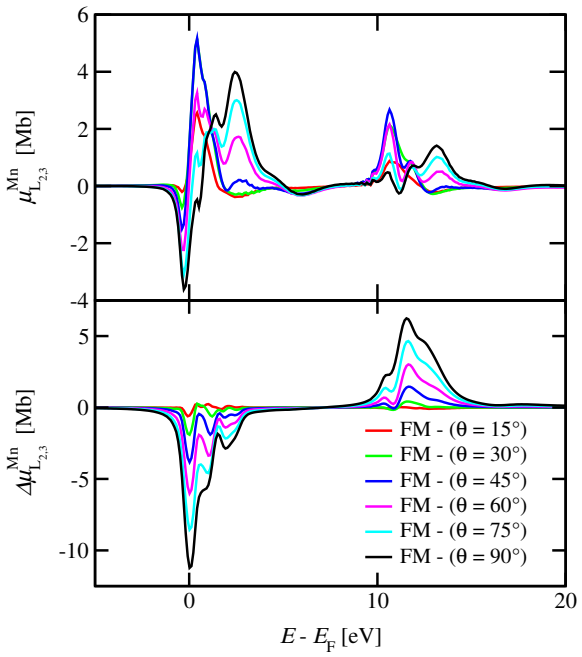

FIG. 9. Difference between ferromagnetic and non-collinear polarization-averaged XAS spectra (top) and X-ray magnetic circular dichroism (XMCD) spectra (bottom) at the Mn $\mathrm{L}_{2,3}$-edge in the chiral magnetic structure ncpM0. The polar angle θ gives the tilt of the moments w.r.t. the [0001] direction.

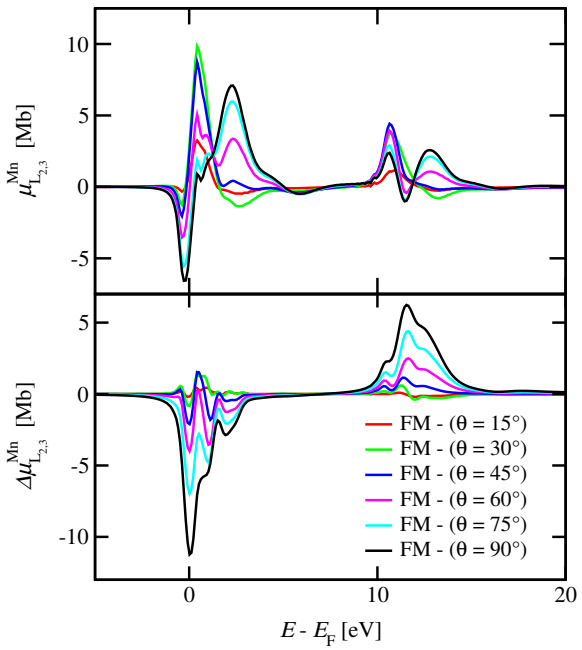

FIG. 10. Difference between ferromagnetic and non-collinear polarization-averaged XAS spectra (top) and X-ray magnetic circular dichroism (XMCD) spectra (bottom) at the Mn $\mathrm{L}_{2,3}$-edge in the achiral magnetic structure ncpM9. The polar angle θ gives the tilt of the moments w.r.t. the [0001] direction.

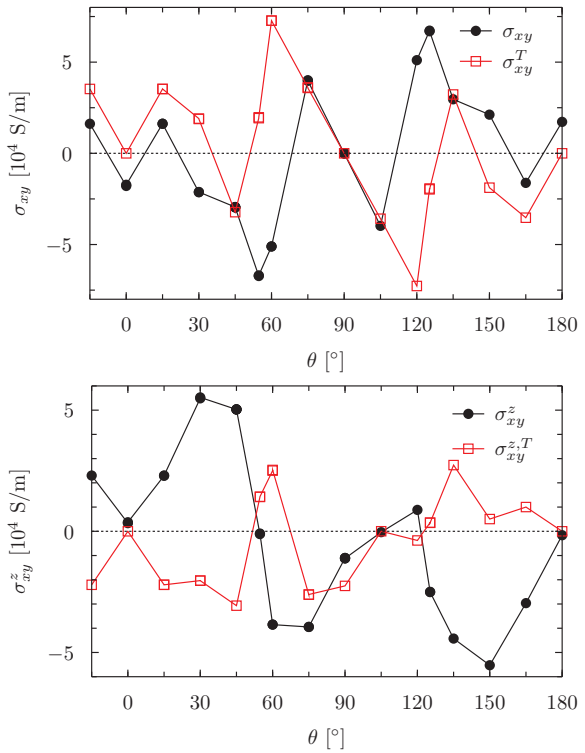

FIG. 11. Top: Anomalous Hall conductivity σ_{xy} and its chirality-induced or topological contribution σ_{xy}^{T} as functions of polar angle θ in ncpM0. Bottom: Corresponding results for the (topological) spin Hall conductivity σ_{xy} ($\sigma_{xy}^{z,T}$).

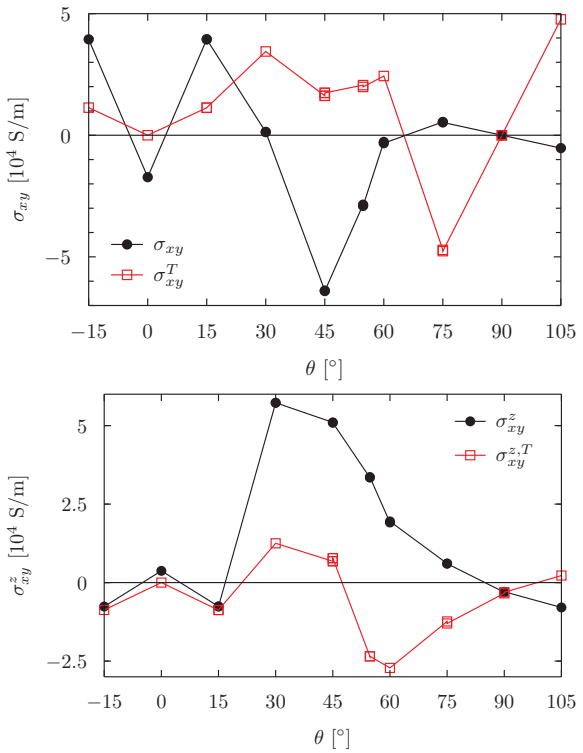

FIG. 12. Top: Anomalous Hall conductivity σ_{xy} and its chirality-induced or topological contribution σ_{xy}^{T} as functions of polar angle θ in ncpM9. Bottom: Corresponding results for the (topological) spin Hall conductivity σ_{xy} ($\sigma_{xy}^{z,T}$).

model (AAM).[79] This was done in order to circumvent the numerical difficulties arising for the $\vec{k}$-space integration in perfectly ordered systems, however the conductivities are almost entirely intrinsic in the sense of negligible relevance of the so-called vertex corrections associated with the thermally-induced disorder. Accordingly it is the magnetic band structure that determines the angular dependence of the AHC, are alternatively its Berry curvature.[80,81] Skew scattering contributions arising from the presence of impurities[82] or locally correlated fluctuating spins[83] will not be considered herein. The spin Hall conductivity in the relativistic and non-relativistic limits, σ_{xy}^{z} and $\sigma_{xy}^{z,T}$, given in the lower panel of Fig. 11 is even around the ferromagnetic limits 0° and 180°, but shows no distinctly symmetric angular dependence in-between. It is however strongly dependent on the non-coplanar spin texture and quite differently so for its spin-orbit- and chirality-induced contributions. These can be of the same or of different sign, leading to partial or even nearly complete cancellation as for $\theta \approx 54.7356°$. Quite interestingly, at $\theta = 105°$ both appear to vanish. Note that in the ferromagnetic limit at $\theta = 0°$ and 180° the total value is small but non-zero, while the topological contribution $\sigma_{xy}^{z,T}$ vanishes.

Quite similar observations can be made in Figure 12 for the achiral spin structure ncpM9 shown for the range $\theta = -15 - 105°$. As can be seen, the AHC in the top panel is found to be anti-symmetric (odd) w.r.t. magnetization reversal whereas the SHC in the bottom panel is asymmetric. The detailed angular dependence is distinct from that in ncpM0 for both quantities, i.e., the two hypothetical structures could be distinguished experimentally. We propose that the abundance of assumed spin configurations in hexagonal Mn_3X compounds could be confirmed or discarded via corresponding transport measurements rotating an applied magnetic field supported by first-principles calculations.

The longitudinal charge transport is even w.r.t. magnetization reversal and anisotropic, i.e., $\sigma_{xx} = \sigma_{yy} \neq \sigma_{zz}$. In the absence of spin-orbit coupling and the associated anisotropic magneto-resistance, the anisotropy of the spin texture as well as the bare crystalline anisotropy already present in the non-magnetic case remain. Similar observations can be reported for the longitudinal spin conductivities $\sigma_{xx}^{z} = \sigma_{yy}^{z} \neq \sigma_{zz}^{z}$, however these are not fully even w.r.t. magnetization reversal. The other polarizations either show large chirality-induced contributions as well ($\sigma_{xy}^{k} = -\sigma_{yx}^{k}$ with $k = \{x, y\}$) or are exclusively SOC-induced ($\sigma_{iz}^{k} \neq -\sigma_{zi}^{k}$ with $i \neq k = \{x, y\}$). Note that all of them are even w.r.t. magnetization reversal.

E. Spinorbitronic effects: (T)SOT and (T)EE

Naturally the question arises whether the so-called spinorbitronic phenomena spin-orbit torque (SOT) and Edelstein effect (EE) also exhibit chirality-induced contributions leading to finite values in the absence of spin-orbit coupling. Employing the same Kubo linear response framework used for the charge and spin transport calculations in the previous section, but exchanging the operator for the response, the (spin) current density operators, by either the magnetic torque operator[60] or the spin magnetization operator[61], the torkances t_{ij} and Edelstein polarizations p_{ij} can be computed from first principles. Figure 13 shows the polar-angle dependence of the torkance tensor elements $t_{xx} = t_{yy}$ (top), $t_{xy} = -t_{yx}$ (middle), and t_{zz} (bottom) in the chiral compound ncpM0. The diagonal torkances in the top and bottom panels are obviously even w.r.t. magnetization reversal, i.e., anti-symmetric w.r.t. $\theta = 90°$, while the off-diagonal anti-symmetric element $t_{xy} = -t_{yx}$ in the middle panel is odd. For this as well as for the $t_{xx} = t_{yy}$ indeed a sizable chirality-induced contribution is found that appears to be largest at $\theta = 30°$ and 150°. The diagonal torkance t_{zz} in the bottom panel, corresponding to a rotation of the moments about the [0001] or z axis coinciding with the direction of the applied electric field, is almost exclusively spin-orbit-driven. In all three cases the full torkances vanish in the ferromagnetic limit ($\theta = 0°$ and 180°) due to inversion symmetry.

The Edelstein polarization is one of the two microscopic mechanisms usually discussed as a source for the SOT, namely the (Rashba-)Edelstein torque, while the spin-Hall torque is attributed to the spin-transfer-torque-like action of a spin-polarized current on the local magnetization. The elements of the tensor $\underline{\boldsymbol{p}}$ are shown in Fig. 14 as a function of polar angle θ. The elements p_{ij} are found to behave very similar to the corresponding elements of $\underline{\boldsymbol{t}}$, i.e., the diagonal elements are even, the off-diagonal ones are odd, and $p_{xx} = p_{yy}$ (top) as well as $p_{xy} = -p_{yx}$ (middle) are overall chirality-dominated while p_{zz} in the bottom panel is again essentially SOC-induced. Note however, that the correspondence between t_{ij} and p_{ij} is not trivial, as an additional crossproduct with the local magnetization is contained in the response operator for the torkance. This leads for example for the odd torkance $t_{xy} = -t_{yx}$ in the middle panel of Fig. 13 to a different angular dependence as compared to $p_{xy} = -p_{yx}$ in particular close to the ferromagnetic limits at the left and right ends. For the topological contributions this is even more pronounced. While the odd Edelstein polarization is chirality-dominated close to the antiferromagnetic configuration at $\theta = 90°$, the SOT- and chirality-induced torkances are even of different sign here. The achiral coplanar and non-coplanar structures ncAFM9 and ncpM9 are found to be numerically zero as demanded by the inversion symmetry (see Section III A).

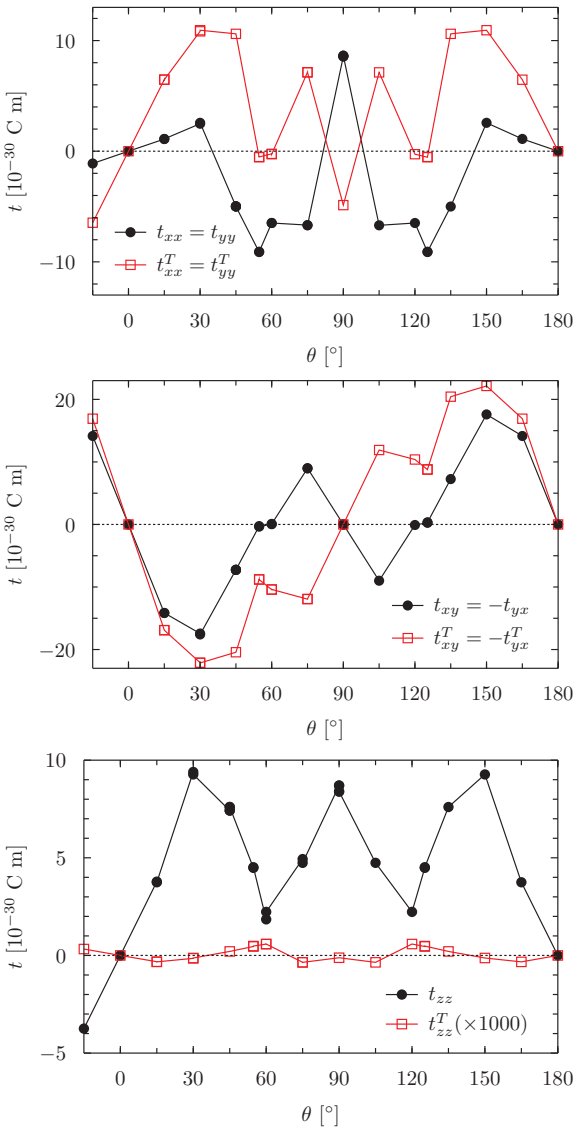

FIG. 13. Spin-orbit torkances $t_{xx} = t_{yy}$ (top), $t_{xy} = -t_{yx}$ (middle), and t_{zz} (bottom) as functions of polar angle θ in ncpM0. The chirality-induced contributions t^T_{ij} are given as red open squares.

F. Non-coplanar antiferromagnets

By rotating the moments in the two Kagome planes in opposite directions by the same angle θ, non-coplanar antiferromagnetic structures as shown in Fig. 15 for $\theta = \pm 45°$ are obtained. The upper panel is derived from the co-planar AFM structure ncAFM0, while the ncpAFM9 structure in the lower panel is obtained from the achiral ncAFM9 structure. As θ differs for both magnetic sub-lattices, the inversion symmetry is obviously broken, i.e., a chiral structure results. Note, that for ncpAFM0 inversion combined with time-reversal ($\bar{1}'$) is still

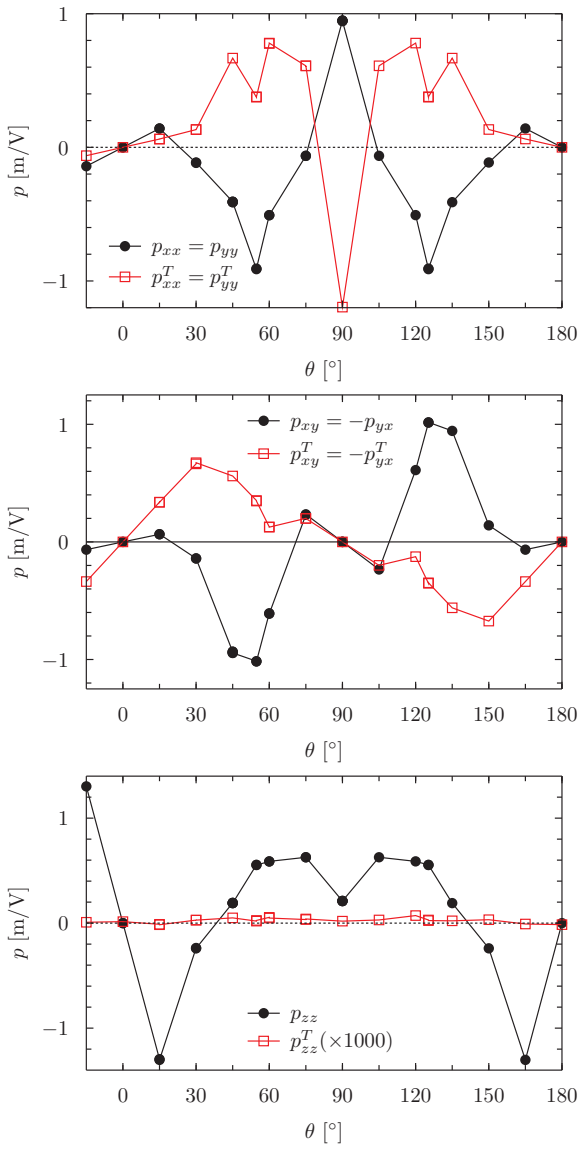

FIG. 14. Edelstein polarizations $p_{xx} = p_{yy}$ (top), $p_{xy} = -p_{yx}$ (middle), and p_{zz} (bottom) as functions of polar angle θ in ncpM0. The chirality-induced contributions p^T_{ij} are given as red open squares.

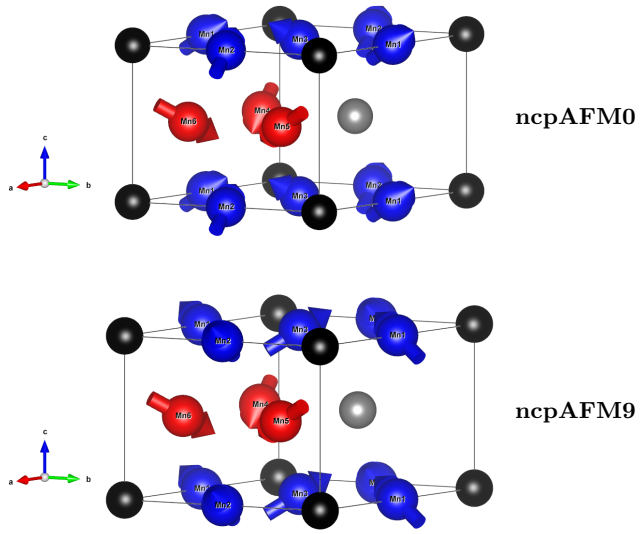

FIG. 15. Non-coplanar antiferromagnetic structures obtained from Fig. 3 by rotating the moments in the two Kagome planes into opposite directions by the same angle. The structure in the top panel has the same chirality in both sub-lattices (ncpAFM0), while in the lower panel they are of opposite sign (ncpAFM9).[72]

a symmetry operation.

The tensor shapes for charge and z-polarized spin conductivity correspond for both structures to the non-magnetic case, i.e., diagonal with $\sigma_{xx} = \sigma_{yy} \neq \sigma_{zz}$ and only one independent element of $\underline{\boldsymbol{\sigma}}^z$, the spin Hall conductivity $\sigma^z_{xy} = -\sigma^z_{yx}$. The shapes of $\underline{\boldsymbol{\sigma}}^x$ and $\underline{\boldsymbol{\sigma}}^y$ for ncpAFM0 and ncpAFM9, however, differ from each other as well as from the ones for the NM structure.[59] For the torkance and the Edelstein polarization the tensor shapes are given in Eqs. (7) and (8). Obviously there is a finite Edelstein polarization as well as spin-orbit torkance present for both structures. However, the corresponding tensor shapes differ from each other, as the magnetic point group has to be considered here.[60,61]

Figure 18 shows the Edelstein polarization tensor elements p_{xx}, p_{xy}, and p_{zz} for both structures at $\theta = \pm 45°$ as a function of a scaled speed of light c (see Appendix A for details). Confirming the tensor shapes in Eqs. (7) and (8), in the upper panel only the diagonal elements are non-zero, while in the lower panel only p_{xy} is. Furthermore it can be stated that for ncpAFM0 again p_{zz} is smaller than p_{xx} and vanishes in the non-relativistic limit ($c_0/c \to 0$), while p_{xx} has a large chirality-induced contribution. The anti-symmetric Edelstein polarization p_{xy} for ncpAFM9 shown in the bottom panel of Fig. 18 is even almost exclusively arising from the spin texture.

In agreement with the absence of off-diagonal anti-symmetric conductivity tensor elements the XMCD signals of the two chiral magnetic sub-lattices cancel each other numerically exactly (not shown). The same applies to the anomalous Hall conductivity shown in Fig. 17, while the spin Hall conductivities are found to be finite with sizable topological contributions.

IV. CONCLUSIONS

To summarize, the effect of a non-collinear and non-coplanar spin texture on orbital moments, X-ray absorption, charge and spin transport as well as spin-orbit torque and Edelstein polarization has been investigated by first-principles calculations in hexagonal Mn_3Ge. By

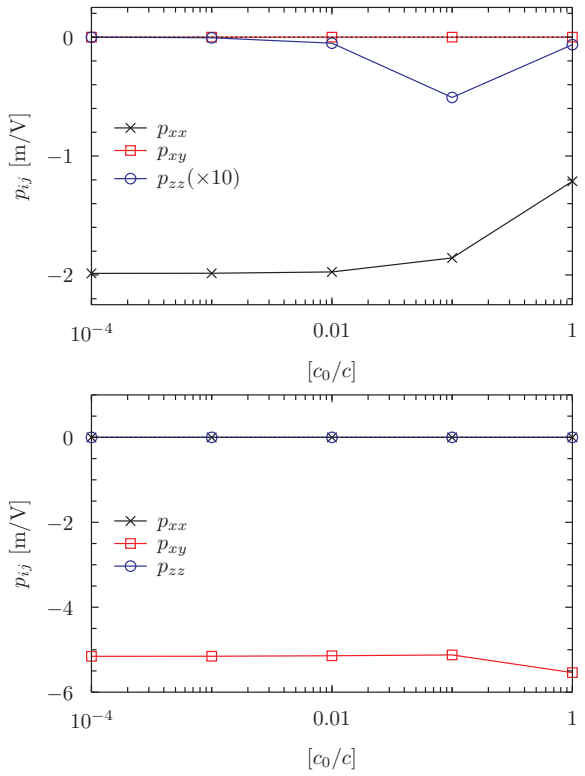

FIG. 16. Edelstein polarizations p_{xx}, p_{xy}, and p_{zz} in ncpAFM0 (top) and ncpAFM9 (bottom) as functions of c_0/c. For both structures the polar angle θ is 45°. The relativistic limit is on the right ($c_0/c = 1$), the non-relativistic one on the left ($c_0/c \to 0$).

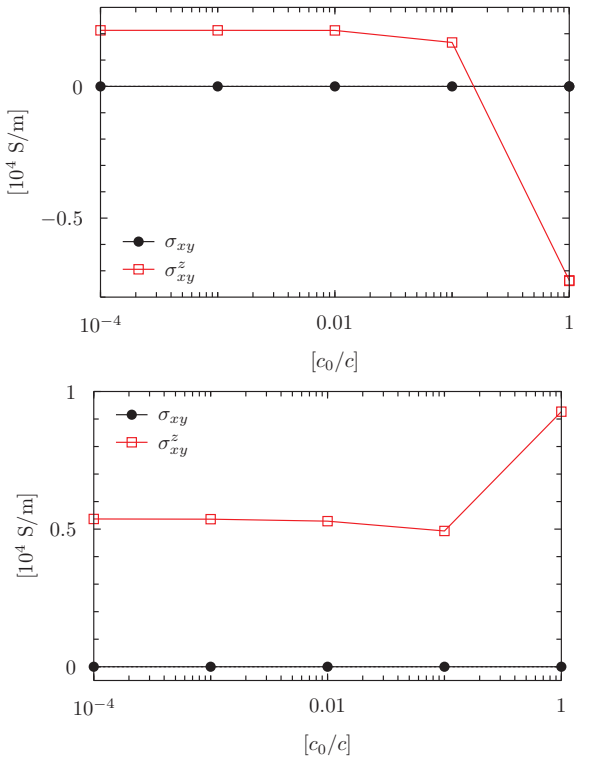

FIG. 17. Anomalous and spin Hall conductivities, σ_{xy} and σ^z_{xy}, respectively, in ncpAFM0 (top) and ncpAFM9 (bottom) as functions of c_0/c. For both structures the polar angle θ is 45°. The relativistic limit is on the right ($c_0/c = 1$), the non-relativistic one on the left ($c_0/c \to 0$).

smoothly varying the polar angle w.r.t. to the Kagome planes of corner-sharing triangles in two hypothetical reference structures, one globally chiral one achiral, the chirality-induced or topological contributions are compared to the spin-orbit-induced parts. To obtain the former in absence of the latter, the non-relativistic limit has been taken by scaling the speed of light c. The key findings are first of all the occurrence of topological orbital moments in presence and absence of global inversion symmetry, in the latter case following the angular dependence expected from the scalar spin chirality. A proposal of its experimental verification by XMCD measurements in a rotating external magnetic field is supported by a comparison of spectra for the field-aligned ferromagnetic case with those of non-coplanar spin configurations. Also here the limit of vanishing spin-orbit coupling has been investigated, conclusive statements could however not yet been made due to limitations of the standard XMCD sum rules. Furthermore the presence, angular dependence, as well as magnitude of the chirality-induced contributions to the anomalous and spin Hall conductivities has been demonstrated. Similar calculations of the spin-orbit torkance and the Edelstein polarization reveal sizable topological contributions also here, that can, depending on which quantity and which tensor element is considered as well as on the polar angle, enhance or suppress the spin-orbit-induced effects and be either dominating or vanishing.

Future studies on realistic non-collinear antiferromagnets of the hexagonal Mn_3X type with X = Ga, Ge, or Sn based on the experimentally assumed or theoretically proposed spin structures could help determining the actual configuration and the relevance of chirality-induced contributions in measured response properties. A proposed extension of the XMCD sum rules to non-collinear magnetic order and the absence of spin-orbit coupling should be able to support experimental efforts on the quantification of topological orbital moments.

ACKNOWLEDGMENTS

Financial support by the DFG via SFB 1277 (*Emergente relativistische Effekte in der Kondensierten Materie*) is gratefully acknowledged.

Appendix A: Manipulating the spin-orbit coupling

The topological contributions to the various response quantities discussed were determined by either setting the spin-orbit coupling explicitly to zero in the self-consistent calculations (orbital moments) or by scaling the speed of light c in the X-ray absorption and Kubo linear response calculations. The limit $c_0/c \to 0$ with the speed of light in vacuum c_0, or equivalently $c/c_0 \to \infty$, corresponds to the non-relativistic case. Obviously not only the spin-orbit coupling is affected this way, but also the so-called scalar-relativistic effects. However, for the properties relevant to this work it is the by far dominating term.

Figure 18 shows the anomalous (black symbols) and spin Hall (red symbols) conductivities as a function of the scaled speed of light c_0/c for the ferromagnetic state (top), the non-coplanar magnetic state ncpM0 depicted in the top panel of Fig. 4 (middle), and the coplanar non-collinear antiferromagnetic state ncAFM0 (bottom). Going from the relativistic limit on the right side to the non-relativistic on the left, both σ_{xy} and σ^z_{xy} vanish for the ferromagnet, revealing their purely SOC-driven nature. In the non-coplanar magnetic state ($\theta = 45°$) in the middle panel both are finite for $c_0/c \to 0$, i.e., they exhibit a chirality-induced or topological contribution arising from the spin texture. For both quantities this is sizable, the so-called topological Hall effect (THE) is even dominating in the relativistic limit, while the topological spin Hall effect (TSHE) is of opposite sign when compared to the SOC-induced contribution and about half as large. For the non-collinear antiferromagnetic structure ncAFM0 in the bottom panel the anomalous Hall effect vanishes due to symmetry (see Table I and Eq. 1), while the TSHE is even larger than the total SHE. This means that here the contribution due to spin-orbit coupling is again of opposite sign and but now the chirality-induced part is about twice as large.

Corresponding results for the structures ncpM9 (again for $\theta = 45°$) and ncAFM9 are presented in Fig. 19. Here the relation of chirality- and SOC-induced contributions is somewhat different. The former is smaller and of opposite sign for the AHE, while of the same sign for the SHE in the non-coplanar magnetic structure (top). In the coplanar antiferromagnetic state (bottom) the AHE is again vanishing, whereas the SHE is predominantly chirality-induced.

* sebastian.wimmer@cup.uni-muenchen.de

[1] M. Bode, M. Heide, K. von Bergmann, P. Ferriani, S. Heinze, G. Bihlmayer, A. Kubetzka, O. Pietzsch, S. Blügel, and R. Wiesendanger, Nature **447**, 190 (2007).

[2] C. Train, R. Gheorghe, V. Krstic, L.-M. Chamoreau, N. S. Ovanesyan, G. L. J. A. Rikken, M. Gruselle, and M. Verdaguer, Nature Materials **7**, 729 (2008).

[3] H.-B. Braun, Advances in Physics **61**, 1 (2012).

[4] J. Stein, M. Baum, S. Holbein, T. Finger, T. Cronert, C. Tölzer, T. Fröhlich, S. Biesenkamp, K. Schmalzl, P. Steffens, C. H. Lee, and M. Braden, Phys. Rev. Lett. **119**, 177201 (2017).

[5] C. S. Spencer, J. Gayles, N. A. Porter, S. Sugimoto, Z. Aslam, C. J. Kinane, T. R. Charlton, F. Freimuth, S. Chadov, S. Langridge, J. Sinova, C. Felser, S. Blügel, Y. Mokrousov, and C. H. Marrows, Phys. Rev. B **97**, 214406 (2018).

[6] T. Skyrme, Nuclear Physics **31**, 556 (1962).

[7] S. Mühlbauer, B. Binz, F. Jonietz, C. Pfleiderer, A. Rosch, A. Neubauer, R. Georgii, and P. Böni, Science **323**, 915 (2009).

[8] A. Neubauer, C. Pfleiderer, B. Binz, A. Rosch, R. Ritz, P. G. Niklowitz, and P. Böni, Phys. Rev. Lett. **102**, 186602 (2009), erratum: Phys. Rev. Lett. **110**, 209902 (2013).

[9] S. Heinze, K. von Bergmann, M. Menzel, J. Brede, A. Kubetzka, R. Wiesendanger, G. Bihlmayer, and S. Blugel, Nat. Phys. **7**, 713 (2011).

[10] B. Dupe, M. Hoffmann, C. Paillard, and S. Heinze, Nature Communications **5**, 4030 (2014).

[11] H. Reichlová, D. Kriegner, V. Holý, K. Olejník, V. Novák, M. Yamada, K. Miura, S. Ogawa, H. Takahashi, T. Jungwirth, and J. Wunderlich, Phys. Rev. B **92**, 165424 (2015).

[12] C. Moreau-Luchaire, C. Moutas, N. Reyren, J. Sampaio, C. A. F. Vaz, N. Van Horne, K. Bouzehouane, K. Garcia, C. Deranlot, P. Warnicke, P. Wohlhüter, J.-M. George, M. Weigand, J. Raabe, V. Cros, and A. Fert, Nature Nanotechnology **11**, 444 (2016).

[13] S. Woo, K. Litzius, B. Krüger, M.-Y. Im, L. Caretta, K. Richter, M. Mann, A. Krone, R. M. Reeve, M. Weigand, P. Agrawal, I. Lemesh, M.-A. Mawass, P. Fischer, M. Kläui, and G. S. D. Beach, Nature Materials **15**, 501 (2016).

[14] A. K. Nayak, V. Kumar, T. Ma, P. Werner, E. Pippel, R. Sahoo, F. Damay, U. K. Rößler, C. Felser, and S. S. P. Parkin, Nature **548**, 561 (2017).

[15] X. Z. Yu, N. Kanazawa, W. Z. Zhang, T. Nagai, T. Hara, K. Kimoto, Y. Matsui, Y. Onose, and Y. Tokura, Nature Communications **3**, 988 (2012).

[16] J. Sampaio, V. Cros, S. Rohart, A. Thiaville, and A. Fert, Nature Nanotechnology **8**, 839 (2013).

[17] A. Fert, V. Cros, and J. Sampaio, Nature Nanotechnology **8**, 152 (2013).

[18] R. Tomasello, E. Martinez, R. Zivieri, L. Torres, M. Carpentieri, and G. Finocchio, Scientific Reports **4**, 6784 (2014).

[19] A. Fert, N. Reyren, and V. Cros, Nature Reviews Materials **2**, 17031 (2017).

[20] W. Koshibae and N. Nagaosa, Nature Communications **7**, 10542 (2016).

[21] R. Shindou and N. Nagaosa, Phys. Rev. Lett. **87**, 116801 (2001).

[22] K. Nakamura, T. Ito, and A. J. Freeman, Phys. Rev. B **68**, 180404 (2003).

[23] M. Hoffmann, J. Weischenberg, B. Dupé, F. Freimuth,

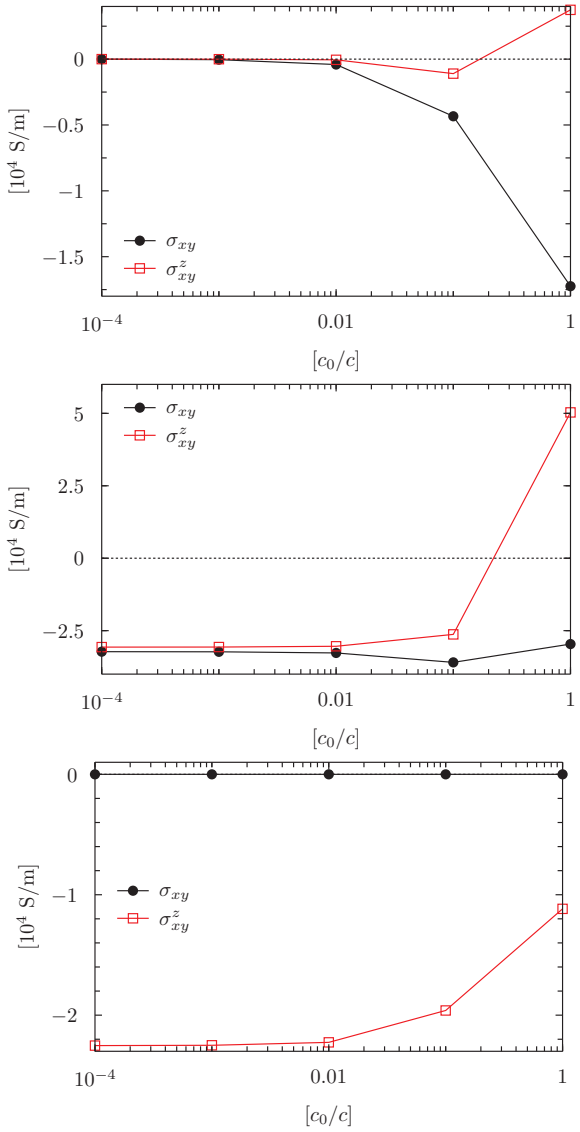

FIG. 18. Anomalous and spin Hall conductivity as a function of c_0/c in the ferromagnetic state (top), the non-coplanar chiral magnetic state ncpM0 (middle) for $\theta = 45°$, and the co-planar non-collinear chiral state ncAFM0 (bottom). The relativistic limit is on the right ($c_0/c = 1$), the non-relativistic one on the left ($c_0/c \to 0$).

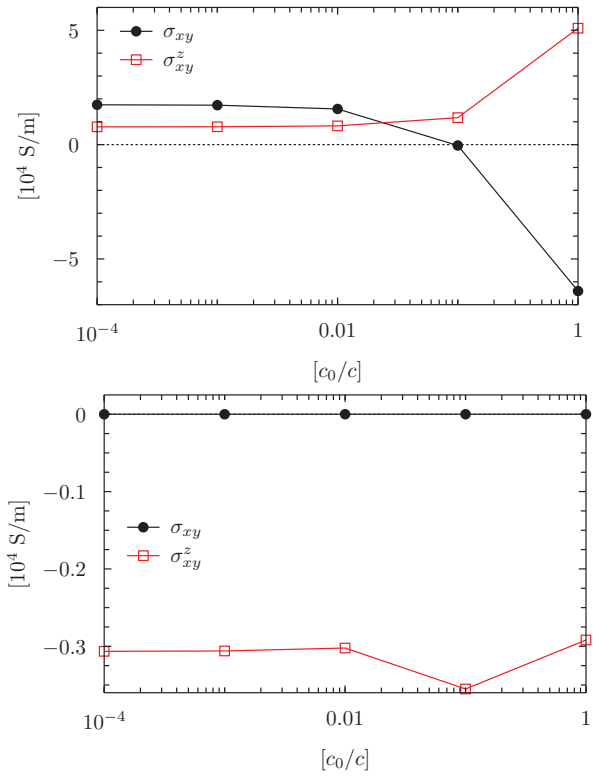

FIG. 19. Anomalous and spin Hall conductivity as a function of c_0/c in the non-coplanar achiral magnetic state ncpM9 (top) for $\theta = 45°$, and the co-planar non-collinear achiral state ncAFM9 (bottom). The relativistic limit is on the right ($c_0/c = 1$), the non-relativistic one on the left ($c_0/c \to 0$).

P. Ferriani, Y. Mokrousov, and S. Heinze, Phys. Rev. B **92**, 020401 (2015).

[24] J.-P. Hanke, F. Freimuth, A. K. Nandy, H. Zhang, S. Blügel, and Y. Mokrousov, Phys. Rev. B **94**, 121114 (2016).

[25] M. dos Santos Dias, J. Bouaziz, M. Bouhassoune, S. Blügel, and S. Lounis, Nature Communications **7**, 13613 (2016).

[26] J.-P. Hanke, F. Freimuth, S. Blügel, and Y. Mokrousov, Scientific Reports **7**, 41078 (2017).

[27] Y. Taguchi, Y. Oohara, H. Yoshizawa, N. Nagaosa, and Y. Tokura, Science **291**, 2573 (2001).

[28] G. Tatara and H. Kawamura, J. Phys. Soc. Japan **71**, 2613 (2002).

[29] M. Onoda and N. Nagaosa, Journal of the Physical Society of Japan **71**, 19 (2002).

[30] P. Bruno, V. K. Dugaev, and M. Taillefumier, Phys. Rev. Lett. **93**, 096806 (2004).

[31] T. Tomizawa and H. Kontani, Phys. Rev. B **82**, 104412 (2010).

[32] T. Schulz, R. Ritz, A. Bauer, M. Halder, M. Wagner, C. Franz, C. Pfleiderer, K. Everschor, M. Garst, and A. Rosch, Nature Physics **8**, 301 (2012).

[33] N. Nagaosa and Y. Tokura, Nature Nanotechnology **8**, 899 (2013).

[34] C. Franz, F. Freimuth, A. Bauer, R. Ritz, C. Schnarr, C. Duvinage, T. Adams, S. Blügel, A. Rosch, Y. Mokrousov, and C. Pfleiderer, Phys. Rev. Lett. **112**, 186601 (2014).

[35] G. Yin, Y. Liu, Y. Barlas, J. Zang, and R. K. Lake, Phys. Rev. B **92**, 024411 (2015).

[36] P. M. Buhl, F. Freimuth, S. Blügel, and Y. Mokrousov, physica status solidi (RRL) Rapid Research Letters **11**, 1700007 (2017), 1700007.

[37] H. Chen, Q. Niu, and A. H. MacDonald, Phys. Rev. Lett. **112**, 017205 (2014).

[38] J. Kübler and C. Felser, EPL (Europhysics Letters) **108**, 67001 (2014).

[39] Y. Zhang, Y. Sun, H. Yang, J. Železný, S. P. P. Parkin,

C. Felser, and B. Yan, Phys. Rev. B **95**, 075128 (2017).
[40] D. Boldrin and A. S. Wills, Advances in Condensed Matter Physics **2012**, 615295 (2012).
[41] C. Sürgers, G. Fischer, P. Winkel, and H. v. Löhneysen, Nature Communications **5**, 3400 (2014).
[42] S. Nakatsuji, N. Kiyohara, and T. Higo, Nature **527**, 212 (2015).
[43] N. Kiyohara, T. Tomita, and S. Nakatsuji, Phys. Rev. Applied **5**, 064009 (2016).
[44] A. K. Nayak, J. E. Fischer, Y. Sun, B. Yan, J. Karel, A. C. Komarek, C. Shekhar, N. Kumar, W. Schnelle, J. Kübler, C. Felser, and S. S. P. Parkin, Sci. Adv. **2**, e1501870 (2016).
[45] C. Sürgers, T. Wolf, P. Adelmann, W. Kittler, G. Fischer, and H. v. Löhneysen, Scientific Reports **7**, 42982 (2017).
[46] Z. H. Liu, Y. J. Zhang, G. D. Liu, B. Ding, E. K. Liu, H. M. Jafri, Z. P. Hou, W. H. Wang, X. Q. Ma, and G. H. Wu, Scientific Reports **7**, 515 (2017).
[47] J. Orenstein and J. E. Moore, Phys. Rev. B **87**, 165110 (2013).
[48] W. Feng, G.-Y. Guo, J. Zhou, Y. Yao, and Q. Niu, ArXiv e-prints (2015), arXiv:1509.02865 [cond-mat.mtrl-sci], arXiv:1509.02865 [cond-mat.mtrl-sci].
[49] S. Wimmer, J. Minár, S. Mankovsky, A. N. Yaresko, and H. Ebert, "Magneto-optic and transverse transport properties of noncollinear antiferromagnets," unpublished (2018).
[50] O. Gomonay, Phys. Rev. B **91**, 144421 (2015).
[51] J. Železný, Y. Zhang, C. Felser, and B. Yan, Phys. Rev. Lett. **119**, 187204 (2017).
[52] Y. Zhang, J. Zelezny, Y. Sun, J. van den Brink, and B. Yan, ArXiv e-prints (2017), arXiv:1704.03917 [cond-mat.mtrl-sci].
[53] J. B. S. Mendes, R. O. Cunha, O. Alves Santos, P. R. T. Ribeiro, F. L. A. Machado, R. L. Rodríguez-Suárez, A. Azevedo, and S. M. Rezende, Phys. Rev. B **89**, 140406 (2014).
[54] W. Zhang, W. Han, S.-H. Yang, Y. Sun, Y. Zhang, B. Yan, and S. S. P. Parkin, Sci. Adv. **2**, e1600759 (2016).
[55] G.-Y. Guo and T.-C. Wang, Phys. Rev. B **96**, 224415 (2017).
[56] M. Ikhlas, T. Tomita, T. Koretsune, M.-T. Suzuki, D. Nishio-Hamane, R. Arita, Y. Otani, and S. Nakatsuji, Nat. Phys. **13**, 1085 (2017).
[57] L. Šmejkal, Y. Mokrousov, B. Yan, and A. H. MacDonald, Nature Physics **14**, 242 (2018).
[58] W. H. Kleiner, Phys. Rev. **142**, 318 (1966).
[59] M. Seemann, D. Ködderitzsch, S. Wimmer, and H. Ebert, Phys. Rev. B **92**, 155138 (2015).
[60] S. Wimmer, K. Chadova, M. Seemann, D. Ködderitzsch, and H. Ebert, Phys. Rev. B **94**, 054415 (2016).
[61] S. Wimmer, K. Chadova, and H. Ebert, "Symmetry and magnitude of the direct and inverse Edelstein effect: A KKR-CPA-Kubo approach," unpublished (2018).
[62] H. T. Stokes, D. M. Hatch, and B. J. Campbell, ISOTROPY Software Suite, `iso.byu.edu`.
[63] H. T. Stokes and D. M. Hatch, J. Appl. Crystallogr, **38**, 237 (2005).
[64] R. Kubo, Can. J. Phys. **34**, 1274 (1956).
[65] R. Kubo, J. Phys. Soc. Japan **12**, 570 (1957).
[66] W. H. Butler, Phys. Rev. B **31**, 3260 (1985).
[67] A. Crépieux and P. Bruno, Phys. Rev. B **64**, 014416 (2001).
[68] D. Ködderitzsch, K. Chadova, and H. Ebert, Phys. Rev. B **92**, 184415 (2015).
[69] H. Ebert, Rep. Prog. Phys. **59**, 1665 (1996).
[70] *The Munich SPR-KKR package*, H. Ebert *et al.* `http://olymp.cup.uni-muenchen.de/ak/ebert/SPRKKR`.
[71] P. Středa, J. Phys. C: Solid State Phys. **15**, L717 (1982).
[72] This figure has been created using the software VESTA[84].
[73] D. Zhang, B. Yan, S.-C. Wu, J. Kübler, G. Kreiner, S. S. P. Parkin, and C. Felser, J. Phys.: Cond. Mat. **25**, 206006 (2013).
[74] *International Tables for Crystallography, Volume A: Space Group Symmetry* (Springer, 2002).
[75] The sum over all sites is shown, which leaves only the z-component non-zero.
[76] J. L. Erskine and E. A. Stern, Phys. Rev. B **12**, 5016 (1975).
[77] B. T. Thole, P. Carra, F. Sette, and G. van der Laan, Phys. Rev. Lett. **68**, 1943 (1992).
[78] P. Carra, B. T. Thole, M. Altarelli, and X. Wang, Phys. Rev. Lett. **70**, 694 (1993).
[79] H. Ebert, S. Mankovsky, K. Chadova, S. Polesya, J. Minár, and D. Ködderitzsch, Phys. Rev. B **91**, 165132 (2015).
[80] M. V. Berry, Proceedings of the Royal Society of London A: Mathematical, Physical and Engineering Sciences **392**, 45 (1984).
[81] D. Xiao, M.-C. Chang, and Q. Niu, Rev. Mod. Phys. **82**, 1959 (2010).
[82] K. Nakazawa and H. Kohno, Journal of the Physical Society of Japan **83**, 073707 (2014).
[83] H. Ishizuka and N. Nagaosa, Sci. Adv. **4**, aap9962 (2018).
[84] K. Momma and F. Izumi, J. Appl. Crystallogr. **44**, 1272 (2011).

3.5 Spin-orbit torque & Edelstein effect

Spin orbitronics [103] is one of the latest developments in the wider field of spintronics, adding a number of spin-orbit induced phenomena that include in particular the so-called spin-orbit torque (SOT) and the Edelstein effect (EE), as well as their Onsager reciprocals. The spin-orbit torque holds great promise for a spin-based logic in ever greater efficiency and smaller size, as it allows switching magnetic layers in, e.g., MRAM devices without the need for magnetic reference layers as its *predecessor*, the spin-transfer torque, does. The Edelstein effect or inverse spin-galvanic effect has certainly been revived by studies on the SOT, first discussed mainly as a prominent contribution to the torkance due to interface inversion asymmetry, the Rashba-Edelstein torque. But it deserves to be regarded as a phenomenon on its own, in particular as it may occur also in non-magnetic systems.

In the following two published articles and one unpublished manuscript will be presented. The first publication, Ref. 335, deals with the space-time symmetry restrictions on the spin-orbit torque as an extension to earlier work, Ref. 283, reprinted in Section 3.3 on page 175. The tensor shapes of the torkance, the linear response coefficients describing the correlation of an electric current as perturbation and a magnetic torque as response, as well as of its time-reversed counterpart connected to the inverse spin-orbit torque are presented and discussed. This is accompanied by first-principles calculations for a model tri-layer alloy system and a discussion of the results focussing on the various contributions and underlying mechanisms. The second article, Ref. 368, is concerned with the SOT and its relation to the so-called Dzyaloshinskii-Moriya interaction, another manifestation of spin-orbit coupling, that leads to a non-collinear alignment of spin moments in non-centrosymmetric systems. In addition the transverse transport properties of the system under study are discussed, the $Mn_{1-x}Fe_xGe$ alloy with B20 crystal structure. It is an important exemplar of those materials in which so-called Skyrmions, i.e, mesoscopic quasiparticles composed of a defined arrangement of non-collinear spins can be observed. Finally, in Section 3.5.2 so far unpublished work on the direct and inverse Edelstein effect will be presented, again focussing first on group-theoretical aspects, followed by numerical investigations on the same model system as used in the work on the SOT [335]. Particular emphasis is put here on the close connection of the two spinorbitronic phenomena concerning symmetry properties and underlying mechanisms, in addition the relation to the charge and spin conductivity is investigated.

3.5.1 Published results on the spin-orbit torque

The following is a copy of the article *Fully relativistic description of spin-orbit torques by means of linear response theory* [335], reprinted with permission from

S. Wimmer, K. Chadova, M. Seemann, D. Ködderitzsch, and H. Ebert,
Phys. Rev. B **94**, 054415 (2016).

PHYSICAL REVIEW B **94**, 054415 (2016)

Fully relativistic description of spin-orbit torques by means of linear response theory

S. Wimmer,* K. Chadova, M. Seemann, D. Ködderitzsch, and H. Ebert†
Department Chemie/Phys. Chemie, Ludwig-Maximilians-Universität München, Germany
(Received 12 April 2016; revised manuscript received 21 June 2016; published 11 August 2016)

Symmetry and magnitude of spin-orbit torques (SOT), i.e., current-induced torques on the magnetization of systems lacking inversion symmetry, are investigated in a fully relativistic linear response framework based on the Kubo formalism. By applying all space-time symmetry operations contained in the magnetic point group of a solid to the relevant response coefficient, the torkance expressed as torque-current correlation function, restrictions to the shape of the direct and inverse response tensors are obtained. These are shown to apply to the corresponding thermal analogs as well, namely the direct and inverse thermal SOT in response to a temperature gradient or heat current. Using an implementation of the Kubo-Bastin formula for the torkance into a first-principles multiple-scattering Green function framework and accounting for disorder effects via the so-called coherent potential approximation, all contributions to the SOT in pure systems, dilute as well as concentrated alloys can be treated on equal footing. This way, material specific values for all torkance tensor elements in the fcc (111) trilayer alloy system Pt|Fe_xCo_{1-x}|Cu are obtained over a wide concentration range and discussed in comparison to results for electrical and spin conductivity, as well as to previous work—in particular concerning symmetry with respect to magnetization reversal and the nature of the various contributions.

DOI: 10.1103/PhysRevB.94.054415

I. INTRODUCTION

Spin-orbit torques (SOT), denoting the response of a magnetization to an electric current by changing its orientation, have evolved from a theoretical conjecture [1–3] via experimental verification [4–6] to their imminent technological application in SOT-MRAM devices [7] in a remarkably short period of time. This can be attributed to the fact that unlike most [8] other ways of defined manipulation of magnetic moments it does not require external magnetic fields or auxiliary magnetic layers, offering an enormous advantage concerning information storage density, nonvolatility, and scalability [9]. The combined effect of spin-orbit interaction and exchange coupling in systems lacking inversion symmetry offers thus the possibility to switch the magnetization of spintronics devices by applying an electric current. Unlike its close relative, the spin-transfer torque mechanism [10,11], it does not rely on the presence of a "polarizer" magnetic layer, allowing for much simpler device architecture and reducing necessary critical current densities [12]. The intrinsic relativistic spin-orbit interaction can transfer orbital to spin angular momentum in a magnetic material having a suitable structure, leading to an effective magnetic field exerting a torque on the magnetization.

Recent experiments [13–15] were able to measure the SOT directly as a function of magnetization direction, whereas earlier evidence has only been indirect [4–6,9,16–18]. Two symmetrically distinct contributions to the SOT could be observed this way, one being even and the other odd with respect to magnetization reversal. To lowest order in the magnetization direction $\hat{\mathbf{m}}$, the even torque in response to an in-plane current $\mathbf{j}$ was found to go by $\hat{\mathbf{m}} \times (\mathbf{j} \times \hat{\mathbf{m}})$, whereas the odd one scales with $\hat{\mathbf{m}} \times \mathbf{j}$. While initial work on spin-orbit torques was focused on transition metal FM | NM bilayers [5,6] or dilute magnetic semiconductors [4], recent experiments [19–22] demonstrate the possibility to switch ferromagnetic moments by SOTs originating from antiferromagnets, and Wadley *et al.* [23] were even able to switch the antiferromagnet itself. Corresponding predictions of so-called Néel-order spin-orbit torques, the local SOTs of alternating (collinear) spin sublattices, had been made earlier [24]. On the ferromagnetic side it could be shown that magnetic insulators can be switched by SOTs as well [25]. Exploiting the large spin-orbit coupling of bismuth and the pronounced ferromagnetism of Cr-doped $Bi_xSb_{1-x}Te_3$, topological insulator heterostructures were shown to be promising candidates for SOT-based memory and logic devices [26,27]. Although the nature of the spin-orbit torque certainly is not yet fully understood in all details, its ability to deterministically switch magnetic moments, without the need for external magnetic fields [28], has been demonstrated beyond doubt. Currently, experimental research is already heading towards fully functional devices [29,30], en route exposing further interesting aspects of SOTs [31,32].

Early theoretical work on the SOT in bilayer systems proposed two distinct mechanisms, namely a torque arising from the Rashba effect at the asymmetric interface [2,33–35], and a spin transfer torque due to the spin current generated in the heavy-metal layer by the spin Hall effect [17,18,36]. The "Rashba" torque was initially found to be dominated by a fieldlike component [3,33,37] being odd with respect to magnetization reversal, whereas the "spin Hall" torque was believed to consist mostly of an even (anti-)damping- or spin transfer-like contribution [9,17,18,37]. This picture has however turned out to be too simple [13,14], as these mechanisms appear to be only the limiting cases of a more complex scenario [13,38], involving terms of higher orders in the magnetization direction [13] and in addition an intrinsic contribution, arising from the band structure in a single ferromagnetic layer alone [39,40]. First-principles calculations of the torkance tensor [41–43] can be used to help to disentangle the various contributions by providing model-independent material parameters. The pioneering works of Freimuth *et al.* [42,43] demonstrated this for FM | NM bilayer systems using

*sebastian.wimmer@cup.uni-muenchen.de
†hubert.ebert@cup.uni-muenchen.de

the Kubo linear response formalism to calculate layer-resolved torkances.

It has been noted quite early on [44] that there exists of course an Onsager reciprocal to the spin-orbit torque, i.e., by interchanging perturbation (electric field or charge current) and response (torque on the magnetization) one arrives at the inverse spin-orbit torque (ISOT), describing the electric field induced by magnetization dynamics [45]. The reciprocity of the two, SOT and ISOT, has been discussed recently in great detail by Freimuth *et al.* [46], who noted that both phenomena can be described by the torkance tensor. In this work, by performing a symmetry analysis of the linear response expressions describing SOT and ISOT, we will give explicit tensor shapes for both properties in terms of the torkance, thereby demonstrating, where applicable, the presence and exact form of their reciprocity. As will be shown, these shapes remain unchanged when replacing the electric field by a temperature gradient, giving a justification for the use of a Mott-like expression for direct and inverse thermal SOT discussed by Géranton *et al.* [47] and Freimuth *et al.* [48].

The present paper focuses on two aspects of the spin-orbit torque. First, an extensive space-time symmetry analysis based on group-theoretical grounds and not restricted to special cases is performed that allows determining the tensor shapes of both direct and inverse SOT from their respective Kubo linear response expressions, based on the magnetic point group alone [49]. Secondly, by making use of the coherent potential approximation (CPA) within multiple scattering theory the possibility to study the concentration dependence of the torkance in alloys is demonstrated, thereby paving the way for a materials design approach to the SOT.

This paper is organized as follows. In Sec. II we introduce the underlying linear response formalism used to calculate the torkance tensor, discuss its implementation into a multiple scattering framework, with particular emphasis on the treatment of disorder, and finally outline the application of symmetry considerations leading to restrictions to the tensor shapes of both direct and inverse spin-orbit torques. The outcome of this group-theoretical analysis for all magnetic point groups allowing for the existence of a locally finite magnetization, as in ferro-, ferri-, as well as antiferromagnets, will be presented together with corresponding results for the electrical and spin conductivity tensors. In Sec. III we present the results of our numerical investigations on a Pt|Fe_xCo_{1-x}|Cu trilayer system, elucidating the impact of substitutional disorder on the various contributions to the torkance. By comparing concentration-dependent results for the torkance tensor with such for electrical and spin conductivity we will discuss their (partial) interconnection. Finally, contact will be made to previous work, in particular concerning the separation of the torkance into contributions based on the structure of the linear response expression (Fermi sea and Fermi surface terms) and on symmetry arguments (even or odd symmetry with respect to magnetization reversal). We conclude with a summary of the presented and an outlook on future work in Sec. IV.

II. FORMALISM

A well-known application of Kubo's linear response formalism is the derivation of an expression for the electrical conductivity tensor $\underline{\underline{\sigma}}$ that describes the electric current density $\mathbf{j} = \underline{\underline{\sigma}}\,\mathbf{E}$ in response to an electric field $\mathbf{E}$. In analogy one can derive an expression for the torkance tensor $\underline{\underline{t}}$ that gives the torque $\mathbf{T} = \underline{\underline{t}}\,\mathbf{E}$ as a response to $\mathbf{E}$ [42,43]. Replacing the operator $\hat{j}_\mu$ representing the component μ of the current by the operator $\hat{T}_\mu$ for the torque one can straightforwardly adopt the derivation of the so-called Kubo-Bastin formula for $\underline{\underline{\sigma}}$ [50,51] leading to a corresponding expression for the torkance $\underline{\underline{t}}$ [52]:

$$t_{\mu\nu} = -\frac{\hbar}{4\pi}\int_{-\infty}^{\infty} d\varepsilon \frac{df(\varepsilon)}{d\varepsilon}\mathrm{Tr}\langle \hat{T}_\mu (G^+ - G^-)\hat{j}_\nu G^- - \hat{T}_\mu G^+ \hat{j}_\nu (G^+ - G^-)\rangle + \frac{\hbar}{4\pi}\int_{-\infty}^{\infty} d\varepsilon\, f(\varepsilon)\mathrm{Tr} \times \left\langle \hat{T}_\mu G^+ \hat{j}_\nu \frac{dG^+}{d\varepsilon} - \hat{T}_\mu \frac{dG^+}{d\varepsilon}\hat{j}_\nu G^+ - \text{“}(G^+ \to G^-)\text{”}\right\rangle, \tag{1}$$

where $f(\varepsilon) = [e^{(\varepsilon-\mu)/k_B T} + 1]^{-1}$ is the Fermi-Dirac distribution with the electrochemical potential μ [$E_F = \mu(T = 0\,\mathrm{K})$] and $G^{+(-)}$ is the retarded (advanced) Green function. This implies that in the limit $T \to 0$ K for the temperature the first term in Eq. (1) has to be evaluated only for the Fermi energy E_F (Fermi surface term $t^I_{\mu\nu}$), while the second one requires an integration over the occupied part of the valence band (Fermi sea term $t^{II}_{\mu\nu}$).

The operator $\hat{j}_\nu = -|e|c\alpha_\nu$ in Eq. (1) represents the perturbation due to the electric field component E_ν. Adopting a fully relativistic formulation to account coherently for the impact of SOC, $\hat{j}_\nu$ is expressed by the corresponding velocity operator $\hat{v}_\nu = c\alpha_\nu$, where c is the speed of light and α_ν is one of the standard 4×4 Dirac matrices [53]. The torque operator $\hat{T}_\mu$ on the other hand represents the response in form of a change of the magnetization component m_μ with time. Using the classical definition of the torque on the magnetization $\mathbf{m}$ due to an effective field $\mathbf{B}_{\mathrm{eff}}$, $\mathbf{T} = \mathbf{m} \times \mathbf{B}_{\mathrm{eff}} = \hat{u} \times \frac{\partial E}{\partial \hat{u}}$ with $\hat{u} = \mathbf{m}/|\mathbf{m}|$ and the total energy E, and applying the Hellmann-Feynman theorem, the torque operator can be written as [54,55]

$$\hat{T}_\mu = \frac{\partial}{\partial u_\mu}\hat{\mathcal{H}}(\hat{u} \times \hat{n})_\mu = \beta(\boldsymbol{\sigma} \times \hat{e}_z)_\mu B_{xc}(\mathbf{r}). \tag{2}$$

For the second line use has been made of the specific form of $\hat{\mathcal{H}}$ for a magnetic solid within the framework of local spin density formalism (LSDA) where $B_{xc}(\mathbf{r})$ stands for the difference in the exchange potential for electrons with spin up and down [56] in reference to the local quantization axis $\hat{e}_z \parallel \hat{n}$ and $\boldsymbol{\sigma}$ is the vector of the 4×4 Pauli spin matrices [53].

In Eq. (1) the electronic structure is represented in terms of the retarded and advanced Green functions $G^+(E)$ and $G^-(E)$, respectively. Using this approach has the big advantage that one can deal straightforwardly with disordered systems. Considering for example chemical disorder the brackets $\langle\cdots\rangle$ in Eq. (1) stand for the configurational average in a disordered alloy. For the applications presented below relativistic multiple scattering theory was used to determine the Green function [57,58]. The average over alloy configurations was determined by means of the coherent potential approximation (CPA) alloy

theory as done in the context of the electrical conductivity [59,60], spin conductivity [61], and Gilbert damping parameter [55]. This implies in particular that the so-called vertex corrections, that ensure that the proper average $\langle \hat{T}_\mu G^\pm \hat{j}_\nu G^\pm \rangle$ is taken instead of the simpler one $\langle \hat{T}_\mu G^\pm \rangle \langle \hat{j}_\nu G^\pm \rangle$, are included in the calculations.

Expressing the electric field induced torque by means of linear response formalism allows investigating straightforwardly the condition for which the SOT may show up or not. This can be done using a scheme worked out by Kleiner [62] and extended recently by Seemann *et al.* [63]. Making use of the behavior of the torque operator $\hat{T}_\mu$ and of the current density operator j_ν under symmetry operations one is led to the relations that restrict the shape of the torkance tensor $\underline{\boldsymbol{t}}$:

$$t_{\mu\nu} = \sum_{\kappa\lambda} t_{\kappa\lambda} D(R)_{\kappa\mu} D(R)_{\lambda\nu} \det(R), \tag{3}$$

$$t_{\mu\nu} = -\sum_{\kappa\lambda} t'_{\lambda\kappa} D(R)^*_{\kappa\mu} D(R)^*_{\lambda\nu} \det(R), \tag{4}$$

where $\underline{\boldsymbol{D}}(R)$ is the 3×3 transformation matrix associated with the pure spatial operation R and $\det(R)$ is the corresponding determinant of that matrix. In Eq. (3) only unitary pure spatial symmetry operations are considered, while in Eq. (4) antiunitary operations are considered that involve apart from the spatial operation R also the time reversal operation. As a consequence Eq. (4) relates the torkance tensor $\underline{\boldsymbol{t}}$ with the tensor $\underline{\boldsymbol{t}}'$ that is associated with the effect inverse to the SOT, i.e., Eq. (4) is equivalent to an Onsager relation for $\underline{\boldsymbol{t}}$.

Considering Eq. (3) for all symmetry operations of a magnetic point group, the corresponding symmetry-allowed shape of the direct and inverse torkance tensors, $\underline{\boldsymbol{t}}$ and $\underline{\boldsymbol{t}}'$, can be determined. Tables I to VI give the results for all magnetic point groups leading to a nonvanishing torkance tensor. Note that the symmetry analysis was performed for a general direction of the local magnetization. If this axis is uniquely fixed by the magnetic point group, all direct (inverse) torkance elements with corresponding first (second) Cartesian index vanish due to the additional restriction imposed by the form of Eq. (2). In addition the tensor shapes for electrical and spin conductivity for polarization along the principal axis are given for the respective magnetic Laue groups obtained by adding the spatial inversion operation [62,63]. Naturally, this leads to redundancies since different magnetic point groups have the same magnetic Laue group.

Magnetic symmetry groups that allow for locally finite magnetization in general can be subdivided into two categories [62,63], one without any time-reversal symmetry, neither as an operation on its own nor in combination with a spatial operation, category (b) (Table I), the other containing time reversal only connected with a spatial operation, category (c) (Tables II–VI). Naturally, this excludes all magnetic point groups of category (a) corresponding to a nonmagnetic solid, i.e., that contain time reversal as a separate element [62,63]. Groups that permit existence of a ferromagnetic state are given in boldface.

Comparing the results for magnetic point groups of categories (b) in Table I and (c) in Tables II–VI, one notes that those of the former exhibit identical direct and inverse torkance tensor shapes, $\underline{\boldsymbol{t}}$ and $\underline{\boldsymbol{t}}'$, while for those of the latter the two tensors usually differ in shape but nevertheless are connected to each other. This becomes obvious when looking at Eq. (4): if there was time reversal as a separate operation, as in a group of category (a), the corresponding spatial operation R would be the identity, and therefore $t_{\mu\nu} = -t'_{\nu\mu}$ for all tensor elements, i.e., something quite similar to the usual Onsager relations would hold [64]. When there are no time-reversal-connected, that is, antiunitary, operations in the group, as in category (b), Eq. (4) does not apply at all and the shape of $\underline{\boldsymbol{t}}'$ is given exclusively by Eq. (3) and thus identical to that of $\underline{\boldsymbol{t}}$. For the magnetic point groups of category (c), where time reversal appears only in connection with a spatial operation R, the shapes are determined by $\underline{\boldsymbol{D}}(R)$, the nature of the operation(s) connecting $\underline{\boldsymbol{t}}$ and $\underline{\boldsymbol{t}}'$.

In addition one notices that none of the magnetic point groups listed in Tables I–VI contains the spatial inversion as an element. This central restriction—missing inversion symmetry—has been pointed out before by Manchon and Zhang [1,2] as well as Garate and MacDonald [3] on the basis of restricted model considerations. This basic requirement is explained here on group-theoretical grounds by the transformation properties of the operators appearing in the linear response expression. The torque operator, represented by the vector product of magnetization and effective magnetic field—both pseudovectors symmetric under spatial inversion but antisymmetric under time reversal—hence transforms as a time-reversal symmetric pseudovector, while the electric current operator as a proper vector is antisymmetric under both. Therefore, the product of the two is both time-reversal and inversion antisymmetric. Correspondingly, the shapes of direct and inverse torkance tensors are determined by the magnetic point group of a solid, in contrast for example to the electrical conductivity and thermoelectric tensors [62], as well as to the spin conductivity and related spincaloritronic transport tensors [63]. Note however, that missing inversion symmetry is not a sufficient precondition for the occurrence of a finite torkance (to zeroth order in the magnetization direction [66]), as can be seen from the absence of the noncentrosymmetric groups $\bar{6}$, $\bar{6}2m$, and $\bar{4}3m$ from Table I.

Since the operators for electric and heat current densities transform identical under all space-time symmetry operations relevant for solids [62,63], the tensor shapes will stay unaltered when the electric field is replaced by a temperature gradient. In other words, the shapes given here apply also for the direct and inverse thermal spin-orbit torque effect discussed recently by Géranton *et al.* [47] and Freimuth *et al.* [48].

A special remark is in order concerning collinear antiferromagnets: here the two spin sublattices can be transformed into each other by the combination of a spatial operation plus time reversal, i.e., the lattice belongs to category (c). Therefore, the tensor shapes of the torkance on the individual sublattices are described by the tensors $\underline{\boldsymbol{t}}$ and $\underline{\boldsymbol{t}}'$ in Tables II–VI, which can—but not necessarily has to—lead to a vanishing net torkance. However, although there is no net magnetization the moments of the individual sublattices nevertheless are subject to *local* spin-orbit torques provided the magnetic point group does not contain spatial inversion [65] and can therefore be switched by an applied electric field [23,24,66].

TABLE I. Shape of the direct and inverse torkance tensors, $\underline{\boldsymbol{t}}$ and $\underline{\boldsymbol{t}}'$, for all magnetic point groups of category (b). Note that since these do not contain time reversal, neither as an element on its own nor in combination with a spatial operation, the two tensors are unconnected and identical in shape. The third and fourth columns show the electrical conductivity tensor $\underline{\boldsymbol{\sigma}}$ and the spin conductivity tensor $\underline{\boldsymbol{\sigma}}^k$ for polarization along the principal axis k, respectively, for the corresponding magnetic Laue groups. See Ref. [63] for the two remaining polarization directions and further details on conventions and notation. Magnetic point groups that allow for the existence of a ferromagnetic state are given in boldface.

Magnetic point group	$\underline{\boldsymbol{t}}$	$\underline{\boldsymbol{t}}'$	Magnetic Laue group	$\underline{\boldsymbol{\sigma}}$	$\underline{\boldsymbol{\sigma}}^k$
1	$\begin{pmatrix} t_{xx} & t_{xy} & t_{xz} \\ t_{yx} & t_{yy} & t_{yz} \\ t_{zx} & t_{zy} & t_{zz} \end{pmatrix}$	$\begin{pmatrix} t'_{xx} & t'_{xy} & t'_{xz} \\ t'_{yx} & t'_{yy} & t'_{yz} \\ t'_{zx} & t'_{zy} & t'_{zz} \end{pmatrix}$	$\bar{1}$	$\begin{pmatrix} \sigma_{xx} & \sigma_{xy} & \sigma_{xz} \\ \sigma_{yx} & \sigma_{yy} & \sigma_{yz} \\ \sigma_{zx} & \sigma_{zy} & \sigma_{zz} \end{pmatrix}$	$\begin{pmatrix} \sigma^z_{xx} & \sigma^z_{xy} & \sigma^z_{xz} \\ \sigma^z_{yx} & \sigma^z_{yy} & \sigma^z_{yz} \\ \sigma^z_{zx} & \sigma^z_{zy} & \sigma^z_{zz} \end{pmatrix}$
2	$\begin{pmatrix} t_{xx} & 0 & t_{xz} \\ 0 & t_{yy} & 0 \\ t_{zx} & 0 & t_{zz} \end{pmatrix}$	$\begin{pmatrix} t'_{xx} & 0 & t'_{xz} \\ 0 & t'_{yy} & 0 \\ t'_{zx} & 0 & t'_{zz} \end{pmatrix}$	$2/m$	$\begin{pmatrix} \sigma_{xx} & 0 & \sigma_{xz} \\ 0 & \sigma_{yy} & 0 \\ \sigma_{zx} & 0 & \sigma_{zz} \end{pmatrix}$	$\begin{pmatrix} \sigma^y_{xx} & 0 & \sigma^y_{xz} \\ 0 & \sigma^y_{yy} & 0 \\ \sigma^y_{zx} & 0 & \sigma^y_{zz} \end{pmatrix}$
m	$\begin{pmatrix} 0 & t_{xy} & 0 \\ t_{yx} & 0 & t_{yz} \\ 0 & t_{zy} & 0 \end{pmatrix}$	$\begin{pmatrix} 0 & t'_{xy} & 0 \\ t'_{yx} & 0 & t'_{yz} \\ 0 & t'_{zy} & 0 \end{pmatrix}$	$2/m$	$\begin{pmatrix} \sigma_{xx} & 0 & \sigma_{xz} \\ 0 & \sigma_{yy} & 0 \\ \sigma_{zx} & 0 & \sigma_{zz} \end{pmatrix}$	$\begin{pmatrix} \sigma^y_{xx} & 0 & \sigma^y_{xz} \\ 0 & \sigma^y_{yy} & 0 \\ \sigma^y_{zx} & 0 & \sigma^y_{zz} \end{pmatrix}$
222	$\begin{pmatrix} t_{xx} & 0 & 0 \\ 0 & t_{yy} & 0 \\ 0 & 0 & t_{zz} \end{pmatrix}$	$\begin{pmatrix} t'_{xx} & 0 & 0 \\ 0 & t'_{yy} & 0 \\ 0 & 0 & t'_{zz} \end{pmatrix}$	mmm	$\begin{pmatrix} \sigma_{xx} & 0 & 0 \\ 0 & \sigma_{yy} & 0 \\ 0 & 0 & \sigma_{zz} \end{pmatrix}$	$\begin{pmatrix} 0 & \sigma^z_{xy} & 0 \\ \sigma^z_{yx} & 0 & 0 \\ 0 & 0 & 0 \end{pmatrix}$
$mm2$	$\begin{pmatrix} 0 & t_{xy} & 0 \\ t_{yx} & 0 & 0 \\ 0 & 0 & 0 \end{pmatrix}$	$\begin{pmatrix} 0 & t'_{xy} & 0 \\ t'_{yx} & 0 & 0 \\ 0 & 0 & 0 \end{pmatrix}$	mmm	$\begin{pmatrix} \sigma_{xx} & 0 & 0 \\ 0 & \sigma_{yy} & 0 \\ 0 & 0 & \sigma_{zz} \end{pmatrix}$	$\begin{pmatrix} 0 & \sigma^z_{xy} & 0 \\ \sigma^z_{yx} & 0 & 0 \\ 0 & 0 & 0 \end{pmatrix}$
4	$\begin{pmatrix} t_{xx} & t_{xy} & 0 \\ -t_{xy} & t_{xx} & 0 \\ 0 & 0 & t_{zz} \end{pmatrix}$	$\begin{pmatrix} t'_{xx} & t'_{xy} & 0 \\ -t'_{xy} & t'_{xx} & 0 \\ 0 & 0 & t'_{zz} \end{pmatrix}$	$4/m$	$\begin{pmatrix} \sigma_{xx} & \sigma_{xy} & 0 \\ -\sigma_{xy} & \sigma_{xx} & 0 \\ 0 & 0 & \sigma_{zz} \end{pmatrix}$	$\begin{pmatrix} \sigma^z_{xx} & \sigma^z_{xy} & 0 \\ -\sigma^z_{xy} & \sigma^z_{xx} & 0 \\ 0 & 0 & \sigma^z_{zz} \end{pmatrix}$
$\bar{4}$	$\begin{pmatrix} t_{xx} & t_{xy} & 0 \\ t_{xy} & -t_{xx} & 0 \\ 0 & 0 & 0 \end{pmatrix}$	$\begin{pmatrix} t'_{xx} & t'_{xy} & 0 \\ t'_{xy} & -t'_{xx} & 0 \\ 0 & 0 & 0 \end{pmatrix}$	$4/m$	$\begin{pmatrix} \sigma_{xx} & \sigma_{xy} & 0 \\ -\sigma_{xy} & \sigma_{xx} & 0 \\ 0 & 0 & \sigma_{zz} \end{pmatrix}$	$\begin{pmatrix} \sigma^z_{xx} & \sigma^z_{xy} & 0 \\ -\sigma^z_{xy} & \sigma^z_{xx} & 0 \\ 0 & 0 & \sigma^z_{zz} \end{pmatrix}$
422	$\begin{pmatrix} t_{xx} & 0 & 0 \\ 0 & t_{xx} & 0 \\ 0 & 0 & t_{zz} \end{pmatrix}$	$\begin{pmatrix} t'_{xx} & 0 & 0 \\ 0 & t'_{xx} & 0 \\ 0 & 0 & t'_{zz} \end{pmatrix}$	$4/mmm$	$\begin{pmatrix} \sigma_{xx} & 0 & 0 \\ 0 & \sigma_{xx} & 0 \\ 0 & 0 & \sigma_{zz} \end{pmatrix}$	$\begin{pmatrix} 0 & \sigma^z_{xy} & 0 \\ -\sigma^z_{xy} & 0 & 0 \\ 0 & 0 & 0 \end{pmatrix}$
$4mm$	$\begin{pmatrix} 0 & t_{xy} & 0 \\ -t_{xy} & 0 & 0 \\ 0 & 0 & 0 \end{pmatrix}$	$\begin{pmatrix} 0 & t'_{xy} & 0 \\ -t'_{xy} & 0 & 0 \\ 0 & 0 & 0 \end{pmatrix}$	$4/mmm$	$\begin{pmatrix} \sigma_{xx} & 0 & 0 \\ 0 & \sigma_{xx} & 0 \\ 0 & 0 & \sigma_{zz} \end{pmatrix}$	$\begin{pmatrix} 0 & \sigma^z_{xy} & 0 \\ -\sigma^z_{xy} & 0 & 0 \\ 0 & 0 & 0 \end{pmatrix}$
$\bar{4}2m$	$\begin{pmatrix} t_{xx} & 0 & 0 \\ 0 & -t_{xx} & 0 \\ 0 & 0 & 0 \end{pmatrix}$	$\begin{pmatrix} t'_{xx} & 0 & 0 \\ 0 & -t'_{xx} & 0 \\ 0 & 0 & 0 \end{pmatrix}$	$4/mmm$	$\begin{pmatrix} \sigma_{xx} & 0 & 0 \\ 0 & \sigma_{xx} & 0 \\ 0 & 0 & \sigma_{zz} \end{pmatrix}$	$\begin{pmatrix} 0 & \sigma^z_{xy} & 0 \\ -\sigma^z_{xy} & 0 & 0 \\ 0 & 0 & 0 \end{pmatrix}$
3	$\begin{pmatrix} t_{xx} & t_{xy} & 0 \\ -t_{xy} & t_{xx} & 0 \\ 0 & 0 & t_{zz} \end{pmatrix}$	$\begin{pmatrix} t'_{xx} & t'_{xy} & 0 \\ -t'_{xy} & t'_{xx} & 0 \\ 0 & 0 & t'_{zz} \end{pmatrix}$	$\bar{3}$	$\begin{pmatrix} \sigma_{xx} & \sigma_{xy} & 0 \\ -\sigma_{xy} & \sigma_{xx} & 0 \\ 0 & 0 & \sigma_{zz} \end{pmatrix}$	$\begin{pmatrix} \sigma^z_{xx} & \sigma^z_{xy} & 0 \\ -\sigma^z_{xy} & \sigma^z_{xx} & 0 \\ 0 & 0 & \sigma^z_{zz} \end{pmatrix}$
312	$\begin{pmatrix} t_{xx} & 0 & 0 \\ 0 & t_{xx} & 0 \\ 0 & 0 & t_{zz} \end{pmatrix}$	$\begin{pmatrix} t'_{xx} & 0 & 0 \\ 0 & t'_{xx} & 0 \\ 0 & 0 & t'_{zz} \end{pmatrix}$	$\bar{3}1m$	$\begin{pmatrix} \sigma_{xx} & 0 & 0 \\ 0 & \sigma_{xx} & 0 \\ 0 & 0 & \sigma_{zz} \end{pmatrix}$	$\begin{pmatrix} 0 & \sigma^z_{xy} & 0 \\ -\sigma^z_{xy} & 0 & 0 \\ 0 & 0 & 0 \end{pmatrix}$
$31m$	$\begin{pmatrix} 0 & t_{xy} & 0 \\ -t_{xy} & 0 & 0 \\ 0 & 0 & 0 \end{pmatrix}$	$\begin{pmatrix} 0 & t'_{xy} & 0 \\ -t'_{xy} & 0 & 0 \\ 0 & 0 & 0 \end{pmatrix}$	$\bar{3}1m$	$\begin{pmatrix} \sigma_{xx} & 0 & 0 \\ 0 & \sigma_{xx} & 0 \\ 0 & 0 & \sigma_{zz} \end{pmatrix}$	$\begin{pmatrix} 0 & \sigma^z_{xy} & 0 \\ -\sigma^z_{xy} & 0 & 0 \\ 0 & 0 & 0 \end{pmatrix}$
6	$\begin{pmatrix} t_{xx} & t_{xy} & 0 \\ -t_{xy} & t_{xx} & 0 \\ 0 & 0 & t_{zz} \end{pmatrix}$	$\begin{pmatrix} t'_{xx} & t'_{xy} & 0 \\ -t'_{xy} & t'_{xx} & 0 \\ 0 & 0 & t'_{zz} \end{pmatrix}$	$6/m$	$\begin{pmatrix} \sigma_{xx} & \sigma_{xy} & 0 \\ -\sigma_{xy} & \sigma_{xx} & 0 \\ 0 & 0 & \sigma_{zz} \end{pmatrix}$	$\begin{pmatrix} \sigma^z_{xx} & \sigma^z_{xy} & 0 \\ -\sigma^z_{xy} & \sigma^z_{xx} & 0 \\ 0 & 0 & \sigma^z_{zz} \end{pmatrix}$
622	$\begin{pmatrix} t_{xx} & 0 & 0 \\ 0 & t_{xx} & 0 \\ 0 & 0 & t_{zz} \end{pmatrix}$	$\begin{pmatrix} t'_{xx} & 0 & 0 \\ 0 & t'_{xx} & 0 \\ 0 & 0 & t'_{zz} \end{pmatrix}$	$6/mmm$	$\begin{pmatrix} \sigma_{xx} & 0 & 0 \\ 0 & \sigma_{xx} & 0 \\ 0 & 0 & \sigma_{zz} \end{pmatrix}$	$\begin{pmatrix} 0 & \sigma^z_{xy} & 0 \\ -\sigma^z_{xy} & 0 & 0 \\ 0 & 0 & 0 \end{pmatrix}$
$6mm$	$\begin{pmatrix} 0 & t_{xy} & 0 \\ -t_{xy} & 0 & 0 \\ 0 & 0 & 0 \end{pmatrix}$	$\begin{pmatrix} 0 & t'_{xy} & 0 \\ -t'_{xy} & 0 & 0 \\ 0 & 0 & 0 \end{pmatrix}$	$6/mmm$	$\begin{pmatrix} \sigma_{xx} & 0 & 0 \\ 0 & \sigma_{xx} & 0 \\ 0 & 0 & \sigma_{zz} \end{pmatrix}$	$\begin{pmatrix} 0 & \sigma^z_{xy} & 0 \\ -\sigma^z_{xy} & 0 & 0 \\ 0 & 0 & 0 \end{pmatrix}$

TABLE I. (*Continued.*)

Magnetic point group	$\underline{t}$	$\underline{t}'$	Magnetic Laue group	$\underline{\sigma}$	$\underline{\sigma}^k$
23	$\begin{pmatrix} t_{xx} & 0 & 0 \\ 0 & t_{xx} & 0 \\ 0 & 0 & t_{xx} \end{pmatrix}$	$\begin{pmatrix} t'_{xx} & 0 & 0 \\ 0 & t'_{xx} & 0 \\ 0 & 0 & t'_{xx} \end{pmatrix}$	$m\bar{3}$	$\begin{pmatrix} \sigma_{xx} & 0 & 0 \\ 0 & \sigma_{xx} & 0 \\ 0 & 0 & \sigma_{xx} \end{pmatrix}$	$\begin{pmatrix} 0 & \sigma^z_{xy} & 0 \\ \sigma^y_{xz} & 0 & 0 \\ 0 & 0 & 0 \end{pmatrix}$
432	$\begin{pmatrix} t_{xx} & 0 & 0 \\ 0 & t_{xx} & 0 \\ 0 & 0 & t_{xx} \end{pmatrix}$	$\begin{pmatrix} t'_{xx} & 0 & 0 \\ 0 & t'_{xx} & 0 \\ 0 & 0 & t'_{xx} \end{pmatrix}$	$m\bar{3}m$	$\begin{pmatrix} \sigma_{xx} & 0 & 0 \\ 0 & \sigma_{xx} & 0 \\ 0 & 0 & \sigma_{xx} \end{pmatrix}$	$\begin{pmatrix} 0 & \sigma^z_{xy} & 0 \\ -\sigma^z_{xy} & 0 & 0 \\ 0 & 0 & 0 \end{pmatrix}$

Finally, it should be mentioned that the results for the torkance tensors presented in Tables I–VI have been independently checked for a number of systems, including $m'm'm$, $4/mm'm'$, $6/mm'm'$, $\bar{3}m'$ with vanishing torkance and 1, $\bar{1}'$, m', $2/m'$, $2'/m$, $m'm'2$, $\bar{4}2'm'$, $3m'$, $\bar{6}'2m'$, $6/m'm'm'$ with finite torkance, by numerical calculations using the implementation described above.

III. RESULTS

To investigate the impact of chemical disorder and the ability to tailor the torkance via the alloy composition the multilayer system Pt|Fe_xCo_{1-x}|Cu has been investigated over the full range of concentration x (0.01 − 0.99). Figure 1 shows the hexagonal structure of the model system for which a

TABLE II. Shape of the direct and inverse torkance tensors, $\underline{t}$ and $\underline{t}'$, for magnetic point groups of category (c). Note that the two tensors usually differ in shape, depending on which spatial operation(s) is (are) combined with time reversal. The third and fourth columns show the electrical conductivity tensor $\underline{\sigma}$ and the spin conductivity tensor $\underline{\sigma}^k$ for polarization along the principal axis k, respectively, for the corresponding magnetic Laue groups. See Ref. [63] for the two remaining polarization directions and further details on conventions and notation. Magnetic point groups that allow for the existence of a ferromagnetic state are given in boldface. This table contains only groups with a principal axis of order $O(k) \leqslant 2$ (triclinic, monoclinic, and orthorhombic groups) and is continued in Tables III–VI.

Magnetic point group	$\underline{t}$	$\underline{t}'$	Magnetic Laue group	$\underline{\sigma}$	$\underline{\sigma}^k$
$\bar{1}'$	$\begin{pmatrix} t_{xx} & t_{xy} & t_{xz} \\ t_{yx} & t_{yy} & t_{yz} \\ t_{zx} & t_{zy} & t_{zz} \end{pmatrix}$	$\begin{pmatrix} t_{xx} & t_{yx} & t_{zx} \\ t_{xy} & t_{yy} & t_{zy} \\ t_{xz} & t_{yz} & t_{zz} \end{pmatrix}$	$\bar{1}1'$	$\begin{pmatrix} \sigma_{xx} & \sigma_{xy} & \sigma_{xz} \\ \sigma_{xy} & \sigma_{yy} & \sigma_{yz} \\ \sigma_{xz} & \sigma_{yz} & \sigma_{zz} \end{pmatrix}$	$\begin{pmatrix} \sigma^z_{xx} & \sigma^z_{xy} & \sigma^z_{xz} \\ \sigma^z_{yx} & \sigma^z_{yy} & \sigma^z_{yz} \\ \sigma^z_{zx} & \sigma^z_{zy} & \sigma^z_{zz} \end{pmatrix}$
2′	$\begin{pmatrix} t_{xx} & t_{xy} & t_{xz} \\ t_{yx} & t_{yy} & t_{yz} \\ t_{zx} & t_{zy} & t_{zz} \end{pmatrix}$	$\begin{pmatrix} -t_{xx} & t_{yx} & -t_{zx} \\ t_{xy} & -t_{yy} & t_{zy} \\ -t_{xz} & t_{yz} & -t_{zz} \end{pmatrix}$	$2'/m'$	$\begin{pmatrix} \sigma_{xx} & \sigma_{xy} & \sigma_{xz} \\ -\sigma_{xy} & \sigma_{yy} & \sigma_{yz} \\ \sigma_{xz} & -\sigma_{yz} & \sigma_{zz} \end{pmatrix}$	$\begin{pmatrix} \sigma^y_{xx} & \sigma^y_{xy} & \sigma^y_{xz} \\ \sigma^y_{yx} & \sigma^y_{yy} & \sigma^y_{yz} \\ \sigma^y_{zx} & \sigma^y_{zy} & \sigma^y_{zz} \end{pmatrix}$
m′	$\begin{pmatrix} t_{xx} & t_{xy} & t_{xz} \\ t_{yx} & t_{yy} & t_{yz} \\ t_{zx} & t_{zy} & t_{zz} \end{pmatrix}$	$\begin{pmatrix} t_{xx} & -t_{yx} & t_{zx} \\ -t_{xy} & t_{yy} & -t_{zy} \\ t_{xz} & -t_{yz} & t_{zz} \end{pmatrix}$	$2'/m'$	$\begin{pmatrix} \sigma_{xx} & \sigma_{xy} & \sigma_{xz} \\ -\sigma_{xy} & \sigma_{yy} & \sigma_{yz} \\ \sigma_{xz} & -\sigma_{yz} & \sigma_{zz} \end{pmatrix}$	$\begin{pmatrix} \sigma^y_{xx} & \sigma^y_{xy} & \sigma^y_{xz} \\ \sigma^y_{yx} & \sigma^y_{yy} & \sigma^y_{yz} \\ \sigma^y_{zx} & \sigma^y_{zy} & \sigma^y_{zz} \end{pmatrix}$
$2/m'$	$\begin{pmatrix} t_{xx} & 0 & t_{xz} \\ 0 & t_{yy} & 0 \\ t_{zx} & 0 & t_{zz} \end{pmatrix}$	$\begin{pmatrix} t_{xx} & 0 & t_{zx} \\ 0 & t_{yy} & 0 \\ t_{xz} & 0 & t_{zz} \end{pmatrix}$	$2/m1'$	$\begin{pmatrix} \sigma_{xx} & 0 & \sigma_{xz} \\ 0 & \sigma_{yy} & 0 \\ \sigma_{xz} & 0 & \sigma_{zz} \end{pmatrix}$	$\begin{pmatrix} \sigma^y_{xx} & 0 & \sigma^y_{xz} \\ 0 & \sigma^y_{yy} & 0 \\ \sigma^y_{zx} & 0 & \sigma^y_{zz} \end{pmatrix}$
$2'/m$	$\begin{pmatrix} 0 & t_{xy} & 0 \\ t_{yx} & 0 & t_{yz} \\ 0 & t_{zy} & 0 \end{pmatrix}$	$\begin{pmatrix} 0 & t_{yx} & 0 \\ t_{xy} & 0 & t_{zy} \\ 0 & t_{yz} & 0 \end{pmatrix}$	$2/m1'$	$\begin{pmatrix} \sigma_{xx} & 0 & \sigma_{xz} \\ 0 & \sigma_{yy} & 0 \\ \sigma_{xz} & 0 & \sigma_{zz} \end{pmatrix}$	$\begin{pmatrix} \sigma^y_{xx} & 0 & \sigma^y_{xz} \\ 0 & \sigma^y_{yy} & 0 \\ \sigma^y_{zx} & 0 & \sigma^y_{zz} \end{pmatrix}$
2′2′2	$\begin{pmatrix} t_{xx} & t_{xy} & 0 \\ t_{yx} & t_{yy} & 0 \\ 0 & 0 & t_{zz} \end{pmatrix}$	$\begin{pmatrix} -t_{xx} & t_{yx} & 0 \\ t_{xy} & -t_{yy} & 0 \\ 0 & 0 & -t_{zz} \end{pmatrix}$	$m'm'm$	$\begin{pmatrix} \sigma_{xx} & \sigma_{xy} & 0 \\ -\sigma_{xy} & \sigma_{yy} & 0 \\ 0 & 0 & \sigma_{zz} \end{pmatrix}$	$\begin{pmatrix} \sigma^z_{xx} & \sigma^z_{xy} & 0 \\ \sigma^z_{yx} & \sigma^z_{yy} & 0 \\ 0 & 0 & \sigma^z_{zz} \end{pmatrix}$
m′m′2	$\begin{pmatrix} t_{xx} & t_{xy} & 0 \\ t_{yx} & t_{yy} & 0 \\ 0 & 0 & t_{zz} \end{pmatrix}$	$\begin{pmatrix} t_{xx} & -t_{yx} & 0 \\ -t_{xy} & t_{yy} & 0 \\ 0 & 0 & t_{zz} \end{pmatrix}$	$m'm'm$	$\begin{pmatrix} \sigma_{xx} & \sigma_{xy} & 0 \\ -\sigma_{xy} & \sigma_{yy} & 0 \\ 0 & 0 & \sigma_{zz} \end{pmatrix}$	$\begin{pmatrix} \sigma^z_{xx} & \sigma^z_{xy} & 0 \\ \sigma^z_{yx} & \sigma^z_{yy} & 0 \\ 0 & 0 & \sigma^z_{zz} \end{pmatrix}$
m′m2′	$\begin{pmatrix} 0 & t_{xy} & 0 \\ t_{yx} & 0 & t_{yz} \\ 0 & t_{zy} & 0 \end{pmatrix}$	$\begin{pmatrix} 0 & -t_{yx} & 0 \\ -t_{xy} & 0 & t_{zy} \\ 0 & t_{yz} & 0 \end{pmatrix}$	$m'm'm$	$\begin{pmatrix} \sigma_{xx} & 0 & \sigma_{xz} \\ 0 & \sigma_{yy} & 0 \\ -\sigma_{xz} & 0 & \sigma_{zz} \end{pmatrix}$	$\begin{pmatrix} 0 & \sigma^z_{xy} & 0 \\ \sigma^z_{yx} & 0 & \sigma^z_{yz} \\ 0 & \sigma^z_{zy} & 0 \end{pmatrix}$
$m'm'm'$	$\begin{pmatrix} t_{xx} & 0 & 0 \\ 0 & t_{yy} & 0 \\ 0 & 0 & t_{zz} \end{pmatrix}$	$\begin{pmatrix} t_{xx} & 0 & 0 \\ 0 & t_{yy} & 0 \\ 0 & 0 & t_{zz} \end{pmatrix}$	$mmm1'$	$\begin{pmatrix} \sigma_{xx} & 0 & 0 \\ 0 & \sigma_{yy} & 0 \\ 0 & 0 & \sigma_{zz} \end{pmatrix}$	$\begin{pmatrix} 0 & \sigma^z_{xy} & 0 \\ \sigma^z_{yx} & 0 & 0 \\ 0 & 0 & 0 \end{pmatrix}$
$m'mm$	$\begin{pmatrix} 0 & 0 & 0 \\ 0 & 0 & t_{yz} \\ 0 & t_{zy} & 0 \end{pmatrix}$	$\begin{pmatrix} 0 & 0 & 0 \\ 0 & 0 & t_{zy} \\ 0 & t_{yz} & 0 \end{pmatrix}$	$mmm1'$	$\begin{pmatrix} \sigma_{xx} & 0 & 0 \\ 0 & \sigma_{yy} & 0 \\ 0 & 0 & \sigma_{zz} \end{pmatrix}$	$\begin{pmatrix} 0 & \sigma^z_{xy} & 0 \\ \sigma^z_{yx} & 0 & 0 \\ 0 & 0 & 0 \end{pmatrix}$

TABLE III. Table II continued for tetragonal groups with $O(k) = 4$.

Magnetic point group	$\underline{t}$	$\underline{t}'$	Magnetic Laue group	$\underline{\sigma}$	$\underline{\sigma}^k$
$4'$	$\begin{pmatrix} t_{xx} & t_{xy} & 0 \\ t_{yx} & t_{yy} & 0 \\ 0 & 0 & t_{zz} \end{pmatrix}$	$\begin{pmatrix} -t_{yy} & t_{xy} & 0 \\ t_{yx} & -t_{xx} & 0 \\ 0 & 0 & -t_{zz} \end{pmatrix}$	$4'/m$	$\begin{pmatrix} \sigma_{xx} & 0 & 0 \\ 0 & \sigma_{xx} & 0 \\ 0 & 0 & \sigma_{zz} \end{pmatrix}$	$\begin{pmatrix} \sigma^z_{xx} & \sigma^z_{xy} & 0 \\ \sigma^z_{yx} & \sigma^z_{yy} & 0 \\ 0 & 0 & \sigma^z_{zz} \end{pmatrix}$
$\bar{4}'$	$\begin{pmatrix} t_{xx} & t_{xy} & 0 \\ t_{yx} & t_{yy} & 0 \\ 0 & 0 & t_{zz} \end{pmatrix}$	$\begin{pmatrix} t_{yy} & -t_{xy} & 0 \\ -t_{yx} & t_{xx} & 0 \\ 0 & 0 & t_{zz} \end{pmatrix}$	$4'/m$	$\begin{pmatrix} \sigma_{xx} & 0 & 0 \\ 0 & \sigma_{xx} & 0 \\ 0 & 0 & \sigma_{zz} \end{pmatrix}$	$\begin{pmatrix} \sigma^z_{xx} & \sigma^z_{xy} & 0 \\ \sigma^z_{yx} & \sigma^z_{yy} & 0 \\ 0 & 0 & \sigma^z_{zz} \end{pmatrix}$
$4/m'$	$\begin{pmatrix} t_{xx} & t_{xy} & 0 \\ -t_{xy} & t_{xx} & 0 \\ 0 & 0 & t_{zz} \end{pmatrix}$	$\begin{pmatrix} t_{xx} & -t_{xy} & 0 \\ t_{xy} & t_{xx} & 0 \\ 0 & 0 & t_{zz} \end{pmatrix}$	$4/m1'$	$\begin{pmatrix} \sigma_{xx} & 0 & 0 \\ 0 & \sigma_{xx} & 0 \\ 0 & 0 & \sigma_{zz} \end{pmatrix}$	$\begin{pmatrix} \sigma^z_{xx} & \sigma^z_{xy} & 0 \\ -\sigma^z_{xy} & \sigma^z_{xx} & 0 \\ 0 & 0 & \sigma^z_{zz} \end{pmatrix}$
$4'/m'$	$\begin{pmatrix} t_{xx} & t_{xy} & 0 \\ t_{xy} & -t_{xx} & 0 \\ 0 & 0 & 0 \end{pmatrix}$	$\begin{pmatrix} t_{xx} & t_{xy} & 0 \\ t_{xy} & -t_{xx} & 0 \\ 0 & 0 & 0 \end{pmatrix}$	$4/m1'$	$\begin{pmatrix} \sigma_{xx} & 0 & 0 \\ 0 & \sigma_{xx} & 0 \\ 0 & 0 & \sigma_{zz} \end{pmatrix}$	$\begin{pmatrix} \sigma^z_{xx} & \sigma^z_{xy} & 0 \\ -\sigma^z_{xy} & \sigma^z_{xx} & 0 \\ 0 & 0 & \sigma^z_{zz} \end{pmatrix}$
$4'22'$	$\begin{pmatrix} t_{xx} & 0 & 0 \\ 0 & t_{yy} & 0 \\ 0 & 0 & t_{zz} \end{pmatrix}$	$\begin{pmatrix} -t_{yy} & 0 & 0 \\ 0 & -t_{xx} & 0 \\ 0 & 0 & -t_{zz} \end{pmatrix}$	$4'/mmm'$	$\begin{pmatrix} \sigma_{xx} & 0 & 0 \\ 0 & \sigma_{xx} & 0 \\ 0 & 0 & \sigma_{zz} \end{pmatrix}$	$\begin{pmatrix} 0 & \sigma^z_{xy} & 0 \\ \sigma^z_{yx} & 0 & 0 \\ 0 & 0 & 0 \end{pmatrix}$
$42'2'$	$\begin{pmatrix} t_{xx} & t_{xy} & 0 \\ -t_{xy} & t_{xx} & 0 \\ 0 & 0 & t_{zz} \end{pmatrix}$	$\begin{pmatrix} -t_{xx} & -t_{xy} & 0 \\ t_{xy} & -t_{xx} & 0 \\ 0 & 0 & -t_{zz} \end{pmatrix}$	$4/mm'm'$	$\begin{pmatrix} \sigma_{xx} & \sigma_{xy} & 0 \\ -\sigma_{xy} & \sigma_{xx} & 0 \\ 0 & 0 & \sigma_{zz} \end{pmatrix}$	$\begin{pmatrix} \sigma^z_{xx} & \sigma^z_{xy} & 0 \\ -\sigma^z_{xy} & \sigma^z_{xx} & 0 \\ 0 & 0 & \sigma^z_{zz} \end{pmatrix}$
$4'mm'$	$\begin{pmatrix} 0 & t_{xy} & 0 \\ t_{yx} & 0 & 0 \\ 0 & 0 & 0 \end{pmatrix}$	$\begin{pmatrix} 0 & t_{xy} & 0 \\ t_{yx} & 0 & 0 \\ 0 & 0 & 0 \end{pmatrix}$	$4'/mmm'$	$\begin{pmatrix} \sigma_{xx} & 0 & 0 \\ 0 & \sigma_{xx} & 0 \\ 0 & 0 & \sigma_{zz} \end{pmatrix}$	$\begin{pmatrix} 0 & \sigma^z_{xy} & 0 \\ \sigma^z_{yx} & 0 & 0 \\ 0 & 0 & 0 \end{pmatrix}$
$4m'm'$	$\begin{pmatrix} t_{xx} & t_{xy} & 0 \\ -t_{xy} & t_{xx} & 0 \\ 0 & 0 & t_{zz} \end{pmatrix}$	$\begin{pmatrix} t_{xx} & t_{xy} & 0 \\ -t_{xy} & t_{xx} & 0 \\ 0 & 0 & t_{zz} \end{pmatrix}$	$4/mm'm'$	$\begin{pmatrix} \sigma_{xx} & \sigma_{xy} & 0 \\ -\sigma_{xy} & \sigma_{xx} & 0 \\ 0 & 0 & \sigma_{zz} \end{pmatrix}$	$\begin{pmatrix} \sigma^z_{xx} & \sigma^z_{xy} & 0 \\ -\sigma^z_{xy} & \sigma^z_{xx} & 0 \\ 0 & 0 & \sigma^z_{zz} \end{pmatrix}$
$\bar{4}'2m'$	$\begin{pmatrix} t_{xx} & 0 & 0 \\ 0 & t_{yy} & 0 \\ 0 & 0 & t_{zz} \end{pmatrix}$	$\begin{pmatrix} t_{yy} & 0 & 0 \\ 0 & t_{xx} & 0 \\ 0 & 0 & t_{zz} \end{pmatrix}$	$4'/mmm'$	$\begin{pmatrix} \sigma_{xx} & 0 & 0 \\ 0 & \sigma_{xx} & 0 \\ 0 & 0 & \sigma_{zz} \end{pmatrix}$	$\begin{pmatrix} 0 & \sigma^z_{xy} & 0 \\ \sigma^z_{yx} & 0 & 0 \\ 0 & 0 & 0 \end{pmatrix}$
$\bar{4}'m2'$	$\begin{pmatrix} 0 & t_{xy} & 0 \\ t_{yx} & 0 & 0 \\ 0 & 0 & 0 \end{pmatrix}$	$\begin{pmatrix} 0 & -t_{xy} & 0 \\ -t_{yx} & 0 & 0 \\ 0 & 0 & 0 \end{pmatrix}$	$4'/mmm'$	$\begin{pmatrix} \sigma_{xx} & 0 & 0 \\ 0 & \sigma_{xx} & 0 \\ 0 & 0 & \sigma_{zz} \end{pmatrix}$	$\begin{pmatrix} 0 & \sigma^z_{xy} & 0 \\ \sigma^z_{yx} & 0 & 0 \\ 0 & 0 & 0 \end{pmatrix}$
$\bar{4}2'm'$	$\begin{pmatrix} t_{xx} & t_{xy} & 0 \\ t_{xy} & -t_{xx} & 0 \\ 0 & 0 & 0 \end{pmatrix}$	$\begin{pmatrix} -t_{xx} & t_{xy} & 0 \\ t_{xy} & t_{xx} & 0 \\ 0 & 0 & 0 \end{pmatrix}$	$4/mm'm'$	$\begin{pmatrix} \sigma_{xx} & \sigma_{xy} & 0 \\ -\sigma_{xy} & \sigma_{xx} & 0 \\ 0 & 0 & \sigma_{zz} \end{pmatrix}$	$\begin{pmatrix} \sigma^z_{xx} & \sigma^z_{xy} & 0 \\ -\sigma^z_{xy} & \sigma^z_{xx} & 0 \\ 0 & 0 & \sigma^z_{zz} \end{pmatrix}$
$4/m'm'm'$	$\begin{pmatrix} t_{xx} & 0 & 0 \\ 0 & t_{xx} & 0 \\ 0 & 0 & t_{zz} \end{pmatrix}$	$\begin{pmatrix} t_{xx} & 0 & 0 \\ 0 & t_{xx} & 0 \\ 0 & 0 & t_{zz} \end{pmatrix}$	$4/mmm1'$	$\begin{pmatrix} \sigma_{xx} & 0 & 0 \\ 0 & \sigma_{xx} & 0 \\ 0 & 0 & \sigma_{zz} \end{pmatrix}$	$\begin{pmatrix} 0 & \sigma^z_{xy} & 0 \\ -\sigma^z_{xy} & 0 & 0 \\ 0 & 0 & 0 \end{pmatrix}$
$4/m'mm$	$\begin{pmatrix} 0 & t_{xy} & 0 \\ -t_{xy} & 0 & 0 \\ 0 & 0 & 0 \end{pmatrix}$	$\begin{pmatrix} 0 & -t_{xy} & 0 \\ t_{xy} & 0 & 0 \\ 0 & 0 & 0 \end{pmatrix}$	$4/mmm1'$	$\begin{pmatrix} \sigma_{xx} & 0 & 0 \\ 0 & \sigma_{xx} & 0 \\ 0 & 0 & \sigma_{zz} \end{pmatrix}$	$\begin{pmatrix} 0 & \sigma^z_{xy} & 0 \\ -\sigma^z_{xy} & 0 & 0 \\ 0 & 0 & 0 \end{pmatrix}$
$4'/m'm'm$	$\begin{pmatrix} t_{xx} & 0 & 0 \\ 0 & -t_{xx} & 0 \\ 0 & 0 & 0 \end{pmatrix}$	$\begin{pmatrix} t_{xx} & 0 & 0 \\ 0 & -t_{xx} & 0 \\ 0 & 0 & 0 \end{pmatrix}$	$4/mmm1'$	$\begin{pmatrix} \sigma_{xx} & 0 & 0 \\ 0 & \sigma_{xx} & 0 \\ 0 & 0 & \sigma_{zz} \end{pmatrix}$	$\begin{pmatrix} 0 & \sigma^z_{xy} & 0 \\ -\sigma^z_{xy} & 0 & 0 \\ 0 & 0 & 0 \end{pmatrix}$

stacking of fcc (111) atomic planes along the z axis has been assumed, using the lattice spacing of Pt (7.408 a_0).

To examine the connection of the torkance with other related response quantities we calculated the electrical and spin conductivity tensors in addition. Replacing the torque operator $\hat{T}_\mu$ in Eq. (1) by the operator $\hat{j}_\mu$ one gets, apart from some constants, the corresponding expressions for the electrical conductivity tensor $\underline{\sigma}$. From this one can see immediately that the longitudinal conductivities σ_{ii} are connected only with the first Fermi surface term in Eq. (1); accordingly they are determined for $T = 0$ K by the electronic structure at the Fermi energy E_F while the second Fermi sea term vanishes. Due to the magnetic Laue group ($\bar{3}m'$) of the investigated system the conductivity tensor $\underline{\sigma}$ has only the nonvanishing elements $\sigma_{xx} = \sigma_{yy} \neq \sigma_{zz}$ and $\sigma_{xy} = -\sigma_{yx}$ [63], the well-known shape of ferromagnetic systems with a principal axis k of order $O(k) \geqslant 3$ and neither additional purely spatial rotation axes perpendicular to it, nor vertical mirror planes. The corresponding results for Pt|Fe_xCo_{1-x}|Cu are shown in Fig. 2 as a function of the concentration x. As to be expected

TABLE IV. Table II continued for trigonal groups with $O(k) = 3$.

Magnetic point group	$\underline{t}$	$\underline{t}'$	Magnetic Laue group	$\underline{\sigma}$	$\underline{\sigma}^k$
$\bar{3}'$	$\begin{pmatrix} t_{xx} & t_{xy} & 0 \\ -t_{xy} & t_{xx} & 0 \\ 0 & 0 & t_{zz} \end{pmatrix}$	$\begin{pmatrix} t_{xx} & -t_{xy} & 0 \\ t_{xy} & t_{xx} & 0 \\ 0 & 0 & t_{zz} \end{pmatrix}$	$\bar{3}1'$	$\begin{pmatrix} \sigma_{xx} & 0 & 0 \\ 0 & \sigma_{xx} & 0 \\ 0 & 0 & \sigma_{zz} \end{pmatrix}$	$\begin{pmatrix} \sigma^z_{xx} & \sigma^z_{xy} & 0 \\ -\sigma^z_{xy} & \sigma^z_{xx} & 0 \\ 0 & 0 & \sigma^z_{zz} \end{pmatrix}$
312′	$\begin{pmatrix} t_{xx} & t_{xy} & 0 \\ -t_{xy} & t_{xx} & 0 \\ 0 & 0 & t_{zz} \end{pmatrix}$	$\begin{pmatrix} -t_{xx} & -t_{xy} & 0 \\ t_{xy} & -t_{xx} & 0 \\ 0 & 0 & -t_{zz} \end{pmatrix}$	$\bar{3}1m'$	$\begin{pmatrix} \sigma_{xx} & \sigma_{xy} & 0 \\ -\sigma_{xy} & \sigma_{xx} & 0 \\ 0 & 0 & \sigma_{zz} \end{pmatrix}$	$\begin{pmatrix} \sigma^z_{xx} & \sigma^z_{xy} & 0 \\ -\sigma^z_{xy} & \sigma^z_{xx} & 0 \\ 0 & 0 & \sigma^z_{zz} \end{pmatrix}$
31m′	$\begin{pmatrix} t_{xx} & t_{xy} & 0 \\ -t_{xy} & t_{xx} & 0 \\ 0 & 0 & t_{zz} \end{pmatrix}$	$\begin{pmatrix} t_{xx} & t_{xy} & 0 \\ -t_{xy} & t_{xx} & 0 \\ 0 & 0 & t_{zz} \end{pmatrix}$	$\bar{3}1m'$	$\begin{pmatrix} \sigma_{xx} & \sigma_{xy} & 0 \\ -\sigma_{xy} & \sigma_{xx} & 0 \\ 0 & 0 & \sigma_{zz} \end{pmatrix}$	$\begin{pmatrix} \sigma^z_{xx} & \sigma^z_{xy} & 0 \\ -\sigma^z_{xy} & \sigma^z_{xx} & 0 \\ 0 & 0 & \sigma^z_{zz} \end{pmatrix}$
$\bar{3}'1m'$	$\begin{pmatrix} t_{xx} & 0 & 0 \\ 0 & t_{xx} & 0 \\ 0 & 0 & t_{zz} \end{pmatrix}$	$\begin{pmatrix} t_{xx} & 0 & 0 \\ 0 & t_{xx} & 0 \\ 0 & 0 & t_{zz} \end{pmatrix}$	$\bar{3}1m1'$	$\begin{pmatrix} \sigma_{xx} & 0 & 0 \\ 0 & \sigma_{xx} & 0 \\ 0 & 0 & \sigma_{zz} \end{pmatrix}$	$\begin{pmatrix} 0 & \sigma^z_{xy} & 0 \\ -\sigma^z_{xy} & 0 & 0 \\ 0 & 0 & 0 \end{pmatrix}$
$\bar{3}'1m$	$\begin{pmatrix} 0 & t_{xy} & 0 \\ -t_{xy} & 0 & 0 \\ 0 & 0 & 0 \end{pmatrix}$	$\begin{pmatrix} 0 & -t_{xy} & 0 \\ t_{xy} & 0 & 0 \\ 0 & 0 & 0 \end{pmatrix}$	$\bar{3}1m1'$	$\begin{pmatrix} \sigma_{xx} & 0 & 0 \\ 0 & \sigma_{xx} & 0 \\ 0 & 0 & \sigma_{zz} \end{pmatrix}$	$\begin{pmatrix} 0 & \sigma^z_{xy} & 0 \\ -\sigma^z_{xy} & 0 & 0 \\ 0 & 0 & 0 \end{pmatrix}$

TABLE V. Table II continued for hexagonal groups with $O(k) = 6$.

Magnetic point group	$\underline{t}$	$\underline{t}'$	Magnetic Laue group	$\underline{\sigma}$	$\underline{\sigma}^k$
$6'$	$\begin{pmatrix} t_{xx} & t_{xy} & 0 \\ -t_{xy} & t_{xx} & 0 \\ 0 & 0 & t_{zz} \end{pmatrix}$	$\begin{pmatrix} -t_{xx} & t_{xy} & 0 \\ -t_{xy} & -t_{xx} & 0 \\ 0 & 0 & -t_{zz} \end{pmatrix}$	$6'/m'$	$\begin{pmatrix} \sigma_{xx} & 0 & 0 \\ 0 & \sigma_{xx} & 0 \\ 0 & 0 & \sigma_{zz} \end{pmatrix}$	$\begin{pmatrix} \sigma^z_{xx} & \sigma^z_{xy} & 0 \\ -\sigma^z_{xy} & \sigma^z_{xx} & 0 \\ 0 & 0 & \sigma^z_{zz} \end{pmatrix}$
$\bar{6}'$	$\begin{pmatrix} t_{xx} & t_{xy} & 0 \\ -t_{xy} & t_{xx} & 0 \\ 0 & 0 & t_{zz} \end{pmatrix}$	$\begin{pmatrix} t_{xx} & -t_{xy} & 0 \\ t_{xy} & t_{xx} & 0 \\ 0 & 0 & t_{zz} \end{pmatrix}$	$6'/m'$	$\begin{pmatrix} \sigma_{xx} & 0 & 0 \\ 0 & \sigma_{xx} & 0 \\ 0 & 0 & \sigma_{zz} \end{pmatrix}$	$\begin{pmatrix} \sigma^z_{xx} & \sigma^z_{xy} & 0 \\ -\sigma^z_{xy} & \sigma^z_{xx} & 0 \\ 0 & 0 & \sigma^z_{zz} \end{pmatrix}$
$6/m'$	$\begin{pmatrix} t_{xx} & t_{xy} & 0 \\ -t_{xy} & t_{xx} & 0 \\ 0 & 0 & t_{zz} \end{pmatrix}$	$\begin{pmatrix} t_{xx} & -t_{xy} & 0 \\ t_{xy} & t_{xx} & 0 \\ 0 & 0 & t_{zz} \end{pmatrix}$	$6/m1'$	$\begin{pmatrix} \sigma_{xx} & 0 & 0 \\ 0 & \sigma_{xx} & 0 \\ 0 & 0 & \sigma_{zz} \end{pmatrix}$	$\begin{pmatrix} \sigma^z_{xx} & \sigma^z_{xy} & 0 \\ -\sigma^z_{xy} & \sigma^z_{xx} & 0 \\ 0 & 0 & \sigma^z_{zz} \end{pmatrix}$
$6'22'$	$\begin{pmatrix} t_{xx} & 0 & 0 \\ 0 & t_{xx} & 0 \\ 0 & 0 & t_{zz} \end{pmatrix}$	$\begin{pmatrix} -t_{xx} & 0 & 0 \\ 0 & -t_{xx} & 0 \\ 0 & 0 & -t_{zz} \end{pmatrix}$	$6'/m'mm'$	$\begin{pmatrix} \sigma_{xx} & 0 & 0 \\ 0 & \sigma_{xx} & 0 \\ 0 & 0 & \sigma_{zz} \end{pmatrix}$	$\begin{pmatrix} 0 & \sigma^z_{xy} & 0 \\ -\sigma^z_{xy} & 0 & 0 \\ 0 & 0 & 0 \end{pmatrix}$
62′2′	$\begin{pmatrix} t_{xx} & t_{xy} & 0 \\ -t_{xy} & t_{xx} & 0 \\ 0 & 0 & t_{zz} \end{pmatrix}$	$\begin{pmatrix} -t_{xx} & -t_{xy} & 0 \\ t_{xy} & -t_{xx} & 0 \\ 0 & 0 & -t_{zz} \end{pmatrix}$	$6/mm'm'$	$\begin{pmatrix} \sigma_{xx} & \sigma_{xy} & 0 \\ -\sigma_{xy} & \sigma_{xx} & 0 \\ 0 & 0 & \sigma_{zz} \end{pmatrix}$	$\begin{pmatrix} \sigma^z_{xx} & \sigma^z_{xy} & 0 \\ -\sigma^z_{xy} & \sigma^z_{xx} & 0 \\ 0 & 0 & \sigma^z_{zz} \end{pmatrix}$
$6'mm'$	$\begin{pmatrix} 0 & t_{xy} & 0 \\ -t_{xy} & 0 & 0 \\ 0 & 0 & 0 \end{pmatrix}$	$\begin{pmatrix} 0 & t_{xy} & 0 \\ -t_{xy} & 0 & 0 \\ 0 & 0 & 0 \end{pmatrix}$	$6'/m'mm'$	$\begin{pmatrix} \sigma_{xx} & 0 & 0 \\ 0 & \sigma_{xx} & 0 \\ 0 & 0 & \sigma_{zz} \end{pmatrix}$	$\begin{pmatrix} 0 & \sigma^z_{xy} & 0 \\ -\sigma^z_{xy} & 0 & 0 \\ 0 & 0 & 0 \end{pmatrix}$
6m′m′	$\begin{pmatrix} t_{xx} & t_{xy} & 0 \\ -t_{xy} & t_{xx} & 0 \\ 0 & 0 & t_{zz} \end{pmatrix}$	$\begin{pmatrix} t_{xx} & t_{xy} & 0 \\ -t_{xy} & t_{xx} & 0 \\ 0 & 0 & t_{zz} \end{pmatrix}$	$6/mm'm'$	$\begin{pmatrix} \sigma_{xx} & \sigma_{xy} & 0 \\ -\sigma_{xy} & \sigma_{xx} & 0 \\ 0 & 0 & \sigma_{zz} \end{pmatrix}$	$\begin{pmatrix} \sigma^z_{xx} & \sigma^z_{xy} & 0 \\ -\sigma^z_{xy} & \sigma^z_{xx} & 0 \\ 0 & 0 & \sigma^z_{zz} \end{pmatrix}$
$\bar{6}'2m'$	$\begin{pmatrix} t_{xx} & 0 & 0 \\ 0 & t_{xx} & 0 \\ 0 & 0 & t_{zz} \end{pmatrix}$	$\begin{pmatrix} t_{xx} & 0 & 0 \\ 0 & t_{xx} & 0 \\ 0 & 0 & t_{zz} \end{pmatrix}$	$6'/m'mm'$	$\begin{pmatrix} \sigma_{xx} & 0 & 0 \\ 0 & \sigma_{xx} & 0 \\ 0 & 0 & \sigma_{zz} \end{pmatrix}$	$\begin{pmatrix} 0 & \sigma^z_{xy} & 0 \\ -\sigma^z_{xy} & 0 & 0 \\ 0 & 0 & 0 \end{pmatrix}$
$\bar{6}'m2'$	$\begin{pmatrix} 0 & t_{xy} & 0 \\ -t_{xy} & 0 & 0 \\ 0 & 0 & 0 \end{pmatrix}$	$\begin{pmatrix} 0 & -t_{xy} & 0 \\ t_{xy} & 0 & 0 \\ 0 & 0 & 0 \end{pmatrix}$	$6'/m'mm'$	$\begin{pmatrix} \sigma_{xx} & 0 & 0 \\ 0 & \sigma_{xx} & 0 \\ 0 & 0 & \sigma_{zz} \end{pmatrix}$	$\begin{pmatrix} 0 & \sigma^z_{xy} & 0 \\ -\sigma^z_{xy} & 0 & 0 \\ 0 & 0 & 0 \end{pmatrix}$
$6/m'm'm'$	$\begin{pmatrix} t_{xx} & 0 & 0 \\ 0 & t_{xx} & 0 \\ 0 & 0 & t_{zz} \end{pmatrix}$	$\begin{pmatrix} t_{xx} & 0 & 0 \\ 0 & t_{xx} & 0 \\ 0 & 0 & t_{zz} \end{pmatrix}$	$6/mmm1'$	$\begin{pmatrix} \sigma_{xx} & 0 & 0 \\ 0 & \sigma_{xx} & 0 \\ 0 & 0 & \sigma_{zz} \end{pmatrix}$	$\begin{pmatrix} 0 & \sigma^z_{xy} & 0 \\ -\sigma^z_{xy} & 0 & 0 \\ 0 & 0 & 0 \end{pmatrix}$
$6/m'mm$	$\begin{pmatrix} 0 & t_{xy} & 0 \\ -t_{xy} & 0 & 0 \\ 0 & 0 & 0 \end{pmatrix}$	$\begin{pmatrix} 0 & -t_{xy} & 0 \\ t_{xy} & 0 & 0 \\ 0 & 0 & 0 \end{pmatrix}$	$6/mmm1'$	$\begin{pmatrix} \sigma_{xx} & 0 & 0 \\ 0 & \sigma_{xx} & 0 \\ 0 & 0 & \sigma_{zz} \end{pmatrix}$	$\begin{pmatrix} 0 & \sigma^z_{xy} & 0 \\ -\sigma^z_{xy} & 0 & 0 \\ 0 & 0 & 0 \end{pmatrix}$

TABLE VI. Table II continued for cubic groups.

Magnetic point group	$\underline{t}$	$\underline{t'}$	Magnetic Laue group	$\underline{\sigma}$	$\underline{\sigma^k}$
$m'\bar{3}'$	$\begin{pmatrix} t_{xx} & 0 & 0 \\ 0 & t_{xx} & 0 \\ 0 & 0 & t_{xx} \end{pmatrix}$	$\begin{pmatrix} t_{xx} & 0 & 0 \\ 0 & t_{xx} & 0 \\ 0 & 0 & t_{xx} \end{pmatrix}$	$m\bar{3}1'$	$\begin{pmatrix} \sigma_{xx} & 0 & 0 \\ 0 & \sigma_{xx} & 0 \\ 0 & 0 & \sigma_{xx} \end{pmatrix}$	$\begin{pmatrix} 0 & \sigma^z_{xy} & 0 \\ \sigma^y_{xz} & 0 & 0 \\ 0 & 0 & 0 \end{pmatrix}$
$4'32'$	$\begin{pmatrix} t_{xx} & 0 & 0 \\ 0 & t_{xx} & 0 \\ 0 & 0 & t_{xx} \end{pmatrix}$	$\begin{pmatrix} -t_{xx} & 0 & 0 \\ 0 & -t_{xx} & 0 \\ 0 & 0 & -t_{xx} \end{pmatrix}$	$m\bar{3}m'$	$\begin{pmatrix} \sigma_{xx} & 0 & 0 \\ 0 & \sigma_{xx} & 0 \\ 0 & 0 & \sigma_{xx} \end{pmatrix}$	$\begin{pmatrix} 0 & \sigma^z_{xy} & 0 \\ \sigma^y_{xz} & 0 & 0 \\ 0 & 0 & 0 \end{pmatrix}$
$\bar{4}'3m'$	$\begin{pmatrix} t_{xx} & 0 & 0 \\ 0 & t_{xx} & 0 \\ 0 & 0 & t_{xx} \end{pmatrix}$	$\begin{pmatrix} t_{xx} & 0 & 0 \\ 0 & t_{xx} & 0 \\ 0 & 0 & t_{xx} \end{pmatrix}$	$m\bar{3}m'$	$\begin{pmatrix} \sigma_{xx} & 0 & 0 \\ 0 & \sigma_{xx} & 0 \\ 0 & 0 & \sigma_{xx} \end{pmatrix}$	$\begin{pmatrix} 0 & \sigma^z_{xy} & 0 \\ \sigma^y_{xz} & 0 & 0 \\ 0 & 0 & 0 \end{pmatrix}$
$m'\bar{3}'m'$	$\begin{pmatrix} t_{xx} & 0 & 0 \\ 0 & t_{xx} & 0 \\ 0 & 0 & t_{xx} \end{pmatrix}$	$\begin{pmatrix} t_{xx} & 0 & 0 \\ 0 & t_{xx} & 0 \\ 0 & 0 & t_{xx} \end{pmatrix}$	$m\bar{3}m1'$	$\begin{pmatrix} \sigma_{xx} & 0 & 0 \\ 0 & \sigma_{xx} & 0 \\ 0 & 0 & \sigma_{xx} \end{pmatrix}$	$\begin{pmatrix} 0 & \sigma^z_{xy} & 0 \\ -\sigma^z_{xy} & 0 & 0 \\ 0 & 0 & 0 \end{pmatrix}$

for $T = 0$ K one finds a divergent behavior for the longitudinal conductivities σ_{xx} and σ_{zz} in the dilute regime, i.e., when x goes to 0 or 1, respectively. In both cases the variation with x is rather symmetric around the composition $x = 0.5$ as the two alloying components, Fe and Co, respectively, do not differ too much concerning their electronic properties in this fcc (111)-like structure. Apart from this general behavior one notes that one has $\sigma_{xx} > \sigma_{zz}$ for all concentrations. This is due to the simple fact that for σ_{xx} one has electronic transport parallel to the atomic layers while σ_{zz} implies transport perpendicular to the layers; the finite conductivity is not only because of the chemical disorder in the Fe-Co layers but in addition due to a strong geometrical confinement and corresponding interface scattering. Figure 2 (top) shows also the conductivity σ_{xx} and σ_{zz} calculated without the vertex corrections. As one can see, this restriction hardly changes the numerical results. This finding is very typical for transition metal systems with a high density of states at the Fermi energy implying a short mean free path length [67]. In contrast to the longitudinal conductivity σ_{ii} the transverse conductivity σ_{xy} has contributions from the Fermi surface as well as Fermi sea terms [see Eq. (1)] when the Kubo-Bastin formula is used (see comment below). Corresponding results for Pt|Fe_xCo_{1-x}|Cu are shown in the middle panel of Fig. 2. As one notes, the Fermi surface and sea contributions are comparable in magnitude but have opposite sign leading to a partial cancellation. Obviously, both contributions vary rather smoothly with concentration and show for the considered concentration range ($0.01 \leqslant x \leqslant 0.99$) in contrast for example to the binary alloys Fe_xPd_{1-x} and Ni_xPd_{1-x} [60] practically no divergent behavior in the dilute limit ($x \to 0$ or $x \to 1$). As discussed before [60] a divergent behavior of σ_{xy} can be ascribed to a strong skew scattering contribution that scales with the longitudinal conductivity σ_{xx} [68]. On the other hand, this extrinsic source for the transverse transport is accounted for by the contribution to σ_{xy} that is connected with the vertex corrections [60]. Inspecting Fig. 2 (middle) that shows results for the Fermi surface contribution to σ_{xy} obtained with and without the vertex corrections, one finds that these give rise only to minor corrections throughout the considered concentration regime. With the skew scattering mechanism being negligible and the intrinsic contribution dominating the system is obviously in the so-called dirty regime [68,69]. Considering the Fermi sea contribution to σ_{xy} (Fig. 2, middle) one finds no impact of the vertex corrections at all. This is fully in line with the findings of Turek *et al.* [70] who could show that this property has to be fulfilled for formal reasons within the TB-LMTO-CPA formalism. As a consequence, this implies that the skew scattering mechanism is, as to be expected, connected only to the Fermi surface contribution to σ_{xy}. This is a seemingly trivial precondition to get the full skew scattering contribution to σ_{xy} when performing Boltzmann type of calculations for the dilute regime that are restricted to the Fermi energy E_F [71]. In fact, this is to be expected because for the electrical conductivity tensor it is possible for the case $T = 0$ K to go from the Kubo-Bastin to the Kubo-Středa equation that has only contributions from the Fermi surface [51,72], i.e., the Fermi sea term can be eliminated exactly.

Considering the spin conductivity tensor the nonvanishing tensor elements σ^k_{ij} can again be found from symmetry

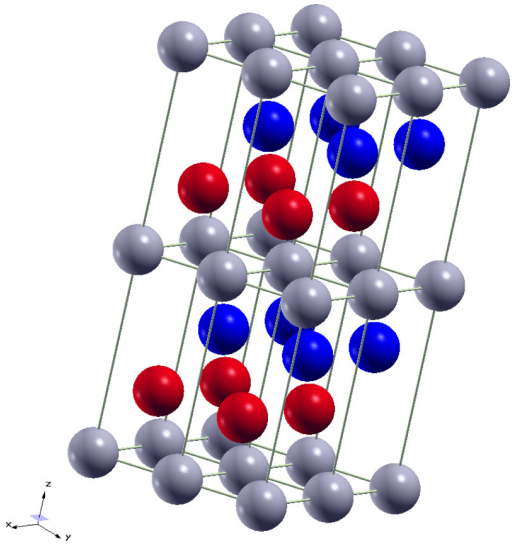

FIG. 1. Structure of the investigated multilayer system Pt|Fe_xCo_{1-x}|Cu consisting of a stacking of fcc (111) planes along the z axis. Cu atoms are colored in blue, Fe_xCo_{1-x} sites in red, and Pt atoms are represented in light gray.

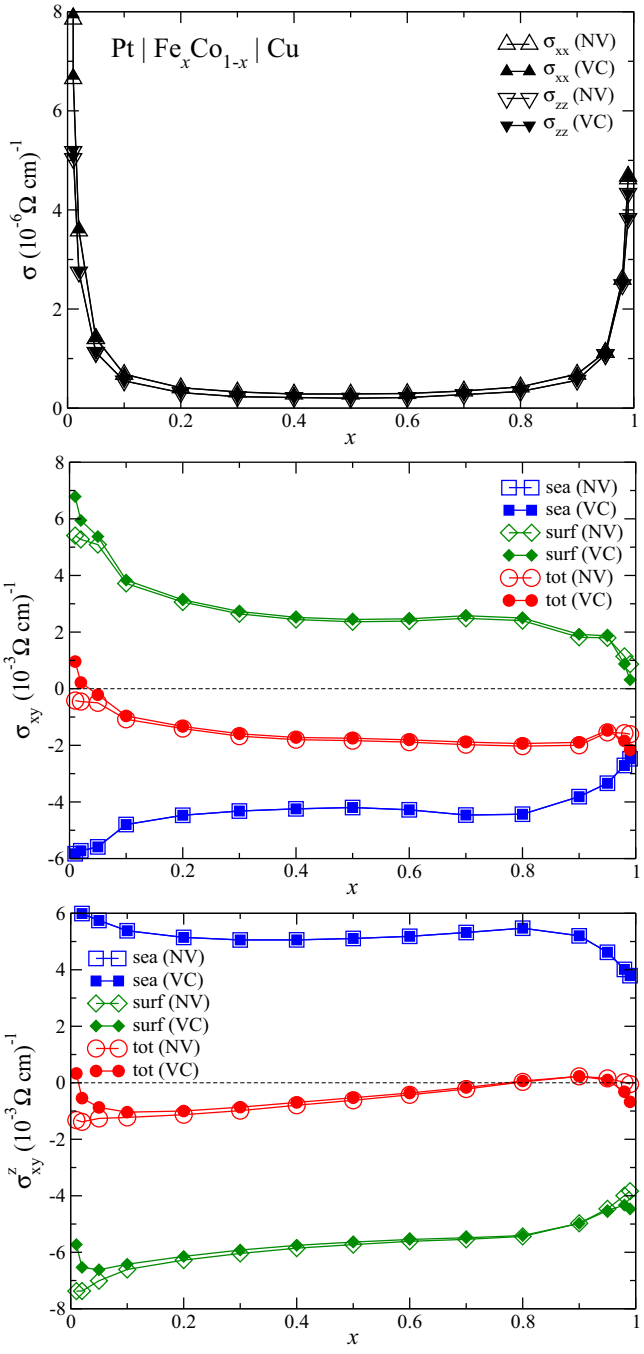

FIG. 2. Top: the longitudinal components $\sigma_{xx} = \sigma_{yy}$ and σ_{zz} of the conductivity tensor $\underline{\boldsymbol{\sigma}}$ of Pt|Fe$_x$Co$_{1-x}$|Cu as a function of the concentration x. Middle: the corresponding anomalous Hall conductivity $\sigma_{xy} = -\sigma_{yx}$. Bottom: the spin Hall conductivity $\sigma^z_{xy} = -\sigma^z_{yx}$. Open symbols represent calculations without vertex corrections (NV) and filled symbols those including vertex corrections (VC). The blue squares correspond to the Fermi sea contribution (sea), the green diamonds represent contributions from the Fermi surface (surf), and red circles give the total result (tot).

considerations [63]. Restricting here to the z component of the spin polarization one has the nonvanishing elements $\sigma^z_{xx} = \sigma^z_{yy} \neq \sigma^z_{zz}$ and $\sigma^z_{xy} = -\sigma^z_{yx}$, i.e., $\underline{\boldsymbol{\sigma}}^z$ has the same shape as $\underline{\boldsymbol{\sigma}}$. Comparing the corresponding numerical results for the transverse spin conductivity shown in the lower panel of Fig. 2 with their counterparts connected with the transverse conductivity σ_{xy} one finds a very similar behavior in the investigated concentration regime as follows. (i) The Fermi sea and surface contributions are comparable in magnitude but have different sign leading to a partial cancellation. (ii) The individual terms vary only slightly with concentration without showing a pronounced divergent behavior in the investigated range ($0.01 \leqslant x \leqslant 0.99$). (iii) The Fermi surface contribution shows a very weak impact of the vertex corrections. (iv) The Fermi sea contribution is hardly affected at all by them . The findings (iii) and (iv) again imply that the extrinsic contributions and with this the skew scattering contribution are very small. Finding (iv) that so far has been demonstrated only numerically is now (in contrast to the case of the electrical conductivity) by no means trivial. While the use of a Kubo-Středa-like equation for σ^z_{xy} turned out to be very successful when applied to metallic alloys [61], it nevertheless has to be seen as approximate [73]. For that reason the finding that there are hardly any vertex corrections to the Fermi sea part but essentially only for the Fermi surface part is now an important precondition for getting all relevant skew scattering contributions to σ^z_{xy} when performing calculations exclusively at the Fermi surface, e.g., based on the Boltzmann equation [71,74,75].

For the magnetization along the z axis Pt|Fe$_x$Co$_{1-x}$|Cu has the magnetic point group $3m'$ [76] leading to an antisymmetric torkance tensor with nonvanishing elements $t_{xx} = t_{yy} \neq t_{zz}$ and $t_{xy} = -t_{yx}$ (see third row of Table IV). Actually, because of the restrictions imposed by the form of the torque operator given in Eq. (2) the element t_{zz} that would represent a change in the magnitude of the magnetic moment along the z direction does not show up in the calculations. This impact of an external electric field has to be considered as a direct manifestation of the Edelstein effect [77,78] and can be described by a response quantity formulated appropriately. To this end, the torque operator in Eq. (2) has to be replaced by $\beta\boldsymbol{\sigma}$, the bare spin polarization operator. Accordingly, the difference between the two response phenomena only lies in the interaction with the local magnetization, if present [79]. The top panel of Fig. 3 gives the numerical results for the diagonal torkance element t_{xx}. As one can see, it has many properties in common with the longitudinal conductivity σ_{xx} as follows. (i) There is no Fermi sea contribution. (ii) It shows a divergent behavior in the dilute limit $x \to 0$ or $x \to 1$, respectively. (iii) The variation with composition is moreover again quite symmetric around the equiatomic center. (iv) Finally, as for σ_{xx}, we find only a very weak impact of the vertex corrections on the Fermi surface contribution that furthermore does not significantly increase towards the pure limits. This implies that there are no significant contributions due to skew scattering or the side-jump mechanism and accordingly the odd torkance t_{xx} is dominated by the intrinsic contribution. As a consequence, this torkance tensor element will only to a very limited extent be accessible by calculations based on the Boltzmann formalism. Considering t_{xy} one finds from Figs. 2 and 3 that this tensor element behaves much like σ_{xy} and σ^z_{xy} as follows. (i) The Fermi sea and surface contributions are quite comparable in magnitude but have different sign leading to a partial cancellation. (ii) Both parts are weakly concentration dependent with a more pronounced variation for the Fermi surface term on the Co-rich side. (iii)

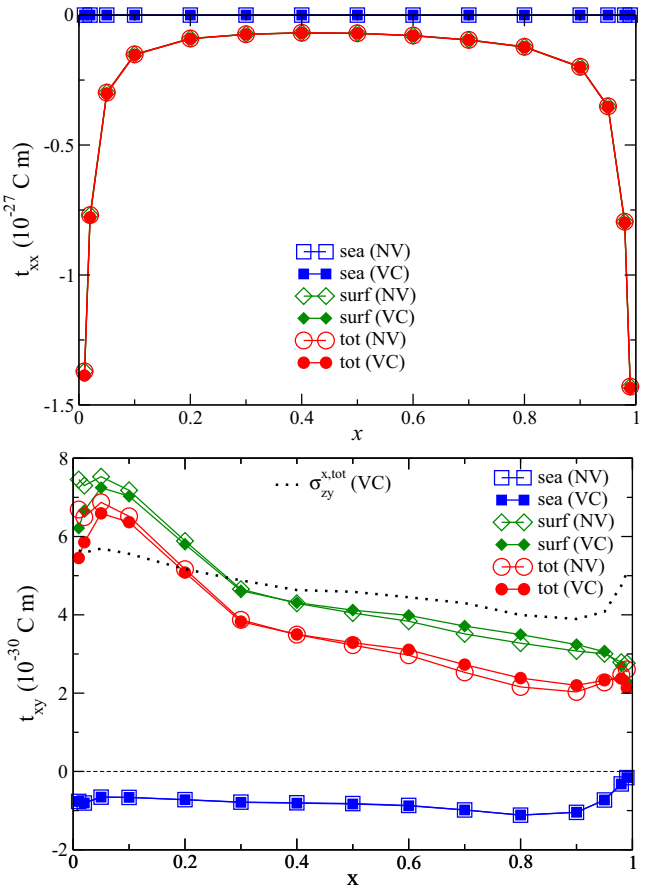

FIG. 3. Top: the longitudinal component $t_{xx} = t_{yy}$ of the SOT depending on the concentration. Bottom: the transverse component $t_{xy} = -t_{yx}$ of the SOT depending on the concentration. Use of symbols and colors as in Fig. 2. The black dotted line represents the total spin conductivity σ^{x}_{zy} in $(10^{-3}\ \Omega\,\mathrm{cm})^{-1}$ including vertex corrections.

The Fermi surface contribution shows a very weak impact of the vertex corrections. (iv) The Fermi sea contribution is almost unaffected by them. Again, from (iii) and (iv) one may conclude that the extrinsic contributions due to, e.g., the skew scattering are very small. As for t_{xx}, calculations based on the Boltzmann formalism are only able to account for this minor contribution to t_{xy}. The comparable concentration dependence of the spin "Hall" conductivity $\sigma^{x}_{zy} = -\sigma^{y}_{zx}$ (black dotted line in Fig. 3, bottom) and the even torkance t_{xy} seems to support previous suggestions that they are intimately connected [80].

The first *ab initio* investigations on the spin-orbit torque by Freimuth *et al.* [42,43] were dealing among others with Co/Pt(111) having the same symmetry as the system Pt|Fe_xCo_{1-x}|Cu considered here. As shown by these authors, the mirror planes perpendicular to the atomic layers imply the t_{xx} and t_{xy} to be odd and even, respectively, under reversal of the magnetization direction, i.e., one has $t_{xx}(\mathbf{m}) = -t_{xx}(-\mathbf{m})$ and $t_{xy}(\mathbf{m}) = t_{xy}(-\mathbf{m})$. Our numerical results are fully in line with this basic symmetry restriction. Freimuth *et al.* also used the Kubo-Bastin formalism, however, with the Green function represented in terms of Bloch functions and energy eigenvalues. This restricted the investigation to the very dilute limit with the impact of chemical or structural disorder represented by a broadening parameter Γ. Calculating the diagonal torkance element t_{xx} as a function of Γ leads in the limit $\Gamma \to 0$ to a divergent behavior. This is obviously in full accordance with the CPA results shown in Fig. 3 (top) that also show a divergence for the concentration $x \to 0$ or $x \to 1$, implying that the major impact of disorder on the diagonal torkance is essentially independent of the impurity type and does not arise due to the vertex corrections. Accordingly, the relevant aspect appears to be the lifetime broadening that is sufficiently well accounted for within the framework of the Gaussian disorder model used by Freimuth *et al.* [43]. A qualitative agreement between the two approaches in the dilute limit is also observed for the off-diagonal element t_{xy}. While t_{xy} given in Fig. 3 appears to vary between two finite values for pure Co ($x = 0$) and Fe ($x = 1$), without any sign of divergence in the considered composition regime, t_{xy} of Co/Pt(111) as calculated by Freimuth *et al.* [43] as a function of the broadening parameter takes a constant and finite value in the limit $\Gamma \to 0$. This suggests that in the dilute limit both approaches give access to the intrinsic contribution to the torkance. Concerning the decomposition of the torkance into Fermi sea and Fermi surface contributions, the results in Fig. 3 are again in qualitative agreement with the findings of Freimuth *et al.* [42,43]: the odd torkance element t_{xx} (top) has no Fermi sea contribution, whereas to the even t_{xy} (bottom) both Fermi sea and Fermi surface contribute significantly. Finally, as suggested before—amongst others by the aforementioned authors—the similar composition dependence of t_{xy} and the spin conductivity σ^{x}_{zy} seems to support at least in part the notion "spin Hall" torque.

IV. CONCLUSIONS

In summary, based on Kubo's linear response formalism, the symmetry and magnitude of spin-orbit torques in metals and alloys can be investigated using group-theoretical considerations for the former and an implementation of the Kubo-Bastin formula for the torkance in a multiple-scattering framework for the latter. The resulting tensor shapes for direct and inverse torkance for all magnetic point groups allowing for locally finite magnetization, as in ferro-, ferri-, as well as antiferromagnets, have been presented. The former have been independently confirmed for a number of systems by numerical calculations. For nonmagnetic point groups, i.e., neglecting the antiunitary operations involving time-reversal altogether, Železný *et al.* [66] obtained results for the direct torkance that are completely in line with Table I. By investigating the concentration dependence of two symmetrically distinct tensor elements in an fcc (111) trilayer system, contact and extensions could be made to previous work concerning the various contributions to the SOT and possible underlying mechanisms. While the odd torkance was found to bear a striking resemblance to the electrical conductivity concerning its dependence on the alloy composition in the ferromagnetic layer, the even component could be demonstrated to behave more like the transverse transport properties anomalous and spin Hall conductivity. The key advantage of the CPA alloy theory over simpler models of disorder is the possibility to calculate material-specific parameters very efficiently, paving the way for a computational materials design approach to

direct and inverse spin-orbit torques. As has been shown, the electronic contribution to the corresponding thermally induced phenomena, direct and inverse thermal spin-orbit torques, can in principle be calculated from the torkance employing a Mott-like expression. Future work will focus on the close connection between direct and inverse SOTs to the direct and inverse Edelstein effects as well as spin conductivities.

ACKNOWLEDGMENTS

The authors would like to thank Dr. S. Mankovsky for helpful discussions. Financial support by the *Deutsche Forschungsgemeinschaft* (German Science Foundation, DFG) via the programmes SPP 1538 and SFB 689 is gratefully acknowledged.

[1] A. Manchon and S. Zhang, Phys. Rev. B **78**, 212405 (2008).
[2] A. Manchon and S. Zhang, Phys. Rev. B **79**, 094422 (2009).
[3] I. Garate and A. H. MacDonald, Phys. Rev. B **80**, 134403 (2009).
[4] A. Chernyshov, M. Overby, X. Liu, J. K. Furdyna, Y. Lyanda-Geller, and L. P. Rokhinson, Nat. Phys. **5**, 656 (2009).
[5] I. M. Miron, G. Gaudin, S. Auffret, B. Rodmacq, A. Schuhl, S. Pizzini, J. Vogel, and P. Gambardella, Nat. Mater. **9**, 230 (2010).
[6] U. H. Pi, K. Won Kim, J. Y. Bae, S. C. Lee, Y. J. Cho, K. S. Kim, and S. Seo, Appl. Phys. Lett. **97**, 162507 (2010).
[7] G. Gaudin, I. M. Miron, P. Gambardella, and A. Schuhl, Magnetic memory element, Patent, US Patent applications No. 12/899,072, No. 12/899,091, and No. 12/959,980 (2010).
[8] For alternatives to the SOT for *control of magnetism by electric fields* see, for example, the same-titled review by Matsukara *et al.* [81].
[9] I. M. Miron, K. Garello, G. Gaudin, P.-J. Zermatten, M. V. Costache, S. Auffret, S. Bandiera, B. Rodmacq, A. Schuhl, and P. Gambardella, Nature (London) **476**, 189 (2011).
[10] J. Slonczewski, J. Magn. Magn. Mater. **159**, L1 (1996).
[11] L. Berger, Phys. Rev. B **54**, 9353 (1996).
[12] P. Gambardella and I. M. Miron, Philos. Trans. R. Soc. A **369**, 3175 (2011).
[13] K. Garello, I. M. Miron, C. O. Avci, F. Freimuth, Y. Mokrousov, S. Blügel, S. Auffret, O. Boulle, G. Gaudin, and P. Gambardella, Nat. Nanotechnol. **8**, 587 (2013).
[14] J. Kim, J. Sinha, M. Hayashi, M. Yamanouchi, S. Fukami, T. Suzuki, S. Mitani, and H. Ohno, Nat. Mater. **12**, 240 (2013).
[15] X. Qiu, P. Deorani, K. Narayanapillai, K.-S. Lee, K.-J. Lee, H.-W. Lee, and H. Yang, Sci. Rep. **4**, 4491 (2014).
[16] I. M. Miron, T. Moore, H. Szambolics, L. D. Buda-Prejbeanu, S. Auffret, B. Rodmacq, S. Pizzini, J. Vogel, M. Bonfim, A. Schuhl, and G. Gaudin, Nat. Mater. **10**, 419 (2011).
[17] L. Liu, O. J. Lee, T. J. Gudmundsen, D. C. Ralph, and R. A. Buhrman, Phys. Rev. Lett. **109**, 096602 (2012).
[18] L. Liu, C.-F. Pai, Y. Li, H. W. Tseng, D. C. Ralph, and R. A. Buhrman, Science **336**, 555 (2012).
[19] H. Reichlová, D. Kriegner, V. Holý, K. Olejník, V. Novák, M. Yamada, K. Miura, S. Ogawa, H. Takahashi, T. Jungwirth, and J. Wunderlich, Phys. Rev. B **92**, 165424 (2015).
[20] V. Tshitoyan, C. Ciccarelli, A. P. Mihai, M. Ali, A. C. Irvine, T. A. Moore, T. Jungwirth, and A. J. Ferguson, Phys. Rev. B **92**, 214406 (2015).
[21] W. Zhang, M. B. Jungfleisch, F. Freimuth, W. Jiang, J. Sklenar, J. E. Pearson, J. B. Ketterson, Y. Mokrousov, and A. Hoffmann, Phys. Rev. B **92**, 144405 (2015).
[22] S. Fukami, C. Zhang, S. Dutta Gupta, A. Kurenkov, and H. Ohno, Nat. Mater. **15**, 535 (2016).
[23] P. Wadley, B. Howells, J. Železný, C. Andrews, V. Hills, R. P. Campion, V. Novák, K. Olejník, F. Maccherozzi, S. S. Dhesi, S. Y. Martin, T. Wagner, J. Wunderlich, F. Freimuth, Y. Mokrousov, J. Kuneš, J. S. Chauhan, M. J. Grzybowski, A. W. Rushforth, K. W. Edmonds, B. L. Gallagher, and T. Jungwirth, Science **351**, 587 (2016).
[24] J. Železný, H. Gao, K. Výborný, J. Zemen, J. Mašek, A. Manchon, J. Wunderlich, J. Sinova, and T. Jungwirth, Phys. Rev. Lett. **113**, 157201 (2014).
[25] A. Hamadeh, O. d'Allivy Kelly, C. Hahn, H. Meley, R. Bernard, A. H. Molpeceres, V. V. Naletov, M. Viret, A. Anane, V. Cros, S. O. Demokritov, J. L. Prieto, M. Muñoz, G. de Loubens, and O. Klein, Phys. Rev. Lett. **113**, 197203 (2014).
[26] Y. Fan, P. Upadhyaya, X. Kou, M. Lang, S. Takei, Z. Wang, J. Tang, L. He, L.-T. Chang, M. Montazeri, G. Yu, W. Jiang, T. Nie, R. N. Schwartz, Y. Tserkovnyak, and K. L. Wang, Nat. Mater. **13**, 699 (2014).
[27] Y. Wang, P. Deorani, K. Banerjee, N. Koirala, M. Brahlek, S. Oh, and H. Yang, Phys. Rev. Lett. **114**, 257202 (2015).
[28] G. Yu, P. Upadhyaya, Y. Fan, J. G. Alzate, W. Jiang, K. L. Wong, S. Takei, S. A. Bender, L.-T. Chang, Y. Jiang, M. Lang, J. Tang, Y. Wang, Y. Tserkovnyak, P. K. Amiri, and K. L. Wang, Nat. Nanotechnol. **9**, 548 (2014).
[29] M. Cubukcu, O. Boulle, M. Drouard, K. Garello, C. O. Avci, I. M. Miron, J. Langer, B. Ocker, P. Gambardella, and G. Gaudin, Appl. Phys. Lett. **104**, 042406 (2014).
[30] G. Prenat, K. Jabeur, G. Pendina, O. Boulle, and G. Gaudin, *Spintronics-based Computing* (Springer International Publishing, Cham, 2015), Chap. Beyond STT-MRAM, Spin Orbit Torque RAM SOT-MRAM for High Speed and High Reliability Applications, p. 145.
[31] C. K. Safeer, E. Jué, A. Lopez, L. Buda-Prejbeanu, S. Auffret, S. Pizzini, O. Boulle, I. M. Miron, and G. Gaudin, Nat. Nanotechnol. **11**, 143 (2016).
[32] M. Yang, K. Cai, H. Ju, K. W. Edmonds, G. Yang, S. Liu, B. Li, B. Zhang, Y. Sheng, S. Wang, Y. Ji, and K. Wang, Sci. Rep. **6**, 20778 (2016).
[33] A. Matos-Abiague and R. L. Rodríguez-Suárez, Phys. Rev. B **80**, 094424 (2009).
[34] K.-W. Kim, J.-H. Moon, K.-J. Lee, and H.-W. Lee, Phys. Rev. Lett. **108**, 217202 (2012).
[35] G. Tatara, N. Nakabayashi, and K.-J. Lee, Phys. Rev. B **87**, 054403 (2013).
[36] L. Liu, T. Moriyama, D. C. Ralph, and R. A. Buhrman, Phys. Rev. Lett. **106**, 036601 (2011).
[37] P. M. Haney, H.-W. Lee, K.-J. Lee, A. Manchon, and M. D. Stiles, Phys. Rev. B **87**, 174411 (2013).
[38] A. Manchon, arXiv:1204.4869 [cond-mat.mes-hall].

[39] H. Kurebayashi, J. Sinova, D. Fang, A. C. Irvine, T. D. Skinner, J. Wunderlich, V. Novak, R. P. Campion, B. L. Gallagher, E. K. Vehstedt, P. L. Zarbo, K. Vyborny, A. J. Ferguson, and T. Jungwirth, Nat. Nanotechnol. **9**, 211 (2014).
[40] K.-W. Kim, K.-J. Lee, H.-W. Lee, and M. D. Stiles, Phys. Rev. B **92**, 224426 (2015).
[41] P. M. Haney, H.-W. Lee, K.-J. Lee, A. Manchon, and M. D. Stiles, Phys. Rev. B **88**, 214417 (2013).
[42] F. Freimuth, S. Blügel, and Y. Mokrousov, J. Phys.: Condens. Matter **26**, 104202 (2014).
[43] F. Freimuth, S. Blügel, and Y. Mokrousov, Phys. Rev. B **90**, 174423 (2014).
[44] K. M. D. Hals, A. Brataas, and Y. Tserkovnyak, Europhys. Lett. **90**, 47002 (2010).
[45] C. Ciccarelli, K. M. D. Hals, A. Irvine, V. Novak, Y. Tserkovnyak, H. Kurebayashi, A. Brataas, and A. Ferguson, Nat. Nanotechnol. **10**, 50 (2015).
[46] F. Freimuth, S. Blügel, and Y. Mokrousov, Phys. Rev. B **92**, 064415 (2015).
[47] G. Géranton, F. Freimuth, S. Blügel, and Y. Mokrousov, Phys. Rev. B **91**, 014417 (2015).
[48] F. Freimuth, S. Blügel, and Y. Mokrousov, J. Phys.: Condens. Matter **28**, 316001 (2016).
[49] During review, we became aware of related group-theoretical work by Železný *et al.* [66] on direct SOTs in ferro- and antiferromagnets, leading to completely identical results for point groups without time-reversal symmetry (see Table I).
[50] A. Bastin, C. Lewiner, O. Betbeder-matibet, and P. Nozieres, J. Phys. Chem. Solids **32**, 1811 (1971).
[51] A. Crépieux and P. Bruno, Phys. Rev. B **64**, 014416 (2001).
[52] The expression for the torkance tensor given here differs slightly from that given by Freimuth *et al.* [42,43] but is in full accordance with the corresponding expression for the conductivity tensor as given, for example, by Crépieux and Bruno [51].
[53] M. E. Rose, *Relativistic Electron Theory* (John Wiley & Sons, Inc., New York, London, 1961).
[54] T. L. Gilbert, IEEE Trans. Magn. **40**, 3443 (2004).
[55] H. Ebert, S. Mankovsky, D. Ködderitzsch, and P. J. Kelly, Phys. Rev. Lett. **107**, 066603 (2011).
[56] A. H. MacDonald and S. H. Vosko, J. Phys. C **12**, 2977 (1979).
[57] H. Ebert, in *Electronic Structure and Physical Properties of Solids*, edited by H. Dreyssé, Lecture Notes in Physics Vol. 535 (Springer, Berlin, Heidelberg, 2000), p. 191.
[58] H. Ebert, D. Ködderitzsch, and J. Minár, Rep. Prog. Phys. **74**, 096501 (2011).
[59] W. H. Butler, Phys. Rev. B **31**, 3260 (1985).
[60] S. Lowitzer, D. Ködderitzsch, and H. Ebert, Phys. Rev. Lett. **105**, 266604 (2010).
[61] S. Lowitzer, M. Gradhand, D. Ködderitzsch, D. V. Fedorov, I. Mertig, and H. Ebert, Phys. Rev. Lett. **106**, 056601 (2011).
[62] W. H. Kleiner, Phys. Rev. **142**, 318 (1966).
[63] M. Seemann, D. Ködderitzsch, S. Wimmer, and H. Ebert, Phys. Rev. B **92**, 155138 (2015).
[64] See, e.g., Eq. (11) of Ref. [82].
[65] The tensor shapes of the local torkances can also be determined by the magnetic point group of the sublattices that is a subgroup of the global group obtained by removing the antiunitary operation connecting them. If the parent group does not contain $\bar{1}$, the corresponding subgroup is also noncentrosymmetric.
[66] J. Železný, H. Gao, A. Manchon, F. Freimuth, Y. Mokrousov, J. Zemen, J. Mašek, J. Sinova, and T. Jungwirth, arXiv:1604.07590 [cond-mat.mtrl-sci].
[67] J. Banhart, H. Ebert, and A. Vernes, Phys. Rev. B **56**, 10165 (1997).
[68] N. Nagaosa, J. Sinova, S. Onoda, A. H. MacDonald, and N. P. Ong, Rev. Mod. Phys. **82**, 1539 (2010).
[69] R. Bianco, R. Resta, and I. Souza, Phys. Rev. B **90**, 125153 (2014).
[70] I. Turek, J. Kudrnovský, and V. Drchal, Phys. Rev. B **89**, 064405 (2014).
[71] B. Zimmermann, K. Chadova, D. Ködderitzsch, S. Blügel, H. Ebert, D. V. Fedorov, N. H. Long, P. Mavropoulos, I. Mertig, Y. Mokrousov, and M. Gradhand, Phys. Rev. B **90**, 220403 (2014).
[72] P. Středa, J. Phys. C **15**, L717 (1982).
[73] D. Ködderitzsch, K. Chadova, and H. Ebert, Phys. Rev. B **92**, 184415 (2015).
[74] M. Gradhand, D. V. Fedorov, P. Zahn, and I. Mertig, Phys. Rev. B **81**, 020403 (2010).
[75] C. Herschbach, D. V. Fedorov, I. Mertig, M. Gradhand, K. Chadova, H. Ebert, and D. Ködderitzsch, Phys. Rev. B **88**, 205102 (2013).
[76] More precisely $31m'$ or $3m'1$, depending on the axis convention for the corresponding space group. Results for the former are given here; the tensors for the other can be obtained by a rotation of the coordinate system by $\pi/2$ around the principal axis. See Ref. [63] for details .
[77] A. G. Aronov and Y. B. Lyanda-Geller, JETP Lett. **50**, 431 (1989).
[78] V. M. Edelstein, Solid State Commun. **73**, 233 (1990).
[79] The close connection between spin-orbit torques and the Edelstein effect has already been mentioned earlier [3–5] and we find that, as also Železný *et al.* [66] point out, the tensor forms for direct torkance and direct Edelstein response are indeed identical when considering a general direction of the magnetization for the former.
[80] See, e.g., Eq. (76) of Ref. [63] for an explicit relation.
[81] F. Matsukura, Y. Tokura, and H. Ohno, Nat. Nanotechnol. **10**, 209 (2015).
[82] K. M. D. Hals and A. Brataas, Phys. Rev. B **91**, 214401 (2015).

The following is a copy of the article *Composition-dependent magnetic response properties of* $Mn_{1-x}Fe_xGe$ *alloys* [368], reprinted with permission from

S. Mankovsky, S. Wimmer, S. Polesya, and H. Ebert,
Phys. Rev. B **97**, 024403 (2018).

PHYSICAL REVIEW B **97**, 024403 (2018)

Composition-dependent magnetic response properties of $Mn_{1-x}Fe_xGe$ alloys

S. Mankovsky, S. Wimmer, S. Polesya, and H. Ebert
Dept. Chemie/Phys. Chemie, LMU Munich, Butenandtstrasse 11, D-81377 Munich, Germany

(Received 23 October 2017; published 3 January 2018)

The composition-dependent behavior of the Dzyaloshinskii–Moriya interaction (DMI), the spin-orbit torque (SOT), as well as anomalous and spin Hall conductivities of $Mn_{1-x}Fe_xGe$ alloys have been investigated by first-principles calculations using the relativistic multiple scattering Korringa–Kohn–Rostoker (KKR) formalism. The D_{xx} component of the DMI exhibits a strong dependence on the Fe concentration, changing sign at $x \approx 0.85$ in line with previous theoretical calculations as well as with experimental results demonstrating the change of spin helicity at $x \approx 0.8$. A corresponding behavior with a sign change at $x \approx 0.5$ is predicted also for the Fermi-sea contribution to the SOT, because this is closely related to the DMI. In the case of anomalous and spin Hall effects it is shown that the calculated Fermi-sea contributions are rather small and the composition-dependent behavior of these effects are determined mainly by the electronic states at the Fermi level. The spin-orbit-induced scattering mechanisms responsible for both these effects suggest a common origin of the minimum of the anomalous Hall effect and the sign change of the spin Hall effect conductivities.

DOI: 10.1103/PhysRevB.97.024403

I. INTRODUCTION

During the last decade skyrmionic magnetic materials have moved into the focus of scientific interest because their unique properties hold promise for various applications in magnetic storage and spintronic devices [1]. The key role for the formation of a skyrmion magnetic texture is played by the Dzyaloshinskii–Morirya interaction (DMI) [2,3]. Its competition with the isotropic exchange interaction, magnetic anisotropy, and the Zeeman interaction in the presence of an external magnetic field determines the size of skyrmions and the region of stability in the corresponding phase diagram. Another important characteristic feature of skyrmions is their helicity (i.e., the spin spiraling direction), which is determined by the orientation of the involved Dzyaloshinskii–Morirya interaction vectors and can be exploited as an additional degree of freedom for the manipulation of skyrmions [4–6]. The correlation between the skyrmion helicity and crystal chirality has already been discussed in the literature [7,8]. Recent experiments have demonstrated in addition a change of the skyrmion helicity with the chemical composition in the case of B20 alloys [9,10] while the crystal chirality was unaltered. This finding opens an alternative possibility for DMI engineering in order to manipulate the skyrmion helicity.

This holds particularly true for the $Mn_{1-x}Fe_xGe$ alloy system which is in the center of interest for the present investigation. Experimentally, it was found [9,11] that the size of skyrmions in this material can be tuned by changing the Fe concentration, reaching a maximum at $x \sim 0.8$ [11], i.e., at the concentration when the skyrmion helicity changes sign without a change of the crystal chirality. This behavior was investigated theoretically [12,13] via first-principles calculations of the DMI and analyzing the details of the electronic structure that may have an influence on it. Gayles *et al.* [12] have demonstrated that the sign of the DMI in $Mn_{1-x}Fe_xGe$ can be explained by the relative positions in energy of the $d^{\uparrow}_{xy}$ and $d^{\downarrow}_{x^2-y^2}$ states of Fe which change when the Fe concentration increases above $x \sim 0.8$. As a consequence, a flip of the chirality of the magnetic texture occurs. Similar conclusions have been drawn by Koretsune *et al.* [13]. While these calculations have been done by treating chemical disorder within the virtual crystal approximation (Ref. [12]) or even by employing the rigid-band approximation (Ref. [13]), the present work is based on the coherent-potential approximation (CPA) alloy theory, which should give more reliable results for the electronic structure of disordered alloys.

In addition we investigate the concentration dependence of the response properties connected to spin-orbit coupling (SOC) in the presence of an applied electric field, i.e., the spin-orbit torque (SOT), the anomalous Hall effect (AHE), and the spin Hall effect (SHE), because these are important for practical applications. Especially, we focus on the SOT, expecting common features with the DMI according to recent findings by Freimuth *et al.* [14].

This article is organized as follows: We start with theoretical details on the formalisms employed to calculate DMI parameters and linear-response coefficients from first principles in Sec. II. Results for the $Mn_{1-x}Fe_xGe$ alloy system are presented and discussed in Sec. III, subdivided into Dzyaloshinskii–Morirya interaction (III A), spin-orbit torque (III B), anomalous and spin Hall conductivity (III C), and symmetry considerations (III D). We conclude with a brief summary in Sec. IV. Additional derivations connected to the expressions in Sec. II are given in the appendix.

II. THEORETICAL DETAILS

All calculations were performed by using the fully relativistic Korringa–Kohn–Rostoker (KKR) Green's function method [15,16] within the framework of local spin-density approximation (LSDA) to density functional theory (DFT) and the parametrization scheme for the exchange and correlation potential as given by Vosko *et al.* [17]. A cutoff $l_{\max} = 3$

was used for the angular-momentum expansion of the Green's function. The chemical disorder was treated within the coherent-potential approximation (CPA) alloy theory [18,19].

To investigate the composition-dependent behavior of the skyrmion size and helicity observed in experiment, we have calculated the D_{xx} element of the micromagnetic DMI tensor as a function of Fe concentration x. As was demonstrated previously [20], this quantity can be calculated in two different ways: Either by performing a direct evaluation of the expression

$$D_{\mu\nu} = \frac{1}{\pi}\mathrm{Re}\,\mathrm{Tr}\int^{E_\mathrm{F}} dE(E-E_\mathrm{F}) \times\frac{1}{\Omega_{BZ}}\int d^3k\Big[\underline{O}(E)\underline{\tau}(\mathbf{k},E)\underline{T}_\mu(E)\frac{\partial}{\partial k_\nu}\underline{\tau}(\mathbf{k},E) - \underline{T}_\mu(E)\underline{\tau}(\mathbf{k},E)\underline{O}(E)\frac{\partial}{\partial k_\nu}\underline{\tau}(\mathbf{k},E)\Big], \quad (1)$$

with the overlap integrals and the matrix elements of the torque operator $\hat{T}_\mu = \beta[\boldsymbol{\sigma}\times\hat{z}]_\mu B_{xc}(\mathbf{r})$ [21],

$$[\underline{O}]_{\Lambda\Lambda'} = \int_\Omega d^3r\, Z^\times_\Lambda(\mathbf{r},E)Z^j_{\Lambda'}(\mathbf{r},E),$$
$$[\underline{T}_\mu]_{\Lambda\Lambda'} = \int_\Omega d^3r\, Z^\times_\Lambda(\mathbf{r},E)\hat{T}_\mu Z^j_{\Lambda'}(\mathbf{r},E), \quad (2)$$

or by using the interatomic D^{ij}_μ interactions

$$D_{\mu\nu} = \sum_{ij} D^{ij}_\mu(\mathbf{R}_j-\mathbf{R}_i)_\nu, \quad (3)$$

which are calculated in an analogous way [20].

The current-induced torkance [22] and the anomalous [23] and spin [24] Hall conductivities were calculated within the Kubo linear-response formalism using the expression

$$\mathcal{R}_{\mu\nu} = \mathcal{R}^I_{\mu\nu} + \mathcal{R}^{II}_{\mu\nu} = -\frac{\hbar}{4\pi\Omega}\int_{-\infty}^{\infty}\frac{df(E)}{dE}\mathrm{Tr}\langle\hat{B}_\mu(\hat{G}^+-\hat{G}^-)\hat{A}_\nu\hat{G}^- - \hat{B}_\mu\hat{G}^+\hat{A}_\nu(\hat{G}^+-\hat{G}^-)\rangle dE + \frac{\hbar}{4\pi\Omega}\int_{-\infty}^{\infty}f(E) \times\mathrm{Tr}\Big\langle\Big(\hat{B}_\mu\hat{G}^+\hat{A}_\nu\frac{d\hat{G}^+}{dE} - \hat{B}_\mu\frac{d\hat{G}^+}{dE}\hat{A}_\nu\hat{G}^+\Big) - ([\cdots\hat{G}^-\cdots])\Big\rangle dE, \quad (4)$$

where $\mathcal{R}^I_{\mu\nu}$ and $\mathcal{R}^{II}_{\mu\nu}$ are the Fermi-surface and Fermi-sea contributions, respectively. The operator $\hat{A}_\nu$ representing in all three cases the perturbation is the electric current-density operator $\hat{j}_\nu = -|e|c\alpha_\nu$. For the calculations of the anomalous Hall conductivity one has for the response $\hat{\mathbf{B}} = \hat{\mathbf{A}}$, for the spin Hall conductivity $\hat{\mathbf{B}} = \hat{\mathbf{P}}\hat{\mathbf{A}}$ with the relativistic spin-polarization operator $\hat{\mathbf{P}}$ [25,26], while for the calculations of the spin-orbit torkances $t_{\mu\nu}$ the torque operator $\hat{B}_\mu = \hat{T}_\mu$ has to be used. Additional calculations for the Fermi-sea torkance have been performed by following the relationship between this quantity and the DMI parameters as suggested by Freimuth *et al.* [14]. In line with Eq. (2), these calculations were based on the expression

$$t^{\mathrm{sea}}_{\mu\nu} = -\frac{e}{\pi}\mathrm{Re}\,\mathrm{Tr}\int^{E_\mathrm{F}} dE \times\frac{1}{\Omega_{BZ}}\int d^3k\Big[\underline{O}(E)\underline{\tau}(\mathbf{k},E)\underline{T}_\mu(E)\frac{\partial}{\partial k_\nu}\underline{\tau}(\mathbf{k},E) - \underline{T}_\mu(E)\underline{\tau}(\mathbf{k},E)\underline{O}(E)\frac{\partial}{\partial k_\nu}\underline{\tau}(\mathbf{k},E)\Big], \quad (5)$$

which obviously differs, apart from prefactors, from Eq. (2) only by the weighting factor $(E-E_\mathrm{F})$. Both expressions for $t^{\mathrm{sea}}_{\mu\nu}$ should be equivalent, as can be demonstrated for the particular case of a translationally invariant system. In this case the relationship between Eq. (6) and the Fermi-sea term $t^{\mathrm{sea}}_{\mu\nu}$ in Eq. (4) can be established by using the expression for the group velocity suggested by Shilkova and Shirokovskii discussed below [27–29] (see Sec. A).

Alternatively, we have

$$t_{\mu\nu} = \sum_{ij} t^{ij}_\mu(\mathbf{R}_j-\mathbf{R}_i)_\nu, \quad (6)$$

with the interatomic torkance terms

$$t^{ij}_\mu = -\Big(\frac{e}{2\pi}\Big)\mathrm{Im}\,\mathrm{Tr}\int^{E_\mathrm{F}} dE\sum_{\Lambda_1\Lambda_2\Lambda_3\Lambda_4} \times\big[O^j_{\Lambda_4\Lambda_1}(E)\tau^{ji}_{\Lambda_1\Lambda_2}(E)T^i_{\mu,\Lambda_2\Lambda_3}(E)\tau^{ij}_{\Lambda_3\Lambda_4}(E) - O^i_{\Lambda_4\Lambda_1}(E)\tau^{ij}_{\Lambda_1\Lambda_2}(E)T^j_{\mu,\Lambda_2\Lambda_3}(E)\tau^{ji}_{\Lambda_3\Lambda_4}(E)\big], \quad (7)$$

which are obtained in analogy to the interatomic DMI parameters.

III. RESULTS AND DISCUSSION

A. Dzyaloshinskii–Moriya interaction

In the following we first focus on the behavior of the DMI in $Mn_{1-x}Fe_xGe$ as a function of Fe concentration x. The dependence of the DMI parameter $D_{xx}(x)$ on x is plotted in Fig. 1(a) in comparison with available theoretical results from other groups [12,30]. The results calculated by using an explicit expression for D_{xx} derived recently [20] are given by open diamonds, while those based on the interatomic interaction parameters $\mathbf{D}^{ij}$ are given by solid circles. Although the latter value has contributions only from the $\mathbf{D}^{ij}_{\text{Fe-Fe}}$, $\mathbf{D}^{ij}_{\text{Mn-Mn}}$, and $\mathbf{D}^{ij}_{\text{Fe-Mn}}$ interatomic DMI pair interaction terms, both results are in very good agreement with each other. They also fit reasonably well to the theoretical results by other groups shown by dashed [12] and dashed-dotted [30] lines. The deviations between these and the present work are most likely caused by the different approach used to treat the chemical disorder in the alloy. As was mentioned above, the CPA alloy theory was used in the present work, while the previous results [12,30] have been obtained by using the so-called virtual crystal approximation. As follows from Fig. 1(a), $D_{xx}(x)$ changes sign at $x\approx 0.8$, in line with the experimental observation [11]. A very similar concentration dependence is also observed for the $D_{yy}(x)$ component (open squares). The deviation from $D_{xx}(x)$, which is allowed by crystal symmetry (see Sec. III D), is itself a function of x but small throughout. From the element-projected plots shown in Fig. 1(b) one can see that $D^{\mathrm{Fe}}_{xx}(x)$ and $D^{\mathrm{Mn}}_{xx}(x)$

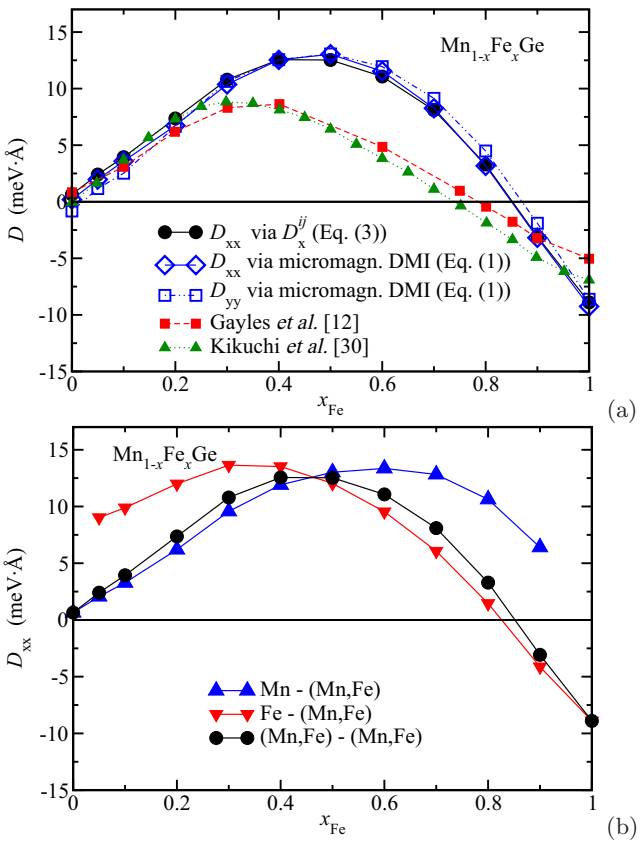

FIG. 1. (a) Results for $D_{xx}(x)$ in $Mn_{1-x}Fe_xGe$ calculated by using Eq. (3) (circles) and for $D_{xx}(x)$ (diamonds) and $D_{yy}(x)$ (empty squares) calculated by using using Eq. (2) in comparison with the results of other calculations from Ref. [12] (filled squares) and Ref. [30] (triangles). (b) The element-resolved Dzyaloshinskii–Moriya interaction in $Mn_{1-x}Fe_xGe$ D_{xx}^{Mn} (triangles up) and D_{xx}^{Fe} (triangles down). The total $D_{xx}(x)$ function is again shown as circles as in panel (a).

have their maxima at a different Fe concentration, i.e., at $x \approx 0.3$ and $x \approx 0.6$ for Fe and Mn, respectively. As one notes, $D_{xx}^{Fe}(x)$ changes its sign at $x \sim 0.8$ if x increases, while $D_{xx}^{Mn}(x)$ does not change sign. In the case of the DMI strength approaching zero, the system exhibits a ferromagnetically (FM) ordered structure. Grigoriev *et al.* [11] have reported the experimentally measured Curie temperature $T_C = 234.3$ K for the $Mn_{1-x}Fe_xGe$ alloy at $x = 0.75$. The Curie temperature calculated via Monte Carlo simulations in the present work for $x = 0.8$ is $T_C \approx 290$ K, slightly overestimating the experimental value. Note however, that these calculations are based on exchange coupling parameters calculated for the FM reference state at $T = 0$ K, while more accurate results require calculations based on the magnetically disordered state, which can be performed within the so-called disordered local moment (DLM) scheme [31,32].

The observed concentration dependence of the DMI was associated in the literature [12,13,30] with specific features of the electronic structure and their modification with the Fe concentration x. Figure 2 shows corresponding results of electronic structure calculations making use of the CPA alloy theory, i.e., the spin- and element-resolved density of states (DOS) on Mn [Fig. 2(a)] and Fe [Fig. 2(b)] sites in $Mn_{1-x}Fe_xGe$ for the three different concentrations $x = 0.1$, 0.5, and 0.9. As one can see in the bottom panels, the occupied majority-spin states of Mn and Fe are very close to each other and hardly depend on the Fe concentration. Obviously, chemical disorder has only a weak impact for this spin subsystem, leading to a rather weak disorder-induced smearing of the energy bands. This can be seen as well in Figs. 3(c) and 3(d), which show the Bloch spectral function for majority-spin states in $Mn_{0.9}Fe_{0.1}Ge$ and $Mn_{0.1}Fe_{0.9}Ge$, respectively. On the other hand, the different exchange splitting for the electronic states on Mn and Fe sites leads to different positions for their minority-spin states and as a consequence to a pronounced disorder-induced smearing of the energy bands for the disordered $Mn_{1-x}Fe_xGe$ alloys. Again this can be seen in the upper panels of Figs. 2(a) and 2(b), as well as in Figs. 3(a) and 3(b), showing the Bloch spectral function for minority-spin states in case of $x = 0.1$ and 0.9, respectively. Moreover, the exchange splitting for Fe and Mn both decreases upon increasing the Fe concentration. As a consequence, the Fe and Mn spin magnetic moments decrease simultaneously, as can be seen in Fig. 4.

Figure 2 indicates that the concentration-dependent modification of the electronic structure has twofold character. First, the Fe minority-spin $d^{\downarrow}_{x^2-y^2}$ states move down in energy from their position above the Fermi level at small Fe concentration [$x = 0.1$, solid line in Fig. 2(b)] to a position below the Fermi energy at high Fe content [$x = 0.9$, dashed line in Fig. 2(b)]. Additionally, a weak shift of the majority-spin $d^{\uparrow}_{xy}$ states of Fe towards the Fermi energy can be observed. This behavior, as discussed previously [12,13], leads to a sign change of the Fe-projected as well as the total DMI at $x \sim 0.8$. At the same time, Fig. 2(a) shows that the minority-spin $d^{\downarrow}_{x^2-y^2}$ states of Mn stay essentially unoccupied over the whole concentration range. As a consequence, $D_{xx}^{Mn}(x)$ does not exhibit any sign changes. As the positions of the element-projected minority-spin states of Fe and Mn are rather different (see Fig. 2), the increase of the contributions of minority-spin Fe states with increasing x in parallel with the decreasing contribution of corresponding Mn states leads for the alloy system to an apparent shift of the electronic energy bands. According to Refs. [12,13], this should also lead to a sign change of the DMI parameter.

Finally, it is worth mentioning that there are different trends in the behavior of the DMI parameter in the Mn-rich limit when comparing theoretical results (both present and previous) with experimental data [11]. As was remarked by Gayles *et al.* [12], the origin of this difference is not clear and the authors suggest certain mechanisms to be responsible for that. We would like to add here that the micromagnetic DMI components are the results of a summation of pair interactions over all neighbors. Although the Mn-Mn DMI have in general even larger magnitude than the Fe-Fe interactions, their summation leads to a small total DMI due to their oscillating behavior as a function of distance. This leads in the case of MnGe to a significant compensation of all contributions. For a more realistic description of the experimental situation at finite temperature, involving in particular noncollinear spin texture, Monte Carlo simulations based on atomistic spin models might be important [33].

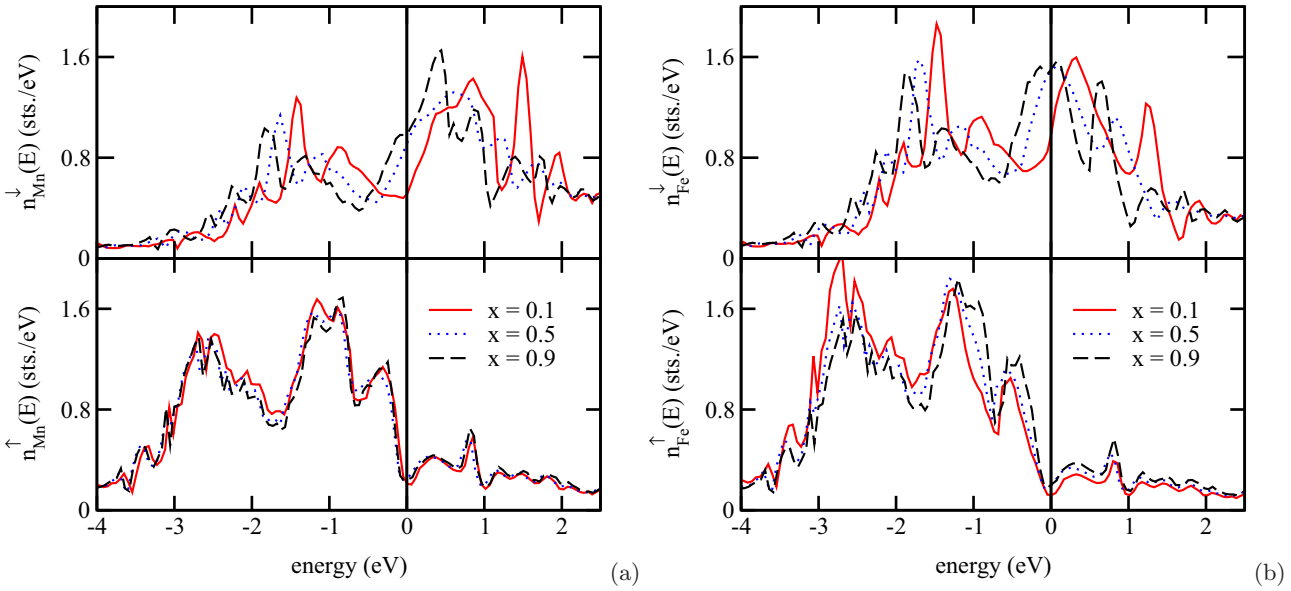

FIG. 2. The spin- and element-resolved DOS on (a) Mn and (b) Fe atoms in $Mn_{1-x}Fe_xGe$ for $x = 0.1$, 0.5, and 0.9.

B. Spin-orbit torque

The torkance tensor element $t_{xx}(x)$ representing the spin-orbit torque (SOT) calculated for $Mn_{1-x}Fe_xGe$ within the Kubo formalism [22] is represented in Fig. 5(a) by filled squares. In contrast to $D_{xx}(x)$, it changes sign three times when x increases. However, one has to note that this behavior is caused by two contributions to the torkance, showing a quite different concentration dependence: the Fermi-surface contribution from electronic states at the Fermi energy (open circles) and the Fermi-sea contribution due to all states below the Fermi energy (filled circles). Both contributions vary nonmonotonically with x and both change sign at $x \sim 0.5$, having however an opposite slope in the vicinity of this point. As a consequence, their combination leads to a partial cancellation in the total torkance that has a completely different concentration dependence when compared with the individual contributions.

Despite similarities in the behavior of $D_{xx}(x)$ and the Fermi-sea torkance $t^{\text{sea}}_{xx}(x)$, they change sign at different x values (0.8 and 0.5, respectively). To make a more detailed comparison, we calculate the Fermi-sea torkance by using the expressions in Eqs. (5) and (6). The results are plotted in Fig. 5(b) (triangles and squares, respectively) in comparison with the results based on the linear-response expression Eq. (4) (circles), demonstrating good agreement between all three types of

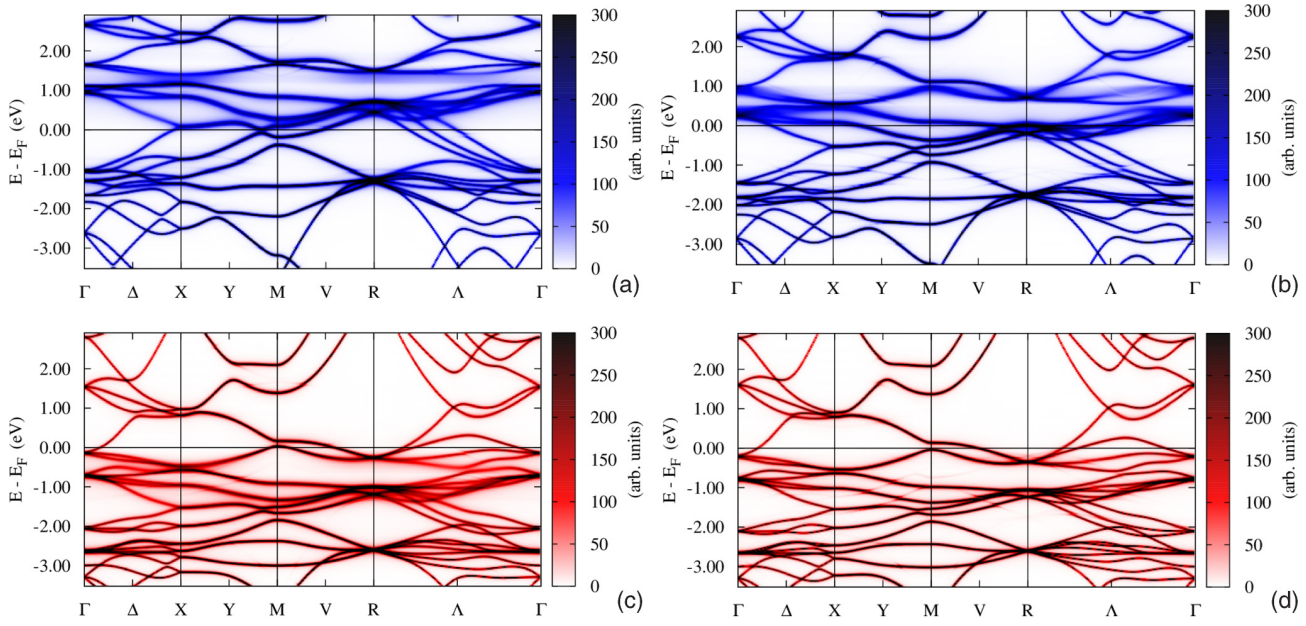

FIG. 3. The spin-resolved Bloch spectral function in $Mn_{0.9}Fe_{0.1}Ge$ and $Mn_{0.1}Fe_{0.9}Ge$ for (a), (b) minority- and (c), (d) majority-spin states, respectively.

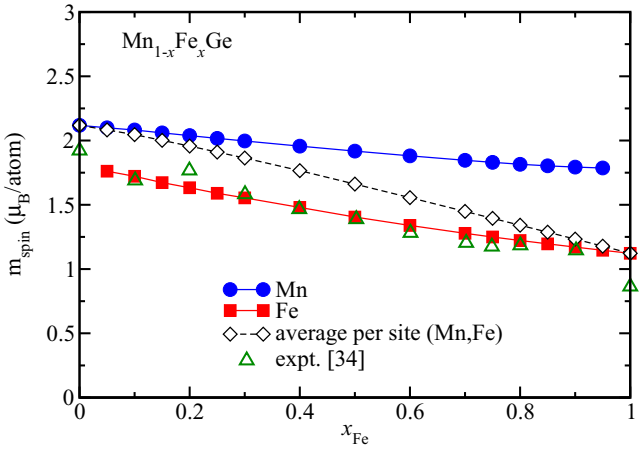

FIG. 4. Spin magnetic moments of Mn (circles) and Fe (squares) in $Mn_{1-x}Fe_xGe$ alloy, and the average magnetic moment per site (diamonds). Experimental results of Kanazawa *et al.* [34] are shown as green triangles.

calculations. The difference in the concentrations when the $D_{xx}(x)$ and $t_{xx}^{\rm sea}(x)$ functions change sign can obviously be attributed to the weighting factor $(E - E_{\rm F})$ in the expression for the DMI [20], which results in a different energy region

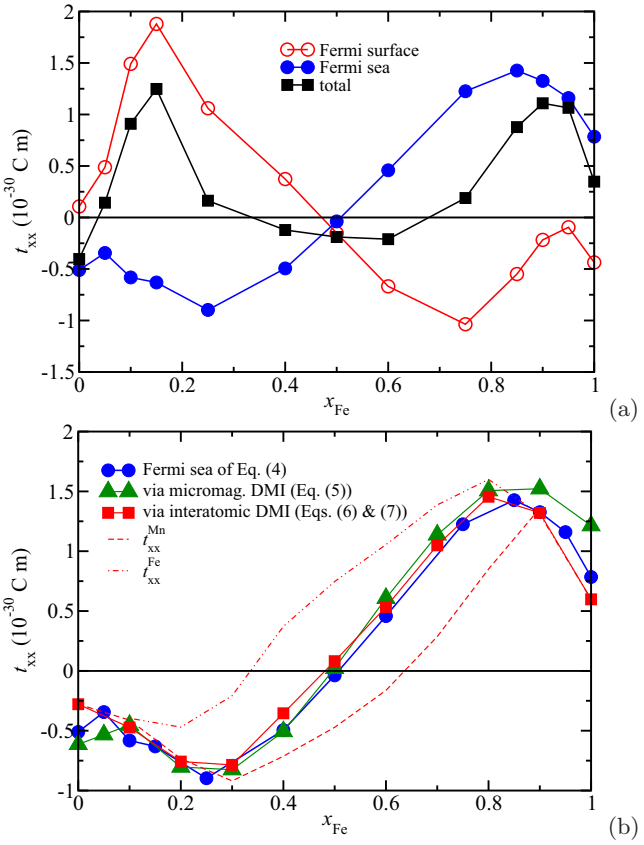

FIG. 5. (a) Total torkance per unit cell (solid squares) as well as its Fermi surface (empty circles) and Fermi sea (filled circles) contributions in $Mn_{1-x}Fe_xGe$ calculated via the Kubo–Bastin formalism [Eq. (4)]. (b) Comparison of Fermi-sea contribution to the torkance calculated via Eq. (4) (circles) with results obtained using the expressions (5) (triangles) and (6) (squares).

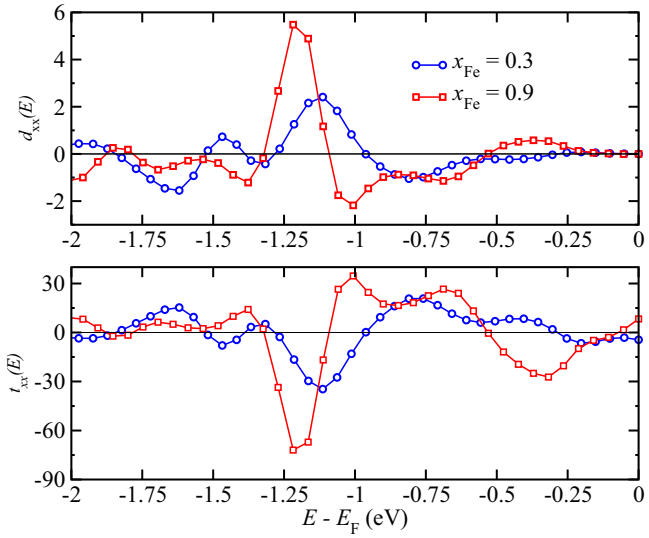

FIG. 6. Energy dependence of the DMI parameter $D_{xx}(E)$ (upper panel) and the torkance $t_{xx}(E)$ (lower panel) in $Mn_{0.7}Fe_{0.3}Ge$ (circles) and $Mn_{0.1}Fe_{0.9}Ge$ (squares). Integrated up to the Fermi energy $E_{\rm F}$, these functions give t_{xx} and D_{xx}.

for the dominating contributions to the $D_{xx}(x)$ function when compared with the torkance term $t_{xx}^{\rm sea}(x)$. This is demonstrated in Fig. 6, which gives the energy-resolved DMI parameter and the Fermi-sea torkance for two different Fe concentrations. In addition, note that the contributions to $t_{xx}^{\rm sea}(x)$ associated with the alloy components Mn and Fe, shown in Fig. 5(b) by dashed and dash-dotted curves, change sign at different concentrations x. Nevertheless, because of the strong exchange interaction between these two components located on the same sublattice, one has to discuss the component-averaged torkance when considering the SOT in the alloy.

Finally, considering the Fermi-surface and Fermi-sea contributions to the SOT separately in the pure limits, i.e., for the MnGe and FeGe compounds [see Fig. 5(a)], one finds a different sign for these contributions. This allows us to conclude that the intrinsic torkance is mainly responsible for the sign change of the SOT when the Fe concentration changes from 0 to 1. It is determined by the characteristics of the electronic structure discussed above. On the other hand, in the case of disordered $Mn_{1-x}Fe_xGe$ alloys the extrinsic contributions to the SOT cannot be completely neglected. Although small and only relevant at the Fermi surface, they are responsible together with the intrinsic contribution for the concentration dependence of the SOT and jointly determine the exact composition at which the torkance changes its sign.

C. Anomalous and spin Hall conductivity

To have a more complete picture of the SOC-induced response to an external electric field in $Mn_{1-x}Fe_xGe$, we briefly discuss the corresponding results for the transport-properties anomalous Hall effect (AHE) and spin Hall effect (SHE) (see, e.g., Refs. [35,36], respectively). As is the case for the current-induced spin-orbit torkance, these phenomena are caused by a SOC-induced spin asymmetry in the electron scattering.

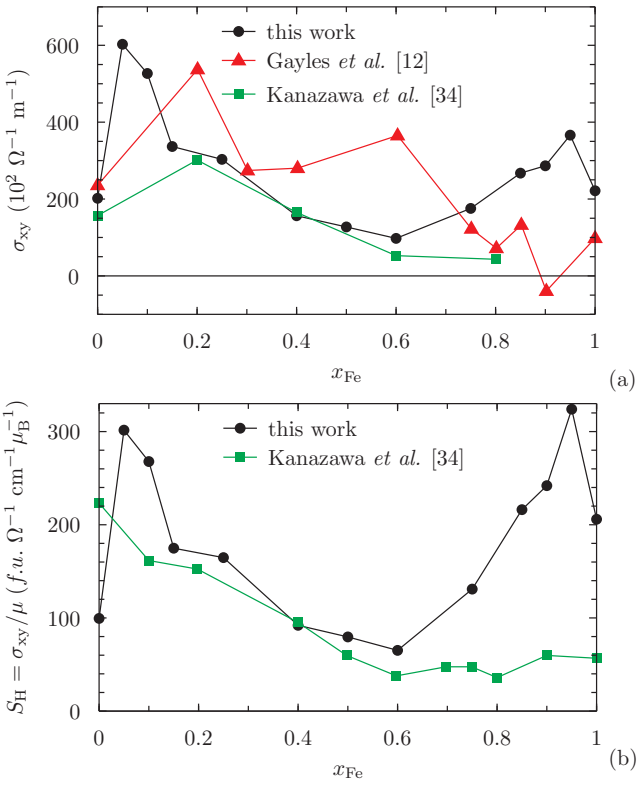

FIG. 7. (a) Anomalous Hall conductivity calculated for $Mn_{1-x}Fe_xGe$ via the CPA–Kubo–Bastin formalism (circles), compared with calculations using the Berry-curvature approach and the virtual crystal approximation [12] (triangles), and with low-temperature experimental data (squares) [34]. (b) Anomalous Hall coefficient calculated via the Kubo–Bastin equation (circles) compared with experimental data at 50 K (squares) [34].

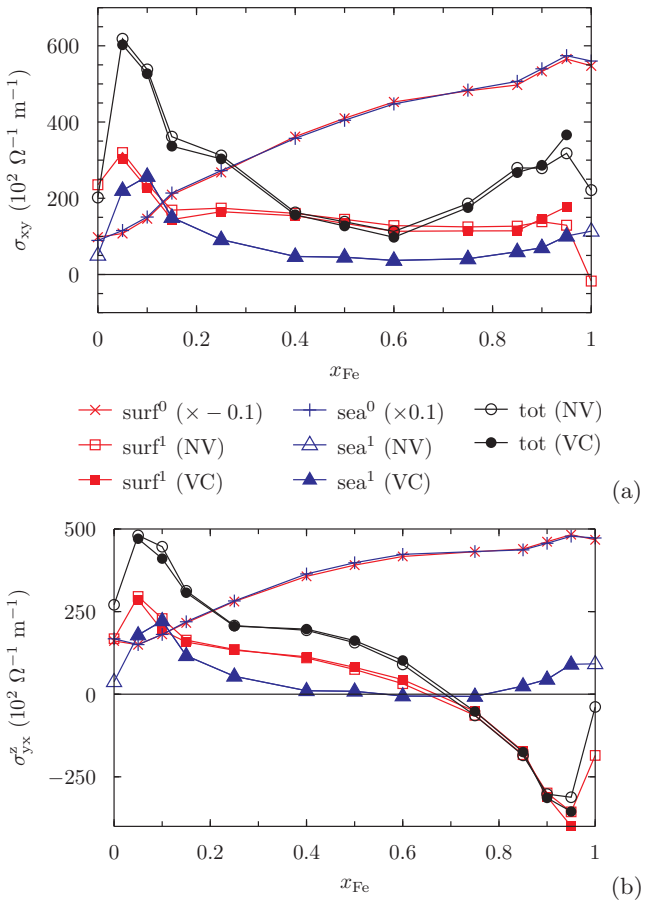

FIG. 8. (a) Anomalous and (b) spin Hall conductivities σ_{xy} and σ^z_{xy}, respectively, as functions of x in $Mn_{1-x}Fe_xGe$ calculated via the Kubo–Bastin formalism. Fermi- surface contributions are given in red, those from the Fermi sea in blue, and their sum in black. The superscripts 0 and 1 indicate on- and off-site terms. Results for the latter are shown excluding (NV) and including vertex corrections (VC).

Because of this, one can expect certain correlations concerning their composition-dependent behavior.

For the investigated alloy system $Mn_{1-x}Fe_xGe$, the anomalous Hall conductivity (AHC) σ_{xy} calculated within the Kubo–Bastin formalism [Eq. (4)] is given in Fig. 7(a) as full circles. As can be seen, σ_{xy} does not change sign in going from MnGe to FeGe, in agreement with previous first-principles calculations [12] and experiment [34]. Note that the chemical disorder is treated on fundamentally different levels in the two theoretical approaches. While the present work employs the coherent-potential approximation, the results of Ref. [12] are based on the virtual crystal approximation. This difference should be mainly responsible for the deviations between the two sets of theory data visible in the upper panel of Fig. 7, which are most pronounced on the Fe-rich side of the concentration range where even the signs appears to differ. As shown later, however, this is not due to the extrinsic or incoherent contributions. Unfortunately, reliable experimental data in this region could not be obtained because both the Hall and the longitudinal resistivity are small under the experimental conditions [34].

Comparison of the anomalous Hall coefficient $S_H = \sigma_{xy}/\mu$ to the experimental results of Kanazawa *et al.* [34] in the lower panel of Fig. 7 shows good agreement for the Mn-rich side of the concentration range (except for pure MnGe, see below), while deviations on the Fe-rich side are quite large. Here one should note that the measurements were performed at 50 K while the calculations assume $T = 0$ K, meaning in particular perfect ferromagnetic order. As can be seen in Fig. 3 of Ref. [34], the temperature dependence of magnetization as well as anomalous Hall conductivity is quite substantial for MnGe and even more so for FeGe. As mentioned above for the anomalous Hall conductivity, the experimental uncertainty is in addition rather high in the pure-Fe limit. For a more detailed understanding of these discrepancies investigations including the effects of finite temperature, sample geometry, and noncollinear magnetic structure are necessary.

Having a closer look at the Kubo–Bastin equation (4), one can decompose the full response coefficient into several contributions with distinct physical meaning. Most obviously, the two terms $\mathcal{R}^I_{xy}$ and $\mathcal{R}^{II}_{xy}$ differ in the absence or presence of contributions from occupied states below the Fermi level, i.e., these are the Fermi-surface and Fermi-sea terms, respectively. They are plotted in Fig. 8(a) in red (Fermi surface) and blue (Fermi sea), further decomposed into on-site (surf^0 and sea^0, crosses) and off-site (surf^1 and sea^1, squares and triangles,

respectively) contributions. For the latter results are shown once excluding (NV, empty symbols) and once including the so-called vertex corrections (VC, full symbols) arising from the difference in the product of configuration-averaged Green's functions versus the configuration average of the product. These give rise to the so-called extrinsic or incoherent contribution and are connected to the scattering-in term of the Boltzmann equation [37].

Comparing now the various terms, one first of all notices that on-site terms are large [note that they are scaled by a factor of (−)0.1], opposite in sign and almost identical in magnitude, leading to an almost perfect cancellation. Turning to the off-site terms one observes a similar concentration dependence and a dominance of the Fermi-surface contribution, except for $x \simeq 0.1$ and at the Fe-rich side of the concentration range. This means that the anomalous Hall conductivity is dominated by the states at the Fermi level, in particular for intermediate concentrations. Obviously, already for this reason a clear correlation between anomalous Hall coefficient and DMI strength, as suggested by Kanazawa *et al.* [34], is not supported by our findings. Finally, the vertex corrections are, as observed before [22,38,39], only relevant for the Fermi-surface term and in this system only noticeable in the dilute limits, particularly on the Fe-rich side. Note that, as discussed before, there the density of states at the Fermi level is largest and has predominantly d-like character. Interestingly, the seemingly diverging behavior for $x \to 0$ (1) is not caused by the extrinsic contribution [24].

Because the same spin-dependent scattering mechanisms are responsible for the SHE and AHE, both, transverse spin and charge currents can be present in the FM-ordered $Mn_{1-x}Fe_xGe$ system. However, in contrast to σ_{xy}, the transverse spin conductivity σ^z_{xy} shown in Fig. 8 (bottom) does change its sign at $x \sim 0.7$. Thus, the total transverse current should be dominated by opposite spin characters in these limits. Interestingly, the AHC has a minimum of its absolute value close to the Fe concentration corresponding to the sign change of the SHC. In fact, the Fermi-sea contributions to σ_{xy} and σ^z_{xy} as well as both on-site terms behave very similarly over the entire concentration range, whereas the Fermi-surface contributions agree only on the Mn-rich side up to the minimum or sign change, respectively.

The spin Hall conductivity of the $Mn_{1-x}Fe_xGe$ alloy system presented in Fig. 8 (bottom) as a function of Fe concentration changes sign approximately at the same composition as the DMI parameter D_{xx} and, accordingly, also the torkance t_{xx}. However, one can again see a leading role of the Fermi-surface contribution to the spin Hall conductivity, in particular at the Fe-rich side after the sign change. This implies that the sign of the SHE conductivity is determined to a large extent by the character of the states at the Fermi energy and their spin-orbit coupling, which changes with concentration according to the discussion above. Note however, that in pure FeGe the Fermi-surface and Fermi-sea contributions are of equal magnitude but opposite sign, leading to their partial cancellation. Concerning the importance of the vertex corrections the spin Hall conductivity behaves again similar to the AHC, in as much as they are only present at the Fermi surface and negligible over the entire concentration range considered here—again apart from the Fe-rich limit.

A more detailed analysis of the anomalous and spin Hall conductivities in terms of underlying scattering mechanisms based on their scaling behavior with respect to the longitudinal (charge) conductivity in the dilute limits has been so far precluded by the large numerical cost and is left for future work. Note also, that the anomalous and spin Hall conductivities in the present work were calculated for the FM structure. Introducing a chiral noncollinear spin texture, one can expect additional contributions from the topological anomalous [6] and spin Hall [40] effects, most likely displaying different concentration-dependent features.

D. Symmetry considerations

We conclude with a few remarks on magnetic symmetry and the corresponding shapes of the response tensors discussed above. The B20 structure of the $Mn_{1-x}Fe_xGe$ alloy system has the (nonmagnetic) space group $P2_13$, for ferromagnetic order with magnetization along z (one of the 2_1 axes), this leads to the magnetic space group (MSG) $P2'_12'_12_1$, the magnetic point group (MPG) $2'2'2$, and finally the magnetic Laue group (MLG) $m'm'm$ (or $2'2'2$ in the convention of Ref. [41]). The corresponding symmetry-allowed tensor forms for electrical ($\underline{\sigma}$) and spin ($\underline{\sigma}^\xi$) conductivity [42] and the current-induced torkance [22] are[1]

$$\underline{\sigma}^{(z)} = \begin{pmatrix} \sigma^{(z)}_{xx} & \sigma^{(z)}_{xy} & 0 \\ -\sigma^{(z)}_{xy} & \sigma^{(z)}_{yy} & 0 \\ 0 & 0 & \sigma^{(z)}_{zz} \end{pmatrix}, \tag{8}$$

and

$$\underline{t} = \begin{pmatrix} t_{xx} & t_{xy} & 0 \\ t_{yx} & t_{yy} & 0 \\ 0 & 0 & 0 \end{pmatrix}. \tag{9}$$

Note that this is not the highest symmetric FM-ordered structure because for $\mathbf{m} \parallel (111)$ (along the three-fold axes) one would have MSG $R3$, MPG 3, and MLG $\bar{3}$, leading to the tensor shapes

$$\underline{\sigma}^{(z)} = \begin{pmatrix} \sigma^{(z)}_{xx} & \sigma^{(z)}_{xy} & 0 \\ -\sigma^{(z)}_{xy} & \sigma^{(z)}_{xx} & 0 \\ 0 & 0 & \sigma^{(z)}_{zz} \end{pmatrix}, \tag{10}$$

and

$$\underline{t} = \begin{pmatrix} t_{xx} & t_{xy} & 0 \\ -t_{xy} & t_{xx} & 0 \\ 0 & 0 & 0 \end{pmatrix}. \tag{11}$$

Figure 9 shows all nonzero tensor elements of $\underline{t}$ for $\mathbf{m} \parallel$ z as chosen in this work. Apparently, the deviations between the diagonal torkances t_{xx} and t_{yy} are negligibly small over the whole concentration range; the largest differences occur once more on the Fe-rich side. For the off-diagonal torkances, $t_{yx} \simeq -t_{xy}$ holds as well with the above exception. Note, that these torkances, in contrast with t_{xx} and t_{yy}, only contain contributions from the Fermi surface, as discussed before [22]

[1]The spin conductivity is given for polarization ξ along z here, for x- and y-polarization see Ref. [42].

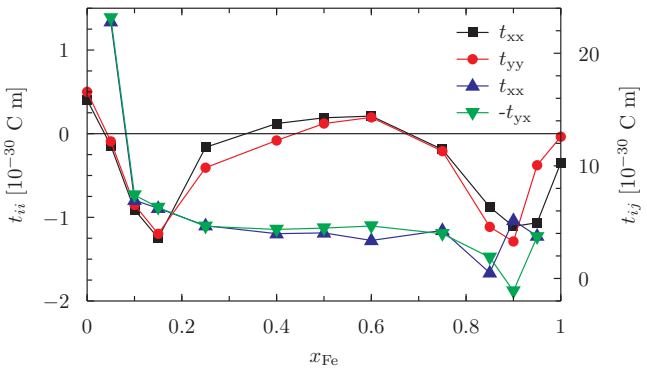

FIG. 9. Comparison of all nonzero torkance tensor elements as functions of x in $Mn_{1-x}Fe_xGe$ calculated via the Kubo–Bastin formalism. The diagonal elements t_{xx} and t_{yy} (left y scale) are given as black squares and red circles, respectively, the off-diagonal torkances (right y scale) t_{xy} and $-t_{yx}$ are given as blue up- and green down-facing triangles.

and, as the diagonal elements, are dominated by the intrinsic contribution. Irrespective of the magnetic point group [$m'm'm$ for $\mathbf{m} \parallel (001)$ or 3 for $\mathbf{m} \parallel (111)$], the diagonal elements are even, while the off-diagonal ones are odd with respect to reversal of the magnetization direction. The same applies to both the electrical and the spin conductivity tensors.

IV. SUMMARY

To summarize, we have presented results of calculations for the D_{xx} and D_{yy} components of the DMI vector in the B20 $Mn_{1-x}Fe_xGe$ alloys as a function of Fe concentration. The sign change of this quantity evidences the change of spin helicity at $x \approx 0.85$, in line with experimental results as well as with theoretical results obtained by other groups. Although the approach used in the present work is more appropriate for disordered systems when compared with those used in the previous investigations, all calculations demonstrate reasonable agreement, because of the virtual-crystal-like behavior of the majority spin states [12,30]. In addition, we discussed the concentration dependence of the total spin-orbit torkance t_{xx} and its Fermi-surface and Fermi-sea contributions. It was shown that, for all Fe concentrations, both parts have the same order of magnitude but their sign is opposite, leading to a significant compensation. By using different approaches to calculate the Fermi-sea contribution to the SOT its composition-dependent features in common with the DMI were discussed. In the case of the AHE and SHE the calculated Fermi sea contributions are rather small and the behavior of these effects as functions of composition are determined mainly by the electronic states at the Fermi level. The common SOC-induced mechanisms responsible for these effects, for the investigated concentration range ($0.05 < x < 0.95$) these are predominantly of intrinsic origin, result in the correlation of their dependence on the Fe concentration. This is demonstrated by the finding that the minimum of the AHE magnitude and the sign change of the SHC occur at approximately the same composition.

ACKNOWLEDGMENTS

Financial support by the DFG (Germany) via SFB 689 (Spinphänomene in reduzierten Dimensionen) and SFB 1277 (Emergent Relativistic Effects in Condensed Matter–From Fundamental Aspects to Electronic Functionality) is gratefully acknowledged.

APPENDIX

According to the suggestion by Shilkova and Shirokovskii [27,28], the electron group velocity can be represented by the expression

$$\mathbf{v}_n(\mathbf{k}) = \frac{\partial \lambda_n(E,\mathbf{k})}{\partial \mathbf{k}}\bigg|_{E=E_n(\mathbf{k})} \Bigg/ \frac{\partial \lambda_n(E,\mathbf{k})}{\partial E}\bigg|_{E=E_n(\mathbf{k})}. \quad \text{(A1)}$$

Here $\lambda_n(E,\mathbf{k})$ are the eigenvalues of the KKR matrix $\underline{M}(E,\mathbf{k}) = \underline{\tau}^{-1}(E,\mathbf{k})$ that are determined by solving the eigenvalue problem [29]

$$\underline{M}(E,\mathbf{k})\mathbf{b}^n(E,\mathbf{k}) = \lambda_n \mathbf{b}^n(E,\mathbf{k}) \quad \text{(A2)}$$

and vanish at $E = E_n(\mathbf{k})$ corresponding to zeros of the determinant $||\underline{M}(E,\mathbf{k})||$. Here $b^n_\Lambda(\mathbf{k})$ are the associated eigenvectors. With this one arrives at the expression

$$\mathbf{b}^{n\dagger}(\mathbf{k})\frac{\partial \underline{\tau}(E,\mathbf{k})}{\partial \mathbf{k}}\mathbf{b}^n(\mathbf{k})\bigg|_{E=E_n(\mathbf{k})} = \mathbf{v}_n(\mathbf{k})\mathbf{b}^{n\dagger}(\mathbf{k})\frac{\partial \underline{\tau}(E,\mathbf{k})}{\partial E}\mathbf{b}^n(\mathbf{k})\bigg|_{E=E_n(\mathbf{k})}. \quad \text{(A3)}$$

Finally, use is made of the relation for the group velocity [27,28]:

$$\mathbf{v}_n(\mathbf{k}) = \sum_{\Lambda,\Lambda'} b^{n\dagger}_\Lambda(\mathbf{k})(c\boldsymbol{\alpha}_{\Lambda,\Lambda'})b^n_{\Lambda'}(\mathbf{k}), \quad \text{(A4)}$$

with

$$\boldsymbol{\alpha}_{\Lambda,\Lambda'} = \int_\Omega d^3r Z^\times_\Lambda(\mathbf{r},E)\boldsymbol{\alpha} Z_{\Lambda'}(\mathbf{r},E), \quad \text{(A5)}$$

where c is the speed of light and $\boldsymbol{\alpha}$ is the vector of Dirac matrices, which represents the relativistic current operator $\hat{\mathbf{j}} = -e\hat{\mathbf{v}} = -ec\boldsymbol{\alpha}$. With this one finally arrives at the relationship between Eq. (6) and the Fermi-sea term in Eq. (4).

[1] N. Kanazawa, S. Seki, and Y. Tokura, Adv. Mater. **29**, 1603227 (2017).
[2] I. Dzyaloshinsky, J. Phys. Chem. Solids **4**, 241 (1958).
[3] T. Moriya, Phys. Rev. **120**, 91 (1960).
[4] S. A. Daz and R. E. Troncoso, J. Phys.: Condens. Matter **28**, 426005 (2016).
[5] Y. Taguchi, Y. Oohara, H. Yoshizawa, N. Nagaosa, and Y. Tokura, Science **291**, 2573 (2001).

[6] P. Bruno, V. K. Dugaev, and M. Taillefumier, Phys. Rev. Lett. **93**, 096806 (2004).
[7] M. Ishida, Y. Endoh, S. Mitsuda, Y. Ishikawa, and M. Tanaka, J. Phys. Soc. Jpn. **54**, 2975 (1985).
[8] V. A. Dyadkin, S. V. Grigoriev, D. Menzel, D. Chernyshov, V. Dmitriev, J. Schoenes, S. V. Maleyev, E. V. Moskvin, and H. Eckerlebe, Phys. Rev. B **84**, 014435 (2011).
[9] K. Shibata, X. Z. Yu, T. Hara, D. Morikawa, N. Kanazawa, K. Kimoto, S. Ishiwata, Y. Matsui, and Y. Tokura, Nat. Nanotechnol. **8**, 723 (2013).
[10] S. V. Grigoriev, S.-A. Siegfried, E. V. Altynbayev, N. M. Potapova, V. Dyadkin, E. V. Moskvin, D. Menzel, A. Heinemann, S. N. Axenov, L. N. Fomicheva *et al.*, Phys. Rev. B **90**, 174414 (2014).
[11] S. V. Grigoriev, N. M. Potapova, S.-A. Siegfried, V. A. Dyadkin, E. V. Moskvin, V. Dmitriev, D. Menzel, C. D. Dewhurst, D. Chernyshov, R. A. Sadykov *et al.*, Phys. Rev. Lett. **110**, 207201 (2013).
[12] J. Gayles, F. Freimuth, T. Schena, G. Lani, P. Mavropoulos, R. A. Duine, S. Blügel, J. Sinova, and Y. Mokrousov, Phys. Rev. Lett. **115**, 036602 (2015).
[13] T. Koretsune, N. Nagaosa, and R. Arita, Sci. Rep. **5**, 13302 (2015).
[14] F. Freimuth, S. Bluegel, and Y. Mokrousov, J. Phys.: Condens. Matter **26**, 104202 (2014).
[15] H. Ebert *et al.*, *The Munich SPR-KKR Package*, version 7.7, http://olymp.cup.uni-muenchen.de/ak/ebert/SPRKKR (2017).
[16] H. Ebert, D. Ködderitzsch, and J. Minár, Rep. Prog. Phys. **74**, 096501 (2011).
[17] S. H. Vosko, L. Wilk, and M. Nusair, Can. J. Phys. **58**, 1200 (1980).
[18] P. Soven, Phys. Rev. **156**, 809 (1967).
[19] B. Velický, Phys. Rev. **184**, 614 (1969).
[20] S. Mankovsky and H. Ebert, Phys. Rev. B **96**, 104416 (2017).
[21] H. Ebert and S. Mankovsky, Phys. Rev. B **79**, 045209 (2009).
[22] S. Wimmer, K. Chadova, M. Seemann, D. Ködderitzsch, and H. Ebert, Phys. Rev. B **94**, 054415 (2016).
[23] S. Lowitzer, D. Ködderitzsch, and H. Ebert, Phys. Rev. B **82**, 140402(R) (2010).
[24] S. Lowitzer, M. Gradhand, D. Ködderitzsch, D. V. Fedorov, I. Mertig, and H. Ebert, Phys. Rev. Lett. **106**, 056601 (2011).
[25] V. Bargmann and E. P. Wigner, Proc. Natl. Acad. Sci. USA **34**, 211 (1948).
[26] A. Vernes, B. L. Györffy, and P. Weinberger, Phys. Rev. B **76**, 012408 (2007).
[27] V. P. Shirokovskii, N. A. Shilkova, and N. A. Trubitsina, Phys. Status Solidi B **133**, 593 (1986).
[28] N. A. Shilkova and V. P. Shirokovskii, Phys. Status Solidi B **149**, 571 (1988).
[29] M. Gradhand, D. V. Fedorov, F. Pientka, P. Zahn, I. Mertig, and B. L. Györffy, Phys. Rev. B **84**, 075113 (2011).
[30] T. Kikuchi, T. Koretsune, R. Arita, and G. Tatara, Phys. Rev. Lett. **116**, 247201 (2016).
[31] J. Staunton, B. L. Gyorffy, A. J. Pindor, G. M. Stocks, and H. Winter, J. Phys. F: Met. Phys. **15**, 1387 (1985).
[32] A. V. Ruban, S. Khmelevskyi, P. Mohn, and B. Johansson, Phys. Rev. B **75**, 054402 (2007).
[33] S. Polesya, S. Mankovsky, S. Bornemann, D. Ködderitzsch, J. Minár, and H. Ebert, Phys. Rev. B **89**, 184414 (2014).
[34] N. Kanazawa, K. Shibata, and Y. Tokura, New J. Phys. **18**, 045006 (2016).
[35] N. Nagaosa, J. Sinova, S. Onoda, A. H. MacDonald, and N. P. Ong, Rev. Mod. Phys. **82**, 1539 (2010).
[36] J. Sinova, S. O. Valenzuela, J. Wunderlich, C. H. Back, and T. Jungwirth, Rev. Mod. Phys. **87**, 1213 (2015).
[37] W. H. Butler, Phys. Rev. B **31**, 3260 (1985).
[38] I. Turek, J. Kudrnovský, and V. Drchal, Phys. Rev. B **89**, 064405 (2014).
[39] D. Ködderitzsch, K. Chadova, and H. Ebert, Phys. Rev. B **92**, 184415 (2015).
[40] G. Yin, Y. Liu, Y. Barlas, J. Zang, and R. K. Lake, Phys. Rev. B **92**, 024411 (2015).
[41] W. H. Kleiner, Phys. Rev. **142**, 318 (1966).
[42] M. Seemann, D. Ködderitzsch, S. Wimmer, and H. Ebert, Phys. Rev. B **92**, 155138 (2015).

3.5.2 Additional results on the Edelstein effect

The following is an unpublished manuscript on the Edelstein effect and its reciprocal phenomenon, focussing on space-time symmetry aspects as well as first-principles results, both based on Kubo's linear response formalism. As the Edelstein effect is closely related to the spin-orbit torque discussed in particular in Ref. 335 reprinted in Section 3.5 on page 228, the two effects will be extensively compared.

Symmetry and magnitude of the direct and inverse Edelstein effect: A KKR-CPA-Kubo approach

S. Wimmer,* K. Chadova, and H. Ebert
Department Chemie/Phys. Chemie, Ludwig-Maximilians-Universität München, Germany

The symmetry restrictions concerning the occurrence of the direct and inverse Edelstein or inverse and direct spin-galvanic effects are investigated. The shapes of the corresponding response tensors are given for all non-centrosymmetric magnetic point groups. These group theoretical considerations are accompanied by first-principles calculations of the Edelstein response on the basis of the corresponding Kubo-Bastin equation. Results for the fcc(111) tri-layer alloy-system Pt | Fe_xCo_{1-x} | Cu are presented and discussed in relation to results for the electrical and spin conductivity as well as the spin-orbit-induced torkance.

I. INTRODUCTION

The Edelstein effect (EE) denotes the phenomenon that an electric field applied to a non-centrosymmetric solid may induce a spin polarization.[1,2] While there was previous work on a corresponding photo-galvanic effect,[3,4] it seems that the *magneto-electric effect* proposed by Edelstein[2] is the first unambiguous prediction of what is nowadays understood as the EE.[5] Attempts to highlight also the (somewhat) close relation to the (Bychkov-)Rashba effect[6] or to recognize the contribution by Aronov and Lyanda-Geller[1] led to the alternative names Rashba-Edelstein effect (REE)[7,8] and Aronov-Lyanda-Geller-Edelstein effect (ALGE)[9]. Yet another, so to speak more diplomatic, term in use is *current-induced spin polarization* (CISP)[10].

The Edelstein effect could be unambiguously verified in experiment presumably for the first time by Silov *et al.*[11] and Kato *et al.*[12] (see also Refs. 13, 14, and 15).[16] As the EE can be identified with the inverse of the so-called spin-galvanic effect[17] or the closely related circular photo-galvanic effect[18], it is accordingly also called inverse spin-galvanic effect (see, e.g., Refs. 19 and 20). The first experimental realization of the inverse Edelstein effect (IEE) in non-magnetic materials was achieved by Rojas Sánchez *et al.*[21].

Following the works of Aronov and Lyanda-Geller[1] and Edelstein[2] a theoretical description of the EE/ISGE was developed by various groups. Most work in this field was based so far on simplified (Rashba) models.[22–25] The same holds true for theoretical efforts on the inverse Edelstein effect.[26–29] First-principles calculations on the other hand are rather rare in the literature so far.[10,30] Ref. 10 in particular also dealt with the restrictions imposed on the EE by the crystallographic symmetry of the system under investigation, aiming at the tensor shapes of the so-called spin-orbit torkance[31–35] in ferro- and antiferromagnets. The close connection between those two linear response phenomena was realized (in fact utilized) already by Manchon and Zhang[31]. While the absence of inversion symmetry as a precondition for both effects was of course well-known, it was Železný *et al.*[10] who did the first systematic analysis based on group theoretical considerations. Focusing on a projection of the Edelstein polarization or torkance on sub-lattices in collinear antiferromagnets those authors however neglect the effect of time-reversal giving in particular rise to the *generalized Onsager relations*[36] between direct and inverse effects. In the present work the full space-time symmetry of all relevant (non-centrosymmetric) magnetic space groups will be considered. Moreover, based on considerations of the transformation properties of charge and heat current operators, corresponding statements for the thermal analogues, direct and inverse thermal Edelstein effects can be made. The former has recently been considered as a possible contribution or side effect in the spin Nernst magnetothermopower (SMT)[37] by Tölle *et al.*[38]. The latest member of the Edelstein family, the orbital Edelstein effect[39] will not be discussed herein.

The present work focuses, besides group-theoretical analysis, on the magnitude of the Edelstein response tensor or polarization as obtained from linear response calculations of a suitable Kubo formula for the charge current-spin polarization correlation. A corresponding Kubo-Bastin implementation into a fully-relativistic KKR-CPA framework[40,41] allows in particular giving material specific values of the Edelstein polarization in alloys as well as the discussion of intrinsic and extrinsic scattering mechanisms and the relevance of Fermi sea and Fermi surface terms. By comparison with other linear response phenomena, electrical and spin conductivity as well as of course with the spin-orbit torque, their partial interconnection is elucidated.

This article is organized as follows: In Section II we introduce the underlying linear response formalism used to calculate the Edelstein tensor, discuss its implementation into a multiple scattering framework, with particular emphasis on the treatment of disorder, and finally outline the application of symmetry considerations leading to restrictions to the tensor shapes of both, direct and inverse Edelstein effect. The outcome of this group-theoretical analysis for all magnetic point groups will be presented together with corresponding results for the electrical and spin conductivity tensors. The connection between Edelstein effect, spin-orbit torque, and spin conductivity will be discussed. In Section III we present the results of our numerical investigations on a Pt | Fe_xCo_{1-x} | Cu tri-layer system, highlighting the impact of disorder effects (impu-

rity scattering) on the various contributions to the Edelstein response. By comparing concentration-dependent results for the Edelstein tensor with such for torkance and spin conductivity we will discuss their interrelation.

II. FORMALISM

A well-known application of Kubo's linear response formalism is the derivation of an expression for the electrical conductivity tensor $\underline{\boldsymbol{\sigma}}$ that allows giving the electrical current density $\mathbf{j} = \underline{\boldsymbol{\sigma}}\,\mathbf{E}$ in response to an electrical field $\mathbf{E}$. In analogy one can derive an expression for the Edelstein tensor $\underline{\boldsymbol{p}}$ that gives the spin polarization $\mathbf{s} = \underline{\boldsymbol{p}}\,\mathbf{E}$ induced by $\mathbf{E}$.[1,2] Replacing the operator for the response, $\hat{j}_\mu$ representing the component μ of the current density, by an operator for the spin polarization along the μ axis, which in relativistic four-component Dirac notation reads[42,43]

$$\hat{P}_\mu = \beta\Sigma_\mu = \begin{pmatrix} \mathrm{I}_2 & 0_2 \\ 0_2 & -\mathrm{I}_2 \end{pmatrix} (\sigma_\mu \otimes \mathrm{I}_2) = \begin{pmatrix} \sigma_\mu & 0_2 \\ 0_2 & -\sigma_\mu \end{pmatrix} \ , \quad (1)$$

with σ_μ being one of the standard 2×2 Pauli matrices, one can straightforwardly adopt the derivation of the so-called Kubo-Bastin formula for $\underline{\boldsymbol{\sigma}}$,[44] leading to a corresponding expression for the Edelstein response tensor $\underline{\boldsymbol{p}}$:

$$\begin{aligned} p_{\mu\nu} = &-\frac{\hbar}{4\pi}\int_{-\infty}^{\infty} d\varepsilon \frac{df(\varepsilon)}{d\varepsilon} \mathrm{Tr}\left\langle \hat{P}_\mu (G^+ - G^-)\hat{j}_\nu G^- - \hat{P}_\mu G^+ \hat{j}_\nu (G^+ - G^-) \right\rangle \\ &+\frac{\hbar}{4\pi}\int_{-\infty}^{\infty} d\varepsilon f(\varepsilon) \mathrm{Tr}\left\langle \hat{P}_\mu G^+ \hat{j}_\nu \frac{dG^+}{d\varepsilon} - \hat{P}_\mu \frac{dG^+}{d\varepsilon}\hat{j}_\nu G^+ - \text{“}\left(G^+ \to G^-\right)\text{”} \right\rangle \ , \end{aligned} \quad (2)$$

where $f(\varepsilon)$ is the Fermi-Dirac distribution and G^+ (G^-) is the retarded (advanced) single-particle Green function at energy ε (arguments have been dropped for the sake of readability). This implies that in the limit $T \to 0$ K for the temperature the first term in Eq. (2) has to be evaluated only for the Fermi energy E_F (Fermi surface term $p^I_{\mu\nu}$), while the second one requires an integration over the occupied part of the valence band (Fermi sea term $p^{II}_{\mu\nu}$).

The current (density) operator $\hat{j}_\nu = -|e|c\alpha_\nu$ in Eq. (2) represents the perturbation due to the electric field component E_ν. Adopting a fully relativistic formulation to account coherently for the impact of SOC, $\hat{j}_\nu$ is expressed by the corresponding velocity operator $\hat{v}_\nu = c\alpha_\nu$, where c is the speed of light and α_ν is one of the standard 4×4 Dirac matrices.[43] The spin-polarization operator $\hat{P}_\mu$ on the other hand represents the spin-magnetic moment along the μ axis induced by the electric field, and is therefore most conveniently expressed by Eq. (1).

In Eq. (2) the electronic structure is represented in terms of the retarded and advanced Green functions $G^+(\varepsilon)$ and $G^-(\varepsilon)$, respectively. Using this approach has the big advantage that one can deal straightforwardly with disordered systems. Considering for example chemical disorder the brackets $\langle ... \rangle$ in Eq. (2) stand for the configurational average for a disordered alloy. For the applications presented below relativistic multiple scattering theory was used to determine the Green functions $G^\pm(\varepsilon)$.[40,45] The configurational averaging over alloy configurations was determined by means of the Coherent Potential Approximation (CPA) alloy theory as done in the context of the electrical conductivity,[46,47] spin conductivity,[48] Gilbert damping parameter,[49] and recently to the spin-orbit torque.[50] This implies in particular that the so-called vertex corrections, that ensure that the proper average $\langle \hat{P}_\mu G^\pm \hat{j}_\nu G^\pm \rangle$ is taken instead of the simpler product $\langle \hat{P}_\mu G^\pm \rangle \langle \hat{j}_\nu G^\pm \rangle$, are included in the calculations.

Expressing the electric field induced spin-polarization by means of linear response formalism allows to investigate straightforwardly the condition for which the Edelstein effect may show up or not. This can be done using a scheme worked out by Kleiner[51], recently extended by Seemann *et al.*,[52] and already applied to direct and inverse spin-orbit torques.[50] Making use of the behavior of the spin-polarization operator $\hat{P}_\mu$ and of the current density operator j_ν under symmetry operations one is led to the relations that restrict the shape of the Edelstein response tensor $\underline{\boldsymbol{p}}$:

$$p_{\mu\nu} = \sum_{\kappa\lambda} p_{\kappa\lambda} D(R)_{\kappa\mu} D(R)_{\lambda\nu} \det(R) \quad (3)$$

$$p_{\mu\nu} = \sum_{\kappa\lambda} p'_{\lambda\kappa} D(R)^*_{\kappa\mu} D(R)^*_{\lambda\nu} \det(R) \ , \quad (4)$$

where $\underline{\boldsymbol{D}}(R)$ is the 3×3 transformation matrix associated with the pure spatial operation R and $\det(R)$ is the corresponding determinant of that matrix. In Eq. (3) only unitary pure spatial symmetry operations are considered, while in Eq. (4) anti-unitary operations are considered that involve apart form the spatial operation R also the time reversal operation. As a consequence Eq. (4) relates the Edelstein tensor $\underline{\boldsymbol{p}}$ with the tensor $\underline{\boldsymbol{p}}'$ that is associated with the time-reversed effect, i.e., Eq. (4) is

a *generalized* Onsager relation for the direct and inverse Edelstein effect.

Considering Eqs. (3) and (4) for all symmetry operations of a magnetic point group, the corresponding symmetry-allowed shape of the direct and inverse Edelstein response tensors, $\underline{\boldsymbol{p}}$ and $\underline{\boldsymbol{p}}'$, can be determined. Tables I to VII give the results for all magnetic point groups leading to a non-vanishing Edelstein polarization tensor. These groups can be subdivided into three categories[36,52], one with time-reversal as a symmetry operation, category (a), one without time-reversal involved, neither as an operation on its own nor in combination with a spatial rotation, category (b), the other containing time-reversal in connection with a spatial rotation, category (c). The groups $\bar{6}1'$, $\bar{6}2m1'$ ($\bar{6}m21'$), $\bar{4}3m1'$ of category (a), $\bar{6}$, $\bar{6}2m$ ($\bar{6}m2$), $\bar{4}3m$ of category (b), and $\bar{6}2'm'$ ($\bar{6}m'2'$) of category (c) are non-centrosymmetric but nevertheless have vanishing Edelstein response (at least to zeroth order in the magnetization direction[10]).

In addition, one notices that none of the magnetic point groups listed in Tables I through VII has the spatial inversion as an element. This central restriction – missing inversion symmetry – has been pointed out for the torkance before by Manchon and Zhang[32] as well as Garate and MacDonald[33] on the basis of restricted model considerations and proven on group-theoretical grounds by the present authors.[50] The torkance and Edelstein response both are describing the response to an electric current represented by the current density operator $\hat{j}_\nu$. As the operators for the torque, $\hat{T}_\mu$, and the spin polarization due to the Edelstein effect, $\hat{P}_\mu$, are both pseudo vectors[53] that are transforming identically under unitary symmetry operations (see below), the absence of spatial inversion symmetry is a precondition[54] for the Edelstein effect as well. Moreover, for the same reason the shapes of the direct torkance[50] and Edelstein response tensors are identical for all magnetic point groups of categories (b) and (c). It should be noted that the magnetic point groups under category (a) apply to non-magnetic materials only. In this case the Edelstein effect may show up, while there is no (global) torkance as this requires a finite spontaneous magnetization.

Železný *et al.*[10] obtain completely identical results for the current induced spin polarization (CISP) or direct Edelstein response for crystallographic (non-magnetic) point groups (category (a), see Table I) using a similar approach. These authors discuss in addition an expansion of the response tensor in powers of the magnetization direction, of which only the zeroth order term is considered here. Note, that in Ref. 10 only non-magnetic non-centrosymmetric solids are considered, i.e., those 21 point groups of category (a) that have no spatial inversion symmetry. This is done having in particular the projection onto the sub-lattices of collinear (Néel) antiferromagnets in mind, where the operations connecting the two sub-lattices are spatial operations combined with time-reversal that reverses the direction of the moments. It is however precisely this kind of symmetry operation that gives the connection between direct and inverse effects, SOT and ISOT. Therefore these *generalized Onsager relations*[36] are not contained in the prescription of Železný *et al.*[10].

The close connection between spin-orbit torques and the Edelstein effect has already been mentioned earlier[10,31–33,55–57]. It derives from the identical transformation properties of the operators representing the responses in the two cases, magnetic torque and spin polarization, under spatial operations. However, since the spin-polarization operator $\hat{P}_\mu$, representing in principle a spin magnetic moment, is a pseudo vector anti-symmetric w.r.t. time-reversal, in contrast to the torque operator $\hat{T}_\mu$, which is given as a cross-product of two time-reversal anti-symmetric operators leading to a time-reversal symmetric pseudo vector, the torkance and the Edelstein response differ concerning their transformation behavior under anti-unitary operations (by a minus sign). This can in fact be deduced already by inspection of the explicit forms of the two operators, given in Eq. (1) above for $\hat{P}_\mu$ and in Eq. (2) of Ref. 50 for $\hat{T}_\mu$. The additional factor $B_{xc}(\mathbf{r})$ in the latter, the spin-polarized exchange potential, is of course time-reversal anti-symmetric, as the operator $\beta\Sigma_\mu$ itself. This leads to slightly modified *generalized Onsager relations* for the two.

Since the operators for electrical and heat current (density) transform identical under all space-time symmetry operations relevant for solids, the tensor forms will stay unaltered when the electric field is replaced by a temperature gradient. This means that the shapes given here apply also for the direct[58] and inverse thermal Edelstein effect.

A close connection between the Edelstein polarization and the spin conductivity, in particular the spin Hall effect, has been proposed based on model considerations by numerous authors. See for example Refs. 25 and 59,[60] as well as the review on the SHE by Sinova *et al.*[20]. Comparing the tensor shapes for $\underline{\boldsymbol{p}}$ and $\underline{\boldsymbol{\sigma}}^k$ in Tables I-VII however one has to state that there is no universal relationship between the two phenomena concerning their space-time symmetry. The Edelstein polarization tensor $\underline{\boldsymbol{p}}$ sometimes is identical in shape to one of the tensors $\underline{\boldsymbol{\sigma}}^k$, sometimes to that of the electrical conductivity tensor $\underline{\boldsymbol{\sigma}}$ and cases where it is distinct from all four of them can be found as well. In fact, a general rule for their interrelation is not to be expected as, although the same form of the polarization operator can also be employed in the spin current density operator and the operator representing the perturbation is the same in both cases, the additional current density operator for the response of course affects the space-time symmetry properties as well. Accordingly, the only definite statement concerning the shape of $\underline{\boldsymbol{p}}$ that can be made, is that it is identical in shape to $\underline{\boldsymbol{t}}$.

From the mechanistic point of view one might find a rather indirect connection between the two phenomena, the link being the spin-orbit torque. It has been stated early on[61], that two distinct contribution to the torkance

4

mpg	$\underline{\boldsymbol{p}}$	$\underline{\boldsymbol{p}}'$	mLg	$\underline{\boldsymbol{\sigma}}$	$\underline{\boldsymbol{\sigma}}^x$	$\underline{\boldsymbol{\sigma}}^y$	$\underline{\boldsymbol{\sigma}}^z$
$11'$	$\begin{pmatrix} p_{xx} & p_{xy} & p_{xz} \\ p_{yx} & p_{yy} & p_{yz} \\ p_{zx} & p_{zy} & p_{zz} \end{pmatrix}$	$\begin{pmatrix} p_{xx} & p_{yx} & p_{zx} \\ p_{xy} & p_{yy} & p_{zy} \\ p_{xz} & p_{yz} & p_{zz} \end{pmatrix}$	$\bar{1}1'$	$\begin{pmatrix} \sigma_{xx} & \sigma_{xy} & \sigma_{xz} \\ \sigma_{xy} & \sigma_{yy} & \sigma_{yz} \\ \sigma_{xz} & \sigma_{yz} & \sigma_{zz} \end{pmatrix}$	$\begin{pmatrix} \sigma_{xx}^x & \sigma_{xy}^x & \sigma_{xz}^x \\ \sigma_{yx}^x & \sigma_{yy}^x & \sigma_{yz}^x \\ \sigma_{zx}^x & \sigma_{zy}^x & \sigma_{zz}^x \end{pmatrix}$	$\begin{pmatrix} \sigma_{xx}^y & \sigma_{xy}^y & \sigma_{xz}^y \\ \sigma_{yx}^y & \sigma_{yy}^y & \sigma_{yz}^y \\ \sigma_{zx}^y & \sigma_{zy}^y & \sigma_{zz}^y \end{pmatrix}$	$\begin{pmatrix} \sigma_{xx}^z & \sigma_{xy}^z & \sigma_{xz}^z \\ \sigma_{yx}^z & \sigma_{yy}^z & \sigma_{yz}^z \\ \sigma_{zx}^z & \sigma_{zy}^z & \sigma_{zz}^z \end{pmatrix}$
$21'$	$\begin{pmatrix} p_{xx} & 0 & p_{xz} \\ 0 & p_{yy} & 0 \\ p_{zx} & 0 & p_{zz} \end{pmatrix}$	$\begin{pmatrix} p_{xx} & 0 & p_{zx} \\ 0 & p_{yy} & 0 \\ p_{xz} & 0 & p_{zz} \end{pmatrix}$	$2/m1'$	$\begin{pmatrix} \sigma_{xx} & 0 & \sigma_{xz} \\ 0 & \sigma_{yy} & 0 \\ \sigma_{xz} & 0 & \sigma_{zz} \end{pmatrix}$	$\begin{pmatrix} 0 & \sigma_{xy}^x & 0 \\ \sigma_{yx}^x & 0 & \sigma_{yz}^x \\ 0 & \sigma_{zy}^x & 0 \end{pmatrix}$	$\begin{pmatrix} \sigma_{xx}^y & 0 & \sigma_{xz}^y \\ 0 & \sigma_{yy}^y & 0 \\ \sigma_{zx}^y & 0 & \sigma_{zz}^y \end{pmatrix}$	$\begin{pmatrix} 0 & \sigma_{xy}^z & 0 \\ \sigma_{yx}^z & 0 & \sigma_{yz}^z \\ 0 & \sigma_{zy}^z & 0 \end{pmatrix}$
$m1'$	$\begin{pmatrix} 0 & p_{xy} & 0 \\ p_{yx} & 0 & p_{yz} \\ 0 & p_{zy} & 0 \end{pmatrix}$	$\begin{pmatrix} 0 & p_{yx} & 0 \\ p_{xy} & 0 & p_{zy} \\ 0 & p_{yz} & 0 \end{pmatrix}$	$2/m1'$	$\begin{pmatrix} \sigma_{xx} & 0 & \sigma_{xz} \\ 0 & \sigma_{yy} & 0 \\ \sigma_{xz} & 0 & \sigma_{zz} \end{pmatrix}$	$\begin{pmatrix} 0 & \sigma_{xy}^x & 0 \\ \sigma_{yx}^x & 0 & \sigma_{yz}^x \\ 0 & \sigma_{zy}^x & 0 \end{pmatrix}$	$\begin{pmatrix} \sigma_{xx}^y & 0 & \sigma_{xz}^y \\ 0 & \sigma_{yy}^y & 0 \\ \sigma_{zx}^y & 0 & \sigma_{zz}^y \end{pmatrix}$	$\begin{pmatrix} 0 & \sigma_{xy}^z & 0 \\ \sigma_{yx}^z & 0 & \sigma_{yz}^z \\ 0 & \sigma_{zy}^z & 0 \end{pmatrix}$
$2221'$	$\begin{pmatrix} p_{xx} & 0 & 0 \\ 0 & p_{yy} & 0 \\ 0 & 0 & p_{zz} \end{pmatrix}$	$\begin{pmatrix} p_{xx} & 0 & 0 \\ 0 & p_{yy} & 0 \\ 0 & 0 & p_{zz} \end{pmatrix}$	$mmm1'$	$\begin{pmatrix} \sigma_{xx} & 0 & 0 \\ 0 & \sigma_{yy} & 0 \\ 0 & 0 & \sigma_{zz} \end{pmatrix}$	$\begin{pmatrix} 0 & 0 & 0 \\ 0 & 0 & \sigma_{yz}^x \\ 0 & \sigma_{zy}^x & 0 \end{pmatrix}$	$\begin{pmatrix} 0 & 0 & \sigma_{xz}^y \\ 0 & 0 & 0 \\ \sigma_{zx}^y & 0 & 0 \end{pmatrix}$	$\begin{pmatrix} 0 & \sigma_{xy}^z & 0 \\ \sigma_{yx}^z & 0 & 0 \\ 0 & 0 & 0 \end{pmatrix}$
$mm21'$	$\begin{pmatrix} 0 & p_{xy} & 0 \\ p_{yx} & 0 & 0 \\ 0 & 0 & 0 \end{pmatrix}$	$\begin{pmatrix} 0 & p_{yx} & 0 \\ p_{xy} & 0 & 0 \\ 0 & 0 & 0 \end{pmatrix}$	$mmm1'$	$\begin{pmatrix} \sigma_{xx} & 0 & 0 \\ 0 & \sigma_{yy} & 0 \\ 0 & 0 & \sigma_{zz} \end{pmatrix}$	$\begin{pmatrix} 0 & 0 & 0 \\ 0 & 0 & \sigma_{yz}^x \\ 0 & \sigma_{zy}^x & 0 \end{pmatrix}$	$\begin{pmatrix} 0 & 0 & \sigma_{xz}^y \\ 0 & 0 & 0 \\ \sigma_{zx}^y & 0 & 0 \end{pmatrix}$	$\begin{pmatrix} 0 & \sigma_{xy}^z & 0 \\ \sigma_{yx}^z & 0 & 0 \\ 0 & 0 & 0 \end{pmatrix}$
$41'$	$\begin{pmatrix} p_{xx} & p_{xy} & 0 \\ -p_{xy} & p_{xx} & 0 \\ 0 & 0 & p_{zz} \end{pmatrix}$	$\begin{pmatrix} p_{xx} & -p_{xy} & 0 \\ p_{xy} & p_{xx} & 0 \\ 0 & 0 & p_{zz} \end{pmatrix}$	$4/m1'$	$\begin{pmatrix} \sigma_{xx} & 0 & 0 \\ 0 & \sigma_{xx} & 0 \\ 0 & 0 & \sigma_{zz} \end{pmatrix}$	$\begin{pmatrix} 0 & 0 & \sigma_{xz}^x \\ 0 & 0 & -\sigma_{xz}^y \\ \sigma_{zx}^x & -\sigma_{zx}^y & 0 \end{pmatrix}$	$\begin{pmatrix} 0 & 0 & \sigma_{xz}^y \\ 0 & 0 & \sigma_{xz}^x \\ \sigma_{zx}^y & \sigma_{zx}^x & 0 \end{pmatrix}$	$\begin{pmatrix} \sigma_{xx}^z & \sigma_{xy}^z & 0 \\ -\sigma_{xy}^z & \sigma_{xx}^z & 0 \\ 0 & 0 & \sigma_{zz}^z \end{pmatrix}$
$\bar{4}1'$	$\begin{pmatrix} p_{xx} & p_{xy} & 0 \\ p_{xy} & -p_{xx} & 0 \\ 0 & 0 & 0 \end{pmatrix}$	$\begin{pmatrix} p_{xx} & p_{xy} & 0 \\ p_{xy} & -p_{xx} & 0 \\ 0 & 0 & 0 \end{pmatrix}$	$4/m1'$	$\begin{pmatrix} \sigma_{xx} & 0 & 0 \\ 0 & \sigma_{xx} & 0 \\ 0 & 0 & \sigma_{zz} \end{pmatrix}$	$\begin{pmatrix} 0 & 0 & \sigma_{xz}^x \\ 0 & 0 & -\sigma_{xz}^y \\ \sigma_{zx}^x & -\sigma_{zx}^y & 0 \end{pmatrix}$	$\begin{pmatrix} 0 & 0 & \sigma_{xz}^y \\ 0 & 0 & \sigma_{xz}^x \\ \sigma_{zx}^y & \sigma_{zx}^x & 0 \end{pmatrix}$	$\begin{pmatrix} \sigma_{xx}^z & \sigma_{xy}^z & 0 \\ -\sigma_{xy}^z & \sigma_{xx}^z & 0 \\ 0 & 0 & \sigma_{zz}^z \end{pmatrix}$
$4221'$	$\begin{pmatrix} p_{xx} & 0 & 0 \\ 0 & p_{xx} & 0 \\ 0 & 0 & p_{zz} \end{pmatrix}$	$\begin{pmatrix} p_{xx} & 0 & 0 \\ 0 & p_{xx} & 0 \\ 0 & 0 & p_{zz} \end{pmatrix}$	$4/mmm1'$	$\begin{pmatrix} \sigma_{xx} & 0 & 0 \\ 0 & \sigma_{xx} & 0 \\ 0 & 0 & \sigma_{zz} \end{pmatrix}$	$\begin{pmatrix} 0 & 0 & 0 \\ 0 & 0 & -\sigma_{xz}^y \\ 0 & -\sigma_{zx}^y & 0 \end{pmatrix}$	$\begin{pmatrix} 0 & 0 & \sigma_{xz}^y \\ 0 & 0 & 0 \\ \sigma_{zx}^y & 0 & 0 \end{pmatrix}$	$\begin{pmatrix} 0 & \sigma_{xy}^z & 0 \\ -\sigma_{xy}^z & 0 & 0 \\ 0 & 0 & 0 \end{pmatrix}$
$4mm1'$	$\begin{pmatrix} 0 & p_{xy} & 0 \\ -p_{xy} & 0 & 0 \\ 0 & 0 & 0 \end{pmatrix}$	$\begin{pmatrix} 0 & -p_{xy} & 0 \\ p_{xy} & 0 & 0 \\ 0 & 0 & 0 \end{pmatrix}$	$4/mmm1'$	$\begin{pmatrix} \sigma_{xx} & 0 & 0 \\ 0 & \sigma_{xx} & 0 \\ 0 & 0 & \sigma_{zz} \end{pmatrix}$	$\begin{pmatrix} 0 & 0 & 0 \\ 0 & 0 & -\sigma_{xz}^y \\ 0 & -\sigma_{zx}^y & 0 \end{pmatrix}$	$\begin{pmatrix} 0 & 0 & \sigma_{xz}^y \\ 0 & 0 & 0 \\ \sigma_{zx}^y & 0 & 0 \end{pmatrix}$	$\begin{pmatrix} 0 & \sigma_{xy}^z & 0 \\ -\sigma_{xy}^z & 0 & 0 \\ 0 & 0 & 0 \end{pmatrix}$
$\bar{4}2m1'$	$\begin{pmatrix} p_{xx} & 0 & 0 \\ 0 & -p_{xx} & 0 \\ 0 & 0 & 0 \end{pmatrix}$	$\begin{pmatrix} p_{xx} & 0 & 0 \\ 0 & -p_{xx} & 0 \\ 0 & 0 & 0 \end{pmatrix}$	$4/mmm1'$	$\begin{pmatrix} \sigma_{xx} & 0 & 0 \\ 0 & \sigma_{xx} & 0 \\ 0 & 0 & \sigma_{zz} \end{pmatrix}$	$\begin{pmatrix} 0 & 0 & 0 \\ 0 & 0 & -\sigma_{xz}^y \\ 0 & -\sigma_{zx}^y & 0 \end{pmatrix}$	$\begin{pmatrix} 0 & 0 & \sigma_{xz}^y \\ 0 & 0 & 0 \\ \sigma_{zx}^y & 0 & 0 \end{pmatrix}$	$\begin{pmatrix} 0 & \sigma_{xy}^z & 0 \\ -\sigma_{xy}^z & 0 & 0 \\ 0 & 0 & 0 \end{pmatrix}$
$31'$	$\begin{pmatrix} p_{xx} & p_{xy} & 0 \\ -p_{xy} & p_{xx} & 0 \\ 0 & 0 & p_{zz} \end{pmatrix}$	$\begin{pmatrix} p_{xx} & -p_{xy} & 0 \\ p_{xy} & p_{xx} & 0 \\ 0 & 0 & p_{zz} \end{pmatrix}$	$\bar{3}1'$	$\begin{pmatrix} \sigma_{xx} & 0 & 0 \\ 0 & \sigma_{xx} & 0 \\ 0 & 0 & \sigma_{zz} \end{pmatrix}$	$\begin{pmatrix} \sigma_{xx}^x & \sigma_{xx}^y & \sigma_{xz}^x \\ \sigma_{xx}^y & -\sigma_{xx}^x & -\sigma_{xz}^y \\ \sigma_{zx}^x & -\sigma_{zx}^y & 0 \end{pmatrix}$	$\begin{pmatrix} \sigma_{xx}^y & -\sigma_{xx}^x & \sigma_{xz}^y \\ -\sigma_{xx}^x & -\sigma_{xx}^y & \sigma_{xz}^x \\ \sigma_{zx}^y & \sigma_{zx}^x & 0 \end{pmatrix}$	$\begin{pmatrix} \sigma_{xx}^z & \sigma_{xy}^z & 0 \\ -\sigma_{xy}^z & \sigma_{xx}^z & 0 \\ 0 & 0 & \sigma_{zz}^z \end{pmatrix}$
$3121'$	$\begin{pmatrix} p_{xx} & 0 & 0 \\ 0 & p_{xx} & 0 \\ 0 & 0 & p_{zz} \end{pmatrix}$	$\begin{pmatrix} p_{xx} & 0 & 0 \\ 0 & p_{xx} & 0 \\ 0 & 0 & p_{zz} \end{pmatrix}$	$\bar{3}1m1'$	$\begin{pmatrix} \sigma_{xx} & 0 & 0 \\ 0 & \sigma_{xx} & 0 \\ 0 & 0 & \sigma_{zz} \end{pmatrix}$	$\begin{pmatrix} \sigma_{xx}^x & 0 & 0 \\ 0 & -\sigma_{xx}^x & -\sigma_{xz}^y \\ 0 & -\sigma_{zx}^y & 0 \end{pmatrix}$	$\begin{pmatrix} 0 & -\sigma_{xx}^x & \sigma_{xz}^y \\ -\sigma_{xx}^x & 0 & 0 \\ \sigma_{zx}^y & 0 & 0 \end{pmatrix}$	$\begin{pmatrix} 0 & \sigma_{xy}^z & 0 \\ -\sigma_{xy}^z & 0 & 0 \\ 0 & 0 & 0 \end{pmatrix}$
$31m1'$	$\begin{pmatrix} 0 & p_{xy} & 0 \\ -p_{xy} & 0 & 0 \\ 0 & 0 & 0 \end{pmatrix}$	$\begin{pmatrix} 0 & -p_{xy} & 0 \\ p_{xy} & 0 & 0 \\ 0 & 0 & 0 \end{pmatrix}$	$\bar{3}1m1'$	$\begin{pmatrix} \sigma_{xx} & 0 & 0 \\ 0 & \sigma_{xx} & 0 \\ 0 & 0 & \sigma_{zz} \end{pmatrix}$	$\begin{pmatrix} \sigma_{xx}^x & 0 & 0 \\ 0 & -\sigma_{xx}^x & -\sigma_{xz}^y \\ 0 & -\sigma_{zx}^y & 0 \end{pmatrix}$	$\begin{pmatrix} 0 & -\sigma_{xx}^x & \sigma_{xz}^y \\ -\sigma_{xx}^x & 0 & 0 \\ \sigma_{zx}^y & 0 & 0 \end{pmatrix}$	$\begin{pmatrix} 0 & \sigma_{xy}^z & 0 \\ -\sigma_{xy}^z & 0 & 0 \\ 0 & 0 & 0 \end{pmatrix}$
$61'$	$\begin{pmatrix} p_{xx} & p_{xy} & 0 \\ -p_{xy} & p_{xx} & 0 \\ 0 & 0 & p_{zz} \end{pmatrix}$	$\begin{pmatrix} p_{xx} & -p_{xy} & 0 \\ p_{xy} & p_{xx} & 0 \\ 0 & 0 & p_{zz} \end{pmatrix}$	$6/m1'$	$\begin{pmatrix} \sigma_{xx} & 0 & 0 \\ 0 & \sigma_{xx} & 0 \\ 0 & 0 & \sigma_{zz} \end{pmatrix}$	$\begin{pmatrix} 0 & 0 & \sigma_{xz}^x \\ 0 & 0 & -\sigma_{xz}^y \\ \sigma_{zx}^x & -\sigma_{zx}^y & 0 \end{pmatrix}$	$\begin{pmatrix} 0 & 0 & \sigma_{xz}^y \\ 0 & 0 & \sigma_{xz}^x \\ \sigma_{zx}^y & \sigma_{zx}^x & 0 \end{pmatrix}$	$\begin{pmatrix} \sigma_{xx}^z & \sigma_{xy}^z & 0 \\ -\sigma_{xy}^z & \sigma_{xx}^z & 0 \\ 0 & 0 & \sigma_{zz}^z \end{pmatrix}$
$6221'$	$\begin{pmatrix} p_{xx} & 0 & 0 \\ 0 & p_{xx} & 0 \\ 0 & 0 & p_{zz} \end{pmatrix}$	$\begin{pmatrix} p_{xx} & 0 & 0 \\ 0 & p_{xx} & 0 \\ 0 & 0 & p_{zz} \end{pmatrix}$	$6/mmm1'$	$\begin{pmatrix} \sigma_{xx} & 0 & 0 \\ 0 & \sigma_{xx} & 0 \\ 0 & 0 & \sigma_{zz} \end{pmatrix}$	$\begin{pmatrix} 0 & 0 & 0 \\ 0 & 0 & -\sigma_{xz}^y \\ 0 & -\sigma_{zx}^y & 0 \end{pmatrix}$	$\begin{pmatrix} 0 & 0 & \sigma_{xz}^y \\ 0 & 0 & 0 \\ \sigma_{zx}^y & 0 & 0 \end{pmatrix}$	$\begin{pmatrix} 0 & \sigma_{xy}^z & 0 \\ -\sigma_{xy}^z & 0 & 0 \\ 0 & 0 & 0 \end{pmatrix}$
$6mm1'$	$\begin{pmatrix} 0 & p_{xy} & 0 \\ -p_{xy} & 0 & 0 \\ 0 & 0 & 0 \end{pmatrix}$	$\begin{pmatrix} 0 & -p_{xy} & 0 \\ p_{xy} & 0 & 0 \\ 0 & 0 & 0 \end{pmatrix}$	$6/mmm1'$	$\begin{pmatrix} \sigma_{xx} & 0 & 0 \\ 0 & \sigma_{xx} & 0 \\ 0 & 0 & \sigma_{zz} \end{pmatrix}$	$\begin{pmatrix} 0 & 0 & 0 \\ 0 & 0 & -\sigma_{xz}^y \\ 0 & -\sigma_{zx}^y & 0 \end{pmatrix}$	$\begin{pmatrix} 0 & 0 & \sigma_{xz}^y \\ 0 & 0 & 0 \\ \sigma_{zx}^y & 0 & 0 \end{pmatrix}$	$\begin{pmatrix} 0 & \sigma_{xy}^z & 0 \\ -\sigma_{xy}^z & 0 & 0 \\ 0 & 0 & 0 \end{pmatrix}$
$231'$	$\begin{pmatrix} p_{xx} & 0 & 0 \\ 0 & p_{xx} & 0 \\ 0 & 0 & p_{xx} \end{pmatrix}$	$\begin{pmatrix} p_{xx} & 0 & 0 \\ 0 & p_{xx} & 0 \\ 0 & 0 & p_{xx} \end{pmatrix}$	$m\bar{3}1'$	$\begin{pmatrix} \sigma_{xx} & 0 & 0 \\ 0 & \sigma_{xx} & 0 \\ 0 & 0 & \sigma_{xx} \end{pmatrix}$	$\begin{pmatrix} 0 & 0 & 0 \\ 0 & 0 & \sigma_{xy}^z \\ 0 & \sigma_{xz}^y & 0 \end{pmatrix}$	$\begin{pmatrix} 0 & 0 & \sigma_{xz}^y \\ 0 & 0 & 0 \\ \sigma_{xy}^z & 0 & 0 \end{pmatrix}$	$\begin{pmatrix} 0 & \sigma_{xy}^z & 0 \\ \sigma_{xz}^y & 0 & 0 \\ 0 & 0 & 0 \end{pmatrix}$
$4321'$	$\begin{pmatrix} p_{xx} & 0 & 0 \\ 0 & p_{xx} & 0 \\ 0 & 0 & p_{xx} \end{pmatrix}$	$\begin{pmatrix} p_{xx} & 0 & 0 \\ 0 & p_{xx} & 0 \\ 0 & 0 & p_{xx} \end{pmatrix}$	$m\bar{3}m1'$	$\begin{pmatrix} \sigma_{xx} & 0 & 0 \\ 0 & \sigma_{xx} & 0 \\ 0 & 0 & \sigma_{xx} \end{pmatrix}$	$\begin{pmatrix} 0 & 0 & 0 \\ 0 & 0 & \sigma_{xy}^z \\ 0 & -\sigma_{xy}^z & 0 \end{pmatrix}$	$\begin{pmatrix} 0 & 0 & -\sigma_{xy}^z \\ 0 & 0 & 0 \\ \sigma_{xy}^z & 0 & 0 \end{pmatrix}$	$\begin{pmatrix} 0 & \sigma_{xy}^z & 0 \\ -\sigma_{xy}^z & 0 & 0 \\ 0 & 0 & 0 \end{pmatrix}$

Table I. Shape of the direct and inverse Edelstein tensors, $\underline{\boldsymbol{p}}$ and $\underline{\boldsymbol{p}}'$, for all magnetic point groups of category (a). The third column shows the electrical conductivity tensor, $\underline{\boldsymbol{\sigma}}$, and in columns four to six the spin conductivity tensors for polarization along the Cartesian axes k = x, y and z, $\underline{\boldsymbol{\sigma}}^k$, are given. See Ref. 52 for further details on conventions and notation.

5

mpg	$\underline{\boldsymbol{p}}$	$\underline{\boldsymbol{p}}'$	mLg	$\underline{\boldsymbol{\sigma}}$	$\underline{\boldsymbol{\sigma}}^x$	$\underline{\boldsymbol{\sigma}}^y$	$\underline{\boldsymbol{\sigma}}^z$
1	$\begin{pmatrix} p_{xx} & p_{xy} & p_{xz} \\ p_{yx} & p_{yy} & p_{yz} \\ p_{zx} & p_{zy} & p_{zz} \end{pmatrix}$	$\begin{pmatrix} p'_{xx} & p'_{xy} & p'_{xz} \\ p'_{yx} & p'_{yy} & p'_{yz} \\ p'_{zx} & p'_{zy} & p'_{zz} \end{pmatrix}$	$\bar{1}$	$\begin{pmatrix} \sigma_{xx} & \sigma_{xy} & \sigma_{xz} \\ \sigma_{yx} & \sigma_{yy} & \sigma_{yz} \\ \sigma_{zx} & \sigma_{zy} & \sigma_{zz} \end{pmatrix}$	$\begin{pmatrix} \sigma^x_{xx} & \sigma^x_{xy} & \sigma^x_{xz} \\ \sigma^x_{yx} & \sigma^x_{yy} & \sigma^x_{yz} \\ \sigma^x_{zx} & \sigma^x_{zy} & \sigma^x_{zz} \end{pmatrix}$	$\begin{pmatrix} \sigma^y_{xx} & \sigma^y_{xy} & \sigma^y_{xz} \\ \sigma^y_{yx} & \sigma^y_{yy} & \sigma^y_{yz} \\ \sigma^y_{zx} & \sigma^y_{zy} & \sigma^y_{zz} \end{pmatrix}$	$\begin{pmatrix} \sigma^z_{xx} & \sigma^z_{xy} & \sigma^z_{xz} \\ \sigma^z_{yx} & \sigma^z_{yy} & \sigma^z_{yz} \\ \sigma^z_{zx} & \sigma^z_{zy} & \sigma^z_{zz} \end{pmatrix}$
2	$\begin{pmatrix} p_{xx} & 0 & p_{xz} \\ 0 & p_{yy} & 0 \\ p_{zx} & 0 & p_{zz} \end{pmatrix}$	$\begin{pmatrix} p'_{xx} & 0 & p'_{xz} \\ 0 & p_{yy} & 0 \\ p'_{zx} & 0 & p'_{zz} \end{pmatrix}$	$2/m$	$\begin{pmatrix} \sigma_{xx} & 0 & \sigma_{xz} \\ 0 & \sigma_{yy} & 0 \\ \sigma_{zx} & 0 & \sigma_{zz} \end{pmatrix}$	$\begin{pmatrix} 0 & \sigma^x_{xy} & 0 \\ \sigma^x_{yx} & 0 & \sigma^x_{yz} \\ 0 & \sigma^x_{zy} & 0 \end{pmatrix}$	$\begin{pmatrix} \sigma^y_{xx} & 0 & \sigma^y_{xz} \\ 0 & \sigma^y_{yy} & 0 \\ \sigma^y_{zx} & 0 & \sigma^y_{zz} \end{pmatrix}$	$\begin{pmatrix} 0 & \sigma^z_{xy} & 0 \\ \sigma^z_{yx} & 0 & \sigma^z_{yz} \\ 0 & \sigma^z_{zy} & 0 \end{pmatrix}$
m	$\begin{pmatrix} 0 & p_{xy} & 0 \\ p_{yx} & 0 & p_{yz} \\ 0 & p_{zy} & 0 \end{pmatrix}$	$\begin{pmatrix} 0 & p'_{xy} & 0 \\ p'_{yx} & 0 & p'_{yz} \\ 0 & p'_{zy} & 0 \end{pmatrix}$	$2/m$	$\begin{pmatrix} \sigma_{xx} & 0 & \sigma_{xz} \\ 0 & \sigma_{yy} & 0 \\ \sigma_{zx} & 0 & \sigma_{zz} \end{pmatrix}$	$\begin{pmatrix} 0 & \sigma^x_{xy} & 0 \\ \sigma^x_{yx} & 0 & \sigma^x_{yz} \\ 0 & \sigma^x_{zy} & 0 \end{pmatrix}$	$\begin{pmatrix} \sigma^y_{xx} & 0 & \sigma^y_{xz} \\ 0 & \sigma^y_{yy} & 0 \\ \sigma^y_{zx} & 0 & \sigma^y_{zz} \end{pmatrix}$	$\begin{pmatrix} 0 & \sigma^z_{xy} & 0 \\ \sigma^z_{yx} & 0 & \sigma^z_{yz} \\ 0 & \sigma^z_{zy} & 0 \end{pmatrix}$
222	$\begin{pmatrix} p_{xx} & 0 & 0 \\ 0 & p_{yy} & 0 \\ 0 & 0 & p_{zz} \end{pmatrix}$	$\begin{pmatrix} p'_{xx} & 0 & 0 \\ 0 & p'_{yy} & 0 \\ 0 & 0 & p'_{zz} \end{pmatrix}$	mmm	$\begin{pmatrix} \sigma_{xx} & 0 & 0 \\ 0 & \sigma_{yy} & 0 \\ 0 & 0 & \sigma_{zz} \end{pmatrix}$	$\begin{pmatrix} 0 & 0 & 0 \\ 0 & 0 & \sigma^x_{yz} \\ 0 & \sigma^x_{zy} & 0 \end{pmatrix}$	$\begin{pmatrix} 0 & 0 & \sigma^y_{xz} \\ 0 & 0 & 0 \\ \sigma^y_{zx} & 0 & 0 \end{pmatrix}$	$\begin{pmatrix} 0 & \sigma^z_{xy} & 0 \\ \sigma^z_{yx} & 0 & 0 \\ 0 & 0 & 0 \end{pmatrix}$
$mm2$	$\begin{pmatrix} 0 & p_{xy} & 0 \\ p_{yx} & 0 & 0 \\ 0 & 0 & 0 \end{pmatrix}$	$\begin{pmatrix} 0 & p'_{xy} & 0 \\ p'_{yx} & 0 & 0 \\ 0 & 0 & 0 \end{pmatrix}$	mmm	$\begin{pmatrix} \sigma_{xx} & 0 & 0 \\ 0 & \sigma_{yy} & 0 \\ 0 & 0 & \sigma_{zz} \end{pmatrix}$	$\begin{pmatrix} 0 & 0 & 0 \\ 0 & 0 & \sigma^x_{yz} \\ 0 & \sigma^x_{zy} & 0 \end{pmatrix}$	$\begin{pmatrix} 0 & 0 & \sigma^y_{xz} \\ 0 & 0 & 0 \\ \sigma^y_{zx} & 0 & 0 \end{pmatrix}$	$\begin{pmatrix} 0 & \sigma^z_{xy} & 0 \\ \sigma^z_{yx} & 0 & 0 \\ 0 & 0 & 0 \end{pmatrix}$
4	$\begin{pmatrix} p_{xx} & p_{xy} & 0 \\ -p_{xy} & p_{xx} & 0 \\ 0 & 0 & p_{zz} \end{pmatrix}$	$\begin{pmatrix} p'_{xx} & p'_{xy} & 0 \\ -p'_{xy} & p'_{xx} & 0 \\ 0 & 0 & p'_{zz} \end{pmatrix}$	$4/m$	$\begin{pmatrix} \sigma_{xx} & \sigma_{xy} & 0 \\ -\sigma_{xy} & \sigma_{xx} & 0 \\ 0 & 0 & \sigma_{zz} \end{pmatrix}$	$\begin{pmatrix} 0 & 0 & \sigma^x_{xz} \\ 0 & 0 & -\sigma^y_{xz} \\ \sigma^x_{zx} & -\sigma^y_{zx} & 0 \end{pmatrix}$	$\begin{pmatrix} 0 & 0 & \sigma^y_{xz} \\ 0 & 0 & \sigma^x_{xz} \\ \sigma^y_{zx} & \sigma^x_{zx} & 0 \end{pmatrix}$	$\begin{pmatrix} \sigma^z_{xx} & \sigma^z_{xy} & 0 \\ -\sigma^z_{xy} & \sigma^z_{xx} & 0 \\ 0 & 0 & \sigma^z_{zz} \end{pmatrix}$
$\bar{4}$	$\begin{pmatrix} p_{xx} & p_{xy} & 0 \\ p_{xy} & -p_{xx} & 0 \\ 0 & 0 & 0 \end{pmatrix}$	$\begin{pmatrix} p'_{xx} & p'_{xy} & 0 \\ p'_{xy} & -p'_{xx} & 0 \\ 0 & 0 & 0 \end{pmatrix}$	$4/m$	$\begin{pmatrix} \sigma_{xx} & \sigma_{xy} & 0 \\ -\sigma_{xy} & \sigma_{xx} & 0 \\ 0 & 0 & \sigma_{zz} \end{pmatrix}$	$\begin{pmatrix} 0 & 0 & \sigma^x_{xz} \\ 0 & 0 & -\sigma^y_{xz} \\ \sigma^x_{zx} & -\sigma^y_{zx} & 0 \end{pmatrix}$	$\begin{pmatrix} 0 & 0 & \sigma^y_{xz} \\ 0 & 0 & \sigma^x_{xz} \\ \sigma^y_{zx} & \sigma^x_{zx} & 0 \end{pmatrix}$	$\begin{pmatrix} \sigma^z_{xx} & \sigma^z_{xy} & 0 \\ -\sigma^z_{xy} & \sigma^z_{xx} & 0 \\ 0 & 0 & \sigma^z_{zz} \end{pmatrix}$
422	$\begin{pmatrix} p_{xx} & 0 & 0 \\ 0 & p_{xx} & 0 \\ 0 & 0 & p_{zz} \end{pmatrix}$	$\begin{pmatrix} p'_{xx} & 0 & 0 \\ 0 & p'_{xx} & 0 \\ 0 & 0 & p'_{zz} \end{pmatrix}$	$4/mmm$	$\begin{pmatrix} \sigma_{xx} & 0 & 0 \\ 0 & \sigma_{xx} & 0 \\ 0 & 0 & \sigma_{zz} \end{pmatrix}$	$\begin{pmatrix} 0 & 0 & 0 \\ 0 & 0 & -\sigma^y_{xz} \\ 0 & -\sigma^y_{zx} & 0 \end{pmatrix}$	$\begin{pmatrix} 0 & 0 & \sigma^y_{xz} \\ 0 & 0 & 0 \\ \sigma^y_{zx} & 0 & 0 \end{pmatrix}$	$\begin{pmatrix} 0 & \sigma^z_{xy} & 0 \\ -\sigma^z_{xy} & 0 & 0 \\ 0 & 0 & 0 \end{pmatrix}$
$4mm$	$\begin{pmatrix} 0 & p_{xy} & 0 \\ -p_{xy} & 0 & 0 \\ 0 & 0 & 0 \end{pmatrix}$	$\begin{pmatrix} 0 & p'_{xy} & 0 \\ -p'_{xy} & 0 & 0 \\ 0 & 0 & 0 \end{pmatrix}$	$4/mmm$	$\begin{pmatrix} \sigma_{xx} & 0 & 0 \\ 0 & \sigma_{xx} & 0 \\ 0 & 0 & \sigma_{zz} \end{pmatrix}$	$\begin{pmatrix} 0 & 0 & 0 \\ 0 & 0 & -\sigma^y_{xz} \\ 0 & -\sigma^y_{zx} & 0 \end{pmatrix}$	$\begin{pmatrix} 0 & 0 & \sigma^y_{xz} \\ 0 & 0 & 0 \\ \sigma^y_{zx} & 0 & 0 \end{pmatrix}$	$\begin{pmatrix} 0 & \sigma^z_{xy} & 0 \\ -\sigma^z_{xy} & 0 & 0 \\ 0 & 0 & 0 \end{pmatrix}$
$\bar{4}2m$	$\begin{pmatrix} p_{xx} & 0 & 0 \\ 0 & -p_{xx} & 0 \\ 0 & 0 & 0 \end{pmatrix}$	$\begin{pmatrix} p'_{xx} & 0 & 0 \\ 0 & -p'_{xx} & 0 \\ 0 & 0 & 0 \end{pmatrix}$	$4/mmm$	$\begin{pmatrix} \sigma_{xx} & 0 & 0 \\ 0 & \sigma_{xx} & 0 \\ 0 & 0 & \sigma_{zz} \end{pmatrix}$	$\begin{pmatrix} 0 & 0 & 0 \\ 0 & 0 & -\sigma^y_{xz} \\ 0 & -\sigma^y_{zx} & 0 \end{pmatrix}$	$\begin{pmatrix} 0 & 0 & \sigma^y_{xz} \\ 0 & 0 & 0 \\ \sigma^y_{zx} & 0 & 0 \end{pmatrix}$	$\begin{pmatrix} 0 & \sigma^z_{xy} & 0 \\ -\sigma^z_{xy} & 0 & 0 \\ 0 & 0 & 0 \end{pmatrix}$
3	$\begin{pmatrix} p_{xx} & p_{xy} & 0 \\ -p_{xy} & p_{xx} & 0 \\ 0 & 0 & p_{zz} \end{pmatrix}$	$\begin{pmatrix} p'_{xx} & p'_{xy} & 0 \\ -p'_{xy} & p'_{xx} & 0 \\ 0 & 0 & p'_{zz} \end{pmatrix}$	$\bar{3}$	$\begin{pmatrix} \sigma_{xx} & \sigma_{xy} & 0 \\ -\sigma_{xy} & \sigma_{xx} & 0 \\ 0 & 0 & \sigma_{zz} \end{pmatrix}$	$\begin{pmatrix} \sigma^x_{xx} & \sigma^y_{xx} & \sigma^x_{xz} \\ \sigma^y_{xx} & -\sigma^x_{xx} & -\sigma^y_{xz} \\ \sigma^x_{zx} & -\sigma^y_{zx} & 0 \end{pmatrix}$	$\begin{pmatrix} \sigma^y_{xx} & -\sigma^x_{xx} & \sigma^y_{xz} \\ -\sigma^x_{xx} & -\sigma^y_{xx} & \sigma^x_{xz} \\ \sigma^y_{zx} & \sigma^x_{zx} & 0 \end{pmatrix}$	$\begin{pmatrix} \sigma^z_{xx} & \sigma^z_{xy} & 0 \\ -\sigma^z_{xy} & \sigma^z_{xx} & 0 \\ 0 & 0 & \sigma^z_{zz} \end{pmatrix}$
312	$\begin{pmatrix} p_{xx} & 0 & 0 \\ 0 & p_{xx} & 0 \\ 0 & 0 & p_{zz} \end{pmatrix}$	$\begin{pmatrix} p'_{xx} & 0 & 0 \\ 0 & p'_{xx} & 0 \\ 0 & 0 & p'_{zz} \end{pmatrix}$	$\bar{3}1m$	$\begin{pmatrix} \sigma_{xx} & 0 & 0 \\ 0 & \sigma_{xx} & 0 \\ 0 & 0 & \sigma_{zz} \end{pmatrix}$	$\begin{pmatrix} \sigma^x_{xx} & 0 & 0 \\ 0 & -\sigma^x_{xx} & -\sigma^y_{xz} \\ 0 & -\sigma^y_{zx} & 0 \end{pmatrix}$	$\begin{pmatrix} 0 & -\sigma^x_{xx} & \sigma^y_{xz} \\ -\sigma^x_{xx} & 0 & 0 \\ \sigma^y_{zx} & 0 & 0 \end{pmatrix}$	$\begin{pmatrix} 0 & \sigma^z_{xy} & 0 \\ -\sigma^z_{xy} & 0 & 0 \\ 0 & 0 & 0 \end{pmatrix}$
$31m$	$\begin{pmatrix} 0 & p_{xy} & 0 \\ -p_{xy} & 0 & 0 \\ 0 & 0 & 0 \end{pmatrix}$	$\begin{pmatrix} 0 & p'_{xy} & 0 \\ -p'_{xy} & 0 & 0 \\ 0 & 0 & 0 \end{pmatrix}$	$\bar{3}1m$	$\begin{pmatrix} \sigma_{xx} & 0 & 0 \\ 0 & \sigma_{xx} & 0 \\ 0 & 0 & \sigma_{zz} \end{pmatrix}$	$\begin{pmatrix} \sigma^x_{xx} & 0 & 0 \\ 0 & -\sigma^x_{xx} & -\sigma^y_{xz} \\ 0 & -\sigma^y_{zx} & 0 \end{pmatrix}$	$\begin{pmatrix} 0 & -\sigma^x_{xx} & \sigma^y_{xz} \\ -\sigma^x_{xx} & 0 & 0 \\ \sigma^y_{zx} & 0 & 0 \end{pmatrix}$	$\begin{pmatrix} 0 & \sigma^z_{xy} & 0 \\ -\sigma^z_{xy} & 0 & 0 \\ 0 & 0 & 0 \end{pmatrix}$
6	$\begin{pmatrix} p_{xx} & p_{xy} & 0 \\ -p_{xy} & p_{xx} & 0 \\ 0 & 0 & p_{zz} \end{pmatrix}$	$\begin{pmatrix} p'_{xx} & p'_{xy} & 0 \\ -p'_{xy} & p'_{xx} & 0 \\ 0 & 0 & p'_{zz} \end{pmatrix}$	$6/m$	$\begin{pmatrix} \sigma_{xx} & \sigma_{xy} & 0 \\ -\sigma_{xy} & \sigma_{xx} & 0 \\ 0 & 0 & \sigma_{zz} \end{pmatrix}$	$\begin{pmatrix} 0 & 0 & \sigma^x_{xz} \\ 0 & 0 & -\sigma^y_{xz} \\ \sigma^x_{zx} & -\sigma^y_{zx} & 0 \end{pmatrix}$	$\begin{pmatrix} 0 & 0 & \sigma^y_{xz} \\ 0 & 0 & \sigma^x_{xz} \\ \sigma^y_{zx} & \sigma^x_{zx} & 0 \end{pmatrix}$	$\begin{pmatrix} \sigma^z_{xx} & \sigma^z_{xy} & 0 \\ -\sigma^z_{xy} & \sigma^z_{xx} & 0 \\ 0 & 0 & \sigma^z_{zz} \end{pmatrix}$
622	$\begin{pmatrix} p_{xx} & 0 & 0 \\ 0 & p_{xx} & 0 \\ 0 & 0 & p_{zz} \end{pmatrix}$	$\begin{pmatrix} p'_{xx} & 0 & 0 \\ 0 & p'_{xx} & 0 \\ 0 & 0 & p'_{zz} \end{pmatrix}$	$6/mmm$	$\begin{pmatrix} \sigma_{xx} & 0 & 0 \\ 0 & \sigma_{xx} & 0 \\ 0 & 0 & \sigma_{zz} \end{pmatrix}$	$\begin{pmatrix} 0 & 0 & 0 \\ 0 & 0 & -\sigma^y_{xz} \\ 0 & -\sigma^y_{zx} & 0 \end{pmatrix}$	$\begin{pmatrix} 0 & 0 & \sigma^y_{xz} \\ 0 & 0 & 0 \\ \sigma^y_{zx} & 0 & 0 \end{pmatrix}$	$\begin{pmatrix} 0 & \sigma^z_{xy} & 0 \\ -\sigma^z_{xy} & 0 & 0 \\ 0 & 0 & 0 \end{pmatrix}$
$6mm$	$\begin{pmatrix} 0 & p_{xy} & 0 \\ -p_{xy} & 0 & 0 \\ 0 & 0 & 0 \end{pmatrix}$	$\begin{pmatrix} 0 & p'_{xy} & 0 \\ -p'_{xy} & 0 & 0 \\ 0 & 0 & 0 \end{pmatrix}$	$6/mmm$	$\begin{pmatrix} \sigma_{xx} & 0 & 0 \\ 0 & \sigma_{xx} & 0 \\ 0 & 0 & \sigma_{zz} \end{pmatrix}$	$\begin{pmatrix} 0 & 0 & 0 \\ 0 & 0 & -\sigma^y_{xz} \\ 0 & -\sigma^y_{zx} & 0 \end{pmatrix}$	$\begin{pmatrix} 0 & 0 & \sigma^y_{xz} \\ 0 & 0 & 0 \\ \sigma^y_{zx} & 0 & 0 \end{pmatrix}$	$\begin{pmatrix} 0 & \sigma^z_{xy} & 0 \\ -\sigma^z_{xy} & 0 & 0 \\ 0 & 0 & 0 \end{pmatrix}$
23	$\begin{pmatrix} p_{xx} & 0 & 0 \\ 0 & p_{xx} & 0 \\ 0 & 0 & p_{xx} \end{pmatrix}$	$\begin{pmatrix} p'_{xx} & 0 & 0 \\ 0 & p'_{xx} & 0 \\ 0 & 0 & p'_{xx} \end{pmatrix}$	$m\bar{3}$	$\begin{pmatrix} \sigma_{xx} & 0 & 0 \\ 0 & \sigma_{xx} & 0 \\ 0 & 0 & \sigma_{xx} \end{pmatrix}$	$\begin{pmatrix} 0 & 0 & 0 \\ 0 & 0 & \sigma^z_{xy} \\ 0 & \sigma^y_{xz} & 0 \end{pmatrix}$	$\begin{pmatrix} 0 & 0 & \sigma^y_{xz} \\ 0 & 0 & 0 \\ \sigma^z_{xy} & 0 & 0 \end{pmatrix}$	$\begin{pmatrix} 0 & \sigma^z_{xy} & 0 \\ \sigma^y_{xz} & 0 & 0 \\ 0 & 0 & 0 \end{pmatrix}$
432	$\begin{pmatrix} p_{xx} & 0 & 0 \\ 0 & p_{xx} & 0 \\ 0 & 0 & p_{xx} \end{pmatrix}$	$\begin{pmatrix} p'_{xx} & 0 & 0 \\ 0 & p'_{xx} & 0 \\ 0 & 0 & p'_{xx} \end{pmatrix}$	$m\bar{3}m$	$\begin{pmatrix} \sigma_{xx} & 0 & 0 \\ 0 & \sigma_{xx} & 0 \\ 0 & 0 & \sigma_{xx} \end{pmatrix}$	$\begin{pmatrix} 0 & 0 & 0 \\ 0 & 0 & \sigma^z_{xy} \\ 0 & -\sigma^z_{xy} & 0 \end{pmatrix}$	$\begin{pmatrix} 0 & 0 & -\sigma^z_{xy} \\ 0 & 0 & 0 \\ \sigma^z_{xy} & 0 & 0 \end{pmatrix}$	$\begin{pmatrix} 0 & \sigma^z_{xy} & 0 \\ -\sigma^z_{xy} & 0 & 0 \\ 0 & 0 & 0 \end{pmatrix}$

Table II. Shape of the direct and inverse Edelstein tensors, $\underline{\boldsymbol{p}}$ and $\underline{\boldsymbol{p}}'$, for all magnetic point groups of category (b). The third column shows the electrical conductivity tensor, $\underline{\boldsymbol{\sigma}}$, and in columns four to six the spin conductivity tensors for polarization along the Cartesian axes k = x, y and z, $\underline{\boldsymbol{\sigma}}^k$, are given. See Ref. 52 for further details on conventions and notation.

mpg	$\underline{\boldsymbol{p}}$	$\underline{\boldsymbol{p}}'$	mLg	$\underline{\boldsymbol{\sigma}}$	$\underline{\boldsymbol{\sigma}}^x$	$\underline{\boldsymbol{\sigma}}^y$	$\underline{\boldsymbol{\sigma}}^z$
$\bar{1}'$	$\begin{pmatrix} p_{xx} & p_{xy} & p_{xz} \\ p_{yx} & p_{yy} & p_{yz} \\ p_{zx} & p_{zy} & p_{zz} \end{pmatrix}$	$\begin{pmatrix} -p_{xx} & -p_{yx} & -p_{zx} \\ -p_{xy} & -p_{yy} & -p_{zy} \\ -p_{xz} & -p_{yz} & -p_{zz} \end{pmatrix}$	$\bar{1}1'$	$\begin{pmatrix} \sigma_{xx} & \sigma_{xy} & \sigma_{xz} \\ \sigma_{xy} & \sigma_{yy} & \sigma_{yz} \\ \sigma_{xz} & \sigma_{yz} & \sigma_{zz} \end{pmatrix}$	$\begin{pmatrix} \sigma^x_{xx} & \sigma^x_{xy} & \sigma^x_{xz} \\ \sigma^x_{yx} & \sigma^x_{yy} & \sigma^x_{yz} \\ \sigma^x_{zx} & \sigma^x_{zy} & \sigma^x_{zz} \end{pmatrix}$	$\begin{pmatrix} \sigma^y_{xx} & \sigma^y_{xy} & \sigma^y_{xz} \\ \sigma^y_{yx} & \sigma^y_{yy} & \sigma^y_{yz} \\ \sigma^y_{zx} & \sigma^y_{zy} & \sigma^y_{zz} \end{pmatrix}$	$\begin{pmatrix} \sigma^z_{xx} & \sigma^z_{xy} & \sigma^z_{xz} \\ \sigma^z_{yx} & \sigma^z_{yy} & \sigma^z_{yz} \\ \sigma^z_{zx} & \sigma^z_{zy} & \sigma^z_{zz} \end{pmatrix}$
$2'$	$\begin{pmatrix} p_{xx} & p_{xy} & p_{xz} \\ p_{yx} & p_{yy} & p_{yz} \\ p_{zx} & p_{zy} & p_{zz} \end{pmatrix}$	$\begin{pmatrix} p_{xx} & -p_{yx} & p_{zx} \\ -p_{xy} & p_{yy} & -p_{zy} \\ p_{xz} & -p_{yz} & p_{zz} \end{pmatrix}$	$2'/m'$	$\begin{pmatrix} \sigma_{xx} & \sigma_{xy} & \sigma_{xz} \\ -\sigma_{xy} & \sigma_{yy} & \sigma_{yz} \\ \sigma_{xz} & -\sigma_{yz} & \sigma_{zz} \end{pmatrix}$	$\begin{pmatrix} \sigma^x_{xx} & \sigma^x_{xy} & \sigma^x_{xz} \\ \sigma^x_{yx} & \sigma^x_{yy} & \sigma^x_{yz} \\ \sigma^x_{zx} & \sigma^x_{zy} & \sigma^x_{zz} \end{pmatrix}$	$\begin{pmatrix} \sigma^y_{xx} & \sigma^y_{xy} & \sigma^y_{xz} \\ \sigma^y_{yx} & \sigma^y_{yy} & \sigma^y_{yz} \\ \sigma^y_{zx} & \sigma^y_{zy} & \sigma^y_{zz} \end{pmatrix}$	$\begin{pmatrix} \sigma^z_{xx} & \sigma^z_{xy} & \sigma^z_{xz} \\ \sigma^z_{yx} & \sigma^z_{yy} & \sigma^z_{yz} \\ \sigma^z_{zx} & \sigma^z_{zy} & \sigma^z_{zz} \end{pmatrix}$
m'	$\begin{pmatrix} p_{xx} & p_{xy} & p_{xz} \\ p_{yx} & p_{yy} & p_{yz} \\ p_{zx} & p_{zy} & p_{zz} \end{pmatrix}$	$\begin{pmatrix} -p_{xx} & p_{yx} & -p_{zx} \\ p_{xy} & -p_{yy} & p_{zy} \\ -p_{xz} & p_{yz} & -p_{zz} \end{pmatrix}$	$2'/m'$	$\begin{pmatrix} \sigma_{xx} & \sigma_{xy} & \sigma_{xz} \\ -\sigma_{xy} & \sigma_{yy} & \sigma_{yz} \\ \sigma_{xz} & -\sigma_{yz} & \sigma_{zz} \end{pmatrix}$	$\begin{pmatrix} \sigma^x_{xx} & \sigma^x_{xy} & \sigma^x_{xz} \\ \sigma^x_{yx} & \sigma^x_{yy} & \sigma^x_{yz} \\ \sigma^x_{zx} & \sigma^x_{zy} & \sigma^x_{zz} \end{pmatrix}$	$\begin{pmatrix} \sigma^y_{xx} & \sigma^y_{xy} & \sigma^y_{xz} \\ \sigma^y_{yx} & \sigma^y_{yy} & \sigma^y_{yz} \\ \sigma^y_{zx} & \sigma^y_{zy} & \sigma^y_{zz} \end{pmatrix}$	$\begin{pmatrix} \sigma^z_{xx} & \sigma^z_{xy} & \sigma^z_{xz} \\ \sigma^z_{yx} & \sigma^z_{yy} & \sigma^z_{yz} \\ \sigma^z_{zx} & \sigma^z_{zy} & \sigma^z_{zz} \end{pmatrix}$
$2/m'$	$\begin{pmatrix} p_{xx} & 0 & p_{xz} \\ 0 & p_{yy} & 0 \\ p_{zx} & 0 & p_{zz} \end{pmatrix}$	$\begin{pmatrix} -p_{xx} & 0 & -p_{zx} \\ 0 & -p_{yy} & 0 \\ -p_{xz} & 0 & -p_{zz} \end{pmatrix}$	$2/m1'$	$\begin{pmatrix} \sigma_{xx} & 0 & \sigma_{xz} \\ 0 & \sigma_{yy} & 0 \\ \sigma_{xz} & 0 & \sigma_{zz} \end{pmatrix}$	$\begin{pmatrix} 0 & \sigma^x_{xy} & 0 \\ \sigma^x_{yx} & 0 & \sigma^x_{yz} \\ 0 & \sigma^x_{zy} & 0 \end{pmatrix}$	$\begin{pmatrix} \sigma^y_{xx} & 0 & \sigma^y_{xz} \\ 0 & \sigma^y_{yy} & 0 \\ \sigma^y_{zx} & 0 & \sigma^y_{zz} \end{pmatrix}$	$\begin{pmatrix} 0 & \sigma^z_{xy} & 0 \\ \sigma^z_{yx} & 0 & \sigma^z_{yz} \\ 0 & \sigma^z_{zy} & 0 \end{pmatrix}$
$2'/m$	$\begin{pmatrix} 0 & p_{xy} & 0 \\ p_{yx} & 0 & p_{yz} \\ 0 & p_{zy} & 0 \end{pmatrix}$	$\begin{pmatrix} 0 & -p_{yx} & 0 \\ -p_{xy} & 0 & -p_{zy} \\ 0 & -p_{yz} & 0 \end{pmatrix}$	$2/m1'$	$\begin{pmatrix} \sigma_{xx} & 0 & \sigma_{xz} \\ 0 & \sigma_{yy} & 0 \\ \sigma_{xz} & 0 & \sigma_{zz} \end{pmatrix}$	$\begin{pmatrix} 0 & \sigma^x_{xy} & 0 \\ \sigma^x_{yx} & 0 & \sigma^x_{yz} \\ 0 & \sigma^x_{zy} & 0 \end{pmatrix}$	$\begin{pmatrix} \sigma^y_{xx} & 0 & \sigma^y_{xz} \\ 0 & \sigma^y_{yy} & 0 \\ \sigma^y_{zx} & 0 & \sigma^y_{zz} \end{pmatrix}$	$\begin{pmatrix} 0 & \sigma^z_{xy} & 0 \\ \sigma^z_{yx} & 0 & \sigma^z_{yz} \\ 0 & \sigma^z_{zy} & 0 \end{pmatrix}$
$2'2'2$	$\begin{pmatrix} p_{xx} & p_{xy} & 0 \\ p_{yx} & p_{yy} & 0 \\ 0 & 0 & p_{zz} \end{pmatrix}$	$\begin{pmatrix} p_{xx} & -p_{yx} & 0 \\ -p_{xy} & p_{yy} & 0 \\ 0 & 0 & p_{zz} \end{pmatrix}$	$m'm'm$	$\begin{pmatrix} \sigma_{xx} & \sigma_{xy} & 0 \\ -\sigma_{xy} & \sigma_{yy} & 0 \\ 0 & 0 & \sigma_{zz} \end{pmatrix}$	$\begin{pmatrix} 0 & 0 & \sigma^x_{xz} \\ 0 & 0 & \sigma^x_{yz} \\ \sigma^x_{zx} & \sigma^x_{zy} & 0 \end{pmatrix}$	$\begin{pmatrix} 0 & 0 & \sigma^y_{xz} \\ 0 & 0 & \sigma^y_{yz} \\ \sigma^y_{zx} & \sigma^y_{zy} & 0 \end{pmatrix}$	$\begin{pmatrix} \sigma^z_{xx} & \sigma^z_{xy} & 0 \\ \sigma^z_{yx} & \sigma^z_{yy} & 0 \\ 0 & 0 & \sigma^z_{zz} \end{pmatrix}$
$m'm'2$	$\begin{pmatrix} p_{xx} & p_{xy} & 0 \\ p_{yx} & p_{yy} & 0 \\ 0 & 0 & p_{zz} \end{pmatrix}$	$\begin{pmatrix} -p_{xx} & p_{yx} & 0 \\ p_{xy} & -p_{yy} & 0 \\ 0 & 0 & -p_{zz} \end{pmatrix}$	$m'm'm$	$\begin{pmatrix} \sigma_{xx} & \sigma_{xy} & 0 \\ -\sigma_{xy} & \sigma_{yy} & 0 \\ 0 & 0 & \sigma_{zz} \end{pmatrix}$	$\begin{pmatrix} 0 & 0 & \sigma^x_{xz} \\ 0 & 0 & \sigma^x_{yz} \\ \sigma^x_{zx} & \sigma^x_{zy} & 0 \end{pmatrix}$	$\begin{pmatrix} 0 & 0 & \sigma^y_{xz} \\ 0 & 0 & \sigma^y_{yz} \\ \sigma^y_{zx} & \sigma^y_{zy} & 0 \end{pmatrix}$	$\begin{pmatrix} \sigma^z_{xx} & \sigma^z_{xy} & 0 \\ \sigma^z_{yx} & \sigma^z_{yy} & 0 \\ 0 & 0 & \sigma^z_{zz} \end{pmatrix}$
$m'm2'$	$\begin{pmatrix} 0 & p_{xy} & 0 \\ p_{yx} & 0 & p_{yz} \\ 0 & p_{zy} & 0 \end{pmatrix}$	$\begin{pmatrix} 0 & p_{yx} & 0 \\ p_{xy} & 0 & -p_{zy} \\ 0 & -p_{yz} & 0 \end{pmatrix}$	$m'm'm$	$\begin{pmatrix} \sigma_{xx} & 0 & \sigma_{xz} \\ 0 & \sigma_{yy} & 0 \\ -\sigma_{xz} & 0 & \sigma_{zz} \end{pmatrix}$	$\begin{pmatrix} 0 & \sigma^x_{xy} & 0 \\ \sigma^x_{yx} & 0 & \sigma^x_{yz} \\ 0 & \sigma^x_{zy} & 0 \end{pmatrix}$	$\begin{pmatrix} \sigma^y_{xx} & 0 & \sigma^y_{xz} \\ 0 & \sigma^y_{yy} & 0 \\ \sigma^y_{zx} & 0 & \sigma^y_{zz} \end{pmatrix}$	$\begin{pmatrix} 0 & \sigma^z_{xy} & 0 \\ \sigma^z_{yx} & 0 & \sigma^z_{yz} \\ 0 & \sigma^z_{zy} & 0 \end{pmatrix}$
$m'm'm'$	$\begin{pmatrix} p_{xx} & 0 & 0 \\ 0 & p_{yy} & 0 \\ 0 & 0 & p_{zz} \end{pmatrix}$	$\begin{pmatrix} -p_{xx} & 0 & 0 \\ 0 & -p_{yy} & 0 \\ 0 & 0 & -p_{zz} \end{pmatrix}$	$mmm1'$	$\begin{pmatrix} \sigma_{xx} & 0 & 0 \\ 0 & \sigma_{yy} & 0 \\ 0 & 0 & \sigma_{zz} \end{pmatrix}$	$\begin{pmatrix} 0 & 0 & 0 \\ 0 & 0 & \sigma^x_{yz} \\ 0 & \sigma^x_{zy} & 0 \end{pmatrix}$	$\begin{pmatrix} 0 & 0 & \sigma^y_{xz} \\ 0 & 0 & 0 \\ \sigma^y_{zx} & 0 & 0 \end{pmatrix}$	$\begin{pmatrix} 0 & \sigma^z_{xy} & 0 \\ \sigma^z_{yx} & 0 & 0 \\ 0 & 0 & 0 \end{pmatrix}$
$m'mm$	$\begin{pmatrix} 0 & 0 & 0 \\ 0 & 0 & p_{yz} \\ 0 & p_{zy} & 0 \end{pmatrix}$	$\begin{pmatrix} 0 & 0 & 0 \\ 0 & 0 & -p_{zy} \\ 0 & -p_{yz} & 0 \end{pmatrix}$	$mmm1'$	$\begin{pmatrix} \sigma_{xx} & 0 & 0 \\ 0 & \sigma_{yy} & 0 \\ 0 & 0 & \sigma_{zz} \end{pmatrix}$	$\begin{pmatrix} 0 & 0 & 0 \\ 0 & 0 & \sigma^x_{yz} \\ 0 & \sigma^x_{zy} & 0 \end{pmatrix}$	$\begin{pmatrix} 0 & 0 & \sigma^y_{xz} \\ 0 & 0 & 0 \\ \sigma^y_{zx} & 0 & 0 \end{pmatrix}$	$\begin{pmatrix} 0 & \sigma^z_{xy} & 0 \\ \sigma^z_{yx} & 0 & 0 \\ 0 & 0 & 0 \end{pmatrix}$

Table III. Shape of the direct and inverse Edelstein tensors, $\underline{\boldsymbol{p}}$ and $\underline{\boldsymbol{p}}'$, for magnetic point groups of category (c). The third column shows the electrical conductivity tensor, $\underline{\boldsymbol{\sigma}}$, and in columns four to six the spin conductivity tensors for polarization along the Cartesian axes k = x, y and z, $\underline{\boldsymbol{\sigma}}^k$, are given. See Ref. 52 for further details on conventions and notation. This table is continued in Tables IV-VII.

are conceivable: a Rashba(-Edelstein)- or field-like torque and a spin Hall- or (anti-)damping-like torque. The former obviously always contributes, the latter might as well.

III. NUMERICAL INVESTIGATIONS

While the group theoretical considerations presented above allow unambiguous prediction of the occurrence of the direct and inverse Edelstein effect, they give no information concerning the absolute and relative magnitude of the respective tensor elements. In order to get more insight into this aspect, calculations of the Edelstein polarization tensor $\underline{\boldsymbol{p}}$ have been performed on the artificial multilayer alloy-system Pt | Fe_xCo_{1-x} | Cu for the full range of concentration x. Fig. 1 shows the hexagonal structure of this model system for which a stacking of fcc(111)-like atomic planes along the z-axis has been assumed.

For the magnetization along the stacking direction Pt | Fe_xCo_{1-x} | Cu has the magnetic point group $3m'$,[62] leading to an anti-symmetric Edelstein tensor with non-vanishing elements $p_{xx} = p_{yy} \neq p_{zz}$ and $p_{xy} = -p_{yx}$ (see row three of Tab. V). Corresponding numerical results for the elements of the tensor $\underline{\boldsymbol{p}}$ are given in Fig. 2. To provide a wider basis for the discussion of the results for the EE, the non-vanishing elements of the torkance tensor $\underline{\boldsymbol{t}}$ in the same system obtained before are reproduced from Ref. 50 for convenience in Fig. 3. In addition calculations have been performed on the spin conductivity tensors with the corresponding results given in Fig. 4. Results for the electrical conductivity have been presented before as well[50], but will not be repeated here.

The top panel of Fig. 2 gives the numerical results for the concentration dependence of the diagonal Edelstein tensor element p_{xx} ($= p_{yy}$) perpendicular to the magnetization. As in Ref. 50, the so-called Fermi sea contribution, corresponding to the second term in Eq. (2), is represented by blue squares, the Fermi surface contribution, accordingly the first term in Eq. (2), is shown as green diamonds, their sum is given as red circles. Empty symbols are results without vertex corrections (NV), full symbols include them (VC). The antisymmetric off-diagonal el-

7

mpg	$\underline{p}$	$\underline{p}'$	mLg	$\underline{\sigma}$	$\underline{\sigma}^x$	$\underline{\sigma}^y$	$\underline{\sigma}^z$
$4'$	$\begin{pmatrix} p_{xx} & p_{xy} & 0 \\ p_{yx} & p_{yy} & 0 \\ 0 & 0 & p_{zz} \end{pmatrix}$	$\begin{pmatrix} p_{yy} & -p_{xy} & 0 \\ -p_{yx} & p_{xx} & 0 \\ 0 & 0 & p_{zz} \end{pmatrix}$	$4'/m$	$\begin{pmatrix} \sigma_{xx} & 0 & 0 \\ 0 & \sigma_{xx} & 0 \\ 0 & 0 & \sigma_{zz} \end{pmatrix}$	$\begin{pmatrix} 0 & 0 & \sigma^x_{xz} \\ 0 & 0 & \sigma^x_{yz} \\ \sigma^x_{zx} & \sigma^x_{zy} & 0 \end{pmatrix}$	$\begin{pmatrix} 0 & 0 & \sigma^y_{xz} \\ 0 & 0 & \sigma^y_{yz} \\ \sigma^y_{zx} & \sigma^y_{zy} & 0 \end{pmatrix}$	$\begin{pmatrix} \sigma^z_{xx} & \sigma^z_{xy} & 0 \\ \sigma^z_{yx} & \sigma^z_{yy} & 0 \\ 0 & 0 & \sigma^z_{zz} \end{pmatrix}$
$\bar{4}'$	$\begin{pmatrix} p_{xx} & p_{xy} & 0 \\ p_{yx} & p_{yy} & 0 \\ 0 & 0 & p_{zz} \end{pmatrix}$	$\begin{pmatrix} -p_{yy} & p_{xy} & 0 \\ p_{yx} & -p_{xx} & 0 \\ 0 & 0 & -p_{zz} \end{pmatrix}$	$4'/m$	$\begin{pmatrix} \sigma_{xx} & 0 & 0 \\ 0 & \sigma_{xx} & 0 \\ 0 & 0 & \sigma_{zz} \end{pmatrix}$	$\begin{pmatrix} 0 & 0 & \sigma^x_{xz} \\ 0 & 0 & \sigma^x_{yz} \\ \sigma^x_{zx} & \sigma^x_{zy} & 0 \end{pmatrix}$	$\begin{pmatrix} 0 & 0 & \sigma^y_{xz} \\ 0 & 0 & \sigma^y_{yz} \\ \sigma^y_{zx} & \sigma^y_{zy} & 0 \end{pmatrix}$	$\begin{pmatrix} \sigma^z_{xx} & \sigma^z_{xy} & 0 \\ \sigma^z_{yx} & \sigma^z_{yy} & 0 \\ 0 & 0 & \sigma^z_{zz} \end{pmatrix}$
$4/m'$	$\begin{pmatrix} p_{xx} & p_{xy} & 0 \\ -p_{xy} & p_{xx} & 0 \\ 0 & 0 & p_{zz} \end{pmatrix}$	$\begin{pmatrix} -p_{xx} & p_{xy} & 0 \\ -p_{xy} & -p_{xx} & 0 \\ 0 & 0 & -p_{zz} \end{pmatrix}$	$4/m1'$	$\begin{pmatrix} \sigma_{xx} & 0 & 0 \\ 0 & \sigma_{xx} & 0 \\ 0 & 0 & \sigma_{zz} \end{pmatrix}$	$\begin{pmatrix} 0 & 0 & \sigma^x_{xz} \\ 0 & 0 & -\sigma^y_{xz} \\ \sigma^x_{zx} & -\sigma^y_{zx} & 0 \end{pmatrix}$	$\begin{pmatrix} 0 & 0 & \sigma^y_{xz} \\ 0 & 0 & \sigma^x_{xz} \\ \sigma^y_{zx} & \sigma^x_{zx} & 0 \end{pmatrix}$	$\begin{pmatrix} \sigma^z_{xx} & \sigma^z_{xy} & 0 \\ -\sigma^z_{xy} & \sigma^z_{xx} & 0 \\ 0 & 0 & \sigma^z_{zz} \end{pmatrix}$
$4'/m'$	$\begin{pmatrix} p_{xx} & p_{xy} & 0 \\ p_{xy} & -p_{xx} & 0 \\ 0 & 0 & 0 \end{pmatrix}$	$\begin{pmatrix} -p_{xx} & -p_{xy} & 0 \\ -p_{xy} & p_{xx} & 0 \\ 0 & 0 & 0 \end{pmatrix}$	$4/m1'$	$\begin{pmatrix} \sigma_{xx} & 0 & 0 \\ 0 & \sigma_{xx} & 0 \\ 0 & 0 & \sigma_{zz} \end{pmatrix}$	$\begin{pmatrix} 0 & 0 & \sigma^x_{xz} \\ 0 & 0 & -\sigma^y_{xz} \\ \sigma^x_{zx} & -\sigma^y_{zx} & 0 \end{pmatrix}$	$\begin{pmatrix} 0 & 0 & \sigma^y_{xz} \\ 0 & 0 & \sigma^x_{xz} \\ \sigma^y_{zx} & \sigma^x_{zx} & 0 \end{pmatrix}$	$\begin{pmatrix} \sigma^z_{xx} & \sigma^z_{xy} & 0 \\ -\sigma^z_{xy} & \sigma^z_{xx} & 0 \\ 0 & 0 & \sigma^z_{zz} \end{pmatrix}$
$4'22'$	$\begin{pmatrix} p_{xx} & 0 & 0 \\ 0 & p_{yy} & 0 \\ 0 & 0 & p_{zz} \end{pmatrix}$	$\begin{pmatrix} p_{yy} & 0 & 0 \\ 0 & p_{xx} & 0 \\ 0 & 0 & p_{zz} \end{pmatrix}$	$4'/mmm'$	$\begin{pmatrix} \sigma_{xx} & 0 & 0 \\ 0 & \sigma_{xx} & 0 \\ 0 & 0 & \sigma_{zz} \end{pmatrix}$	$\begin{pmatrix} 0 & 0 & 0 \\ 0 & 0 & \sigma^y_{yz} \\ 0 & \sigma^x_{zy} & 0 \end{pmatrix}$	$\begin{pmatrix} 0 & 0 & \sigma^y_{xz} \\ 0 & 0 & 0 \\ \sigma^y_{zx} & 0 & 0 \end{pmatrix}$	$\begin{pmatrix} 0 & \sigma^z_{xy} & 0 \\ \sigma^z_{yx} & 0 & 0 \\ 0 & 0 & 0 \end{pmatrix}$
$42'2'$	$\begin{pmatrix} p_{xx} & p_{xy} & 0 \\ -p_{xy} & p_{xx} & 0 \\ 0 & 0 & p_{zz} \end{pmatrix}$	$\begin{pmatrix} p_{xx} & p_{xy} & 0 \\ -p_{xy} & p_{xx} & 0 \\ 0 & 0 & p_{zz} \end{pmatrix}$	$4/mm'm'$	$\begin{pmatrix} \sigma_{xx} & \sigma_{xy} & 0 \\ -\sigma_{xy} & \sigma_{xx} & 0 \\ 0 & 0 & \sigma_{zz} \end{pmatrix}$	$\begin{pmatrix} 0 & 0 & \sigma^x_{xz} \\ 0 & 0 & -\sigma^y_{xz} \\ \sigma^x_{zx} & -\sigma^y_{zx} & 0 \end{pmatrix}$	$\begin{pmatrix} 0 & 0 & \sigma^y_{xz} \\ 0 & 0 & \sigma^x_{xz} \\ \sigma^y_{zx} & \sigma^x_{zx} & 0 \end{pmatrix}$	$\begin{pmatrix} \sigma^z_{xx} & \sigma^z_{xy} & 0 \\ -\sigma^z_{xy} & \sigma^z_{xx} & 0 \\ 0 & 0 & \sigma^z_{zz} \end{pmatrix}$
$4'mm'$	$\begin{pmatrix} 0 & p_{xy} & 0 \\ p_{yx} & 0 & 0 \\ 0 & 0 & 0 \end{pmatrix}$	$\begin{pmatrix} 0 & -p_{xy} & 0 \\ -p_{yx} & 0 & 0 \\ 0 & 0 & 0 \end{pmatrix}$	$4'/mmm'$	$\begin{pmatrix} \sigma_{xx} & 0 & 0 \\ 0 & \sigma_{xx} & 0 \\ 0 & 0 & \sigma_{zz} \end{pmatrix}$	$\begin{pmatrix} 0 & 0 & 0 \\ 0 & 0 & \sigma^x_{yz} \\ 0 & \sigma^x_{zy} & 0 \end{pmatrix}$	$\begin{pmatrix} 0 & 0 & \sigma^y_{xz} \\ 0 & 0 & 0 \\ \sigma^y_{zx} & 0 & 0 \end{pmatrix}$	$\begin{pmatrix} 0 & \sigma^z_{xy} & 0 \\ \sigma^z_{yx} & 0 & 0 \\ 0 & 0 & 0 \end{pmatrix}$
$4m'm'$	$\begin{pmatrix} p_{xx} & p_{xy} & 0 \\ -p_{xy} & p_{xx} & 0 \\ 0 & 0 & p_{zz} \end{pmatrix}$	$\begin{pmatrix} -p_{xx} & -p_{xy} & 0 \\ p_{xy} & -p_{xx} & 0 \\ 0 & 0 & -p_{zz} \end{pmatrix}$	$4/mm'm'$	$\begin{pmatrix} \sigma_{xx} & \sigma_{xy} & 0 \\ -\sigma_{xy} & \sigma_{xx} & 0 \\ 0 & 0 & \sigma_{zz} \end{pmatrix}$	$\begin{pmatrix} 0 & 0 & \sigma^x_{xz} \\ 0 & 0 & -\sigma^y_{xz} \\ \sigma^x_{zx} & -\sigma^y_{zx} & 0 \end{pmatrix}$	$\begin{pmatrix} 0 & 0 & \sigma^y_{xz} \\ 0 & 0 & \sigma^x_{xz} \\ \sigma^y_{zx} & \sigma^x_{zx} & 0 \end{pmatrix}$	$\begin{pmatrix} \sigma^z_{xx} & \sigma^z_{xy} & 0 \\ -\sigma^z_{xy} & \sigma^z_{xx} & 0 \\ 0 & 0 & \sigma^z_{zz} \end{pmatrix}$
$\bar{4}'2m'$	$\begin{pmatrix} p_{xx} & 0 & 0 \\ 0 & p_{yy} & 0 \\ 0 & 0 & p_{zz} \end{pmatrix}$	$\begin{pmatrix} -p_{yy} & 0 & 0 \\ 0 & -p_{xx} & 0 \\ 0 & 0 & -p_{zz} \end{pmatrix}$	$4'/mmm'$	$\begin{pmatrix} \sigma_{xx} & 0 & 0 \\ 0 & \sigma_{xx} & 0 \\ 0 & 0 & \sigma_{zz} \end{pmatrix}$	$\begin{pmatrix} 0 & 0 & 0 \\ 0 & 0 & \sigma^x_{yz} \\ 0 & \sigma^x_{zy} & 0 \end{pmatrix}$	$\begin{pmatrix} 0 & 0 & \sigma^y_{xz} \\ 0 & 0 & 0 \\ \sigma^y_{zx} & 0 & 0 \end{pmatrix}$	$\begin{pmatrix} 0 & \sigma^z_{xy} & 0 \\ \sigma^z_{yx} & 0 & 0 \\ 0 & 0 & 0 \end{pmatrix}$
$\bar{4}'m2'$	$\begin{pmatrix} 0 & p_{xy} & 0 \\ p_{yx} & 0 & 0 \\ 0 & 0 & 0 \end{pmatrix}$	$\begin{pmatrix} 0 & p_{xy} & 0 \\ p_{yx} & 0 & 0 \\ 0 & 0 & 0 \end{pmatrix}$	$4'/mmm'$	$\begin{pmatrix} \sigma_{xx} & 0 & 0 \\ 0 & \sigma_{xx} & 0 \\ 0 & 0 & \sigma_{zz} \end{pmatrix}$	$\begin{pmatrix} 0 & 0 & 0 \\ 0 & 0 & \sigma^x_{yz} \\ 0 & \sigma^x_{zy} & 0 \end{pmatrix}$	$\begin{pmatrix} 0 & 0 & \sigma^y_{xz} \\ 0 & 0 & 0 \\ \sigma^y_{zx} & 0 & 0 \end{pmatrix}$	$\begin{pmatrix} 0 & \sigma^z_{xy} & 0 \\ \sigma^z_{yx} & 0 & 0 \\ 0 & 0 & 0 \end{pmatrix}$
$\bar{4}2'm'$	$\begin{pmatrix} p_{xx} & p_{xy} & 0 \\ p_{xy} & -p_{xx} & 0 \\ 0 & 0 & 0 \end{pmatrix}$	$\begin{pmatrix} p_{xx} & -p_{xy} & 0 \\ -p_{xy} & -p_{xx} & 0 \\ 0 & 0 & 0 \end{pmatrix}$	$4/mm'm'$	$\begin{pmatrix} \sigma_{xx} & \sigma_{xy} & 0 \\ -\sigma_{xy} & \sigma_{xx} & 0 \\ 0 & 0 & \sigma_{zz} \end{pmatrix}$	$\begin{pmatrix} 0 & 0 & \sigma^x_{xz} \\ 0 & 0 & -\sigma^y_{xz} \\ \sigma^x_{zx} & -\sigma^y_{zx} & 0 \end{pmatrix}$	$\begin{pmatrix} 0 & 0 & \sigma^y_{xz} \\ 0 & 0 & \sigma^x_{xz} \\ \sigma^y_{zx} & \sigma^x_{zx} & 0 \end{pmatrix}$	$\begin{pmatrix} \sigma^z_{xx} & \sigma^z_{xy} & 0 \\ -\sigma^z_{xy} & \sigma^z_{xx} & 0 \\ 0 & 0 & \sigma^z_{zz} \end{pmatrix}$
$4/m'm'm'$	$\begin{pmatrix} p_{xx} & 0 & 0 \\ 0 & p_{xx} & 0 \\ 0 & 0 & p_{zz} \end{pmatrix}$	$\begin{pmatrix} -p_{xx} & 0 & 0 \\ 0 & -p_{xx} & 0 \\ 0 & 0 & -p_{zz} \end{pmatrix}$	$4/mmm1'$	$\begin{pmatrix} \sigma_{xx} & 0 & 0 \\ 0 & \sigma_{xx} & 0 \\ 0 & 0 & \sigma_{zz} \end{pmatrix}$	$\begin{pmatrix} 0 & 0 & 0 \\ 0 & 0 & -\sigma^y_{xz} \\ 0 & -\sigma^y_{zx} & 0 \end{pmatrix}$	$\begin{pmatrix} 0 & 0 & \sigma^y_{xz} \\ 0 & 0 & 0 \\ \sigma^y_{zx} & 0 & 0 \end{pmatrix}$	$\begin{pmatrix} 0 & \sigma^z_{xy} & 0 \\ -\sigma^z_{xy} & 0 & 0 \\ 0 & 0 & 0 \end{pmatrix}$
$4/m'mm$	$\begin{pmatrix} 0 & p_{xy} & 0 \\ -p_{xy} & 0 & 0 \\ 0 & 0 & 0 \end{pmatrix}$	$\begin{pmatrix} 0 & p_{xy} & 0 \\ -p_{xy} & 0 & 0 \\ 0 & 0 & 0 \end{pmatrix}$	$4/mmm1'$	$\begin{pmatrix} \sigma_{xx} & 0 & 0 \\ 0 & \sigma_{xx} & 0 \\ 0 & 0 & \sigma_{zz} \end{pmatrix}$	$\begin{pmatrix} 0 & 0 & 0 \\ 0 & 0 & -\sigma^y_{xz} \\ 0 & -\sigma^y_{zx} & 0 \end{pmatrix}$	$\begin{pmatrix} 0 & 0 & \sigma^y_{xz} \\ 0 & 0 & 0 \\ \sigma^y_{zx} & 0 & 0 \end{pmatrix}$	$\begin{pmatrix} 0 & \sigma^z_{xy} & 0 \\ -\sigma^z_{xy} & 0 & 0 \\ 0 & 0 & 0 \end{pmatrix}$
$4'/m'm'm$	$\begin{pmatrix} p_{xx} & 0 & 0 \\ 0 & -p_{xx} & 0 \\ 0 & 0 & 0 \end{pmatrix}$	$\begin{pmatrix} -p_{xx} & 0 & 0 \\ 0 & p_{xx} & 0 \\ 0 & 0 & 0 \end{pmatrix}$	$4/mmm1'$	$\begin{pmatrix} \sigma_{xx} & 0 & 0 \\ 0 & \sigma_{xx} & 0 \\ 0 & 0 & \sigma_{zz} \end{pmatrix}$	$\begin{pmatrix} 0 & 0 & 0 \\ 0 & 0 & -\sigma^y_{xz} \\ 0 & -\sigma^y_{zx} & 0 \end{pmatrix}$	$\begin{pmatrix} 0 & 0 & \sigma^y_{xz} \\ 0 & 0 & 0 \\ \sigma^y_{zx} & 0 & 0 \end{pmatrix}$	$\begin{pmatrix} 0 & \sigma^z_{xy} & 0 \\ -\sigma^z_{xy} & 0 & 0 \\ 0 & 0 & 0 \end{pmatrix}$

Table IV. Table III continued for tetragonal groups.

ement $p_{xy} = -p_{yx}$ is shown in the middle panel, the use of symbols is the same as in the top panel. In contrast to the torkance tensor for the same magnetic point group, the element p_{zz} in the bottom panel obviously does not vanish. This means that a current parallel to the magnetic moment along the z-direction changes its magnitude. The pronounced concentration dependence of the vertex corrections to the Fermi surface term will be discussed below.

When comparing the results for torkance (see Fig. 3) and Edelstein response one of the first observations is that the concentration dependence of the diagonal (xx) and of the off-diagonal (xy) elements seem to have been interchanged. The former, p_{xx} in the top panel of Fig. 2, is an almost linear and flat function of the concentration, while the latter, p_{xy} in the middle panel, shows the conductivity-like divergences at the boundaries. This inverted behavior of course reflects the additional cross-product of the current-induced spin polarization with the magnetization, that is the essential difference between Edelstein effect and spin-orbit torque.

Analyzing the numerical results in more detail, one finds that all three non-vanishing tensor elements are dominated by the contributions from the Fermi surface. Comparing now t_{xx} (Fig. 3, top) and p_{xy} (Fig. 2, middle) one sees that the slight asymmetry of the torkance is more pronounced for the Edelstein response, and in addition reversed concerning the dependence on x, i.e., p_{xy} is larger (absolutely) for 10 % Fe than for 10 %Co. A similar observation can be made comparing t_{xy} (Fig. 3, bot-

8

mpg	$\underline{p}$	$\underline{p}'$	mLg	$\underline{\sigma}$	$\underline{\sigma}^x$	$\underline{\sigma}^y$	$\underline{\sigma}^z$
$\bar{3}'$	$\begin{pmatrix} p_{xx} & p_{xy} & 0 \\ -p_{xy} & p_{xx} & 0 \\ 0 & 0 & p_{zz} \end{pmatrix}$	$\begin{pmatrix} -p_{xx} & p_{xy} & 0 \\ -p_{xy} & -p_{xx} & 0 \\ 0 & 0 & -p_{zz} \end{pmatrix}$	$\bar{3}1'$	$\begin{pmatrix} \sigma_{xx} & 0 & 0 \\ 0 & \sigma_{xx} & 0 \\ 0 & 0 & \sigma_{zz} \end{pmatrix}$	$\begin{pmatrix} \sigma^x_{xx} & \sigma^y_{xx} & \sigma^x_{xz} \\ \sigma^y_{xx} & -\sigma^x_{xx} & -\sigma^y_{xz} \\ \sigma^x_{zx} & -\sigma^y_{zx} & 0 \end{pmatrix}$	$\begin{pmatrix} \sigma^y_{xx} & -\sigma^x_{xx}\sigma^y_{xz} \\ -\sigma^x_{xx} & -\sigma^y_{xx}\sigma^x_{xz} \\ \sigma^y_{zx} & \sigma^x_{zx} & 0 \end{pmatrix}$	$\begin{pmatrix} \sigma^z_{xx} & \sigma^z_{xy} & 0 \\ -\sigma^z_{xy} & \sigma^z_{xx} & 0 \\ 0 & 0 & \sigma^z_{zz} \end{pmatrix}$
$312'$	$\begin{pmatrix} p_{xx} & p_{xy} & 0 \\ -p_{xy} & p_{xx} & 0 \\ 0 & 0 & p_{zz} \end{pmatrix}$	$\begin{pmatrix} p_{xx} & p_{xy} & 0 \\ -p_{xy} & p_{xx} & 0 \\ 0 & 0 & p_{zz} \end{pmatrix}$	$\bar{3}1m'$	$\begin{pmatrix} \sigma_{xx} & \sigma_{xy} & 0 \\ -\sigma_{xy} & \sigma_{xx} & 0 \\ 0 & 0 & \sigma_{zz} \end{pmatrix}$	$\begin{pmatrix} \sigma^x_{xx} & \sigma^y_{xx} & \sigma^x_{xz} \\ \sigma^y_{xx} & -\sigma^x_{xx} & -\sigma^y_{xz} \\ \sigma^x_{zx} & -\sigma^y_{zx} & 0 \end{pmatrix}$	$\begin{pmatrix} \sigma^y_{xx} & -\sigma^x_{xx}\sigma^y_{xz} \\ -\sigma^x_{xx} & -\sigma^y_{xx}\sigma^x_{xz} \\ \sigma^y_{zx} & \sigma^x_{zx} & 0 \end{pmatrix}$	$\begin{pmatrix} \sigma^z_{xx} & \sigma^z_{xy} & 0 \\ -\sigma^z_{xy} & \sigma^z_{xx} & 0 \\ 0 & 0 & \sigma^z_{zz} \end{pmatrix}$
$31m'$	$\begin{pmatrix} p_{xx} & p_{xy} & 0 \\ -p_{xy} & p_{xx} & 0 \\ 0 & 0 & p_{zz} \end{pmatrix}$	$\begin{pmatrix} -p_{xx} & -p_{xy} & 0 \\ p_{xy} & -p_{xx} & 0 \\ 0 & 0 & -p_{zz} \end{pmatrix}$	$\bar{3}1m'$	$\begin{pmatrix} \sigma_{xx} & \sigma_{xy} & 0 \\ -\sigma_{xy} & \sigma_{xx} & 0 \\ 0 & 0 & \sigma_{zz} \end{pmatrix}$	$\begin{pmatrix} \sigma^x_{xx} & \sigma^y_{xx} & \sigma^x_{xz} \\ \sigma^y_{xx} & -\sigma^x_{xx} & -\sigma^y_{xz} \\ \sigma^x_{zx} & -\sigma^y_{zx} & 0 \end{pmatrix}$	$\begin{pmatrix} \sigma^y_{xx} & -\sigma^x_{xx}\sigma^y_{xz} \\ -\sigma^x_{xx} & -\sigma^y_{xx}\sigma^x_{xz} \\ \sigma^y_{zx} & \sigma^x_{zx} & 0 \end{pmatrix}$	$\begin{pmatrix} \sigma^z_{xx} & \sigma^z_{xy} & 0 \\ -\sigma^z_{xy} & \sigma^z_{xx} & 0 \\ 0 & 0 & \sigma^z_{zz} \end{pmatrix}$
$\bar{3}'1m'$	$\begin{pmatrix} p_{xx} & 0 & 0 \\ 0 & p_{xx} & 0 \\ 0 & 0 & p_{zz} \end{pmatrix}$	$\begin{pmatrix} -p_{xx} & 0 & 0 \\ 0 & -p_{xx} & 0 \\ 0 & 0 & -p_{zz} \end{pmatrix}$	$\bar{3}1m1'$	$\begin{pmatrix} \sigma_{xx} & 0 & 0 \\ 0 & \sigma_{xx} & 0 \\ 0 & 0 & \sigma_{zz} \end{pmatrix}$	$\begin{pmatrix} \sigma^x_{xx} & 0 & 0 \\ 0 & -\sigma^x_{xx} & -\sigma^y_{xz} \\ 0 & -\sigma^y_{zx} & 0 \end{pmatrix}$	$\begin{pmatrix} 0 & -\sigma^x_{xx}\sigma^y_{xz} \\ -\sigma^x_{xx} & 0 & 0 \\ \sigma^y_{zx} & 0 & 0 \end{pmatrix}$	$\begin{pmatrix} 0 & \sigma^z_{xy} & 0 \\ -\sigma^z_{xy} & 0 & 0 \\ 0 & 0 & 0 \end{pmatrix}$
$\bar{3}'1m$	$\begin{pmatrix} 0 & p_{xy} & 0 \\ -p_{xy} & 0 & 0 \\ 0 & 0 & 0 \end{pmatrix}$	$\begin{pmatrix} 0 & p_{xy} & 0 \\ -p_{xy} & 0 & 0 \\ 0 & 0 & 0 \end{pmatrix}$	$\bar{3}1m1'$	$\begin{pmatrix} \sigma_{xx} & 0 & 0 \\ 0 & \sigma_{xx} & 0 \\ 0 & 0 & \sigma_{zz} \end{pmatrix}$	$\begin{pmatrix} \sigma^x_{xx} & 0 & 0 \\ 0 & -\sigma^x_{xx} & -\sigma^y_{xz} \\ 0 & -\sigma^y_{zx} & 0 \end{pmatrix}$	$\begin{pmatrix} 0 & -\sigma^x_{xx}\sigma^y_{xz} \\ -\sigma^x_{xx} & 0 & 0 \\ \sigma^y_{zx} & 0 & 0 \end{pmatrix}$	$\begin{pmatrix} 0 & \sigma^z_{xy} & 0 \\ -\sigma^z_{xy} & 0 & 0 \\ 0 & 0 & 0 \end{pmatrix}$

Table V. Table III continued for trigonal groups.

mpg	$\underline{p}$	$\underline{p}'$	mLg	$\underline{\sigma}$	$\underline{\sigma}^x$	$\underline{\sigma}^y$	$\underline{\sigma}^z$
$6'$	$\begin{pmatrix} p_{xx} & p_{xy} & 0 \\ -p_{xy} & p_{xx} & 0 \\ 0 & 0 & p_{zz} \end{pmatrix}$	$\begin{pmatrix} p_{xx} & -p_{xy} & 0 \\ p_{xy} & p_{xx} & 0 \\ 0 & 0 & p_{zz} \end{pmatrix}$	$6'/m'$	$\begin{pmatrix} \sigma_{xx} & 0 & 0 \\ 0 & \sigma_{xx} & 0 \\ 0 & 0 & \sigma_{zz} \end{pmatrix}$	$\begin{pmatrix} \sigma^x_{xx} & \sigma^y_{xx} & \sigma^x_{xz} \\ \sigma^y_{xx} & -\sigma^x_{xx} & -\sigma^y_{xz} \\ \sigma^x_{zx} & -\sigma^y_{zx} & 0 \end{pmatrix}$	$\begin{pmatrix} \sigma^y_{xx} & -\sigma^x_{xx}\sigma^y_{xz} \\ -\sigma^x_{xx} & -\sigma^y_{xx}\sigma^x_{xz} \\ \sigma^y_{zx} & \sigma^x_{zx} & 0 \end{pmatrix}$	$\begin{pmatrix} \sigma^z_{xx} & \sigma^z_{xy} & 0 \\ -\sigma^z_{xy} & \sigma^z_{xx} & 0 \\ 0 & 0 & \sigma^z_{zz} \end{pmatrix}$
$\bar{6}'$	$\begin{pmatrix} p_{xx} & p_{xy} & 0 \\ -p_{xy} & p_{xx} & 0 \\ 0 & 0 & p_{zz} \end{pmatrix}$	$\begin{pmatrix} -p_{xx} & p_{xy} & 0 \\ -p_{xy} & -p_{xx} & 0 \\ 0 & 0 & -p_{zz} \end{pmatrix}$	$6'/m'$	$\begin{pmatrix} \sigma_{xx} & 0 & 0 \\ 0 & \sigma_{xx} & 0 \\ 0 & 0 & \sigma_{zz} \end{pmatrix}$	$\begin{pmatrix} \sigma^x_{xx} & \sigma^y_{xx} & \sigma^x_{xz} \\ \sigma^y_{xx} & -\sigma^x_{xx} & -\sigma^y_{xz} \\ \sigma^x_{zx} & -\sigma^y_{zx} & 0 \end{pmatrix}$	$\begin{pmatrix} \sigma^y_{xx} & -\sigma^x_{xx}\sigma^y_{xz} \\ -\sigma^x_{xx} & -\sigma^y_{xx}\sigma^x_{xz} \\ \sigma^y_{zx} & \sigma^x_{zx} & 0 \end{pmatrix}$	$\begin{pmatrix} \sigma^z_{xx} & \sigma^z_{xy} & 0 \\ -\sigma^z_{xy} & \sigma^z_{xx} & 0 \\ 0 & 0 & \sigma^z_{zz} \end{pmatrix}$
$6/m'$	$\begin{pmatrix} p_{xx} & p_{xy} & 0 \\ -p_{xy} & p_{xx} & 0 \\ 0 & 0 & p_{zz} \end{pmatrix}$	$\begin{pmatrix} -p_{xx} & p_{xy} & 0 \\ -p_{xy} & -p_{xx} & 0 \\ 0 & 0 & -p_{zz} \end{pmatrix}$	$6/m1'$	$\begin{pmatrix} \sigma_{xx} & 0 & 0 \\ 0 & \sigma_{xx} & 0 \\ 0 & 0 & \sigma_{zz} \end{pmatrix}$	$\begin{pmatrix} 0 & 0 & \sigma^x_{xz} \\ 0 & 0 & -\sigma^y_{xz} \\ \sigma^x_{zx} & -\sigma^y_{zx} & 0 \end{pmatrix}$	$\begin{pmatrix} 0 & 0 & \sigma^y_{xz} \\ 0 & 0 & \sigma^x_{xz} \\ \sigma^y_{zx}\sigma^x_{zx} & 0 \end{pmatrix}$	$\begin{pmatrix} \sigma^z_{xx} & \sigma^z_{xy} & 0 \\ -\sigma^z_{xy} & \sigma^z_{xx} & 0 \\ 0 & 0 & \sigma^z_{zz} \end{pmatrix}$
$6'22'$	$\begin{pmatrix} p_{xx} & 0 & 0 \\ 0 & p_{xx} & 0 \\ 0 & 0 & p_{zz} \end{pmatrix}$	$\begin{pmatrix} p_{xx} & 0 & 0 \\ 0 & p_{xx} & 0 \\ 0 & 0 & p_{zz} \end{pmatrix}$	$6'/m'mm'$	$\begin{pmatrix} \sigma_{xx} & 0 & 0 \\ 0 & \sigma_{xx} & 0 \\ 0 & 0 & \sigma_{zz} \end{pmatrix}$	$\begin{pmatrix} 0 & \sigma^y_{xx} & 0 \\ \sigma^y_{xx} & 0 & -\sigma^y_{xz} \\ 0 & -\sigma^y_{zx} & 0 \end{pmatrix}$	$\begin{pmatrix} \sigma^y_{xx} & 0 & \sigma^y_{xz} \\ 0 & -\sigma^y_{xx} & 0 \\ \sigma^y_{zx} & 0 & 0 \end{pmatrix}$	$\begin{pmatrix} 0 & \sigma^z_{xy} & 0 \\ -\sigma^z_{xy} & 0 & 0 \\ 0 & 0 & 0 \end{pmatrix}$
$62'2'$	$\begin{pmatrix} p_{xx} & p_{xy} & 0 \\ -p_{xy} & p_{xx} & 0 \\ 0 & 0 & p_{zz} \end{pmatrix}$	$\begin{pmatrix} p_{xx} & p_{xy} & 0 \\ -p_{xy} & p_{xx} & 0 \\ 0 & 0 & p_{zz} \end{pmatrix}$	$6/mm'm'$	$\begin{pmatrix} \sigma_{xx} & \sigma_{xy} & 0 \\ -\sigma_{xy} & \sigma_{xx} & 0 \\ 0 & 0 & \sigma_{zz} \end{pmatrix}$	$\begin{pmatrix} 0 & 0 & \sigma^x_{xz} \\ 0 & 0 & -\sigma^y_{xz} \\ \sigma^x_{zx} & -\sigma^y_{zx} & 0 \end{pmatrix}$	$\begin{pmatrix} 0 & 0 & \sigma^y_{xz} \\ 0 & 0 & \sigma^x_{xz} \\ \sigma^y_{zx}\sigma^x_{zx} & 0 \end{pmatrix}$	$\begin{pmatrix} \sigma^z_{xx} & \sigma^z_{xy} & 0 \\ -\sigma^z_{xy} & \sigma^z_{xx} & 0 \\ 0 & 0 & \sigma^z_{zz} \end{pmatrix}$
$6'mm'$	$\begin{pmatrix} 0 & p_{xy} & 0 \\ -p_{xy} & 0 & 0 \\ 0 & 0 & 0 \end{pmatrix}$	$\begin{pmatrix} 0 & -p_{xy} & 0 \\ p_{xy} & 0 & 0 \\ 0 & 0 & 0 \end{pmatrix}$	$6'/m'mm'$	$\begin{pmatrix} \sigma_{xx} & 0 & 0 \\ 0 & \sigma_{xx} & 0 \\ 0 & 0 & \sigma_{zz} \end{pmatrix}$	$\begin{pmatrix} 0 & \sigma^y_{xx} & 0 \\ \sigma^y_{xx} & 0 & -\sigma^y_{xz} \\ 0 & -\sigma^y_{zx} & 0 \end{pmatrix}$	$\begin{pmatrix} \sigma^y_{xx} & 0 & \sigma^y_{xz} \\ 0 & -\sigma^y_{xx} & 0 \\ \sigma^y_{zx} & 0 & 0 \end{pmatrix}$	$\begin{pmatrix} 0 & \sigma^z_{xy} & 0 \\ -\sigma^z_{xy} & 0 & 0 \\ 0 & 0 & 0 \end{pmatrix}$
$6m'm'$	$\begin{pmatrix} p_{xx} & p_{xy} & 0 \\ -p_{xy} & p_{xx} & 0 \\ 0 & 0 & p_{zz} \end{pmatrix}$	$\begin{pmatrix} -p_{xx} & -p_{xy} & 0 \\ p_{xy} & -p_{xx} & 0 \\ 0 & 0 & -p_{zz} \end{pmatrix}$	$6/mm'm'$	$\begin{pmatrix} \sigma_{xx} & \sigma_{xy} & 0 \\ -\sigma_{xy} & \sigma_{xx} & 0 \\ 0 & 0 & \sigma_{zz} \end{pmatrix}$	$\begin{pmatrix} 0 & 0 & \sigma^x_{xz} \\ 0 & 0 & -\sigma^y_{xz} \\ \sigma^x_{zx} & -\sigma^y_{zx} & 0 \end{pmatrix}$	$\begin{pmatrix} 0 & 0 & \sigma^y_{xz} \\ 0 & 0 & \sigma^x_{xz} \\ \sigma^y_{zx}\sigma^x_{zx} & 0 \end{pmatrix}$	$\begin{pmatrix} \sigma^z_{xx} & \sigma^z_{xy} & 0 \\ -\sigma^z_{xy} & \sigma^z_{xx} & 0 \\ 0 & 0 & \sigma^z_{zz} \end{pmatrix}$
$\bar{6}'2m'$	$\begin{pmatrix} p_{xx} & 0 & 0 \\ 0 & p_{xx} & 0 \\ 0 & 0 & p_{zz} \end{pmatrix}$	$\begin{pmatrix} -p_{xx} & 0 & 0 \\ 0 & -p_{xx} & 0 \\ 0 & 0 & -p_{zz} \end{pmatrix}$	$6'/m'mm'$	$\begin{pmatrix} \sigma_{xx} & 0 & 0 \\ 0 & \sigma_{xx} & 0 \\ 0 & 0 & \sigma_{zz} \end{pmatrix}$	$\begin{pmatrix} 0 & \sigma^y_{xx} & 0 \\ \sigma^y_{xx} & 0 & -\sigma^y_{xz} \\ 0 & -\sigma^y_{zx} & 0 \end{pmatrix}$	$\begin{pmatrix} \sigma^y_{xx} & 0 & \sigma^y_{xz} \\ 0 & -\sigma^y_{xx} & 0 \\ \sigma^y_{zx} & 0 & 0 \end{pmatrix}$	$\begin{pmatrix} 0 & \sigma^z_{xy} & 0 \\ -\sigma^z_{xy} & 0 & 0 \\ 0 & 0 & 0 \end{pmatrix}$
$\bar{6}'m2'$	$\begin{pmatrix} 0 & p_{xy} & 0 \\ -p_{xy} & 0 & 0 \\ 0 & 0 & 0 \end{pmatrix}$	$\begin{pmatrix} 0 & p_{xy} & 0 \\ -p_{xy} & 0 & 0 \\ 0 & 0 & 0 \end{pmatrix}$	$6'/m'mm'$	$\begin{pmatrix} \sigma_{xx} & 0 & 0 \\ 0 & \sigma_{xx} & 0 \\ 0 & 0 & \sigma_{zz} \end{pmatrix}$	$\begin{pmatrix} 0 & \sigma^y_{xx} & 0 \\ \sigma^y_{xx} & 0 & -\sigma^y_{xz} \\ 0 & -\sigma^y_{zx} & 0 \end{pmatrix}$	$\begin{pmatrix} \sigma^y_{xx} & 0 & \sigma^y_{xz} \\ 0 & -\sigma^y_{xx} & 0 \\ \sigma^y_{zx} & 0 & 0 \end{pmatrix}$	$\begin{pmatrix} 0 & \sigma^z_{xy} & 0 \\ -\sigma^z_{xy} & 0 & 0 \\ 0 & 0 & 0 \end{pmatrix}$
$6/m'm'm'$	$\begin{pmatrix} p_{xx} & 0 & 0 \\ 0 & p_{xx} & 0 \\ 0 & 0 & p_{zz} \end{pmatrix}$	$\begin{pmatrix} -p_{xx} & 0 & 0 \\ 0 & -p_{xx} & 0 \\ 0 & 0 & -p_{zz} \end{pmatrix}$	$6/mmm1'$	$\begin{pmatrix} \sigma_{xx} & 0 & 0 \\ 0 & \sigma_{xx} & 0 \\ 0 & 0 & \sigma_{zz} \end{pmatrix}$	$\begin{pmatrix} 0 & 0 & 0 \\ 0 & 0 & -\sigma^y_{xz} \\ 0 & -\sigma^y_{zx} & 0 \end{pmatrix}$	$\begin{pmatrix} 0 & 0 & \sigma^y_{xz} \\ 0 & 0 & 0 \\ \sigma^y_{zx} & 0 & 0 \end{pmatrix}$	$\begin{pmatrix} 0 & \sigma^z_{xy} & 0 \\ -\sigma^z_{xy} & 0 & 0 \\ 0 & 0 & 0 \end{pmatrix}$
$6/m'mm$	$\begin{pmatrix} 0 & p_{xy} & 0 \\ -p_{xy} & 0 & 0 \\ 0 & 0 & 0 \end{pmatrix}$	$\begin{pmatrix} 0 & p_{xy} & 0 \\ -p_{xy} & 0 & 0 \\ 0 & 0 & 0 \end{pmatrix}$	$6/mmm1'$	$\begin{pmatrix} \sigma_{xx} & 0 & 0 \\ 0 & \sigma_{xx} & 0 \\ 0 & 0 & \sigma_{zz} \end{pmatrix}$	$\begin{pmatrix} 0 & 0 & 0 \\ 0 & 0 & -\sigma^y_{xz} \\ 0 & -\sigma^y_{zx} & 0 \end{pmatrix}$	$\begin{pmatrix} 0 & 0 & \sigma^y_{xz} \\ 0 & 0 & 0 \\ \sigma^y_{zx} & 0 & 0 \end{pmatrix}$	$\begin{pmatrix} 0 & \sigma^z_{xy} & 0 \\ -\sigma^z_{xy} & 0 & 0 \\ 0 & 0 & 0 \end{pmatrix}$

Table VI. Table III continued for hexagonal groups.

tom) and p_{xx} (Fig. 2, top), here the torkance is stronger on the Co-rich side while the Edelstein response is larger for higher iron content. Note that this is not trivially related to the magnitude of the local spin magnetic moment, which is in fact increasing with x, but has to be attributed to the different selection rules for the operator matrix elements. Another striking difference is the relative importance and sign of the Fermi sea and surface contributions. While for the even torkance t_{xy} the Fermi sea term is not negligible and moreover of opposite sign

9

mpg	$\underline{\boldsymbol{p}}$	$\underline{\boldsymbol{p}}'$	mLg	$\underline{\boldsymbol{\sigma}}$	$\underline{\boldsymbol{\sigma}}^x$	$\underline{\boldsymbol{\sigma}}^y$	$\underline{\boldsymbol{\sigma}}^z$
$m'\bar{3}'$	$\begin{pmatrix} p_{xx} & 0 & 0 \\ 0 & p_{xx} & 0 \\ 0 & 0 & p_{xx} \end{pmatrix}$	$\begin{pmatrix} -p_{xx} & 0 & 0 \\ 0 & -p_{xx} & 0 \\ 0 & 0 & -p_{xx} \end{pmatrix}$	$m\bar{3}1'$	$\begin{pmatrix} \sigma_{xx} & 0 & 0 \\ 0 & \sigma_{xx} & 0 \\ 0 & 0 & \sigma_{xx} \end{pmatrix}$	$\begin{pmatrix} 0 & 0 & 0 \\ 0 & 0 & \sigma^z_{xy} \\ 0 & \sigma^y_{xz} & 0 \end{pmatrix}$	$\begin{pmatrix} 0 & 0 & \sigma^y_{xz} \\ 0 & 0 & 0 \\ \sigma^z_{xy} & 0 & 0 \end{pmatrix}$	$\begin{pmatrix} 0 & \sigma^z_{xy} & 0 \\ \sigma^y_{xz} & 0 & 0 \\ 0 & 0 & 0 \end{pmatrix}$
$4'32'$	$\begin{pmatrix} p_{xx} & 0 & 0 \\ 0 & p_{xx} & 0 \\ 0 & 0 & p_{xx} \end{pmatrix}$	$\begin{pmatrix} p_{xx} & 0 & 0 \\ 0 & p_{xx} & 0 \\ 0 & 0 & p_{xx} \end{pmatrix}$	$m\bar{3}m'$	$\begin{pmatrix} \sigma_{xx} & 0 & 0 \\ 0 & \sigma_{xx} & 0 \\ 0 & 0 & \sigma_{xx} \end{pmatrix}$	$\begin{pmatrix} 0 & 0 & 0 \\ 0 & 0 & \sigma^z_{xy} \\ 0 & \sigma^y_{xz} & 0 \end{pmatrix}$	$\begin{pmatrix} 0 & 0 & \sigma^y_{xz} \\ 0 & 0 & 0 \\ \sigma^z_{xy} & 0 & 0 \end{pmatrix}$	$\begin{pmatrix} 0 & \sigma^z_{xy} & 0 \\ \sigma^y_{xz} & 0 & 0 \\ 0 & 0 & 0 \end{pmatrix}$
$\bar{4}'3m'$	$\begin{pmatrix} p_{xx} & 0 & 0 \\ 0 & p_{xx} & 0 \\ 0 & 0 & p_{xx} \end{pmatrix}$	$\begin{pmatrix} -p_{xx} & 0 & 0 \\ 0 & -p_{xx} & 0 \\ 0 & 0 & -p_{xx} \end{pmatrix}$	$m\bar{3}m'$	$\begin{pmatrix} \sigma_{xx} & 0 & 0 \\ 0 & \sigma_{xx} & 0 \\ 0 & 0 & \sigma_{xx} \end{pmatrix}$	$\begin{pmatrix} 0 & 0 & 0 \\ 0 & 0 & \sigma^z_{xy} \\ 0 & \sigma^y_{xz} & 0 \end{pmatrix}$	$\begin{pmatrix} 0 & 0 & \sigma^y_{xz} \\ 0 & 0 & 0 \\ \sigma^z_{xy} & 0 & 0 \end{pmatrix}$	$\begin{pmatrix} 0 & \sigma^z_{xy} & 0 \\ \sigma^y_{xz} & 0 & 0 \\ 0 & 0 & 0 \end{pmatrix}$
$m'\bar{3}'m'$	$\begin{pmatrix} p_{xx} & 0 & 0 \\ 0 & p_{xx} & 0 \\ 0 & 0 & p_{xx} \end{pmatrix}$	$\begin{pmatrix} -p_{xx} & 0 & 0 \\ 0 & -p_{xx} & 0 \\ 0 & 0 & -p_{xx} \end{pmatrix}$	$m\bar{3}m1'$	$\begin{pmatrix} \sigma_{xx} & 0 & 0 \\ 0 & \sigma_{xx} & 0 \\ 0 & 0 & \sigma_{xx} \end{pmatrix}$	$\begin{pmatrix} 0 & 0 & 0 \\ 0 & 0 & \sigma^z_{xy} \\ 0 & -\sigma^z_{xy} & 0 \end{pmatrix}$	$\begin{pmatrix} 0 & 0 & -\sigma^z_{xy} \\ 0 & 0 & 0 \\ \sigma^z_{xy} & 0 & 0 \end{pmatrix}$	$\begin{pmatrix} 0 & \sigma^z_{xy} & 0 \\ -\sigma^z_{xy} & 0 & 0 \\ 0 & 0 & 0 \end{pmatrix}$

Table VII. Table III continued for cubic groups.

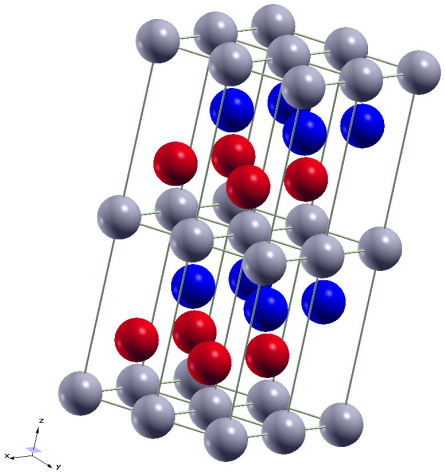

Figure 1. (Color online) Structure of the investigated multilayer system $\mathrm{Pt}\,|\,\mathrm{Fe}_x\mathrm{Co}_{1-x}\,|\,\mathrm{Cu}$ consisting of a stacking of fcc(111) planes along the z axis. Cu atoms are colored in blue, $\mathrm{Fe}_x\mathrm{Co}_{1-x}$ sites in red and Pt atoms are represented in light grey.

compared to the Fermi surface term, for the longitudinal Edelstein response p_{xx} the Fermi sea does not contribute significantly but with the same sign as the Fermi surface term. The vertex corrections are in both cases only significant at the Fermi surface and only in the very dilute limits. For the Edelstein polarization p_{xy} the Fermi sea contribution is numerically zero, in agreement with the situation for the odd torkance t_{xx}. The Fermi surface contribution is essentially purely intrinsic for both, i.e., the vertex corrections are insignificant. The very strong concentration dependence of p_{zz} (bottom panel), including several sign changes is indeed very puzzling, because lacking convergence w.r.t. **k**-point density (usually the biggest numerical challenge in linear response calculations in solids) can be ruled out as a reason for this behavior. In fact, the structure is caused by the vertex corrections to the Fermi-surface contribution (surf), reflecting the very delicate dependence of this term on the various system parameters. The vertex corrections to the Fermi sea term are negligibly small for all elements of $\underline{\boldsymbol{p}}$ and $\underline{\boldsymbol{t}}$.

Concerning the behavior of the tensor elements w.r.t. magnetization reversal, the longitudinal elements $p_{xx} = p_{yy}$ and p_{zz} change sign when changing the magnetization direction from z to −z, i.e., these elements have perfect odd symmetry. The off-diagonal antisymmetric elements $p_{xy} = -p_{yx}$ in contrast remain unchanged and represent therefore a purely even contribution to the Edelstein effect. These symmetry properties are identical to that of the torkance tensor, where also t_{xx} was odd and t_{xy} even w.r.t. magnetization reversal; i.e., completely opposite to the behavior of $\underline{\boldsymbol{\sigma}}$. These findings obviously reflect the transformation properties of the various vector operators involved.

When reversing the layer sequence from $\mathrm{Pt}\,|\,\mathrm{Fe}_x\mathrm{Co}_{1-x}\,|\,\mathrm{Cu}$ to $\mathrm{Cu}\,|\,\mathrm{Fe}_x\mathrm{Co}_{1-x}\,|\,\mathrm{Pt}$ and keeping the global magnetization direction fixed along z, both – symmetric and anti-symmetric – parts of the tensor change sign. Since this corresponds to magnetization reversal plus inversion of the coordinate system (for a rotation around x: x → x' = x, y → y' = −y, z → z' = −z), this of course does not mean both are odd, since $p_{x'y'}(z') = -p_{xy}(z') = p_{xy}(z)$.

Finally, it should be noted that when changing the lattice parameter in addition from that of fcc Pt to that of fcc Cu, the absolute values slightly change due to the modified electronic structure (presumably in particular at the interface). This is more pronounced for the Edelstein response than for the torkance, reflecting once more the fact that the polarization tensor is more sensitive to the computational parameters than the torkance tensor.

Figure 4 shows all non-zero elements of the spin conductivity tensors $\underline{\boldsymbol{\sigma}}^x$ and $\underline{\boldsymbol{\sigma}}^y$ (top and middle) and $\underline{\boldsymbol{\sigma}}^z$ (bottom). All results are the sum of Fermi sea and Fermi surface terms and include the vertex corrections. In agreement with the predicted tensor shapes the former two are related such that six elements suffice to express all spin conductivities with polarization perpendicular to

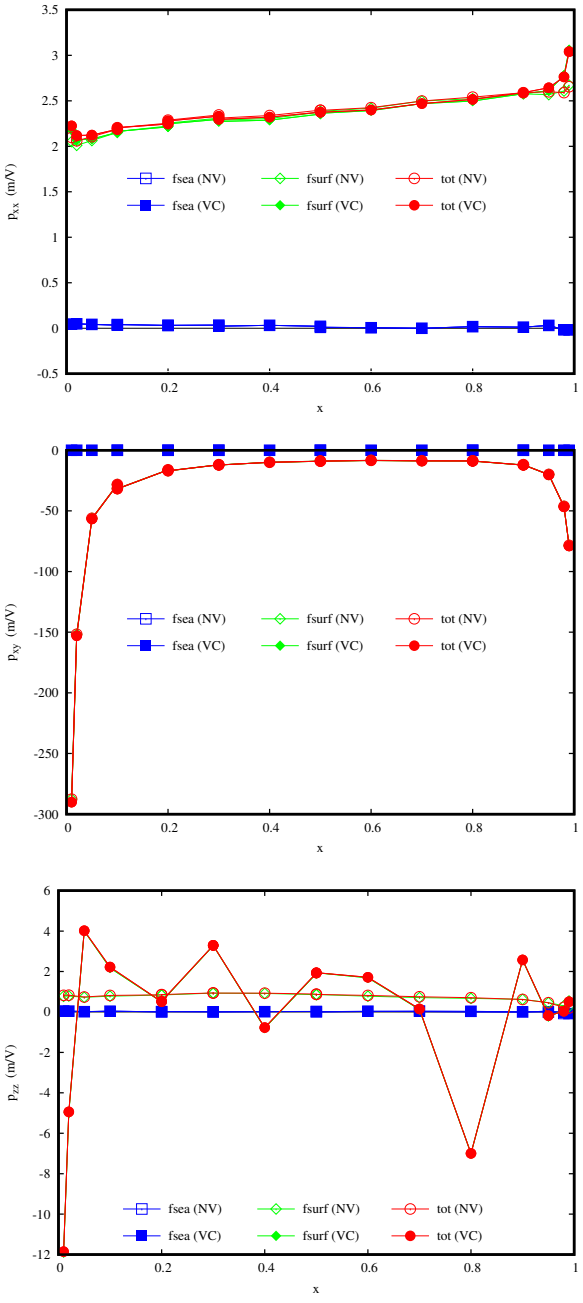

Figure 2. (Color online) Longitudinal component $p_{xx} = p_{yy}$ (top), transverse component $p_{xy} = -p_{yx}$ (middle), and longitudinal component $p_{zz} \neq p_{xx}$ (bottom) of the Edelstein polarization depending on the concentration x in $\mathrm{Pt}\,|\,\mathrm{Fe}_x\mathrm{Co}_{1-x}\,|\,\mathrm{Cu}$. Open symbols represent calculations without vertex corrections (NV) and filled symbols such including vertex corrections (VC). The blue squares correspond to the Fermi sea contribution, the green diamonds represent contributions from the Fermi surface and red circles give the total results.

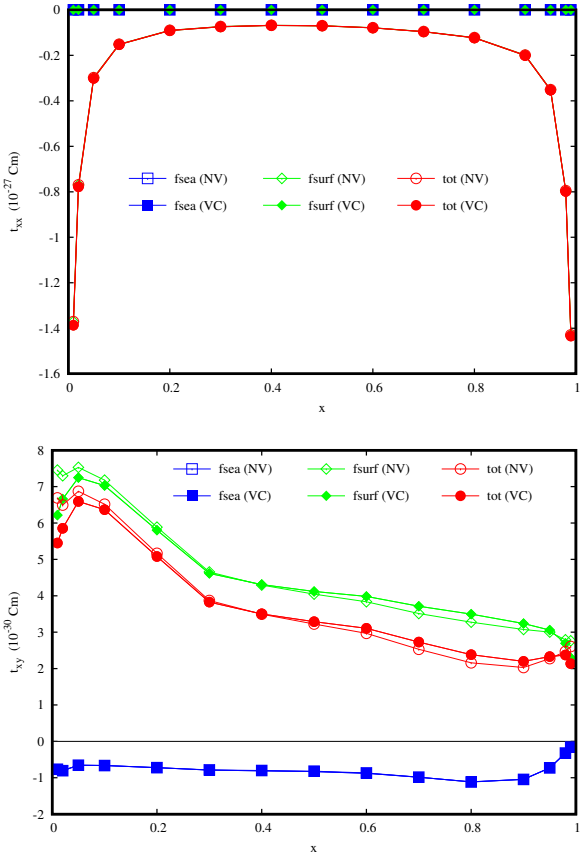

Figure 3. (Color online) The longitudinal component $t_{xx} = t_{yy}$ (top) and the transverse component $t_{xy} = -t_{yx}$ of the SOT depending on the concentration x in $\mathrm{Pt}\,|\,\mathrm{Fe}_x\mathrm{Co}_{1-x}\,|\,\mathrm{Cu}$. Use of symbols and colors corresponds to Fig. 2. Reprinted from our previous work on the SOT, Ref. 50.

the layer stacking (x and y). Furthermore there is no relation to the elements of $\underline{\boldsymbol{\sigma}}^z$ (bottom), of which there are only 3 independent ones: the longitudinal in-plane spin conductivity $\sigma^z_{xx} = \sigma^z_{yy}$, the longitudinal perpendicular spin conductivity σ^z_{zz}, and the transverse and antisymmetric spin Hall conductivity $\sigma^z_{xy} = -\sigma^z_{yx}$.

For the tensor elements shown in the top panel of Fig. 4 with direction of spin polarization (superscript) and electric field (second subscript) coinciding with either p_{xx} or p_{xy} (first index polarization, second electric field) in the top and middle panels of Fig. 2, respectively, no immediate connection can be made to the corresponding elements of $\underline{\boldsymbol{p}}$. While two show divergences in the dilute limits and two do not, the overall concentration dependence is clearly distinct from both that of p_{xx} or p_{xy}. Note, however, that also here the vertex corrections are essentially negligible over the whole concentration range for all elements (not shown). The same applies also to the spin conductivities in response to an electric field along z shown in the middle panel. For the elements of $\underline{\boldsymbol{\sigma}}^z$ in the bottom panel the above-mentioned observation can be made, that the diagonal elements behave

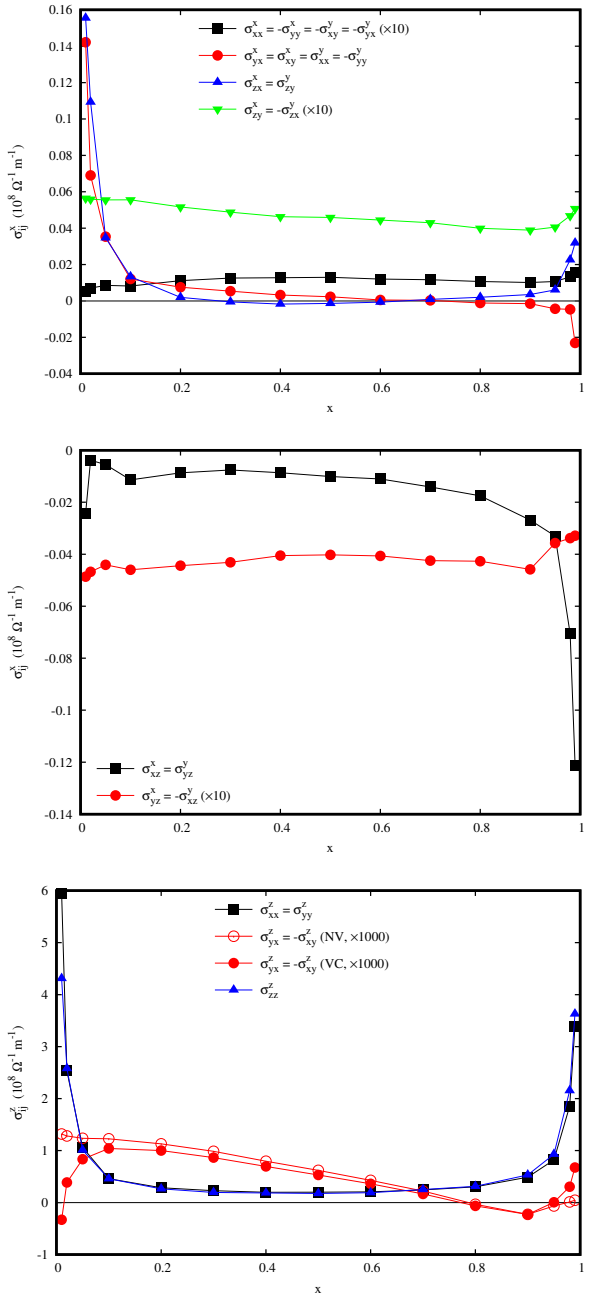

Figure 4. (Color online) Top: All independent non-zero elements of the spin conductivity tensors $\underline{\boldsymbol{\sigma}}^x$ and $\underline{\boldsymbol{\sigma}}^y$ where the direction of electric field and polarization are the same as for either p_{xx} or p_{xy} Middle: Independent non-zero elements of the spin conductivity tensors $\underline{\boldsymbol{\sigma}}^x$ and $\underline{\boldsymbol{\sigma}}^y$ with the direction of the electric field along z. Bottom: Independent non-zero elements of the spin conductivity tensor $\underline{\boldsymbol{\sigma}}^z$. In all cases the total spin conductivities are shown, i.e., including all terms and the vertex corrections, for σ^z_{xy} in the bottom panel results excluding them (NV) are shown in addition.

very much conductivity-like and in that respect are similar to p_{xy} and t_{xx}, while the spin Hall conductivity σ^z_{xy} shows a pronounced variation with concentration including in particular three sign changes. The first of these at low Fe concentration x is caused entirely by the vertex corrections, the other two at large x are present in the intrinsic contribution. Moreover, the relevance of the vertex corrections in the dilute limits is considerably greater here than in any of the other responses discussed. In conclusion, the earlier suggestions that there might be a close connection between Edelstein polarization and spin (Hall) conductivity cannot be unequivocally supported by our results.

IV. SUMMARY

Based on Kubo's linear response theory, the symmetry and magnitude of the direct and inverse Edelstein effects in metals and alloys can be investigated using group-theoretical considerations for the former and an implementation of the Kubo-Bastin formula for the Edelstein response tensor (or Edelstein conductivity, as it is sometime called[29,59]) in a multiple-scattering framework for the latter. The resulting tensor shapes for direct and inverse Edelstein response for all magnetic point groups have been presented. These have been independently verified for a number of systems by numerical calculations using the implementation described herein. By investigating the concentration dependence of three distinct tensor elements in an fcc(111) tri-layer alloy model system and comparing these results to those for the torkance and spin conductivity tensors, the partial interconnection of the three phenomena was elucidated. It was found that the behavior of even and odd Edelstein polarization as a function of concentration x in $\mathrm{Pt}\,|\,\mathrm{Fe}_x\mathrm{Co}_{1-x}\,|\,\mathrm{Cu}$ is reversed to that of the corresponding torkance tensor elements. The odd polarization $p_{xx} = p_{yy}$ exhibits a mild, almost linear increase with increasing Fe content, similar to the variation of the transverse transport properties anomalous and spin Hall conductivity, $\sigma_{xy} = -\sigma_{yx}$ and $\sigma^z_{xy} = -\sigma^z_{yx}$. The latter, however, decreases approximately linearly with x for intermediate concentrations, while in the dilute limits the typical divergent behavior can be observed, preceded by changes in sign. A similar behavior has been found earlier[50] for the even torkance $t_{xy} = -t_{yx}$. The even component of the Edelstein response tensor $\underline{\boldsymbol{p}}$, $p_{xy} = -p_{yx}$, in contrast behaves concerning its concentration dependence more like the longitudinal electrical conductivity as well as the diagonal elements of the spin conductivity tensor $\underline{\boldsymbol{\sigma}}^z$, showing a pronounced variation as a function of x with a divergence-like behavior towards the dilute limits. The symmetry w.r.t. reversal of the magnetization direction, i.e., which tensor elements are even or odd in that respect, is however the same for torkance and Edelstein polarization. The zz-element of $\underline{\boldsymbol{p}}$, describing the electric-field-induced spin polarization in the direction of the magnetization, leading to modification of its magnitude, was found to be most sensitive to computational parameters.

Although a simple lack of convergence can be ruled out, its strong variation with concentration involving several sign changes has to be taken with caution. In particular it should be noted, that the corresponding element of the torkance is zero by definition.

A trivial connection between Edelstein polarization and spin (Hall) conductivity could not be established, neither on a group-theoretical level comparing the space-time symmetry-allowed tensor shapes, nor by analyzing their concentration dependence and the relevance of the various contributions (Fermi surface vs. Fermi sea, intrinsic vs. extrinsic mechanisms) based on a first-principles Kubo-Bastin implementation within the KKR-CPA framework.

The key advantage of the CPA alloy theory over simpler models of disorder is the possibility to calculate material-specific parameters very efficiently, opening the way to a computational materials design approach to the direct and inverse Edelstein polarization. As has been shown, the electronic contribution to the corresponding thermally-induced phenomena, direct and inverse thermal Edelstein effect, can in principle be calculated from the Edelstein polarization employing a Mott-like expression and using, if present, generalized Onsager relations between the reciprocal effects.

Future investigations should be aimed at a first-principles determination of the Edelstein polarization tensor in realistic non-centrosymmetric and conductive bulk materials such as for example Weyl semi-metals, or in metallic surface or interface systems where the inversion symmetry is broken *by construction*. Of particular use for experimental investigations might be, symmetry considerations left aside, the relative magnitude of the tensor elements and, in case of magnetic systems, their relation to the corresponding spin-orbit-induced torkances.

ACKNOWLEDGMENTS

The authors would like to thank the *Deutsche Forschungsgemeinschaft* (German Science Foundation, DFG) for financial support via the programmes SPP 1538 and SFB 689.

* sebastian.wimmer@cup.uni-muenchen.de

1 A. G. Aronov and Y. B. Lyanda-Geller, JETP Lett. **50**, 431 (1989), Russian original: ZhETF **50**, 398 (1989).
2 V. M. Edelstein, Solid State Commun. **73**, 233 (1990).
3 E. L. Ivchenko and G. E. Pikus, JETP Letters **27**, 604 (1978), Russian original: ZhETF **27**, 640 (1978).
4 F. T. Vas'ko and N. A. Prima, Sov. Phys. Solid State **21**, 994 (1979), Russian original: Fiz. Tverd. Tela **21**, 1734 (1979).
5 See however also Ref. 63, which deals with a *kinetic magnetoelectric effect [...] in non-magnetic conductors which lack a center of symmetry.*
6 Y. A. Bychkov and E. I. Rashba, JETP Lett. **39**, 78 (1984), Russian original: ZhETF **39**, 66 (1984).
7 H. J. Zhang, S. Yamamoto, B. Gu, H. Li, M. Maekawa, Y. Fukaya, and A. Kawasuso, Phys. Rev. Lett. **114**, 166602 (2015).
8 G. Vignale and I. V. Tokatly, Phys. Rev. B **93**, 035310 (2016).
9 A. Johansson, J. Henk, and I. Mertig, Phys. Rev. B **93**, 195440 (2016).
10 J. Železný, H. Gao, A. Manchon, F. Freimuth, Y. Mokrousov, J. Zemen, J. Mašek, J. Sinova, and T. Jungwirth, Phys. Rev. B **95**, 014403 (2017).
11 A. Y. Silov, P. A. Blajnov, J. H. Wolter, R. Hey, K. H. Ploog, and N. S. Averkiev, Appl. Phys. Lett. **85**, 5929 (2004).
12 Y. K. Kato, R. C. Myers, A. C. Gossard, and D. D. Awschalom, Phys. Rev. Lett. **93**, 176601 (2004).
13 S. D. Ganichev, S. N. Danilov, P. Schneider, V. V. Bel'kov, L. E. Golub, W. Wegscheider, D. Weiss, and W. Prettl, eprint arXiv:cond-mat/0403641 (2004), cond-mat/0403641.
14 V. Sih, R. C. Myers, Y. K. Kato, W. H. Lau, A. C. Gossard, and D. D. Awschalom, Nat. Phys. **1**, 31 (2005).
15 J. Wunderlich, B. Kaestner, J. Sinova, and T. Jungwirth, Phys. Rev. Lett. **94**, 047204 (2005).
16 The earlier predictions of the optical analogue in Refs. 3 and 4 were soon afterwards verified by Vorob´ev *et al.*[64].
17 S. D. Ganichev, E. L. Ivchenko, V. V. Bel'kov, S. A. Tarasenko, M. Sollinger, D. Weiss, W. Wegscheider, and W. Prettl, Nature **417**, 153 (2002).
18 S. D. Ganichev, E. L. Ivchenko, S. N. Danilov, J. Eroms, W. Wegscheider, D. Weiss, and W. Prettl, Phys. Rev. Lett. **86**, 4358 (2001).
19 I. Garate and M. Franz, Phys. Rev. Lett. **104**, 146802 (2010).
20 J. Sinova, S. O. Valenzuela, J. Wunderlich, C. H. Back, and T. Jungwirth, Rev. Mod. Phys. **87**, 1213 (2015).
21 J. C. Rojas Sánchez, L. Vila, G. Desfonds, S. Gambarelli, J. P. Attané, J. M. De Teresa, C. Magén, and A. Fert, Nat. Commun. **4**, 2944 (2013).
22 J. Inoue, G. E. W. Bauer, and L. W. Molenkamp, Phys. Rev. B **67**, 033104 (2003).
23 E. G. Mishchenko, A. V. Shytov, and B. I. Halperin, Phys. Rev. Lett. **93**, 226602 (2004).
24 B. K. Nikolić, S. Souma, L. P. Zârbo, and J. Sinova, Phys. Rev. Lett. **95**, 046601 (2005).
25 R. Raimondi, P. Schwab, C. Gorini, and G. Vignale, Ann. Phys. **524**, 153 (2012).
26 I. Žutić, J. Fabian, and S. Das Sarma, Phys. Rev. Lett. **88**, 066603 (2002).
27 T. Kondo, J. Hayafuji, and H. Munekata, Japanese Journal of Applied Physics **45**, L663 (2006).
28 I. Adagideli, M. Scheid, M. Wimmer, G. E. W. Bauer, and K. Richter, New J. Phys. **9**, 382 (2007).
29 K. Shen, G. Vignale, and R. Raimondi, Phys. Rev. Lett. **112**, 096601 (2014).
30 I. V. Tokatly, E. E. Krasovskii, and G. Vignale, Phys. Rev. B **91**, 035403 (2015).

[31] A. Manchon and S. Zhang, Phys. Rev. B **78**, 212405 (2008).
[32] A. Manchon and S. Zhang, Phys. Rev. B **79**, 094422 (2009).
[33] I. Garate and A. H. MacDonald, Phys. Rev. B **80**, 134403 (2009).
[34] A. Chernyshov, M. Overby, X. Liu, J. K. Furdyna, Y. Lyanda-Geller, and L. P. Rokhinson, Nat. Phys. **5**, 656 (2009).
[35] I. Mihai Miron, G. Gaudin, S. Auffret, B. Rodmacq, A. Schuhl, S. Pizzini, J. Vogel, and P. Gambardella, Nat. Mater. **9**, 230 (2010).
[36] W. H. Kleiner, Phys. Rev. **142**, 318 (1966).
[37] S. Meyer, Y.-T. Chen, S. Wimmer, M. Althammer, T. Wimmer, R. Schlitz, S. Geprägs, H. Huebl, D. Ködderitzsch, H. Ebert, G. E. W. Bauer, R. Gross, and S. T. B. Goennenwein, Nat. Mater. **16**, 977 (2017).
[38] S. Tölle, M. Dzierzawa, U. Eckern, and C. Gorini, Ann. Phys. **530**, 1700303 (2018).
[39] T. Yoda, T. Yokoyama, and S. Murakami, Nano Letters **18**, 916 (2018).
[40] H. Ebert, D. Ködderitzsch, and J. Minár, Rep. Prog. Phys. **74**, 096501 (2011).
[41] D. Ködderitzsch, K. Chadova, and H. Ebert, Phys. Rev. B **92**, 184415 (2015).
[42] M. E. Rose, *Elementary Theory of Angular Momentum* (John Wiley & Sons, Inc. - New York, Chapman & Hall, Ltd. - London, 1957).
[43] M. E. Rose, *Relativistic Electron Theory* (John Wiley & Sons, Inc. - New York, London, 1961).
[44] A. Crépieux and P. Bruno, Phys. Rev. B **64**, 014416 (2001).
[45] H. Ebert, in *Electronic Structure and Physical Properties of Solids*, Lecture Notes in Physics, Vol. 535, edited by H. Dreyssé (Springer Berlin / Heidelberg, Berlin, 2000) pp. 191–246.
[46] W. H. Butler, Phys. Rev. B **31**, 3260 (1985).
[47] S. Lowitzer, D. Ködderitzsch, and H. Ebert, Phys. Rev. Lett. **105**, 266604 (2010).
[48] S. Lowitzer, M. Gradhand, D. Ködderitzsch, D. V. Fedorov, I. Mertig, and H. Ebert, Phys. Rev. Lett. **106**, 056601 (2011).
[49] H. Ebert, S. Mankovsky, D. Ködderitzsch, and P. J. Kelly, Phys. Rev. Lett. **107**, 066603 (2011).
[50] S. Wimmer, K. Chadova, M. Seemann, D. Ködderitzsch, and H. Ebert, Phys. Rev. B **94**, 054415 (2016).
[51] W. H. Kleiner, Phys. Rev. **153**, 726 (1967).
[52] M. Seemann, D. Ködderitzsch, S. Wimmer, and H. Ebert, Phys. Rev. B **92**, 155138 (2015).
[53] Note that, when comparing Eq. (1) with Eq. (2) of Ref. 50, they differ just by a factor $B_{xc}(\mathbf{r})$, the spin-polarized exchange potential. This transforms, concerning spatial operations, of course according to the symmetry of the Hamiltonian.
[54] But not a sufficient one, as noted before[10] there are non-centrosymmetric magnetic point groups where the Edelstein response vanishes for other reasons.
[55] F. Freimuth, S. Blügel, and Y. Mokrousov, Phys. Rev. B **90**, 174423 (2014).
[56] F. Freimuth, S. Blügel, and Y. Mokrousov, Phys. Rev. B **92**, 064415 (2015).
[57] H. Li, H. Gao, L. P. Zârbo, K. Výborný, X. Wang, I. Garate, F. Doğan, A. Čejchan, J. Sinova, T. Jungwirth, and A. Manchon, Phys. Rev. B **91**, 134402 (2015).
[58] S. Tölle, C. Gorini, and U. Eckern, Phys. Rev. B **90**, 235117 (2014).
[59] J. Borge, C. Gorini, G. Vignale, and R. Raimondi, Phys. Rev. B **89**, 245443 (2014), erratum: Phys. Rev. B **91**, 239904 (2015).
[60] Note however also the erratum[65] to the work by Borge *et al.*[59], where it is admitted that the *heuristic arguments* employed in Ref. 59 *have to be slightly modified*.
[61] A. Manchon, arXiv:1204.4869 [cond-mat.mes-hall] (2012).
[62] 31m' or 3m'1, depending on the axis-convention. The former is given in the tables, tensor forms for the other can be obtained by a $\pi/2$-rotation around the principal axis.
[63] L. Levitov, Y. V. Nazarov, and G. Eliashberg, JETP Lett. **61**, 133 (1985), Russian original: ZhETF **88**, 229 (1985).
[64] L. E. Vorob´ev, E. L. Ivchenko, G. E. Pikus, I. Farbshtein, V. A. Shalygin, and A. V. Shturbin, JETP Letters **29**, 441 (1979), Russian original: ZhETF **29**, 485 (1979).
[65] J. Borge, C. Gorini, G. Vignale, and R. Raimondi, Phys. Rev. B **91**, 239904 (2015).

3.6 Charge and spin transport at finite temperatures

The movement of electrons through a solid is fundamentally affected by scattering at deviations from the ideal periodic lattice at absolute zero. Interaction with a modified potential at a lattice site is usually termed impurity scattering. In this context, the most prominent sources for scattering are random occupation with different atoms in an alloy and dislocation of atoms from their ideal positions, so-called Frenkel defects, creating interstitial defects and vacancies. These effects lead to a finite resistivity already at $T = 0\,\mathrm{K}$: The residual resistivity. At finite temperature additional lattice imperfections arise due to atomic vibrations and, in magnetic solids, also due to fluctuations concerning direction and amplitude of the magnetic moments. While the coherent motion of atoms and moments, phonons and magnons, and their interactions with the electrons are a true challenge concerning a first-principles linear response description, the so-called alloy analogy model (AAM) [202] provides an efficient yet realistic scheme to treat the elastic scattering of electrons due to thermally-induced disorder. As the name suggests, it boroughs the concept of a mean-field description of disorder from the coherent potential approximation (CPA) to the theory of alloys. Both, CPA as well as AAM, were briefly introduced in Chapter 2, Section 2.2.5. In the following, two applications of the alloy analogy model to charge and spin transport at finite temperatures are presented in the form of reprints of published articles.

The first one, Ref. 369, is a joint experimental and theoretical study of the spin Hall angle in $\mathrm{Au}_x\mathrm{Pt}_{1-x}$ alloys as a function of concentration x and temperature. The first-principles calculations, based on a relativistic implementation of the Kubo-Bastin equation for spin-polarised conductivities (see Section 2.3.1), could demonstrate that the large spin Hall angle observed for intermediate concentrations arises due to an interplay of an only weakly temperature-dependent intrinsic contribution to the spin Hall conductivity and a strongly supressed longitudinal charge conductivity. An additional remark is made on page 277.

The second publication [340] is a theoretical investigation on the anomalous Hall effect in the compensated (at $T = 0\,\mathrm{K}$) ferrimagnetic Heusler alloy $\mathrm{Mn}_{1.5}\mathrm{V}_{0.5}\mathrm{FeAl}$. Again the alloy analogy model is employed to account for thermally-induced lattice vibrations and, in particular, transverse spin fluctuations. For the latter an approximate projection of the experimentally determined temperature dependence of the magnetisation on the different magnetic sub-lattices has been applied. The results for residual resistivity and anomalous Hall effect are in very satisfying agreement with recent experiments [370]. Moreover, by tuning the individual sub-lattice magnetic moments to full compensation the symmetry-allowed occurrence of the AHE in spite of a vanishing net-magnetisation could be numerically demonstrated.

3.6.1 Published results on the spin Hall angle in AuPt alloys

The following is a copy of the article *Tuning Spin Hall Angles by Alloying* [369], reprinted (including Supplemental Material) with permission from

M. Obstbaum, M. Decker, A.K. Greiner, M. Haertinger, T.N.G. Meier, M. Kronseder, K. Chadova, S. Wimmer, D. Ködderitzsch, H. Ebert, and C.H. Back, Phys. Rev. Lett. **117**, 167204 (2016).

PRL 117, 167204 (2016) PHYSICAL REVIEW LETTERS week ending 14 OCTOBER 2016

Tuning Spin Hall Angles by Alloying

M. Obstbaum,[1] M. Decker,[1] A. K. Greitner,[1] M. Haertinger,[1] T. N. G. Meier,[1] M. Kronseder,[1] K. Chadova,[2] S. Wimmer,[2] D. Ködderitzsch,[2] H. Ebert,[2] and C. H. Back[1]

[1]*Institut für Experimentelle und Angewandte Physik, Universität Regensburg, 93040 Regensburg, Germany*

[2]*Department Chemie, Ludwig-Maximilians-Universität (LMU) München, 81377 Munich, Germany*

(Received 20 March 2016; revised manuscript received 16 September 2016; published 14 October 2016)

Within a combined experimental and theoretical study it is shown that the spin Hall angle of a substitutional alloy system can be continuously varied via its composition. For the alloy system Au_xPt_{1-x} a substantial increase of the maximum spin Hall angle compared to the pure alloy partners could be achieved this way. The experimental findings for the longitudinal charge conductivity σ, the transverse spin Hall conductivity σ_{SH}, and the spin Hall angle α_{SH} could be confirmed by calculations based on Kubo's linear response formalism. Calculations of these response quantities for different temperatures show that the divergent behavior of σ and σ_{SH} is rapidly suppressed with increasing temperature. As a consequence, σ_{SH} is dominated at higher temperatures by its intrinsic contribution that has only a rather weak temperature dependence.

DOI: 10.1103/PhysRevLett.117.167204

Magnetization switching in thin ferromagnetic films under the influence of spin transfer torques (STTs) [1–3] enables universal memory concepts. Focusing on ferromagnetic–normal-metal (FM-NM) bilayers, a pronounced STT on the magnetization of the FM can be achieved by utilizing the spin Hall effect (SHE) in the NM [4–6]. For that reason, the SHE and its inverse, i.e., the ISHE, have received a lot of interest over the last decade. In this context, many different experimental techniques have been applied to study the efficiency of the SHE in various NMs, with the corresponding figure of merit given by the spin Hall angle α_{SH}. When using a combination of electrical spin injection with nonlocal spin detection in the experiments [7–11], α_{SH} is usually defined as the ratio between the transverse (spin Hall) and the longitudinal conductivity of the NM, i.e., $\alpha_{SH} = \sigma_{SH}/\sigma$. Examining, on the other hand, in experiment the magnetization dynamics in the presence of STT and/or spin pumping [12–20], α_{SH} is defined via the ratio of generated to injected spin and charge currents, J_s and J_c, respectively. However, one should stress that the two different definitions of α_{SH} are fully consistent with each other as demonstrated, for example, in Ref. [21].

Concerning the charge to spin current conversion, the most efficient elemental NMs found so far are Pt, Pd, W, and Ta. Their spin Hall angles could be exceeded for some dilute alloys as for example Pt in Au [11] and Bi in Cu [10]. In these cases, the rather large observed spin Hall angles were ascribed to the skew scattering mechanism, although a reliable confirmation of this by means of numerically reliable *ab initio* electronic structure methods is by no means trivial [22].

Because of the complexity of the relativistic band structure of metals [23] and the ensuing transport properties [24], simple models are not capable of obtaining spin Hall angles in a material specific way. In recent years, efforts to calculate transverse transport properties from first principles succeeded in solving this task. Approaches calculating transverse transport properties with a formulation employing the Berry phase are able to describe perfect crystalline systems [25,26]. On the other hand, approaches employing the Boltzmann formalism [24,27], and Green function techniques that are used to solve the Kubo-Středa or Bastin transport equations [28] are able to treat disordered systems.

In this Letter we report on an experimental study on the ISHE in $Ni_{81}Fe_{19}/Au_xPt_{1-x}$ bilayers with the spin Hall angles α_{SH} determined for a wide range of composition. Our experimental findings that are confirmed by accompanying first principles calculations clearly show that α_{SH} can be tuned for Au_xPt_{1-x} over an extremely wide span with a pronounced maximum value for $x \approx 0.5$.

In our experimental setup (see Fig. 1), pure spin currents are injected via spin pumping [29–32] into Au_xPt_{1-x} by means of ferromagnetic resonance (FMR). To unambiguously extract voltage signals caused by the ISHE, the experimental approach already applied successfully to investigate pure Pt and Au on $Ni_{81}Fe_{19}$ [20] is used. A similar approach has been used by other authors to determine α_{SH} for $Ni_{81}Fe_{19}/Pt$ [19] who pointed out the reliability of the experimental method. By varying the angle ϕ_H between the static magnetization component and the attached voltage probes the contribution to the measured signal due to the anisotropic magnetoresistance (AMR) can be reliably separated from that due to the ISHE for the investigated $Ni_{81}Fe_{19}/Au_xPt_{1-x}$ bilayer systems. This way the voltage signals caused by the ISHE in the Au_xPt_{1-x} alloys can unambiguously be obtained. The subsequent determination of the spin Hall angle α_{SH} is performed by

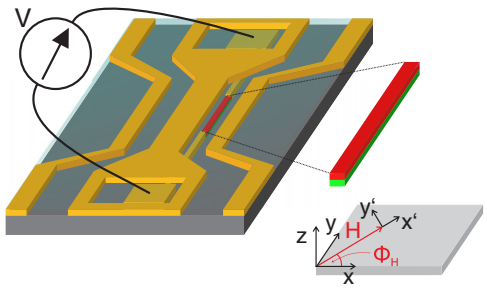

FIG. 1. Integration of a $Ni_{81}Fe_{19}/Au_xPt_{1-x}$-bilayer wire together with voltage probes in the experimental setup. The $Ni_{81}Fe_{19}$ layer is shown in green and the Au_xPt_{1-x} layer is shown in red. In this geometry the excitation field is perpendicular to the bilayer. The angle ϕ_H gives the angle between the voltage probes and the static magnetization. x', y', z define the local coordinate system of the magnetization.

fitting the pure ISHE voltage spectra at FMR to a Lorentzian line shape. Figure 2 shows a typical voltage trace for the $Ni_{81}Fe_{19}/Au_{0.47}Pt_{0.53}$ bilayer recorded for $\phi_H = 45°$ at a frequency of 12 GHz. Using the expressions (see Supplemental Material [33]) for the dc-voltage signals due to the AMR and the ISHE, V_{ISHE} and V_{AMR}, respectively, the measured voltage V can be split into a symmetric and antisymmetric part, as shown in Fig. 2. As the symmetric part at distinct angles stems only from the ISHE, one gets direct access to the corresponding spin Hall angle α_{SH} that is proportional to V_{ISHE}.

To quantify α_{SH} it is advantageous to keep the magnetization at $\phi_H = 0°$ allowing for a frequency dependent recording of the voltages V_{ISHE}^{oop}. In this case the formula for α_{SH} [15,20,34,35] reduces to

$$\alpha_{SH} = \frac{V_{ISHE}^{oop}\sigma(t_{NM}+t_{FM})M_S^2}{efg_F^{\uparrow\downarrow}\Im(\chi_{z'z'}^{res})\chi_{y'z'}^{res}|h_z|^2 l\lambda_{sd}\tanh(\frac{t_{NM}}{2\lambda_{sd}})}, \quad (1)$$

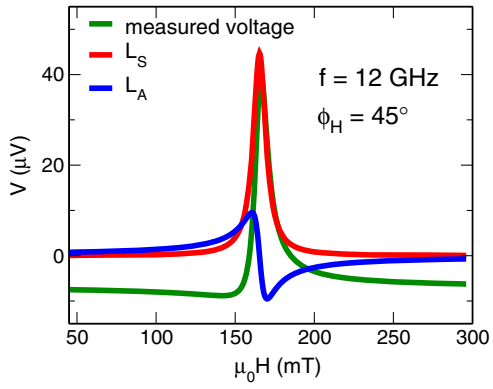

FIG. 2. Measured dc-voltage signal at FMR (green curve) for $\phi_H = 45°$ and a precession frequency of 12 GHz for a $Ni_{81}Fe_{19}/Au_{0.47}Pt_{0.53}$ bilayer. L_S and L_A denote the symmetric (red curve) and antisymmetric (blue curve), respectively, contribution according to a fit to a Lorentzian line shape.

where $\sigma(t_{NM}+t_{FM})$ is the conductivity of the bilayer system depending on the individual thicknesses t_{NM} and t_{FM}, respectively, M_S is the saturation magnetization of the FM film, $g_F^{\uparrow\downarrow}$ is the effective spin mixing conductance which contains the backflow correction, $\chi_{z'z'}^{res}$ and $\chi_{y'z'}^{res}$ are elements of the Polder susceptibility tensor, l is the length of the wire and λ_{sd} is the spin diffusion length.

Obviously, the spin Hall angle depends on several parameters and their quantification is crucial for obtaining reliable results for α_{SH}. The effective spin mixing conductance $g_F^{\uparrow\downarrow}$ of the different $Ni_{81}Fe_{19}/Au_xPt_{1-x}$ interfaces is extracted from spin pumping experiments (again including the backflow correction) performed on corresponding calibration squares next to the wire. For this, the increase of the Gilbert damping constant α relative to the damping constant α_0 of uncapped $Ni_{81}Fe_{19}$ is used. For the data analysis it is assumed that the spin mixing conductance of the bilayer system $Ni_{81}Fe_{19}/Au_xPt_{1-x}$ decreases linearly with Au concentration x. This is well justified by measurements of $g_F^{\uparrow\downarrow}$ for various compositions (see Supplemental Material [33]). Most of the other magnetic parameters, including the susceptibility tensor elements, are determined on the basis of available data from experimental investigations on $Ni_{81}Fe_{19}/Au_xPt_{1-x}$ bilayers [36]. The excitation field h_z generated by the coplanar waveguide is estimated using electromagnetic simulation software and subsequent numerical evaluation. Since the spin diffusion length λ_{sd} enters Eq. (1) in an exponential manner, it is a crucial parameter concerning the determination of α_{SH}. In order to estimate λ_{sd} for all investigated Au_xPt_{1-x} alloys, V_{ISHE} has been measured as a function of the thickness for selected Au_xPt_{1-x}-layers. The analysis of the data (see Supplemental Material [33]) suggests that the λ_{sd} increases with increasing conductivity of the Au_xPt_{1-x} alloys (see Fig. 3 and Supplemental Material [33]). Using these data together with the measured value of $\lambda_{sd}(Pt) = 1.9$ nm for pure Pt, leads to the estimated values for λ_{sd} given in Fig. 3. For pure Au, $\lambda_{sd} = 34$ nm is assumed

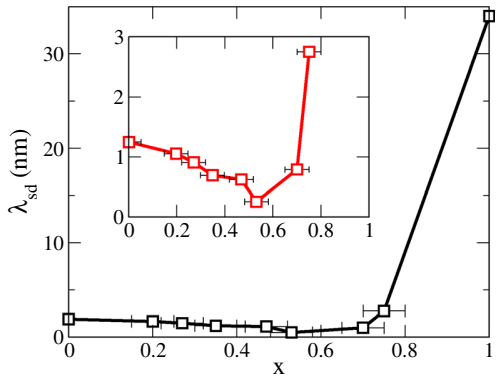

FIG. 3. Spin diffusion length λ_{sd}, of Au_xPt_{1-x} alloys determined assuming a linear dependence of λ_{sd} on the conductivity σ_{AuPt}. The inset shows λ_{sd} on an enlarged scale for the investigated concentration x below 0.8

[37]. Figure 3 shows that the spin diffusion length drops quickly when Pt is added to Au and that it is already comparable to the value for pure Pt for about 30% Pt in Au.

With a reliable estimate for the spin diffusion length available, the spin Hall angle α_{SH} of Au_xPt_{1-x} can finally be evaluated on the basis of Eq. (1), where σ stands for the conductivity of the complete $Ni_{81}Fe_{19}/Au_xPt_{1-x}$ bilayer (see Fig. 4 and Supplemental Material [33]). The corresponding values for α_{SH} are given in the top panel of Fig. 4 as a function of the composition. In particular, because of the

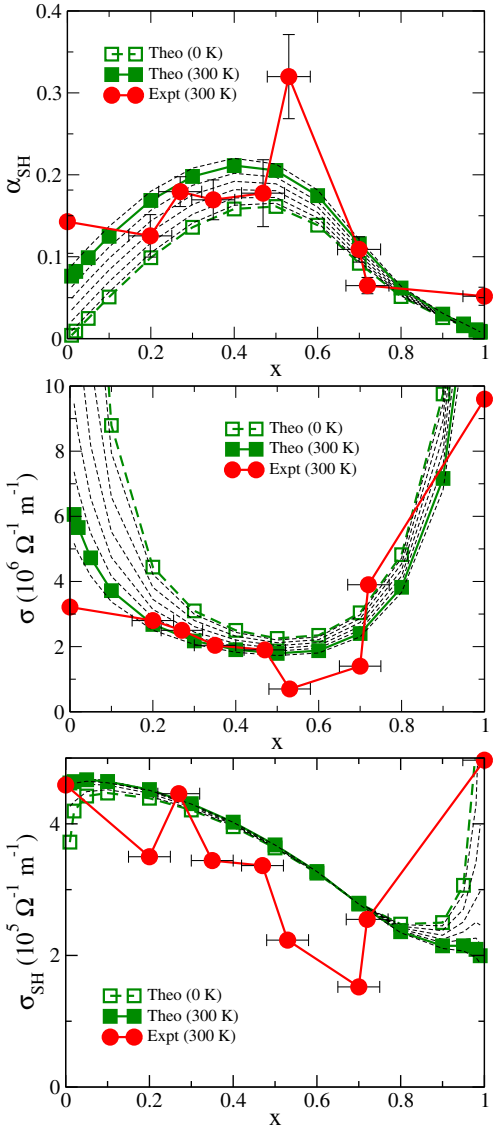

FIG. 4. Spin Hall angle α_{SH} (top), longitudinal charge conductivity σ (middle), transverse spin Hall conductivity σ_{SH} (bottom), of Au_xPt_{1-x} as a function of the concentration x. The full red circles give experimental data for $T = 300$ K, while the full (open) squares give results obtained using Kubo's linear response formalism in combination with the alloy analog model for $T = 300$ K ($T = 0$ K). The thin dashed lines give theoretical results for the temperature range between 0 and 350 K in steps of 50 K.

delicate dependence of α_{SH} on λ_{sd} as given by Eq. (1), the errors bars are relatively large. Nevertheless, it is obvious that α_{SH} for the concentrated alloys substantially exceeds the values for the pure components Pt and Au, respectively. This major experimental result of the present work clearly demonstrates that alloying and working with concentrated alloys opens a promising route to tune the spin Hall angle in a simple and robust way (see discussion below). Figure 4 gives the longitudinal charge conductivity σ (middle panel) of Au_xPt_{1-x} corresponding to the resistivity given in the Supplemental Material [33] and the transverse spin conductivity σ_{SH} (bottom panel) as deduced from α_{SH} and σ. As one notes, σ_{SH} varies for the considered composition regime nearly linearly with concentration x.

To support the interpretation of our experiments, *ab initio* investigations on the transport properties of Au_xPt_{1-x} alloys have been performed on the basis of Kubo's linear response formalism. These are based on a calculation of the underlying electronic structure by means of the KKR-GF (Korringa-Kohn-Rostoker Green function) method that gives direct access to the electronic GF. This allows us to account straightforwardly for random disorder in substitutional alloys by means of the coherent potential approximation (CPA). The CPA also offers a very reliable platform to deal with the so-called vertex corrections that occur when dealing with response functions. In the present case they give rise in particular to the extrinsic contribution to the spin Hall conductivity that is dominated by the skew scattering mechanism [28,38]. A most reliable treatment of this central spin-orbit induced transport property is ensured by using the fully relativistic formulation of the KKR-GF formalism [40]. For technical details see Ref. [41] and the Supplemental Material [33].

In contrast to previous theoretical work in the field, we accounted explicitly for the impact of finite temperatures on the transport properties. This is achieved by treating thermal lattice vibrations using the alloy analogy model [42]. Within this approach that is based on the adiabatic approximation, the temperature induced atomic displacements are seen as a random, quasistatic and temperature dependent distortion of the lattice with a corresponding distortion of the potential. The resulting temperature induced disorder of the potential is treated using the CPA as it is done for chemical disorder due to alloying.

The results for the longitudinal conductivity $\sigma(x, T)$ for $T = 0$ K given in Fig. 4 (middle, open squares) show as a prominent feature the typical divergent behavior $\sigma(x, 0) \approx \bar{\sigma}_{\mathrm{host(solute)}}/x_{\mathrm{solute}}$ in the dilute regime [43], where we find for the reduced conductivities $\bar{\sigma}_{\mathrm{Pt(Au)}} \lesssim \bar{\sigma}_{\mathrm{Au(Pt)}}$ [28], i.e., for Pt in Au and Au in Pt, respectively. This behavior reflects the fact that $\sigma(x, 0)$ for a perfectly periodic solid ($x = 0$ or 1) at $T = 0$ K becomes infinite and accordingly its resistivity becomes zero. On the other hand, for concentrations $0 < x < 1$ one has even for $T = 0$ K a finite conductivity corresponding to the residual resistivity. For finite

temperatures, $\sigma(x,T)$ becomes finite even in the case of pure elements due to electron-phonon scattering or, equivalently, thermally induced disorder [44]. As to be expected, because of the very different density of states at the Fermi energy, the corresponding conductivity drops much faster with temperature for pure Pt than for pure Au. For the dilute Au_xPt_{1-x} alloys with $x \lesssim 0.1$ or $x \gtrsim 0.9$, respectively, one finds $\sigma(x,T)$ also to be finite but one still notices a reminiscence of the divergence of $\sigma(x,0)$ for $x \to 0$ or 1, respectively. For the concentrated alloys ($0.2 \lesssim x \lesssim 0.8$), on the other hand, only a moderate change of about 20% for $\sigma(x,T)$ is found when going from $T = 0$ to 300 K. This implies that the scattering due to chemical disorder is more pronounced than that due to thermal lattice vibrations. Figure 4 (middle) shows that the calculations reproduce the experimental data for the conductivity σ measured at room temperature very well. This obviously also holds for the spin conductivity σ_{SH} that is given in Fig. 4 (bottom).

For the dilute regimes, the theoretical spin conductivity $\sigma_{SH}(x,T)$ also shows a $1/x_{solute}$ divergence reflecting that $\sigma_{SH}(x,T)$ is dominated by its skew scattering contribution $\sigma_{SH}^{skew}(x,T)$ as this scales for $T = 0$ K linearly with $\sigma(x,0)$ according to $\sigma_{SH}^{skew}(x,0) \approx S_{host(solute)}\sigma(x,0) = S_{host(solute)}\bar{\sigma}_{host(solute)}/x_{solute}$, where $S_{host(solute)}$ is the so-called skewness factor (see Supplemental Material [33]) [28,39,45]. Because $\bar{\sigma}_{Pt(Au)} \lesssim \bar{\sigma}_{Au(Pt)}$ and $S_{Pt(Au)} \approx -S_{Au(Pt)}/7.2$ [28] the divergent behavior of $\sigma_{SH}(x,0)$ is much more pronounced on the Au-rich side of the system than on the Pt-rich side. As found before for several other systems [28], one notes that the divergence leads to a strong increase of σ_{SH} on the Au-rich side while σ_{SH} decreases on the Pt-rich side for $x_{solute} \to 0$. This behavior again reflects the fact that the divergence is primarily due to the skew scattering (represented by the skewness factor S) with its magnitude and sign determined by the difference in the strength of the spin-orbit coupling for the host and solute atom [27]. As Fig. 4 shows, the divergent behavior of σ_{SH} in the dilute regime disappears very rapidly with rising temperature. In line with the behavior of σ, this change with temperature is much more pronounced for the Pt-rich than for the Au-rich side. For both sides of the system, however, the divergent behavior disappears completely at room temperature. In contrast to σ, the spin conductivity σ_{SH} shows only a very weak temperature dependence in the concentrated alloy regime. Further inspection of the theoretical results clearly shows that the extrinsic contributions to σ_{SH} connected with the vertex corrections hardly contribute in that regime. This means that the skew scattering mechanism can be ignored while the intrinsic contribution to σ_{SH} dominates. The data in Fig. 4 then imply in particular that the intrinsic contribution is essentially temperature independent as it is indeed found by the calculations (see Supplemental Material [33]).

Altogether, one notes that for the concentrated composition regime, Au_xPt_{1-x} shows the so-called *dirty* behavior [45] with negligible contributions to σ_{SH} due to the skew scattering mechanism and its intrinsic part dominating. This counterintuitive behavior was recently discussed in the context of the impact of chemical disorder on the anomalous Hall effect [46]. Here we find that not only chemical but also thermal disorder may drive a system into the dirty limiting behavior.

The spin Hall angle α_{SH} resulting from the calculated σ and σ_{SH} values is given in the top panel of Fig. 4. Because of the dependence of the individual conductivities on temperature and composition (see Supplemental Material [33]) one finds a very pronounced temperature dependence for α_{SH} on the Pt-rich side of the system that continuously gets diminished by alloying until it more or less disappears at the Au-rich end. This temperature dependence of α_{SH} for a given concentration x is primarily determined by that of σ as σ_{SH} depends rather weakly on T. In line with this, one finds that α_{SH} increases monotonically with temperature when x is kept fixed. Also the strongly asymmetric temperature dependence of α_{SH} is explained this way as the temperature dependence of σ is much more pronounced on the Pt-rich than on the Au-rich side of the system. Because of the pronounced minimum of σ that is located around $x \approx 0.5$ and the moderate concentration dependence of σ_{SH} one finds a clear maximum for α_{SH} more or less for the same alloy composition. Because of the very different temperature dependence of σ and σ_{SH} discussed, the maximum occurs for all temperatures with a weak shift towards pure Pt with increasing temperature. Finally, it should be noted that α_{SH} is not well defined in the case of pure systems ($x = 0$, or 1) at $T = 0$ K as σ becomes infinite (see Supplemental Material [33]). The corresponding limiting value $\alpha_{SH} \approx S_{host(solute)}$ for $x_{solute} \to 0$ to be expected from the properties of σ and σ_{SH} discussed above is obviously not yet reached for the compositions considered in Fig. 4 as the intrinsic contribution to σ_{SH} is that large (see Supplemental Material [33]).

In summary, it has been demonstrated that the FMR-based experimental setup used before to determine the spin Hall angle for pure elements can also be applied successfully for the investigation of substitutional alloy systems throughout the whole concentration regime. Working with concentrated alloys has the big advantage that one avoids the delicate dependence of the spin conductivity σ_{SH} on the concentration that is in general found for dilute alloys because of the divergent behavior of the skew scattering contribution. As it was demonstrated for the alloy system Au_xPt_{1-x}, it is nevertheless possible to surpass substantially the spin Hall angle α_{SH} of the pure components in the concentrated regime, i.e., to vary α_{SH} over a wide range via the concentration. All experimental findings could be quantitatively confirmed by the accompanying theoretical work based on Kubo's linear response formalism. As a new feature of such a type of calculations, the effect of finite temperatures could be accounted for. These calculations

clearly demonstrated that the divergent behavior of σ_{SH} in the dilute regime due to the skew scattering is rapidly suppressed with increasing temperature. For its intrinsic contribution, on the other hand, only a weak temperature dependence has been found.

Financial support by the DFG through the SFB 689 *Spin Phenomena in Reduced Dimensions* as well as SPP 1538 *Spin Caloric Transport* is gratefully acknowledged.

[1] L. Berger, Phys. Rev. B **54**, 9353 (1996).
[2] J. C. Slonczewski, J. Magn. Magn. Mater. **159**, L1 (1996).
[3] A. Brataas, A. D. Kent, and H. Ohno, Nat. Mater. **11**, 372 (2012).
[4] M. I. Dyakonov, Phys. Lett. **35A**, 459 (1971).
[5] J. E. Hirsch, Phys. Rev. Lett. **83**, 1834 (1999).
[6] K. Garello, I. M. Miron, C. O. Avci, F. Freimuth, Y. Mokrousov, S. Blügel, S. Auffret, O. Boulle, G. Gaudin, and P. Gambardella, Nat. Nanotechnol. **8**, 587 (2013).
[7] S. O. Valenzuela and M. Tinkham, Nature (London) **442**, 176 (2006).
[8] T. Kimura, Y. Otani, T. Sato, S. Takahashi, and S. Maekawa, Phys. Rev. Lett. **98**, 156601 (2007).
[9] T. Seki, I. Sugai, Y. Hasegawa, S. Mitani, and K. Takanashi, Solid State Commun. **150**, 496 (2010).
[10] Y. Niimi, Y. Kawanishi, D. H. Wei, C. Deranlot, H. X. Yang, M. Chshiev, T. Valet, A. Fert, and Y. Otani, Phys. Rev. Lett. **109**, 156602 (2012).
[11] B. Gu, I. Sugai, T. Ziman, G. Y. Guo, N. Nagaosa, T. Seki, K. Takanashi, and S. Maekawa, Phys. Rev. Lett. **105**, 216401 (2010).
[12] E. Saitoh, M. Ueda, H. Miyajima, and G. Tatara, Appl. Phys. Lett. **88**, 182509 (2006).
[13] K. Ando, S. Takahashi, K. Harii, K. Sasage, J. Ieda, S. Maekawa, and E. Saitoh, Phys. Rev. Lett. **101**, 036601 (2008).
[14] O. Mosendz, J. E. Pearson, F. Y. Fradin, G. E. W. Bauer, S. D. Bader, and A. Hoffmann, Phys. Rev. Lett. **104**, 046601 (2010).
[15] A. Azevedo, L. H. Vilela-Leão, R. L. Rodríguez-Suárez, A. F. Lacerda Santos, and S. M. Rezende, Phys. Rev. B **83**, 144402 (2011).
[16] L. Liu, T. Moriyama, D. C. Ralph, and R. A. Buhrman, Phys. Rev. Lett. **106**, 036601 (2011).
[17] L. Liu, C. F. Pai, Y. Li, H. W. Tseng, D. C. Ralph, and R. A. Buhrman, Science **336**, 555 (2012).
[18] C. F. Pai, L. Liu, Y. Li, H. W. Tseng, D. C. Ralph, and R. A. Buhrman, Appl. Phys. Lett. **101**, 122404 (2012).
[19] Z. Feng, J. Hu, L. Sun, B. You, D. Wu, J. Du, W. Zhang, A. Hu, Y. Yang, D. M. Tang, B. S. Zhang, and H. F. Ding, Phys. Rev. B **85**, 214423 (2012).
[20] M. Obstbaum, M. Härtinger, H. G. Bauer, T. Meier, F. Swientek, C. H. Back, and G. Woltersdorf, Phys. Rev. B **89**, 060407 (2014).
[21] L. Liu, R. A. Buhrmann, and D. C. Ralph, arXiv:1111.3702.
[22] D. V. Fedorov, C. Herschbach, A. Johansson, S. Ostanin, I. Mertig, M. Gradhand, K. Chadova, D. Ködderitzsch, and H. Ebert, Phys. Rev. B **88**, 085116 (2013).
[23] J. Sinova, S. O. Valenzuela, J. Wunderlich, C. H. Back, and T. Jungwirth, Rev. Mod. Phys. **87**, 1213 (2015).
[24] B. Zimmermann, K. Chadova, D. Ködderitzsch, S. Blügel, H. Ebert, D. V. Fedorov, N. H. Long, P. Mavropoulos, I. Mertig, Y. Mokrousov, and M. Gradhand, Phys. Rev. B **90**, 220403 (2014).
[25] G. Y. Guo, S. Murakami, T.-W. Chen, and N. Nagaosa, Phys. Rev. Lett. **100**, 096401 (2008).
[26] F. Freimuth, S. Blügel, and Y. Mokrousov, Phys. Rev. Lett. **105**, 246602 (2010).
[27] M. Gradhand, D. V. Fedorov, P. Zahn, and I. Mertig, Phys. Rev. Lett. **104**, 186403 (2010).
[28] S. Lowitzer, M. Gradhand, D. Ködderitzsch, D. V. Fedorov, I. Mertig, and H. Ebert, Phys. Rev. Lett. **106**, 056601 (2011).
[29] S. Mizukami, Y. Ando, and T. Miyazaki, J. Magn. Magn. Mater. **230**, 1640 (2001).
[30] B. Heinrich, Y. Tserkovnyak, G. Woltersdorf, A. Brataas, R. Urban, and G. E. W. Bauer, Phys. Rev. Lett. **90**, 187601 (2003).
[31] Y. Tserkovnyak, A. Brataas, and G. E. W. Bauer, Phys. Rev. Lett. **88**, 117601 (2002).
[32] Y. Tserkovnyak, A. Brataas, and G. E. W. Bauer, Phys. Rev. B **66**, 224403 (2002).
[33] See Supplemental Material at http://link.aps.org/supplemental/10.1103/PhysRevLett.117.167204 for more information on the experimental and theoretical background as well as additional supporting results.
[34] N. Mecking, Y. S. Gui, and C. M. Hu, Phys. Rev. B **76**, 224430 (2007).
[35] H. J. Jiao and G. E. W. Bauer, Phys. Rev. Lett. **110**, 217602 (2013).
[36] Z. Celinski, K. B. Urquhart, and B. Heinrich, J. Magn. Magn. Mater. **166**, 6 (1997).
[37] O. Mosendz, G. Woltersdorf, B. Kardasz, B. Heinrich, and C. H. Back, Phys. Rev. B **79**, 224412 (2009).
[38] For the sake of brevity, in the following we use the term *skew scattering* synonymously for all extrinsic contributions [27,39].
[39] K. Chadova, D. V. Fedorov, C. Herschbach, M. Gradhand, I. Mertig, D. Ködderitzsch, and H. Ebert, Phys. Rev. B **92**, 045120 (2015).
[40] H. Ebert, D. Ködderitzsch, and J. Minár, Rep. Prog. Phys. **74**, 096501 (2011).
[41] D. Ködderitzsch, K. Chadova, and H. Ebert, Phys. Rev. B **92**, 184415 (2015).
[42] H. Ebert, S. Mankovsky, K. Chadova, S. Polesya, J. Minár, and D. Ködderitzsch, Phys. Rev. B **91**, 165132 (2015).
[43] A. Crépieux and P. Bruno, Phys. Rev. B **64**, 014416 (2001).
[44] M. Jonson and G. D. Mahan, Phys. Rev. B **21**, 4223 (1980).
[45] N. Nagaosa, J. Sinova, S. Onoda, A. H. MacDonald, and N. P. Ong, Rev. Mod. Phys. **82**, 1539 (2010).
[46] R. Bianco, R. Resta, and I. Souza, Phys. Rev. B **90**, 125153 (2014).

Tuning spin Hall angles by alloying

M. Obstbaum[1], M. Decker[1], A. K. Greitner[1], M. Härtinger[1], T. N. G. Meier[1], M. Kronseder[1], K. Chadova[2], S. Wimmer[2], D. Ködderitzsch[2], H. Ebert[2] and C. H. Back[1]
[1]*Institut für Experimentelle und Angewandte Physik, Universität Regensburg, Germany,* [2]*Ludwig-Maximilians-Universität (LMU) München, Department Chemie*

Supplemental Material

A. Sample preparation

The investigated $Ni_{81}Fe_{19}$ and Au_xPt_{1-x} films are successively deposited onto a GaAs substrate using magnetron sputtering in a UHV chamber. Unless stated differently, each layer is 12 nm thick. In order to cover the full composition range of Au_xPt_{1-x} alloys the following procedure is used. A 1 cm^2 piece of GaAs substrate was put across a lateral gradient of a Au_xPt_{1-x} particle beam. The gradient is achieved by simultaneous operation of neighboring sputtering sources with the substrate located at the lateral mid-position above them. The GaAs substrate is covered by a mask of electron beam lithography (EBL) resist, allowing fabrication of wires and 1 mm^2 square patterns onto the GaAs substrate. The wires are 5 μm wide and 400 μm long. They are electrically connected to voltage probes and integrated into coplanar waveguides (CPW) by successive EBL-steps.

For a sketch of the sample design and the integrated bilayer wire see Fig. 1 of the manuscript. The overlap of the electrical connections leads to an effective wire length of 350 μm. Each wire is exposed to the same Au-Pt beam as a corresponding calibration square which is used for the determination of its composition via x-ray photo electron spectroscopy (XPS). For the analysis the well separated $4p_{3/2}$ core level peaks of Au and Pt are used. The resulting error for the concentration x is estimated to be ± 5 %.

B. Experimental determination of the Spin Hall angle

For the investigated $Ni_{81}Fe_{19}/Au_xPt_{1-x}$-wires the voltage signals are recorded at FMR. For this the static component of the magnetization is always in the x-y-plane and saturated along the external field $\mathbf{H}$ with its orientation specified by the in-plane angle ϕ_{H} (see Fig. 1 of the manuscript). As the excursion angles of the magnetization $\mathbf{M}$ are kept small it is helpful to define a second coordinate system whose x'-axis points along the static component of $\mathbf{M}$. The magnetization dynamics is then confined to the y'-z-plane and the equation of motion for the magnetization components $M_{y'}$ and M_z reduces to a two dimensional problem. In this framework the possible dc-voltage signals due to AMR and ISHE are given by the following two equations [15,20,34,35]:

$$\begin{aligned} V_{\mathrm{ISHE}} &= \alpha_{\mathrm{SH}} \frac{e}{\sigma} \frac{g_{\mathrm{F}}^{\uparrow\downarrow} \omega}{2\pi M_{\mathrm{S}}^2} \frac{\lambda_{\mathrm{sd}}}{t_{\mathrm{NM}} + t_{\mathrm{FM}}} \tanh\left(\frac{t_{\mathrm{NM}}}{2\lambda_{\mathrm{sd}}}\right) l \\ &\quad \times \left(\Im(\chi^{\mathrm{res}}_{y'y'}) \chi^{\mathrm{res}}_{z'y'} h_x^2 \cos(\phi_{\mathrm{H}}) \sin^2(\phi_{\mathrm{H}}) + \Im(\chi^{\mathrm{res}}_{z'z'}) \chi^{\mathrm{res}}_{y'z'} h_z^2 \cos(\phi_{\mathrm{H}}) \right) \frac{(\Delta H)^2}{(H - H_0)^2 + (\Delta H)^2} \qquad (1) \\ V_{\mathrm{AMR}} &= \frac{1}{2} \frac{I R_{\mathrm{A}}}{M_{\mathrm{S}}} \sin(2\phi_{\mathrm{H}}) \\ &\quad \times \left(\Big(-\Im\{\chi^{\mathrm{res}}_{y'y'}\} h_x \sin(\phi_{\mathrm{H}}) + \chi^{\mathrm{res}}_{y'z} h_z \sin(\xi) \Big) \Big(\frac{\Delta H (H - H_0)}{(H - H_0)^2 + (\Delta H)^2} \Big) \right. \\ &\qquad \left. + \chi^{\mathrm{res}}_{y'z} h_z \cos(\xi) \Big(\frac{(\Delta H)^2}{(H - H_0)^2 + (\Delta H)^2} \Big) \right) . \qquad (2) \end{aligned}$$

Here α_{SH} is the spin Hall angle, e the electron's charge, σ is the conductivity of the bilayer, $g_{\mathrm{F}}^{\uparrow\downarrow}$ is the effective spin mixing conductance which contains the backflow correction, ω the angular frequency M_s the saturation magnetization of $Ni_{81}Fe_{19}$, λ_{sd} the spin diffusion length in the normal metal and t_{NM} and t_{FM} are the thicknesses of the normal metal and the ferromagnetic layers, respectively. l is the length of our device. $\chi^{\mathrm{res}}_{y'y'}$, $\chi^{\mathrm{res}}_{z'y'}$, $\chi^{\mathrm{res}}_{z'z'}$ and $\chi^{\mathrm{res}}_{y'z'}$ are elements

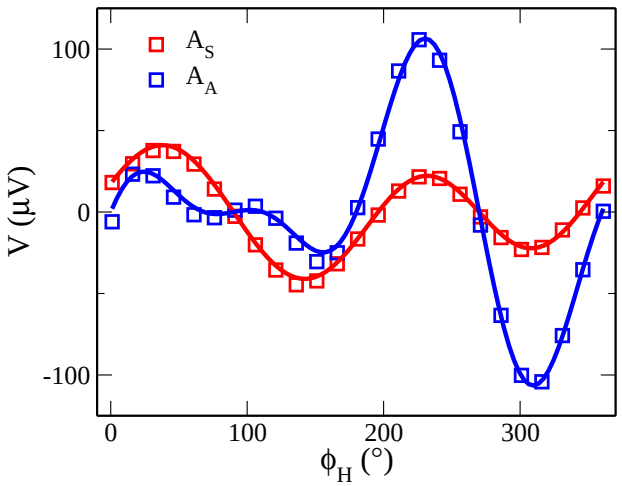

FIG. 1: The amplitudes of the fitted symmetric (A_S, red open squares) and antisymmetric (A_A, blue open squares) parts of the Lorentzian line plotted as a function of ϕ_H for the $Ni_{81}Fe_{19}/Au_{0.47}Pt_{0.53}$ bilayer. The amplitudes A_S and A_A are fitted to the expressions $(c\sin(\phi_H)+d)\sin(2\phi_H)+e\cos(\phi_H)$ and $(a\sin(\phi_H)+b)\sin(2\phi_H)$, respectively.

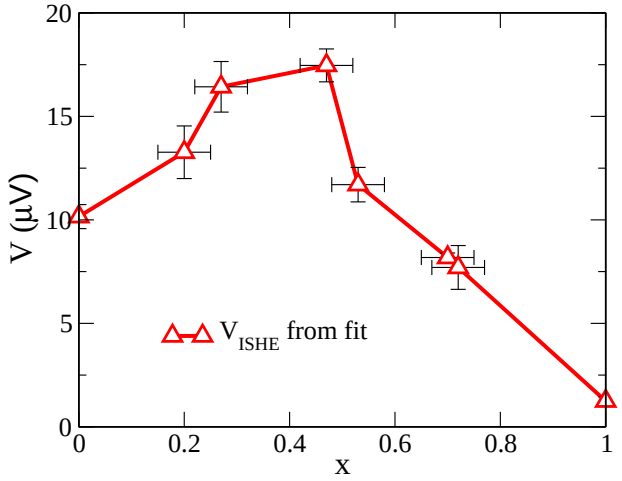

FIG. 2: The value of V_{ISHE} from the fit of angular dependent measurements at 12 GHz plotted as a function of the concentration x for the Au_xPt_{1-x} alloy system.

of the Polder susceptibility tensor. The microwave driving field components are h_z and h_x. I is the current through the device and R_A its resistivity. Finally the resonance field is given by H_0 and the line width at resonance by ΔH. As shown in [20] it is important to include terms for in-plane excitation even for the out-of-plane excitation scheme used here and shown in Fig. 1 of the manuscript.

In-plane fields are generated at the position of the $Ni_{81}Fe_{19}$-layer due to a current flowing through the conductive NM-capping. This effect is always present to a certain extent due to capacitive and inductive coupling between CPW and bilayer-wire. The mutual phase shift of the currents flowing through the CPW and the bilayer-wire is denoted by ξ. While not done here, from this phase shift one might determine the relative amplitude of the excitation field due to CPW and NM as well as obtain information about the type of coupling. The term $\lambda_{sd}/(t_{NM}+t_{FM})\tanh(t_{NM}/2\lambda_{sd})$ in Eq. (1) assumes spin diffusion and gives the average spin current density in the NM [14,15,19,20].

From Eqs. (1) and (2) it is obvious that a voltage signal across FMR caused by the ISHE is characterized by a symmetric Lorentzian function whereas the contribution due to AMR has both symmetric and antisymmetric parts (see Fig. 2 of the manuscript). These parts of the voltage trace are determined by fits to the data. Their amplitudes A_S and A_A are plotted as a function of ϕ_H in Fig. 1. The solid lines are angular dependent fits to the data according to Eqs. (1) and (2). This data analysis is done for all $Ni_{81}Fe_{19}/Au_xPt_{1-x}$-bilayers. The resulting voltage signal V_{ISHE} due to the ISHE under the influence of h_z is plotted in Fig. 2 as a function of the concentration x. These data already suggest that there is a sizable ISHE for the whole composition range of Au_xPt_{1-x}.

Another central quantity entering the determination of the spin Hall angle is the conductivity of the system. The experimental data measured for Au_xPt_{1-x} are represented in Fig. 3 in terms of the corresponding measured resistivity ρ for $Ni_{81}Fe_{19}/Au_xPt_{1-x}$ bilayer wires as well as bare alloy films.

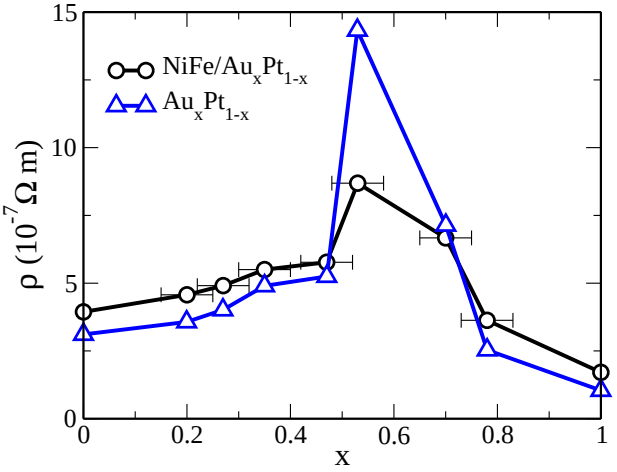

FIG. 3: The resistivity of the 5 μm wide and 400 μm $Ni_{81}Fe_{19}/Au_xPt_{1-x}$ bilayer wires (black open circles) plotted as a function of Au_xPt_{1-x}-composition and compared to the resistivity of the bare alloy films (blue open triangles).

Setting $\phi_H = 0°$ allows to deduce the spin Hall angle α_{SH} from Eq. (1) of the manuscript, with the spin diffusion length λ_{sd} being one of the most crucial parameters that enters this expression. To determine λ_{sd} in a reliable manner it has been measured as a function of the thickness for selected Au_xPt_{1-x} layers. Corresponding results for $Au_{0.72}Pt_{0.28}$ and $Au_{0.66}Pt_{0.34}$ are shown in Fig. 4. V_{ISHE} is measured for frequencies of 7 to 12 GHz in steps of 0.5 GHz. Each data point displayed in Fig. 4 is the average of in total 10 voltage traces which are normalized with respect to frequency dependent parameters (the susceptibilities and the applied microwave power) and furthermore in terms of bilayer resistance and frequency.

The solid lines plotted in Fig. 4 show the function $A\tanh(t_{NM}/2\lambda_{sd})$ for various values of λ_{sd} ranging from λ_{sd} = 0.6 nm to 4.0 nm. The measured data are best represented by $\lambda_{sd} = 2.8$ nm and 0.8 nm, respectively, for $Au_{0.72}Pt_{0.28}$ and $Au_{0.66}Pt_{0.34}$. This suggests that the spin diffusion length increases with increasing conductivity of the Au_xPt_{1-x} alloys. Note that we use the results for the $Au_{0.72}Pt_{0.28}$ alloy ($\lambda_{sd} = 2.8$ nm), the literature value for pure Au ($\lambda_{sd} = 34$ nm [37]) and the results for pure Pt (λ_{sd}(Pt) = 1.9 nm) together with the resistivity data to obtain an estimate for the spin diffusion length of all the alloys. Corresponding results are summarized in Fig. 3 of the manuscript. The overall trend shows that the spin diffusion length is already very short for an amount of approximately 30 % of Pt in Au.

The effective spin mixing conductance $g_F^{\uparrow\downarrow}$ of the different $Ni_{81}Fe_{19}/Au_xPt_{1-x}$-interfaces is extracted from spin pumping experiments (again including the backflow correction) performed on corresponding calibration squares next to the wire. For this the increase of the Gilbert damping constant α relative to the damping constant α_0 of uncapped $Ni_{81}Fe_{19}$ is used. As can be seen in Fig. 5 a linear dependence of the effective spin mixing conductance can be observed as a function of Au concentration x.

C. Computational details and additional theoretical results

In order to support the interpretation of our experimental results the conductivities are calculated using a particular form of the Kubo-Bastin equation [41] implemented using the fully relativistic multiple-scattering Korringa-Kohn-Rostoker Green function (KKR-GF) method [40]

$$\sigma^{z}_{\mu\nu} = \sigma^{z,I}_{\mu\nu} + \sigma^{z,II}_{\mu\nu} \tag{3}$$

$$\sigma^{z,I}_{\mu\nu} = \frac{\hbar}{4\pi\Omega}\mathrm{Tr}\left\langle \hat{J}^z_\mu(\hat{G}^+ - \hat{G}^-)\hat{j}_\nu\hat{G}^- - \hat{J}^z_\mu\hat{G}^+\hat{j}_\nu(\hat{G}^+ - \hat{G}^-)\right\rangle \tag{4}$$

$$\sigma^{z,II}_{\mu\nu} = \frac{\hbar}{4\pi\Omega}\int_{-\infty}^{E_F}\mathrm{Tr}\left\langle \hat{J}^z_\mu\hat{G}^+\hat{j}_\nu\frac{d\hat{G}^+}{dE} - \hat{J}^z_\mu\frac{d\hat{G}^+}{dE}\hat{j}_\nu\hat{G}^+ - \left(\hat{J}^z_\mu\hat{G}^- j_\nu\frac{d\hat{G}^-}{dE} - \hat{J}^z_\mu\frac{d\hat{G}^-}{dE}\hat{j}_\nu\hat{G}^-\right)\right\rangle \mathrm{d}E\,, \tag{5}$$

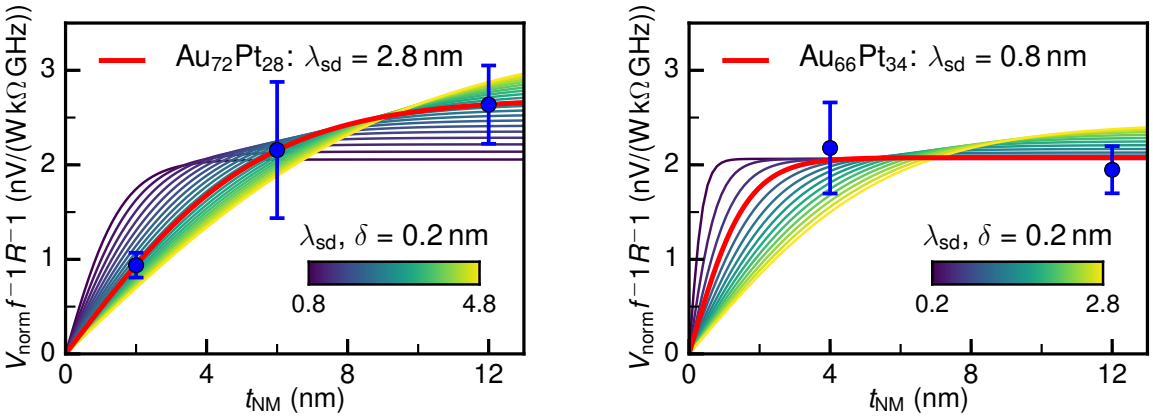

FIG. 4: ISHE-voltage amplitudes for different alloy thicknesses normalized with respect to magnetic properties, microwave power, resistance of the respective bilayer wire and frequency. Every data point is the average of 10 voltage amplitudes from fits in a frequency range of 7 to 12 GHz.

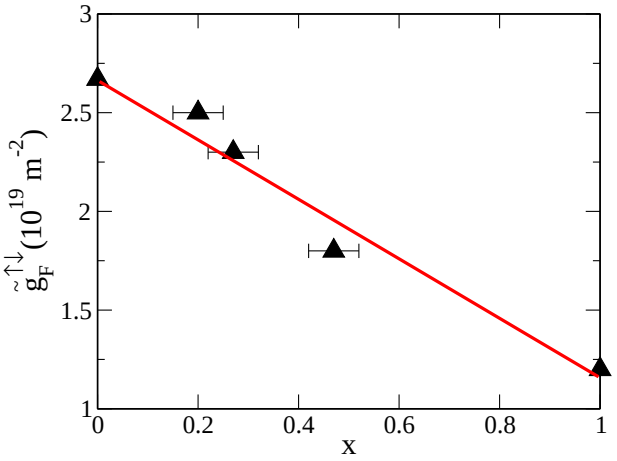

FIG. 5: Effective spin mixing conductance determined from spin pumping experiments as a function of alloy concentration.

where here the form applicable for $T = 0$ K is given. In this case terms I and II denote contributions from the Fermi-surface and Fermi-sea, respectively. Accordingly, the Green functions in Eq. (4) are evaluated at the Fermi energy E_{F} and the energy arguments of the GFs have been omitted throughout. In the employed relativistic formalism the electric current operator is given by $\hat{\mathbf{j}} = -|e|c\boldsymbol{\alpha}$, while the relativistic spin (z-polarization) current density operator $\hat{\mathbf{J}}^z$, used for the calculation of the spin conductivity is given by $\hat{J}^z_\mu = \left(\beta\Sigma_z - \frac{\gamma_5\hat{p}_z}{mc}\right)|e|c\alpha_\mu\,, \quad \mu \in \{x, y\}$ [28]. Here the quantities e, m, c and $\hat{p}_z$ have their usual meaning, while the other quantities are the standard 4×4 matrices occurring in the Dirac formalism.

The real space representation of the Green function operator $\hat{G}$ was obtained by using the spin-polarized relativistic version of multiple-scattering (MS) theory [40] with a cutoff of $\ell_{\max} = 3$ for the MS-expansion. The electronic structure embodied in the underlying effective single-particle Dirac Hamiltonian for the GF is determined employing the framework of Kohn-Sham-Dirac (KSD) spin density functional theory (KSD-SDFT) using the LDA as approximation for the xc-functional. The atomic sphere approximation has been used as shape approximation in the construction of the cell potentials. The lattice constants for the pure systems Au and Pt have been taken as 4.08 $\mathring{A}$ and 3.92 $\mathring{A}$ respectively and have been linearly interpolated between these values in the alloy case.

To describe the effect of disorder the Coherent Potential Approximation (CPA) has been used in the self-consistent determination of the single particle potentials as well as in the configurational averaging of the transport expression as indicated by the angular brackets in Eqs. (4) and (5). In the latter case the so-called vertex corrections are included that are crucial to describe the scattering processes at impurities (e.g. skew- and side-jump scattering) [23,43]. In fact this approach allows a decomposition of the spin Hall conductivity σ_{SH} into its intrinsic and extrinsic parts, $\sigma^{\mathrm{intr}}_{\mathrm{SH}}$

and $\sigma_{\rm SH}^{\rm extr}$, respectively. In the dilute alloy regime the latter one is dominated by its skew scattering contribution [28]. As has been shown in the context of the anamolous Hall conductivity [45]. One may therefore write for the spin Hall conductivity $\sigma_{\rm SH}$ in the dilute alloy regime [28]:

$$\begin{aligned} \sigma_{\rm SH} &= \sigma_{\rm SH}^{\rm intr} + \sigma_{\rm SH}^{\rm extr} \\ &\approx \sigma_{\rm SH}^{\rm intr} + \sigma_{\rm SH}^{\rm skew} \\ &\approx \sigma_{\rm SH}^{\rm intr} + S\,\sigma \end{aligned} \tag{6}$$

where the scaling behavior $\sigma_{\rm SH}^{\rm skew} = S\,\sigma$ has been used with S the so-called skewness factor and σ the longitudinal conductivity. These expressions show in particular that the asymptotic behavior of the Hall angle $\alpha_{\rm SH} = \sigma_{\rm SH}/\sigma$ in the dilute limit approaches for $\sigma_{\rm SH}^{\rm intr} \approx$ constant asymptotically the limit $\alpha_{\rm SH} = S$ because σ scales with the concentration of the solute $x_{\rm solute}$ as $1/x_{\rm solute}$ [43]. The values for $\alpha_{\rm SH}$ given in Fig. 4 (top panel) are in line with this, i.e. the limiting value for $x \to 0$ or 1 is non-zero (see the detailed discussion of the scaling behavior below). For $x = 0$ or $x = 1$ and $T = 0$ K, on the other hand, $\alpha_{\rm SH}$ is not well defined as σ gets infinite.

As mentioned in the manuscript the implementation of the Kubo-Bastin equation on the basis of the KKR-CPA formalism has been used to account simultaneously for chemical as well as thermally induced disorder. Corresponding results for the intrinsic contribution $\sigma_{\rm SH}^{\rm intr}$ to the spin Hall conductivity $\sigma_{\rm SH}$ are shown in Fig. 6 as a function of the concentration for a sequence of temperatures from 50 to 350 K. Obviously, only in the dilute limit a noteworthy

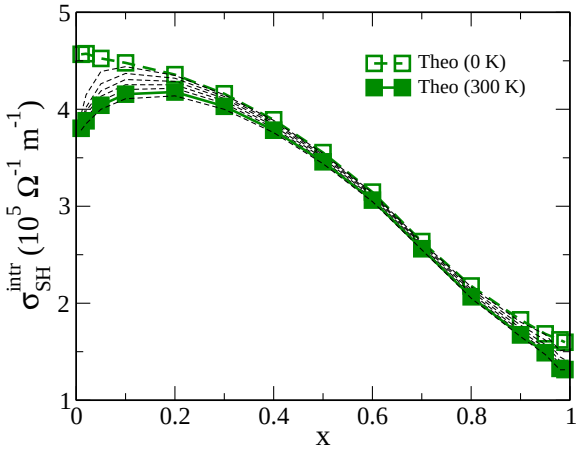

FIG. 6: Calculated intrinsic contribution $\sigma_{\rm SH}^{\rm intr}$ to the spin Hall conductivity $\sigma_{\rm SH}$ of $\rm Au_xPt_{1-x}$ as a function of the concentration x for a sequence of temperatures T from 50 to 350 K.

dependence of $\sigma_{\rm SH}$ on the temperature is found.

The scaling behavior of the spin Hall conductivity expressed in Eq. (6) has been investigated in detail in Ref. 28 for the case $T = 0$ K. The corresponding plot of $\sigma_{\rm SH}(x, 0)$ versus $\sigma(x, 0)$ for $T = 0$ K is given in the left panel of Fig. 7 by the thick dashed line. This curve clearly shows the linear variation of $\sigma_{\rm SH}(x, 0)$ with $\sigma(x, 0)$ on the Au and Pt rich sides of the system if the concentration x seen as an implicit parameter is varied from 0 to 1. The thin dashed lines give corresponding plots for $\sigma_{\rm SH}(x, T)$ and $\sigma(x, T)$ for a sequence of fixed temperatures from 50 to 350 K. As one notices, the slope of the curves in the dilute regime diminishes quickly implying that the skewness parameter correspondingly diminishes with rising temperature. This again implies that the temperature induced disorder has the same impact on $\sigma_{\rm SH}(x, T)$ as the chemical disorder due to alloying.

As in Ref. 28 the total spin Hall conductivity was considered in the left panel of Fig. 7. The right panel shows corresponding plots restricting to the extrinsic contribution to $\sigma_{\rm SH}(x, T)$ stemming primarily from the skew scattering mechanism, i.e. without the intrinsic part $\sigma_{\rm SH}^{\rm intr}$ shown in Fig. 6. These curves once more demonstrate the linear scaling behavior expressed by Eq. (6) and clearly show a different sign of the skewness parameter on the Au and Pt rich sides of the system that can be related to the difference in spin-orbit strength of the alloy partners (see e.g. [28]). These curves also demonstrate that the rather large positive intrinsic spin Hall conductivity $\sigma_{\rm SH}^{\rm intr}(x, T)$ throughout the concentration regime of $\rm Au_xPt_{1-x}$ is responsible that the total spin Hall conductivity $\sigma_{\rm SH}(x, T)$ is also positive for the full concentration and temperature range.

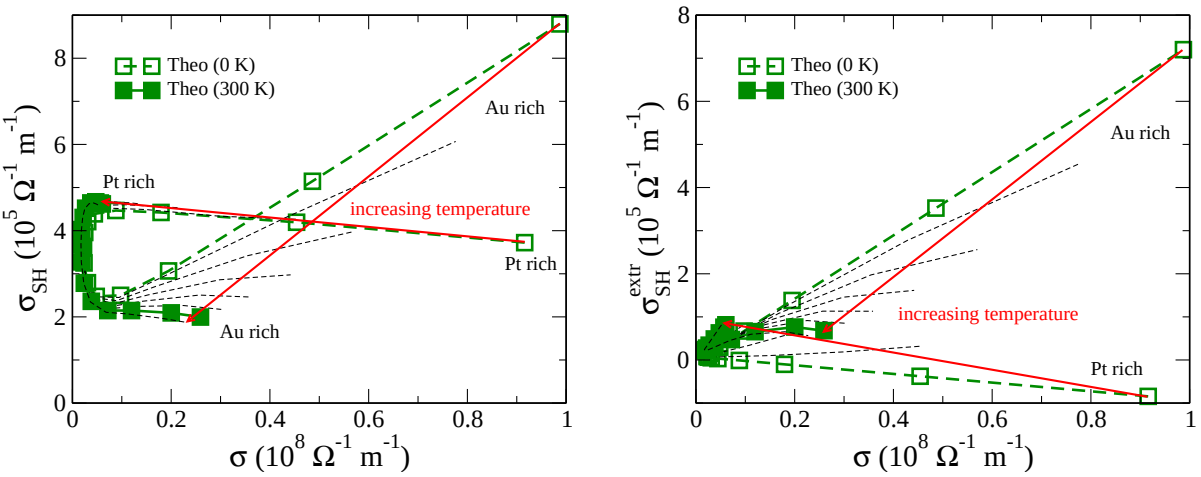

FIG. 7: Scaling behavior of the spin Hall conductivity $\sigma_{\mathrm{SH}}(x,T)$ of $\mathrm{Au}_x\mathrm{Pt}_{1-x}$ w.r.t. its longitudinal conductivity $\sigma(x,T)$ with the concentration x as an implicit parameter for a sequence of temperatures T from 50 to 350 K with the red arrow indicating increasing temperature. Left: total spin Hall conductivity $\sigma_{\mathrm{SH}}(x,T)$; right: extrinsic contribution $\sigma_{\mathrm{SH}}^{\mathrm{extr}}$ to the spin Hall conductivity. Thick dashed (full) lines represent results for $T = 50$ (300) K.

References

The references refer to the references of the associated manuscript.

Additional remark

- The measurements on AuPt have been repeated by Zhu *et al.* [371], qualitatively confirming the concentration dependence, but reporting twice as large values for σ_{SH} and θ_{SH}. This is attributed to a considerably larger spin diffusion length found in the direct spin-orbit torque experiments as compared to that obtained using spin pumping and inverse spin Hall measurements in Ref. 369.

3.6.2 Additional results on galvanomagnetic effects in a ferrimagnet

The following is a reprint of the article *Temperature-dependent charge transport in the compensated ferrimagnet $Mn_{1.5}V_{0.5}FeAl$ from first principles* [340], reprinted from

R. Stinshoff, S. Wimmer, H. Ebert, G.H. Fecher, C. Felser, and S. Chadov, arXiv:1710.04453 [cond-mat.mtrl-sci] (2017), submitted to Phys. Rev. B.

Temperature-dependent charge transport in the compensated ferrimagnet $Mn_{1.5}V_{0.5}FeAl$ from first principles

R. Stinshoff,[1] S. Wimmer,[2] H. Ebert,[2] G. H. Fecher,[1] C. Felser,[1] and S. Chadov[1]

[1] *Max-Planck-Institut für Chemische Physik fester Stoffe, 01187 Dresden, Germany*
[2] *Ludwig-Maximilians-Universität, Dept. Chemie, Butenandtstr. 11, 81377 München, Germany*

We present an *ab-initio* study of the temperature-dependent longitudinal and anomalous Hall resistivities in the compensated collinear ferrimagnet $Mn_{1.5}V_{0.5}FeAl$. Its transport properties are calculated using the general fully relativistic Kubo–Bastin formalism and their temperature dependency is accounted for magnetic and structural disorder. Both scattering sources, together with the residual chemical disorder, were treated equally provided by the CPA (Coherent Potential Approximation) SPR-KKR (Spin-Polarized Relativistic Korringa-Kohn-Rostoker) method. All calculated properties showed good agreement with a recent experimental results, providing useful specific information on the chemical and magnetic arrangement as well as on the influence of disorder. Finally, we demonstrated that the anomalous Hall effect in such compensated systems occurs regardless of the vanishing net spin moment.

PACS numbers: 75.50.Gg, 72.80.Ng, 85.30.Fg
Keywords: compensated ferrimagnets, conductivity, anomalous Hall effect, disorder

Magnetically compensated systems provide an attractive base for the next generation of spintronic devices [1]. Their investigation is motivated by potential applications in various technological fields, such as new types of RAM, detectors, microscopic tips, etc, in which the interest is focused on an alternative manipulation of spins, absence of stray fields and higher operating frequencies. Magnetically compensated systems have different order parameters than ferromagnets, such as staggered magnetization [2, 3] or magnetic chirality [4–6], which can be manipulated and detected by either magnetic fields or pulsed electric currents. However, the absence of net magnetization does not exclude the possibility that such materials will exhibit the anomalous Hall effect (AHE) [7], Kerr effect [8] or high spin-polarization [9–11]. For example, in case of the planar noncollinear antiferromagnets (e.g., Mn_3Ir) AHE has been predicted [12] for the case when the mirror symmetry is broken. By considering magnetic compensation in the cubic ferrimagnets, it is important to note that, both typical cubic structures with $Fm\bar{3}m$ or $F\bar{4}3m$ space groups correspond to $I4/mm'm'$ or $I\bar{4}m'2'$ magnetic space groups, respectively. Both cases belong to the magnetic Laue group $4/mm'm'$ [13, 14] which leads to the following shape of the conductivity tensor:

$$\underline{\sigma} = \begin{pmatrix} \sigma_{xx} & \sigma_H & 0 \\ -\sigma_H & \sigma_{xx} & 0 \\ 0 & 0 & \sigma_{zz} \end{pmatrix}, \qquad (1)$$

where σ_H is the anomalous Hall component. Obviously, σ_H will have a non-vanishing amplitude if there is a difference between the spin-up and -down projections of the electronic structure, which can be fulfilled if the magnetic moment of one atom type is compensated by the antiparallel moments from the other atom types. It is particularly easy to realize such systems using cubic Heusler alloys since most of them obey the Slater–Pauling rule [15, 16], suggesting that compensated ferrimagnets can be found among compounds having 24 electron formula units. Some compensated Heusler ferrimagnets have been already reported, such as $MnCo_{4/3}Ga_{5/3}$ [17]. Ferrimagnetic compensation can also be induced in the tetragonal structures [18], e.g., in the case of $Mn_{1.4}Pt_{0.6}Ga$ [19]; however, the deviation from the Slater–Pauling rule does not allow for a clear recipe for the exact compensating stoichiometry.

The first experimental evidence of non-zero AHE in compensated cubic ferrimagnets was given recently [20, 21] for the Heusler compound $Mn_{1.5}V_{0.5}FeAl$. Additional calculations [21] have shown that this system is half-metallic in agreement with the Slater-Pauling rule, indicating that the observed AHE is due to the aforementioned strong asymmetry of the spin-channels. Here, we investigate this scenario by first-principles calculations on the system $Mn_{1.5}V_{0.5}FeAl$ and verify that the experimental non-zero AHE is an intrinsic property of the compensated ferrimagnets, rather than a consequence of the small remaining magnetization induced by deviations from stoichiometry. We employed the fully-relativistic SPR-KKR (Spin-Polarized Relativistic Korringa-Kohn-Rostoker) method using the standard generalized gradient approximation [22] for the exchange-correlation potential. The structural information on $Mn_{1.5}V_{0.5}FeAl$ is taken from a recent experiment [20].

Though the origins of AHE being well understood theoretically, a realistic combined first-principles description still remains a challenging computational task. At present, the most general approach for equally considering the sources of AHE is the so-called Kubo-Bastin formalism. Being implemented within the SPR-KKR method [23, 24], it allows us to deal with the charge transport in solids by treating various disorder effects on the basis of the CPA (Coherent Potential Approxima-

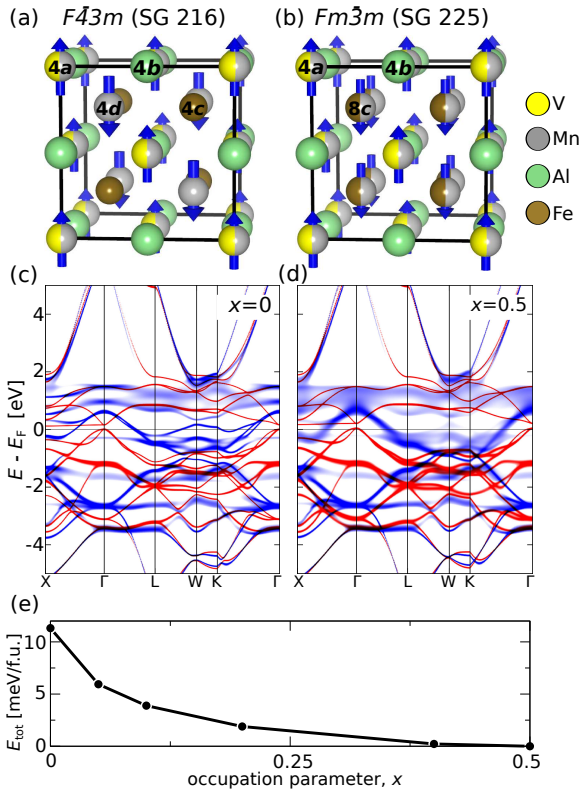

FIG. 1: $Mn_{1.5}V_{0.5}FeAl$ within (a) $F\bar{4}3m$ (SG 216, with 4*c* and 4*d* Wyckoff sites occupied by Mn and Fe, respectively) and (b) $Fm\bar{3}m$ (SG 225, for which 4*c* and 4*d* sites become equivalent by changing to common type 8*c* with random $Mn_{0.5}Fe_{0.5}$ occupation). Other sites, 4*a* and 4*b*, occupied by $Mn_{0.5}V_{0.5}$ and Al, respectively, remain the same in both structures. Arrows indicate the spin moments of Mn atoms. (c) and (d) show the corresponding (to (a) and (b), respectively) spin-resolved (red - spin-up, blue - spin-down) spectral densities. (e) The total energy as a function of x (occupation parameter), i.e., the amount of Mn in 4*d* position: $x = 0$ corresponds to (a), $x = 0.5$ - to (b).

tion) [25, 26].

Since the X-ray diffraction (XRD) refinement [20] does not unambiguously resolve the occupancies of the 4*c* and 4*d* Wyckoff positions, we first specified the chemical order in the system. Most of the integral characteristics of the system, such as the magnetization, are not very sensitive to the partial ordering; however partial ordering might significantly influence the charge transport. Treating our system within the $F\bar{4}3m$ symmetry, we assumed 4*c* and 4*d* sites were different. This allowed us to mix Mn with Fe, gradually going from the most ordered case $(Mn)_{4d}(Fe)_{4c}$ ($F\bar{4}3m$) to the most disordered case $(Mn_{0.5}Fe_{0.5})_{4d}(Mn_{0.5}Fe_{0.5})_{4c}$, which has higher effective symmetry ($Fm\bar{3}m$). Both variants are shown in Fig. 1 a and b. Even though their electronic structures (Fig. 1 c, d) were looking similar, increased broadening of the spin-down states was observed in the vicinity of the

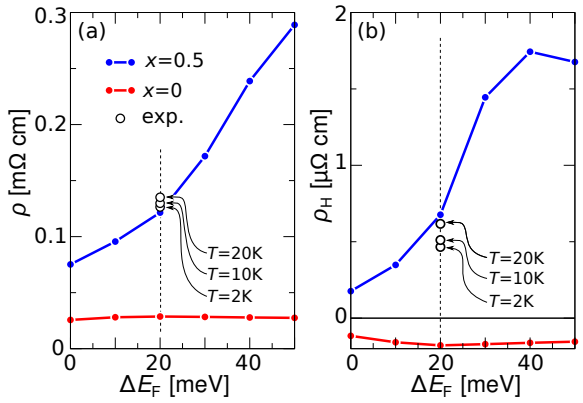

FIG. 2: Residual resistivities as a function of the Fermi energy shift $\Delta E_F = E'_F - E_F$. (a) Longitudinal resistivity ρ, (b) anomalous Hall resistivity ρ_H. Red and blue curves correspond to the $x = 0$ and $x = 0.5$ variants; empty circles are the experimental values [21] measured at low temperatures (indicated explicitly).

Fermi energy E_F for the case (d), which was caused by the additional Mn/Fe disorder. This broadening should impose a drastic difference in the transport properties of the case (d) with respect to case (c). Calculating the total energy as a function of the occupation rate x: $(Mn_xFe_{1-x})_{4d}(Mn_{1-x}Fe_x)_{4c}$, $0 \le x \le 0.5$, provided information concerning the most stable phase. As shown in Fig. 1 e, the total energy decreased monotonically with x and reached its minimum at $x = 0.5$. This behavior indicates that $Mn_{1.5}V_{0.5}FeAl$ effectively has $Fm\bar{3}m$ symmetry.

Having specified the chemical order, we proceeded with the precise calibration of the Fermi energy E_F. Again, small deviations of E_F do not influence the integral properties as the magnetization, but might be crucial for the transport properties. These deviations can occur both in experiment (e.g., due to chemical and structural imperfections) as well as in calculations (e.g., due to the spherical approximation of the atomic potentials). For this reason, we computed both $\rho = 1/3 \cdot (2\rho_{xx} + \rho_{zz})$ and $\rho_H = \rho_{xy}$ as functions of the E_F position (Fig. 2). For $x = 0.5$ we observed a strong dependence on E_F for both ρ and ρ_H, which showed the best simultaneous agreement with experiment at ~ 20 meV above the nominal E_F. At the same time, for $x = 0$ both quantities strongly deviated from experiment within the whole range of ΔE_F.

The temperature dependency of the charge transport for $x = 0.5$ was examined by considering two basic sources of disorder induced by temperature: phonons and magnons. Here they are considered in an approximate way as an additional quasi-static disorder: phonons - as positional disorder, magnons - as spin-orientation disorder [27]. In addition, we neglected the T-dependency of the Fermi-Dirac statistics and identified the actual chemical potential $\mu(T)$ with E_F. The ability to treat

both thermal disorder sources within the CPA formalism made this approach especially convenient. Even though the non-local details and the specific features of the thermal oscillatory modes are neglected, the practical use of this approach has been convincingly demonstrated [27–29].

The T-dependency of the mean amplitude of the atomic displacements was determined here by the Debye theory (the effective Debye temperature was taken as an average over atomic types), whereas the directions of displacements were selected along the basis vectors to keep the conformity with the lattice. The atomic spins were assumed to have T-independent amplitudes m_i ($i = 1, .., N$; N is the number of atoms in the unit cell), and thus were calculated from first principles, but the adequateness of the T-dependency of their angular distribution expressed by weights, must be determined. At a fixed temperature T, the angular distribution of the i-th atomic spin gives its effective average value: $m_i \sum_\nu p_{i\nu}(T)\vec{e}_\nu = \langle \vec{m}_i \rangle (T)$ ($\{\vec{e}_\nu\}$ is a fixed set of all possible spatial directions). The angular distribution was assumed to be Gibbs-like (see Eqs. 13-15 in Ref. [27]) with weights $\{p_{i\nu}(T)\}$ determined by fitting the experimental value: $\langle \vec{m}_i \rangle (T) = \vec{m}_i^{\,\mathrm{exp}}(T)$. Such a mapping is unique only for a single magnetic sublattice, where the experimental magnetization unambiguously defines the angular distribution of each atomic spin, since $\forall i : m_{iz}^{\mathrm{exp}} = M_{\mathrm{exp}}/N$ (index "z" denotes a projection on the common magnetization axis). In the present case, even though $M_{\mathrm{exp}}(T)$ is known, the unit cell contains five different magnetic sublattices: i = V($4a$), Mn($4a$), V($4b$), Fe($8c$) and Mn($8c$). We simplified this situation by assuming that the same form of the T-dependency applies to all atomic spins that randomly share the same Wyckoff site, which reduced the number of magnetic sublattices from five to three (i.e., $i = 4a$, $4b$ and $8c$). To avoid the remaining ambiguity, we assumed some reasonable form of the T-dependency for each sublattice, e.g., by implying a sublattice-specific Bloch's law: $\langle m_{iz} \rangle (T) = m_{iz}\,(1 - (T/T_i)^{\alpha_i})^{\beta_i}$, where α_i, β_i and T_i (playing the role of an ordering temperature for the i-th sublattice) are T-independent fitting parameters and $m_{iz} = m_{iz}(0)$ - the ground-state atomic spin moments calculated from first principles. Thus, we fitted $M_{\mathrm{exp}}(T)$ by using the following expression: $\sum_i m_{iz}\,(1 - (T/T_i)^{\alpha_i})^{\beta_i} = M_{\mathrm{fit}}(T) \longrightarrow M_{\mathrm{exp}}(T)$, with i running over three atomic sublattices entering the unit cell with the corresponding multiplicities, which are implicitly included in m_{iz}. The fit (see Fig. 3) resulted in rather close sets for the ordering temperatures T_i = 345.6, 345.0 and 345.0 K, as well as for the power factors α_i = 2.52, 2.92 and 3.10, β_i = 0.56, 0.35 and 0.55 for sites $4a$, $4b$ and $8c$, respectively. These factors appeared to have the same order of magnitude as those in the conventional Bloch's law ($\alpha = 3/2$, $\beta = 1/3$).

The conductivities σ and σ_{H} calculated as functions of T are shown in Fig. 4. The effects of spin-fluctuations and atomic vibrations are demonstrated by two additional curves, where the calculation accounts either only for spin-fluctuations (marked as "fluct.") or only for atomic vibrations ("vib."). These scattering sources cannot be combined, neither as parallel nor as sequential resistors (i.e., neither of these combinations gives the blue curve), even at low temperatures. On the other hand, the result based on the spin-fluctuations alone (green) followed the total curve (blue) more closely indicating that the spin disorder is the dominant scattering source. Both computed σ and σ_{H} reasonably agreed with the experimental values over the whole temperature range. The strongest deviation from experiment was simultaneously observed around 100 K for both quantities (in case of σ_{H}@100 K the deviation was more than 50 %, however due to $\sigma_{\mathrm{H}}/\sigma \sim 10^{-3}$, for the absolute deviation the relation $\delta\sigma_{\mathrm{H}} \sim \sigma_{\mathrm{H}} \ll \delta\sigma \ll \sigma$ holds). The main reason for the deviations are the aforementioned assumptions about the angular distribution of the spin moments, which might deviate from the actual distribution more strongly in the T-range where the dispersion is already large, but the distribution is still far from uniform. The adequate description of this temperature regime becomes rather complicated, but it can be improved by systematically considering different aspects influencing the distribution of the local moments, such as the specific features of the magnon dispersion, additional angular correlations imposed by relativistic effects, and possible longitudinal spin fluctuations.

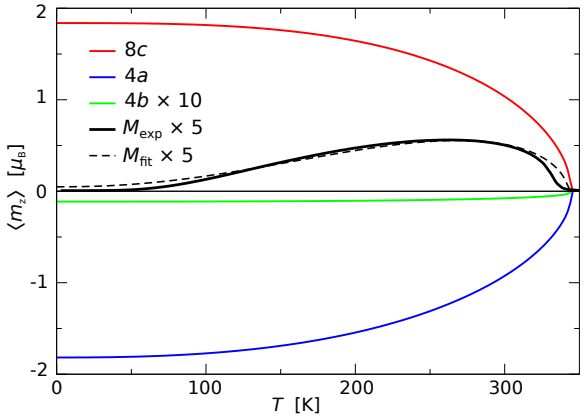

FIG. 3: Experimental magnetization [21] in μ_{B}/f.u. (black solid line) versus fit (black dashed line) together with the z-projections of the sublattice spin moments derived from the fit (red, blue and green correspond to $8c$ ($Mn_{0.5}Fe_{0.5}$), $4a$ ($Mn_{0.5}V_{0.5}$) and $4b$ (Al), respectively).

In addition to the determination of the chemical order, the present calculations explain several aspects specific to ferrimagnets, such as the directions of local moments in the magnetically compensated state. Since the reversal of local moment occurs simultaneously with the sign change

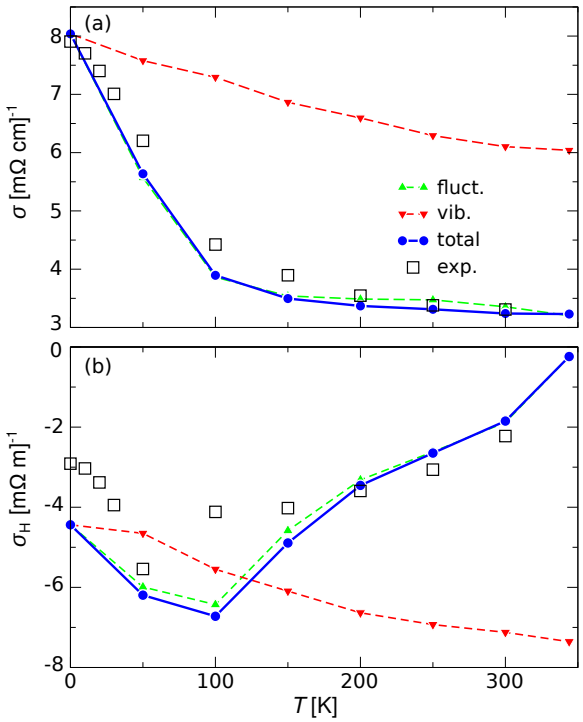

FIG. 4: (a) Longitudinal σ and (b) anomalous Hall σ_{H} conductivities. Dashed green (up-triangles) and red (down-triangles) curves correspond to the case when only either magnetic fluctuation or atomic vibrations, respectively, are taken into account. The blue curve (circles) corresponds to the simultaneous inclusion of both scattering sources. Hollow squares stand for experimental values [21].

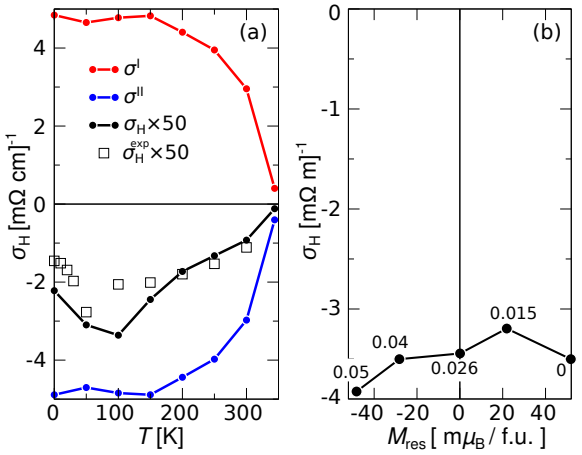

FIG. 5: (a) Anomalous Hall conductivities versus temperature. Red and blue curves correspond to the Fermi-surface σ^{I} and Fermi-sea σ^{II} terms. The black solid line is their sum σ_{H}, scaled up by a factor 50, as well as the experimental values [21] ($\sigma_{\mathrm{H}}^{\mathrm{exp}}$, hollow squares). (b) σ_{H} vs residual magnetization M_{res}. Annotated values correspond to the stoichiometric variation δ on $4a$ site, $\mathrm{Mn}_{0.5+\delta}\mathrm{V}_{0.5-\delta}$, which controls M_{res}.

of σ_{H}, $\sigma_{\mathrm{H}} < 0$, the moments of Mn and Fe on $8c$ positions are positive (aligned along an infinitesimal small external magnetic field), whereas those of Mn and V on $4a$ are negative. Further, the residual chemical disorder is shown to reduce the AHE: in the Kubo–Bastin formalism [24], the transverse conductivity is the sum of the Fermi-surface term (σ^{I}, the contribution from the conducting electrons at E_{F}) and the Fermi-sea term (σ^{II}, the contribution from the occupied states), $\sigma_{\mathrm{H}} = \sigma^{\mathrm{I}} + \sigma^{\mathrm{II}} \sim -10^{-5}\,(\mu\Omega\mathrm{cm})^{-1}$, which appear to be large quantities with opposite sign: $\sigma^{\mathrm{I}} \sim -\sigma^{\mathrm{II}} \sim 5 \cdot 10^{-3}\,(\mu\Omega\mathrm{cm})^{-1}$. This relation holds in the whole temperature range up to the magnetic critical point, where both terms simultaneously vanish (see Fig. 5 a). While σ^{II} is almost insensitive to the residual disorder, σ^{I} is strongly dependent on disorder and vanishes only close to the perfect limit, thereby increasing the total sum σ_{H}. However, this does not apply to the present material as it is strongly disordered.

The non-trivial observation in which the ideally compensated collinear ferrimagnet can exhibit a non-zero AHE does not unambiguously follow from the above data since neither the experimental nor the theoretical situations are ideal. Small residual magnetization is present both in experiment and in the ground-state calculations; the computed value is $M_{\mathrm{res}} = M_{\mathrm{spin}} + M_{\mathrm{orbital}} = 0.0097 + 0.0421 = 0.05\,\mu_{\mathrm{B}}$/f.u. for the nominal (non-shifted) E_{F}. The applied calibration shift $\Delta E_{\mathrm{F}} = 20\,\mathrm{meV}$ slightly influences M_{res} further. To demonstrate the nonzero AHE at $M = 0$, we have adjusted the stoichiometry so that $M_{\mathrm{res}} = 0$ within the numerical precision (see Fig. 5 b). This can be achieved, for instance, by a slight excess of Mn on the $4a$ site: $\mathrm{Mn}_{0.5+\delta}\mathrm{V}_{0.5-\delta}$. Some non-zero values of M_{res} are negative since we do not change the directions of the atomic moments, in order to preserve the sign of σ_{H}. As it follows, σ_{H} continuously changes with M_{res} and does not show any minimum in the amplitude by approaching $M_{\mathrm{res}} = 0$. Thus, the AHE should not vanish in the ferrimagnets because of magnetic compensation. We emphasize that the aspect of full compensation is rather fundamentally than technologically relevant, since it is almost impossible in practice to remove small rest of the magnetization even in antiferromagnets. On the other hand, this makes the verification of a non-vanishing AHE technically difficult, since σ_{H} (or ρ_{H}) changes its sign with the reversal of the external magnetic field and thus passes through zero [20, 30].

To conclude, we provided an extended first-principles description of the temperature-dependent charge transport in the compensated ferrimagnet $\mathrm{Mn}_{1.5}\mathrm{V}_{0.5}\mathrm{FeAl}$, which was in good agreement with experiment. In particular, we analyzed the influence of disorder on a charge transport and proved the possibility of a non-zero anomalous Hall effect in the ideally compensated state.

[1] A. H. MacDonald and M. Tsoi, Phil. Trans. R. Soc. A **369**, 3098 (2011).

[2] V. M. T. S. Barthem, C. V. Colin, H. Mayaffre, M.-H. Julien, and D. Givord, Nat. Commun. **4**, 2892 (2013).

[3] P. Wadley, B. Howells, J. Železný, C. Andrews, V. Hills, R. P. Campion, V. Novák, K. Olejník, F. Maccherozzi, S. S. Dhesi, et al., Science **351**, 192404 (2016).

[4] E. van der Bijl, R. E. Troncoso, and R. A. Duine, Phys. Rev. B **88**, 064417 (2013).

[5] H. Watanabe, K. Hoshi, and J.-I. Ohe, Phys. Rev. B **94**, 125143 (2016).

[6] S. Singh, S. W. D'Souza, J. Nayak, E. Suard, L. Chapon, A. Senyshyn, V. Petricek, Y. Skourski, M. Nicklas, C. Felser, et al., Nat. Commun. **7**, 12671 (2016).

[7] J. Kübler and C. Felser, Europhys. Lett. **108**, 67001 (2014).

[8] W. Feng, G.-Y. Guo, J. Zhou, Y. Yao, and Q. Niu, Phys. Rev. B **92**, 144426 (2015).

[9] S. Chadov, J. Kiss, and C. Felser, Adv. Func. Mater. **23**, 832 (2013).

[10] L. Wollmann, G. H. Fecher, S. Chadov, and C. Felser, J. Phys. D: Appl. Phys. **48**, 164004 (2015).

[11] S. Chadov, S. W. D'Souza, L. Wollmann, J. Kiss, G. H. Fecher, and C. Felser, Phys. Rev. B **91**, 094203 (2015).

[12] H. Chen, Q. Niu, and A. H. MacDonald, Phys. Rev. Lett. **112**, 017205 (2014).

[13] W. H. Kleiner, Phys. Rev. **142**, 318 (1966).

[14] M. Seemann, D. Ködderitzsch, S. Wimmer, and H. Ebert, Phys. Rev. B **92**, 155138 (2015).

[15] J. C. Slater, Phys. Rev. **49**, 931 (1936).

[16] L. Pauling, Phys. Rev. **54**, 899 (1938).

[17] G. J. Li, E. K. Liu, Y. J. Zhang, Y. Du, H. W. Zhang, W. H. Wang, and G. H. Wu, J. Appl. Phys. **113**, 103903 (2013).

[18] L. Wollmann, S. Chadov, J. Kübler, and C. Felser, Phys. Rev. B **92**, 064417 (2015).

[19] A. K. Nayak, M. Nicklas, S. Chadov, P. Khuntia, C. Shekhar, A. Kalache, M. Baenitz, Y. Skourski, V. K. Guduru, A. Puri, et al., Nat. Mater. **14**, 679 (2015).

[20] R. Stinshoff, A. K. Nayak, G. H. Fecher, B. Balke, S. Ouardi, Y. Skourski, T. Nakamura, and C. Felser, Phys. Rev. B **95**, 060410 (2017).

[21] R. Stinshoff, G. H. Fecher, S. Chadov, A. K. Nayak, B. Balke, S. Ouardi, T. Nakamura, and C. Felser, accepted in AIP Advances (2017).

[22] J. P. Perdew, K. Burke, and M. Ernzerhof, Phys. Rev. Lett. **77**, 3865 (1996).

[23] H. Ebert, D. Ködderitzsch, and J. Minár, Rep. Prog. Phys. **74**, 096501 (2011).

[24] D. Ködderitzsch, K. Chadova, and H. Ebert, Phys. Rev. B **92**, 184415 (2015).

[25] P. Soven, Phys. Rev. **156**, 809 (1967).

[26] D. W. Taylor, Phys. Rev. **156**, 1017 (1967).

[27] H. Ebert, S. Mankovsky, K. Chadova, S. Polesya, J. Minár, and D. Ködderitzsch, Phys. Rev. B **91**, 165132 (2015).

[28] K. Chadova, S. Mankovsky, J. Minár, and H. Ebert, Phys. Rev. B **95**, 125109 (2017).

[29] S. Mankovsky, S. Polesya, K. Chadova, H. Ebert, J. B. Staunton, T. Gruenbaum, M. A. W. Schoen, C. H. Back, X. Z. Chen, and C. Song, Phys. Rev. B **95**, 155139 (2017).

[30] V. N. Novogrudskii and I. G. Fakidov, Sov. Phys. J.E.T.P. **47**, 20 (1965).

Chapter 4

Conclusion

The main aim of the present work as part of the DFG priority program "Spin Caloric Transport (SpinCaT)" was to apply the combination of a spin-polarised relativistic band structure method and a corresponding linear response transport formalism to the first-principles determination of spin-dependent thermoelectric coefficients of metals and alloys. To this end the Korringa-Kohn-Rostoker multiple scattering formalism and Kubo's linear response theory as implemented in the Munich SPR-KKR program package were extended by a generalisation of Mott's formula for the thermoelectric power. Making furthermore use of the coherent potential approximation, a single-site alloy theory, and an analogous scheme for the mean-field description of thermally-induced lattice vibrations and spin fluctuations, the so-called alloy analogy model, finite-temperature transport properties of ordered as well as (chemically) disordered systems could be investigated. In addition, group-theoretical concepts were applied to the symmetry analysis of electric and thermoelectric responses and extended to spintronic and spincaloritronic effects as well as to the spinorbitronic phenomena spin-orbit torque and Edelstein effect.

The underlying methods and formalisms were introduced in Chapter 2. Starting with a short treatise on density functional theory focused on the aspects relevant to this work in Section 2.1, an overview over the KKR multiple scattering framework giving access to the single-electron Green function as the fundamental object for the description of the electronic structure of a system and its properties was given in Section 2.2. Of particular relevance to the results presented in Chapter 3 is Section 2.3, that sketches Kubo's linear response formalism and focuses on its application to thermoelectric and spincaloritronic transport properties. A historical overview on the field was given and alternative approaches to the phenomenological description of charge and heat currents in response to electric fields and temperature gradients were reviewed. Generalisations to the Mott formula for the thermopower were outlined and an extensive comparison of spin-projected and spin-polarised approaches to spincaloritronics was made. A brief introduction to a model-independent group-theoretical approach to the space-time symmetry of linear response phenomena was given in addition.

Chapter 3 presented a collection of published articles and unpublished manuscripts on spincaloritronic and related response properties. Examples for phenomena that could be quantitatively studied using all or a subset of the above-mentioned methods are the anisotropy of the Seebeck effect or anisotropic magneto-thermopower and

the anomalous Nernst effect in ferromagnets (Section 3.1), as well as the spin Nernst effect and its manifestation in the spin Nernst magneto-thermopower (Section 3.2). An extensive study on electric, thermoelectric, and thermal transport in $Co_{1-x}Fe_x$ alloys aimed at supporting experimental investigations in search for signatures of quasiparticles was presented in Section 3.1 as well. The spin-orbit-induced scattering mechanisms known from the theory of the anomalous and spin Hall effects could be shown to give rise to distinct contributions also to the spin Nernst effect (Section 3.2). Its role in the so-called spin Nernst magneto-thermopower used for its experimental verification was supported by first-principles calculations of finite temperature spin Hall and spin Nernst angles. The space-time symmetry of linear response phenomena based on their respective flux-force correlation in terms of the Kubo formula were investigated. An extension to three operators for the description of direct and inverse spin conductivities in response to electric fields or temperature gradients led in particular to the prediction and numerical confirmation of longitudinal spin currents in non-magnetic systems (Section 3.3). Transverse transport and related magneto-optical properties in non-collinear antiferromagnets were investigated in Section 3.4. Their occurrence was shown to be most generally deductible from established group-theoretical considerations. In addition, the so-called topological or chirality-induced contributions to various linear response phenomena in chiral coplanar and non-coplanar spin configurations were studied numerically in the non-relativistic limit. Extending the group-theoretical framework of Section 3.3 to the spin-orbit torque and the Edelstein effect allowed giving tensor shapes for direct and inverse effects in all magnetic point groups (Section 3.5). Supporting first-principles calculations for a non-centrosymmetric tri-layer alloy system could be used to investigate the relevance of various contributions and underlying mechanisms to these effects. Finite temperature effects beyond the Fermi-Dirac statistics, namely thermally-induced lattice displacements and spin fluctuations were studied concerning their effect on the spin and anomalous Hall effects in Section 3.6. In a joint experimental and theoretical study it could be shown that the intrinsic contribution to the spin Hall effect dominates at elevated temperatures. Moreover, the temperature dependence of the galvanomagnetic response properties of an uncompensated ferrimagnet were demonstrated to be accurately modelled based on a projection of the temperature-dependent magnetisation on sub-lattices .

Furthermore, the implementation of the generalised Mott relations used for the first-principles determination of thermoelectric and spincaloritronic response coefficients was presented in Appendix A.2. Implementations of a two-dimensional formulation of the Kubo formalism and the non-equilibrium Green function formalism for layered systems, both not used throughout this thesis, were sketched and applied in Appendices A.5 and A.6, respectively. The latter two hold great promises for future investigations of more complex scenarios such as electric-field- or thermally-induced linear response phenomena of heterostructures as for example multilayer and surface systems with complex non-collinear and non-coplanar magnetic structures as well as non-equilibrium phenomena under applied external biases. One particularly interesting application in this respect is the proposed first-principles description of the so-called electric-field-induced X-ray magnetic circular dichroism (EFI-XMCD) employed for the detection of transient spin polarisation in non-magnetic metals [372, 373].

To some extent one has to admit that the comment by Vilenkin and Tylor in 1978 [282], that there were *an embarrassment of richly suitable phenomena with which to explain almost any result*[1] stills holds largely true. Using a currently quite popular expression, this is of course to a great deal owed to the fact that many effects are *emergent phenomena* [374], coming about precisely due to the intricate interplay of several complicated individual processes. In particular electronic correlations and collective excitations such as phonons and magnons still pose a great challenge to their first-principles description. But to end on a less gloomy tone, the steady progress in the computational physics approach to transport coefficients allowing ever more complications to be included on a first-principles level enables us to give reliable numbers for already quite complex scenarios. Based on these, in oftentimes even quantitative comparison with likewise increasingly reliable experimental results, the discrepancies can be ascribed to physical phenomena that lie beyond the present capabilities of a first-principles approach.

Future first-principles investigations in the field of spincaloritronics based on the methodology and extending the applications presented in this work should certainly be aimed at two-dimensional structures such as surfaces and interfaces. To the remarkable achievements already made in the direction towards a realistic description of experimental conditions [18, 62, 63, 302, 303, 375–378], the approach presented herein could add the merits of a fully-relativistic description of linear response phenomena in chemically, structurally as well as thermally disordered systems.

[1] Which itself was a somewhat disappointed update of earlier statements by Wilson (1936 and 1953, see references in Ref. 282) that experiment and theory of thermoelectric phenomena are irreconcilable.

Appendices

A.1 Linear response coefficients as used by Kubo *et al.*

Supplementary to the discussion in Section 2.3.2.1, pp. 43, the connection between the phenomenological equations for charge and heat current densities, Eq. (4.2) of Ref. 109, and the commonly used response tensors given in Eq. (4.5) is revisited in the following.

The starting point is Eq. (4.2) of Kubo *et al.* [109]:

$$\boldsymbol{j} = \mathcal{S}^{(1)}(\boldsymbol{E} + \frac{T}{e}\boldsymbol{\nabla}\xi) + \mathcal{S}^{(2)}\frac{1}{T}\boldsymbol{\nabla}T \tag{A.1}$$

$$\boldsymbol{q} = -\mathcal{S}^{(3)}(\boldsymbol{E} + \frac{T}{e}\boldsymbol{\nabla}\xi) - \mathcal{S}^{(4)}\frac{1}{T}\boldsymbol{\nabla}T\ , \tag{A.2}$$

where a first apparent misprint, a missing T in the prefactor of $\boldsymbol{\nabla}\xi$ in the second line, has been corrected already by Kleiner [271]. Here $\mathcal{S}^{(n)}$ are tensors of rank two, $\boldsymbol{E}$ is as usual the electric field, and $\xi = \zeta/T$ is the reduced chemical potential.

From the first line for the electric(al) current density one obtains via

$$\boldsymbol{E} = \left(\boldsymbol{j} - \mathcal{S}^{(2)}\frac{1}{T}\boldsymbol{\nabla}T\right)(\mathcal{S}^{(1)})^{-1} - \frac{T}{e}\boldsymbol{\nabla}\xi \tag{A.3}$$

and by using the first line of Eq. (4.5) of Ref. 109,

$$\rho = (\mathcal{S}^{(1)})^{-1} = \sigma^{-1}\ , \tag{A.4}$$

as well as

$$\begin{aligned}\frac{T}{e}\boldsymbol{\nabla}\xi = \frac{T}{e}\boldsymbol{\nabla}\frac{\zeta}{T} &= \frac{T}{e}\frac{T\boldsymbol{\nabla}\zeta - \zeta\boldsymbol{\nabla}T}{T^2} \\ &= \frac{1}{e}\boldsymbol{\nabla}\zeta - \frac{\zeta}{eT}\boldsymbol{\nabla}T\ ,\end{aligned} \tag{A.5}$$

the expression for the electric field in the first line of Eq. (4.4) of Ref. 109:

$$\boldsymbol{E} = \rho\boldsymbol{j} - \frac{1}{e}\mathcal{S}\boldsymbol{\nabla}T - \frac{1}{e}\boldsymbol{\nabla}\zeta\ . \tag{A.6}$$

Here

$$\mathcal{S} = \frac{e(\mathcal{S}^{(1)})^{-1}\mathcal{S}^{(2)} - \zeta}{T} \tag{A.7}$$

is $-e$ times the *absolute thermoelectric power per unit temperature difference* [109].

Inserting Eq. (A.3) into the second line of Eq. (A.1) gives

$$\begin{aligned}\boldsymbol{q} &= -\mathcal{S}^{(3)}\left[\left(\rho\boldsymbol{j} - \frac{1}{eT}(e\mathcal{S}^{(1)})^{-1}\mathcal{S}^{(2)} - \zeta)\boldsymbol{\nabla}T - \frac{1}{e}\boldsymbol{\nabla}\zeta\right) + \frac{T}{e}\boldsymbol{\nabla}\xi\right] - \mathcal{S}^{(4)}\frac{1}{T}\boldsymbol{\nabla}T \\ &= -\mathcal{S}^{(3)}\rho\boldsymbol{j} + \left(\frac{\mathcal{S}^{(3)}(\mathcal{S}^{(1)})^{-1}\mathcal{S}^{(2)} - \mathcal{S}^{(4)}}{T}\right)\boldsymbol{\nabla}T \\ &\quad + \mathcal{S}^{(3)}\left(\frac{1}{eT}\zeta\boldsymbol{\nabla}T - \frac{1}{e}\boldsymbol{\nabla}\zeta + \frac{T}{e}\boldsymbol{\nabla}\xi\right) \ . \end{aligned} \tag{A.8}$$

Using Eq. (A.5), the three terms in the last bracket of the second line cancel each other, and one may write

$$\boldsymbol{q} = \underbrace{\left(-\mathcal{S}^{(3)}\rho - \frac{\zeta}{T}\right)}_{\pi}\boldsymbol{j} - \underbrace{\left(\frac{\mathcal{S}^{(4)} - \mathcal{S}^{(3)}(\mathcal{S}^{(1)})^{-1}\mathcal{S}^{(2)}}{T}\right)}_{\kappa}\boldsymbol{\nabla}T + \frac{\zeta}{T}\boldsymbol{j} \ , \tag{A.9}$$

which is, apart from the prefactor of the last term, identical to the second line of Eq. (4.4) of Kubo *et al.* [109]. As this term serves as a compensation for the second term in π, the prefactor $-\frac{1}{e}$ of Kubo *et al.* seems to be erroneous, which can be seen already when inspecting the units.

A.2 Implementation of the generalised Mott relations

In this appendix first tests and applications of an implementation of the generalised Mott relations [Eqs. (2.156)-(2.158)] and their low temperature limits, Mott's formula for the thermopower [Eq. (2.268)] and Sondheimer's for the (anomalous) Nernst conductivity [Eq. (2.270)] will be presented. These calculations have been performed as preliminary work for Sections 3.1 and 3.2. Computational details can be found in Appendix A.7.

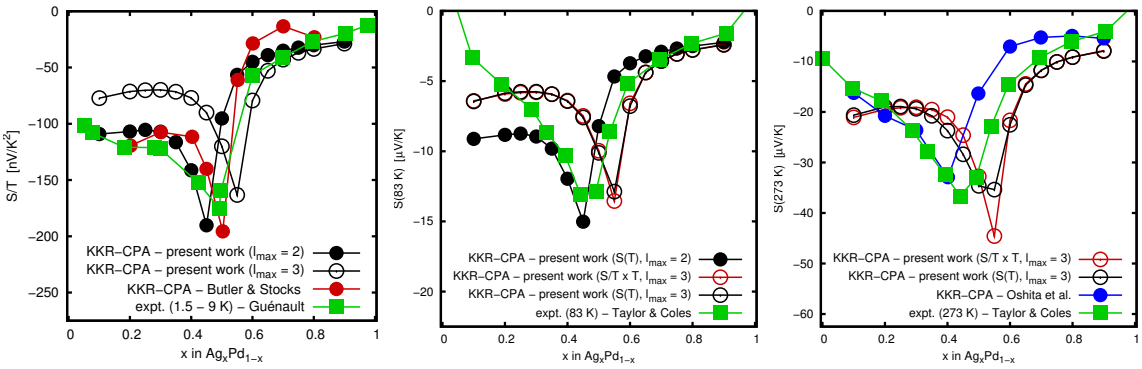

Figure A.1: Thermoelectric power of Ag_xPd_{1-x} as a function of x at $T = 1\,\mathrm{K}$ (left), 83 K (middle) and 237 K (right). Comparison is made to experimental data [379, 380] and other first-principles calculations [264, 296]. Moreover the Mott formula and its finite-temperature generalisation as well as two different angular momentum expansions are compared.

Figure A.1 shows the concentration dependence of the Seebeck coefficient in fcc Ag_xPd_{1-x} alloys at three different temperatures. In the left panel the low temperature limit S/T at $T = 1\,\mathrm{K}$ calculated via Eq. (2.268) is compared for two different angular momentum expansions (full black circles: $\ell_{\max} = 2$, empty circles: $\ell_{\max} = 3$) against results by Butler and Stocks [264] (red full circles, $\ell_{\max} = 2$) and experimental low-temperature data from Guénault [379] (green squares). For a discussion of the concentration dependence and the relevance of vertex corrections see Refs. 264 and 265. These authors also discuss the impact of the angular momentum expansion cut-off ($\ell_{\max}$), which is less pronounced w.r.t. the magnitude as in the resistivity, but leads to a shift of the extremum in the middle of the concentration range. Results obtained from the generalised Mott formula [Eq. (2.266)] at $T = 1\,\mathrm{K}$ are indistinguishable from the Mott results shown here. The central panel gives results for $T = 83\,\mathrm{K}$ using the generalised Mott formula in comparison to experimental data obtained by Taylor and Coles [380]. Again the theoretical results for smaller $\ell_{\max}$ accidentally compare more favourable to experiment. In addition to $S(T)$ also data for $S/T \times T$ is shown, i.e., the Mott results from the left panel multiplied by $T = 83\,\mathrm{K}$. Only minor differences in the vicinity of the extremum are visible. For $T = 273\,\mathrm{K}$ in the right panel these differences obviously become more pronounced, the reduced magnitude and the broadening of the extremum are in agreement with experiment. Its slightly wrong position is again due to the use of $\ell_{\max} = 3$, the results obtained by Oshita *et al.* [296] for $\ell_{\max} = 2$ and using Eq. (2.266) are however not substantially better.

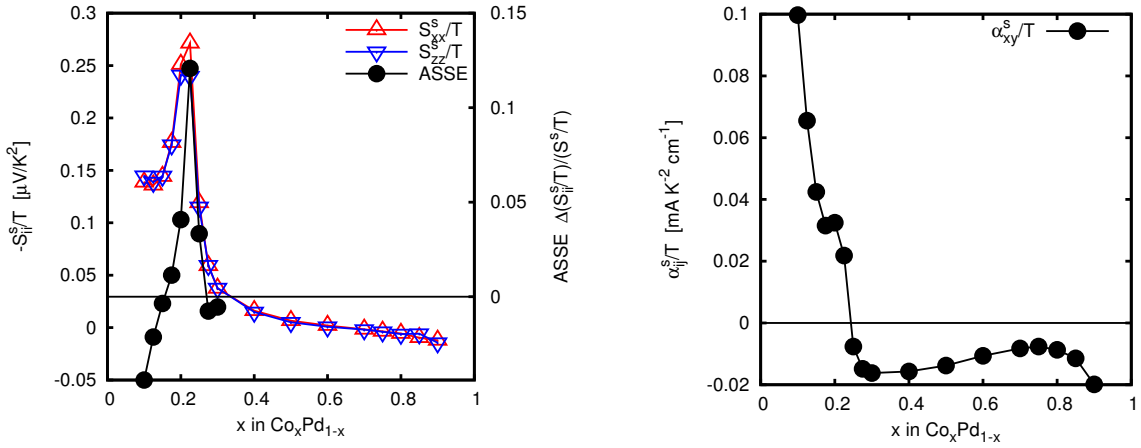

Figure A.2: Spin-dependent Seebeck coefficient and its magnetic anisotropy (left) and spin Nernst conductivity (right) as a function of x in $\mathrm{Co}_x\mathrm{Pd}_{1-x}$. In both cases the low temperature limits obtained from Mott- or Sondheimer-like formulae are shown.

In Figure A.2 the spincaloritronic response properties spin-dependent Seebeck coefficient (left) and spin(-dependent) Nernst conductivity (right) are shown for the ferromagnetic alloy $\mathrm{Co}_x\mathrm{Pd}_{1-x}$. Both were calculated from spin-polarised conductivities ($s \equiv \mathrm{z}$) using the Mott and Sondheimer formulae, Eqs. (2.268) and (2.270), respectively. The spin-dependent Seebeck effect shows, as its charge counterpart discussed in Ref. 267, a dependence on the relative orientation of applied temperature gradient and magnetisation (along z). The difference of the spin-polarised Seebeck coefficients in relation to the isotropic value, $\Delta(S^s_{ii}/T)/(S^s/T)$, is termed anisotropy of the spin-dependent Seebeck effect (ASSE) in analogy to the anisotropic Seebeck effect (ASE) and the anisotropic magnetoresistance (AMR). As the individual S^s_{ii}/T, it is largest for $x \approx 0.2$, in line with most other response properties of $\mathrm{Co}_x\mathrm{Pd}_{1-x}$ [267]. Note that a spin-projected formulation of the spin-dependent Seebeck coefficient as $S^\uparrow - S^\downarrow$ leads to appreciable differences (not shown). Moreover, the quite commonly employed definition of a spin-dependent Seebeck coefficient $S^s = (\sigma^\uparrow S^\uparrow - \sigma^\downarrow S^\downarrow)/(\sigma^\uparrow + \sigma^\downarrow)$ differs from the spin-polarised Seebeck coefficient used here in that it relates a spincaloritronic response in the numerator to the electric conductivity $\sigma = \sigma^\uparrow + \sigma^\downarrow$ in the denominator. The right panel of Fig. A.2 shows the spin(-polarised) Nernst conductivity in the athermal limit, α^s_{xy}/T as a function of x. Again the most prominent feature, the sign change, occurs at $x \approx 0.2$, the concentration for which, e.g., the anomalous Nernst conductivity shows a maximum [267]. For this quantity a definition in terms of spin-projected Nernst conductivities is possible, provided a suitable spin projection scheme [223] is employed.

A.3 Spin-dependent thermoelectrics

By defining spin-projected thermoelectric coefficients and using their sum and difference for charge and spin-dependent Seebeck tensor elements respectively, Tauber *et al.* [20] obviously combine the information about charge and spin related processes. Thereby, without explicitly mentioning it, their expression for the diagonal part of the Seebeck coefficient in reduced dimensions contains a term which we interpret as the combination of the spin(-dependent) Nernst and the inverse spin Hall effect. This gives in total a contribution to the electric field in the direction of the temperature gradient which one would miss when considering Eq. (1) of Ref. 266 alone. By explicitly combining the charge and spin-polarised parts, Eqs. (1) and (3) of Ref. 266,

$$\boldsymbol{j}^c + \boldsymbol{J}^{s,\xi} = (\underline{\boldsymbol{L}}^{cc} + \underline{\boldsymbol{\mathcal{L}}}^{sc,\xi})\,\boldsymbol{E} - (\underline{\boldsymbol{L}}^{cq} + \underline{\boldsymbol{\mathcal{L}}}^{sq,\xi})\,\frac{\boldsymbol{\nabla} T}{eT}\,, \tag{A.10}$$

and setting both currents to zero it is possible to obtain a relation between the electric field created by both charge and spin-polarisation rearrangement due to the temperature gradient. So for $\boldsymbol{j}^c = 0$ and independently $\boldsymbol{J}^{s,\xi} = 0$,

$$\boldsymbol{E} = (\underline{\boldsymbol{A}}^{\xi})^{-1}\,\underline{\boldsymbol{B}}^{\xi}\,(-\frac{\boldsymbol{\nabla} T}{eT}) = \underline{\boldsymbol{S}}^{c+s,\xi}\;\boldsymbol{\nabla} T\,. \tag{A.11}$$

Here $\underline{\boldsymbol{A}}^{\xi} = \underline{\boldsymbol{L}}^{cc} + \underline{\boldsymbol{\mathcal{L}}}^{sc,\xi}$ and $\underline{\boldsymbol{B}}^{\xi} = \underline{\boldsymbol{L}}^{cq} + \underline{\boldsymbol{\mathcal{L}}}^{sq,\xi}$ where we assume that the polarisation axes are orthogonal and hence the inversion of the third rank tensor $\underline{\boldsymbol{\mathcal{L}}}^{sc}$ can be performed as an inversion of separate second rank tensors. Considering now only the polarisation along z, we obtain for a cubic system the charge- and spin-dependent Seebeck tensor $\underline{\boldsymbol{S}}^{c+s,z}$, which in matrix form is

$$\underline{\boldsymbol{S}}^{c+s,z} = -\frac{1}{eT}\frac{1}{N}\begin{pmatrix} A^z_{\mathrm{xx}} & -A^z_{\mathrm{xy}} & 0 \\ A^z_{\mathrm{xy}} & A^z_{\mathrm{xx}} & 0 \\ 0 & 0 & \frac{N}{A^z_{\mathrm{zz}}} \end{pmatrix}\begin{pmatrix} B^z_{\mathrm{xx}} & B^z_{\mathrm{xy}} & 0 \\ -B^z_{\mathrm{xy}} & B^z_{\mathrm{xx}} & 0 \\ 0 & 0 & B^z_{\mathrm{zz}} \end{pmatrix}\,, \tag{A.12}$$

where $N = (A^z_{\mathrm{xx}})^2 + (A^z_{\mathrm{xy}})^2$.

Assuming now a non-magnetic system where off-diagonal charge- and diagonal spin-dependent elements of the response tensors of type $\underline{\boldsymbol{L}}$ and $\underline{\boldsymbol{\mathcal{L}}}$ vanish, i.e.,

$$L^{cc}_{\mathrm{xy}} = L^{cq}_{\mathrm{xy}} = \mathcal{L}^{sc,z}_{\mathrm{xx}} = \mathcal{L}^{sq,z}_{\mathrm{xx}} = 0\,, \tag{A.13}$$

the diagonal elements $S^{c+s,z}_{\mathrm{xx}}$ referring to an axis (x) orthogonal to the spin quantisation axis become

$$S^{c+s,z}_{\mathrm{xx}} = -\frac{1}{eT}\frac{L^{cc}_{\mathrm{xx}}L^{cq}_{\mathrm{xx}} + \mathcal{L}^{sc,z}_{\mathrm{xy}}\mathcal{L}^{sq,z}_{\mathrm{xy}}}{(L^{cc}_{\mathrm{xx}})^2 + (\mathcal{L}^{sc,z}_{\mathrm{xy}})^2}. \tag{A.14}$$

This expression is exactly identical to the one given by Tauber *et al.* [20] [Eq. (8)], but obviously not to Eq. (6) of Ref. 266. Numerically they give almost the same result, since the off diagonal spin-dependent contributions are orders of magnitude smaller than the diagonal charge-dependent ones. As stated above, the additional information contained in Eq. (A.14) is connected to the coupling of the temperature gradient to the longitudinal charge rearrangement via two transverse effects, namely the spin Nernst and the inverse spin Hall effect.

Analogously, the off-diagonal charge- and spin-dependent Seebeck coefficient $S_{\mathrm{yx}}^{c+s,z}$, which connects the field created in y direction to the temperature gradient in x direction, which is given for a cubic system by

$$S_{\mathrm{yx}}^{c+s,z} = -\frac{1}{eT}\frac{A_{\mathrm{xx}}^{z}B_{\mathrm{yx}}^{z} - A_{\mathrm{yx}}^{z}B_{\mathrm{xx}}^{z}}{(A_{\mathrm{xx}}^{z})^2 + (A_{\mathrm{xy}}^{z})^2}\ , \tag{A.15}$$

can in the non-magnetic limit be reduced to

$$S_{\mathrm{yx}}^{c+s,z} = -\frac{1}{eT}\frac{L_{\mathrm{xx}}^{cc}\mathcal{L}_{\mathrm{yx}}^{sq,z} - \mathcal{L}_{\mathrm{yx}}^{sc,z}L_{\mathrm{xx}}^{cq}}{(L_{\mathrm{xx}}^{cc})^2 + (\mathcal{L}_{\mathrm{yx}}^{sc,z})^2} \tag{A.16}$$

by using Eq. (A.13). Again one finds this expression to be identical to the corresponding expression given in Ref. 20, namely

$$S_{\mathrm{yx}}^{s} = -\frac{1}{eT}\frac{L_{0,\mathrm{xx}}^{\uparrow}L_{1,\mathrm{yx}}^{\uparrow} - L_{0,\mathrm{yx}}^{\uparrow}L_{1,\mathrm{xx}}^{\uparrow}}{(L_{0,\mathrm{xx}}^{\uparrow})^2 + (L_{0,\mathrm{yx}}^{\uparrow})^2}, \tag{A.17}$$

which actually contains information about charge as well as spin-polarisation.

Furthermore it has to be stressed, that $\underline{\boldsymbol{S}}^{c+s}$ is not the simple sum of a charge- and a spin-dependent thermoelectric tensor. Additionally it is of course only in the non-magnetic case valid to construct it from spin-projected thermoelectric tensors by taking their sum and difference for diagonal and off-diagonal elements, respectively. In particular one has to be aware of the fact that when doing so one is explicitly mixing charge and spin.

A.4 Magnetic Laue groups and rotation of spin conductivity tensors

Alternative definitions of magnetic Laue groups

Kleiner [271] defines a magnetic Laue group (MLG) as the group obtained from the magnetic point group by removing the improper part of every rotation (operator), if present. Seemann *et al.* [283, 338, 339] instead adhered to the commonly used definition of a Laue group, namely the group obtained from a (magnetic) point group upon addition of the spatial inversion operator ($\bar{1}$). So the MLGs obtained this or that way are really different groups of symmetry operations and can, in principle, lead to different tensor shapes for certain response functions. The reason why there are no such cases concerning the symmetry of $\underline{\boldsymbol{\tau}}'$, $\underline{\boldsymbol{\tau}}$ and $\underline{\boldsymbol{\sigma}}$ is that the improper part of the operator is irrelevant for the restriction it imposes on the shape of the electrical conductivity and the thermoelectric tensors. This is because the symmetry operation acts twice on identically transforming operators (electrical and heat current density) and its improper part gives just a factor of $-\mathrm{I}_3$, twice. Hence if two MLGs just differ by additional (or missing) improper rotations generated by adding the space inversion (or removing the improper part from every improper rotation), their tensor shapes must be identical. The proper rotations de facto determining the tensor shapes are, as demanded, the same in both cases.

Spin conductivity tensors in equivalent coordinate systems

In Ref. 283, reprinted in Section 3.3, the tensor forms for the inverse thermoelectric tensor $\underline{\boldsymbol{\tau}}$ of the magnetic Laue groups $4'/mm'm$ and $4'/mmm'$ of category (c) [p. 180] and the direct and inverse spin conductivity tensors of the groups $\bar{3}1m1'$ and $\bar{3}m11'$ of category (a) [p. 182], $\bar{3}1m$ and $\bar{3}m1$ of category (b) [p. 183], as well as $4'/mm'm$ and $4'/mmm'$, $\bar{3}1m'$ and $\bar{3}m'1$, and $6'/m'm'm$ and $6'/m'mm'$ of category (c) [p. 184] were stated to be pairwise related to each other by rotations of the coordinate system around the respective principal axes. This shall be demonstrated here for the direct (reduced) and inverse spin conductivity tensors in category (c), collected in Tables A.1 and A.2, respectively.

Rotation around the principal axis (z), corresponding to the generator at the first position of the group symbol or the *primary direction*, by the angle between the secondary and tertiary directions leads to the tensors in Tables A.3 and A.4. The respective angles are $\theta = \pi/4$ for $4'/mm'm$ and $4'/mmm'$ and $\theta = \pi/2$ for $\bar{3}1m'$ and $\bar{3}m'1$ as well as for $6'/m'm'm$ and $6'/m'mm'$. Note that the full third-rank tensors have to be rotated. Relabelling the elements $\sigma_{ij}^{k}(\theta)$ of Tab. A.3 and accounting for degeneracies leads for the reduced tensor forms to Table A.5. Doing the same with Tab. A.4 and using furthermore the elements of Tab. A.5, one obtains Table A.6.

Now when comparing Tables A.5 and A.1 as well as Tables A.6 and A.2 the equivalence of the pairs of magnetic Laue groups becomes obvious. Note, that the lines are of course swapped, i.e., $\underline{\boldsymbol{\sigma}}^{(\prime)x}(\theta)$ of $4'/mm'm$ is to be compared to $\underline{\boldsymbol{\sigma}}^{(\prime)x}$ of $4'/mmm'$, etc., since the equivalent coordinate systems have been transformed into each other.

magnetic Laue group	$\underline{\boldsymbol{\sigma}}^x$	$\underline{\boldsymbol{\sigma}}^y$	$\underline{\boldsymbol{\sigma}}^z$
$4'/mm'm$	$\begin{pmatrix} 0 & 0 & \sigma_{xz}^x \\ 0 & 0 & -\sigma_{xz}^y \\ \sigma_{zx}^x & -\sigma_{zx}^y & 0 \end{pmatrix}$	$\begin{pmatrix} 0 & 0 & \sigma_{xz}^y \\ 0 & 0 & -\sigma_{xz}^x \\ \sigma_{zx}^y & -\sigma_{zx}^x & 0 \end{pmatrix}$	$\begin{pmatrix} \sigma_{xx}^z & \sigma_{xy}^z & 0 \\ -\sigma_{xy}^z & -\sigma_{xx}^z & 0 \\ 0 & 0 & 0 \end{pmatrix}$
$4'/mmm'$	$\begin{pmatrix} 0 & 0 & 0 \\ 0 & 0 & \sigma_{yz}^x \\ 0 & \sigma_{zy}^x & 0 \end{pmatrix}$	$\begin{pmatrix} 0 & 0 & \sigma_{xz}^y \\ 0 & 0 & 0 \\ \sigma_{zx}^y & 0 & 0 \end{pmatrix}$	$\begin{pmatrix} 0 & \sigma_{xy}^z & 0 \\ \sigma_{yx}^z & 0 & 0 \\ 0 & 0 & 0 \end{pmatrix}$
$\bar{3}1m'$, $\bar{3}m'1$	$\begin{pmatrix} \sigma_{xx}^x & \sigma_{xx}^y & \sigma_{xz}^x \\ \sigma_{xx}^y & -\sigma_{xx}^x & -\sigma_{xz}^y \\ \sigma_{zx}^x & -\sigma_{zx}^y & 0 \end{pmatrix}$	$\begin{pmatrix} \sigma_{xx}^y & -\sigma_{xx}^x & \sigma_{xz}^y \\ -\sigma_{xx}^x & -\sigma_{xx}^y & \sigma_{xz}^x \\ \sigma_{zx}^y & \sigma_{zx}^x & 0 \end{pmatrix}$	$\begin{pmatrix} \sigma_{xx}^z & \sigma_{xy}^z & 0 \\ -\sigma_{xy}^z & \sigma_{xx}^z & 0 \\ 0 & 0 & \sigma_{zz}^z \end{pmatrix}$
$6'/m'm'm$	$\begin{pmatrix} \sigma_{xx}^x & 0 & 0 \\ 0 & -\sigma_{xx}^x & -\sigma_{xz}^y \\ 0 & -\sigma_{zx}^y & 0 \end{pmatrix}$	$\begin{pmatrix} 0 & -\sigma_{xx}^x & \sigma_{xz}^y \\ -\sigma_{xx}^x & 0 & 0 \\ \sigma_{zx}^y & 0 & 0 \end{pmatrix}$	$\begin{pmatrix} 0 & \sigma_{xy}^z & 0 \\ -\sigma_{xy}^z & 0 & 0 \\ 0 & 0 & 0 \end{pmatrix}$
$6'/m'mm'$	$\begin{pmatrix} 0 & \sigma_{xx}^y & 0 \\ \sigma_{xx}^y & 0 & -\sigma_{xz}^y \\ 0 & -\sigma_{zx}^y & 0 \end{pmatrix}$	$\begin{pmatrix} \sigma_{xx}^y & 0 & \sigma_{xz}^y \\ 0 & -\sigma_{xx}^y & 0 \\ \sigma_{zx}^y & 0 & 0 \end{pmatrix}$	$\begin{pmatrix} 0 & \sigma_{xy}^z & 0 \\ -\sigma_{xy}^z & 0 & 0 \\ 0 & 0 & 0 \end{pmatrix}$

Table A.1: Reduced polarisation tensor forms for magnetic Laue groups of category (c).

magnetic Laue group	$\underline{\boldsymbol{\sigma}}'^x$	$\underline{\boldsymbol{\sigma}}'^y$	$\underline{\boldsymbol{\sigma}}'^z$
$4'/mm'm$	$\begin{pmatrix} 0 & 0 & \sigma_{xz}^x \\ 0 & 0 & -\sigma_{xz}^y \\ \sigma_{xx}^z & -\sigma_{xy}^z & 0 \end{pmatrix}$	$\begin{pmatrix} 0 & 0 & \sigma_{xz}^y \\ 0 & 0 & -\sigma_{xz}^x \\ \sigma_{xy}^z & -\sigma_{xx}^z & 0 \end{pmatrix}$	$\begin{pmatrix} \sigma_{zx}^x & \sigma_{zx}^y & 0 \\ -\sigma_{zx}^y & -\sigma_{zx}^x & 0 \\ 0 & 0 & 0 \end{pmatrix}$
$4'/mmm'$	$\begin{pmatrix} 0 & 0 & 0 \\ 0 & 0 & \sigma_{yz}^x \\ 0 & \sigma_{yx}^z & 0 \end{pmatrix}$	$\begin{pmatrix} 0 & 0 & \sigma_{xz}^y \\ 0 & 0 & 0 \\ \sigma_{xy}^z & 0 & 0 \end{pmatrix}$	$\begin{pmatrix} 0 & \sigma_{zx}^y & 0 \\ \sigma_{zy}^x & 0 & 0 \\ 0 & 0 & 0 \end{pmatrix}$
$\bar{3}1m'$	$\begin{pmatrix} -\sigma_{xx}^x & \sigma_{xx}^y & \sigma_{xz}^x \\ \sigma_{xx}^y & \sigma_{xx}^x & -\sigma_{xz}^y \\ \sigma_{xx}^z & -\sigma_{xy}^z & 0 \end{pmatrix}$	$\begin{pmatrix} \sigma_{xx}^y & \sigma_{xx}^x & \sigma_{xz}^y \\ \sigma_{xx}^x & -\sigma_{xx}^y & \sigma_{xz}^x \\ \sigma_{xy}^z & \sigma_{xx}^z & 0 \end{pmatrix}$	$\begin{pmatrix} \sigma_{zx}^x & \sigma_{zx}^y & 0 \\ -\sigma_{zx}^y & \sigma_{zx}^x & 0 \\ 0 & 0 & \sigma_{zz}^z \end{pmatrix}$
$\bar{3}m'1$	$\begin{pmatrix} \sigma_{xx}^x & -\sigma_{xx}^y & \sigma_{xz}^x \\ -\sigma_{xx}^y & -\sigma_{xx}^x & -\sigma_{xz}^y \\ \sigma_{xx}^z & -\sigma_{xy}^z & 0 \end{pmatrix}$	$\begin{pmatrix} -\sigma_{xx}^y & -\sigma_{xx}^x & \sigma_{xz}^y \\ -\sigma_{xx}^x & \sigma_{xx}^y & \sigma_{xz}^x \\ \sigma_{xy}^z & \sigma_{xx}^z & 0 \end{pmatrix}$	$\begin{pmatrix} \sigma_{zx}^x & \sigma_{zx}^y & 0 \\ -\sigma_{zx}^y & \sigma_{zx}^x & 0 \\ 0 & 0 & \sigma_{zz}^z \end{pmatrix}$
$6'/m'm'm$	$\begin{pmatrix} \sigma_{xx}^x & 0 & 0 \\ 0 & -\sigma_{xx}^x & -\sigma_{xz}^y \\ 0 & -\sigma_{xy}^z & 0 \end{pmatrix}$	$\begin{pmatrix} 0 & -\sigma_{xx}^x & \sigma_{xz}^y \\ -\sigma_{xx}^x & 0 & 0 \\ \sigma_{xy}^z & 0 & 0 \end{pmatrix}$	$\begin{pmatrix} 0 & \sigma_{zx}^y & 0 \\ -\sigma_{zx}^y & 0 & 0 \\ 0 & 0 & 0 \end{pmatrix}$
$6'/m'mm'$	$\begin{pmatrix} 0 & \sigma_{xx}^y & 0 \\ \sigma_{xx}^y & 0 & -\sigma_{xz}^y \\ 0 & -\sigma_{xy}^z & 0 \end{pmatrix}$	$\begin{pmatrix} \sigma_{xx}^y & 0 & \sigma_{xz}^y \\ 0 & -\sigma_{xx}^y & 0 \\ \sigma_{xy}^z & 0 & 0 \end{pmatrix}$	$\begin{pmatrix} 0 & \sigma_{zx}^y & 0 \\ -\sigma_{zx}^y & 0 & 0 \\ 0 & 0 & 0 \end{pmatrix}$

Table A.2: Polarisation tensor forms for magnetic Laue groups of category (c).

magnetic Laue group	$\underline{\boldsymbol{\sigma}}^{x}(\theta)$	$\underline{\boldsymbol{\sigma}}^{y}(\theta)$	$\underline{\boldsymbol{\sigma}}^{z}(\theta)$
$4'/mm'm$	$\begin{pmatrix} 0 & 0 & 0 \\ 0 & 0 & (-\sigma^{x}_{xz}-\sigma^{y}_{xz}) \\ 0 & (-\sigma^{x}_{zx}-\sigma^{y}_{zx}) & 0 \end{pmatrix}$	$\begin{pmatrix} 0 & 0 & (-\sigma^{x}_{xz}+\sigma^{y}_{xz}) \\ 0 & 0 & 0 \\ (-\sigma^{x}_{zx}+\sigma^{y}_{zx}) & 0 & 0 \end{pmatrix}$	$\begin{pmatrix} 0 & (-\sigma^{z}_{xx}+\sigma^{z}_{xy}) & 0 \\ (-\sigma^{z}_{xx}-\sigma^{z}_{xy}) & 0 & 0 \\ 0 & 0 & 0 \end{pmatrix}$
$4'/mmm'$	$\begin{pmatrix} 0 & 0 & \frac{(\sigma^{x}_{yz}+\sigma^{y}_{xz})}{2} \\ 0 & 0 & \frac{(\sigma^{x}_{yz}-\sigma^{y}_{xz})}{2} \\ \frac{(\sigma^{x}_{zy}+\sigma^{y}_{zx})}{2} & \frac{(\sigma^{x}_{zy}-\sigma^{y}_{zx})}{2} & 0 \end{pmatrix}$	$\begin{pmatrix} 0 & 0 & \frac{(-\sigma^{x}_{yz}+\sigma^{y}_{xz})}{2} \\ 0 & 0 & \frac{(-\sigma^{x}_{yz}-\sigma^{y}_{xz})}{2} \\ \frac{(-\sigma^{x}_{zy}+\sigma^{y}_{zx})}{2} & \frac{(-\sigma^{x}_{zy}-\sigma^{y}_{zx})}{2} & 0 \end{pmatrix}$	$\begin{pmatrix} \frac{(\sigma^{z}_{xy}+\sigma^{z}_{yx})}{2} & \frac{(\sigma^{z}_{xy}-\sigma^{z}_{yx})}{2} & 0 \\ \frac{(-\sigma^{z}_{xy}+\sigma^{z}_{yx})}{2} & \frac{(-\sigma^{z}_{xy}-\sigma^{z}_{yx})}{2} & 0 \\ 0 & 0 & 0 \end{pmatrix}$
$\bar{3}1m'$, $\bar{3}m'1$	$\begin{pmatrix} -\sigma^{y}_{xx} & \sigma^{x}_{xx} & \sigma^{x}_{xz} \\ \sigma^{x}_{xx} & \sigma^{y}_{xx} & -\sigma^{y}_{xz} \\ \sigma^{y}_{zx} & -\sigma^{x}_{zx} & 0 \end{pmatrix}$	$\begin{pmatrix} \sigma^{x}_{xx} & \sigma^{y}_{xx} & \sigma^{y}_{xz} \\ \sigma^{y}_{xx} & -\sigma^{x}_{xx} & \sigma^{x}_{xz} \\ \sigma^{y}_{zx} & \sigma^{x}_{zx} & 0 \end{pmatrix}$	$\begin{pmatrix} \sigma^{z}_{xx} & \sigma^{z}_{xy} & 0 \\ -\sigma^{z}_{xy} & \sigma^{z}_{xx} & 0 \\ 0 & 0 & \sigma^{z}_{zz} \end{pmatrix}$
$6'/m'm'm$	$\begin{pmatrix} 0 & \sigma^{x}_{xx} & 0 \\ \sigma^{x}_{xx} & 0 & -\sigma^{y}_{xz} \\ 0 & -\sigma^{y}_{zx} & 0 \end{pmatrix}$	$\begin{pmatrix} \sigma^{x}_{xx} & 0 & \sigma^{y}_{xz} \\ 0 & -\sigma^{x}_{xx} & 0 \\ \sigma^{y}_{zx} & 0 & 0 \end{pmatrix}$	$\begin{pmatrix} 0 & \sigma^{z}_{xy} & 0 \\ -\sigma^{z}_{xy} & 0 & 0 \\ 0 & 0 & 0 \end{pmatrix}$
$6'/m'mm'$	$\begin{pmatrix} -\sigma^{y}_{xx} & 0 & 0 \\ 0 & \sigma^{y}_{xz} & -\sigma^{y}_{xz} \\ 0 & -\sigma^{y}_{zx} & 0 \end{pmatrix}$	$\begin{pmatrix} 0 & \sigma^{y}_{xx} & \sigma^{y}_{xz} \\ \sigma^{y}_{xx} & 0 & 0 \\ \sigma^{y}_{zx} & 0 & 0 \end{pmatrix}$	$\begin{pmatrix} 0 & \sigma^{z}_{xy} & 0 \\ -\sigma^{z}_{xy} & 0 & 0 \\ 0 & 0 & 0 \end{pmatrix}$

Table A.3: Reduced polarisation tensor forms for magnetic Laue groups of category (c) (see Tab. A.1), transformed by a rotation of the coordinate system around the principal (z) axis.

magnetic Laue group	$\underline{\boldsymbol{\sigma}}'^{x}(\theta)$	$\underline{\boldsymbol{\sigma}}'^{y}(\theta)$	$\underline{\boldsymbol{\sigma}}'^{z}(\theta)$
$4'/mm'm$	$\begin{pmatrix} 0 & 0 & 0 \\ 0 & 0 & (-\sigma^{x}_{xz}-\sigma^{y}_{xz}) \\ 0 & (-\sigma^{z}_{xx}-\sigma^{z}_{xy}) & 0 \end{pmatrix}$	$\begin{pmatrix} 0 & 0 & (-\sigma^{x}_{xz}+\sigma^{y}_{xz}) \\ 0 & 0 & 0 \\ (-\sigma^{z}_{xx}+\sigma^{z}_{xy}) & 0 & 0 \end{pmatrix}$	$\begin{pmatrix} 0 & (-\sigma^{x}_{xx}+\sigma^{y}_{xx}) & 0 \\ (-\sigma^{x}_{xx}-\sigma^{y}_{xx}) & 0 & 0 \\ 0 & 0 & 0 \end{pmatrix}$
$4'/mmm'$	$\begin{pmatrix} 0 & 0 & \frac{(\sigma^{x}_{yz}+\sigma^{y}_{xz})}{2} \\ 0 & 0 & \frac{(\sigma^{x}_{yz}-\sigma^{y}_{xz})}{2} \\ \frac{(\sigma^{z}_{xy}+\sigma^{z}_{yx})}{2} & \frac{(-\sigma^{z}_{xy}+\sigma^{z}_{yx})}{2} & 0 \end{pmatrix}$	$\begin{pmatrix} 0 & 0 & \frac{(-\sigma^{x}_{yz}+\sigma^{y}_{xz})}{2} \\ 0 & 0 & \frac{(-\sigma^{x}_{yz}-\sigma^{y}_{xz})}{2} \\ \frac{(\sigma^{z}_{xy}-\sigma^{z}_{yx})}{2} & \frac{(-\sigma^{z}_{xy}-\sigma^{z}_{yx})}{2} & 0 \end{pmatrix}$	$\begin{pmatrix} \frac{(\sigma^{x}_{zy}+\sigma^{y}_{zx})}{2} & \frac{(-\sigma^{x}_{zy}+\sigma^{y}_{zx})}{2} & 0 \\ \frac{(\sigma^{x}_{zy}-\sigma^{y}_{zx})}{2} & \frac{(-\sigma^{x}_{zy}-\sigma^{y}_{zx})}{2} & 0 \\ 0 & 0 & 0 \end{pmatrix}$
$\bar{3}1m'$	$\begin{pmatrix} -\sigma^{y}_{xx} & -\sigma^{x}_{xx} & \sigma^{x}_{xz} \\ -\sigma^{x}_{xx} & \sigma^{y}_{xx} & -\sigma^{y}_{xz} \\ \sigma^{z}_{xx} & -\sigma^{z}_{xy} & 0 \end{pmatrix}$	$\begin{pmatrix} -\sigma^{x}_{xx} & \sigma^{y}_{xx} & \sigma^{y}_{xz} \\ \sigma^{y}_{xx} & \sigma^{x}_{xx} & \sigma^{x}_{xz} \\ \sigma^{z}_{xy} & \sigma^{z}_{xx} & 0 \end{pmatrix}$	$\begin{pmatrix} \sigma^{x}_{zy} & \sigma^{y}_{zy} & 0 \\ -\sigma^{y}_{zx} & \sigma^{x}_{zx} & 0 \\ 0 & 0 & \sigma^{z}_{zz} \end{pmatrix}$
$\bar{3}m'1$	$\begin{pmatrix} \sigma^{y}_{xx} & \sigma^{x}_{xx} & \sigma^{x}_{xz} \\ \sigma^{x}_{xx} & -\sigma^{y}_{xx} & -\sigma^{y}_{xz} \\ \sigma^{z}_{xx} & -\sigma^{z}_{xy} & 0 \end{pmatrix}$	$\begin{pmatrix} \sigma^{x}_{xx} & -\sigma^{y}_{xx} & \sigma^{y}_{xz} \\ -\sigma^{y}_{xx} & -\sigma^{x}_{xx} & \sigma^{x}_{xz} \\ \sigma^{z}_{xy} & \sigma^{z}_{xx} & 0 \end{pmatrix}$	$\begin{pmatrix} \sigma^{x}_{zy} & \sigma^{y}_{zy} & 0 \\ -\sigma^{y}_{zx} & \sigma^{x}_{zx} & 0 \\ 0 & 0 & \sigma^{z}_{zz} \end{pmatrix}$
$6'/m'm'm$	$\begin{pmatrix} 0 & \sigma^{x}_{xx} & 0 \\ \sigma^{x}_{xx} & 0 & -\sigma^{y}_{xz} \\ 0 & -\sigma^{z}_{xy} & 0 \end{pmatrix}$	$\begin{pmatrix} \sigma^{x}_{xx} & 0 & \sigma^{y}_{xz} \\ 0 & -\sigma^{x}_{xx} & 0 \\ \sigma^{z}_{xy} & 0 & 0 \end{pmatrix}$	$\begin{pmatrix} 0 & \sigma^{y}_{zx} & 0 \\ -\sigma^{y}_{zx} & 0 & 0 \\ 0 & 0 & 0 \end{pmatrix}$
$6'/m'mm'$	$\begin{pmatrix} -\sigma^{y}_{xx} & 0 & 0 \\ 0 & \sigma^{y}_{xz} & -\sigma^{y}_{xz} \\ 0 & -\sigma^{z}_{xy} & 0 \end{pmatrix}$	$\begin{pmatrix} 0 & \sigma^{y}_{xx} & \sigma^{y}_{xz} \\ \sigma^{y}_{xx} & 0 & 0 \\ \sigma^{z}_{xy} & 0 & 0 \end{pmatrix}$	$\begin{pmatrix} 0 & \sigma^{y}_{zx} & 0 \\ -\sigma^{y}_{zx} & 0 & 0 \\ 0 & 0 & 0 \end{pmatrix}$

Table A.4: Polarisation tensor forms for magnetic Laue groups of category (c) (see Tab. A.2), transformed by a rotation of the coordinate system around the principal (z) axis.

magnetic Laue group	$\underline{\boldsymbol{\sigma}}^x(\theta)$	$\underline{\boldsymbol{\sigma}}^y(\theta)$	$\underline{\boldsymbol{\sigma}}^z(\theta)$
$4'/mm'm$	$\begin{pmatrix} 0 & 0 & 0 \\ 0 & 0 & \sigma^x_{yz}(\theta) \\ 0 & \sigma^x_{zy}(\theta) & 0 \end{pmatrix}$	$\begin{pmatrix} 0 & 0 & \sigma^y_{xz}(\theta) \\ 0 & 0 & 0 \\ \sigma^y_{zx}(\theta) & 0 & 0 \end{pmatrix}$	$\begin{pmatrix} 0 & \sigma^z_{xy}(\theta) & 0 \\ \sigma^z_{yx}(\theta) & 0 & 0 \\ 0 & 0 & 0 \end{pmatrix}$
$4'/mmm'$	$\begin{pmatrix} 0 & 0 & \sigma^x_{xz}(\theta) \\ 0 & 0 & -\sigma^y_{xz}(\theta) \\ \sigma^x_{zx}(\theta) & -\sigma^y_{zx}(\theta) & 0 \end{pmatrix}$	$\begin{pmatrix} 0 & 0 & \sigma^y_{xz}(\theta) \\ 0 & 0 & -\sigma^x_{xz}(\theta) \\ \sigma^y_{zx}(\theta) & -\sigma^x_{zx}(\theta) & 0 \end{pmatrix}$	$\begin{pmatrix} \sigma^z_{xx}(\theta) & \sigma^z_{xy}(\theta) & 0 \\ -\sigma^z_{xy}(\theta) & -\sigma^z_{xx}(\theta) & 0 \\ 0 & 0 & 0 \end{pmatrix}$
$\bar{3}1m'$, $\bar{3}m'1$	$\begin{pmatrix} \sigma^x_{xx}(\theta) & \sigma^y_{xx}(\theta) & \sigma^x_{xz}(\theta) \\ \sigma^y_{xx}(\theta) & -\sigma^x_{xx}(\theta) & -\sigma^y_{xz}(\theta) \\ \sigma^x_{zx}(\theta) & -\sigma^y_{zx}(\theta) & 0 \end{pmatrix}$	$\begin{pmatrix} \sigma^y_{xx}(\theta) & -\sigma^x_{xx}(\theta) & \sigma^y_{xz}(\theta) \\ -\sigma^x_{xx}(\theta) & -\sigma^y_{xx}(\theta) & \sigma^x_{xz}(\theta) \\ \sigma^y_{zx}(\theta) & \sigma^x_{zx}(\theta) & 0 \end{pmatrix}$	$\begin{pmatrix} \sigma^z_{xx}(\theta) & \sigma^z_{xy}(\theta) & 0 \\ -\sigma^z_{xy}(\theta) & \sigma^z_{xx}(\theta) & 0 \\ 0 & 0 & \sigma^z_{zz}(\theta) \end{pmatrix}$
$6'/m'm'm$	$\begin{pmatrix} 0 & \sigma^y_{xx}(\theta) & 0 \\ \sigma^y_{xx}(\theta) & 0 & -\sigma^y_{xz}(\theta) \\ 0 & -\sigma^y_{zx}(\theta) & 0 \end{pmatrix}$	$\begin{pmatrix} \sigma^y_{xx}(\theta) & 0 & \sigma^y_{xz}(\theta) \\ 0 & -\sigma^y_{xx}(\theta) & 0 \\ \sigma^y_{zx}(\theta) & 0 & 0 \end{pmatrix}$	$\begin{pmatrix} 0 & \sigma^z_{xy}(\theta) & 0 \\ -\sigma^z_{xy}(\theta) & 0 & 0 \\ 0 & 0 & 0 \end{pmatrix}$
$6'/m'mm'$	$\begin{pmatrix} \sigma^x_{xx}(\theta) & 0 & 0 \\ 0 & -\sigma^x_{xx}(\theta) & -\sigma^y_{xz}(\theta) \\ 0 & -\sigma^y_{zx}(\theta) & 0 \end{pmatrix}$	$\begin{pmatrix} 0 & -\sigma^x_{xx}(\theta) & \sigma^y_{xz}(\theta) \\ -\sigma^x_{xx}(\theta) & 0 & 0 \\ \sigma^y_{zx}(\theta) & 0 & 0 \end{pmatrix}$	$\begin{pmatrix} 0 & \sigma^z_{xy}(\theta) & 0 \\ -\sigma^z_{xy}(\theta) & 0 & 0 \\ 0 & 0 & 0 \end{pmatrix}$

Table A.5: Rotated reduced polarisation tensor forms $\underline{\boldsymbol{\sigma}}^k(\theta)$ for magnetic Laue groups of category (c), i.e., same content as in Tab. A.3, relabelled to facilitate the recognition of degeneracies.

magnetic Laue group	$\underline{\boldsymbol{\sigma}}'^x(\theta)$	$\underline{\boldsymbol{\sigma}}'^y(\theta)$	$\underline{\boldsymbol{\sigma}}'^z(\theta)$
$4'/mm'm$	$\begin{pmatrix} 0 & 0 & 0 \\ 0 & 0 & \sigma^x_{yz}(\theta) \\ 0 & \sigma^z_{yx}(\theta) & 0 \end{pmatrix}$	$\begin{pmatrix} 0 & 0 & \sigma^y_{xz}(\theta) \\ 0 & 0 & 0 \\ \sigma^z_{xy}(\theta) & 0 & 0 \end{pmatrix}$	$\begin{pmatrix} 0 & \sigma^y_{zx}(\theta) & 0 \\ \sigma^x_{zy}(\theta) & 0 & 0 \\ 0 & 0 & 0 \end{pmatrix}$
$4'/mmm'$	$\begin{pmatrix} 0 & 0 & \sigma^x_{xz}(\theta) \\ 0 & 0 & -\sigma^y_{xz}(\theta) \\ \sigma^z_{xx}(\theta) & -\sigma^z_{xy}(\theta) & 0 \end{pmatrix}$	$\begin{pmatrix} 0 & 0 & \sigma^y_{xz}(\theta) \\ 0 & 0 & -\sigma^x_{xz}(\theta) \\ \sigma^z_{xy}(\theta) & -\sigma^z_{xx}(\theta) & 0 \end{pmatrix}$	$\begin{pmatrix} \sigma^x_{zx}(\theta) & \sigma^y_{zx}(\theta) & 0 \\ -\sigma^y_{zx}(\theta) & -\sigma^x_{zx}(\theta) & 0 \\ 0 & 0 & 0 \end{pmatrix}$
$\bar{3}1m'$	$\begin{pmatrix} \sigma^x_{xx}(\theta) & -\sigma^y_{xx}(\theta) & \sigma^x_{xz}(\theta) \\ -\sigma^y_{xx}(\theta) & -\sigma^x_{xx}(\theta) & -\sigma^y_{xz}(\theta) \\ \sigma^z_{xx}(\theta) & -\sigma^z_{xy}(\theta) & 0 \end{pmatrix}$	$\begin{pmatrix} -\sigma^y_{xx}(\theta) & -\sigma^x_{xx}(\theta) & \sigma^y_{xz}(\theta) \\ -\sigma^x_{xx}(\theta) & \sigma^y_{xx}(\theta) & \sigma^x_{xz}(\theta) \\ \sigma^z_{xy}(\theta) & \sigma^z_{xx}(\theta) & 0 \end{pmatrix}$	$\begin{pmatrix} \sigma^x_{zx}(\theta) & \sigma^y_{zx}(\theta) & 0 \\ -\sigma^y_{zx}(\theta) & \sigma^x_{zx}(\theta) & 0 \\ 0 & 0 & \sigma^z_{zz}(\theta) \end{pmatrix}$
$\bar{3}m'1$	$\begin{pmatrix} -\sigma^x_{xx}(\theta) & \sigma^y_{xx}(\theta) & \sigma^x_{xz}(\theta) \\ \sigma^y_{xx}(\theta) & \sigma^x_{xx}(\theta) & -\sigma^y_{xz}(\theta) \\ \sigma^z_{xx}(\theta) & -\sigma^z_{xy}(\theta) & 0 \end{pmatrix}$	$\begin{pmatrix} \sigma^y_{xx}(\theta) & \sigma^x_{xx}(\theta) & \sigma^y_{xz}(\theta) \\ \sigma^x_{xx}(\theta) & -\sigma^y_{xx}(\theta) & \sigma^x_{xz}(\theta) \\ \sigma^z_{xy}(\theta) & \sigma^z_{xx}(\theta) & 0 \end{pmatrix}$	$\begin{pmatrix} \sigma^x_{zx}(\theta) & \sigma^y_{zx}(\theta) & 0 \\ -\sigma^y_{zx}(\theta) & \sigma^x_{zx}(\theta) & 0 \\ 0 & 0 & \sigma^z_{zz}(\theta) \end{pmatrix}$
$6'/m'm'm$	$\begin{pmatrix} 0 & \sigma^y_{xx}(\theta) & 0 \\ \sigma^y_{xx}(\theta) & 0 & -\sigma^y_{xz}(\theta) \\ 0 & -\sigma^z_{xy}(\theta) & 0 \end{pmatrix}$	$\begin{pmatrix} \sigma^y_{xx}(\theta) & 0 & \sigma^y_{xz}(\theta) \\ 0 & -\sigma^y_{xx}(\theta) & 0 \\ \sigma^z_{xy}(\theta) & 0 & 0 \end{pmatrix}$	$\begin{pmatrix} 0 & \sigma^y_{zx}(\theta) & 0 \\ -\sigma^y_{zx}(\theta) & 0 & 0 \\ 0 & 0 & 0 \end{pmatrix}$
$6'/m'mm'$	$\begin{pmatrix} \sigma^x_{xx}(\theta) & 0 & 0 \\ 0 & -\sigma^x_{xx}(\theta) & -\sigma^y_{xz}(\theta) \\ 0 & -\sigma^z_{xy}(\theta) & 0 \end{pmatrix}$	$\begin{pmatrix} 0 & -\sigma^x_{xx}(\theta) & \sigma^y_{xz}(\theta) \\ -\sigma^x_{xx}(\theta) & 0 & 0 \\ \sigma^z_{xy}(\theta) & 0 & 0 \end{pmatrix}$	$\begin{pmatrix} 0 & \sigma^y_{zx}(\theta) & 0 \\ -\sigma^y_{zx}(\theta) & 0 & 0 \\ 0 & 0 & 0 \end{pmatrix}$

Table A.6: Rotated polarisation tensor forms $\underline{\boldsymbol{\sigma}}'^k(\theta)$ for magnetic Laue groups of category (c), i.e., same content as in Tab. A.4, relabelled using the elements of $\underline{\boldsymbol{\sigma}}^k(\theta)$ in Tab. A.5.

A.5 Implementation of the Kubo formalism for 2D transport

Based on earlier work by Butler *et al.* [381] a fully-relativistic formulation of the Kubo linear response formalism suitable for the description of transport in layered systems has been implemented into the Munich SPR-KKR program package [382]. The layer-resolved conductivity, relating the current J_μ^I on layer I in the direction μ to the electric field E_ν^J on layer J in the direction ν as in a discrete formulation of Ohm's law,

$$J_\mu^I = \sum_{J,\nu} \sigma_{\mu\nu}^{IJ} E_\nu^J \; , \tag{A.18}$$

can essentially be expressed by an integral over the two-dimensional Brillouin zone of area Ω,

$$\sigma_{\mu\nu}^{IJ} \propto \frac{1}{4} \sum_{p,p'=\pm 1} (pp') \int_\Omega d^2\boldsymbol{k}_\parallel \, M_\mu^I(z) \, \tau^{IJ}(\boldsymbol{k}_\parallel, z) \, M_\nu^J(z') \, \tau^{JI}(\boldsymbol{k}_\parallel, z') \; . \tag{A.19}$$

Here $z^{(\prime)} = E + ip^{(\prime)}\eta$ is the complex (Fermi) energy with a small imaginary part $p^{(\prime)}\eta$, $M_{\mu/\mu}^{I/J}$ are the current operator matrix elements, and τ^{IJ} is the scattering path operator connecting layers I and J. As further details can be found in Refs. 381 and 232, in the following only results of test calculations and first applications will be presented.

Figure A.3 shows a direct comparison to the results by Butler *et al.* [381] for three different test cases: a free-electron-like jellium model, a non-magnetic Cu, and a ferromagnetic Co system. As can be seen, the agreement is satisfying in all cases, in particular when a sufficiently large angular momentum cut-off ℓ_{max} is chosen. Remaining discrepancies, most prominent for the on-site contribution σ_{ii}^{00}, might be attributed to numerical details as well as to the difference in the current operator formulation (non- vs fully-relativistic).

An important consistency check for a layer-resolved formulation is of course its convergence towards the bulk values of the conductivity with increasing number of layers. Figure A.4 shows corresponding results for a system of bcc (001) Fe layers, longitudinal conductivities summed over layers, $\sigma_{ii} = \sum_{IJ} \sigma_{ii}^{IJ}$, are given in the left panel and the transverse anti-symmetric anomalous Hall conductivity $\sigma_{\mathrm{xy}} = -\sigma_{\mathrm{yx}}$, $\sigma_{ij} = \sum_{IJ} \sigma_{ij}^{IJ}$ with $i \neq j$, is shown on the right. The magnetisation is oriented along the [001] or z direction. Obviously, the on-site terms σ_{ij}^0 do not depend on the number of layers (NI) in a homogeneous system, while the inter-site contributions σ_{ij}^1 show a rather slow convergence towards the bulk value with increasing NI. One should note here, that only layers within the finite 2D structure are summed over, i.e., the translation symmetry along the z direction is neglected. When looking only at the layer-resolved conductivity $\sigma_{ij}^I = \sum_J \sigma_{ij}^{IJ}$ of the central layer the convergence is obviously much faster (not shown).

This is exemplified in Fig. A.5 (left) for the spin-polarized conductivities $\sigma_{\mathrm{xy}}^{I,z}$, i.e., the spin Hall conductivity, and $\sigma_{\mathrm{xx}}^{I,z}$, i.e., the in-plane longitudinal spin conductivity, in a 56 layer bcc (001) Fe system. Starting from the left- or rightmost layer and

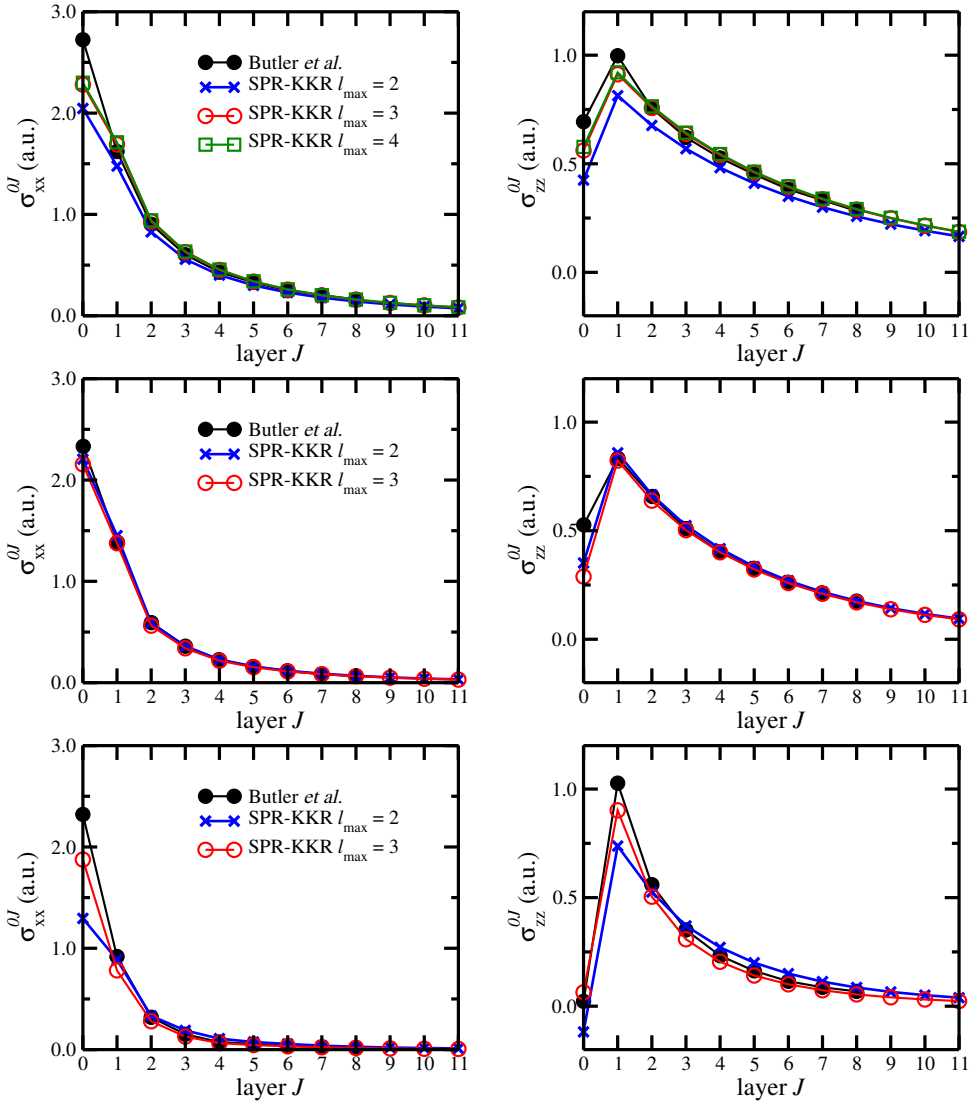

Figure A.3: Layer-resolved in-plane ($\sigma_{\mathrm{xx}}^{0J}$, left) and perpendicular-to-plane ($\sigma_{\mathrm{zz}}^{0J}$, right) conductivities for the first layer ($I = 0$) in a free-electron-like (jellium) model (top), non-magnetic fcc Cu (middle), and ferromagnetic fcc Co (bottom), always with stacking direction along [111] (z). For comparison the results of Butler *et al.* [381] are shown in black, calculations using SPR-KKR are given for different angular momentum expansions.

going towards the center, the spin Hall conductivity (left y axis) converges extremely fast to the bulk value shown as a red horizontal line, even faster than $\sigma_{\mathrm{xx}}^{I,z}$ (right y axis). The right panel of Fig. A.5 shows the temperature dependence of the longitudinal layer-integrated conductivity in fcc (111) Cu. The temperature is accounted for by employing the alloy analogy model [202] for thermally-induced uncorrelated lattice displacements. The behaviour as a function of T is similar for all system sizes shown and corresponds to that of the bulk conductivities shown in black. Only results including the vertex corrections (VC) are shown, which are however of minor relevance here. It should be noted that they apply only to the so-called interaction zone of layers with two-dimensional periodicity, while the semi-infinite leads were neglected. With increasing system size the artificial geometric anisotropy of σ_{xx} and σ_{zz} decreases and the absolute values approach those of the bulk.

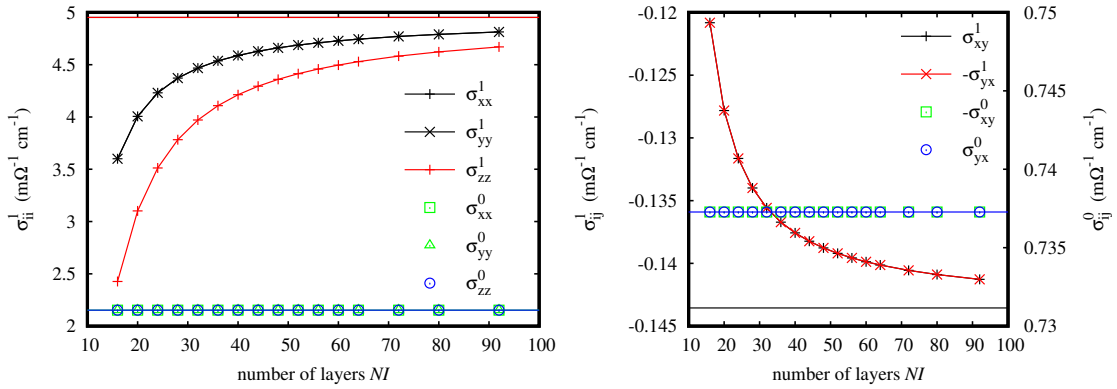

Figure A.4: Layer-integrated longitudinal (left) and transverse (right) conductivities in a bcc (001) Fe system as a function of total number of layers NI. A decomposition into on-site (σ^0_{ij}) and multiple scattering contributions (σ^1_{ij}) is made. The horizontal lines give the corresponding bulk conductivities.

Figure A.6 (left) shows results for the layer-integrated charge Seebeck coefficient in fcc (111) $Cu_{0.5}Au_{0.5}$ as a function of temperature. Results were obtained using the generalised Mott formula, Eq. (2.266), based on energy-dependent layer-integrated conductivities. The vertex corrections are taken into account, again only for the interaction zone while the leads are composed of pure fcc Cu. With growing number of layers the pronounced non-linearity appears to vanish and the bulk result shown in black is approached. The middle panel of Fig. A.6 shows corresponding results for the layer-integrated spin Nernst conductivity. Here as well the strongest deviation from linearity is found for the smallest system, the convergence with increasing systems size is faster than for the Seebeck coefficient, however it appears not to be towards the bulk result. In the right panel of Fig. A.6 the layer-resolved spin Nernst conductivity is shown, ex- (NV, empty symbols) and including vertex corrections (VC, full symbols), for the outermost alloy layers (4 & 57), the innermost layers (30 & 31), and for intermediate layers (7 & 54). One notices that: 1) mirror symmetry (left-right) is obeyed, 2) the vertex corrections are less significant for the outermost layers, while they lead to a sign change already three layers away from the $Cu|Cu_{0.5}Au_{0.5}$ interface, and 3) the innermost layers are obviously very much bulk-like.

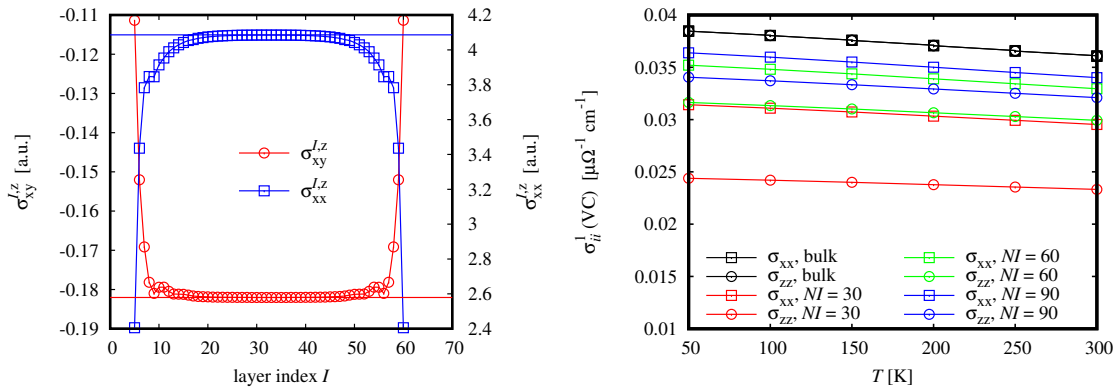

Figure A.5: Left: Layer-resolved spin-polarized conductivities as a function of layer index I in bcc (001) Fe. Right: Layer-integrated longitudinal charge conductivities in fcc Cu (111) as a function of temperature, represented by uncorrelated lattice vibrations via the alloy analogy model, and number of layers NI.

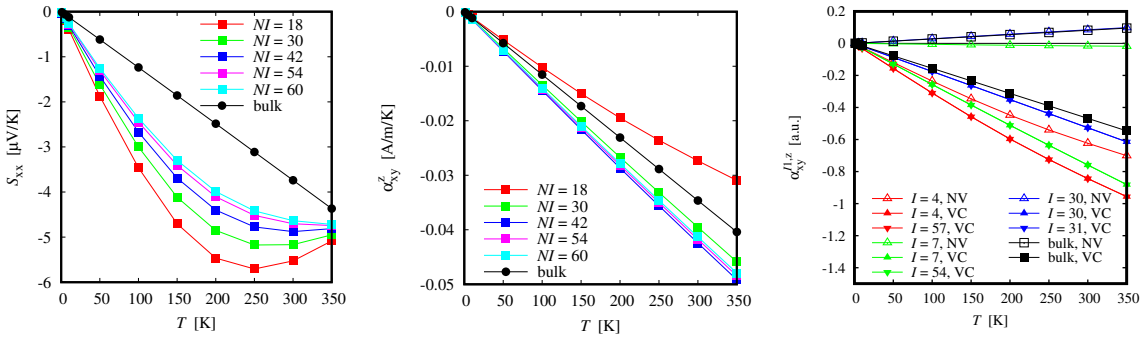

Figure A.6: Left: Layer-integrated charge Seebeck coefficient as a function of temperature and system size in fcc (111) $Cu_{0.5}Au_{0.5}$. Middle: Layer-integrated spin Nernst conductivity. Right: Layer-resolved spin Nernst conductivity for selected layers (see text) of the 60-layer system. In all cases corresponding bulk results are given in black.

As a first application to systems of physical relevance the GaAs(001)/Fe structure was chosen, for which Hupfauer *et al.* [383] observed an anisotropy of the in-plane transport in the bcc (001) Fe film induced by the lower (C_{2v}) symmetry of the Zincblende structure of the GaAs substrate. Figure A.7 (left) shows a top view of the system. For simplicity only one layer of Fe is shown, its atoms are positioned either on top of Ga atoms of the sub-interface layer of the As-terminated substrate or on top of Ga sites in the fourth layer. To be clear, the sequence is: bulk-Ga-As-Ga-As-Fe-vacuum. The results presented here were performed on systems with an Fe film consisting of 6 layers. In the middle panel of Figure A.7 the layer-resolved in-plane conductivities σ^I_{xx} and σ^I_{yy} are shown for $T = 100$ and 300 K, represented by uncorrelated lattice displacements via the alloy analogy model. The magnetisation is oriented along the [010] direction, i.e., along the diagonal in between [110] (x) and $\bar{1}10$ (y). Accordingly, a magnetic anisotropy (planar Hall effect or AMR) is not responsible for the observed anisotropy, it is the lowered rotational symmetry (2- vs. 4-fold) due to the substrate that modifies the electronic structure of the Fe film. Note that the difference of σ^I_{xx} and σ^I_{yy} is largest actually not for the Fe layer closest to the interface but for the surface layer. This can be attributed to a resonance of the interface states at the surface due to the small thickness of the film. With increasing temperature not only the absolute values of the conductivities decrease, but the anisotropy does as well. A similar trend was observed experimentally [383], it is caused by the fact that the thermally-induced disorder tends to make the Fermi surface more isotropic. Figure A.7 (right) shows the angular dependence of the layer-integrated conductivities, σ_{xx} and σ_{yy}, in the same system. Clearly the behaviour of $\sigma_{ii}(\phi)$ is different for longitudinal transport along x and y, the angular dependence is a combination of the magnetic and the crystallographic anisotropy. Based on these preliminary results corresponding investigations were performed in support of experiments on the anisotropy of the Gilbert damping parameter in the same system [384].

In a second application the in-plane transport properties of a Bi_2Se_3 (111) surface system were studied. Figure A.8 (left) shows the BSF relative to the Fermi level arbitrarily shifted into the bulk band gap in order to directly probe the topological surface state that is characterised by its Dirac-cone-like dispersion. In the right panel all symmetry-allowed in-plane charge and spin conductivity tensor elements are shown as a function of layer index represented by the occupying species. The (111)

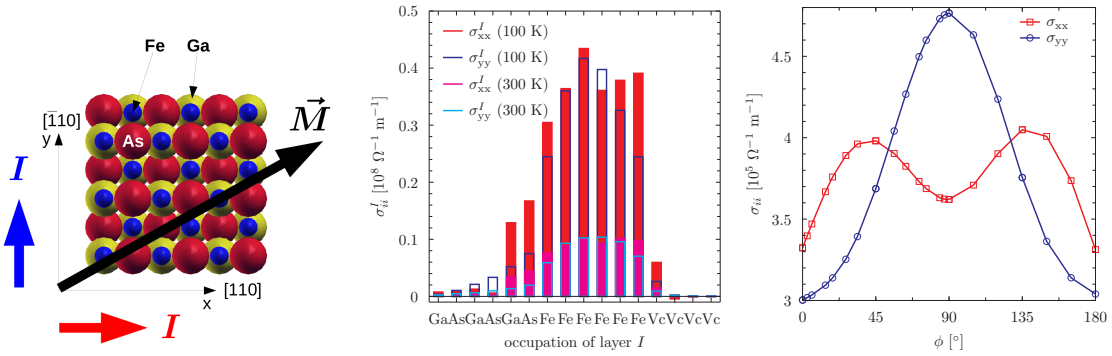

Figure A.7: Left: Structural model of the GaAs(001)/Fe system with indicated crystallographic in-plane directions and their correspondence to the Cartesian coordinates. The coloured symbols I indicate the high-symmetry directions of the current, the magnetisation $\boldsymbol{M}$ is arbitrarily oriented in between. Middle: Layer-resolved in-plane conductivities σ^I_{ii} for two different temperatures accounted for by means of the alloy analogy model for vibrational disorder. The Cartesian indices correspond to the left sub-figure, the magnetisation is pointing along [010]. Right: Angular dependence of the layer-integrated in-plane conductivities for the same system. ϕ denotes the angle between the magnetisation and the [110] direction.

surface has the magnetic Laue group $\bar{3}1m1'$. Accordingly, see Tables IV and VII of Ref. 283, the relevant conductivities are $\sigma_{\mathrm{xx}} = \sigma_{yy}$, $\sigma^{\mathrm{x}}_{\mathrm{xx}} = -\sigma^{\mathrm{x}}_{yy} = -\sigma^{\mathrm{y}}_{\mathrm{xy}} = -\sigma^{\mathrm{y}}_{\mathrm{yx}}$, and $\sigma^{z}_{\mathrm{xy}} = -\sigma^{z}_{\mathrm{yx}}$. As to be expected, the conducting region is more or less limited to the surface region, the largest values are however found in sub-surface layers. Moreover the surface state appears to penetrate quite deep into the bulk and the spin-polarised transport is found to be of longer range than the charge transport.

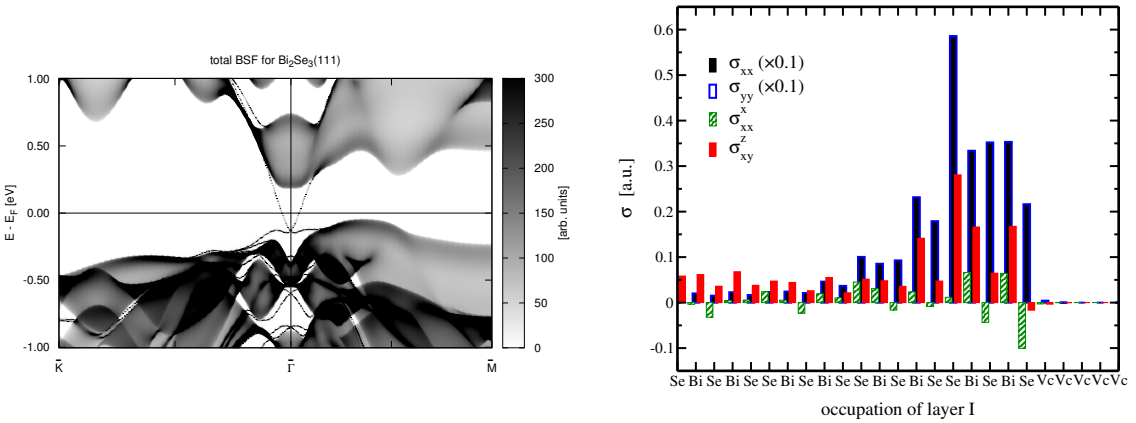

Figure A.8: Left: Bloch spectral function of the surface Se layer in $Bi_2Se_3(111)$ along the high-symmetry directions $\bar{\Gamma} - \bar{K}$ and $\bar{\Gamma} - \bar{M}$. The energy is given relative to the arbitrarily chosen Fermi level indicated by the horizontal line. Right: In-plane charge and spin conductivities as a function of layer index I, represented by the corresponding occupying atomic type.

In summary, a two-dimensional version of the Kubo linear response formalism has been implemented into the SPR-KKR program package. Test calculations in comparison to previous work by Butler *et al.* [381] demonstrated its reliability. The internal consistency between the two- and three-dimensional formulations has been extensively checked, including more advanced features such as chemical and thermally-

induced vibrational disorder. First real applications were the calculation of thermoelectric and spincaloritronic response quantities via the generalised Mott relations in $Cu_{0.5}Au_{0.5}$ alloys, the crystallographic anisotropy of the charge transport in bcc(001) Fe films deposited on GaAs(001), and the charge and spin transport properties of the topological surface state in Bi_2Se_3(111). Current investigations are aimed at transport through coplanar (Bloch and Néel) and non-coplanar domain walls.

A.6 Implementation of the non-equilibrium Green function formalism

This appendix deals with an implementation of the so-called non-equilibrium Green function (NEGF) formalism into the Munich SPR-KKR program package [382]. The work has been based on two alternative approaches to the self-energy appearing in the fundamental Keldysh equation [385] for the non-equilibrium or lesser Green function,

$$G^{<}(\varepsilon) = -\sum_{\alpha=L,R} G^{+}(\varepsilon)\left[(\Sigma_{\alpha}(\varepsilon^{+}) - \Sigma_{\alpha}(\varepsilon^{-}))f(\varepsilon-\mu_{\alpha})\right]G^{-}(\varepsilon)\,, \tag{A.20}$$

that describes the coupling of a system out of equilibrium to its surroundings in terms of the self energies Σ_{α}. For the definition of retarded and advanced Green functions, $G^{\pm}(\varepsilon)$, see Section 2.2. The formulation chosen for Eq. (A.20) is adapted to the layered geometry that will be considered in the following. Accordingly, two self energies appear, one for each interface between the region of interest (*interaction zone*) to the left ($\alpha = L$) or right ($\alpha = R$) semi-infinite bulks or *leads*. In the work by Achilles [386] (see also Ref. 387 and references therein), the self-energy is obtained by introducing an artificially decoupled reference system, while Ogura and Akai [388] exploited the so-called tight-binding KKR scheme [187, 389] where the connection between interaction zone and semi-infinite bulk is described by the so-called surface Green function (SGF). Both approaches are aimed at the description of layered systems under the effect of externally applied biases, as for example electric fields.[2] A potential difference between left and right lead can be imposed by shifting the chemical potentials μ_{α} against each other. In the following only results of the two alternative implementations will be presented, for details of the formalisms the reader is referred to the original publications. The approach of Achilles *et al.* [387], itself based on earlier work by Henk *et al.* [390] and Heiliger *et al.* [391], was implemented in a fully-relativistic way in cooperation with S. Achilles and M. Ogura. It will be called SA approach in the following. The alternative scheme proposed by Ogura and Akai [388] was implemented in cooperation with M. Ogura in Osaka, accordingly it will be referred to as MO approach.

Figure A.9 shows results for the layer-resolved density of states (DOS) at the Fermi level in a homogeneous layered bcc Li system, stacked in the [001] direction. The results in the left figure are obtained from the decoupling-potential approach to the self-energy (SA approach [386, 387, 390, 391]). As can be seen, the DOS calculated from $G^{<}$ converges with decreasing imaginary part of the energy $\mathrm{Im}(\varepsilon)$ to the one obtained from G^{+}, as expected since only in this limit the equivalence of both is given (in fact Eq. (A.20) is valid only for $\mathrm{Im}(\varepsilon) \to 0$). One notices a quite pronounced layer-dependent *bowing* of the NEGF results, that can be attributed to the neglect of contributions that would ensure a connection between $G^{<}$ and G^{+} also for finite $\mathrm{Im}(\varepsilon)$ (see also Ref. 386). Those contributions are proportional to the imaginary part of ε, accordingly with its decrease the bowing gets less pronounced. In addition one notices an oscillation of the DOS as a function of layer index, that is an artefact of the decoupling-potential approach. The self-energy Σ is obtained by a *comparison* between the physical and a reference system, where the coupling of the interaction

[2] This can of course be extended to temperature gradients based on a (generalised) Mott expression, as done by Heiliger *et al.* [17, 18].

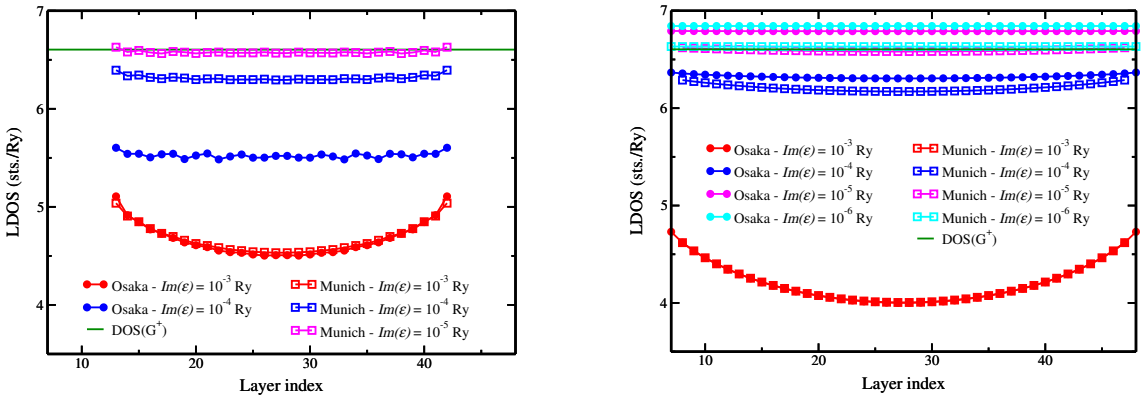

Figure A.9: Comparison of the DOS at the Fermi level in bcc(001) Li calculated from $G^<$ within the SA approach (left) and the MO approach (right). In both cases the corresponding implementations by the Osaka and Munich groups are compared directly against each other and against the DOS calculated from the retarded Green function, DOS(G^+). Different colours represent the finite imaginary part of the energy used (see text).

zone to the leads has been cut by introducing a *barrier region* with constant repulsive potentials. This creates a quantum-well like situation with corresponding eigenstates whose signatures are precisely those oscillations just mentioned. The self-energy is defined here only in the barrier region, chosen to consist of six layers on each side, and $G^<$ can accordingly only be computed in the remainder of the interaction zone. Turning to the results based on the MO approach [388] on the right side of Fig. A.9, one notices a slightly stronger dependence on Im(ε) and the absence of quantum-well states. Both findings are connected to the different way of obtaining the self energies of the leads, i.e., not by introducing an artificially decoupled reference system, but instead by exploiting the fact that in the TB-KKR method for layered systems, the connection between leads and interaction zone is expressed by the SGF. From these, one for each lead, the corresponding self energies can be derived (see Ref. 388 for details), which in particular contain *by construction* no single-site contribution as opposed to the ones in the SA approach. One could argue that, as Σ is describing the coupling between two systems it is formally only defined at the interface. This should also hold true in the limit of infinitesimally small width. It is also because of the SGF-approach to the self energies that $G^<$ is defined over the whole range of the interaction zone, accordingly the DOS can be obtained for all non-bulk layers.

Due its higher robustness, in particular against artefacts connected to the decoupling, and its reduced computational effort, as only the physical system has to be considered, the Osaka or MO approach has been chosen as the basis for subsequent developments. One of these shall be presented in the following, the implementation of a scheme to calculate the transmission through layered systems under an, in principle, finite bias. The expression used for the transmission function is based on work by Caroli *et al.* [392]:

$$T(\varepsilon) = \mathrm{Tr}\left[\Gamma_L(\varepsilon) G^+(\varepsilon) \Gamma_R(\varepsilon) G^-(\varepsilon)\right] \ , \tag{A.21}$$

with the anti-Hermitian part of the self-energy

$$\Gamma_\alpha(\varepsilon) = i\left(\Sigma_\alpha(\varepsilon^+) - \Sigma_\alpha(\varepsilon^-)\right) \ . \tag{A.22}$$

Further details can be found in Refs. 386–388, and references therein. Note in particular, that the limit of zero bias is assumed herein.

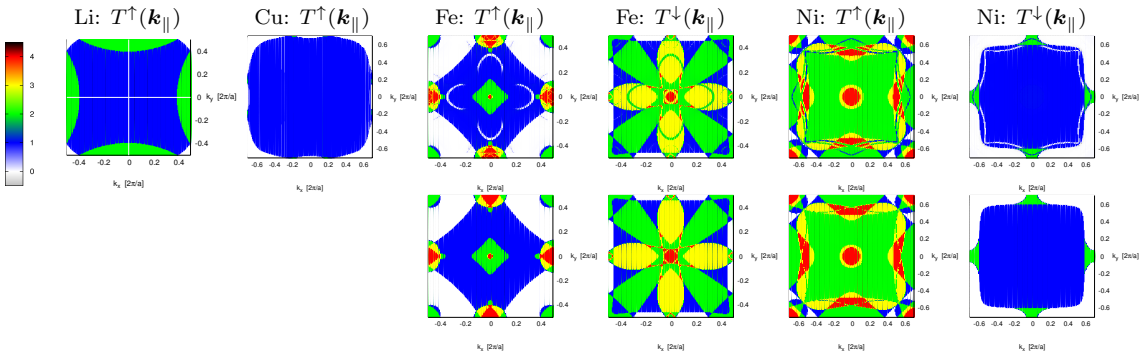

Figure A.10: Spin-projected transmission in [001] direction through 42 layers of, from left to right, bcc Li, fcc Cu, bcc Fe, and fcc Ni, in the latter two cases first for spin up, then for spin down. Results are given for the Fermi level and as a function of $\boldsymbol{k}_{\parallel} = (k_x, k_y, 0)$ with $N_{k_x} = N_{k_y} = 200$ for the full Brillouin zone. In the upper row the fully-relativistic implementation has been used, in the lower row the spin-orbit coupling has been switched off (scalar-relativistic limit).

Figure A.10 shows the $\boldsymbol{k}_{\parallel}$-resolved transmission through a number of layered homogeneous test systems for a small but finite imaginary part of the energy. Note that the transmission is very close to integer values for all $\boldsymbol{k}_{\parallel}$ in all systems, indicating the number of contributing bands. In the top row the results were obtained using the fully-relativistic implementation, while in the bottom row the spin-orbit coupling (SOC) was switched off to make contact to a corresponding scalar-relativistic implementation by Achilles *et al.* [387]. Comparison to Fig. 5 of Ref. 387 indicates excellent agreement for Fe and Ni without SOC (bottom row of Fig. A.10) and for Li and Cu including it. While for the latter two the impact of SOC is obviously negligible, for Fe and Ni in the top row one notices a number of minor changes brought about by SOC-induced lifting of degeneracies. Spin-orbit coupling of course leads in addition to a mixed spin character, because of which the separation into $T^{\uparrow}(\boldsymbol{k}_{\parallel})$ and $T^{\downarrow}(\boldsymbol{k}_{\parallel})$ is only approximate. This corresponds to a neglect of the so-called spin-flip terms, which however have not been investigated in detail.

As a first application to physically more relevant systems, the transmission through a Co|Cu|Co spin-valve has been calculated. Changing the relative orientation of the magnetisation in the two Co regions separated by a non-magnetic Cu spacer, the so-called giant magnetoresistance (GMR) effect can be observed. Figure A.11 (left) shows test calculations for a small system composed of 4 layers Co in the leads with a fixed orientation of the magnetisation M^1 in either [001] (z, stacking direction) or [100] (x, in-plane direction), 6 layers Cu spacers, and again 4 layers Co in which the magnetisation M^2 is rotated. The dependence of the $\boldsymbol{k}$-integrated transmission per area, or conductance $G = \frac{2e}{hA}T$, on the direction of the fixed magnetisation M^1 and on the precise SCF treatment is obviously only minor. On the right side several different systems with either Co or Cu in the leads and varying thickness of magnetic and non-magnetic regions are compared against each other and against literature ([1]: Ref. 393, [2]: Ref. 391). Here G is seen to be quite significantly dependent on the setup of the system, in particular the fact that all test systems were chosen to be mirror symmetric (left-right) while the literature geometries are not, appears to be relevant. In all cases a collinear self-consistent calculation was taken as the starting point, the non-collinear situations were not re-converged.

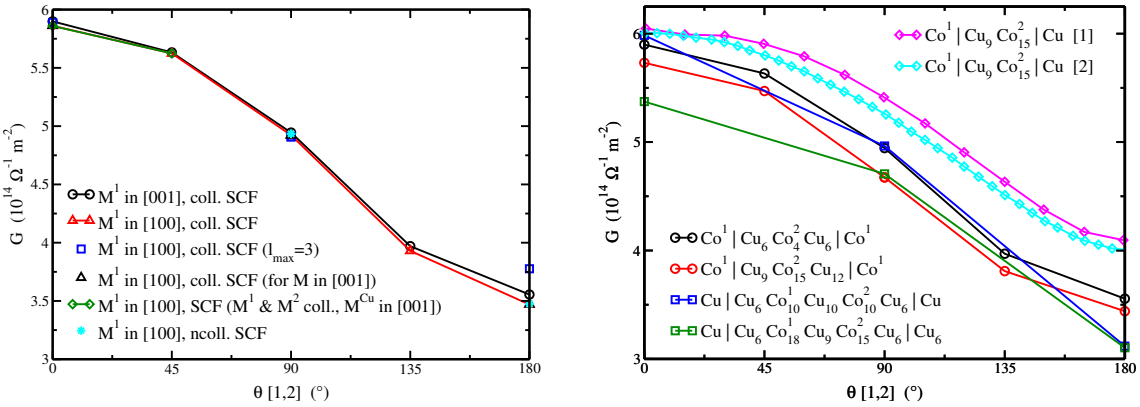

Figure A.11: Conductance $G = \frac{2e}{hA}T$ (see text) in a Co|Cu|Co spin-valve test system as a function of θ, the angle between the magnetisation directions in the two ferromagnetic regions (M^1 and M^2). Left: Dependence on absolute orientation of M^1 and self consistency conditions. Right: Dependence on sequence of regions and their thickness.

To summarise, an implementation of the NEGF formalism into SPR-KKR has been presented. Two alternative formulations of the self-energy have been compared. The one based on the surface Green function inherent to the TB-KKR scheme (Osaka or MO approach [388]) has been found to be more promising for future applications. An implementation of a Caroli-like [392] transmission expression has been demonstrated to give reliable results in agreement with previous work in the scalar-relativistic limit. Based on this, as a first application calculations for a Co|Cu|Co spin-valve system have been performed. The resulting GMR curves show a certain dependence on computational parameters but compare quite well to literature.

Future developments could be aimed at the so-called spin transfer torque (STT), following the work of Haney *et al.* [393] and Heiliger *et al.* [391]. First attempts have been made, but the results are not convincing yet. Another transport-related application of the NEGF formalism is the so-called spin mixing conductance, which allows a proper description of the scattering processes at interfaces. Corresponding developments have been made in the LMTO scheme by Carva and Turek [394]. A current development is the extension to finite biases, with the aim of a first-principles description of X-ray magnetic circular dichroism experiments on electric-field induced (transient) spin polarisation in non-magnetic materials [372, 373].

A.7 Computational details

The electronic structure of all investigated bulk and layered systems was treated in the framework of spin density functional theory within the local spin density approximation (LSDA) using the parametrisation for exchange and correlation potential by Vosko *et al.* [161]. If not noted otherwise, a fully relativistic implementation of the Korringa-Kohn-Rostoker (KKR) multiple scattering formalism based on the Dirac equation for spin-polarised potentials was used [382]. For surface and layer structures a tight-binding version of the KKR method was employed that, by making use of an artificial reference system of repulsive potentials, allows treatment of a large number of atoms. In general, lattice parameters were taken from experiment when available or, in case of alloys, obtained by interpolation of concentration-dependent data. Apart from the results on GaAs(001)/Fe (Appendix A.5), where structural relaxations were obtained self-consistently using VASP [395–397] by S. Polesya, the atoms were assumed to occupy ideal lattice positions. The atomic sphere approximation (ASA) to the potential shape was used throughout.

For the self-consistent part of the calculation a well converged Fermi level (5-6 significant digits) was the primary aim, having in mind subsequent calculations of transport properties that are fully (or at least to a great extent) determined by the states at E_{F}. For the energy integration first 32 and then 64 points on a semi-circular grid (`GRID` $= 5$) in the complex energy plane were used. Convergence w.r.t. $\boldsymbol{k}$-point density for the integration over the irreducible part of the Brillouin zone (BZ) using a regular sampling was ensured by step-wise increasing the input parameter `NKTAB`, roughly corresponding to the number of points in the irreducible BZ, up to 5000 for bulk systems. For layered systems approximately 100×100 points in the full BZ were used (Appendices A.5 and A.6). For the expansion of the Green function in angular momenta, the cut-off value ℓ_{max} was set to 3 (`NL` $= 4$), i.e., including f-like functions to ensure proper description of final states for scattering of d electrons. The tolerance criteria for the potential and the CPA were set to `TOL` $= 10^{-8}$. Lloyd's formula was used to determine E_{F}. For tight-binding calculations of layered systems the radius of the real space cluster for the reference Green function was chosen such as to contain at least 60 atoms. Before moving on to linear response calculations, the ground state properties (band structure, i.e., Bloch spectral function (BSF), density of states, magnetic moments) were confirmed to be in satisfying agreement with available experimental and first-principles theoretical literature data.

In the Kubo linear response calculations, all results were converged w.r.t. the $\boldsymbol{k}$-space integration as far as possible, e.g., up to $(\frac{2^{32}}{2} - 1)/48$ points in the irreducible BZ for cubic systems. All results are for `NL` $= 4$, except for most 2D systems (Appendices A.5 and A.6) where memory limitations usually enforced `NL` $= 3$. To obtain the intrinsic contributions to linear response coefficients in pure systems, an $\mathrm{Im}(E) \to 0$ convergence was performed, usually down to `IME` $= 10^{-5}$ Ry, while ensuring in parallel convergence w.r.t. `NKTAB`. In some very clean metals (usually low impurity concentration) this had to be done as well. In Kubo-Bastin calculations the number of energy points on `GRID` $= 5$ was set to `NE` $= 32$. In case of doubt the convergence w.r.t. this was checked. For finite temperatures within the alloy analogy model (AAM), the lattice displacements were applied in the 14 highest-symmetry directions of a cubic lattice ($6 \times \langle 001 \rangle$, $8 \times \langle 111 \rangle$), the Debye temperatures defining

the mean square displacements were in general used as implemented in SPR-KKR. On very few occasions NL had to be increased for large displacements. In case of spin fluctuations in magnetic systems the $M(T)$ data were usually taken from literature and interpolated numerically, convergence w.r.t. number of polar (NFTET) and azimuthal (NFPHI) angles was ensured. While the required NFTET strongly depends on temperature, the lower T, the more angles on an equidistant spherical mesh are necessary to represent $M(T)$, NFPHI $= 3$ was found to be sufficient in most situations. The tolerance criterion for CPA and/or AAM was set to TOL $= 10^{-8}$.

For the evaluation of the generalised Mott relations [Eqs. (2.156)-(2.158)] a series of Kubo-Středa or Kubo-Bastin calculations of $\underline{\boldsymbol{\sigma}}^{(k)}(E)$ were performed on, usually two, interleaved equidistant energy meshes. Each consisted of 8-10 points, one with smaller increment to ensure reasonable integration at low temperature, the other wider to reduce computational effort at higher T. The conductivity at $E = E_{\mathrm{F}}$ was always included in addition. The difference between chemical potential μ_{c} and Fermi energy E_{F} was assumed to be negligible for the materials and temperature ranges considered in this work, i.e., $k_{\mathrm{B}}T << E_{\mathrm{F}}$ [268]. The energy range necessary for $L_{ij}^{AB}(T)$ at a given T was estimated from the decaying behaviour of $\frac{\partial f(E,E_F,T)}{\partial E}$ as a function of energy E following Ref. 325. If finite temperature effects were included in the underlying conductivity calculations via the AAM, the *electronic* temperature (T_{el}) was chosen to match the *vibrational* and/or *fluctuational* ones (T_v, T_f, or T_{vf}). In case of low T and pure systems or little scattering in one spin channel, the convergence w.r.t. the density of the energy mesh occasionally had to be ensured by adding or removing points or by imposing a finite $\mathrm{Im}(E)$ in the Kubo calculations. In some cases $\sigma_{ij}^{(k)}(E)$ was approximated by non-linear least-squares fits. The convergence of the conductivity calculations was ensured as described above. The obtained set of $\sigma_{ij}^{(k)}(E)$ values was interpolated using third-order Lagrangian polynomials, the subsequent energy integrations were performed using the (extended) three-point Simpson's rule. The convergence of the generalised Mott relations in the limit $T \to 0\,\mathrm{K}$ towards the classical expressions in terms of energy derivatives was always confirmed. As a final note, quite regularly the diagonal elements of, in particular, $\underline{\boldsymbol{L}}^{cq}$ probing the asymmetry of $\sigma_{ii}(E)$ in the vicinity of E_{F} were numerically most demanding, the critical parameter usually being NKTAB. The difference between charge and spin conductivity is only minor in this respect, since the computational effort concerns the BZ integration of the product of two scattering path operators, the operator matrix elements are of little relevance w.r.t. convergence.

A.8 List of used software

- BibTeX
- cctbx [398]
- cif2cell [399] (https://sourceforge.net/projects/cif2cell/)
- git (https://github.com/git/git)
- gnuplot (http://www.gnuplot.info/)
- (xm)grace (http://plasma-gate.weizmann.ac.il/Grace/)
- Inkscape (https://inkscape.org/en/)
- ISOTROPY software suite [400, 401]
- kile (http://kile.sourceforge.net)
- LaTeX 2_ε
- linux (https://github.com/torvalds/linux)
- LRZ Sync+Share (https://syncandshare.lrz.de)
- (wx)maxima (http://andrejv.github.io/wxmaxima/)
- POV-Ray (http://www.povray.org/)
- PY-LMTO [402, 403]
- Python (https://www.python.org/)
- pyxplot (http://pyxplot.org.uk/)
- sage (http://www.sagemath.org/)
- Space-Time-Symmetry code by Seemann [339]
- SPR-KKR [382]
- SymPy [404]
- VASP [395–397]
- vasp2cif (https://github.com/egplar/vasp2cif)
- Vesta [405]
- xband (olymp.phys.chemie.uni-muenchen.de/ak/ebert/xband.html)

A.9 List of acronyms

- AAM alloy analogy model
- AFM antiferromagnet(ic)
- AH(A/C/E) anomalous Hall (angle/conductivity/effect)
- AMR anisotropic magnetoresistance
- AMTEP anisotropic magneto-thermopower
- AN(C/E) anomalous Nernst (conductivity/effect)
- ASA atomic sphere approximation
- ASE anisotropy of the Seebeck effect
- bcc body-centered cubic
- BSF Bloch spectral function
- CPA coherent potential approximation
- DFT density functional theory
- DOS density of states
- EE Edelstein effect
- expt experimental
- ext external
- fcc face-centered cubic
- FM ferromagnet(ic)
- GF Green function
- HK Hohenberg-Kohn
- KB Kubo-Bastin
- KG Kubo-Greenwood
- KKR Korringa-Kohn-Rostoker
- KS Kohn-Sham or Kubo-Středa
- L(S)DA local (spin) density approximation
- LMTO linear(-ized) muffin-tin orbital (method)
- LS(C/T) longitudinal spin (conductivity/transport)
- MLG/MPG/MSG magnetic Laue/point/space group

- MOKE magneto-optical Kerr effect
- MS(T) multiple scattering (theory)
- MT(A) muffin-tin (approximation)
- ncAFM non-collinear antiferromagnet(ic)
- ncp(AF)M non-coplanar (antiferro)magnet(ic)
- NEGF non-equilibrium Green function (method)
- NM non-magnet(ic)
- NV no (/without) vertex corrections
- SDSE spin-dependent Seebeck effect
- SH(A/C/E) spin Hall (angle/conductivity/effect)
- SMT spin Nernst magneto-thermopower
- SN(A/C/E) spin Nernst (angle/conductivity/effect)
- SOC spin-orbit coupling
- SOT spin-orbit torque
- SPR spin-polarised relativistic
- TB tight-binding
- theo theoretical
- T(M)E thermo(magneto)electric
- TM transition metal
- VC (including) vertex corrections
- VWN Vosko-Wilk-Nusair (E_{xc} parametrisation)
- WS Wigner-Seitz
- XAS X-ray absorption spectroscopy
- XM(C/L)D X-ray magnetic (circular/linear) dichroism
- xc exchange-correlation

Bibliography

[1] G. E. Bauer, A. H. MacDonald, and S. Maekawa, Solid State Commun. **150**, 459 (2010).

[2] M. Johnson and R. H. Silsbee, Phys. Rev. B **35**, 4959 (1987).

[3] M. Schmid, S. Srichandan, D. Meier, T. Kuschel, J.-M. Schmalhorst, M. Vogel, G. Reiss, C. Strunk, and C. H. Back, Phys. Rev. Lett. **111**, 187201 (2013).

[4] K. Uchida, S. Takahashi, K. Harii, J. Ieda, W. Koshibae, K. Ando, S. Maekawa, and E. Saitoh, Nature **455**, 778 (2008).

[5] K. Uchida, T. Ota, K. Harii, K. Ando, K. Sasage, H. Nakayama, K. Ikeda, and E. Saitoh, IEEE Trans. Magn. **45**, 2386 (2009).

[6] K. Uchida, H. Adachi, T. Ota, H. Nakayama, S. Maekawa, and E. Saitoh, Appl. Phys. Lett. **97**, 172505 (2010).

[7] K. Uchida, T. Ota, K. Harii, S. Takahashi, S. Maekawa, Y. Fujikawa, and E. Saitoh, Solid State Commun. **150**, 524 (2010).

[8] K. Uchida, J. Xiao, H. Adachi, J. Ohe, S. Takahashi, J. Ieda, T. Ota, Y. Kajiwara, H. Umezawa, H. Kawai, G. E. W. Bauer, S. Maekawa, and E. Saitoh, Nat. Mater. **9**, 894 (2010).

[9] C. M. Jaworski, J. Yang, S. Mack, D. D. Awschalom, J. P. Heremans, and R. C. Myers, Nat. Mater. **9**, 898 (2010).

[10] S. Bosu, Y. Sakuraba, K. Uchida, K. Saito, T. Ota, E. Saitoh, and K. Takanashi, Phys. Rev. B **83**, 224401 (2011).

[11] S. Y. Huang, W. G. Wang, S. F. Lee, J. Kwo, and C. L. Chien, Phys. Rev. Lett. **107**, 216604 (2011).

[12] S. Geprägs, A. Kehlberger, F. D. Coletta, Z. Qiu, E.-J. Guo, T. Schulz, C. Mix, S. Meyer, A. Kamra, M. Althammer, H. Huebl, G. Jakob, Y. Ohnuma, H. Adachi, J. Barker, S. Maekawa, G. E. W. Bauer, E. Saitoh, R. Gross, S. T. B. Goennenwein, and M. Kläui, Nat. Commun. **7**, 10452 (2016).

[13] F. L. Bakker, A. Slachter, J.-P. Adam, and B. J. van Wees, Phys. Rev. Lett. **105**, 136601 (2010).

[14] A. Slachter, F. L. Bakker, J.-P. Adam, and B. J. van Wees, Nat. Phys. **6**, 879 (2010).

[15] A. Slachter, F. L. Bakker, and B. J. van Wees, Phys. Rev. B **84**, 020412 (2011).

[16] J. Flipse, F. L. Bakker, A. Slachter, F. K. Dejene, and B. J. van Wees, Nat. Nanotechnol. **7**, 166 (2012).

[17] M. Walter, J. Walowski, V. Zbarsky, M. Münzenberg, M. Schäfers, D. Ebke, G. Reiss, A. Thomas, P. Peretzki, M. Seibt, J. S. Moodera, M. Czerner, M. Bachmann, and C. Heiliger, Nat. Mater. **10**, 742 (2011).

[18] M. Czerner, M. Bachmann, and C. Heiliger, Phys. Rev. B **83**, 132405 (2011).

[19] M. Weiler, M. Althammer, F. D. Czeschka, H. Huebl, M. S. Wagner, M. Opel, I.-M. Imort, G. Reiss, A. Thomas, R. Gross, and S. T. B. Goennenwein, Phys. Rev. Lett. **108**, 106602 (2012).

[20] K. Tauber, M. Gradhand, D. V. Fedorov, and I. Mertig, Phys. Rev. Lett. **109**, 026601 (2012).

[21] S. Meyer, Y.-T. Chen, S. Wimmer, M. Althammer, T. Wimmer, R. Schlitz, S. Geprägs, H. Huebl, D. Ködderitzsch, H. Ebert, G. E. W. Bauer, R. Gross, and S. T. B. Goennenwein, Nat. Mater. **16**, 977 (2017).

[22] G. E. Bauer, A. H. MacDonald, and S. Maekawa (eds.), Solid State Commun., **150** (2010).

[23] C. Back, G. Bauer, and B. Zink (eds.), Sol. Phys. D: Appl. Phys., **51** (2018).

[24] G. E. W. Bauer, E. Saitoh, and B. J. van Wees, Nat. Mater. **11**, 391 (2012).

[25] S. R. Boona, R. C. Myers, and J. P. Heremans, Energy Environ. Sci. **7**, 885 (2014).

[26] H. Yu, S. D. Brechet, and J.-P. Ansermet, Phys. Lett. A **381**, 825 (2017).

[27] M. Hatami, G. E. Bauer, S. Takahashi, and S. Maekawa, Solid State Commun. **150**, 480 (2010).

[28] P. Machon, M. Eschrig, and W. Belzig, Phys. Rev. Lett. **110**, 047002 (2013).

[29] P. Machon, M. Eschrig, and W. Belzig, New J. Phys. **16**, 073002 (2014).

[30] S. Kolenda, M. J. Wolf, and D. Beckmann, Phys. Rev. Lett. **116**, 097001 (2016).

[31] H. Adachi, K. Uchida, E. Saitoh, J. Ohe, S. Takahashi, and S. Maekawa, Appl. Phys. Lett. **97**, 252506 (2010).

[32] J. Xiao, G. E. W. Bauer, K. Uchida, E. Saitoh, and S. Maekawa, Phys. Rev. B **81**, 214418 (2010).

[33] C. M. Jaworski, J. Yang, S. Mack, D. D. Awschalom, R. C. Myers, and J. P. Heremans, Phys. Rev. Lett. **106**, 186601 (2011).

[34] K. Uchida, T. Ota, H. Adachi, J. Xiao, T. Nonaka, Y. Kajiwara, G. E. W. Bauer, S. Maekawa, and E. Saitoh, J. Appl. Phys. **111**, 103903 (2012).

[35] M. Schreier, A. Kamra, M. Weiler, J. Xiao, G. E. W. Bauer, R. Gross, and S. T. B. Goennenwein, Phys. Rev. B **88**, 094410 (2013).

[36] H. Adachi, K. Uchida, E. Saitoh, and S. Maekawa, Rep. Prog. Phys. **76**, 036501 (2013).

[37] K. M. Hals, A. Brataas, and G. E. Bauer, Solid State Commun. **150**, 461 (2010).

[38] J. C. Slonczewski, Phys. Rev. B **82**, 054403 (2010).

[39] M. V. Costache, G. Bridoux, I. Neumann, and S. O. Valenzuela, Nat. Mater. **11**, 199 (2012).

[40] J. Flipse, F. K. Dejene, D. Wagenaar, G. E. W. Bauer, J. B. Youssef, and B. J. van Wees, Phys. Rev. Lett. **113**, 027601 (2014).

[41] L. Berger, Phys. Rev. B **54**, 9353 (1996).

[42] J. Slonczewski, J. Magn. Magn. Materials **159**, L1 (1996).

[43] M. Tsoi, A. G. M. Jansen, J. Bass, W.-C. Chiang, M. Seck, V. Tsoi, and P. Wyder, Phys. Rev. Lett. **80**, 4281 (1998), erratum: Phys. Rev. Lett. **81**, 493 (1998).

[44] J. A. Katine, F. J. Albert, R. A. Buhrman, E. B. Myers, and D. C. Ralph, Phys. Rev. Lett. **84**, 3149 (2000).

[45] R. Urban, G. Woltersdorf, and B. Heinrich, Phys. Rev. Lett. **87**, 217204 (2001).

[46] Y. Tserkovnyak, A. Brataas, and G. E. W. Bauer, Phys. Rev. Lett. **88**, 117601 (2002).

[47] Y. Tserkovnyak, A. Brataas, and G. E. W. Bauer, Phys. Rev. B **66**, 224403 (2002).

[48] B. Heinrich, Y. Tserkovnyak, G. Woltersdorf, A. Brataas, R. Urban, and G. E. W. Bauer, Phys. Rev. Lett. **90**, 187601 (2003).

[49] K. Lenz, T. Toliński, J. Lindner, E. Kosubek, and K. Baberschke, Phys. Rev. B **69**, 144422 (2004).

[50] K.-W. Kim, J.-H. Moon, K.-J. Lee, and H.-W. Lee, Phys. Rev. Lett. **108**, 217202 (2012).

[51] G. Tatara, N. Nakabayashi, and K.-J. Lee, Phys. Rev. B **87**, 054403 (2013).

[52] K. M. D. Hals and A. Brataas, Phys. Rev. B **91**, 214401 (2015).

[53] I. Garate and A. MacDonald, Phys. Rev. B **79**, 064403 (2009).

[54] A. Manchon and S. Zhang, Phys. Rev. B **79**, 149901(E) (2009).

[55] A. Chernyshov, M. Overby, X. Liu, J. K. Furdyna, Y. Lyanda-Geller, and L. P. Rokhinson, Nat. Phys. **5**, 656 (2009).

[56] I. Mihai Miron, G. Gaudin, S. Auffret, B. Rodmacq, A. Schuhl, S. Pizzini, J. Vogel, and P. Gambardella, Nat. Mater. **9**, 230 (2010).

[57] K. M. D. Hals, A. Brataas, and Y. Tserkovnyak, EPL (Europhysics Letters) **90**, 47002 (2010).

[58] C. Ciccarelli, K. M. D. Hals, A. Irvine, V. Novak, Y. Tserkovnyak, H. Kurebayashi, A. Brataas, and A. Ferguson, Nat. Nanotechnol. **10**, 50 (2015).

[59] M. Hatami, G. E. W. Bauer, Q. Zhang, and P. J. Kelly, Phys. Rev. Lett. **99**, 066603 (2007).

[60] M. Hatami, G. E. W. Bauer, Q. Zhang, and P. J. Kelly, Phys. Rev. B **79**, 174426 (2009).

[61] H. Yu, S. Granville, D. P. Yu, and J.-P. Ansermet, Phys. Rev. Lett. **104**, 146601 (2010).

[62] G. Géranton, F. Freimuth, S. Blügel, and Y. Mokrousov, Phys. Rev. B **91**, 014417 (2015).

[63] F. Freimuth, S. Blügel, and Y. Mokrousov, J. Phys.: Cond. Mat. **28**, 316001 (2016).

[64] S. Tölle, C. Gorini, and U. Eckern, Phys. Rev. B **90**, 235117 (2014).

[65] A. G. Aronov and Y. B. Lyanda-Geller, JETP Lett. **50**, 431 (1989), Russian original: ZhETF **50**, 398 (1989).

[66] V. M. Edelstein, Solid State Commun. **73**, 233 (1990).

[67] S. D. Ganichev, E. L. Ivchenko, V. V. Bel'kov, S. A. Tarasenko, M. Sollinger, D. Weiss, W. Wegscheider, and W. Prettl, Nature **417**, 153 (2002).

[68] S. Tölle, M. Dzierzawa, U. Eckern, and C. Gorini, Ann. Phys. **530**, 1700303 (2018).

[69] W. Thomson, Proc. Roy. Soc. Lond. **8**, 546 (1856).

[70] T. McGuire and R. Potter, IEEE Trans. Magn. **11**, 1018 (1975).

[71] E. H. Hall, Am. J. Math. **2**, 287 (1879).

[72] E. M. Pugh, Phys. Rev. **36**, 1503 (1930).

[73] E. M. Pugh and N. Rostoker, Rev. Mod. Phys. **25**, 151 (1953).

[74] R. Karplus and J. M. Luttinger, Phys. Rev. **95**, 1154 (1954).

[75] N. Nagaosa, J. Sinova, S. Onoda, A. H. MacDonald, and N. P. Ong, Rev. Mod. Phys. **82**, 1539 (2010).

[76] M. I. D'Yakonov and V. I. Perel', JETP Lett. **13**, 467 (1971), Russian original: ZhETF **13**, 657 (1971).

[77] J. E. Hirsch, Phys. Rev. Lett. **83**, 1834 (1999).

[78] Y. K. Kato, R. C. Myers, A. C. Gossard, and D. D. Awschalom, Science **306**, 1910 (2004).

[79] J. Wunderlich, B. Kaestner, J. Sinova, and T. Jungwirth, Phys. Rev. Lett. **94**, 047204 (2005).

[80] J. Sinova, S. O. Valenzuela, J. Wunderlich, C. H. Back, and T. Jungwirth, Rev. Mod. Phys. **87**, 1213 (2015).

[81] Leduc, A., J. Phys. Theor. Appl. **7**, 519 (1888).

[82] E. H. Hall and L. L. Campbell, Proc. Am. Acad. Arts Sci. **46**, 625 (1911).

[83] C. Strohm, G. L. J. A. Rikken, and P. Wyder, Phys. Rev. Lett. **95**, 155901 (2005).

[84] Y. Onose, T. Ideue, H. Katsura, Y. Shiomi, N. Nagaosa, and Y. Tokura, Science **329**, 297 (2010).

[85] A. von Ettingshausen and W. Nernst, Ann. Phys. **265**, 343 (1886).

[86] T. J. Seebeck, Ann. Phys. **82**, 253 (1826).

[87] V. D. Ky, phys. stat. sol. (b) **17**, K207 (1966).

[88] J. C. A. Peltier, Annales de Chimie et de Physique **LVI**, 371 (1834).

[89] K. Uchida, S. Daimon, R. Iguchi, and E. Saitoh, Nature **558**, 95 (2018).

[90] E. Kondorskii, Sov. Phys. JETP **18**, 351 (1964), Russian original: ZhETF **45**, 511 (1964).

[91] T. Seki, R. Iguchi, K. Takanashi, and K. Uchida, Appl. Phys. Lett. **112**, 152403 (2018).

[92] S. Wimmer, M. Seemann, K. Chadova, D. Ködderitzsch, and H. Ebert, Phys. Rev. B **92**, 041101(R) (2015).

[93] S. O. Valenzuela and M. Tinkham, Nature **442**, 176 (2006).

[94] E. Saitoh, M. Ueda, H. Miyajima, and G. Tatara, Appl. Phys. Lett. **88**, 182509 (2006).

[95] T. Kimura, Y. Otani, T. Sato, S. Takahashi, and S. Maekawa, Phys. Rev. Lett. **98**, 156601 (2007), erratum: Phys. Rev. Lett. **98**, 249901 (2007).

[96] J. Sakurai, M. Horie, S. Araki, H. Yamamoto, and T. Shinjo, J. Phys. Soc. Japan **60**, 2522 (1991).

[97] M. Conover, M. Brodsky, J. Mattson, C. Sowers, and S. Bader, J. Magn. Magn. Materials **102**, L5 (1991).

[98] J.-E. Wegrowe, Q. Anh Nguyen, M. Al-Barki, J.-F. Dayen, T. L. Wade, and H.-J. Drouhin, Phys. Rev. B **73**, 134422 (2006).

[99] V. P. Amin, J. Zemen, J. Železný, T. Jungwirth, and J. Sinova, Phys. Rev. B **90**, 140406 (2014).

[100] C. López-Monís, A. Matos-Abiague, and J. Fabian, Phys. Rev. B **90**, 174426 (2014).

[101] J. Shan, F. K. Dejene, J. C. Leutenantsmeyer, J. Flipse, M. Münzenberg, and B. J. van Wees, Phys. Rev. B **92**, 020414 (2015).

[102] J. Wunderlich, B.-G. Park, A. C. Irvine, L. P. Zârbo, E. Rozkotová, P. Nemec, V. Novák, J. Sinova, and T. Jungwirth, Science **330**, 1801 (2010).

[103] T. Kuschel and G. Reiss, Nat. Nanotechnol. **10**, 22 (2015).

[104] A. Manchon and S. Zhang, Phys. Rev. B **78**, 212405 (2008).

[105] A. Manchon and S. Zhang, Phys. Rev. B **79**, 094422 (2009).

[106] I. Garate and A. H. MacDonald, Phys. Rev. B **80**, 134403 (2009).

[107] U. H. Pi, K. Won Kim, J. Y. Bae, S. C. Lee, Y. J. Cho, K. S. Kim, and S. Seo, Appl. Phys. Lett. **97**, 162507 (2010).

[108] G. Prenat, K. Jabeur, G. Di Pendina, O. Boulle, and G. Gaudin, "Beyond STT-MRAM, Spin Orbit Torque RAM SOT-MRAM for High Speed and High Reliability Applications," in *Spintronics-based Computing*, edited by W. Zhao and G. Prenat (Springer International Publishing, Cham, 2015) pp. 145–157.

[109] R. Kubo, M. Yokota, and S. Nakajima, J. Phys. Soc. Japan **12**, 1203 (1957).

[110] P. Hohenberg and W. Kohn, Phys. Rev. **136**, B864 (1964).

[111] W. Kohn and L. J. Sham, Phys. Rev. **140**, A1133 (1965).

[112] U. von Barth and L. Hedin, J. Phys. C: Solid State Phys. **5**, 1629 (1972).

[113] A. K. Rajagopal and J. Callaway, Phys. Rev. B **7**, 1912 (1973).

[114] M. V. Ramana and A. K. Rajagopal, J. Phys. C: Solid State Phys. **12**, L845 (1979).

[115] A. H. MacDonald and S. H. Vosko, J. Phys. C: Solid State Phys. **12**, 2977 (1979).

[116] G. Vignale and M. Rasolt, Phys. Rev. Lett. **59**, 2360 (1987).

[117] G. Vignale and M. Rasolt, Phys. Rev. B **37**, 10685 (1988), erratum: Phys. Rev. B **39**, 5475 (1989).

[118] G. Vignale and M. Rasolt, Phys. Rev. B **39**, 5475 (1989).

[119] J. Kübler, K.-H. Höck, J. Sticht, and A. R. Williams, J. Phys. F: Met. Phys. **18**, 469 (1988).

[120] L. M. Sandratskii, Adv. Phys. **47**, 91 (1998).

[121] L. Nordström and D. J. Singh, Phys. Rev. Lett. **76**, 4420 (1996).

[122] L. N. Oliveira, E. K. U. Gross, and W. Kohn, Phys. Rev. Lett. **60**, 2430 (1988).

[123] E. Runge and E. K. U. Gross, Phys. Rev. Lett. **52**, 997 (1984).

[124] K. Krieger, J. K. Dewhurst, P. Elliott, S. Sharma, and E. K. U. Gross, J. Chem. Theory Comput. **11**, 4870 (2015).

[125] K. Capelle, ArXiv e-prints (2002), arXiv:cond-mat/0211443 .

[126] K. Capelle, Braz. J. Phys. **36**, 1318 (2006).

[127] C. R. Jacob and M. Reiher, Int. J. Quantum Chem. **112**, 3661 (2012).

[128] H. Eschrig, *The Fundamentals of Density Functional Theory* (Edition am Gutenbergplatz, Leipzig, 2003).

[129] K. Burke, *The ABC of DFT* (2007).

[130] E. Engel and R. M. Dreizler, *Density Functional Theory - An Advanced Course*, Theoretical and Mathematical Physics (Springer-Verlag Berlin Heidelberg, 2011).

[131] M. Born and R. Oppenheimer, Ann. Phys. **389**, 457 (1927).

[132] E. Schrödinger, Phys. Rev. **28**, 1049 (1926).

[133] L. H. Thomas, Math. Proc. Cam. Phil. Soc. **23**, 542 (1927).

[134] E. Fermi, Rend. Lincei **6**, 602 (1927), reprinted in: E. Fermi, *Collected Papers (Note e Memorie)*, E. Amaldi *et al.* (eds.), The University of Chicago Press, Chicago and Accademia Nazional dei Lincei, Rome (1962).

[135] M. Levy, Proc. Nat. Acad. Sci. **76**, 6062 (1979).

[136] M. Levy, Phys. Rev. A **26**, 1200 (1982).

[137] E. H. Lieb, Int. J. Quantum Chem. **24**, 243 (1983).

[138] E. H. Lieb, "Density functionals for coulomb systems," in *Density Functional Methods in Physics*, NATO ASI Series, Vol. 123, edited by R. M. Dreizler and J. da Providência (Plenum, New York, 1985).

[139] T. L. Gilbert, Phys. Rev. B **12**, 2111 (1975).

[140] J. E. Harriman, Phys. Rev. A **24**, 680 (1981).

[141] J. C. Slater, Phys. Rev. **34**, 1293 (1929).

[142] W. Heisenberg, Z. Phys. **38**, 411 (1926).

[143] P. A. M. Dirac, Proc. Roy. Soc. Lond. A **112**, 661 (1926).

[144] W. Pauli, Z. Phys. **31**, 765 (1925).

[145] P. A. M. Dirac, Math. Proc. Cam. Phil. Soc. **26**, 376 (1930).

[146] D. M. Ceperley and B. J. Alder, Phys. Rev. Lett. **45**, 566 (1980).

[147] D. C. Langreth and M. J. Mehl, Phys. Rev. Lett. **47**, 446 (1981).

[148] J. P. Perdew, Phys. Rev. Lett. **55**, 1665 (1985), erratum: Phys. Rev. Lett. **55**, 2370 (1985).

[149] J. P. Perdew and W. Yue, Phys. Rev. B **33**, 8800 (1986), erratum: Phys. Rev. B **40**, 3399 (1989).

[150] A. D. Becke, J. Chem. Phys. **98**, 5648 (1993).

[151] J. P. Perdew, M. Ernzerhof, and K. Burke, J. Chem. Phys. **105**, 9982 (1996).

[152] S. Grimme, WIREs Comput. Mol. Sci. **1**, 211 (2011).

[153] J. P. Perdew, S. Kurth, A. c. v. Zupan, and P. Blaha, Phys. Rev. Lett. **82**, 2544 (1999), erratum: Phys. Rev. Lett. **82**, 5179 (1999).

[154] J. Tao, J. P. Perdew, V. N. Staroverov, and G. E. Scuseria, Phys. Rev. Lett. **91**, 146401 (2003).

[155] F. Tran and P. Blaha, Phys. Rev. Lett. **102**, 226401 (2009).

[156] V. I. Anisimov and O. Gunnarsson, Phys. Rev. B **43**, 7570 (1991).

[157] V. I. Anisimov, J. Zaanen, and O. K. Andersen, Phys. Rev. B **44**, 943 (1991).

[158] A. Georges, G. Kotliar, W. Krauth, and M. J. Rozenberg, Rev. Mod. Phys. **68**, 13 (1996).

[159] D. Vollhardt, Ann. Phys. **524**, 1 (2011).

[160] G. Kotliar, S. Y. Savrasov, K. Haule, V. S. Oudovenko, O. Parcollet, and C. A. Marianetti, Rev. Mod. Phys. **78**, 865 (2006).

[161] S. H. Vosko, L. Wilk, and M. Nusair, Can. J. Phys. **58**, 1200 (1980).

[162] M. E. Rose, *Relativistic Electron Theory* (John Wiley & Sons, Inc. - New York, London, 1961).

[163] S. Bornemann, *Theoretical Investigations on the Magnetic Properties of Fe and Co Nanostructures on Noble Metal Surfaces*, Ph.D. thesis, Ludwig-Maximilians-Universität München (2011).

[164] J. P. Perdew, K. Burke, and M. Ernzerhof, Phys. Rev. Lett. **77**, 3865 (1996), erratum: Phys. Rev. Lett. **78**, 1396 (1997).

[165] C. Lee, W. Yang, and R. G. Parr, Phys. Rev. B **37**, 785 (1988).

[166] A. D. Becke, Phys. Rev. A **38**, 3098 (1988).

[167] J. P. Perdew and Y. Wang, Phys. Rev. B **45**, 13244 (1992).

[168] J. P. Perdew and A. Zunger, Phys. Rev. B **23**, 5048 (1981).

[169] K. Lejaeghere, G. Bihlmayer, T. Björkman, P. Blaha, S. Blügel, V. Blum, D. Caliste, I. E. Castelli, S. J. Clark, A. Dal Corso, S. de Gironcoli, T. Deutsch, J. K. Dewhurst, I. Di Marco, C. Draxl, M. Dułak, O. Eriksson, J. A. Flores-Livas, K. F. Garrity, L. Genovese, P. Giannozzi, M. Giantomassi, S. Goedecker, X. Gonze, O. Grånäs, E. K. U. Gross, A. Gulans, F. Gygi, D. R. Hamann, P. J. Hasnip, N. A. W. Holzwarth, D. Iuşan, D. B. Jochym, F. Jollet, D. Jones, G. Kresse, K. Koepernik, E. Küçükbenli, Y. O. Kvashnin, I. L. M. Locht, S. Lubeck, M. Marsman, N. Marzari, U. Nitzsche, L. Nordström, T. Ozaki, L. Paulatto, C. J. Pickard, W. Poelmans, M. I. J. Probert, K. Refson, M. Richter, G.-M. Rignanese, S. Saha, M. Scheffler, M. Schlipf, K. Schwarz, S. Sharma, F. Tavazza, P. Thunström, A. Tkatchenko, M. Torrent, D. Vanderbilt, M. J. van Setten, V. Van Speybroeck, J. M. Wills, J. R. Yates, G.-X. Zhang, and S. Cottenier, Science **351**, aad3000 (2016).

[170] J. Korringa, Physica **13**, 392 (1947).

[171] W. Kohn and N. Rostoker, Phys. Rev. **94**, 1111 (1954).

[172] J. L. Beeby, Proc. Roy. Soc. Lond. A **302**, 113 (1967).

[173] J. S. Faulkner, Prog. Mater. Sci. **27**, 1 (1982).

[174] A. Gonis, *Green functions for ordered and disordered systems* (North-Holland, Amsterdam, 1992).

[175] A. Gonis and W. H. Butler, *Multiple scattering in solids*, Graduate Texts in Contemporary Physics (Springer, Berlin, 1999).

[176] J. Zabloudil, R. Hammerling, L. Szunyogh, and P. Weinberger, *Electron Scattering in Solid Matter: A Theoretical and Computational Treatise*, Springer Series in Solid-State Sciences (Springer, 2004).

[177] E. N. Economou, *Green's Functions in Quantum Physics*, Vol. 7 (Springer-Verlag Berlin Heidelberg, 2006).

[178] W. van Haeringen, B. Farid, and D. Lenstra, Phys. Scr. **1987**, 282 (1987).

[179] E. Tamura, Phys. Rev. B **45**, 3271 (1992).

[180] H. Ebert, J. Braun, D. Ködderitzsch, and S. Mankovsky, Phys. Rev. B **93**, 075145 (2016).

[181] I. Mertig, E. Mrosan, and P. Ziesche, *Multiple-scattering theory of point defects in metals: Electronic properties*, Teubner-Texte zur Physik, Vol. 11 (B. G. Teubner Verlagsgesellschaft, 1987).

[182] P. A. M. Dirac, Proc. Roy. Soc. Lond. A **117**, 610 (1928).

[183] P. Strange, H. Ebert, J. B. Staunton, and B. L. Gyorffy, J. Phys.: Cond. Mat. **1**, 2959 (1989).

[184] B. A. Lippmann and J. Schwinger, Phys. Rev. **79**, 469 (1950).

[185] M. Born, Z. Phys. **38**, 803 (1926).

[186] B. H. Drittler, *KKR-Greensche Funktionsmethode fuer das volle Zellpotential*, Ph.D. thesis, RWTH Aachen (1990).

[187] R. Zeller, P. H. Dederichs, B. Újfalussy, L. Szunyogh, and P. Weinberger, Phys. Rev. B **52**, 8807 (1995).

[188] J. S. Faulkner, Phys. Rev. B **19**, 6186 (1979).

[189] J. S. Faulkner and G. M. Stocks, Phys. Rev. B **21**, 3222 (1980).

[190] J. C. Slater, Phys. Rev. **51**, 846 (1937).

[191] O. K. Andersen, Phys. Rev. B **12**, 3060 (1975).

[192] B. L. Györffy and M. J. Stott, "A one-electron theory of soft x-ray emission from random alloys," in *Band Structure Spectroscopy of Metals and Alloys*, edited by D. J. Fabian and L. M. Watson (Academic Press, London and New York, 1973).

[193] P. P. Ewald, Ann. Phys. **369**, 253 (1921).

[194] L. Nordheim, Ann. Phys. **401**, 607 (1931).

[195] R. H. Parmenter, Phys. Rev. **97**, 587 (1955).

[196] J. Korringa, J. Phys. Chem. Sol. **7**, 252 (1958).

[197] J. L. Beeby, Proc. Roy. Soc. Lond. A **279**, 82 (1964).

[198] P. Soven, Phys. Rev. **156**, 809 (1967).

[199] D. A. Rowlands, J. B. Staunton, and B. L. Györffy, Phys. Rev. B **67**, 115109 (2003).

[200] H. Ebert, S. Mankovsky, D. Ködderitzsch, and P. J. Kelly, Phys. Rev. Lett. **107**, 066603 (2011).

[201] S. Mankovsky, D. Ködderitzsch, G. Woltersdorf, and H. Ebert, Phys. Rev. B **87**, 014430 (2013).

[202] H. Ebert, S. Mankovsky, K. Chadova, S. Polesya, J. Minár, and D. Ködderitzsch, Phys. Rev. B **91**, 165132 (2015).

[203] P. Zhang and Q. Niu, ArXiv e-prints (2004), arXiv:cond-mat/0406436 .

[204] J. Shi, P. Zhang, D. Xiao, and Q. Niu, Phys. Rev. Lett. **96**, 076604 (2006).

[205] L. Onsager, Phys. Rev. **37**, 405 (1931).

[206] L. Onsager, Phys. Rev. **38**, 2265 (1931).

[207] H. B. Callen, Phys. Rev. **73**, 1349 (1948).

[208] S. R. de Groot, *Thermodynamik irreversibler Prozesse*, Hochschultaschenbücher, Vol. 18/18a (Bibliographisches Institut, Mannheim, 1960).

[209] S. R. de Groot and P. Mazur, *Grundlagen der Thermodynamik irreversibler Prozesse*, Hochschultaschenbücher (Bibliographisches Institut, Mannheim, 1969).

[210] H. B. Callen, *Thermodynamics and an Introduction to Thermostatistics*, 2nd ed. (John Wiley & Sons, Inc., New York, 1985).

[211] J. R. Cleveland and C. L. Foiles, J. Appl. Phys. **50**, 1898 (1979).

[212] Y. Pu, E. Johnston-Halperin, D. D. Awschalom, and J. Shi, Phys. Rev. Lett. **97**, 036601 (2006).

[213] E. I. Kondorskii, R. P. Vasil'eva, Y. N. Arkhipov, and A. V. Cheremushkina, JETP Lett. **10**, 49 (1969), Russian original: ZhETF **10**, 78 (1969).

[214] D. Xiao, Y. Yao, Z. Fang, and Q. Niu, Phys. Rev. Lett. **97**, 026603 (2006).

[215] Y. Pu, D. Chiba, F. Matsukura, H. Ohno, and J. Shi, Phys. Rev. Lett. **101**, 117208 (2008).

[216] M. S. Green, J. Chem. Phys. **20**, 1281 (1952).

[217] M. S. Green, J. Chem. Phys. **22**, 398 (1954).

[218] H. Mori, Phys. Rev. **112**, 1829 (1958).

[219] R. Kubo, Can. J. Phys. **34**, 1274 (1956).

[220] R. Kubo, J. Phys. Soc. Japan **12**, 570 (1957).

[221] V. Bargmann and E. P. Wigner, Proc. Natl. Acad. Sci. U.S.A. **34**, 211 (1948).

[222] A. Vernes, B. L. Györffy, and P. Weinberger, Phys. Rev. B **76**, 012408 (2007).

[223] S. Lowitzer, D. Ködderitzsch, and H. Ebert, Phys. Rev. B **82**, 140402(R) (2010).

[224] S. Lowitzer, M. Gradhand, D. Ködderitzsch, D. V. Fedorov, I. Mertig, and H. Ebert, Phys. Rev. Lett. **106**, 056601 (2011).

[225] S. Lowitzer, *Relativistic electronic transport theory - The spin Hall effect and related phenomena*, Ph.D. thesis, Ludwig-Maximilians-Universität München (2010).

[226] G. D. Mahan, *Many-particle physics, 2nd ed.*, Physics of Solids and Liquids (Plenum Press, New York, 1993).

[227] A. Bastin, C. Lewiner, O. Betbeder-Matibet, and P. Nozieres, J. Phys. Chem. Solids **32**, 1811 (1971).

[228] A. Crépieux and P. Bruno, Phys. Rev. B **64**, 014416 (2001).

[229] K. Chadova, *Electronic transport within the Kubo-Bastin Formalism*, Ph.D. thesis (2017).

[230] P. Středa, J. Phys. C: Solid State Phys. **15**, L717 (1982).

[231] D. A. Greenwood, Proc. Phys. Soc. **71**, 585 (1958).

[232] W. H. Butler, Phys. Rev. B **31**, 3260 (1985).

[233] J. Banhart, Phil. Mag. B **77**, 85 (1998).

[234] J. Banhart, Phil. Mag. B **77**, 105 (1998).

[235] J. Banhart and H. Ebert, EPL (Europhysics Letters) **32**, 517 (1995).

[236] S. Lowitzer, D. Ködderitzsch, and H. Ebert, Phys. Rev. Lett. **105**, 266604 (2010).

[237] D. Ködderitzsch, K. Chadova, and H. Ebert, Phys. Rev. B **92**, 184415 (2015).

[238] I. Turek, J. Kudrnovský, and V. Drchal, Phys. Rev. B **86**, 014405 (2012).

[239] I. Turek, J. Kudrnovský, and V. Drchal, Phys. Rev. B **89**, 064405 (2014).

[240] J. M. Luttinger, Phys. Rev. **135**, A1505 (1964).

[241] A. Einstein, Ann. Phys. **14**, 182 (1905).

[242] B. Deo and S. N. Behera, Phys. Rev. **141**, 738 (1966).

[243] N. F. Mott and H. Jones, *The Theory of the Properties of Metals and Alloys* (Oxford University Press (Clarendon Press, Oxford, England), 1936).

[244] G. V. Chester and A. Thellung, Proc. Phys. Soc. **77**, 1005 (1961).

[245] M. Jonson and G. D. Mahan, Phys. Rev. B **21**, 4223 (1980).

[246] T. J. Seebeck, *Magnetische Polarisation der Metalle und Erze durch Temperatur-Differenz*, Abhandlungen der Königlichen Preussischen Akademie der Wissenschaften zu Berlin, 265–373 (1822).

[247] W. Thomson, Proc. Roy. Soc. Edin. **3**, 9198 (1857), actual year of Thomsons's proceeding is 1851.

[248] G. Wiedemann and R. Franz, Ann. Phys. **165**, 497 (1853).

[249] V. D. Ky, phys. stat. sol. (b) **17**, K203 (1966).

[250] D. J. Demars, *Measurements of the magneto-Seebeck and the Nernst-Ettingshausen effects in $Ga_xIn_{1-x}As$ and GaSb*, Ph.D. thesis, University of Ottawa (1972).

[251] A. D. Avery, M. R. Pufall, and B. L. Zink, Phys. Rev. Lett. **109**, 196602 (2012).

[252] L. Gravier, A. Fábián, A. Rudolf, A. Cachin, J.-E. Wegrowe, and J.-P. Ansermet, J. Magn. Magn. Materials **271**, 153 (2004).

[253] L. Gravier, S. Serrano-Guisan, F. Reuse, and J.-P. Ansermet, Phys. Rev. B **73**, 052410 (2006).

[254] L. Gravier, S. Serrano-Guisan, and J.-P. Ansermet, J. Appl. Phys. **97**, 10C501 (2005).

[255] B. Madon, D. C. Pham, J.-E. Wegrowe, D. Lacour, M. Hehn, V. Polewczyk, A. Anane, and V. Cros, Phys. Rev. B **94**, 144423 (2016).

[256] A. Sommerfeld, Z. Phys. **47**, 43 (1928).

[257] A. Sommerfeld and N. H. Frank, Rev. Mod. Phys. **3**, 1 (1931).

[258] E. H. Sondheimer, Proc. Roy. Soc. Lond. A **193**, 484 (1948).

[259] M. Kohler, Ann. Phys. **432**, 601 (1942).

[260] M. Kohler, Z. Phys. **126**, 481 (1949).

[261] L. Nordheim and C. Gorter, Physica **2**, 383 (1935).

[262] M. Jonson and G. D. Mahan, Phys. Rev. B **42**, 9350 (1990).

[263] K. Levin, B. Velický, and H. Ehrenreich, Phys. Rev. B **2**, 1771 (1970).

[264] W. H. Butler and G. M. Stocks, Phys. Rev. B **29**, 4217 (1984).

[265] J. Banhart and H. Ebert, Solid State Commun. **94**, 445 (1995).

[266] S. Wimmer, D. Ködderitzsch, K. Chadova, and H. Ebert, Phys. Rev. B **88**, 201108(R) (2013).

[267] S. Wimmer, D. Ködderitzsch, and H. Ebert, Phys. Rev. B **89**, 161101(R) (2014).

[268] R. Gross and A. Marx, *Festkörperphysik* (Oldenbourg Verlag, München, 2012).

[269] H. B. Callen and T. A. Welton, Phys. Rev. **83**, 34 (1951).

[270] S. R. de Groot and P. Mazur, Physica **23**, 73 (1957).

[271] W. H. Kleiner, Phys. Rev. **142**, 318 (1966).

[272] R. D. Barnard, *Thermoelectricity in Metals and Alloys* (Taylor & Francis Ltd, 10-14 Macklin Street, London WC2B 5NF, 1972).

[273] C. A. Domenicali, Phys. Rev. **112**, 1863 (1958).

[274] S. M. Girvin and M. Jonson, J. Phys. C: Solid State Phys. **15**, L1147 (1982).

[275] M. Jonson and S. M. Girvin, Bull. Am. Phys. Soc. **28**, 323 (1983).

[276] M. Jonson and S. M. Girvin, Phys. Rev. B **29**, 1939 (1984).

[277] C. A. Domenicali, Rev. Mod. Phys. **26**, 237 (1954).

[278] C. A. Domenicali and F. A. Otter, Phys. Rev. **95**, 1134 (1954).

[279] C. A. Domenicali, Phys. Rev. **117**, 984 (1960).

[280] J. M. Ziman, *Electrons and Phonons* (Clarendon, Oxford, England, 1960).

[281] L. Smrčka and P. Středa, J. Phys. C: Solid State Phys. **10**, 2153 (1977).

[282] A. Vilenkin and P. L. Taylor, Phys. Rev. B **18**, 5280 (1978).

[283] M. Seemann, D. Ködderitzsch, S. Wimmer, and H. Ebert, Phys. Rev. B **92**, 155138 (2015).

[284] A. Sommerfeld, Z. Phys. **47**, 1 (1928).

[285] A. Sommerfeld and H. Bethe, "Elektronentheorie der Metalle," in *Aufbau der zusammenhängenden Materie*, Handbuch der Physik, Vol. 24 (Springer Berlin Heidelberg, Berlin, Heidelberg, 1933) pp. 333–622.

[286] N. W. Ashcroft and N. D. Mermin, *Solid State Physics* (Holt, Rinehart and Winston, New York, 1976).

[287] N. W. Ashcroft and N. D. Mermin, *Festkörperphysik*, 2nd ed. (Oldenbourg Verlag, München Wien, 2005).

[288] A. M. Guénault, Phil. Mag. A **15**, 17 (1967).

[289] J. Kondo, Progress of Theoretical Physics **34**, 523 (1965).

[290] H. Kontani, Phys. Rev. B **67**, 014408 (2003).

[291] M. Cutler and N. F. Mott, Phys. Rev. **181**, 1336 (1969).

[292] I. Proskurin and M. Ogata, J. Phys. Soc. Japan **82**, 063712 (2013).

[293] Y. Jiong, L. Huanming, W. Ting, Z. Wenqing, C. Lidong, and Y. Jihui, Adv. Funct. Mater. **18**, 2880 (2008).

[294] J. Barth, G. H. Fecher, B. Balke, S. Ouardi, T. Graf, C. Felser, A. Shkabko, A. Weidenkaff, P. Klaer, H. J. Elmers, H. Yoshikawa, S. Ueda, and K. Kobayashi, Phys. Rev. B **81**, 064404 (2010).

[295] N. F. Hinsche, I. Mertig, and P. Zahn, J. Phys.: Cond. Mat. **23**, 295502 (2011).

[296] M. Oshita, S. Yotsuhashi, H. Adachi, and H. Akai, J. Phys. Soc. Japan **78**, 024708 (2009).

[297] U. Sivan and Y. Imry, Phys. Rev. B **33**, 551 (1986).

[298] R. Landauer, IBM Journal of Research and Development **1**, 223 (1957).

[299] M. Büttiker, IBM Journal of Research and Development **32**, 63 (1988).

[300] H. U. Baranger and A. D. Stone, Phys. Rev. B **40**, 8169 (1989).

[301] A. M. Lunde and K. Flensberg, J. Phys.: Cond. Mat. **17**, 3879 (2005).

[302] V. Popescu and P. Kratzer, Phys. Rev. B **88**, 104425 (2013).

[303] R. Kováčik, P. Mavropoulos, D. Wortmann, and S. Blügel, Phys. Rev. B **89**, 134417 (2014).

[304] F. J. Blatt, Can. J. Phys. **50**, 2836 (1972).

[305] W.-L. Lee, S. Watauchi, V. L. Miller, R. J. Cava, and N. P. Ong, Phys. Rev. Lett. **93**, 226601 (2004).

[306] J. Weischenberg, F. Freimuth, S. Blügel, and Y. Mokrousov, Phys. Rev. B **87**, 060406 (2013).

[307] G. Y. Guo, Q. Niu, and N. Nagaosa, Phys. Rev. B **89**, 214406 (2014).

[308] N. Wakeham, A. F. Bangura, X. Xu, J.-F. Mercure, M. Greenblatt, and N. E. Hussey, Nat. Commun. **2**, 396 (2011).

[309] S. Srichandan, S. Wimmer, S. Pöllath, M. Kronseder, H. Ebert, C. H. Back, and C. Strunk, Phys. Rev. B **98**, 020406 (2018).

[310] Y. Liu, A. A. Starikov, Z. Yuan, and P. J. Kelly, Phys. Rev. B **84**, 014412 (2011).

[311] R. P. Huebener, Phys. Rev. **140**, A1834 (1965).

[312] R. P. Huebener, Phys. Rev. **146**, 502 (1966).

[313] M. Bailyn, Phys. Rev. **126**, 2040 (1962).

[314] M. E. Lucassen, C. H. Wong, R. A. Duine, and Y. Tserkovnyak, Appl. Phys. Lett. **99**, 262506 (2011).

[315] B. Flebus, R. A. Duine, and Y. Tserkovnyak, EPL (Europhysics Letters) **115**, 57004 (2016).

[316] M. Johnson and R. H. Silsbee, Phys. Rev. Lett. **55**, 1790 (1985).

[317] M. Johnson and R. H. Silsbee, Phys. Rev. B **37**, 5312 (1988).

[318] M. Johnson, Solid State Commun. **150**, 543 (2010).

[319] H. B. Callen, *Thermodynamics* (New York, London, Sydney, 1960).

[320] A. G. Aronov, JETP **44**, 193 (1976), Russian original: ZhETF **71**, 371 (1976).

[321] L. Gravier, S. Serrano-Guisan, F. Reuse, and J.-P. Ansermet, Phys. Rev. B **73**, 024419 (2006).

[322] S. Wimmer, D. Ködderitzsch, K. Chadova, and H. Ebert, ArXiv e-prints (2013), arXiv:1306.0621 [cond-mat.mtrl-sci].

[323] M. Misiorny and J. Barnaś, Phys. Rev. B **91**, 155426 (2015).

[324] Z. Ma, Solid State Commun. **150**, 510 (2010).

[325] K. Tauber, *Spin Nernst and spin Hall effect in dilute metallic alloys*, Ph.D. thesis, Institut für Physik der Naturwissenschaftlichen Fakultät II der Martin-Luther-Universität Halle-Wittenberg (2014).

[326] K. Tauber, D. V. Fedorov, M. Gradhand, and I. Mertig, Phys. Rev. B **87**, 161114 (2013).

[327] A. Slachter, F. L. Bakker, and B. J. van Wees, Phys. Rev. B **84**, 174408 (2011).

[328] N. F. Mott, Proc. Roy. Soc. Lond. A **153**, 699 (1936).

[329] A. Fert, J. Phys. C: Solid State Phys. **2**, 1784 (1969).

[330] H. B. G. Casimir, Rev. Mod. Phys. **17**, 343 (1945).

[331] S. R. de Groot and P. Mazur, Phys. Rev. **94**, 218 (1954).

[332] P. Mazur and S. R. de Groot, Phys. Rev. **94**, 224 (1954).

[333] W. H. Kleiner, Phys. Rev. **153**, 726 (1967).

[334] W. H. Kleiner, Phys. Rev. **182**, 705 (1969).

[335] S. Wimmer, K. Chadova, M. Seemann, D. Ködderitzsch, and H. Ebert, Phys. Rev. B **94**, 054415 (2016).

[336] S. Wimmer, K. Chadova, and H. Ebert, "Symmetry and magnitude of the direct and inverse Edelstein effect: A KKR-CPA-Kubo approach," unpublished (2018).

[337] H. Grimmer, Acta Cryst. A **49**, 763 (1993).

[338] M. Seemann, "Space-time symmetry of transport coefficients in relativistic electron transport," (2013), master thesis, Department Chemie, Ludwig-Maximilians-Universität München.

[339] M. Seemann, "Space-time symmetry of transport coefficients in relativistic electron transport," (2014), master thesis, Department Physik, Ludwig-Maximilians-Universität München.

[340] R. Stinshoff, S. Wimmer, H. Ebert, G. H. Fecher, C. Felser, and S. Chadov, ArXiv e-prints (2017), arXiv:1710.04453 [cond-mat.mtrl-sci] .

[341] S. Wimmer, S. Mankovsky, S. Srichandan, M. Kronseder, C. H. Back, C. Strunk, and H. Ebert, "Galvanomagnetic, thermogalvanomagnetic, and thermal transport properties of ferromagnetic bcc Fe_xCo_{1-x} bulk-alloys from first principles," unpublished (2018).

[342] A. P. Cracknell, Phys. Rev. B **7**, 2145 (1973).

[343] A. Pourghazi, G. A. Saunders, and Y. C. Akgöz, Phil. Mag. A **33**, 781 (1976).

[344] H.-D. Butzal, Physica A **114**, 522 (1982).

[345] J. Železný, *Electronic Structure and Magnetic Properties of Antiferromagnetic Semiconductors and Metals*, Ph.D. thesis, Institute of Physics of the Czech Academy of Sciences, Department of Spintronics and Nanoelectronics and Faculty of Mathematics and Physics, Charles University in Prague (2016).

[346] J. Železný, H. Gao, A. Manchon, F. Freimuth, Y. Mokrousov, J. Zemen, J. Mašek, J. Sinova, and T. Jungwirth, Phys. Rev. B **95**, 014403 (2017).

[347] H.-D. Butzal and R. Birss, Physica A **114**, 518 (1982).

[348] S. Shtrikman and H. Thomas, Solid State Commun. **3**, 147 (1965).

[349] P. Bruno, Y. Suzuki, and C. Chappert, Phys. Rev. B **53**, 9214 (1996).

[350] P. Bruno, "The Berry Phase in Magnetism and the Anomalous Hall Effect," in *Handbook of Magnetism and Advanced Magnetic Materials*, Vol. 1, edited by H. Kronmüller and S. Parkin (John Wiley & Sons, Ltd, 2007) pp. 540–558.

[351] H. Chen, Q. Niu, and A. H. MacDonald, Phys. Rev. Lett. **112**, 017205 (2014).

[352] S. Nakatsuji, N. Kiyohara, and T. Higo, Nature **527**, 212 (2015).

[353] T. Huhne, *Magneto-optical Kerr effect of multilayer and surface layer systems*, Ph.D. thesis, Ludwig-Maximilians-Universität München (2000).

[354] J. Kudrnovský, V. Drchal, and I. Turek, Phys. Rev. B **92**, 224421 (2015).

[355] M. Johnson, Phys. Rev. Lett. **70**, 2142 (1993).

[356] F. J. Jedema, A. T. Filip, and B. J. van Wees, Nature **410**, 345 (2001).

[357] D. Ellsworth, L. Lu, J. Lan, H. Chang, P. Li, Z. Wang, J. Hu, B. Johnson, Y. Bian, J. Xiao, R. Wu, and M. Wu, Nat. Phys. **12**, 861 (2016).

[358] S. G. Cheng, Y. Xing, Q. F. Sun, and X. C. Xie, Phys. Rev. B **78**, 045302 (2008).

[359] X. Liu and X. Xie, Solid State Commun. **150**, 471 (2010).

[360] P. Sheng, Y. Sakuraba, Y.-C. Lau, S. Takahashi, S. Mitani, and M. Hayashi, Sci. Adv. **3**, e1701503 (2017).

[361] D.-J. Kim, C.-Y. Jeon, J.-G. Choi, J. W. Lee, S. Surabhi, J.-R. Jeong, K.-J. Lee, and B.-G. Park, Nat. Commun. **8**, 1400 (2017).

[362] L. K. Zou, S. H. Wang, Y. Zhang, J. R. Sun, J. W. Cai, and S. S. Kang, Phys. Rev. B **93**, 014422 (2016).

[363] Y.-T. Chen, S. Takahashi, H. Nakayama, M. Althammer, S. T. B. Goennenwein, E. Saitoh, and G. E. W. Bauer, Phys. Rev. B **87**, 144411 (2013).

[364] Y.-T. Chen, S. Takahashi, H. Nakayama, M. Althammer, S. T. B. Goennenwein, E. Saitoh, and G. E. W. Bauer, J. Phys.: Cond. Mat. **28**, 103004 (2016).

[365] S. U. Meyer, *Spin Caloritronics in Ferromagnet/Normal Metal Hybrid Structures*, Ph.D. thesis, Technische Universität München (2015).

[366] S. Wimmer, J. Minár, S. Mankovsky, A. N. Yaresko, and H. Ebert, "Magneto-optic and transverse transport properties of noncollinear antiferromagnets," unpublished (2018).

[367] S. Wimmer, S. Mankovsky, and H. Ebert, "Chirality-induced linear response properties in non-coplanar Mn_3Ge," unpublished (2018).

[368] S. Mankovsky, S. Wimmer, S. Polesya, and H. Ebert, Phys. Rev. B **97**, 024403 (2018).

[369] M. Obstbaum, M. Decker, A. K. Greitner, M. Haertinger, T. N. G. Meier, M. Kronseder, K. Chadova, S. Wimmer, D. Ködderitzsch, H. Ebert, and C. H. Back, Phys. Rev. Lett. **117**, 167204 (2016).

[370] R. Stinshoff, A. K. Nayak, G. H. Fecher, B. Balke, S. Ouardi, Y. Skourski, T. Nakamura, and C. Felser, Phys. Rev. B **95**, 060410 (2017).

[371] L. Zhu, D. C. Ralph, and R. A. Buhrman, ArXiv e-prints (2018), arXiv:1805.02329 [cond-mat.mtrl-sci] .

[372] R. Kukreja, S. Bonetti, Z. Chen, D. Backes, Y. Acremann, J. A. Katine, A. D. Kent, H. A. Dürr, H. Ohldag, and J. Stöhr, Phys. Rev. Lett. **115**, 096601 (2015).

[373] J. Li, L. R. Shelford, P. Shafer, A. Tan, J. X. Deng, P. S. Keatley, C. Hwang, E. Arenholz, G. van der Laan, R. J. Hicken, and Z. Q. Qiu, Phys. Rev. Lett. **117**, 076602 (2016).

[374] A. Soumyanarayanan, N. Reyren, A. Fert, and C. Panagopoulos, Nature **539**, 509 (2016).

[375] F. Rittweger, N. F. Hinsche, P. Zahn, and I. Mertig, Phys. Rev. B **89**, 035439 (2014).

[376] R. Kováčik, P. Mavropoulos, and S. Blügel, Phys. Rev. B **91**, 014421 (2015).

[377] V. Popescu and P. Kratzer, New J. Phys. **17**, 033036 (2015).

[378] N. H. Long, P. Mavropoulos, B. Zimmermann, S. Blügel, and Y. Mokrousov, Phys. Rev. B **93**, 180406 (2016).

[379] A. M. Guénault, Phil. Mag. **30**, 641 (1974).

[380] J. C. Taylor and B. R. Coles, Phys. Rev. **102**, 27 (1956).

[381] W. H. Butler, X.-G. Zhang, D. M. C. Nicholson, and J. M. MacLaren, Phys. Rev. B **52**, 13399 (1995).

[382] *The Munich SPR-KKR package*,
H. Ebert *et al.*
`http://olymp.cup.uni-muenchen.de/ak/ebert/SPRKKR`.

[383] T. Hupfauer, A. Matos-Abiague, M. Gmitra, F. Schiller, J. Loher, D. Bougeard, C. Back, J. Fabian, and D. Weiss, Nat. Commun. **6**, 7374 (2015).

[384] L. Chen, S. Mankovsky, S. Wimmer, M. A. W. Schoen, H. S. Körner, M. Kronseder, D. Schuh, D. Bougeard, H. Ebert, D. Weiss, and C. H. Back, Nat. Phys. **14**, 490 (2018).

[385] L. Keldysh, JETP **20**, 1018 (1965), Russian original: ZhETF **47**, 1515 (1965).

[386] S. Achilles, *Nichtgleichgewichts-Green-Funktionen zur Beschreibung mesoskopischer Systeme*, Ph.D. thesis, Martin-Luther-Universität Halle-Wittenberg (2012).

[387] S. Achilles, M. Czerner, J. Henk, I. Mertig, and C. Heiliger, Phys. Rev. B **88**, 125411 (2013).

[388] M. Ogura and H. Akai, J. Phys. Soc. Japan **85**, 104715 (2016).

[389] L. Szunyogh, B. Újfalussy, P. Weinberger, and J. Kollár, Phys. Rev. B **49**, 2721 (1994).

[390] J. Henk, A. Ernst, K. K. Saha, and P. Bruno, J. Phys.: Cond. Mat. **18**, 2601 (2006).

[391] C. Heiliger, M. Czerner, B. Y. Yavorsky, I. Mertig, and M. D. Stiles, J. Appl. Phys. **103**, 07A709 (2008).

[392] C. Caroli, R. Combescot, P. Nozieres, and D. Saint-James, J. Phys. C: Solid State Phys. **4**, 916 (1971).

[393] P. M. Haney, D. Waldron, R. A. Duine, A. S. Núñez, H. Guo, and A. H. MacDonald, Phys. Rev. B **76**, 024404 (2007), erratum: Phys. Rev. B **77**, 059901 (2008).

[394] K. Carva and I. Turek, Phys. Rev. B **76**, 104409 (2007).

[395] G. Kresse and J. Hafner, Phys. Rev. B **47**, 558 (1993).

[396] G. Kresse and J. Furthmüller, Comput. Mater. Sci. **6**, 15 (1996).

[397] G. Kresse and J. Furthmüller, Phys. Rev. B **54**, 11169 (1996).

[398] R. W. Grosse-Kunstleve, N. K. Sauter, N. W. Moriarty, and P. D. Adams, J. Appl. Crystallogr. **35**, 126 (2002).

[399] T. Björkman, Comput. Phys. Commun. **182**, 1183 (2011).

[400] H. T. Stokes, D. M. Hatch, and B. J. Campbell, ISOTROPY Software Suite, `iso.byu.edu`.

[401] H. T. Stokes and D. M. Hatch, J. Appl. Crystallogr, **38**, 237 (2005).

[402] A. Y. Perlov, A. N. Yaresko, and V. N. Antonov, "PY-LMTO, A Spin-polarized Relativistic Linear Muffin-tin Orbitals Package for Electronic Structure Calculations," (unpublished).

[403] V. Antonov, B. Harmon, and A. Yaresko, *Electronic Structure and Magneto-Optical Properties of Solids* (Springer Netherlands, 2004).

[404] SymPy Development Team, *SymPy: Python library for symbolic mathematics* (2016).

[405] K. Momma and F. Izumi, J. Appl. Crystallogr. **44**, 1272 (2011).

Curriculum Vitae

Persönliche Angaben

- Name: Sebastian Wimmer
- Geburtsdatum: 7. Juli 1985
- Geburtsort: München, Deutschland

Schulbildung

- 1991 – 1993: Grundschule an der Oselstraße in München
- 1993 – 1995: Grundschule an der Grandlstraße 5 in München
- 1995 – 2004: Louise-Schroeder-Gymnasium in München
- 06/2004: Abschluss mit Abitur

Zivildienst

- 09/2004 – 07/2005: Montessori-Schule der gemeinnützigen Schul-GmbH der Aktion Sonnenschein (Lehrassistenz, ISB-K)

Studium

- 2005 – 2011: Studium der Chemie an der LMU München
- 01 – 07/2011: Masterarbeit in Physikalischer Chemie, Titel: "Theoretische Untersuchungen zu Struktur und Eigenschaften von Antimon-Zinndioxid Legierungen" (AK Ebert)
- Juli 2011: Masterprüfung (Note: 1,28)

Beruf

- 11 – 12/2008: Studentische Hilfskraft am Department Chemie der Ludwig-Maximilians-Universität München, Lehrbereich Physikalische Chemie (AK de Vivie-Riedle)
- 09/2011 – 02/2016, 06/2016 – heute: Wissenschaftlicher Angestellter und Doktorand am Department Chemie der Ludwig-Maximilians-Universität München, Lehrbereich Physikalische Chemie (AK Ebert)

List of publications

1. *First-principles linear response description of the spin Nernst effect*,
S. Wimmer, D. Ködderitzsch, K. Chadova, and H. Ebert,
Phys. Rev. B **88**, 201108(R) (2013), arXiv:1306.0621 [cond-mat.mtrl-sci] (2013).
Reprinted in this thesis in Section 3.2.1 on page 122.

2. *Galvanomagnetic and thermogalvanomagnetic transport effects in ferromagnetic fcc Co_xPd_{1-x} alloys from first principles*,
S. Wimmer, D. Ködderitzsch, and H. Ebert,
Phys. Rev. B **89**, 161101(R) (2014), arXiv:1311.2498 [cond-mat.mtrl-sci] (2013).
Reprinted in this thesis in Section 3.1.1 on page 80.

3. *Spin-orbit-induced longitudinal spin-polarized currents in non-magnetic solids*,
S. Wimmer, M. Seemann, K. Chadova, D. Ködderitzsch, and H. Ebert,
Phys. Rev. B **92**, 041101(R) (2015), arXiv:1502.04947 [cond-mat.mes-hall] (2015).
Reprinted in this thesis in Section 3.3.2 on page 189.

4. *Direct in situ measurement of coupled magnetostructural evolution in a ferromagnetic shape memory alloy and its theoretical modeling*,
A. Pramanick, A. Glavic, G. Samolyuk, A.A. Aczel, V. Lauter, H. Ambaye, Z. Gai, J. Ma, A.D. Stoica, G.M. Stocks, S. Wimmer, S.M. Shapiro, and X.-L. Wang,
Phys. Rev. B **92**, 134109 (2015).

5. *Symmetry-imposed shape of linear response tensors*,
M. Seemann, D. Ködderitzsch, S. Wimmer, and H. Ebert,
Phys. Rev. B **92**, 155138 (2015), arXiv:1507.04947 [cond-mat.mtrl-sci] (2015).
Reprinted in this thesis in Section 3.3.1 on page 175.

6. *Tailoring of the extrinsic spin Hall effect in disordered metal alloys*,
K. Chadova, S. Wimmer, H. Ebert, and D. Ködderitzsch,
Phys. Rev. B **92**, 235142 (2015).

7. *Fully relativistic description of spin-orbit torques by means of linear response theory*,
S. Wimmer, K. Chadova, M. Seemann, D. Ködderitzsch, and H. Ebert,
Phys. Rev. B **94**, 054415 (2016), arXiv:1604.02798 [cond-mat.mtrl-sci] (2016).
Reprinted in this thesis in Section 3.5.1 on page 228.

8. *Observation of the spin Nernst effect*,
S. Meyer, Y.-T. Chen, S. Wimmer, M. Althammer, S. Geprägs, H. Huebl, D. Ködderitzsch, H. Ebert, G.E.W. Bauer, R. Gross, and S.T.B. Goennenwein,
Nat. Mater. **16**, 977 (2017), arXiv:1607.02277 [cond-mat.mtrl-sci] (2016).
Reprinted in this thesis in Section 3.2.2 on page 133.

9. *In-plane anisotropic magnetoresistance in antiferromagnetic $Ba(Fe_{1-x}Co_x)_2As_2$, $(Ba_{1-x}K_x)Fe_2As_2$ and $Ba(Fe_{1-x}Ru_x)_2As_2$*,
G. Derondeau, J. Minár, S. Wimmer, and H. Ebert,
arXiv:1608.08077 [cond-mat.mtrl-sci] (2016), submitted to Phys. Rev. B.

10. *Tuning Spin Hall Angles by Alloying*,
M. Obstbaum, M. Decker, A.K. Greiner, M. Haertinger, T.N.G. Meier, M. Kronseder, K. Chadova, S. Wimmer, D. Ködderitzsch, H. Ebert, and C.H. Back,
Phys. Rev. Lett. **117**, 167204 (2016).
Reprinted in this thesis in Section 3.6.1 on page 266.

11. *Native defects in the Co_2TiZ (Z = Si, Ge, Sn) full Heusler alloys: formation and influence on the thermoelectric properties*,
V. Popescu, P. Kratzer, S. Wimmer, and H. Ebert,
Phys. Rev. B **96**, 054443 (2017), arXiv:1704.00149 [cond-mat.mtrl-sci] (2017).

12. *Composition-dependent magnetic response properties of $Mn_{1-x}Fe_xGe$ alloys*,
S. Mankovsky, S. Wimmer, S. Polesya, and H. Ebert,
Phys. Rev. B **97**, 024403 (2018), arXiv:1710.07248 [cond-mat.mtrl-sci] (2017).
Reprinted in this thesis in Section 3.5.1 on page 241.

13. *Temperature-dependent charge transport in the compensated ferrimagnet $Mn_{1.5}V_{0.5}FeAl$ from first principles*,
R. Stinshoff, S. Wimmer, H. Ebert, G.H. Fecher, C. Felser, and S. Chadov,
arXiv:1710.04453 [cond-mat.mtrl-sci] (2017), submitted to Phys. Rev. B.
Reprinted in this thesis in Section 3.6.2 on page 279.

14. *Large Spin Hall Effect in an Amorphous Binary Alloy*,
K. Fritz, S. Wimmer, H. Ebert, and M. Meinert,
Phys. Rev. B **98**, 094433 (2018), arXiv:1801.02524 [cond-mat.mtrl-sci] (2018).

15. *Magnon scattering in the transport coefficients of CoFe thin films*,
S. Srichandan, S. Wimmer, S. Pöllath, M. Kronseder, H. Ebert, C.H. Back, and C. Strunk,
Phys. Rev. B **98**, 020406(R) (2018), arXiv:1802.01038 [cond-mat.mtrl-sci] (2018).
Reprinted in this thesis in Section 3.1.2 on page 89.

16. *Emergence of anisotropic Gilbert damping in ultrathin Fe layers on GaAs(001)*,
L. Chen, S. Mankovsky, S. Wimmer, M.A.W. Schoen, M. Kronseder, D. Schuh, D. Bougeard, H. Ebert, D. Weiss, and C.H. Back,
Nat. Phys. **14**, 490 (2018).

17. *Thermal conductivity and electrical resistivity of solid iron at Earths core conditions from first principles*,
J. Xu, P. Zhang, K. Haule, J. Minár, S. Wimmer, H. Ebert, and R.E. Cohen,
Phys. Rev. Lett. **121**, 096601 (2018), arXiv:1710.03564 [cond-mat.mtrl-sci] (2017).

18. *Gilbert damping in non-collinear magnetic systems*,
S. Mankovsky, S. Wimmer, and H. Ebert,
Phys. Rev. B **98**, 104406 (2018), arXiv:1805.11468 [cond-mat.mtrl-sci] (2018).

19. *Uncovering electron scattering mechanisms in alloys possessing extreme disorder*,
S. Mu, G.D. Samolyuk, S. Wimmer, M.C. Troparevsky, S. Khan, S. Mankovsky, H. Ebert, and G.M. Stocks,
arXiv:1806.03785 [cond-mat.mtrl-sci] (2018), accepted at npj Comp. Mat..

20. *Spin caloric transport from density-functional theory*,
V. Popescu, P. Kratzer, P. Entel, C. Heiliger, M. Czerner, K. Tauber, F. Töpler, C. Herschbach, D.V. Fedorov, M. Gradhand, I. Mertig, R. Kováčik, P. Mavropoulos, D. Wortmann, S. Blügel, F. Freimuth, Y. Mokrousov, S. Wimmer, D. Ködderitzsch, M. Seemann, K. Chadova, and H. Ebert,
accepted at J. Phys. D (2018).

21. *Temperature dependent electronic transport in concentrated solid solutions of the 3d-transition metals Ni, Fe, Co and Cr from first principles*,
G.D. Samolyuk, S. Mu, A. F. May, B. C. Sales, S. Wimmer, S. Mankovsky, H. Ebert, and G.M. Stocks,
Phys. Rev. B **98**, 165141 (2018).

22. *Galvanomagnetic, thermogalvanomagnetic, and thermal transport properties of ferromagnetic bcc Fe_xCo_{1-x} bulk-alloys from first principles*,
S. Wimmer, S. Mankovsky, S. Srichandan, M. Kronseder, C.H. Back, C. Strunk, and H. Ebert,
unpublished (2018).
Printed in this thesis in Section 3.1.3 on page 105.

23. *Magneto-optic and transverse transport properties of non-collinear antiferromagnets*,
S. Wimmer, J. Minár, S. Mankovsky, A.N. Yaresko and H. Ebert,
unpublished (2018).
Printed in this thesis in Section 3.4.1 on page 201.

24. *Chirality-induced linear response properties of non-coplanar Mn_3Ge*,
S. Wimmer, S. Mankovsky, and H. Ebert,
unpublished (2018).
Printed in this thesis in Section 3.4.2 on page 213.

25. *Symmetry and magnitude of the direct and inverse Edelstein effect: A KKR-CPA-Kubo approach*,
S. Wimmer, K. Chadova, and H. Ebert,
unpublished (2018).
Printed in this thesis in Section 3.5.1 on page 251.

26. *Magnetism and transport properties in fcc-NiCoMn alloys at finite temperatures and hydrostatic pressures*,
S. Mu, J. Yin, G.D. Samolyuk, S. Wimmer, S. Mankovsky, H. Ebert, M. Eisenbach, and G.M. Stocks,
in preparation (2018).

27. *Thermoelectric and thermomagnetoelectric effects in transition metal alloys: A first-principles Kubo-Mott approach*,
S. Wimmer, D. Ködderitzsch, and H. Ebert,
in preparation (2018).

28. *Electronic Structure - Metals and Insulators*,
H. Ebert, S. Mankovsky, and S. Wimmer,

volume 1 of *Handbook of Magnetism and Advanced Magnetic Materials*, Wiley-VCH, Weinheim,
in preparation (2018).

List of conference contributions

Talks

1. *Electronic structure, transport and spectroscopic properties of $Sn_{1-x}Sb_xO_2$ alloys*,
S. Wimmer, J. Minár, D. Ködderitzsch, and H. Ebert,
talk at:
3rd Munich DFT and Beyond Workshop, München, Germany, 10.02.2012.

2. *Anisotropy of the Seebeck effect and anomalous Nernst effect from Kubo linear response formalism*,
S. Wimmer, D. Ködderitzsch, and H. Ebert,
talk at:
DPG-Frühjahrstagung (DPG Spring Meeting), Regensburg, Germany, 30.03.2012.

3. *Anisotropy of the Seebeck effect and anomalous Nernst effect from Kubo linear response formalism*,
S. Wimmer, D. Ködderitzsch, and H. Ebert,
seminar talk at:
Department of Physics, Osaka University, Osaka, Japan, 21.05.2012.

4. *A relativistic implementation of the non-equilibrium Green's function formalism for layered systems*,
S. Wimmer, M. Ogura, H. Akai, and H. Ebert,
talk at:
DPG-Frühjahrstagung (DPG Spring Meeting), Regensburg, Germany, 10.-15.03.2013.

5. *Longitudinal transport properties of Fe films on GaAs(001)*,
S. Wimmer, S. Bornemann, D. Ködderitzsch, J. Minár, H. Ebert, T. Hupfauer, and D. Weiss
talk at:
DPG-Frühjahrstagung (DPG Spring Meeting), Regensburg, Germany, 10.-15.03.2013.

6. *Spin Hall and Spin Nernst effect in paramagnetic alloys*,
S. Wimmer, D. Ködderitzsch, K. Chadova, and H. Ebert,
talk at:
DFG Kolloquium (SPP 1538) "Spin Caloric Transport", Bad Honnef, Germany, 22.-23.04.2013.

7. *Spin Hall and Spin Nernst effect in paramagnetic alloys*,
S. Wimmer, D. Ködderitzsch, K. Chadova, and H. Ebert,
seminar talk at:
Ångström Laboratory, Uppsala Universitet, Uppsala, Sweden, 31.05.2013.

8. *Anomalous and Spin Nernst effect from Kubo linear response formalism*,
S. Wimmer, D. Ködderitzsch, K. Chadova, and H. Ebert,
invited talk at:
JSPS Core-to-Core Program Workshop, Awaji-city, Japan, 16.-19.06.2013.

9. *Anomalous and Spin Nernst effect from Kubo linear response formalism*,
S. Wimmer, D. Ködderitzsch, K. Chadova, and H. Ebert,
seminar talk at:
Department of Physics, Osaka University, Osaka, Japan, 24.06.2013.

10. *Spin caloric transport in alloys from first-principles*,
S. Wimmer, D. Ködderitzsch, K. Chadova, S. Mankovsky, and H. Ebert,
talk at:
DPG-Frühjahrstagung (DPG Spring Meeting), Dresden, Germany, 03.04.2014.

11. *Calculating transport properties for spintronics*,
S. Wimmer, D. Ködderitzsch, K. Chadova, and H. Ebert,
seminar talk at:
Department of Nanoscience, Chiba University, Chiba, Japan, 25.06.2014.

12. *Kubo formalism applied in spintronics - transport and spin-orbit torque in layered systems*,
S. Wimmer, D. Ködderitzsch, S. Bornemann, K. Chadova, M. Seemann, S. Mankovsky, T. Hupfauer, D. Weiss, and H. Ebert,
invited talk at:
JSPS Core-to-Core Program Workshop, Osaka, Japan, 01.-03.06.2014.

13. *Transverse charge and spin transport driven by electric fields and temperature gradients*,
S. Wimmer, K. Chadova, D. Ködderitzsch, and H. Ebert,
talk at:
Material Science Engineering (MSE) 2014, Darmstadt, Germany, 23.-25.10.2014.

14. *Description of (mostly) galvanomagnetic transport using Kubo's linear response formalism*,
S. Wimmer,
tutorial talk at:
SPR-KKR Hands-on Course 2014, München, Germany, 20.-22.10.2014.

15. *Transverse charge and spin transport driven by electric fields and temperature gradients*,
S. Wimmer, K. Chadova, D. Ködderitzsch, and H. Ebert,
talk at:
2nd Mainz-Lanna meeting, Mainz, Germany, 03.-04.12.2014.

16. *Impact of finite temperatures on spin caloric transport properties using the alloy analogy model*,
S. Wimmer, S. Mankovsky, K. Chadova, S. Polesya, D. Ködderitzsch, and H. Ebert,
talk at:
DFG Kolloquium (SPP 1538) "Spin Caloric Transport", Bad Honnef, Germany, 02.-03.02.2015.

17. *Spin-orbit induced longitudinal spin transport in non-magnetic solids*,
S. Wimmer, M. Seemann, K. Chadova, D. Ködderitzsch, and H. Ebert,
talk at:
DPG-Frühjahrstagung (DPG Spring Meeting), Berlin, Germany, 15.-20.03.2015.

18. *Transverse transport and magneto-optical properties of non-collinear antiferromagnets*,
S. Wimmer, J. Minár, S. Mankovsky, D. Ködderitzsch, and H. Ebert,
talk at:
DPG-Frühjahrstagung (DPG Spring Meeting), Berlin, Germany, 15.-20.03.2015.

19. *X-ray magnetic dichroism, magneto-optic Kerr effect and transverse transport in non-collinear antiferromagnets*,
S. Wimmer, J. Minár, S. Mankovsky, D. Ködderitzsch, and H. Ebert,
talk at:
XAFS16 Satellite Meeting "Application of XAFS to the Study of Magnetic Materials", Stuttgart, Germany, 30.08.-02.09.2015.

20. *Charge and spin transport in two-dimensional systems using the KKR-CPA-Kubo approach*,
S. Wimmer, K. Chadova, S. Bornemann, D. Ködderitzsch, and H. Ebert,
talk at:
DPG-Frühjahrstagung (DPG Spring Meeting), Regensburg, Germany, 06.-11.03.2016.

21. *Description of (mostly) galvanomagnetic transport using Kubo's linear response formalism*,
S. Wimmer,
tutorial talk at:
SPR-KKR Hands-on Course 2016, Daresbury Laboratory, Daresbury, UK, 14.-17.11.2016.

22. *Spin caloric transport: symmetry considerations and first-principles description*,
S. Wimmer,
invited talk at:
Lehrstuhlseminar Theoretische Physik II, Universität Augsburg, Germany, 11.01.2017.

23. *Tuning spin Hall angles by alloying*,
S. Wimmer, K. Chadova, D. Ködderitzsch, M. Obstbaum, M. Decker, A.K. Greitner, M. Härtinger, T.N.G. Meier, M. Kronseder, C.H. Back, and H. Ebert,
talk at:
DPG-Frühjahrstagung (DPG Spring Meeting), Dresden, Germany, 19.-24.03.2017.

24. *Electric-field-induced and magneto-optic properties of chiral magnetic solids*,
S. Wimmer, S. Mankovsky, S. Polesya, and H. Ebert,
talk at:
DPG-Frühjahrstagung (DPG Spring Meeting), Berlin, Germany, 11.-16.03.2018.

Posters

25. *Electronic structure, transport and spectroscopic properties of $Sb_xSn_{1-x}O_2$ alloys*,
S. Wimmer, J. Minár, D. Ködderitzsch, V. Müller, D. Fattakhova-Rohlfing, C. Scheu, and H. Ebert,
poster at:
Ψ_k-workshop on KKR and Related Greens Function Methods, Halle (Saale), Germany, 08.-10.07.2011.

26. *Anisotropic Seebeck effect and Anomalous Nernst effect from Kubo linear response formalism*,
S. Wimmer, D. Ködderitzsch, and H. Ebert,
poster at:
DFG Kolloquium (SPP 1538) "Spin Caloric Transport", Bad Honnef, Germany, 04.-06.01.2012.

27. *Anisotropy of the Seebeck effect and anomalous Nernst effect from Kubo linear response formalism*,
S. Wimmer, D. Ködderitzsch, and H. Ebert,
poster at:
2nd SpinCaT PhD workshop, Göttingen, Germany, 08.-09.10.2012.

28. *In-plane anisotropy of transport in $Fe_n/GaAs$*,
S. Wimmer, S. Bornemann, J. Minár, D. Ködderitzsch, H. Ebert, T. Hupfauer, and D. Weiss,
poster at:
International Spintronics Workshop, Regensburg, Germany, 20.09.2012.

29. *Spin-dependent thermo-galvanic effects – Theory*,
H. Ebert and D. Ködderitzsch,
poster at:
Evaluation workshop for the SPP 1538 "Spin Caloric Transport", Bad Honnef, Germany, 19.-21.02.2014.

30. *Spin-Caloric Transport Phenomena in Alloys: Symmetry Analysis and First-Principles Description*,
S. Wimmer, D. Ködderitzsch, K. Chadova, and H. Ebert,
poster at:
Spincaloritronics VI, Kloster Irsee, Germany, 13.-18.07.2014. :

31. *Spin-orbit induced longitudinal spin transport in non-magnetic solids*,
S. Wimmer, M. Seemann, K. Chadova, D. Ködderitzsch, and H. Ebert,
poster at:
584. Wilhelm und Else Heraeus-Seminar "Green's Functions in *ab initio* Electronic Structure Calculations of Solids: From Implementations to Applications", Bad Honnef, Germany, 08.-11.02.2015.

32. *Charge and spin transport in two-dimensional systems using the KKR-CPA-Kubo approach*,
S. Wimmer, K. Chadova, S. Bornemann, D. Ködderitzsch, and H. Ebert,
poster at:
DFG Kolloquium (SPP 1538) "Spin Caloric Transport", Bad Honnef, Germany, 03.-04.03.2016.

33. *In-plane anisotropy of transport and SOT in $Fe_n/GaAs$*,
S. Wimmer, S. Polesya, K. Chadova, and H. Ebert,
poster at:
International Workshop on "Emergent Relativistic Effects in Condensed Matter", Regensburg, Germany, 27.-29.09.2016.

34. *Spin Caloric Transport from First Principles*,
S. Wimmer, K. Chadova, S. Mankovsky, D. Ködderitzsch, and H. Ebert,
poster at:
Spincaloritronics VIII, Regensburg, Germany, 12.-15.06.2017.

Acknowledgements

First of all, I have to thank Prof. Dr. Hubert Ebert for giving me the opportunity to work on a vast range of interesting subjects, to broaden my horizons at many conferences as well as during my stays in Japan, and in particular for being supportive in times of doubt. Secondly, I would like to express my sincerest gratitude to Dr. habil. Diemo Ködderitzsch for his guidance, motivating criticism, seemingly infatigable enthusiasm, and his patience. I am furthermore indebted to Dr. Sergiy Mankovsky for sharing his insights in countless discussions.

Further, I would like to acknowledge my scientific collaborators Dr. Steven Achilles, Dr. habil. Voicu Popescu, Dr. Sibylle Meyer, Dr. Matthias Althammer, Prof. Dr. Sebastian T.B. Goennenwein, Dr. Yan-Ting Chen, Prof. Dr. Gerrit E.W. Bauer, Dr. Sasmita Srichandan, Prof. Dr. Christian Back, Prof. Dr. Christoph Strunk, Dr. Martin Gradhand, Dr. Junqing Xu, Prof. Dr. Ronald E. Cohen, Dr. Sai Mu, Dr. German Samolyuk, Dr. G. Malcolm Stocks, Dr. Stanislav Chadov, and Dr. Ondřej Šipr.

I am very grateful to Prof. Dr. Hisazumi Akai and, in particular, Dr. Masako Ogura for welcoming me at Osaka University and offering me the possibility to spend several very formative periods of time there. In addition I would like to thank Ms. Tomoko Shimokomaki, who took such good care of the more practical aspects of my stays.

I would like to thank my past and present trenchmates and fellow coffee junkies Dr. Stephan Borek, Dr. Sven Bornemann, Apl. Prof. Dr. Jürgen Braun, Dr. Kristina Chadova, Dr. Gerald Derondeau, Prof. Dr. Keisuke Hatada, Dipl. Phys. Andreas Held, Dr. habil. Diemo Ködderitzsch, Dr. Gerhard Kuhn, Dr. Sergiy Mankovsky, Dr. Alberto Marmodoro, M.Sc. Christian Mende, Prof. Dr. Ján Minár, Dr. Laurent Nicolaï, M.Sc. Martin Offenberger, Dr. Masako Ogura, Dipl. Phys. Svitlana Polesya, Dr. habil. Voicu Popescu, M.Sc. Marius Schulte, Dr. Bogdan Yavorsky and, last but far from least, our secretary Rita Römling and our technician/sysadmin Michael Maaß for the camaraderie. Special acknowledgements are in order for M.Sc. Marten Seemann, from whose brilliant work during his master theses I have profited enormously.

Financial support by the DFG via the priority programme SPP 1538 and by the BA via Alg I is gratefully acknowledged. Moreover, I would like to thank Dr. Andreas Will for allowing me to write part of this thesis in the university library.

My deepest gratitude and sincerest apologies to my family and friends for believing in and having to bear with what little oftentimes was left of me over all those years.

Finally, thank you **DOCTOR WHO** for the sonic blast back into reality...